"Propeller Wing Aerodynamic Interference"

Leo Veldhuis, 28 Juni 2005

1. Computational Fluid Dynamics (CFD) presenteert een fantasiewereld. Alleen het experiment toont de ware natuur.

2. De voordelen van de fiets ten aanzien van problemen als filevorming en de belasting van het milieu, worden zwaar onderschat.

3. Door een aanpassing van de profielwelving in het vleugeldeel dat door de slipstroom wordt getroffen kan het voortstuwingsrendement van propeller vliegtuigen worden verhoogd (Hoofdstuk 7)

4. Door het ontbreken van een zintuig waarmee de waarheid kan worden vastgesteld is onze wetenschap louter gebaseerd op geloof en verbeelding.

5. Alhoewel het erg begrijpelijk is als uiting van blijdschap "een gat in de lucht te springen" is dit op grond van de huidige kennis van de stromingsleer fysisch niet mogelijk.

6. De huidige aanpak van een maatschappelijk probleem binnen de Nederlandse politiek is vergelijkbaar met complexe getallen theorie waarbij het reële deel wordt verwaarloosd en het imaginaire deel tot oplossing van het probleem wordt verheven.

7. Als een goede definitie van 'wetenschap' is: "Het beëindigen van de twijfel en de ontrafeling van het mysterie", bestaat wetenschap niet.

8. Het wis- en natuurkunde-onderwijs op de Nederlandse middelbare scholen heeft een dermate laag peil bereikt dat handhaving van het wetenschappelijk niveau van de Technische Universiteiten ernstig gevaar loopt.

9. Rekencodes waarin de vorm en ontwikkeling van de propellerslipstroom niet expliciet worden gemodelleerd leiden tot een overschatting van de propellereffecten wanneer een "swirl recovery factor" niet wordt toegepast (Hoofdstuk 6).

10. Verlaging van de propellerinvalshoek en contra-rotatie, waarbij de binnenzijde van de propellers omhoog beweegt, leiden beide tot een prestatieverbetering van meermotorige propellervliegtuigen (Hoofdstuk 5 en 6)

Deze stellingen worden verdedigbaar geacht en zijn als zodanig goedgekeurd door de promotor.

Propositions accompanying the thesis

"Propeller Wing Aerodynamic Interference"

Leo Veldhuis, June 28th 2005

1. Computational Fluid Dynamics (CFD) presents a world of fantasy. Only the experiment shows true nature.
2. The benefits of the bicycle with respect to problems like traffic congestion and environmental pollution are seriously underestimated.
3. Adaptation of the airfoil camber in the propeller washed area of the wing may lead to an increase of the propulsive efficiency of multi-engined propeller aircraft (Chapter 7).
4. Due to the absence of a sensory organ that tells us the truth, our science is purely based on belief and imagination.
5. Although it may be very understandable to "jump a hole in the air" (Dutch saying) as an expression of happiness, this is physically impossible based on the current knowledge of fluid dynamics.
6. The current approach in Dutch politics to solve a societal problem is comparable to complex number theory where the real part is neglected and the imaginary part is accepted as solution to the problem.
7. If a correct definition of 'science' is: "the termination of doubt and the unravelling of mystery", science does not exist.
8. Educational programmes in physics and mathematics at Dutch secondary schools have reached a level so low that the scientific level of the Technical Universities is at risk.
9. Prediction codes that do not take into account the geometry and development of the propeller slipstream lead to an overestimation of the propeller effects in case a "swirl recovery factor" is not employed (Chapter 6).
10. Lowering the propeller angle of attack and the application of inboard up rotating propellers both lead to a performance increase of multi-engined propeller aircraft (Chapter 5 and 6)

These propositions are regarded as defendable and have been approved as such by the promoter.

Propeller Wing
Aerodynamic Interference

Proefschrift

ter verkrijging van de graad van Doctor
aan de Technische Universiteit Delft,
op gezag van de Rector Magnificus Prof. Dr. ir. J.T. Fokkema
in het openbaar te verdedigen ten overstaan van een commissie,
door het College voor Promoties aangewezen,

op dinsdag 28 juni om 15:30 uur
door

Leonardus Louis Maria Veldhuis
Vliegtuigbouwkundig ingenieur

geboren te Denekamp

ii

Dit proefschrift is goedgekeurd door de promotor:
Prof. dr. ir. P.G. Bakker

Samenstelling promotiecommissie:

Rector Magnificus	Voorzitter
Prof. dr. ir. P.G. Bakker	Technische Universiteit Delft, promotor
Prof. dr. ir. Th. van Holten	Technische Universiteit Delft
Prof. dr. ir. G.A.M. van Kuik	Technische Universiteit Delft
Prof. dr. ir. J.L. van Ingen	Technische Universiteit Delft
Prof. ir. E. Obert	Technische Universiteit Delft
Prof. D. Favier	Université de la Méditerranée, Marseille (Fr)
A.R. Dyke (Bsc)	Airbus UK, Filton (UK)

Summary

The performance characteristics and the stability and control behavior of propeller powered aircraft are strongly dependent on the contribution of the propulsion system. Hence knowledge of the flow behavior both in the area of the wing part washed by the propeller slipstream and the resulting flow field behind the wing is of key importance for detailed design of propeller powered aircraft. Furthermore, to enable further understanding of the processes that play a role with respect to the thrust and drag bookkeeping, the effects that the propulsion system exerts on the wing and vice versa must be known.

The goal of the present investigation is to gain an improved understanding of the aerodynamic interference between the propeller and the wing in a typical tractor arrangement. This study was realized by performing both experimental and numerical analyses on four different propeller-wing models.

The research is restricted to a typical two-engined tractor propeller wing configuration since this is the most commonly used arrangement.

In the experimental investigations data were obtained from three different models in a low speed windtunnel. The first two models are based on a simple geometry, combining a nacelle, built as a body of revolution, with a straight wing model. The third model is a three-dimensional representation of an existing turbo-prop aircraft that was tested without the horizontal tail present.

To facilitate validation of the numerical prediction techniques an extensive data set was generated comprising force data, surface pressure data, surface flow visualization and flow field data behind the model. The results obtained reveal a strong effect of the axial and the swirl velocity in the slipstream leading to a large deformation of the spanwise lift distribution which affects the lift and the drag of the configuration significantly. The beneficial effect of the propeller mounted in front of the wing is the fact that the swirl loss generated by the propeller is partly recovered by the wing in the form of increased leading edge suction. The amount of swirl recovery and the deformation of the initially circular slipstream envelope were determined by performing 5-hole probe flow field surveys. The study of these data based on a quantitative wake analysis approach led to the important insight in the flow structure and delivered spanwise lift and drag data on the wing. These are important when comparing the performance data with numerical methods that apply a simplified slipstream structure based on (quasi-)circular vorticity tubes.

After acquisition of the main model characteristics, both in low and high power conditions, the second wind tunnel model was used to investigate the effects of the propeller position and inclination with respect to the wing. For this purpose the nacelle was detached from the wing and could be traversed in various directions. Whereas the effect of the streamwise and the spanwise propeller position has little effect on the propulsive efficiency, both the vertical position and the propeller inclination demonstrate considerable influence on the performance. Especially a negative

propeller inclination angle showed an interesting enhancement of the wing lift combined with a reduction in the drag.

To illustrate typical propeller wing interaction effects in case the slipstream is not directly cut by the wing an over-the-wing arrangement was tested as well. In contrast to results found in open literature this unconventional configuration showed no improvement in the propulsive efficiency of the system for propeller location close to the wing. This result could be explained by the reduction in the propeller efficiency which outweighs the lift increase and drag reduction found on the wing.

The numerical simulations were performed at different levels of complexity, ranging from adapted Vortex Lattice Method (VLM) techniques and panel methods to the solution of the Reynolds averaged Navier-Stokes (RANS) equations. The goal of these calculations was twofold: first to verify the level of detail needed to adequately describe the main phenomena that occur in the propeller wing interaction problem and secondly to acquire meticulous flow data, which are needed to understand the mechanisms that play a role in this complex flow field.

The calculations show that the main propeller position effects can be predicted with the VLM code that was enhanced with a blade-element propeller model as long as a swirl recovery factor (SRF) of approximately 0.5 is applied. The panel code combined with a slipstream envelope model overpredicts the propeller effects on the wing due to the lack of a SRF.

Detailed flow data were obtained with the RANS code, applying both realizable a $k - \varepsilon$ model and a Reynolds stress model. Close agreement with experimental data was obtained both in the flow variables behind the model and in the integrated configuration characteristics like the lift and the drag coefficient. The actuator disk boundary conditions, applied at the location of the propeller, that were fed with flow data obtained from earlier experiments, adequately described the propeller slipstream effects in the calculations.

In order to determine possible benefits, which might be obtained from a geometrically adapted wing in a tractor propeller-wing arrangement, an optimization procedure was developed and applied. The main outcome of this optimization study is the fact that a wing with either an adapted twist or chord distribution leads to a small performance improvement in the propulsive efficiency for a the cruise condition of typical twin-engined turbo-prop designs.

Contents

III   Optimization   261

Nomenclature

Symbols

a_a	axial velocity factor (v_a/V_∞), speed of sound
a_t	tangential velocity factor (v_t/V_∞)
a'	tangential velocity factor $(v_t/\Omega R)$
a_{cor}	Coriolis acceleration
A	surface area, aspect ratio
A_n	Fourier coefficients
AR	wing aspect ratio
b	wing span
b_f	flap span
B	number of propeller blades
C_{N_p}	propeller normal force coefficient, definition 1, $(= \frac{N_p}{\rho n^2 D^4})$
C'_{N_p}	propeller normal force coefficient, definition 2, $(= \frac{N_p}{q_\infty S_p})$
$C^*_{N_p}$	propeller normal force coefficient, definition 3, $(= \frac{N_p}{q_\infty S_{wing}})$
$C_{N_{\alpha_p}}$	propeller normal force gradient
C_T	propeller thrust force coefficient, definition 1, $(= \frac{T}{\rho n^2 D^4})$
C_d	local two-dimensional drag coefficient
C_D	three-dimensional drag coefficient
C_l	local two-dimensional lift coefficient
C_L	three-dimensional lift coefficient
C_m	pitching moment coefficient
$C_{m,p}$	pitching moment coefficient
$C_{m,y}$	yawing moment coefficient
$C_{m,r}$	rolling moment coefficient
$C_{m,n}$	influence matrix element
C_Y	side force coefficient
C_P	power coefficient
c_p	pressure coefficient, specific heat at constant pressure
c_{p_t}	total pressure coefficient
c_v	specific heat at constant volume
C_Q	torque coefficient
c	chord, speed of sound
$\bar{c}$	mean aerodynamic chord
d	distance
D	(propeller) diameter
D_v	vortex drag
e_t	total energy
f	Prandtl tip loss factor

F	force vector
F	velocity ratio
h	grid / mesh spacing, helicity
h_r	relative helicity
h_t	total enthalpy
i, j, k	unit vectors in x, y and z-direction
J	advance ratio $(= V_\infty/nD)$
l	(local) two-dimensional lift force, length
L	three-dimensional lift force
m	mass
M	Mach number
M_H	helical Mach number
M_p	pitching moment
M_y	yawing moment
M_r	rolling moment
n	normal vector
n	revolutions per second
n_p	number of propellers
$p(x, y, z)$	point is space
p	static pressure
p_t	total pressure
P	power
P_c	power coefficient
Q	flux
Q_c	torque coefficient
q	dynamic pressure
r	radial coordinate
R	propeller radius, radius, gas constant
R_s	local slipstream radius
Re	Reynolds number
s	local coordinate along the body surface
s_p	propeller relative spanwise position
S	area, wing area
S_p	propeller disk area
t	time
T	thrust, temperature
T_c	thrust coefficient, definition 2, $(= \frac{T}{\rho V^2 D^2})$
T_c'	thrust coefficient, definition 3, $(= \frac{T}{q_\infty S_p})$
T_c^*	thrust coefficient, definition 4, $(= \frac{T}{q_\infty S_{wing}})$
u, v, w	velocity component in x, y and z-direction
U_∞	undisturbed flow velocity

v_a	axial velocity increase
v_t	tangential velocity increase
v_n	normal velocity
V	velocity vector
V	reference velocity
V_e	effective velocity
V_∞	undisturbed reference velocity
$\mathcal{V}$	volume
w_s	vortex sheet velocity
x, y, z	local axis system
x_p, y_p, z_p	propeller position in x, y and z-direction
X, Y, Z	global axis system
α	angle of attack
α_p	propeller angle of attack
α_T	thrust line angle attack
β	yawing angle / local propeller blade angle
γ	specific heat ratio $(=c_p/c_v)$
δ	small increment
δ_f	flap deflection angle
ε	downwash angle, wing twist angle
ε_p	deflection angle of the slipstream tube
Φ	velocity potential
θ	position angle of the propeller blade
θ_s	swirl angle
φ	local angle, perturbation potential
φ_s	vortex sheet angle
Γ	circulation
λ	Lagrange multiplier, wing taper ratio
ρ	air density
σ	solidity factor, source
τ	airfoil camber, wall shear stress
η	efficiency factor
η_p	propulsive efficiency
η_{fa}	free air efficiency
μ	dynamic viscosity, doublet strength
Ω	angular velocity of the propeller
Λ	sweep angle
π	pi $(= 3.1415926)$
ω	angular velocity vector
ω	angular velocity
ξ	dimensionless radius $(= r/R)$

ξ, η, ζ	vorticity components in x, y and z-direction
ψ	azimuthal angle in propeller axis system
Δ	difference

Indices

ap	aircraft parts
cor	corrected
cv	control volume
$c.l.$	center line
eff	effective
f	fuselage
fa	free air
fs	full scale
h	horizontal tail
i	induced
inb	inboard
inv	inviscid
m	model
max	maximum
m, n	matrix element indicators
n	nacelle
nac	nacelle
$outb$	outboard
p	propeller
$spin$	spinner
vis	viscous
w	wing
$wing$	related to the wing
x	x component
y	y component
z	z component
∞	undisturbed quantity

Special symbols

$\otimes$	direction away from the observer
$\odot$	direction toward the observer

Abbreviations

AEM	Actuator Disk envelope Membrane Model
APROPOS	Adaptive Propeller Positioning System
BEM	Blade element model
CFD	Computational Fluid Dynamics
DACU	Data acquisition unit
DBS	Down going blade side
DUT	Delft University of Technology
ECN	Energie Onderzoekscentrum Nederland
FIM	Full interaction mode
HPP	High propeller position
HSC	High speed case
LCO	Lift carry over
LPP	Low propeller position
LR	Faculty of Aerospace Engineering
LSC	Low speed case
LTT	Low turbulence tunnel
MMM	multi manometer
OTW	Over-the-wing
PROWIM	Propeller Wing Interference Model
PTD	Propeller tilt down
Real	Realizable
RKE	Realizable $k - \varepsilon$ model
RNG	Renormalization group
RSM	Reynolds stress model
SA	Spalart-Almaras (turbulence model)
SIM	Single interaction mode
STOL	Short take of landing
UBS	Up going blade side
VLM	Vortex Lattice method
V/STOL	Vertical and Short take off and landing
WSP	wake survey plane
2D	two-dimensional
3D	three-dimensional

Part I

Theoretical background

Chapter 1

Introduction

1.1 Historical context

The first type of propulsion used in powered flight was the propeller as the Wright brothers successfully launched their Wright Flyer III on December 17, 1903 (Fig.1.1). There were no data on air propellers available at that time but they had understood that it was not a difficult matter to secure an efficiency of 50% with marine propellers. The books they used on marine propellers, however, contained formulas on propellers that were of an empirical nature. There was no way of adapting them to calculations of aerial propellers. It was apparent to them that a propeller was simply a wing travelling in a spiral course but the relation between the various parameters that determine the final efficiency of the propeller was too complex for them to understand. Hence the only way to really test the thrust and efficiency of the propeller would be to actually try it on the machine as they did at Kitty Hawk. The Wright propeller was not an optimum design in this respect, but they really were on the right track. When further theoretical methods became available for the analysis of propellers, it became clear that the propeller offers the potential of very high propulsive efficiencies for the subsonic speed regime. As a result the propeller has been the object of many research programs worldwide with extensive programs starting from 1927 on. Somewhat earlier in time one of the great scientists in the field of aerodynamics, the famous Ludwig Prandtl, foresaw that the propeller should not be treated as a separate entity but rather be seen in combination with the trailing wing due to possible mutual influence of the wing and the propeller. His findings are nicely laid down in a very early NACA Technical report [1] where Prandtl describes windtunnel tests that he performed on a propeller-wing model (Fig.1.2). Prandtl knew that the performance of the complete configuration would be affected by interference effects as he states:

> ... it is well to distinguish two kinds of influences, one due to variations
> in velocity, and the other due to variations in direction of the air current.
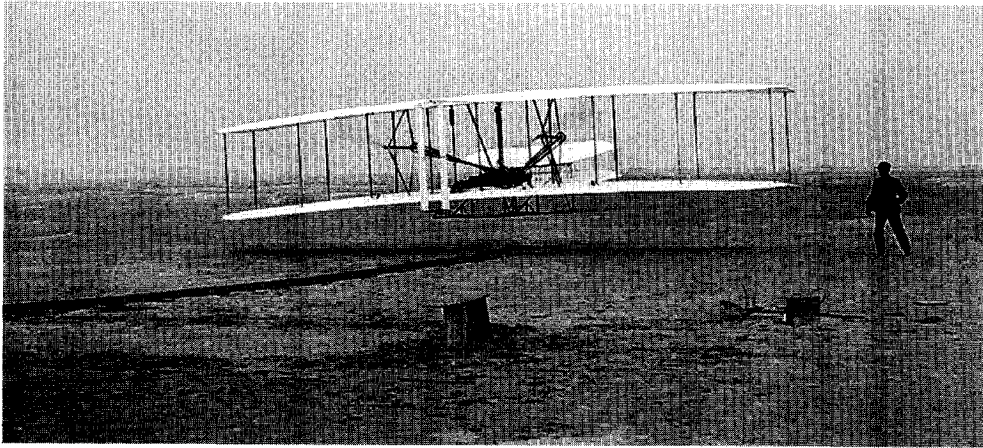
Figure 1.1: *The first manned flight in history: December 17, 1903. At 10:35 a.m. Orville Wright takes off into a 27 mph wind. The distance covered was 120 feet. Time aloft was 12 seconds. Wilbur is seen at right. (Picture: J.T. Daniels)*

> *The propeller is affected mainly by variations in the inflow velocity due to the wing. The wing is also subjected to slight changes in the direction of the air flow, which noticeably affect the drag. This is especially apparent when the aerofoil is outside the slipstream . . .*

The research projects, initiated in the 20's, led to many successful propeller powered aircraft with cruise speeds as high as $M = 0.6$. However, from the mid 50's to the mid 70's there was about a 20-year period of stagnation in propeller research due to the success of the turbojet and the turbofan propulsion systems. In this period of low fuel costs the lower propulsive efficiencies of the latter systems did not matter too much. A turning point arrived with the world energy crisis in 1973-1974 (see Fig.1.3) when NASA started an effort to evaluate the possibilities for high-speed propellers. Various studies indicated that at high cruise speeds , as high as $M = 0.8$, an advanced high-speed turboprop powered aircraft would have a large performance advantage over an equivalent technology high bypass ratio turbofan design.

The increased efficiency is a direct result of the simple thrust-momentum balance which state that the efficiency decreases as the axial velocity increment through the propulsion unit increases. This can be seen in eq. (1.1) where the ideal efficiency is presented as a function of the ratio of axial velocity increase, ΔV, and the undisturbed

(a)

(b)
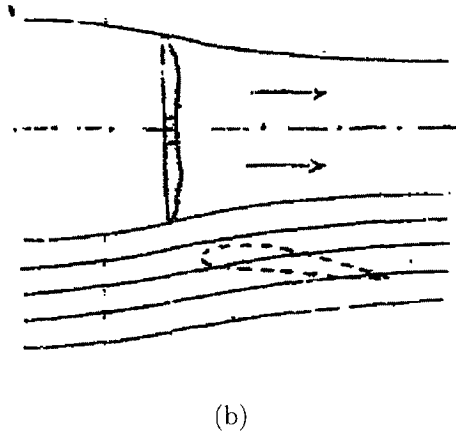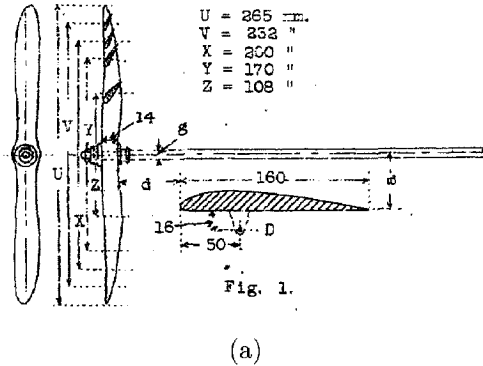
Figure 1.2: *The test set-up (a) and the original drawing (b) by Ludwig Prandtl,
which he used to describe the drag change of a wing placed in close
proximity of a wing.*

speed, V_∞:

$$\eta = \frac{1}{1 + \frac{\Delta V}{V_\infty}} \tag{1.1}$$

Turboprops induce smaller velocity increments, ΔV, to a larger air mass flow than
turbofans do, thereby increasing efficiency by several percentage points. It was envis-
aged that this superior performance could result in large block fuel savings, reduced
life cycle costs, improved range and other benefits for both the civil and military
aircraft market.

The high speed propeller concept (often referred to as the advanced turboprop
concept, see Fig.1.4) that emerged from these investigations, called the "Propfan"
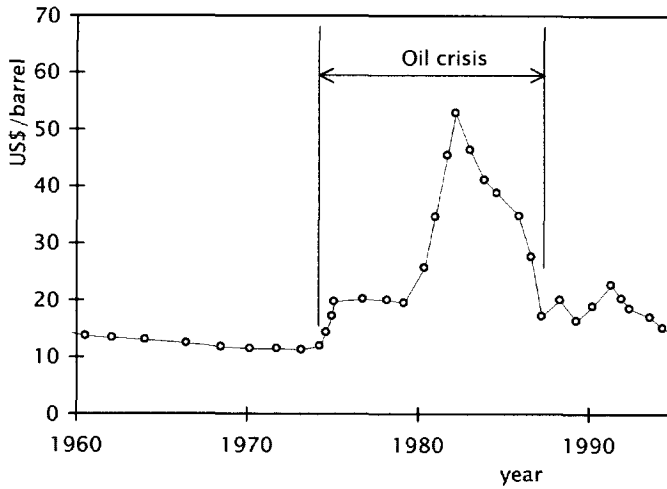
Figure 1.3: *U.S. first purchase crude oil prices expressed in 1996-valued US dol-
lars showing the oil crisis between the year 1973 and 1987 (source:
WTRG, USA, 1998)*

was extensively examined from both structural and aerodynamical point of view as is
demonstrated by numerous references [2, 3, 4, 5]. As a result of the high cruise Mach
number that was aimed at for the propfans the complexity of the propulsion system,
however, confronted designers with serious problems regarding aspects like blade dy-
namic behavior, fatigue and shock wave formation over the wing area immersed in
the slipstream.

But solutions for these problems that gradually emerged from the design offices
were caught up by societal developments that resulted in a sharp decrease of the oil
price. The instantaneous reaction could be expected: the Propfan concept, still in its
infancy state, was put to a halt.

1.2   Status of propeller propulsion

The era of modern turboprop, which started in the 80's with the *Dash-8, BAe ATP,
Fokker 50* and in the 90's with *Dornier 328, Saab 2000* and *BAe Jetstream 41*, initially
showed successful programs. During this period, however, the market transformed by
the arrival of the new-generation regional jet. Although the turbofan powered aircraft
like the *Fokker 70/100* , *Bombardier CRJ* and *BAe 146* gained much popularity it is
doubtful whether any regional aircraft has so far shown to be really profitable.

Jet aircraft indeed show advantages in some directions, but it is justified to acknowledge that there will always be a fair number of short regional routes on which propeller-driven aircraft will have a cost advantage. In this respect an indication for a typical trip length may be found in US domestic flight data where an average regional airline trip of 230 nmi is found. Although operators have rediscovered the advantages of turboprops on shorter routes, the forecast (Fig.1.5) given by Butterworth-Hayes [6], stating that the propeller driven aircraft are likely to hold at least 40% share of the market in future, may be too optimistic. Later market surveys ([7, 8]) show a trend of a decreasing market share of 24% for the turboprop segment with a yearly reduction of about 1% worldwide.

In this changing market it is worthwhile to investigate the technology regarding propeller propulsion versus jet propulsion to see whether new, or adapted, concepts are within reach to optimize current designs.

While worldwide the number of jet-powered aircraft in almost all weight categories is increasing compared to turbo-prop powered aircraft, the absolute numbers of aircraft relying on propellers is still substantial. New concepts like the *Airbus A400M* and the *Hercules 130J* are nice examples of aircraft that make use of the benefits of
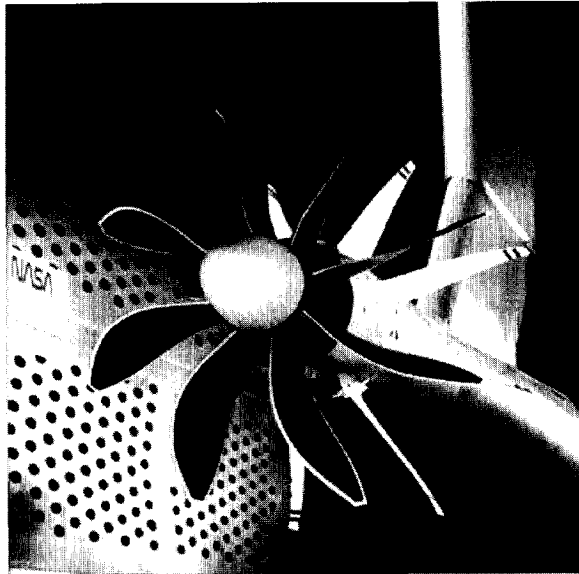
Figure 1.4: *High speed propeller (PROPFAN) tested in the NASA Lewis Research Centre 8 x 6 foot supersonic wind tunnel (Courtesy NASA, photo no. 90-H-78).*
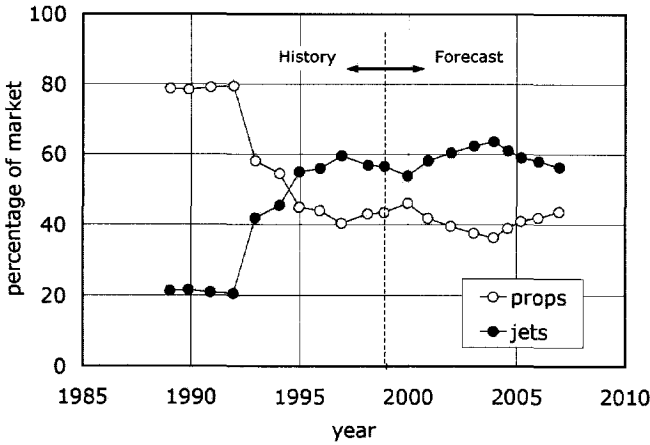
Figure 1.5: *Forecast of turboprop usage compared to jets [6].*

propeller propulsion. Especially the fact that propeller propulsion is inherently more efficient than even advanced turbo-prop concepts (the Propfan) up to Mach 0.8 is important. Expressed in terms of installed propulsive efficiency a comparison between the three major propulsion systems is made in Fig.1.6

Apparently turboprop engines are 10%-30% more efficient than jet engines at cruise condition with Mach numbers below 0.7. Turboprops typically derive 85% of their thrust from a propeller, while the rest is provided by the exhaust jet. Their high thrust specific fuel consumption (TSFC) is the result of the propeller's ability to accelerate large amounts of air at low airspeeds (see (1.1)). This is particularly advantageous during take-off and climb stages of flight when aircraft move relatively slowly. The efficiency of a propeller decreases with increasing airspeed and altitude, limiting the operation of turboprops to Mach numbers between 0.4 and 0.7 and altitudes below 7500 *m*. Hence, turboprop aircraft generally fly more slowly and lower than aircraft with turbofan engines as a trade-off for lower fuel consumption.

Nevertheless, fuel economy does not play the most important role for the selection of the propulsion system today since the relative contribution of fuel costs in the direct operating costs of aircraft has decreased considerably in the last few decades as indicated in Fig.1.7. Other aspects of propeller propulsion that are taken into account during the design process should be noted here as well.

First of all the propeller aircraft shows a wider operational speed range with increasing propulsive efficiency as the speed is decreased from maximum cruise. This typically leads to improved fuel economy when lower speeds can be used and to longer ranges and endurance when necessary (especially important for surveillance tasks).
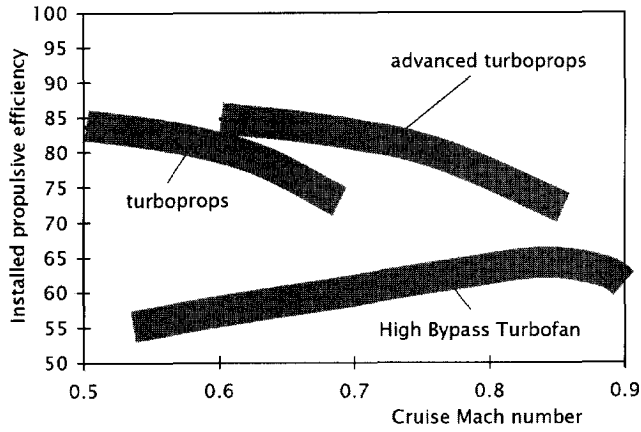
Figure 1.6: *Comparative installed propulsive efficiency of turboprops and turbofans vs. cruise Mach number.*
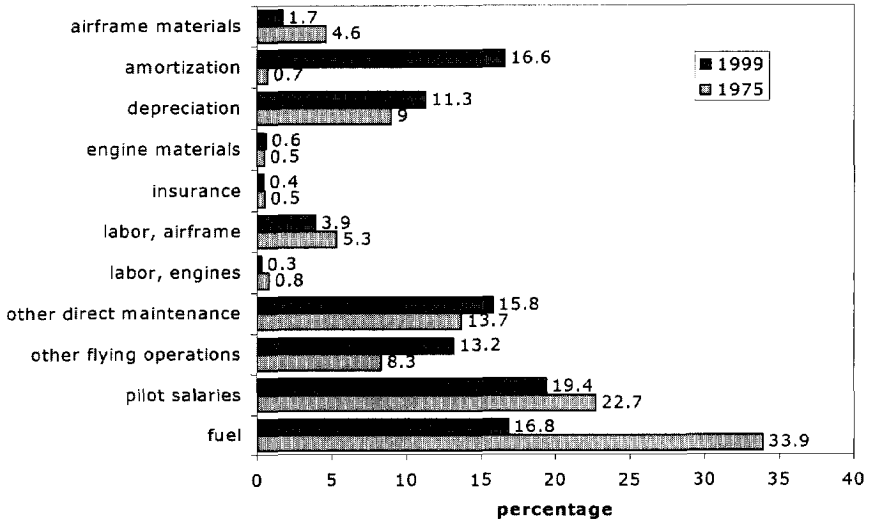
Figure 1.7: *Comparison of Direct Operations and Investment costs of regional jets between 1975 and 1999. Data taken from [9]*

Propellers deliver high thrust at low speeds in taxiing, particularly on semi-prepared terrain, and in take-off and climb. This improved take-off and climb reduces mission / leg fuel consumption and lowers noise for the area around airfields. Due to the high thrust additionally less taxi fuel is used than with turbofan propulsion. An important result of the higher propeller thrust is found in a better "go-around" performance capability than available from a turbofan during an aborted landing.

The availability of thrust reversal for backing on the ground and for braking in flight to produce deceleration and increased steepness of descent is another interesting issue. In addition, thrust reversal is obtained with a smaller weight penalty than occurs with turbofan thrust reversers.

The high slipstream velocities over the wing can be used to increase the wing lift at low speeds which is useful in take-off and landing operations. Thus careful integration of the propeller with the wing can produce improved STOL aircraft designs. The value of the high static thrust available for use in the development of high subsonic V/STOL aircraft is interesting. With the development of $M = 0.7$ to $M = 0.8$ propellers a revival of their use in V/STOL aircraft is a good possibility.

Propellers show quite some flexibility to accommodate different requirements by using the same engine with different propellers and gearboxes. This opens up the possibility to comply to particular preferences in diameter, flight speed, etc.

With the characteristics discussed above it becomes clear that operational, structural and aerodynamic aspects all contribute to the economical operation of propeller powered aircraft. The flight mission requirements certainly determine where the effort with respect to the design is focused.

For multi-engined propeller powered aircraft one of the most important issues, from the aerodynamics and performance point of view, is the interaction between the propeller slipstream and the wing. Modern aircraft concepts, like the European *Airbus A400M* project, exhibit a high disk loading[1] and an increased number of (swept) blades to enable high cruising speed. High disk loading however generates strong swirl velocities in the slipstream, causing considerable deformation of the lift distribution, which has an impact on the aerodynamic behavior and performance of the wing.

The propulsion-airframe installation problem and the experimental and numerical techniques to analyze this topic have been EC-funded since '90 through programs like Gemini I & II, APIAN, DUPRIN I & II and ENIFAIR. Within these research projects specific attention was paid to analysis of current concepts rather than investigation of possible new design strategies.

From earlier investigations it is known that both the position of the powerplant with respect to the wing and the propeller angle of attack play an important role. Carefully designed configurations may reveal some performance benefits when the propeller and the wing are closely coupled.

---

[1] *Disk loading* is the propeller thrust divided by the swept area of the propeller disk.

Rather than an evaluation of the complete design envelope of a propeller powered concept, one typical aspect is further investigated in this dissertation: the aerodynamic aspects of the propeller integration for the cruise phase of the aircraft. In section 1.3 the scope of the dissertation is elucidated further.

1.3   Scope of the thesis

The aerodynamics phenomena that play a role in the characteristics of propeller-driven aircraft constitute a formidable problem that needs to be carefully analyzed understood to arrive at optimized designs.

Hence, in order to achieve the highest possible benefit from propeller propulsion, careful attention should be paid to the integration of the propulsion system and the aircraft. Propeller propulsion systems are in general installed in nacelles that are integrated with the aircraft wing to form a tractor propeller design. Such a closely coupled system has the potential for large installation penalties that are due to possible unfavorable interference effects on the lift distribution over the wing. These effects will certainly be more significant with propeller propulsion systems that exhibit high disk loading due to the higher wake velocities and swirl angles compared to those of lightly loaded propellers. On the other hand, many authors have indicated that well designed propeller aircraft may benefit from the interaction between the propeller slipstream and the trailing wing. The details of the phenomena that play a role in this process will be treated in subsequent chapters.

The effect of various design parameters on the performance may well be accepted as the most important issue. However, with the stronger environmental regulations, regarding the operation of aircraft, one other aspect could be overlooked easily: noise.

The noise production of propellers is a challenging and important issue with respect to the cabin comfort and the effects of the external noise level in relation to community noise. Due to the absence of a shielding duct the pressure distortions generated by the propeller blades directly impinge on the fuselage. In particular for wing mounted propellers the distance to the fuselage is often very small and a very high sound pressure level is observed in the area of minimum clearance. To obtain an acceptable cabin comfort at the present time all new turbo-prop designs incorporate blades with advanced airfoil sections, reduced blade chord and narrow elliptical blade tips. Besides this, the general trend is to use a high number of blades combined with a smaller propeller diameter. Together with the unloading of the tip area this results in reduced noise levels. Although the choices of these typical propeller parameters are prompted by the noise problem, they have a large impact on the aerodynamic characteristics and performance of the propeller. Even though this distinct relation exists, the analysis of the noise production of propellers falls beyond the scope of this study. Therefore existing advanced propellers are used in the subsequent analyses assuming that the designs are optimized already for low noise production. In this respect the

propeller design problem in itself will not be addressed in this dissertation.

The primary goal of this study is to identify and describe the mechanisms that determine the aerodynamic interference between tractor propellers and a wing. Moreover, the effect of various parameters like the propeller position and inclination with respect to the wing will be discussed in detail.

A second goal is to validate which methods can be used to analyze and predict the performance and characteristics of propeller-wing configurations using calculation techniques of distinct complexity. From this analysis the required complexity level of the calculation method to arrive at optimized propeller-wing design is determined.

To arrive at these goals one may be tempted to analyse the complete configuration with the most advanced CFD code available. The separate effects of the propeller on the wing and vice versa are then obtained in a post-processing step. This procedure, in which the propeller and wing are computationally fully coupled hinders a clear understanding of the contribution of the separate parts, especially when the designers needs detailed information on the effects of configuration changes. Therefore, this study focuses on the separate contribution of the propeller and wing by uncoupling them during the experimental and numerical analysis. Hence, the full scope of interaction phenomena is investigated which is beneficial for the design optimization of propeller powered aircraft.

1.4 Outline of the thesis

The dissertation is organized into nine chapters. First of all the basic phenomena that occur when the propeller is brought in close proximity to a wing, the propeller-wing interference effects, are discussed in Chapter 2. Chapter 3 deals with the numerical analysis of propeller wing interference. In this chapter the capabilities of rather simple calculation methods are summarized whereas Chapter 4 illustrates more advanced CFD techniques based on the solution of the Navier-Stokes equations.

To gain further insight in the processes that take place in the interactive flow field, several experiments were performed in a low speed windtunnel. A description and discussion of these experiments is presented in Chapter 5. Chapter 6 contains results of numerical calculations that were performed on the experimentally tested geometries. The goal of these calculations was to study the most important flow variables that determine the complex flow field in the vicinity of the wing and to determine possible performance benefits that could be gained from the propeller-wing interference.

Finally, with the basic phenomena known from the analysis of existing designs, ways to gain benefits from optimizing the wing that interacts with the propeller, are discussed. This topic of optimization is highlighted in Chapter 7. Overall conclusions and recommendations are discussed in Chapter 8.

Chapter 2

Propeller Wing Interference effects

2.1 Introduction

In the design of multi-engined propeller powered aircraft one of the important issues is the interaction between the propeller and the wing. Modern aircraft concepts, exhibit a high disk loading and a high number of blades to enable increased cruising speed or to prevent excessive noise production.

The first problem due to the high disk loading is the direct effect of forces and moments on the propeller especially at non-zero angle of attack. This may cause detrimental effects on the aircraft's stability. Secondly the high energy level in the propeller slipstream will cause strong interference effects on other aircraft parts directly leading to changes in the performance characteristics through adaptation of the wing lift and drag.

The high swirl velocities in the slipstream, that is associated with high disk loading, generate a deformation of the lift distribution which has an impact on the aerodynamic behavior and performance of the wing. Propulsion systems with contra-rotating propellers, developed to recover most of the swirl, seem to be the solution to this problem but they are not used extensively because of their complexity and weight.

Besides this the axial flow increase inside the slipstream might lead to detrimental compressibility effects for aircraft flying at high cruising speed. Hence the interference between propulsion system and the remaining aircraft parts has the potential for large installation penalties.

During the design process of the aircraft the position and the characteristics of the propeller will be based on the result of satisfying various design constraints. Once the layout of a propeller configuration is accepted, the presence of the propeller slipstream

13

that inevitably interacts with the wing, forms part of a tuning process where adjustments should lead to maximum possible performance over a selected speed range of the aircraft. For this reason a detailed analysis of the phenomena that occur for closely coupled propeller wing configurations is highly beneficial.

The rotational kinetic energy in the wake of a conventional single-rotating propeller system is usually considered as a loss term (since it does not contribute to the thrust). However, many authors [10, 11, 12] have indicated that a significant relief of the detrimental drag effect (due to increased dynamic pressure in the slipstream) can be obtained from propeller-wing interaction. Rather than manipulate wing geometry to approach two-dimensional flow, it would seem logical to use some energy source for the task of directing the flow in such way that lower induced drag is produced. The rotational component in the slipstream is in fact available for amplifying or attenuating the wing bound vortex system with a possible reduction of induced drag. In this way the wing in fact acts as a stator vane that recovers some of the swirl loss caused by the propeller. From earlier investigations [13, 11, 14, 15] it is known that the details of the interaction effects are mainly determined by the position of the propulsion system with respect to the wing and propeller angle of attack.

To attain a better understanding of the interactive flows causing the slipstream/wing interference the most important aerodynamic mutual effects between a tractor propeller and a trailing wing are discussed in this chapter.

Although it is known that for cruise speeds above $M = 0.75$ the high velocity in the slipstream might cause shocks on the trailing wing, pushing the wing up to drag rise, this thesis will only deal with the fundamental phenomena arising at moderate to low Mach numbers. Besides the need for enhanced insight in the main phenomena, a major goal is to define an optimum configuration for low speed tractor propeller/wing combinations.

The analysis of the major propeller wing interference effects that are discussed in this thesis is restricted to a typical two-engined turbo-prop configuration as sketched in Fig.2.1. However, the phenomena that occur for these aircraft configurations can be found on 4-engined aircraft as well except for the typical effects that are introduced by possible propeller-overlap.

2.2   Steady versus unsteady analysis

A propeller at an angle of yaw or pitch generates flow that is inherently unsteady as the flow conditions at a blade change with the rotation of the propeller.

Analysis of the unsteady propeller problem (uninstalled) has allowed the calculation of cyclic variation of the propeller blade forces to a reasonable degree of accuracy [16, 17]. A comparison of steady and unsteady analyses of a propeller [16] has shown the steady state analysis to be capable of predicting the mean (time-averaged) result within an acceptable degree of accuracy. Although the unsteady analysis may

(a) Dornier 328
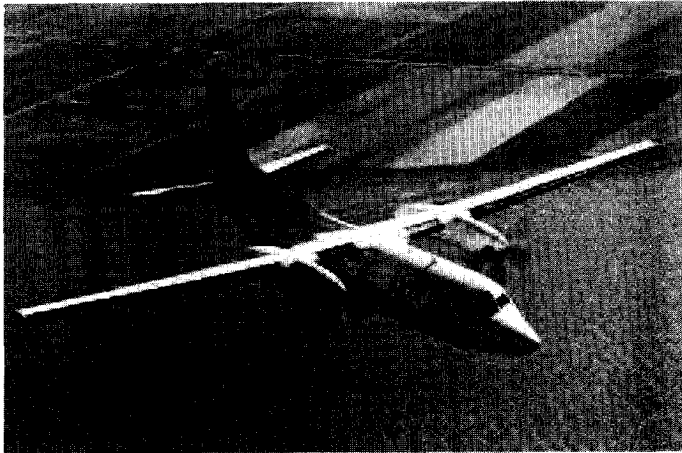
(b) Fokker F50

Figure 2.1: *Examples of two-engined turbo-prop aircraft that are typical for the propeller-wing interference effects discussed herein.*
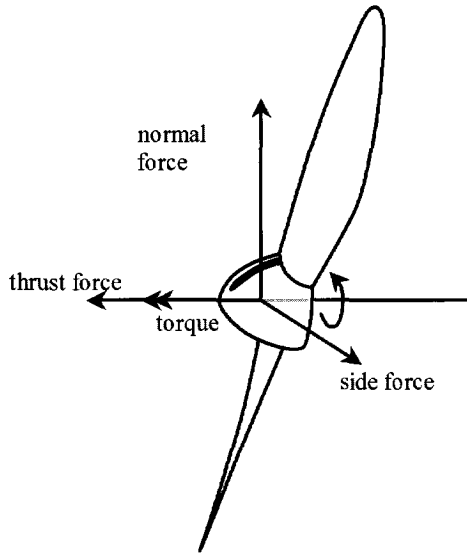
Figure 2.2: *The most important forces and moments acting on the propeller.*

be useful from a structural and vibration point of view it will offer little more than the steady analysis in terms of aircraft performance which requires knowledge of the (quasi-) steady characteristics. As a consequence the major analysis of the propeller-wing interference problem will be based here on the steady state (time averaged effects) assumption.

2.3   Propeller forces and moments

In the first phase of the design process no detailed data are needed for the flow around the propeller blades themselves but rather the disturbed flow field which interacts with the wing is needed. To determine such slipstream data a good starting point is to separate the propeller from the rest of the aircraft and apply procedures to calculate the characteristics of the so-called uninstalled propeller. At a later stage the influence of the other aircraft parts can then be added in such way that the flow exhibits the interaction effects that affect the velocities and pressure imposed by the slipstream.

To find out to what detail and accuracy the propeller forces must be determined regarding their effect on a complete aircraft the magnitude and direction of the forces and moments must be established.

In Fig.2.2 the most important propeller forces and moments that act on the propeller are sketched. The main contributor to the airplane performance is of course

the thrust force. Other forces, however, play an important role as well. In general it can be stated that forces and moments are generated along all three axes in case the propeller is positioned at a non-zero angle of attack to the incoming flow. With the propeller closely coupled to the wing (upwash in front of the wing) and regarding the dynamics of the aircraft (angle of attack) most of the time this non-zero inflow angle will be present. The main contributors that need further attention are:

- the thrust force because of its important role in the thrust-drag bookkeeping

- the propeller normal force for its direct contribution to the aircraft lift coefficient and the considerable influence on the stability of the aircraft [18].

The propeller moments are small compared to the moments produced by the complete aircraft. Hence it is not necessary to treat them in detail. The main contributors to the aircraft's stability and performance are in fact restricted to the normal force and the torque.

2.4 Characteristics of propeller slipstream flow

The description of the interactive flow around the propeller-wing configuration requires detailed information about the characteristics of the slipstream in the presence of the wing. As starting point for the description of this flow the uninstalled propeller may be considered. An attractive way to represent the propeller is the concept of an advancing rotating wing which produces a helical vortex system as sketched in Fig.2.3.
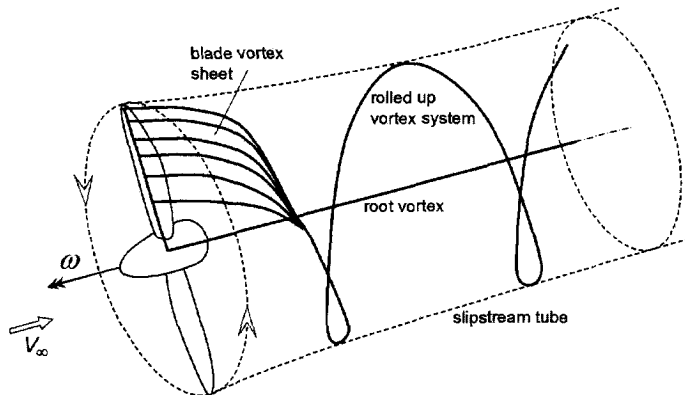
Figure 2.3: *Helical vortex system and slipstream tube generated by a propeller.*

Due to the self-induced velocities produced by the vortex system the vortex wakes tend to deform and roll up which produces a so-called slipstream tube with strong gradients in various flow quantities both in streamwise and radial direction. In case of an asymmetrical loading distribution on the propeller, for example caused by a non-zero angle of attack of the thrust axis, also a variation of the flow quantities in azimuthal direction exists.

The most important flow quantities that characterize the slipstream are:

- Axial velocity profile

- Swirl velocity profile

- Total pressure distribution

- Static pressure distribution

- Vorticity

- Helicity

- Contraction

These quantities will be further explained in the following sections. Additional features of the propeller slipstream and possible ways to determine the propeller forces based on the so-called "Blade Element Method" are summarized in Appendix A.

2.4.1   Axial velocity profile

The local velocity in the 3-dimensional space consists of three components: $V = (u, v, w)^T$ in a Cartesian coordinate system.

In case the propeller thrust axis is directed in the (streamwise) x-direction the u-component becomes the axial velocity component, here denoted with v_a. A typical distribution in radial direction of this component for a general multi-bladed propeller is presented in Fig.2.4.

Due to the non-uniform loading a strong gradient exist in blade spanwise direction and a maximum value is found close to the $\frac{3}{4}R$ location. The low value of v_a close to the blade root is indicative for the relative low blade loading in this region.

As can be seen in Fig.2.5, the axial flow component increases in streamwise direction as a result of the increased length of the vortex system at the particular reference location. When the interaction with a trailing wing is considered, apparently the streamwise distance between the propeller and the wing becomes an important parameter.
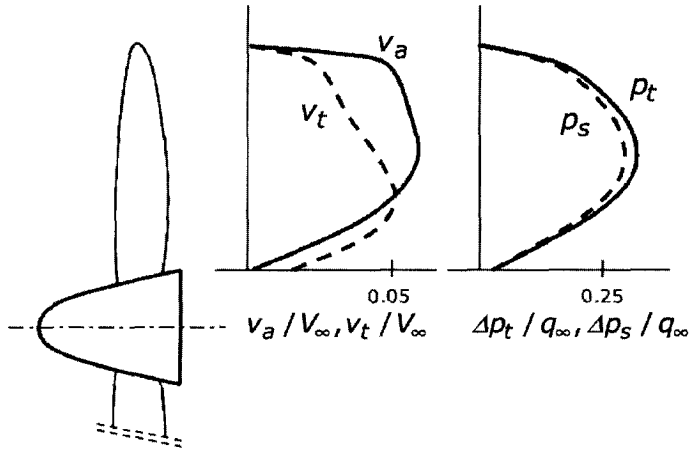
Figure 2.4: *Typical radial distribution of axial velocity, tangential velocity, total pressure and static pressure directly behind a 6 bladed lightly loaded propeller; BEM analysis.*

2.4.2 Swirl velocity profile

To elucidate the distribution of the propeller induced tangential velocity component, $v_t = \sqrt{v^2 + w^2}$, it is helpful to assume an infinite number of blades. This assumption agrees well with the concept of the actuator disk. Since the number of blades is infinite the slipstream domain behind the propeller is completely filled with vortex lines. Based on the simple model, as sketched in Fig.2.6, we find that the bound vortices , attached to the propeller blades, induce no axial velocity in the slipstream. This can be demonstrated by considering two elemental vortices OR and OS located symmetrically with respect to OQ.

The velocities induced by these vortex lines are equal in magnitude but their direction is opposite. By adding all the effects of vortex pairs that constitute the complete bound vortex system it can be concluded that the axial induced flow velocity is the result of the free trailing vortex lines in the slipstream only.

The situation for the tangential velocity, on the other hand, is different. The tangential components, $(v_t)_{OR}$ and $(v_t)_{OS}$ have the same direction which results in a non-zero tangential velocity component in P.

It should be noticed that vortex line OS' induces a tangential component in opposite direction but due to the larger distance to point P the magnitude of this component is smaller than that due to the OS vortex. From Fig.2.6 it becomes clear that the tangential velocity has the same direction as the sense of rotation of the propeller.
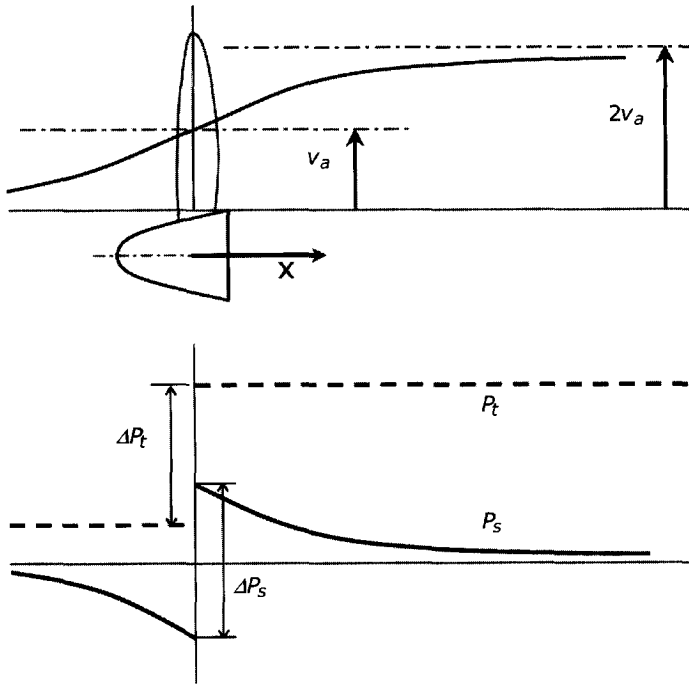
Figure 2.5: *Streamwise development of the axial velocity increase and pressures in the slipstream. The velocity jump increases from v_a at the propeller disk to $2v_a$ far downstream. Pressures are not scaled relatively to each other.*

An equal reasoning can now be followed for a point P' in front of the propeller where the direction of the induced velocity is opposite to the propeller rotation direction. The circulation found over a circle with a radius r and enclosing the propeller axis, should then show a non-zero value. This is physically not possible since the circle, in front of the propeller, does not enclose any vortex line. We may therefore conclude that the tangential velocity in P', induced by the bound vortex system is compensated by the component induced by the free vortices in the slipstream. In Fig.2.7 the distribution in axial direction of the tangential velocity due to both the bound vortex system and the free vortex system is sketched. By adding the effect of both systems, we see that the tangential velocity component is zero everywhere in front of the propeller; its value is w in the propeller plane and becomes $2w$ far behind the propeller.

The tangential velocity component in the slipstream (often referred to as the "swirl velocity") is presented in Fig.2.4 for a typical propeller. As can be seen the form differs
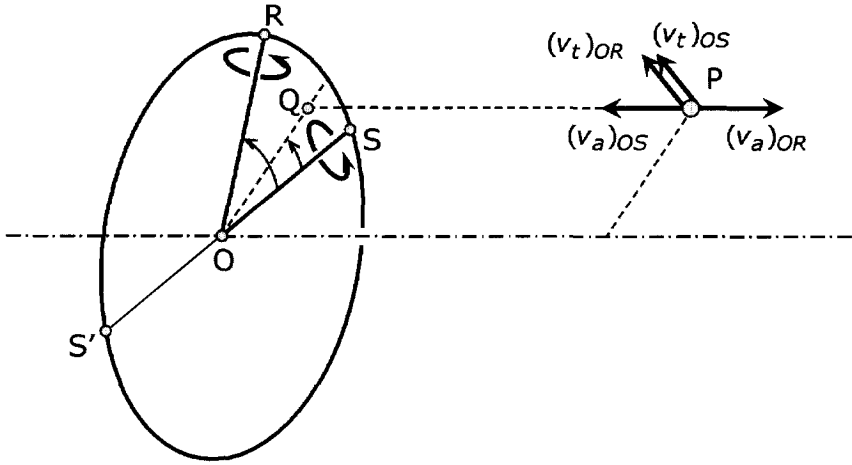
Figure 2.6: *Axial and tangential velocities induced by the propeller blade bound vortex system.*

from the axial velocity profile due to the loading character of the blades.

For varying propeller loading conditions the form of the axial velocity distribution remains unchanged whereas the form of the swirl velocity distribution can change significantly with the propeller advance ratio. An example of this fact is presented in Fig.2.8 for the *Fokker 50* propeller.

The swirl angle, defined as:

$$\theta_{sw} = \tan^{-1}\left(v_t/(V_\infty + v_a)\right) \tag{2.1}$$

depends on both the axial and the tangential velocity component in the slipstream. Since the axial component varies in axial direction and the swirl component stays constant, the swirl angle changes in axial direction. Hence the swirl angle at the location of the wing becomes dependant of the distance, d_p, between the wing and the propeller. Consequently the resulting changes in local angle of attack for a trailing wing will affect the propeller-wing interaction effects. The change in swirl angle for a typical lightly loaded propeller is sketched in Fig.2.9.

2.4.3 Total and static pressure distribution

Both the total and the static pressure rise across the propeller disk, as sketched in Fig.2.4 demonstrate a maximum close to the 0.75R position due to the loading that peaks in this location. A significant difference between the two pressures is
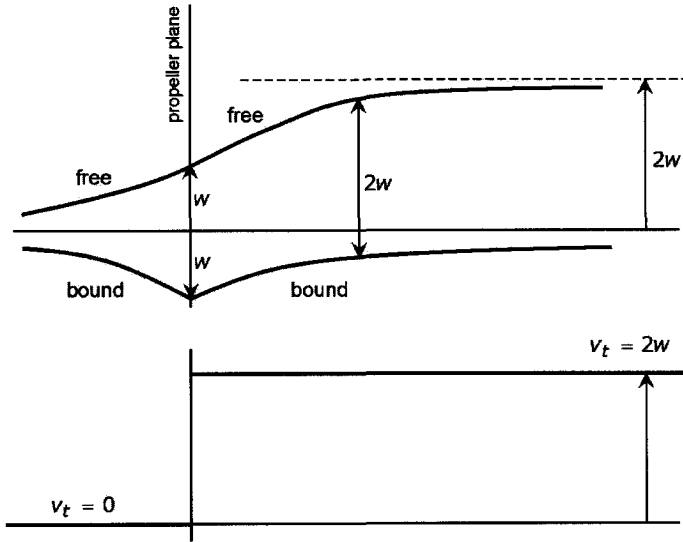
Figure 2.7: *Bound and free vortex contribution to the tangential induced velocity in the propeller slipstream (upper figure) and the resultant component (lower figure).*

noticed when the streamwise development is observed. Where the static pressure jumps locally when passing the disk, the total pressure jumps to a constant value in the slipstream. The small difference between the static pressure and the total pressure at the location of the propeller disk can be attributed to the rotational motion imparted to the slipstream by the reaction of the torque. This can be seen as follows.

Let p be the static pressure immediately in front and Δp the pressure increase behind the propeller. Further, let v_a, v_r and v_t be the axial, the radial and the angular velocity component at a radius r. In the slipstream far downstream, the pressure and the velocity components are denoted with an index s: p_s, v_{a_s}, v_{r_s} and v_{t_s}. When the contraction of the slipstream is neglected the radial velocity component becomes zero: $v_r = v_{r_s} = 0$.

Considering the total pressure of the flow before and behind the propeller disk gives:

$$\begin{aligned} p_{t_\infty} &= p_\infty + \tfrac{1}{2}\rho V_\infty^2 \\ &= p + \tfrac{1}{2}\rho((V_\infty + v_a)^2 + v_t^2) \end{aligned} \tag{2.2}$$
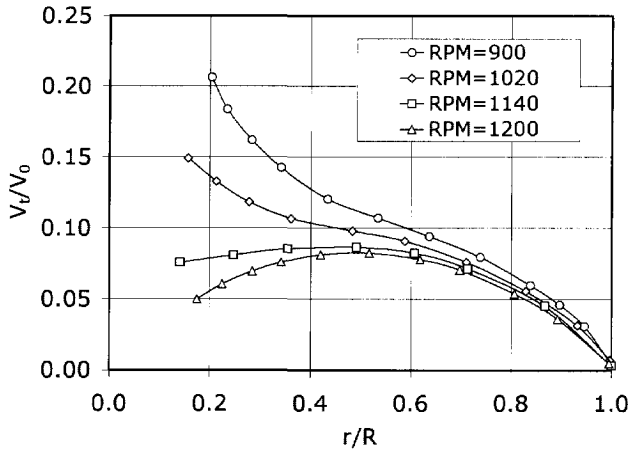
Figure 2.8: *Typical variation of the swirl velocity distribution with propeller speed ; F50 propeller [19]; data taken directly behind the propeller.*
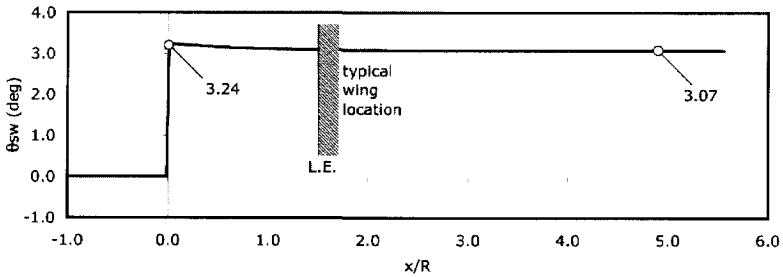
Figure 2.9: *Streamwise variation of the swirl angle for a lightly loaded propeller based on eq. (2.1) ; $v_a/V_\infty = 0.06, v_t/V_\infty = 0.06; r/R = 0.75$. The line L.E. depicts the wing leading edge of a typical twin engine aircraft.*

and:

$$\begin{aligned}
p_{t_s} &= p + \Delta p + \tfrac{1}{2}\rho((V_\infty + v_a)^2 + v_t^2) \\
&= p_s + \tfrac{1}{2}\rho((V_\infty + v_{a_s})^2 + v_{t_s}^2)
\end{aligned} \qquad (2.3)$$

Thus:

$$p_{t_s} - p_{t_\infty} = \Delta p + \tfrac{1}{2}\rho v_t^2 \tag{2.4}$$

which shows that the increase in total pressure on passing through the propeller disk exceeds the static pressure rise Δp by a small term, $\tfrac{1}{2}\rho v_t^2$, which represents the kinetic energy of the rotational motion imposed to the fluid by the torque of the propeller.

It should be noted that an airfoil in the slipstream of a propeller is insensitive to a change of the global value of the static pressure. For the calculation of the propeller wing interference effects the total pressure may be used as part of the definition of boundary conditions in CFD calculations but the parameter for which the wing is sensitive is the dynamic pressure.

2.4.4 Vorticity

The vorticity defined as:

$$\omega = \nabla \times V = \begin{pmatrix} \omega_x \\ \omega_y \\ \omega_z \end{pmatrix} = \begin{pmatrix} \xi \\ \eta \\ \zeta \end{pmatrix} \tag{2.5}$$

gives important insight in the rotational character of the flow that is convected into the slipstream. The spatial distribution of the vorticity in the slipstream is directly related to the blade loading and the position of the blades in time. When the propeller slipstream is treated as an unsteady problem the time dependent position of the vortex sheets that leave the blades will have to be determined. This procedure may be required in case the unsteady loads on a trailing wing are to be determined.

A typical example of the spatial distribution of vorticity behind a 6-bladed high speed propeller is presented in Fig.2.10. Clearly all blades produce their own vortex sheet whose strength and distribution of vorticity is determined by the loading conditions of the specific blade. High values of vorticity are found at the tip side of the vortex sheet were the gradient in the loading is the highest. For most practical design calculations it is acceptable to treat the flow as being steady which implies that the vorticity originally confined to the vorticity sheets is spread over the entire slipstream domain.

Often the streamwise component of the vorticity:

$$\omega_x = \frac{\omega \cdot V}{|V|} \tag{2.6}$$

is presented to indicate the alignment of the blade free vortices with the flow. The selection of this component to illustrate this alignment is in fact not very well-founded. This can be explained by observing the cross-wise components (y and z) of the vorticity vector, an example of which is depicted in Fig.2.11. The values in this figure were taken from a dataset generated by Navier-Stokes computations that are described in
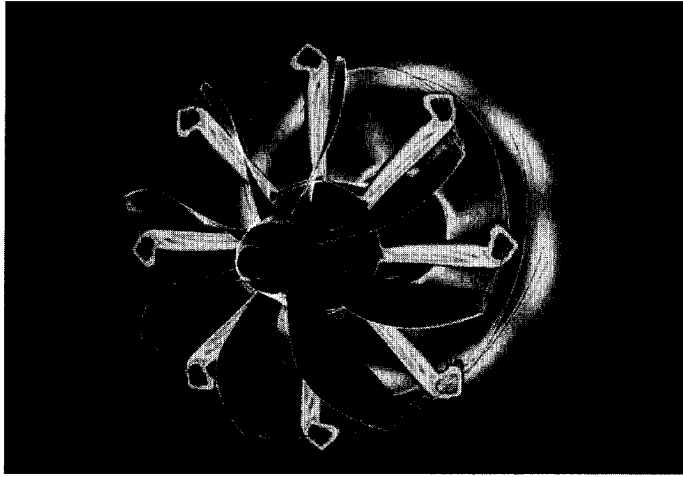
Figure 2.10: *Vorticity distribution in the slipstream of a 6-bladed high speed propeller. CFD-calculation performed by Luursema and Veldhuis [20].*

more detail in Chapter 6. The analysis plane is located directly behind the propeller that was modelled as an actuator disk with representative jump conditions.

In Fig.2.11 calculated vorticity data taken directly behind a 4 bladed propeller are shown. In this case the propeller, that is lightly loaded, is located well in front of a small aspect ratio wing. Further results of this model, denoted PROWIM, are discussed in Chapter 5. As can be clearly seen, an axis-symmetrical distribution of the streamwise component of vorticity, ω_x(Fig.2.11a), is found whereas the cross-wise components, ω_y and ω_z, depicted in Fig.2.11b and Fig.2.11c respectively, are highly non-axis-symmetrical, as expected. The difference between the magnitudes of the three components is relatively small indicating that the oncoming flow is extensively disturbed by the propeller in all 3 directions. This fact certainly is important for a good understanding of the effects of the slipstream may have on the flow over a trailing wing.

2.4.5 Helicity

The helicity density, or simply helicity, is defined as the dot product of the vorticity vector and the velocity vector:

$$h = \omega \cdot V = u\xi + v\eta + w\zeta \tag{2.7}$$

Due to the characteristics of the dot product it is a measure for the alignment between the vorticity vector and the velocity vector.

x-vorticity   y-vorticity   z-vorticity
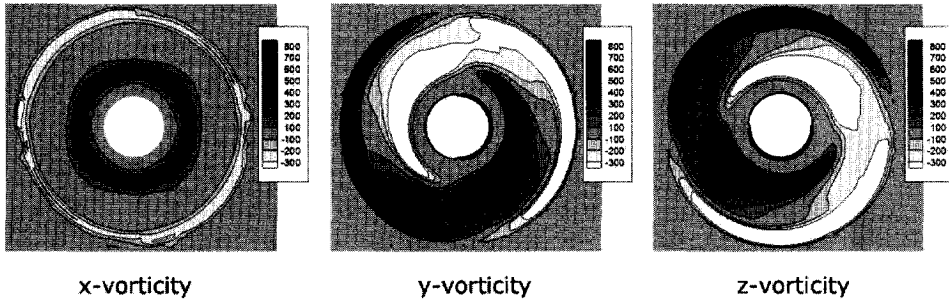
Figure 2.11: *Distribution of x, y and z-component of vorticity in the slipstream directly behind a lightly loaded 4-bladed propeller as taken from a dataset produced by Nebiolo [21].*

A parameter that gives direct insight in the alignment of the flow features is the so-called relative helicity, h_r, which is the normalized value of the helicity density :

$$h_r = \frac{\omega \cdot V}{|\omega| \, |V|} = \cos(\alpha) \qquad (2.8)$$

helicity   relative helicity
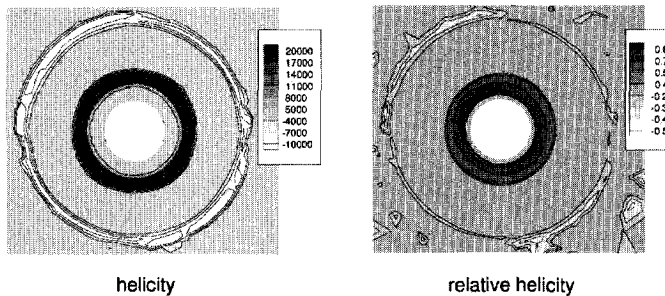
Figure 2.12: *Distributions of helicity and relative helicity directly behind a lightly loaded 4-bladed propeller as taken from a dataset produced by Nebiolo [21].*

It takes a value between -1 and 1 where $h_r = 1$ indicates a perfect screw-like flow with the vorticity vector perfectly aligned with the undisturbed flow velocity vector ($\alpha = 0°$). An example of the distribution of h and h_r is presented in Fig.2.12. In this case the data were again taken from the earlier mentioned CFD-calculations on the

PROWIM propeller-nacelle-wing model (Chapter 5), in a plane directly behind the propeller. Both distributions show a strikingly strong directional bias. The vorticity vector close to the nacelle surface (central part in the pictures) is mainly convected in the direction of the local velocity vector $(\cos(\alpha) \rightarrow 0.8)$ whereas the vortical flow at the outer edge of the slipstream shows the opposite tendency $(\cos(\alpha) \rightarrow -0.5)$. When the slipstream hits the trailing wing this vorticity field will affect the local flow in the wing boundary layer and strong gradients in the local angle of attack are to be expected. As with the high gradients in the total pressure at the tip- and the root-side of the propeller this implies large changes in the local wing spanwise loading due to propeller-wing interference.

2.4.6 Contraction

In order to calculate the loads on a trailing wing it is necessary to determine the dimensions of the wing part that is immersed in the slipstream. Because the slipstream contracts to preserve the mass flow as the velocity is increased through the propeller disk, the diameter of the slipstream tube at the wing location will be somewhat smaller than that at the propeller disk. In general the contraction of the slipstream is quite small but for heavy loaded propellers neglecting the slipstream contraction is not allowed anymore. In this case, the self-induction of the propeller wake has to be taken into account when determining the slipstream geometry and the propeller induction.

As shown by Theodorsen [22] , the contraction of the slipstream in the ultimate wake is only a few percent of the propeller diameter for lightly loaded propellers. In this case small errors are expected if flow calculations are performed without taking the radial component of the velocity vector into account. The analysis performed by Theodorsen is based on the calculation of the velocity field induced by a helix that lies on a perfect cylinder with a constant pitch angle. The radial velocity is obtained using the Biot-Savart law, integrating over the entire discontinuity surface that contains the vortex lines of the helix. Since this procedure is rather laborious (combined with the fact that only mild effects are expected due to the limited contraction ratio), an easier calculation method is preferred.

According to the theory described in Appendix C the contraction ratio, R_s/R, of the slipstream may be approximated by:

$$\frac{R_s(x)}{R} = \sqrt{\frac{1+a}{1 + a\left(1 + \frac{x}{\sqrt{R^2 + x^2}}\right)}} \qquad (2.9)$$

where $a = v_a/V\infty$ is the dimensionless axial velocity factor, related to the thrust coefficient T_c. In Fig.2.13 the contraction ratio of the Theodorsen model is compared with a 3-dimensional analysis of an actuator disk in an inviscid, incompressible flow calculated with a Navier-Stokes code. In both cases a uniform total pressure jump of
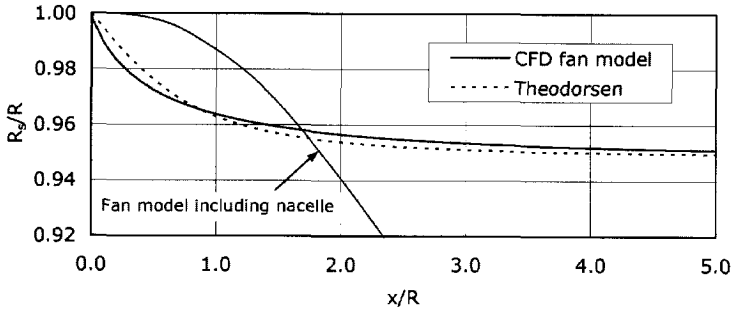
Figure 2.13: *Comparison of slipstream contraction ratio calculated with the model of Theodorsen [22] and a propeller (fan) model with constant total pressure jump across the disk. $C_T = 0.125$; $v_a/V_\infty = 0.074$*
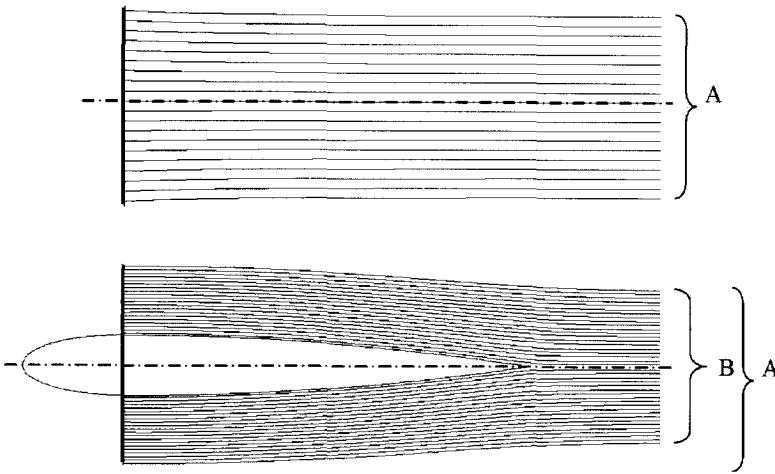
Figure 2.14: *Streamlines leaving the propeller showing the contracting effect of a contoured nacelle as calculated for a 2D-actuator disk model. $C_T = 0.125$; $v_a/V_\infty = 0.074$*

$\Delta p_t/p_{t_\infty} = 0.3$ was applied which results in a thrust coefficient of $C_T = 0.125$ and an axial inflow factor of $a = 0.074$.

Although small differences between the two methods are noticeable the simpler Theodorsen method seems to be acceptable for the purpose of determination of the

slipstream contraction.

Although the contraction, as given by eq.(2.9) leads to acceptable results when the un-installed propeller is considered, it can not cope with the dramatical effect that is introduced by a nacelle. With the blade vortex system now interacting with the (contoured) nacelle, the final contraction ratio, R_s/R, becomes much smaller. An example of this effect is presented in Fig.2.14.

2.5 Disturbance of the propeller flow field

When the propeller is installed on the aircraft it operates in a non-uniform flow field produced by the aircraft components. Axial, vertical and horizontal velocity increments are produced upstream and downstream of the wing.

Besides this a change in the aircraft angle of attack leads to an change in the effective propeller angle of attack which leads to asymmetric loading.

Especially the nacelle and the wing induce a velocity perturbation at the propeller plane and in this way the propeller thrust and power are dependant on the shape of the nacelle and the position of the propeller relative to the wing.

When the propeller performance and slipstream characteristics are considered two cases may be distinguished:

- the axi-symmetrical flow case where the loads relative to the rotating propeller are "steady". This case is important for the aerodynamic design of the propeller itself, for the determination of the slipstream flow and for the installation effects due to the spinner and the hub.

- the asymmetrical flow case which is the usual situation for the installed propeller. This case may require a time-dependent computation to obtain the loads on the propeller blades ($1P$ and multiple P-loads).

2.5.1 Effect of the nacelle on the propeller

An important interference effect is experienced by the propeller due to the nacelle to which it is mounted. Except for the atypical cases, where the nacelle features a strong asymmetric geometry with respect to the location of the thrust axis, in general the interference effects are axis-symmetrical.

As sketched in Fig.2.15 the nacelle will impose a non-uniform axial velocity distribution on the propeller inflow due to blockage. This change in the inflow field will alter the loading distribution along the blades, which in turn will change the apparent thrust for a given value of the shaft power. Although the change in the apparent thrust is usually small at low Mach numbers, the design of the propeller must account for the non-uniform flow by adapting the propeller blade twist distribution when an optimized performance condition is sought after.
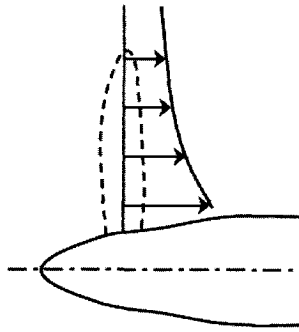
Figure 2.15: *Axial velocity increase due to the blockage effect of the nacelle*

The calculation of the propeller thrust is complicated because the nacelle's perturbation flow field changes the thrust on the propeller while the propeller's pressure field causes a thrust force on the nacelle. In fact the only contribution that is to be known is the sum of the propeller thrust force combined with the nacelle thrust (or drag) force. This is justified by invoking the momentum integral theorem, from which we conclude that the vortex wake far downstream is uniquely determined by the thrust and propulsive efficiency of the object that created it. The details of this object and how the vortex wake was created are irrelevant to the final result. Now the inviscid thrust force on the nacelle is simply the inviscid thrust on the "equivalent propeller" (i.e. on the propeller/nacelle combination) minus the inviscid thrust on the real propeller alone. The inviscid power absorbed by the propeller/nacelle combination, and the inviscid power absorbed by the propeller alone, is always exactly equal by following this procedure.

To get a first impression of the magnitude of the perturbation velocity V_x induced by the nacelle in principle any potential flow calculation method can be used to acceptable accuracy. Fig.2.16 contains an example of results of a simple calculation model, where the (axis-symmetrical) nacelle is replaced by a distribution of sources and sinks along its centerline. Here the source strength σ is related to the nacelle cross-sectional area distribution $S(x)$ through:

$$\sigma = U_\infty \frac{dS(x)}{dx} \tag{2.10}$$

where x is the axial coordinate, positive in downstream direction. The perturbation velocity is then calculated from:

$$V_x(r, x) = \frac{\partial \varphi}{\partial x} \tag{2.11}$$
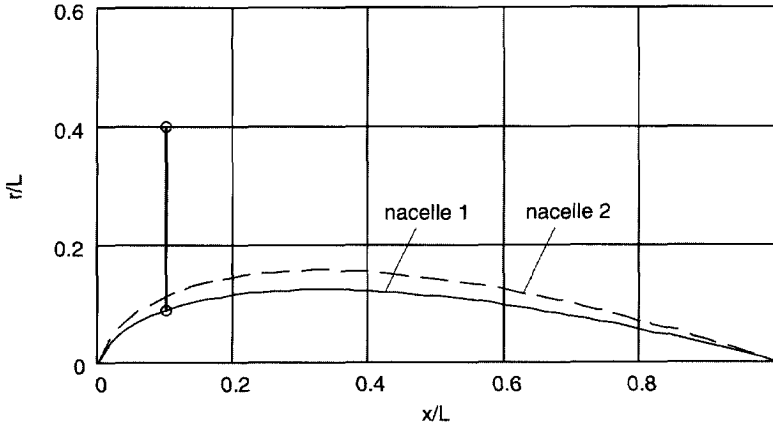
(a)
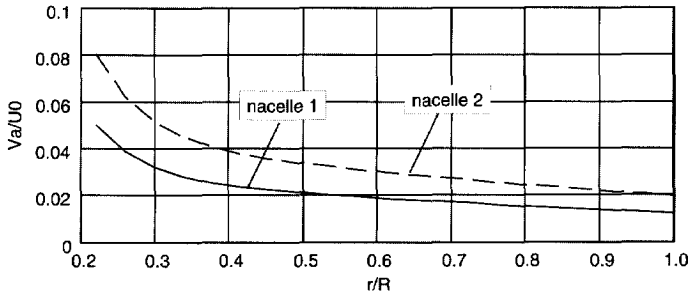
(b)

Figure 2.16: *Example of two arbitrary propeller-nacelle geometries (a) used for the calculation of the axial induced velocity profiles (b), v_a/U_∞ versus the dimensionless radius, r/R*

The perturbation potential, $\varphi(r, x)$, is found by integrating over the source distribution:

$$\varphi(r, x) = -\frac{1}{4\pi} \int_0^{L_n} \frac{\sigma(x_0)d(x_0)}{\sqrt{(x - x_0)^2 + r^2}} \tag{2.12}$$

In this equation the length of the nacelle is denoted with L_n. As can be seen small changes in the nacelle diameter lead to noticeable effects on the axial velocity distribution in the propeller plane which has considerable implications on the blade loading distribution and consequently the total propeller thrust.

When either experimental or calculated slipstream velocities for a zero degree propeller angle of attack ($\alpha_p = 0$) are used in the analysis and optimization process of a propeller-wing configuration some knowledge on the change that the angle of attack generates is needed.

Since the focus of the current research is on the interference between the propeller and the wing a detailed study of the nacelle effects on the inflow field is regarded superfluous. However, the velocities in the slipstream that influence the wing behavior are affected by the presence of the nacelle and as such the nacelle partly affects the interactive flow field. In subsequent analyses the only nacelle effect that will be taken into account is the direct adaptation of the axial flow field. Other effects like the boundary layer development over the nacelle and the nacelle-wing junction as well as the drag changes on the nacelle due to increased dynamic pressure will not be treated.

2.5.2   Wing effect on the propeller

The effect of the wing loading on the inflow field of a tractor propeller is similar to the impact of an incidence angle on an uninstalled propeller. With the non-zero angle of attack of the propeller induced by either the geometrical angle of attack or the effect of the wing, the force and velocity diagram of the propeller blade changes due to the azimuthal variation of the local blade angle of attack Fig.2.17

The only difference between the tilting of the undisturbed velocity vector (case $\alpha_p \neq 0$) and the wing upwash effect is the small local change in the induced velocity field due to the propeller disk position relative to the wing with its typical loading. This can be seen from Fig.2.18 where the effect of propeller angle of attack and a typical wing lift induced velocity perturbation is presented.

As can be seen, the induced velocity distributions for uninstalled propeller (left side) are practically the same as found for the installed propeller in the upwash field of the wing (right side).

Fig.2.19 shows the typical effect of a wing induced angle of attack on the total pressure rise over the propeller disk for four azimuthal positions: $\psi = 0°, 90°, 180°, 270°$. The positions $\psi = 90°$ and $\psi = 270°$ are respectively the downgoing and the upgoing blade position while $\psi = 0°$ and $\psi = 180°$ represent the position of the blade in the upper and lower position. In this case the wing induced velocities were obtained by performing a flow calculation with a 2-dimensional panel code on a NACA64$_2$A015 airfoil with the propeller plane at $1R$ in front of the wing.

Each of the blades that is inclined at an angle of attack to an oncoming flow generates a load which is dependent on the position of the blade in the rotation cycle. The downgoing blade experiences a load increase while the load on the upgoing
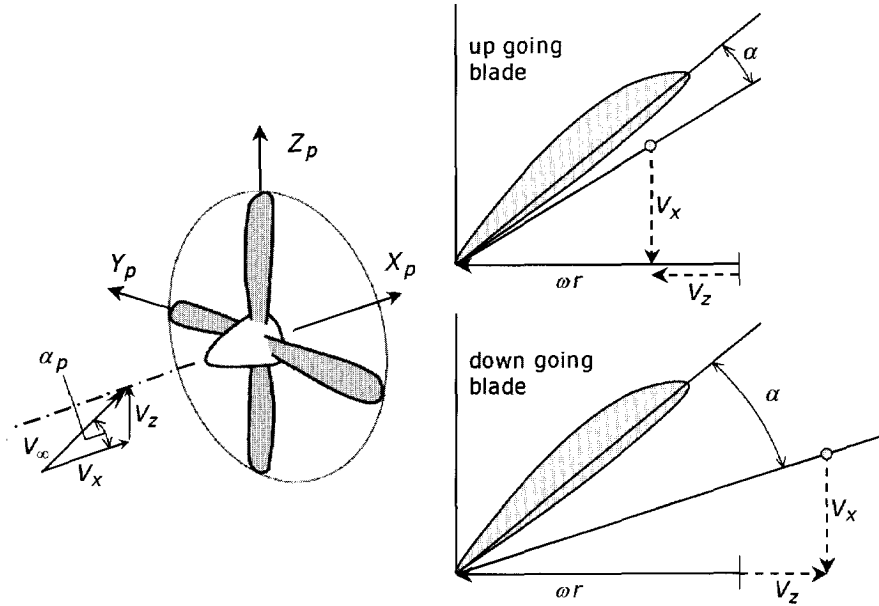
Figure 2.17: *Blade angle of attack variation due to propeller pitch angle. For positive angles of attack, α_p, the down going blade experiences a higher loading that the up going blade.*

blade is relieved. This loading change is due to changes in the angle of attack and dynamic pressure experienced by the blade. The change in the loading of the blade in the vertical position is only due to the blade sweeping motion; forward in the lower position and backward in the upper position. The time-averaged result of these effects is a force along and a moment about all 3 axes, X, Y and Z. It appears that apart from the changes in the thrust and the torque the most important forces and moments due to angle of attack are a normal force, C_{N_p} and a yawing moment,$C_{m,y}$. This situation corresponds to the case of a propeller in yaw – the result of the wing induced side wash – when a side force, C_Y and a pitching moment, $C_{m,p}$, are produced.

From earlier investigations [24, 13, 25] it is known that the resulting moment coefficients are fairly small compared to the total values of the aircraft. The moment has a magnitude of the order of the in-plane force acting at an arm given by the radius of the propeller disc. In practice the in-plane forces and moment behave significantly linearly for inclination angles up to about 20°. The upper limit of this linear behavior depends primarily on the advance ratio, J.

To calculate the in-plane forces and moments Ribner [25] used a method based
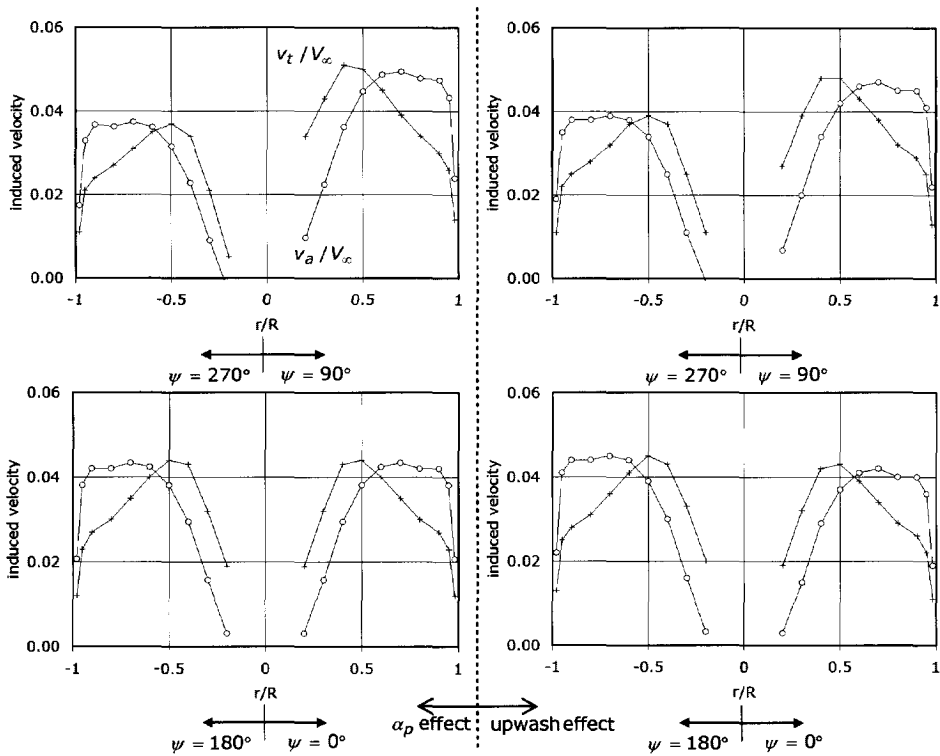
Figure 2.18: *Local induced velocity in the propeller (survey) plane of a typical tractor propeller wing configuration. Left: uninstalled propeller at $\alpha_p = 1.5°$; Right: propeller in the upwash field of the wing at the same average effective propeller angle of attack.*

on the blade element or strip theory (BEM, see Appendix A) which is applicable to small or moderate angles of attack. It was De Young [26] who extended the theory of Ribner to produce a set of simple equations that are applicable to any planform and to high angles of attack.

When the Blade Element Model is applied in the calculation of the propeller characteristics the local blade angle of attack is needed. As described in Appendix A this angle can found by superposition of the propeller and the wing induced blade angle of attack.

The effects of the propeller angle of attack were implemented in a program denoted *prop1b*, which is based on the Blade Element Model including the Prandtl tip loss factor as described in Appendix A. Results from this propeller analysis program were

psi=0 deg

psi= 27 0 deg   psi= 90 deg

psi=180 deg

View : looking upstream
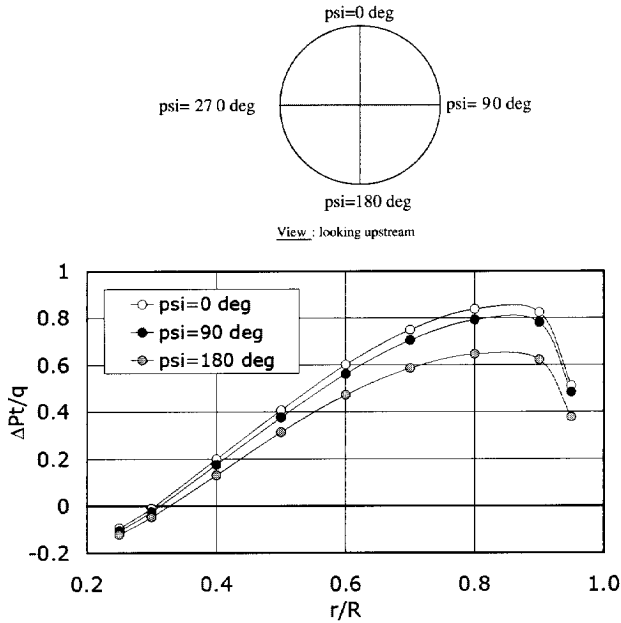
Figure 2.19: *Effect of wing induced velocities on the total pressure rise across the propeller ; "Beaver propeller" [23], positioned at $1R$ in front of a NACA 64_2A015 airfoil ; $J = 0.80$; $\beta_{0.75} = 25°$.*

used in several calculations throughout this thesis.

Some examples of the effect of propeller angle of attack on the so-called "Beaver" propeller, which was used during the experiments described in Chapter 5, are presented in Fig.2.20.

First, as Fig.2.20 indicates, the blade loading becomes dependent on the azimuthal position, as expected, while the thrust coefficient and the torque coefficient for moderate advance ratios increases slightly. This leads to a somewhat smaller propeller efficiency in the case of including wing induced velocities as can be seen in Fig.2.20d. As anticipated, the highest blade loading (highest total pressure rise) is found for the down going blade and the lowest for the up going one. As will be shown in subsequent chapters it is essential to take this slipstream asymmetry into account for accurate propeller-wing interaction calculations.
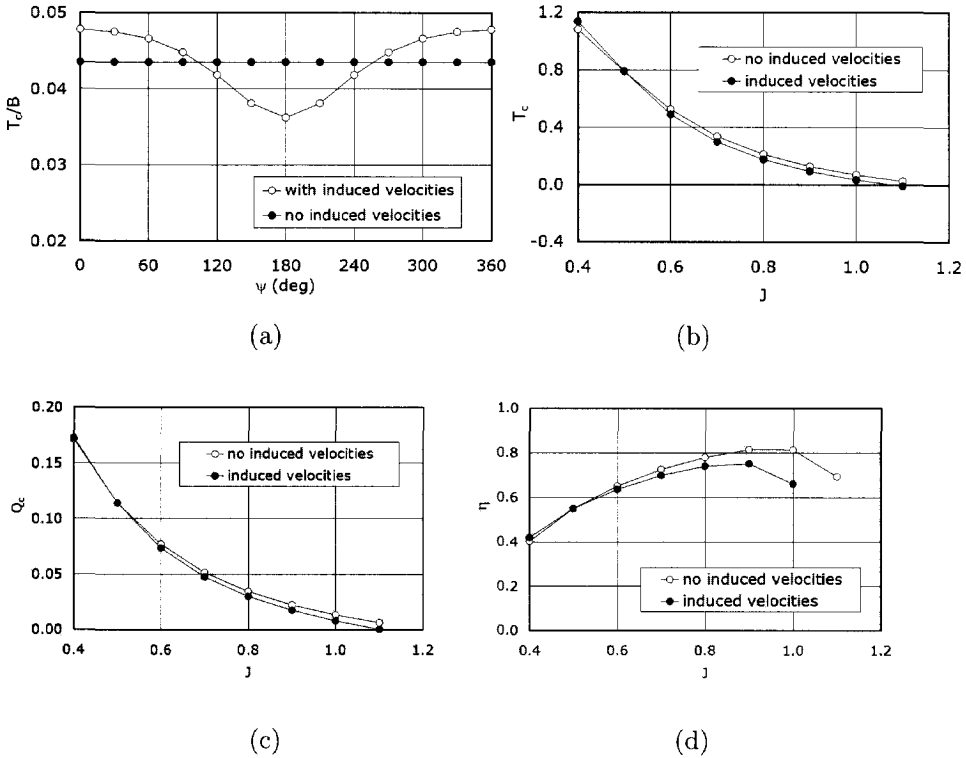
Figure 2.20: *Typical effect of wing induced angle of attack on the propeller: thrust loading per blade versus azimuthal position (a) ; thrust coefficient (b), torque coefficient (c) and the efficiency (d) versus propeller advance ratio; "Beaver" propeller; $\beta_{0.75R} = 25°$; BEM result (prop1b).*

2.6   Propeller slipstream effects on the wing

In a tractor propeller arrangement a considerable part of the wing is directly affected by the propeller slipstream. The larger the proportions of these surfaces and the higher the propeller loading (and angle of attack range), the greater the slipstream effect on the aircraft will be.

Since the slipstream consists of a swirl and an axial velocity component as well as a pressure jump, with reference to the undisturbed flow, the lift distribution and
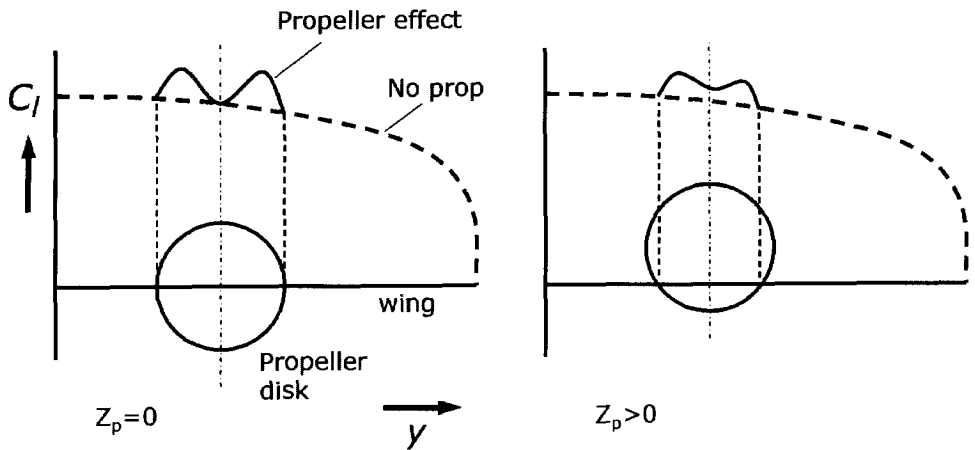
Figure 2.21: *Change in local wing lift coefficient due to the axial velocity increase in the slipstream for a neutral (z=0) and a high (z>0) vertical propeller position. The effect of the propeller outside the slipstream is intentionally left out of the picture.*

with it the overall wing coefficients, are strongly affected. As a result of the modified flow pattern due to the propeller the effects are not confined to the wing part within the slipstream but to parts outside of it as well.

The axial and the swirl velocity induced by the propeller both have their own very specific influence on the flow over the wing. The axial velocity (or alternatively the dynamic pressure) increase does not change the local lift and drag coefficient when based on the local flow conditions inside the slipstream, the local forces, however, are strongly affected. As sketched in section 2.4 the axial velocity distribution is non-uniform; it changes radically in radial direction. Depending on the vertical position of the propeller the wing cross sections are thus more or less affected with higher dynamic pressure values leading to higher values of the local lift- and drag coefficient, based on the undisturbed flow conditions. With the axial velocity distribution symmetrical with respect to the propeller thrust axis (for $\alpha_{p_{eff}} = 0$) the effect on the wing load is equal for both the inboard and outboard side of the nacelle (Fig.2.21).

Contrary to this, the effect of the swirl velocity component is anti-symmetrical. The propeller induced upwash at the upgoing blade side (UBS) introduces an angle of attack increase while the component at the downgoing blade side (DBS) leads to a decreased local wing angle of attack. With the wing at a positive angle of attack the wing generates a positive lift that results in an augmented lift at the UBS and decreased lift at the DBS.

Due to the anti-symmetrical character of the swirl velocity the rotation direction
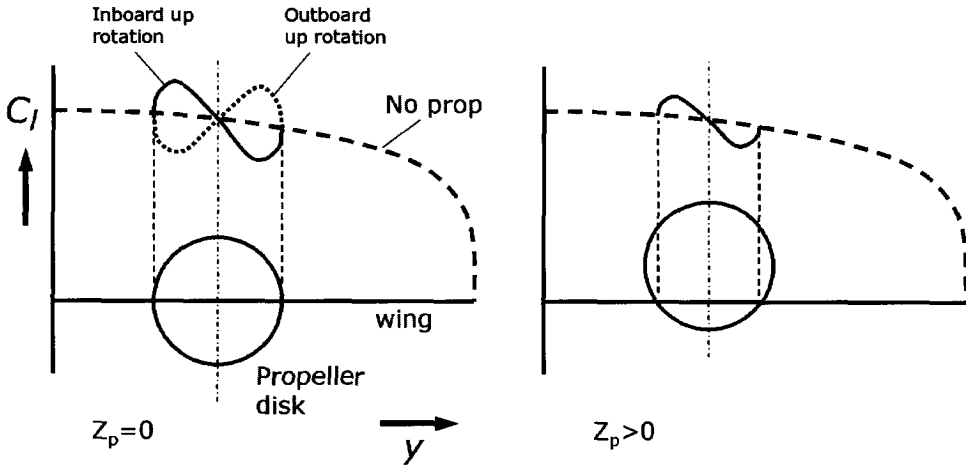
Figure 2.22: *Change in local wing lift coefficient due to the swirl velocity in the slipstream for a neutral (z=0) and a high (z>0) vertical propeller position. The effect of the propeller outside the slipstream is intentionally left out of the picture*

of propeller dominates the final shape of the spanwise wing loading distribution. A simplified sketch of the wing loading affected by the slipstream swirl velocity is depicted in 2.23.

Combining the effects of the axial and the tangential velocity components in the slipstream and taking into account changes in the loading distribution outside the slipstream domain the picture becomes more complicated. As sketched in Fig.2.23 wing regions, W-II and W-III are directly influenced by the slipstream that washes the wing. In W-II the lift effect of the propeller swirl velocity, that changes the local wing angle of attack, is enhanced by the increased dynamic pressure. Considering the inboard up rotation case, in W-III these two slipstream effects counteract each other. The result is a smaller difference between the powered and unpowered case in this region. It can be clearly seen that the propeller effect is not limited to the wing part (with a span equal to the contracted slipstream diameter) directly behind the propeller. Due to the changed wing inflow conditions generated by the propeller the loading in W-I and W-IV changes as well, both for the inboard up and outboard up running propeller. This is the result of the distorted vorticity sheet that leaves the wing.

The consequences of the propeller induced velocities on the wing can be illustrated in more detail by considering a propeller at $z_p = 0$ in front of an infinite wing (Fig.2.24) at $\alpha = 0°$.
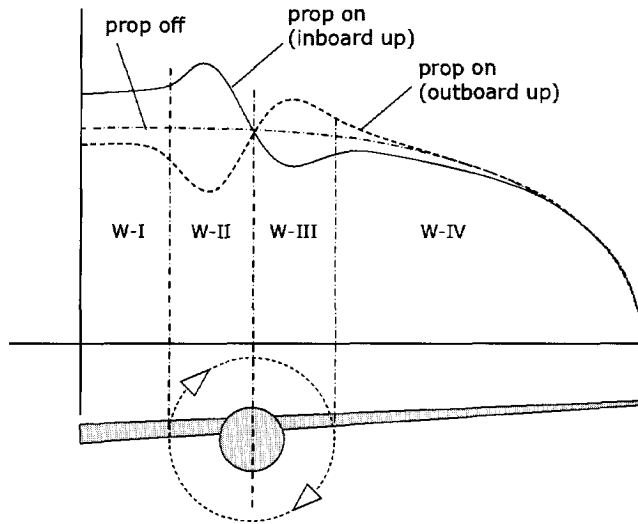
Figure 2.23: *Lift distributions in wing regions affected by the combined effect of the axial and the tangential velocity component in the slipstream*

In the propeller induced upwash region the increase in the local angle of attack tilts the local force vector forward producing components of positive lift and negative drag (increased leading edge suction). Similarly, in the downwash region negative lift and, again, negative drag is produced. The negative components of drag (thrust) can in fact be regarded as an enhancement of the propeller performance with can be interpreted as a reduction in swirl losses. For this reason, in the discussion of the propeller-wing interaction problem, the wing is said to "recover swirl". This phenomenon is comparable to the effect of stator vanes in a turbine engine.

Even with the infinite wing set at a positive angle of attack, now producing positive lift, the net effect of the propeller on the induced drag force is negative. This is due to the fact that the forward rotated forces are augmented while the backward rotated forces are somewhat attenuated. The net result on the wing lift will be positive due to the increased dynamic pressure on both sides of the propeller axis.

The main difference between the infinite wing, sketched in Fig.2.24, and a finite wing is the effect of the wing span loading distribution. In case the loading at the nacelle inboard side is bigger than the outboard side the contribution of the propeller slipstream effect will be stronger here than on the nacelle outboard side.

This means that an inboard up rotating propeller produces a performance increase while the outboard up rotating propeller would lead to some reduction in lift and increase in the net drag.
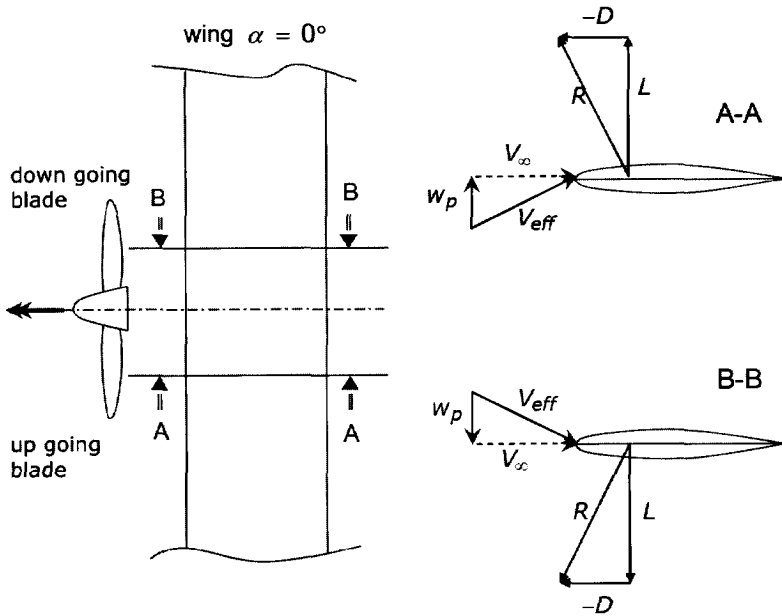
Figure 2.24: *Effect of slipstream swirl velocity on the local forces of an infinite wing at $\alpha = 0°$.*

Apparently the wing span load gradients have a strong impact on the net effect of the propeller slipstream. Since the greatest span loading gradients are found near the wing tip the effect of the propeller will be stronger there. This statement if fully justified by the calculation results presented in Chapter 6.

With the acceptance that a wing drag reduction would require the backward rotated force in the downwash region to be smaller than the forward rotated force in the upwash region it should be noticed that there is a natural tendency to this condition due to the slipstream effect itself. An interesting question, which will be discussed in Chapter 7, is whether further performance improvements can be obtained by enhancing the difference in inboard and outboard loading by appropriate local adaptation of the wing geometry like airfoil camber and twist distribution.

Another important aspect of the way the propeller slipstream influences the wing is the direct effect on the wing boundary layer. Where previous discussions were all based on the inviscid aspects of the interaction, the phenomena that occur with respect to the boundary layer require an analysis of the viscous flow characteristics.

Apart from the investigation of the overall performance benefits of the propeller slipstream interaction with the wing, also studies were conducted to investigate the

effect of the wing boundary layer and the effect of the unsteady pressure distribution [27]. Since the propeller produces an unsteady flow field where the turbulent values from the propeller impinge on the wing, it was thought that the propeller slipstream forced the wing boundary layer to transit from a laminar to a turbulent state. However, experiments using hot-wire anemometry and hot-film [28, 27] showed that in practice the wing boundary layer cycles from a laminar to a transitional turbulent state and back to laminar at the blade pass frequency. Although this phenomenon affects the local wing profile drag coefficient its presence is inevitable and as such it can not be used in a design optimization. Therefore the detailed effect of the propeller slipstream on the boundary layer transition process will not be treated in this thesis.

2.7 Swirl recovery

An important aspect in the calculation of the slipstream-induced velocities with simple models is the reduction of the rotational velocity in the slipstream due to the wing. Both experimental and numerical studies have shown that there is a significant reduction in rotation (swirl velocity) due to the presence of the wing.

Various windtunnel tests have indicated that the amount of the reduction in the rotational velocity depends on numerous factors like the propeller position relative to the wing, the power setting, the wing loading and so forth.

It should be noted that while there is some reduction in rotational velocity due to viscous effects, it is more likely that a change in the slipstream helix angle is the main cause for the reduction in the rotational velocity. In fact the reduction in the slipstream helix angle can be attributed to the wing induced upwash (in front) and downwash (behind).

At the upgoing blade side the angle of rotation is directly reduced by the augmented downwash produced by the wing. The downgoing blade side, on the other hand, experiences a reduction of the rotation angle due tot the wing induced upwash. Consequently, the wing is assumed to reduce the angle of rotation of the slipstream within the part that wash over it. The amount of helix angle reduction is dependent on local flow angle of attack and the location of the wing with respect to the propeller rotation axis. It will be shown in Chapter 7 that it is of vital importance to model swirl recovery properly to arrive at acceptable calculation results.

2.8 Effects of propeller position

A parameter that strongly affects the interaction is the position of the propeller with respect to the wing. Although we may see in subsequent sections that certain configurations lead to considerable performance benefits, it is clear that some layouts are impractical because of structural problems or maintenance complexity. A general

impression of the propeller-wing arrangement of typical twin-engined propeller aircraft is presented in Table 2.1.

Table 2.1: *Typical ranges for the propeller position on twin-engined aircraft.*

Dimension	Range
x_p/R	$0.81 \leftrightarrow 1.56$
$y_p/(b/2)$	$0.23 \leftrightarrow 0.36$
z_p/R	$-0.25 \leftrightarrow 0.42$

As we see, in all three directions x, y and z the ranges are quite limited. Although for most practical applications the propeller positions within the range given in Table 2.1 are to be investigated, analysis of some off-design layouts will be discussed as well, to investigate the limits in the performance of propeller-wing configurations.

A change in the vertical propeller position leads to a noticeable variation of both the dynamic pressure distribution and the local angle of attack due to the radial distribution of the propeller induced velocity components (see Chapter 7 and 8). Besides this, the dimension of wing part immersed in the slipstream will change. Both aspect lead to changes in the interaction effect and the performance.

The slipstream needs some time (distance behind the propeller) to develop to a more or less steady state found at several radii behind the disk. Consequently, variation of the streamwise x-position of the propeller has some (though limited) impact on the wing. In this case the static and the dynamic pressure change with x_p while the swirl velocity stays constant (Fig.2.7). As the swirl velocity has the strongest effects on the wing loading distribution, calculations reveal that the propeller-wing combination exhibits only limited sensitivity to x_p-changes. When the propeller is positioned within the range given in Table 2.1 the wing loading gradients are generally very limited. The small changes that occur are discussed in more detail in Chapter 5 and 6.

High and low propeller position

When the problem of propeller wing interaction is considered it may be beneficial to distinguish 2 special cases:

- the propeller and wing separated by a large distance; hence no interaction occurs

- the propeller and the wing in close proximity but with the wing still outside the slipstream boundary.

Selecting the latter case where the wing is not immersed in the slipstream is attractive from the point of reduced complexity of the interaction problem. Outside
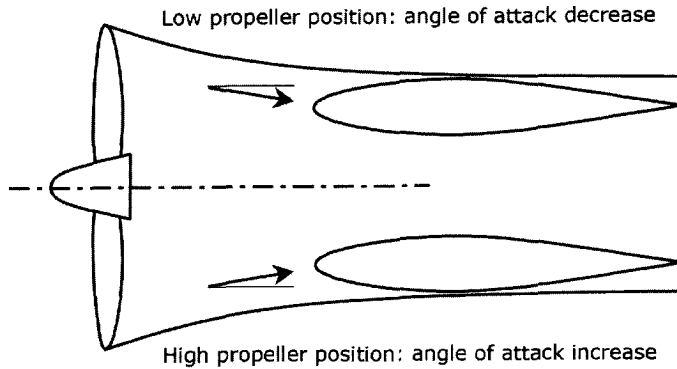
Figure 2.25: *Local wing angle of attack effect for a high and a low propeller position.*

the slipstream the changes in absolute flow velocity are so small that their effect can be neglected. Only the changes in flow direction have to be accounted for, leading to changes in the wing lift and drag that can be easily obtained. In an early experimental investigation [12] it was already found that in the case of a high propeller position, as sketched in Fig.2.25, for a given lift, both the drag and the propeller thrust are reduced compared to the case without interactions (infinite distance between the propeller and the wing). Vice versa an increase in drag and thrust is found for the low propeller position.

An explanation for these findings can simply be given based on the effect of the slipstream contraction.

In case of the high propeller position (HPP) the contraction induced flow field generates an upwash for the wing which leads to a lift increment and a lowering of the drag (the force vector is tilted-forward). For the low propeller position (LPP) the opposite effect occurs as a result of the contraction induced downwash.

Important for the estimation of the total propeller-wing performance is the fact that for the HPP an increase in the axial inflow velocity for the propeller is found due to the presence of the wing (effect of the wing suction side). The consequence now is a lower thrust of the propeller and reduced propeller efficiency. The determination of the total performance should now incorporate the reduction of the drag that, in this case, can be achieved by lowering the wing angle of attack to obtain the constant lift coefficient that is required for an aircraft in equilibrium. For the LPP the opposite reasoning can be set up.

Furthermore, the discussion on the principal effects of the interaction between the propeller and the wing can be extended by considering the flow field characteristics far downstream of the propeller-wing configuration (comparable to the well-known

Trefftz plane analysis).

First of all it may be noted that for a constant lift coefficient (we assume an equilibrium state) no change in the induced drag of the wing will occur. Hence placing the propeller in close proximity to the wing does not lead to a change in the total strength of the vorticity field far downstream. At this point an equivalent propeller is introduced that produces a slipstream with a cross area, S, and an axial velocity increase, v_s, equal to that of the undisturbed propeller. In case of the HPP the diameter of the equivalent propeller should be reduced compared to the undisturbed one because of the higher wing induced axial inflow velocity at the propeller disk location.

In case the same diameter was selected the diameter of the slipstream of the equivalent propeller would have been too high due to the increased mass flow through the disk. The axial velocity increase of the propeller should be adapted and kept constant through an appropriate change in the propeller blade setting.

With the equivalent propeller set at these conditions a thrust and efficiency equal to that of the undisturbed propeller is obtained since slipstream diameter and v_s are equal.

Following the reasoning of the wing induced drag that was unaltered when the propeller was brought close to the wing the flow field far downstream of the propeller is unaltered provided that the original undisturbed propeller is replaced by the given "equivalent" propeller.

One may now conclude that far downstream no interaction between the propeller and the wing is found since the force/energy balance is unaltered compared to the undisturbed configuration (propeller far away from the wing). This conclusion contradicts the earlier observation of mutual interaction between the propeller and the wing.

The only way to explain this apparent contradiction is to accept that the interaction manifests itself solely as an internal force.

For the airplane designer, confronted with a propeller with given diameter (not an equivalent propeller) the interesting question is to determine whether a high or a low propeller position is beneficial from the performance point of view. It was shown earlier that the equivalent propeller should have a smaller diameter than the undisturbed propeller to ensure an equal diameter of the fully developed slipstream.

Hence, leaving the diameter unaltered the mass flow through the disk is increased which, for an equal thrust, results in an increased propeller efficiency. Therefore the result for the high propeller position is an overall gain in propulsive efficiency. In an analogue way the discussion on the low propeller position leads to a lower propulsive efficiency.

To check the validity of the argumentation just discussed some sample calculations were performed with the VLM program (see Chapter 3) on a Fokker 50 like arrangement (further denoted as Model50). The propeller was located at $0.1R$ in front of the wing and calculations were performed for two vertical positions: $+1.1R$ and $-1.1R$

Table 2.2: *Effect of propeller vertical position on effective propulsive efficiency for a wing with high and low propeller position ; Model50 ; high speed case.*

z_p/R	C_L	C'_D	e	$(\eta_p)_{corr}$
+1.1	0.546	-0.01933	1.1032	0.3724
-1.1	0.517	-0.01864	0.9053	0.3405

with respect to the wing leading edge.

The results, summarized in Table 2.2, indeed reveal the highest effective propulsive efficiency for the high propeller position.

The inclined propeller

In the prediction of airplane performance it is often usual to assume that the line of thrust of the propeller is parallel to the flight path. This condition exists, of course, for only one particular angle of attack of the aircraft. For any other angle of attack, especially when climbing or flying horizontally at low speeds, the thrust line is inclined at an angle to the line of flight. Since the propeller, in general, operates in front of a nacelle/wing a considerable angle of attack at the location of the propeller may exist due to upflow generated by these aircraft parts.

When the propeller is inclined with respect to the wing reference line a non-axis symmetrical inflow field is experienced by the blades. As indicated in Appendix A it is possible to determine the resultant propeller normal forces to an acceptable accuracy by using the strip theory. However, in some cases the detailed data about the propeller characteristics, like the blade airfoil lift and drag polars are unavailable. Besides this the effect of the propeller normal force within the complete design cycle is generally needed for many flow conditions. This necessitates the development of an engineering method that produces reliable results in a fast way.

Because of the labor involved in applying the strip-theory to the calculation of the propeller normal force (even at small angles of attack), several simplified methods for calculating the normal force have been developed [25].

Based on the theory of Ribner, extended by De Young [26] a very acceptable procedure is presented in [29]. For single-rotation propellers the propeller-normal force gradient can be written as:

$$\frac{dC_N}{d\alpha_{eff}} = \frac{4.25\sigma_{eff}}{1 + 2\sigma_{eff}} \sin\left(\beta_0 + 3\right) \left[\frac{\pi J^2}{8} + \frac{3\sqrt{\frac{\pi J^2}{8}C_T}}{8\sqrt{\frac{\pi J^2}{8} + \frac{2}{3}C_T}}\right] \qquad (2.13)$$

Here β_0 is the blade pitch angle referred to the zero-lift line of the blade airfoil section at $0.75R$, J is the effective advance ratio and C_T is the propeller thrust coefficient at zero propeller inclination. The effective solidity, σ_{eff}, is given by :

$$\sigma_{eff} = \frac{4B}{3\pi}\left(\frac{\bar{c}_b}{D}\right) \tag{2.14}$$

where $\bar{c}_b$ is the average blade chord from $0.2R$ to the blade tip, given by:

$$\bar{c}_b = \frac{1}{8}\int\limits_{0.2}^{1.0} c_b d\left(\frac{r}{R}\right) \tag{2.15}$$

In most cases the thrust coefficient of the propeller needed in eq.(2.13) will be available, however, an estimate can also be made by using the empirical relation proposed by De Young:

$$C_T = \frac{4.6\sigma_{eff}\cos(\beta_0 + 5)}{1 + 3\sigma_{eff} + \left(\frac{9\sigma_{eff}}{B}\right)}\left(2.2\tan(\beta_0) - J\right) \tag{2.16}$$

Various analyses of propellers at positive angle of attack have been performed and acceptable results were found as long as the parameter restrictions as presented in Table 2.3 are maintained. Fig.2.26 shows that a good agreement is found when the data acquired with eq. (2.16) are compared with experimental values.

Table 2.3: *Parameter range for the applicability of the calculation method of ref.[29], eq. (2.13). Typical errors are within $\pm15\%$.*

Parameter	Range
Number of blades, B	$2 \leq B \leq 10$
Effective solidity, σ_{eff}/B	$0 \leq \sigma_{eff}/B \leq 0.08$
Propeller effective angle of attack, α_p	$\alpha_p \leq 20°$
Mach number, M	$M \leq 0.4$
Thrust coefficient, C_T	$C_T > 0$
Blade pitch angle, β_0	$\beta_0 \geq 5°$
Loading	low to moderate

2.9   Thrust and drag bookkeeping

In the previous sections the main aspects of propeller-wing interference have been discussed to enable insight in the possible effects on the aircraft performance through
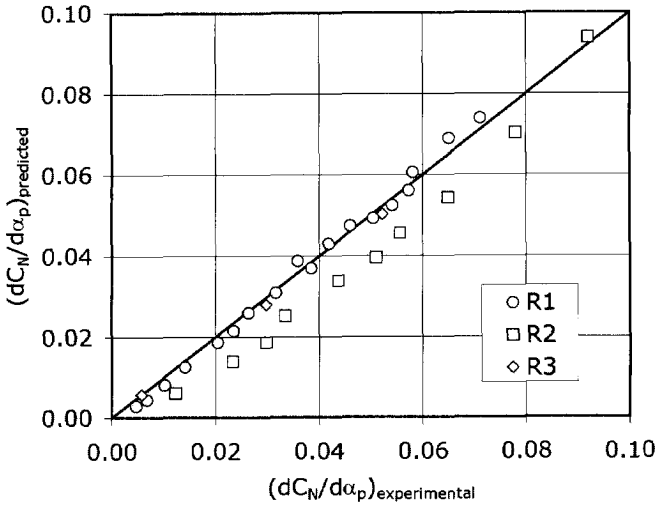
Figure 2.26: *Comparison of propeller test data for the normal force coefficient,*
C_{N_α}, *with the prediction following from eq. (2.13); R1=ref.[30],*
R2=ref.[31], R3=ref.[32].

an adaptation of the wing lift and drag.

For the purpose of aircraft performance calculations as well as the analysis of experimental data obtained in wind tunnels or flight tests an appropriate bookkeeping system of thrust and drag force is needed. The importance of such a system is twofold.

First of all it allows aircraft propeller and engine manufacturers to establish a platform of joint responsibility that can be used in discussions about estimated and real aircraft performance (design versus the full scale product). In this respect it is particularly important that a clear definition of thrust and drag is provided that is well understood by all responsible partners. Important definitions and methodologies that can be used as a guideline for this analysis are presented in Refs. [33, 34, 35, 36].

Secondly it should be appreciated that knowledge about the separate contributors to thrust and drag allow the airplane designer to optimize turbo-prop aircraft configurations. By focusing on the propeller/airframe effects that occur and the means to influence them, a more complete picture of the design space can be attained. Thus adequate choices can be made to further enhance the efficiency and handling qualities of modern turbo-prop aircraft.

Turning back to the first point: because of the importance of an adequate thrust-drag bookkeeping procedure for the purpose of separating responsibilities, some im-

portant conclusions from Ref [134] are summarized.

In Ref [134] a study is presented in which an attempt is made to determine the thrust of a turbo-prop airplane (*Swearingen Metro II*) in flight. Various methods for the measurement of engine power and propeller thrust were used. For the calculation of the propeller shaft power:

- direct measurement of the propeller shaft torque and the engine speed

- measurement of the power lever angle and the engine fuel flow

- measurement of the interstage turbine temperature and the engine speed

The propeller thrust was determined using:

- propeller shaft power combined with a propeller (calculation) model

- measured blade angles combined with a propeller (calculation) model

- measured increase in the total pressure in the slipstream

Both in the shaft power and the thrust calculations typical differences between the methods were in the order of 3%-5%. These values seem to be quite reasonable. However, as inconsistencies were found, the conclusions about the possibility to separate thrust and drag are more worrisome.

Muhammad [35] concludes that serious wing angle of attack effects on the slipstream occur which makes further investigations of propeller-wing interaction necessary. Finally the limited consistency for the different methods to determine the thrust of a turbo-prop in flight leads to the conclusion that separation of thrust and drag is only possible "to a limited degree". Keeping in mind these conclusions as well as the non-conclusive guidelines for thrust and drag bookkeeping in general ([36]) it may be argued that the performance of the aircraft in the design phase should be judged only by some definition of the "total propulsive efficiency". The definition of this efficiency has to be based on the existing knowledge of the various parameters and phenomena that contribute to thrust and drag.

Considering the second point, about the importance of thrust and drag bookkeeping for the aircraft designer some additional thoughts emerge.

If in the design process an optimization of the propeller-wing layout is considered, useful information should be available on all contributors to thrust and drag. From this standpoint, indeed a complete thrust and drag bookkeeping procedure is required as part of complete design cycle. However, in case only minor changes are expected from a design issued earlier, it may be argued that only the factors that influence the flow locally should be considered. For example, the ram drag of the air inlet is one of the factors that determine the total propulsive force but the small changes in the vertical position of the propeller are unlikely to affect the ram drag component for a

fixed propeller setting. Hence design changes can be compared without re-calculating this specific thrust-drag contributor. The same arguing can be followed for many other components of the aircraft.

Chapter 3

Simplified numerical analysis of propeller-wing configurations

3.1 Introduction

Due to the complexity of the propeller-wing interactive flow and restrictions in formulating the problem, approximations are often introduced for the numerical modelling of the interference effects.

In the preliminary design phase of an airplane mainly (semi-) empirical methods are utilized in case the general layout of the aircraft is still undefined. In the detailed design phase more sophisticated surface singularity methods like vortex lattice methods and panel methods form the basis for the fine-tuning of the aircraft design. In case further knowledge is needed regarding the flow characteristics around the aircraft, for example for the sake of more accurate aircraft drag prediction, volume based methods are employed which either solve the inviscid (Euler) or the viscous (Navier-Stokes) flow equations. The degree of complexity, the modelling effort, the calculation effort and the prediction capability of all these methods differ considerably. As a consequence the choice will be based on the required degree of accuracy and the detail of the phenomenon that the designer is interested in. In this respect all techniques ranging from approximate engineering methods to the rather complex Navier-Stokes solver are of equal importance.

A wing positioned behind a rotating propeller experiences a complex unsteady flow field. There will be a periodical impingement of the vortex wakes produced by the propeller which leads to an unsteady wing loading. A strict treatment of this unsteady problem is rather complex and laborious with respect to the velocities induced at the

location of the trailing wing. For this reason the calculation of the propeller induced velocities is often based on time averaged values. This is equivalent to the acceptance of a continuous distribution of the vorticity inside the slipstream. Thus, the numerical treatment of the problem becomes much easier since the wing is now positioned in a steady homogeneous flow field. While a clear advantage arises accepting the steady flow case, the obvious disadvantage is the fact that the unsteady loads on the wing can not be determined and the effects of propeller blade number and rotational speed are radically eliminated from the analysis. When the calculation data are used in the design process and comparison is made with time-averaged experimental data the selection of the steady case, however, is acceptable.

In the next sections the most important simplified numerical modelling techniques for the calculation of the propeller-wing interference problem will be discussed whereas in Chapter 4 the application o the Euler/Navier Stokes methods is treated. The attention is focused on the implementation of the propeller model in the specific method. For detailed information about the methods in general the reader is referred to open literature, where appropriate.

3.2   Empirical methods

For a first-order estimation of the effect of propeller on the performance of the air-craft empirical methods are efficient in the preliminary design phase, especially when windtunnel data of the configuration under consideration are unavailable.

To ensure fast response of the methods when configuration changes are made only simplified models of the configurations are used. Most methods are based on elementary momentum considerations, windtunnel data correlations and/or other relatively simple empirical methods.

One of the first methods to analyze the interaction between a propeller slipstream and a wing was presented by Smelt and Davies [37]. They used a (semi-) empirical method that provided information about the lift distribution on the lifting surfaces and the forces and moments of the entire configuration.

A more accurate method of estimating the thrust decrement and drag increment due to the interaction of propeller flow with a body (or nacelle) at zero incidence is described in ref [38]. It applies to smoothly contoured bodies with a tractor propeller at or near the nose or a pusher propeller at or near the tail and the propellers may be counter-rotating.

Jameson [39] and Fowler [40] present methods to determine the influence of the propeller on the lift and drag characteristics including various flap deflection effects while Marr [41] describes a method for analysing static longitudinal stability, based on the method of Millikan [42].

The DATCOM data sheets [43] provide a systematic summary of methods for estimating basic stability and control derivatives for any given flight condition and

configuration. These DATCOM methods are based on existing theory and/or experimental data. However, their use is restricted to approximations of the aerodynamic characteristics of individual components or based on a simple combination of different components. Although the DATCOM methods can estimate the forces and moments on both free propellers and propeller-wing combinations at low speed, their accuracy is limited and they lack the capability to study the details of the interactive flow since only the integrated aerodynamic characteristics, like total lift and drag of the configuration, are given.

3.3 Momentum theory

A possible starting-point for a simplified analysis is the application of momentum theory, similar to the method described by Kuhn [44] and Obert [45]. One obvious limitation of the usage of the momentum theory is the inability to model the swirl effects of the propeller slipstream that are important for a detailed design of the nacelle-wing layout. Nevertheless the momentum based methods are important for fast acquisition of the various aspects that play a role in the interactive flow like the influence of flap deflection a low speeds.

The method described herein assumes the power-off values of lift and longitudinal force to be known. Subsequently the power-on characteristics of the propeller-wing system are determined by only two slipstream related parameters which are dependent on the thrust coefficient.

In the next paragraphs the most important characteristics of the method will be discussed to enable a comparison with the extended prediction methods (which incorporate swirl velocities in the slipstream as well) described from section 3.4 on.

The method is applied to a propeller/wing/flap system with a tractor propeller mounted ahead of the wing Fig. 3.1.

The flow is represented by a single streamtube around the wing (index w) and separate streamtubes around every propeller (index s). At the location of the wing the cross sectional areas of the wing stream tube and the propeller streamtube are A_w $(= (\pi/4)b^2 - N_p A_s)$ and A_s respectively. The slipstreams produced by the propellers are assumed to be fully developed when they have reached the wing leading edge i.e. no further contraction takes place along the wing.

The forces, that are important for the calculation of the characteristics of the configuration, are resolved in x- and z direction both for the propeller(s) and the wing. Following the momentum theory the forces on the wing streamtube can be written as:

$$X_w = \dot{m}_w V_\infty \left((1 - f_w) \cos \varepsilon_w - 1\right)$$
$$Z_w = \dot{m}_w V_\infty \left((1 - f_w) \sin \varepsilon_w\right)$$

$$(3.1)$$

where $\dot{m}_w$ is the mass flow through A_w while f_w represents the viscous losses that
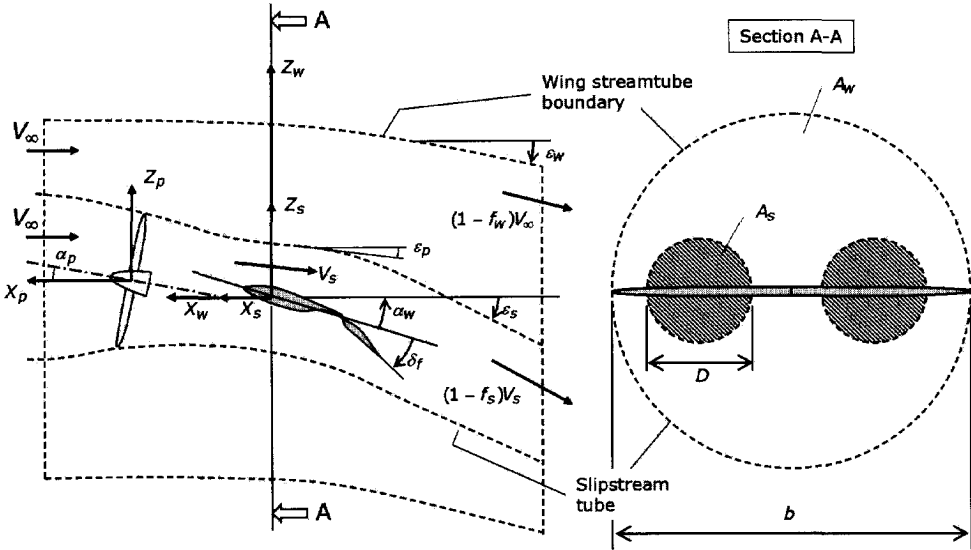
Figure 3.1: *Layout of the propeller-wing-flap system with surrounding stream-tubes used in the momentum method.*

reduce the downstream velocity vector. For the propellers (index p), in an analogue way, we find:

$$
\begin{aligned}
X_p &= N_p \dot{m}_s \left(V_s \cos \, \varepsilon_p - V_\infty \right) \\
Z_p &= N_p \dot{m}_s V_s \sin \, \varepsilon_p
\end{aligned}
\tag{3.2}
$$

while for the complete propeller streamtubes (index s) the forces of all N_p propellers may be written as:

$$
\begin{aligned}
X_p + X_s &= N_p \dot{m}_s \left((1 - f_s) \, V_s \cos \varepsilon_s - V_\infty \right) \\
Z_p + Z_s &= N_p \dot{m}_s \left(1 - f_s \right) V_s \sin \varepsilon_s
\end{aligned}
\tag{3.3}
$$

Expressions (3.1),(3.2) and (3.3) contain pairs of unknowns $((f_w, \varepsilon_w), (\varepsilon_p, \dot{m}_s), (f_s, \varepsilon_s))$ that may be determined by using experimental force measurements, as follows.

First of all for the streamtube of the wing without the slipstream present the inviscid flow case (i.e. $f_w = 0$) leads to the following expression the lift and the drag of the wing:

$$
L = \dot{m} \, \Delta V_z = \rho \frac{\pi b^2}{4} V_\infty \cdot V_\infty \sin \varepsilon_w
\tag{3.4}
$$

$$D = \dot{m} \, \Delta V_x = \frac{\rho \pi b^2}{4} V_\infty \cdot V_\infty \left(\cos \varepsilon_w - 1 \right) \tag{3.5}$$

or in dimensionless form:

$$C_L = \frac{L}{\frac{1}{2} \rho V_\infty^2 \, S} = \frac{\pi b^2}{2S} \sin \varepsilon_w \tag{3.6}$$

$$C_D = \frac{D}{\frac{1}{2} \rho V_\infty^2 \, S} = \frac{\pi b^2}{2S} \left(1 - \cos \varepsilon_w \right) \tag{3.7}$$

When viscous effects are taken into account they tend to reduce the flow velocity at the location of the wing. Therefore eq. (3.6) and (3.7) reduce to:

$$C_L = \frac{\pi}{2} A \left(1 - f_w \right) \sin \varepsilon_w \tag{3.8}$$

$$C_D = \frac{\pi}{2} A \left(1 - \left(1 - f_w \right) \cos \varepsilon_w \right) \tag{3.9}$$

where A is the wing aspect ratio, $A = b^2/S$.

Solving eq. (3.8) and (3.9) for f_w and ε_w leads to:

$$\varepsilon_w = \arctan \left[\frac{\frac{2}{\pi A} C_L}{1 - \frac{2}{\pi A} C_D} \right] \tag{3.10}$$

$$f_w = 1 - \left(\left(\frac{2}{\pi A} C_L \right)^2 + \left(1 - \frac{2}{\pi A} C_D \right)^2 \right)^{\frac{1}{2}} \tag{3.11}$$

The first pair of unknowns, (f_w, ε_w), is now determined by the measured lift and drag coefficient in the unpowered case.

Eq. (3.1) can be written in dimensionless form:

$$C_{X_w} = \frac{\dot{m}_w}{\frac{1}{2} \rho V_s N_p S_p} \frac{V_\infty}{V_s} \left(\left(1 - f_w \right) \cos \varepsilon_w - 1 \right) \tag{3.12}$$

In this case the total propeller disk area, $N_p S_p$ is chosen instead of the wing area, S, as the reference area in the denominator. This is due to fact that in the empirical approach [44] for the determination of f_s and ε_s test data at zero forward speed ($C_T = T/(q_s S_p) = 1$) are used in which the existing forces are related to the propellers only. However, Eq. (3.12) can simly be converted to the more usual form based on kinetic pressure of the free-stream, q_∞, and the wing area, S, by:

$$C_x' = \frac{C_x}{1 - C_T} \frac{N S_p}{S} \tag{3.13}$$

It should be noted that in eq.(3.12) the max flow through the wing streamtube is reduced by the flow through the propeller tubes, $\rho V_\infty N_p A_s$. Therefore:

$$\dot{m}_w = \rho V_\infty \left(\frac{\pi b^2}{4} - N_p A_s \right) \tag{3.14}$$

In the axial momentum theory of propellers uniform flow conditions area assumed across the propeller disk. Hence the area at the slipstream tube is easily found from:

$$A_s = \frac{\frac{1}{2}(V_\infty + V_s)}{V_s} S_p = \frac{1}{2}(1+r) S_p \tag{3.15}$$

where the ratio r is V_∞ / V_s. Combining eq. (3.12), (3.14) and (3.15) now leads to:

$$C_{X_w} = \left(\frac{2}{N_p} \left(\frac{b}{D} \right)^2 - (1+r) \right) r^2 \left((1 - f_w) \cos \varepsilon_w - 1 \right) \tag{3.16}$$

$$C_{Z_w} = \left(\frac{2}{N_p} \left(\frac{b}{D} \right)^2 - (1+r) \right) r^2 (1 - f_w) \sin \varepsilon_w \tag{3.17}$$

The following step is the determination of the unknowns, ε_p and $\dot{m}_s$ in eq. (3.2), which are related to the direct propeller forces. Accepting the small angles restriction, $\alpha_p \leq 12°$, the normal force component that is developed by the propeller is negligible small (this simplification will not be used in the Vortex Lattice method described further on). Hence, only the horizontal and vertical component of the thrust force has to be accounted for:

$$C_{X_p} = C_T \cos \alpha_p \tag{3.18}$$

$$C_{Z_p} = C_T \sin \alpha_p \tag{3.19}$$

The acceptance of the axial momentum theory for the propellers requires that the propeller normal force is ignored. Hence there is no change of momentum perpendicular to the propeller thrust axis. Application of momentum theory in axial direction then leads to relations for the mass flow through the slipstream tube:

$$\dot{m}_s = (1+r) \tfrac{1}{2} \rho S_p V_s \tag{3.20}$$

and the deflection angle of the slipstream tube:

$$\varepsilon_p = \left(1 - (1 - C_T)^{\frac{1}{2}} \right) \alpha_p = (1 - r) \alpha_p \tag{3.21}$$

Finally, eq. (3.3) should be evaluated further to be able to determine the unknowns f_s and ε_s. Writing in dimensionless form leads to:

$$C_{X_p} + C_{X_s} = \frac{\dot{m}_s}{\frac{1}{2}\rho V_s S_p} \left((1 - f_s) \cos \varepsilon_s - r \right) \tag{3.22}$$

$$C_{Z_p} + C_{Z_s} = \frac{\dot{m}_s}{\frac{1}{2}\rho V_s S_p} \left(1 - f_s \right) \sin \varepsilon_s \tag{3.23}$$

As with other coefficients that are used in this semi-empirical approach the force coefficients on the left hand side of (3.22) and (3.23) can be found from force measurements in X-and Z-direction:

$$C_{X_p} + C_{X_s} = (C_X - C_{X_w})_{meas} \tag{3.24}$$

$$C_{Z_p} + C_{Z_s} = (C_Z - C_{Z_w})_{meas} \tag{3.25}$$

Alternatively the components C_{X_w} and C_{Z_w} may be obtained from eq. (3.16) and eq. (3.17). Hence eq. (3.22) and (3.23) become:

$$C_{X_p} + C_{X_s} = (1 + r) \left((1 - f_s) \cos \varepsilon_s - r \right) \tag{3.26}$$

$$C_{Z_p} + C_{Z_s} = (1 + r) \left(1 - f_s \right) \sin \varepsilon_s \tag{3.27}$$

from which the value of ε_s and f_s can be obtained.

Combining eq. (3.16) and (3.26) for the horizontal component and eq. (3.17) and (3.27) for the vertical component leads to the total force coefficient for the complete propeller/wing/flap system:

$$\begin{aligned}
C_X &= C_{X_p} + C_{X_w} \\
&= (1 + r) \left((1 - f_s) \cos \varepsilon_s - r \right) + \\
&\quad \left(\frac{2}{N_p} \left(\frac{b}{D} \right)^2 - (1 + r) \right) r^2 \left((1 - f_{s_0}) \cos \varepsilon_{w_0} - 1 \right)
\end{aligned} \tag{3.28}$$

$$\begin{aligned}
C_Z &= C_{Z_p} + C_{Z_w} \\
&= (1 + r)(1 - f_s) \sin \varepsilon_s + \left(\frac{2}{N} \left(\frac{b}{D} \right)^2 - (1 + r) \right] r^2 \right) (1 - f_{s_0}) \sin \varepsilon_{s_0}
\end{aligned}$$

where the index 0 refers to the power off condition.

With eq. (3.28) the force coefficients in X- and Z-direction of the complete propeller-wing configuration can be calculateted.

Note that he empirical character of the procedure given above is partly due to the information necessary to determine the parameters $\varepsilon_s, \varepsilon_{s_0}, f_s$ and f_{s_0}. The slipstream deflection angle ε_{s_0} and the viscous loss parameter in the power-off case can be determined from eq. (3.10) and (3.11) by using the power-off lift coefficient C_{L_0} and the power-off drag coefficient C_{D_0}.

The estimation of ε_s and f_s for the power-on condition, however, requires a more extensive procedure that relies on empirical relations based on experimental wind tunnel data. Parameters that were found to affect the value of ε_s and f_s are:

- the propeller position and angle of incidence

- the nacelle dimension

- the flap deflection and the flap chord relative to the wing chord which determine the so-called flap the turning effectiveness [13].

- the flap cut-out dimension within the area washed by the slipstream

Chappel et al [38] provides detailed procedures to estimate the effect of these parameters.

The method sketched above provides the separate estimation of forces on the propeller and on the nacelle/wing/flap provided the flow is fully-attached. The accuracy of the method for the predictions of the lift and longitudinal force on the nacelle/wing/flap system is expected to be within 10 and 15 per cent respectively.

Looking at the relations in (3.28) we see that two main effects determine the total lift and drag of the propeller wing combination: the axial velocity increase in the slipstream and its development in streamwise direction combined with the deflection of the streamtubes of the wing and the propeller. As stated before this means that no effect of the swirl velocity is present in the model. It is known from practice, however, that for zero to small flap deflections the total performance of the propeller-wing configuration is affected by the form of the swirl distribution. This is due to the fact that under these conditions the slipstream boundary is very well preserved [46] whereas for moderate to high flap deflection angles the slipstream velocity profiles are completely distorted. Thus the deflection angles induce the most prominent effect on the propeller-wing interactive flow field when flaps are deflected. In the cruise condition the deflection angles of the flow are relatively small which requires an enhanced prediction accuracy to be able to find small effects on the lift and the drag. Consequently the semi-empirical method presented here is best suited to cases with moderately large flap deflections, as found during take-off and landing.

With these restrictions the momentum method may fail in the accurate prediction of propeller-wing performance in the (less complex) cruise condition. As will be discussed in subsequent sections more elaborate calculation methods are available for the cruise phase of the aircraft.

3.4 Vortex lattice method

3.4.1 Background

Although their region of application and absolute accuracy is limited, Vortex lattice Methods (VLM), are still widely used for estimating aircraft aerodynamic characteristics. They have been incorporated in conceptual airplane design to predict the configuration neutral point, lift-curve slope and lifting surface interaction. Limited to subsonic flight speeds, this computational approach is better than using semi-empirical engineering methods as described in section 3.3 and [43] in that unconventional geometric arrangements can be accommodated easily and, important for this research, the implementation of propeller slipstream can be performed in a rather straightforward manner. Since the VLM is based on potential flow theory, its validity is restricted to the linear aerodynamics region, and hence it is principally only valid in the low-angle of attack flight regime (cruise). Furthermore, it does not account for viscous effects nor for leading-edge vortex lift effects. Nevertheless Mach number effects in subcritical flow can be accounted for using the Prandtl-Glauert correction.

Various references are available that describe the theory of the vortex lattice technique in detail [47, 48, 49]. Therefore the description of the form used in this thesis is limited to the aspects needed to model the propeller-wing interaction problem only. Many variations of the vortex lattice method have been developed. Some examples of the application of the VLM-techniques for the purpose of analyzing propeller-wing interaction can be found in [50] and [51].

The VLM scheme used in this study is based on the simplification of the wing vortex system modeled as a series of horseshoe vortices, as illustrated in 6.3.6. The wing thickness is neglected which results in the inability to find accurate values of the chordwise pressure distribution.

The wing is modelled by dividing the planform up into a lattice of quadrilateral panels, and a horseshoe vortex is put on each panel. The bound vortex of the horseshoe vortex is put on the 1/4 chord element line of each panel, in line with the Prandtl lifting line theory, while the control point on the 3/4 chord point of each panel is located at the midpoint in the spanwise direction. An important assumption for the further analysis of the vortex induced velocities at the control point is the fact that the wake is assumed to be flat and lying in the plane of the wing at $z = 0$. This constraint is equivalent to the acceptance of a wake that is not completely force free. Numerical investigations [52], however, have shown that this restriction in general leads to satisfactory lift and induced drag values for wing having moderate to high aspect ratios (say $A > 6$).

The finite number of individual horseshoe vortices that are placed in trapezoidal panels in fact approximate the continuous distribution of vorticity that leaves the wing surface.

The trailing vortices normally follow a curved path when they leave the wing
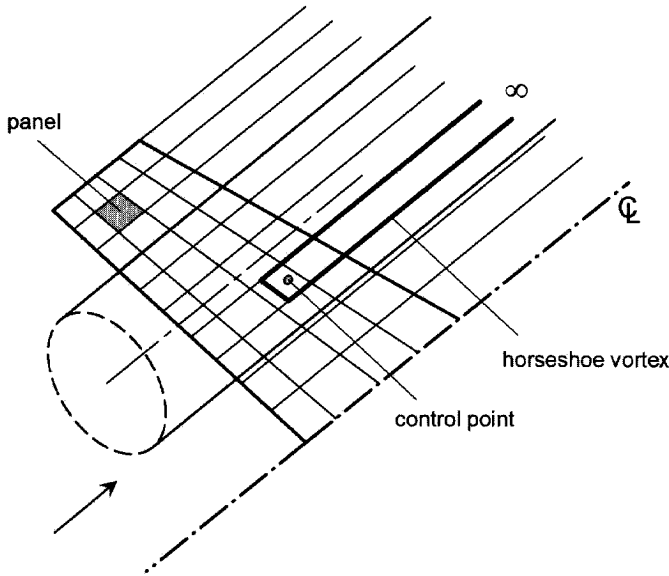
Figure 3.2: *VLM-layout representing the lifting wing behind a propeller. The horseshoe vortex of one panel only was sketched.*

due to the downwash that is the result of positive lift. This curvature is certainly found when a propeller slipstream interacts with the wing vortex sheet. However, for many engineering applications an acceptable accuracy may be obtained assuming the trailing vortex filament to be extending to infinity either parallel to the free stream or parallel to the wing stream-wise axis (x-axis). By selecting the latter direction the calculations become more simplified since the influence coefficient matrix then becomes independent of the wing angle of attack.

To obtain the aerodynamic characteristics, the strengths of each of the horseshoe vortices must be found so that the vector sum of their induced velocity and the free-stream contribution at each control point satisfies the boundary condition of a zero normal velocity component. The induced velocity at a point due to a straight line segment of a vortex filament is given by the Biot-Savart Law.

After solving a system of equations for the vortex strengths they can then be integrated over the surface to obtain the forces and moments.

Is should be noted here that one of the major drawbacks of VLM-technique is its inherent failure at the wing leading edge and the tip were thickness effects are substantial. The problem is in fact the inability of the method to reasonably calculate

the local pressure distribution; the total (and local) forces, however, are predicted to a quite acceptable level.

Although this method constitutes a rather crude model of the real flow around the wing, its simplicity allows some interesting analyses to be performed. The reduced calculation time that is typical for the method allows a quick survey of various configuration layouts.

3.4.2 Propeller effect

The effect of the propeller on the wing loading characteristics is based on the fact that at the control point position an additional velocity vector, V_p, induced by the slipstream is introduced. The differences between earlier VLM-codes, like the one suggested by Marreta et al[51], is typically found in the way these additional velocity components are calculated. In most cases, found in open literature, only a one-way interaction is implemented regarding, e.g. only the propeller effect on the wing (further denoted as single-interaction-mode or SIM) is modeled.

The method presented in this thesis employs a full interaction allowing the wing effect on the propeller as well (full-interaction-mode or FIM).

The various techniques that may be utilized for the calculation of the propeller slipstream induced velocity vector, V_p, are treated in Appendix A. Hence, the description of the VLM method here is restricted to the principal effect of the propeller.

When the VLM algorithm is set up the influence that each horseshoe vortex with index n has on the velocity induced in control point indexed m leads to an expression that gives the total velocity vector due to the wing bound vorticity and the vorticity in the trailing wake. If the model is set with $2N$ vortices the total induced velocity at the control point m then becomes:

$$V_m = \sum_{n=1}^{2N} V_{m,n} = \sum_{n=1}^{2N} C_{m,n} \Gamma_n \qquad (3.29)$$

The $m \times n$ matrix C contains the influence coefficients which solely depend on the geometry of the wing and wake model [48]. To compute the strength of all vortices, Γ_n, the boundary condition of flow tangency at the control should be implemented. This means that the normal component of the free stream velocity balances the induced velocity normal to the wing.

To incorporate the propeller slipstream effect at this point an additional velocity, $\overline{V_p} = (u_p, v_p, w_p)^T$, is added to the free stream velocity at the control points. Hence the total inflow velocity vector becomes:

$$\overline{V_{tot)}} = \overline{V_\infty} + \overline{V_m} + \overline{V_p} \qquad (3.30)$$

Assuming a zero yaw angle, the free stream velocity is given by:

$$\overline{V_\infty} = (V_\infty \cos \alpha)\bar{i} + (V_\infty \sin \alpha)\bar{k} \qquad (3.31)$$

Hence the total velocity at control point m is given by:

$$\overline{V_m} = (V_\infty \cos \alpha + u_{m_i} + u_{m_p})\bar{i} + (v_{m_i} + v_{m_p})\bar{j} + (V_\infty \sin \alpha + w_{m_i} + w_{m_p})\bar{k} \quad (3.32)$$

If the wing surface geometry is described by :

$$G(x, y, z) = 0 \quad (3.33)$$

then the zero normal velocity boundary condition can be written as:

$$\overline{V} \cdot \frac{\overline{\nabla G}}{|\overline{\nabla G}|} = \overline{V} \cdot \overline{\nabla}G = 0 \quad (3.34)$$

This is the general expression that can be used to solve for the unknown circulation. It is complete, insofar, as to contain the effect of the angle of attack as well as the propeller effect. If the surface is in the $x - y$ plane, a simpler form can be obtained. In this case the description of the surface becomes $z = f(x, y)$ and:

$$G(x, y, z) = z - g(x, y) = 0 \quad (3.35)$$

The gradient of G becomes:

$$\frac{\partial G}{\partial x} = -\frac{\partial g}{\partial x}, \quad \frac{\partial G}{\partial y} = -\frac{\partial g}{\partial y}, \quad \frac{\partial G}{\partial z} = -1 \quad (3.36)$$

Substituting this in the equation for the boundary condition leads to:

$$\sum_{n=1}^{2N} \left(C_{m,n_k} - \frac{\partial g}{\partial x}C_{m,n_i} - \frac{\partial g}{\partial y}C_{m,n_j} \right)\Gamma_n = \\ V_\infty \left(\cos \alpha \frac{\partial g}{\partial x} - \sin \alpha \right) + u_{m_p}\frac{\partial g}{\partial x} + v_{m_p}\frac{\partial g}{\partial y} - w_{m_p} \quad (3.37)$$

Now consider a simple planar surface without dihedral and apply the small angles approximation. Then eq. (3.37) reduces to:

$$\sum_{n=1}^{2N} C_{m,n_k}\frac{\Gamma_n}{V_\infty} = \left(\frac{\partial g}{\partial x} - \alpha \right)_m + u_{m_p}\left(\frac{\partial g}{\partial x} \right)_m - w_{m_p} \quad (3.38)$$

This system of linear equations can be solved with standard techniques.

The velocity contribution of the propeller slipstream as given in eq. (3.38) is required both on the lattice elements inside the slipstream tube and outside the slipstream tube since the local flow angles outside the slipstream are changed by the contraction of the slipstream tube. For most VLM models that were published up till now, however, this adaptation outside the slipstream tube was neglected. It will

be shown that this leads to erroneous results when extreme positions of the propeller relative to the wing, like an over-the-wing arrangement are selected.

Once the circulation strength is known the local forces acting on the wing panels can be calculated and subsequently the total lift and induced drag force.

The local lift coefficient, at spanwise location k, is found from:

$$C_{l_k} = \frac{2}{U_\infty c_k} \left(1 + \frac{u_{p_k}}{U_\infty} \right) \Gamma_k \tag{3.39}$$

Summation of the local lift coefficient over the intervals $\Delta y_k = y_{k+1} - y_k$ leads to the wing lift coefficient:

$$C_L = \frac{2 \sum\limits_{k=1}^{2N} \Gamma_k \left(U_\infty + u_{P_k} \right) \Delta y_k}{U_\infty^2 S} \tag{3.40}$$

Once the wing loading is known the local induced angle of attack due to the trailing vortex system and the propeller slipstream can be calculated. Combined with the local lift coefficient the induced drag coefficient is found:

$$C_{D_i} = \frac{1}{S} \sum_{k=1}^{2N} C_{l_k} c_k \alpha_{i_k} \Delta y_k \tag{3.41}$$

where α_{i_k} is the local induced angle of attack as given by:

$$\alpha_{ik} = \frac{-w_k - w_{p_k}}{U_\infty} \tag{3.42}$$

The upwash velocity, w_{p_k}, is given by the propeller slipstream model (Appendix A) while the upwash velocity due to the trailing vortex system is simply found from the Biot-Savart relation:

$$w_k = -\sum_{k=1}^{2N} \frac{1}{4\pi} \frac{\Delta \Gamma_j}{(y_k - y_j)} \quad \text{for } j = 1, 2N \tag{3.43}$$

The VLM-model strictly applies to the inviscid case which means that the profile drag coefficient must be obtained separately. An acceptable approach is to use a function $C_{d_p} = f(\alpha)$ for the specific airfoil section as an input. Since the local angle of attack of all spanwise stations is known from the VLM calculation the profile drag is found from a summation over the wing:

$$C_{Dp} = \frac{1}{S} \sum_{k=1}^{2N} C_{d_{p_k}} \left(1 + \frac{u_{p_k}}{U_\infty} \right)^2 c_k \Delta y_k \tag{3.44}$$

The total coefficients of the propeller-wing configuration can now be calculated with:

$$
\begin{aligned}
C_{L_{tot}} &= C_{L_w} + \Delta C_{L_p} \\
C_{D_{tot}} &= C_{D_i} + C_{D_p} + \Delta C_{D_p}
\end{aligned}
\tag{3.45}
$$

where ΔC_{L_p} and ΔC_{D_p} are respectively the direct lift and the drag contribution of the primary propeller forces (thrust and normal force):

$$
\begin{aligned}
\Delta C_{L_p} &= \frac{S_p}{S} T_c' \sin\left(\alpha_{p_{ref}}\right) + \frac{S_p}{S} C_{N_p} \cos\left(\alpha_{p_{ref}}\right) \\
\Delta C_{D_p} &= -\frac{S_p}{S} T_c' \cos\left(\alpha_{p_{ref}}\right) + \frac{S_p}{S} C_{N_p} \sin\left(\alpha_{p_{ref}}\right)
\end{aligned}
\tag{3.46}
$$

The normal force coefficient is found from the linear relation $C_{N_p} = C_{N_\alpha} \alpha_{p_{eff}}$ (see Appendix A) for which the effective aerodynamic angle of attack of the propeller is required:

$$
\alpha_{p_{eff}} = \alpha_{fus} + \alpha_{prop} + \alpha_{upflow}
\tag{3.47}
$$

This $\alpha_{p_{eff}}$ is composed by contributions of: the fuselage angle of attack (α_{fus}), the propeller incidence angle with respect to the fuselage reference line (α_{prop}) and the upflow angle produced by the wing (α_{upflow}).

The basic VLM-method which incorporates the propeller effect can be extended with the influence of flap deflection and the contribution of the nacelles and the fuselage to the wing loading.

To be able to judge the prediction capabilities for the cruise condition of typical turbo-prop designs, the momentum method and the VLM-method, as described above, are compared. Fig. 3.3 contains some calculation results for a Fokker 50 propeller-wing model (further denoted Model50) at 2 thrust coefficients: a rather low value of $T_c = 0.046$ and a moderate value of $T_c = 0.650$. The calculations were performed for a constant value of the wing angle of the attack of $\alpha = 3.3°$.

The agreement between the VLM-method and the simple momentum theory is reasonable for the low thrust coefficient (Fig. 3.3a) but unacceptable differences are found when the higher thrust case (Fig. 3.3b) is considered. The fact that the propulsion effect on the lift and the drag coefficient is underestimated by the momentum method is caused by the inability of the method to incorporate the swirl component in the slipstream. A negative side effect of the application of the momentum method is that it requires the input of prop-off lift and drag values of both the configurations with flaps deployed and retracted.

The VLM-method directly calculates the required characteristics based on geometrical properties and a swirl component is applied in the BEM-extension of the method. Hence it is expected to deliver more accurate data in case of small angles of attack and low thrust coefficients which are typically found in the cruise condition of the aircraft.
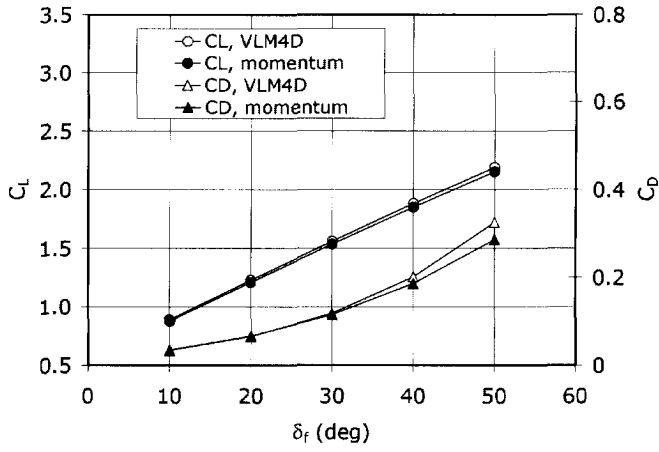
(a)
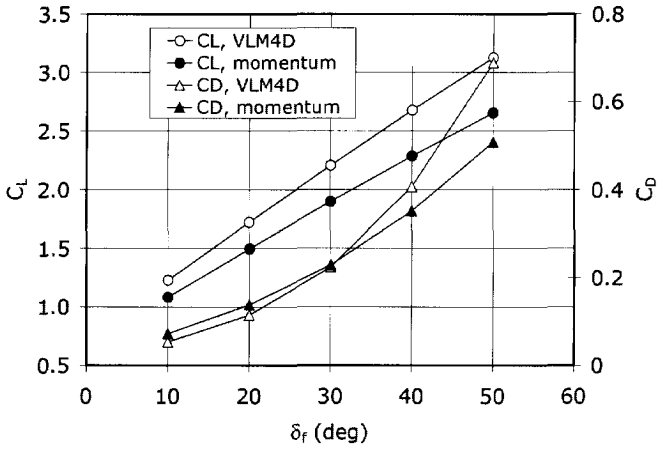
(b)

Figure 3.3: *Comparison of the lift and drag coefficient versus flaps angle cal-culated with the VLM-method and the "momentum" method for a Fokker 50 propeller-wing configuration; prop on ; (a) $T_c = 0.046$; (b) $T_c = 0.650$.*

3.5   Surface singularity method

Along with the description of the VLM-technique for the calculation of the propeller
wing flow field some restrictions of this simplified approach became apparent. The
strongest limitation of the method is the absence of modeling the thickness effect of
both the wing and the nacelles. Considering the flow in chord wise direction this
restriction manifests itself by producing an unrealistic peaky pressure distribution.
The first step to overcome this problem is to cover the actual surface of the aircraft
with a singularity distribution, instead of a reference (camber) surface as used in
VLM-modeling.

The computation technique that incorporates the thickness effect by applying
singularities at the surface is referred to as the panel method. Numerous versions
and implementations are available both applied for research and design purposes and
extensive descriptions are presented in open literature [53, 54, 47]. For a detailed
description of the underlying theory the reader is referred to [49] and many other
sources.

With the vast amount of information available, a general and extensive description
of the panel-method technique is felt overdone and is not incorporated here. However,
taking into account the scope if this study, the implementation of propeller effects in
the panel method will be discussed in subsequent paragraphs of this thesis.

In order to predict the propeller effects on the aircraft performance many attempts
[55, 56, 57] have been made to include the propeller in the panel methods. The
different approaches typically vary in the way the propeller interacts with the other
aircraft parts (SIM or FIM) and the modeling to the propeller itself (time-averaged
effect versus full propeller blade modeling leading to an unsteady analysis).

3.5.1   Summary of panel method technique

To understand the pros and cons of the various techniques that are available to in-
corporate the propeller effect in the panel-code it is beneficial to summarize the basis
equations that are influenced by the propulsion effect.

Panel methods are used for the solution of the linearized potential equation:

$$\left(1 - M_\infty^2\right) \varphi_{xx} + \varphi_{yy} + \varphi_{zz} = 0 \tag{3.48}$$

where φ is the perturbation potential representing first order perturbations with re-
spect to the free stream. The following simplifications of the flow apply:

- inviscid flow

- irrotational flow except for compact regions with vorticity (wakes are formed by
  infinitesimally thin vortex sheets)

- small perturbations allowing subcritical compressible flow (no appearance of shocks)

Eq. (3.48) describes the potential and hence the velocity distribution in the space around the aircraft. To solve this equation, boundary conditions must be implemented. These boundary conditions should be selected such as to obtain a mathematically well-posed problem, i.e. lead to a solution that exists and is physically relevant, is unique and depends smoothly on the boundary conditions. As was sketched in eq.(3.38) of the VLM-technique, it is the adaptation of the boundary conditions that takes care of the propeller slipstream effect in the flow calculation.

Using Green's third identity the solution of the potential-flow problem can be obtained using a surface integral representation for the perturbation potential, [49].

To represent the presence of a body (wing, fuselage etc.) with volume V and surface S_b in the flow the boundary condition should be set such that the body becomes a stream surface. Therefore the normal velocity should become zero:

$$\left(\overline{V_\infty} + \nabla\varphi\right).\overline{n} = 0 \tag{3.49}$$

In eq. (3.49), known as the Neumann boundary condition, n represents the outward directed normal vector on the surface. An additional boundary condition is formed by the fact that the disturbance due to the presence of the body should diminish far away form the body:

$$\nabla\varphi = 0 \qquad |\overline{x_p}| \rightarrow \infty \tag{3.50}$$

where $\overline{x_p}$ is the position vector of an arbitrary point P in space.

An alternative formulation of the boundary condition, that satisfies the Neumann condition indirectly, is the Dirichlet boundary condition which prescribes zero perturbation inside the body with volume V:

$$\varphi = 0 \qquad \text{inside } V \tag{3.51}$$

As indicated, eq. (3.48) assumes inviscid flow which prevents the development of wakes leaving the body that are the result of viscosity. Hence a wake (and a propeller slipstream) must be introduced and modeled explicitly. In the panel method a wake is assumed to form a infinitely thin stream surface denoted S_w. To fix the vorticity strength of the vortex sheet leaving the wing, the Kutta-Joukowsky condition, which requires the velocity at the trailing edge of lifting surface to be finite, is applied.

Since the wake is unable to sustain aerodynamic forces the wake surface is a stream surface and the static pressure on both sides must be equal.

Due to these conditions the wake position is not known a priori and is calculated as part of the solution. This problem is non-linear and difficult to solve. In most cases a sufficient acceptable solution, however, is obtained by explicitly describing the position of the wake. In general the direction of the near wake is taken parallel to the trailing edge bisector.

To find a solution of eq. (3.48) the surface is covered with 2 types of surface singularities: a source and a doublet distribution denoted by $\sigma\left(\xi, \eta\right)$ and $\mu\left(\xi, \eta\right)$ respectively. The latter is needed to be able to produce lift.

With the boundary conditions applied correctly the solution of eq. (3.48) leads to the velocity potential at arbitrary point P in space:

$$\varphi\left(x, y, z\right) = \iint\limits_{s} \left(\kappa_1\left(\sigma\right) + \kappa_2\left(\mu\right)\right) dS \tag{3.52}$$

Where $\kappa_1\left(\sigma\right)$ and $\kappa_2\left(\mu\right)$ represent functions that describe the velocity potential of a surface source and doublet distribution respectively.

Once $\varphi\left(x, y, z\right)$ is found the velocity perturbation distribution on the surface can be found from $\overline{u} = \nabla\varphi$

The calculation of the forces acting on the body is performed in a straightforward manor. With the pressure coefficient defined as:

$$c_p = \frac{p - p_\infty}{\frac{1}{2}\rho_\infty \left|u\right|^2} \tag{3.53}$$

application of the isentropic pressure relation yields:

$$c_p = \frac{2}{\gamma M_\infty^2}\left(\left[1 + \frac{\gamma - 1}{2}M_\infty^2\left(1 - \left(\frac{\left|u\right|}{\left|U_\infty\right|}\right)^2\right)\right]^{\frac{\gamma}{\gamma - 1}} - 1\right) \tag{3.54}$$

Hence the local pressure is directly given by the local velocity vector. The forces and moments can be determined by selecting one of the following methods:

- near field method where the pressures are integrated over all relevant surfaces

- far field approach, known as the Trefftz plane analysis.

For the details of these methods the reader is again referred to open literature on panel methods. The following discussion is focused on the application of propeller flow in the panel method.

3.5.2   Propeller-slipstream envelope model

With the acceptance of an infinite number of helical vortex wakes originating from the disk edge the entire space inside the slipstream is filled with vorticity. Although it is in principle possible to model this with a panel method approach, a simplification can be made here.

Experiments [58] have indicated that most of the vorticity is concentrated at the outer edge of the slipstream. For the current model it is therefore assumed that the
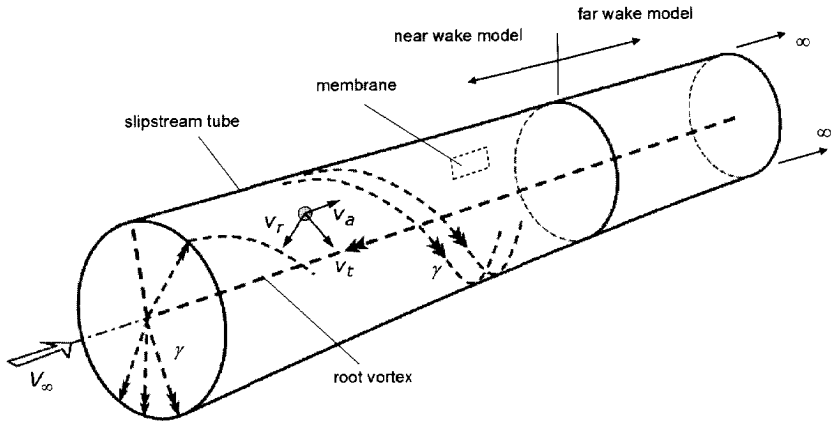
Figure 3.4: *Slipstream tube model used for application in panel methods [56, 55]*

wake rolls up immediately behind the propeller such that the vorticity produced by the propeller blades is concentrated in a thin layer connected to the disk edge and enveloping the slipstream (see Fig. 3.4).

By compacting all the vorticity of the slipstream in the slipstream outer edge the slipstream tube is in fact covered with a continuous distribution of helical shaped vortex lines.

To simplify the problem further the helicoidal vortex sheet can be replaced by two superimposed continuous distributions of vorticity. One distribution consists of axial vorticity. i.e. parallel to the axis of rotation. The other vorticity distribution is located on the same cylindrical surface but directed in planes normal to the slipstream centre line.

The slipstream envelope thus generated may be thought of as the wake of a wing having a closed cylindrical shape and enclosing a region with an energy level that differs from that of the undisturbed outer flow.

The propeller in this model is the generator of the changed energy level producing vortex sheets as sketched above. In fact the model is comparable to the actuator disk model as discussed by Glauert [59] and Horlock [60]. The actuator disk generates the required jump in circumferential (tangential) direction while the axial and the radial velocities are continuous across the disk. To generate the jumps in tangential direction the disk is covered with radial vortex lines.

The vorticity is constant in radial direction and it is continued across the edge of the disk into the cylindrical enveloping vortex sheet. To satisfy the Helmholtz criterion that requires that the vortex lines are closed on themselves at the root side of the propeller blades the distributed vorticity is concentrated in a discrete line vortex

extending downstream (see 3.5.3).

The location of the root vortex is not fixed by the solution procedure. However, the most realistic position would be on the slipstream centre line, thus preventing undesirable interference with other parts like the nacelle and the wing.

3.5.3   Mathematical aspects of the slipstream tube model

The propeller disk

The law for the conservation of energy along a streamline in an inviscid adiabatic flow reads:

$$c_p T + \frac{1}{2} V^2 = H = \text{const} \tag{3.55}$$

Applied between location 1 just in front and location 2 directly behind the propeller disk yields:

$$c_p T_1 + \frac{1}{2} \left(V_{a_1}^2 + V_{t_1}^2 + V_{r_1}^2 \right) = c_p T_2 + \frac{1}{2} \left(V_{a_2}^2 + V_{t_2}^2 + V_{r_2}^2 \right) - \Delta H \tag{3.56}$$

where ΔH is the total enthalpy increase inside the slipstream due to the action of the propeller.

Employing eq. (3.56) at radial position r, in a coordinate system moving with the propeller blades (index rot), there is no increase in the total enthalpy because the propeller performs no work in this system. Moreover the axial and the radial velocity components are unchanged by this transformation and $(V_t)_{rot} = (V_t)_{fixed} - \Omega r$. Then eq. (3.56) becomes:

$$c_p T_1 + \frac{1}{2} \left(V_{a_1}^2 + (V_{t_1} - \Omega r)^2 + V_{r_1}^2 \right) = c_p T_2 + \frac{1}{2} \left(V_{a_2}^2 + (V_{t_2} - \Omega r)^2 + V_{r_2}^2 \right) \tag{3.57}$$

or:

$$c_p (T_2 - T_1) + \frac{1}{2} \left(V_{a_2}^2 - V_{a_1}^2 + V_{r_2}^2 - V_{r_1}^2 + V_{t_2}^2 - V_{t_1}^2 - 2\Omega r (V_{t_2} - V_{t_1}) \right) = 0 \tag{3.58}$$

Combining this with eq. (3.56) we may conclude that:

$$-\Omega r (V_{t_2} - V_{t_1}) = -\Delta H \tag{3.59}$$

or:

$$(V_{t_2} - V_{t_1}) = \frac{\Delta H}{\Omega r} \tag{3.60}$$

Hence the jump in the tangential velocity component is given by the total enthalpy jump (or alternatively the total pressure jump) and the rotational speed of the propeller (or alternatively the advance ratio). The jump in the tangential velocity at the

propeller disk can be related to a doublet distribution, $\mu(s)$, or a vorticity distribution $\gamma(s)$.

When a doublet singularity distribution, μ, is applied on the actuator disk surface the tangential (swirl) velocity for a coordinate s along a circular contour at radius r becomes:

$$V_t(s, 0\pm) = \mp \frac{d\mu(s)}{ds} \tag{3.61}$$

where the plus and the minus sign denote the location just in front of and behind the singularity sheet respectively. Since $ds = rd\psi$ the velocity jump according to eq. (3.61) leads to:

$$(V_{t_2} - V_{t_1}) = \frac{1}{r} \frac{d\mu(\psi)}{d\psi} \tag{3.62}$$

The continuity equation, in incompressible flow, applied at the disk surface yields:

$$\frac{1}{r} \frac{dV_t(\psi)}{d\psi} = 0 \tag{3.63}$$

Substituting eq. (3.63) in eq. (3.62) leads to the following differential equation for μ:

$$\frac{d^2\mu}{d\psi^2} = 0 \tag{3.64}$$

which has the following solution:

$$\mu(\psi) = A_1\psi + A_2 \tag{3.65}$$

where A_1 and A_2 are constants. Choosing $A_2 = 0$ and combining eq. (3.60) and eq. (3.62) yields:

$$(V_{t_2} - V_{t_1}) = \frac{1}{r} A_1 = \frac{1}{r} \frac{\mu}{\psi} \tag{3.66}$$

Hence:

$$\mu = \frac{\Delta H}{\Omega} \psi \tag{3.67}$$

So the doublet strength increases monotonically in circumferential direction. Since the doublet distribution can be replaced by a vorticity distribution through $\gamma(s) = -\frac{d\mu(s)}{ds}$, this is equal to a distribution of vortex lines of equal strength running in radial direction between the axis of rotation and the disk edge. At this axis a discrete vortex is generated running to downstream infinity with strength equal to:

$$\Gamma_{ax} = 2\pi \frac{\Delta H}{\Omega} \tag{3.68}$$
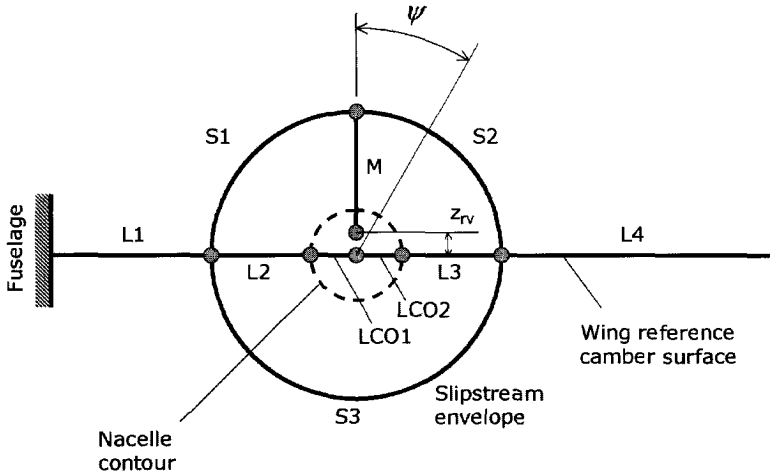
Segment division

Figure 3.5: *Front view of the subdivision of a slipstream / wing combination in the AEM-model in case of Neumann boundary conditions ; Elements: L=lifting surface, S=slipstream envelope, LCO=lift-Carry-Over, M=membrane*

In order to prevent the existence of discrete vortices at physically unrealistic locations as well as to ensure the correct loading on the different parts of the propeller-wing configuration [53, 49] the wing, propeller disk, nacelle and slipstream tube are divided into segments that can carry either a source distribution, a doublet distribution or a combination of both.

To be able to combine the slipstream tube model (further denoted as the "Actuator disk-Envelope-Membrane" or AEM-model) with a realistic propeller-nacelle-wing model intersections have to be defined to reflect the load distribution due to the slipstream on the wing.

When the load distribution is considered discontinuities at the lifting surface / slipstream envelope intersections exist. If a continuous and smoothly varying distribution is accepted for the lifting surface elements, discontinuities can occur only at the edge of a segment. Besides this, strong gradients of the load distribution over a segment are not properly handled by the doublet model. Hence, an appropriate subdivision of the geometry into different interconnected elements is needed, an example of which is given in Fig. 3.5.

The detailed segment layout depends on the choices that are made for the implementation of the boundary conditions.

In case the wing is modeled using a lifting surface approach (boundary conditions
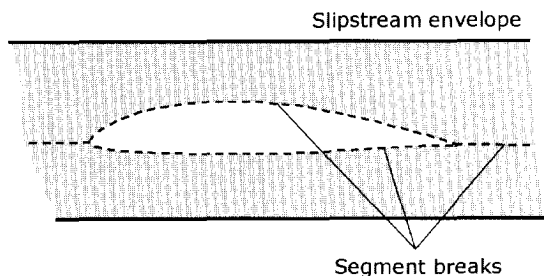
Figure 3.6: *Segment breaks at the slipstream-wing intersection used in case of the Dirichlet boundary condition.*

applied at the reference wing surface) and a Neumann boundary condition used for the nacelle it is sufficient to distribute sources over the nacelle.

The subdivision of the configuration in the slipstream washed area needs special attention in this respect. Since the nacelle is connected to the wing, the lift force at the location of the nacelle does not become zero but rather a part of the lift remains due to the presence of the wing loading. This phenomenon, referred to as lift-carry-over (LCO) requires additional LCO-segments to be positioned inside the nacelle in the case of Neumann boundary conditions [53].

The propeller wake is divided into 3 parts with a connecting membrane element located between the slipstream envelope and the root vortex.

The membrane element which runs from the actuator disk to downstream infinity consists of a sheet with a constant doublet distribution.

As shown by eq. (3.67) the doublet strength, μ, changes monotonically in circumferential direction. This means that discrete vortices are present at $\psi = 0°$ if no special measures are taken. The solution of this problem is to apply a membrane element that is connected to the actuator disk and the slipstream tube at $\psi = 0°$ carrying opposite doublet strength. The result is an irrotational flow in the flow domain bounded by the slipstream tube and the propeller disk.

Although the membrane element can be positioned at any azimuthal position relative to the slipstream axis from the modelling point of view an attractive choice is to take the vertical plane ($\psi = 0°$, Fig. 3.4).

Furthermore the vertical position of the root vortex is not fixed a priori. The variations of the root vortex offset in vertical direction, z_{rv}, is comparable to a small offset of the nacelle from the wing plane ($z = 0$). The proper location of the root vortex is at (or very close to) the propeller axis.

The situation changes slightly for the case where Dirichlet boundary conditions are selected, to enable the correct modeling of wing thickness. To assure a proper lift-

carry-over of the wing loading onto the nacelle a combined doublet/source distribution is needed for the nacelle. Discrete vortices at the nacelle-wing intersection are now prevented by segment breaks as sketched in Fig. 3.6. When (internal) Dirichlet boundary condition are applied, the discrete root vortex can not be placed at the slipstream center line. Instead a section break is located at the membrane-nacelle intersection spreading the discrete vortex effect over the nacelle surface.

To prevent conditions conflicting with the Dirichlet boundary conditions inside the wing the slipstream envelope must be cut at the intersection of the wing, further complicating the geometrical modeling of the propeller-nacelle-wing configuration.

Boundary conditions at the slipstream tube

To determine the position of the slipstream envelope, boundary conditions must be applied. According to van Beek [61] it is beneficial to satisfy the zero pressure jump condition combined with an approximate form of the force free wake condition.

The total pressure outside the slipstream can be written as $p_{t_1} = p_1 + \frac{1}{2}\rho V_1^2$ while for the inside domain $p_{t_2} = p_2 + \frac{1}{2}\rho V_2^2 + \Delta p_t$. Here Δp_t is the total pressure rise due to the propeller. For a zero static pressure jump across the envelope sheet: $p_1 = p_2$ which leads to $\frac{1}{2}\rho(V_2^2 - V_1^2) = \Delta p_t$ or in terms of total enthalpy:

$$\frac{1}{2}\left(V_2{}^2 - V_1{}^2\right) = \Delta H \tag{3.69}$$

The velocity vectors, $\overline{V_2}$ and $\overline{V_1}$ at the outer and the inner side of the slipstream envelope respectively are given by:

$$\begin{aligned}\overline{V_1} &= \overline{U_\infty} + \overline{u^p} - \tfrac{1}{2}\nabla\mu + \tfrac{1}{2}\sigma\overline{n} \\ \overline{V_2} &= \overline{U_\infty} + \overline{u^p} + \tfrac{1}{2}\nabla\mu - \tfrac{1}{2}\sigma\overline{n}\end{aligned} \tag{3.70}$$

where $\nabla\mu$ is the gradient of the doublet strength, σ is the source strength and $\overline{u^p}$ is the mean velocity vector all taken at the slipstream tube induced by all singularity distributions of the rest of the configuration. The vector u^p is given by the Cauchy Principal value [62].

Substitution of eq.(3.70) in eq.(3.69) leads to the first boundary condition (zero pressure jump) for the envelope:

$$\left(\overline{U_\infty} + \overline{u^p}\right) \cdot \left(\nabla\mu - \sigma\overline{n}\right) = \tfrac{1}{2}\Delta H \tag{3.71}$$

which can be solved in an iterative manner [55]. It is interesting to notice that apparently the angle between the velocity vector and the vorticity vector is non-zero in the case of a running propeller ($\Delta H > 0$) leading to the well known helically shaped vorticity distribution.

The second boundary condition is prescribed by the fact that the slipstream tube should be a stream surface.

An approximate form of this force free condition states that the velocity vector at the inner and the outer side of the envelope are parallel. These vectors are the projections on the plane constituted by the vectors $\overline{e_n}$ and $\overline{e_s}$ where the latter is usually taken in the direction of the $x-$axis.

The parallelism condition now yields:

$$\frac{V_{r_1}}{V_{a_1}} = \frac{V_{r_2}}{V_{a_2}} \tag{3.72}$$

where 1 denotes the outer region and 2 the region inside the slipstream envelope. With:

$$V_{r_i} = \left(\overline{V_i} \cdot \overline{e_n}\right) \quad ; \quad V_{a_i} = \left(\overline{V_i} \cdot \overline{e_s}\right) \quad \forall\, i = 1, 2 \tag{3.73}$$

eq. (3.73) leads to:

$$\left(\frac{\overline{V_1} \cdot \overline{e_n}}{\overline{V_1} \cdot \overline{e_s}}\right) = \left(\frac{\overline{V_2} \cdot \overline{e_n}}{\overline{V_2} \cdot \overline{e_s}}\right) \tag{3.74}$$

Combining eq. (3.74) with (3.70) and substituting $\overline{U} = \overline{U_\infty} + \overline{u^p}$ and $\overline{R} = \frac{1}{2}\nabla\mu - \frac{1}{2}\sigma\overline{e_n}$ for simplicity, eq. (3.74) can be written as:

$$\left(\overline{U} \cdot \overline{e_n} + \overline{R} \cdot \overline{e_n}\right)\left(\overline{U} \cdot \overline{e_s} - \overline{R} \cdot \overline{e_s}\right) - \left(\overline{U} \cdot \overline{e_n} - \overline{R} \cdot \overline{e_n}\right)\left(\overline{U} \cdot \overline{e_s} + \overline{R} \cdot \overline{e_s}\right) = 0 \tag{3.75}$$

or:

$$\left(\overline{R} \cdot \overline{e_n}\right)\left(\overline{U} \cdot \overline{e_s}\right) - \left(\overline{U} \cdot \overline{e_n}\right)\left(\overline{R} \cdot \overline{e_s}\right) = 0 \tag{3.76}$$

With the vector identity: $(\overline{a} \times \overline{b})(\overline{c} \times \overline{d}) = (\overline{a} \cdot \overline{c})(\overline{b} \cdot \overline{d}) - (\overline{a} \cdot \overline{d})(\overline{b} \cdot \overline{c})$, eq. (3.76) reduces to:

$$\left(\overline{U_\infty} + \overline{u^p}\right)\left(\nabla\mu - \sigma\overline{e_n}\right) \cdot \overline{e_t} = 0 \tag{3.77}$$

where e_t is the unit vector in tangential direction. The second boundary condition (free stream surface) for the slipstream is now given by eq. (3.77).

3.5.4 Relation between ΔH and the propeller conditions

The effect of the propeller is obtained through an increase in the enthalpy level when the flow has passed the propeller disk. The value of the total enthalpy increase in the slipstream, ΔH, can be related to the propeller thrust and the advance ratio as follows.

First the thrust force is related to the static pressure jump over the propeller:

$$T = \iint\limits_{S_p} (p_2 - p_1)dS \tag{3.78}$$

Combining eq. (3.56) and eq. (3.60) leads to:

$$\frac{1}{\rho_\infty}\frac{\gamma}{\gamma - 1}(p_2 - p_1) + \frac{1}{2}\left(\frac{\Delta H}{\Omega r}\right)^2 = \Delta H \tag{3.79}$$

with eq. (3.78) the thrust force can be written as:

$$T = \iint\limits_{S_p} \left(\frac{\Delta H}{C} - \frac{\Delta H^2}{2C\Omega^2} \frac{1}{r^2} \right) dS \tag{3.80}$$

where $C = \frac{1}{\rho_\infty} \frac{\gamma}{\gamma-1}$.

Performing the integration in eq. (3.80) results in:

$$T = \frac{\Delta H S_p}{C} - \frac{\Delta H^2}{2C\Omega^2} 2\pi \ln \left(\frac{R}{R_{spin}} \right) \tag{3.81}$$

where R and R_{spin} are the propeller tip radius and the spinner radius respectively. This equation can simply be solved for ΔH, yielding:

$$\Delta H = \frac{\frac{S_p}{C} \pm \sqrt{\left(\frac{S_p}{C} \right)^2 - \frac{4\pi \ln \frac{R}{R_{spin}}}{C\Omega^2} T}}{\frac{2\pi \ln \frac{R}{R_{spin}}}{C\Omega^2}} \tag{3.82}$$

With the introduction of the thrust coefficient: $T_c' = T/(\frac{1}{2}\rho U_\infty S_p)$ eq. (3.82) finally results in an expression that can be used to calculate the total enthalpy increase in the slipstream:

$$\frac{\Delta H}{U_\infty^2} = \frac{\frac{\pi}{2} \left(\pi - \sqrt{\pi^2 - 2 \ln \left(\frac{R}{R_{spin}} \right) T_c' \left(\frac{\gamma}{\gamma-1} \right) J^2} \right)}{\ln \left(\frac{R}{R_{spin}} \right) J^2} \tag{3.83}$$

With the propeller properties and flow conditions: T_c', J, R and R_{spin} known, eq. (3.83) gives the total enthalpy jump that is needed to fix the singularity distribution on the disk and the slipstream tube. Accordingly eq. (3.48) can be solved for the complete propeller-wing configuration.

Chapter 4

Flow analysis based on the Euler/Navier-Stokes equations

4.1 Introduction

As discussed in chapter 3 most analyses of propeller slipstream interference effects have largely centered upon simplified (engineering) methods and panel methods.

The advantage of the panel methods is typically to be found in their ease of use and the reduced "flow-through" time that consists of model preparation and CPU time. Since panel methods work with the linearized potential equations a serious disadvantage is the fact that the geometry of the slipstream must be modeled by the user prior to the calculation process. In this respect it is important to note that comparative studies have shown that methods based on the solution of the Euler/Navier Stokes (ENS) equations in the volume surrounding the aircraft have an advantage in that the propeller slipstream is not required to be modeled.

Once the propeller forces are modeled correctly (Appendix A) the slipstream is calculated as part of the flow field, instead. Hence no restrictions are applied with respect to the vorticity in the slipstream domain that, in case of panel methods, is limited to a thin layer defining one or more slipstream tubes. A further advantage of using the Navier-Stokes (NS) equations is the explicit presence of viscous terms. Hence the viscous effect of the propeller slipstream on the nacelle and the wing boundary layer can be determined.

Since in this thesis the emphasis is not on the design of the propeller but on the time-averaged effects of the slipstream on the wing, the problem can greatly be simplified by approximating the propeller blades as an actuator disk boundary

condition as was done in the case of the simpler methods discussed in chapter 3. Data from experiments or separate BEM-like calculation programs are then used to set the boundary conditions at the disk.

In the following sections the theory that is specific to the implementation of the propeller action in the ENS-calculation is described. Some results acquired with these methods are discussed in Chapter 6.

General aspects that are typical for the solution procedure of the Euler/Navier Stokes equations in general can be found in refs. [63, 64, 65].

4.2   Governing equations

In the description of the numerical model for the analysis of the propeller-wing interference problem it is beneficial to start with the inviscid version of the Navier-Stokes equation: the Euler equations.

The Euler equations are based on the conservation laws of mass, momentum and energy for an inviscid flow. Hence in principle flow fields with entropy and vorticity production due to shock waves and total pressure, swirl and total temperature increase due to propeller power effects can be correctly simulated.

The three-dimensional Euler equations, in differential form, may be expressed as:

$$\frac{\partial \overline{Q}}{\partial t} + \frac{\partial \overline{F}}{\partial x} + \frac{\partial \overline{G}}{\partial y} + \frac{\partial \overline{H}}{\partial z} = 0 \tag{4.1}$$

where:

$$
\begin{aligned}
\overline{Q} &= \left(\rho, \rho u, \rho v, \rho w, \rho e_t\right)^T \\
\overline{F} &= \left(\rho u, \rho u^2 + p, \rho u v, \rho u w, \rho u h_t\right)^T \\
\overline{G} &= \left(\rho v, \rho u v, \rho v^2 + p, \rho u w, \rho v h_t\right)^T \\
\overline{H} &= \left(\rho w, \rho u w, \rho v w, \rho w^2 + p, \rho w h_t\right)^T
\end{aligned}
\tag{4.2}
$$

Here $\overline{Q}$ is the conservative state vector while $\overline{F}, \overline{G}$ and $\overline{H}$ are the flux vectors in the x, y and z direction respectively. ρ is the fluid density ; u, v and w are the Cartesian velocity components ; p is the pressure while e_t and h_t are the total energy and the total enthalpy per unit of mass respectively.

The first components of the vector equation form the continuity equation; the second, third and fourth components are the conservation of momentum in the x, y and z direction respectively and the fifth component is the energy equation. The volume integral in eq.(4.1) is the time dependent fluid state while the surface integrals in eq.(4.1) are the fluxes of mass, momentum and energy through the surfaces of the control volume.

A further relation needed to close the system is an equation of state. For a thermally perfect gas this is written as:

$$\frac{p}{\rho} = RT \; ; \; e = c_v T \tag{4.3}$$

where T is the temperature, R is the gas constant ($R = c_p - c_v$), e is the internal energy per unit of mass, c_p and c_v are the specific heats at constant pressure and constant volume respectively. With $\gamma = c_p/c_v$ eq. (4.3) for a perfect gas leads to:

$$p = \frac{R}{c_v}\rho e = (\gamma - 1)\,\rho e = (\gamma - 1)\,\rho \left(e_t - \tfrac{1}{2}\left(u^2 + v^2 + w^2\right)\right) \tag{4.4}$$

where the total energy per unit of mass, e_t, is given by:

$$e_t = e + \frac{1}{2}(u^2 + v^2 + w^2) \tag{4.5}$$

The Euler equations constitute a system of non-linear first order partial differential equations that have to be solved in space. Major steps to find a numerical solution of the system can be summarized as:

- discretization of the equations and the boundary conditions

- solution of the system of ordinary equations

Discretization takes place by subdividing the flow domain into a number of grid cells. The discrete Euler equations are applied to each of the grid cells within the domain. Because of the complexity of the propeller-wing configurations investigated in this report a subdivision must be made into several blocks, an example of which is given in Fig. 4.1

Because of the intrinsic errors that are introduced by the discretization process it is obvious that grid refinement is needed at locations where strong gradients in the flow variables occur. This aspect is especially important at the location of the propeller because of the gradient in the total pressure and the swirl velocity (see Chapter 2 and Appendix A).

Solution of the discretized system of equations is subject to boundary conditions that are specified at the block faces. When the propeller blades are not modeled separately and the actuator disk approach is utilized instead, the propeller face forms a block face as well.

For the cell-centered flow solver, that is assumed here, the fluxes through all the cell-faces are calculated with the average of the flow variables in adjacent grid cells. This is an important aspect once the propeller boundary conditions are implemented.

With the boundary conditions given the solution process requires the calculation of fluxes across the cell faces. For this process various schemes are utilized in practice
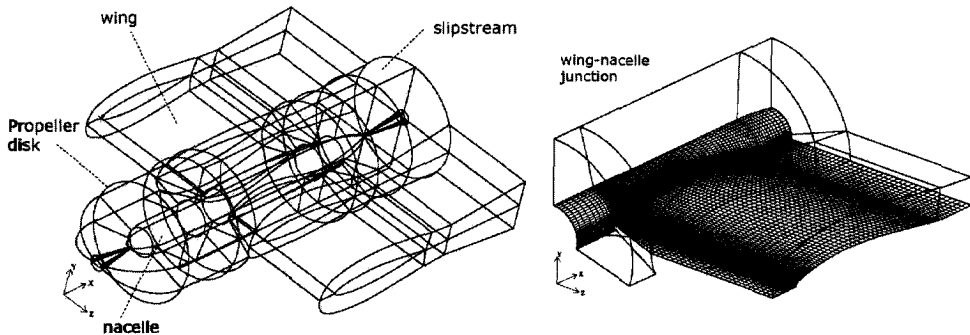
Figure 4.1: *Typical multi-block subdivision of a propeller-nacelle-wing configu-rations for the solution of the ENS-equations.*

like the central differencing method described by Jameson [66] and the approximate solution method based on the solution of the one-dimensional Riemann problem [67, 64, 68].

In the description of the propeller-wing interference effect we restrict ourselves to a time-averaged approach. The acceptance of this limitation was already discussed in Chapter 2. As a consequence of time-averaging the distinct contribution of the separate blades in the form of individual vortex wakes springing from the blades is not resolved in the solution. Instead vorticity is spread continuously in the slipstream flow field. The advantage of this manifests itself in the fact that only a steady flow calculation has to be performed and the propeller is reduced to a discontinuity surface (actuator disk) in the flow domain.

The proper propeller modeling technique that is related to these solution methods is described in more detail in the next sections.

4.3   Propeller model in the ENS-analysis

4.3.1   Actuator disk model

All the calculations and experiments discussed in this report are restricted to subsonic flow conditions. For this reason the considerations for appropriate implementation of the propeller actuator disk model are restricted to flows with $M < M_{crit}$.

The actuator disk forms an interface between two blocks in the flow domain. The boundary conditions at the actuator disk are in principle treated in a manner similar to subsonic inflow and outflow boundary conditions.

At this point it is of vital importance that physically and mathematically correct boundary conditions are used to model the action of the propeller. The fluxes at all

the cell faces that are part of the boundary of the flow domain are determined by the state vector near the boundary and partly by the prescribed boundary conditions.
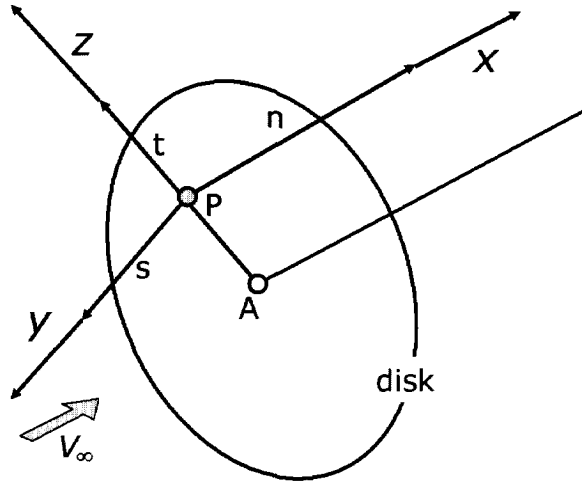

Figure 4.2: *Actuator disk face with local coordinate system.*

For the actuator disk a local Cartesian frame is considered in which the x-axis is directed normal to the propeller disk plane (see Fig. 4.2). The solution procedure requires the fluxes at the faces to be known. Hence, with the (artificial) disk positioned between two block faces (see Fig. 4.3), state vectors given by q_1 and q_2 for block 1 and block 2 respectively need to be determined. However, these fluid states depend on the states found in the cell centers of adjacent cells, q_0 and q_3, and specific boundary conditions. These boundary conditions are not constant throughout the solution process but they depend on the flow variables in the block where they are located.

The boundary conditions of block 1 depend on the flow in block 2 and vice versa. Once the state vectors at each side of the face are known standard routines can be used to calculate the fluxes. Boundary conditions that will be used to model the work performed by the propeller are outflow for block 1 (i.e. flow into the actuator disk region) and inflow for block 2 (i.e. flow out of the disk region).

The following procedures can be used to determine the state vectors q_1 and q_2 for the outflow and the inflow respectively.

4.3.2 Characteristic variable boundary conditions

In the hyperbolic (in time) system of equations, (4.1),(4.2) the quantities that propagate along characteristic lines can be defined and the system can be cast in terms
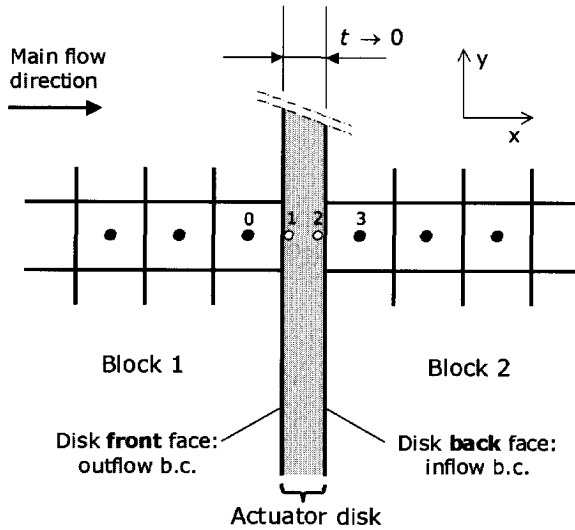
Figure 4.3: *The boundaries at the actuator disk surface.*

of its characteristic form. A set of characteristic variable boundary conditions can be developed, which will finally contribute to a well-posed boundary value problem.

To obtain the eigenvalues that are needed to describe the characteristic lines eq. 4.1 can be written as:

$$\frac{\partial \overline{Q}}{\partial t} + A \frac{\partial \overline{Q}}{\partial x} + B \frac{\partial \overline{Q}}{\partial y} + C \frac{\partial \overline{Q}}{\partial z} = 0 \qquad (4.6)$$

where the Jacobian matrices are given by: $A = \overline{F}/\overline{Q}$, $B = \overline{G}/\overline{Q}$ and $C = \overline{H}/\overline{Q}$. These Jacobian matrices are quite complicated. However, the system can be simplified by expressing them in the primitive variables, $\overline{q} = (\rho, u, v, w, p)^T$.

The quasi-linear non-conservative form of the Euler equations is now given by:

$$\frac{\partial \overline{q}}{\partial t} + \alpha \frac{\partial \overline{q}}{\partial x} + \beta \frac{\partial \overline{q}}{\partial y} + \gamma \frac{\partial \overline{q}}{\partial z} = 0 \qquad (4.7)$$

The transformation between the conserved and non-conserved variables is defined by:

$$M = \frac{\partial \overline{Q}}{\partial \overline{q}} \qquad (4.8)$$

which can be computed easily:

$$M = \begin{pmatrix} 1 & 0 & 0 & 0 & 0 \\ u & \rho & 0 & 0 & 0 \\ v & 0 & \rho & 0 & 0 \\ w & 0 & 0 & \rho & 0 \\ \frac{1}{2}q^2 & \rho u & \rho v & \rho w & \frac{1}{\gamma-1} \end{pmatrix} \qquad (4.9)$$

where $q = \sqrt{u^2 + v^2 + w^2}$ is the flow speed. The Jacobians, A, B and C can be written in general form as $K = \partial \overline{S}/\partial \overline{Q}$, where $\overline{S}$ represents the flux vectors $\overline{F}$, $\overline{G}$ and $\overline{H}$.

The mapping matrix M provides a similarity transformation to describe the relation between the conservative Jacobians, K and the non-conservative Jacobians, k. This can be seen as follows.

Eq. 4.6 can be written as:

$$\frac{\partial \overline{Q}}{\partial \overline{q}}\frac{\partial \overline{q}}{\partial t} + A\frac{\partial \overline{Q}}{\partial \overline{q}}\frac{\partial \overline{q}}{\partial x} + B\frac{\partial \overline{Q}}{\partial \overline{q}}\frac{\partial \overline{q}}{\partial y} + C\frac{\partial \overline{Q}}{\partial \overline{q}}\frac{\partial \overline{q}}{\partial z} = 0 \qquad (4.10)$$

Multiplication by M^{-1} and application of eq. 4.8 yields:

$$\frac{\partial \overline{q}}{\partial t} + M^{-1}AM\frac{\partial \overline{q}}{\partial x} + M^{-1}BM\frac{\partial \overline{q}}{\partial y} + M^{-1}CM\frac{\partial \overline{q}}{\partial z} = 0 \qquad (4.11)$$

Hence the similarity relation for the Jacobians k, of the non-conservative system, and K, of the conservative form, is:

$$k = M^{-1}KM \qquad \text{and} \qquad K = M^{-1}kM \qquad (4.12)$$

With eq. 4.12 matrix k leads to a much simpler form than K:

$$k = \begin{pmatrix} \tilde{u} & \rho n_x & \rho n_y & \rho n_z & 0 \\ 0 & \tilde{u} & 0 & 0 & n_x/\rho \\ 0 & 0 & \tilde{u} & 0 & n_y/\rho \\ 0 & 0 & 0 & \tilde{u} & n_z/\rho \\ 0 & \rho n_x c^2 & \rho n_y c^2 & \rho n_z c^2 & \tilde{u} \end{pmatrix} \qquad (4.13)$$

where c is the speed of sound and $\tilde{u}$ is the projection of the velocity vector in unit normal direction:

$$\tilde{u} = n_x u + n_y v + n_z w \qquad (4.14)$$

Due to the simple structure of matrix k it is easy to find the eigenvalues, λ, by solving:

$$|k - \lambda I| = 0 \qquad (4.15)$$

This results in the following eigenvalues:

$$\lambda_1 = \lambda_2 = \lambda_3 = \tilde{u}$$
$$\lambda_4 = \tilde{u} + c \tag{4.16}$$
$$\lambda_5 = \tilde{u} - c$$

These eigenvalues represent characteristic directions, along which characteristic variables are strictly conserved [68]. That is, each characteristic direction transports given information defined by the characteristic variable. The characteristic directions define the number of physical boundary conditions that can be defined for a given boundary.

Variables which are transported from the boundaries towards the interior can be imposed at a given boundary as 'physical' boundary conditions. The remaining variables depend on the computed flow solution and are referred to as 'numerical' boundary conditions.

At this moment, characteristic variable boundary conditions will have to be developed for the actuator disk sketched in Fig. 4.3.

Subsonic outflow

At the front side of the actuator disk, sketched in Fig. 4.3, the flow leaves the computational domain. This means that in this plane we have outflow boundary conditions. If we restricting ourselves to subsonic flow conditions the first four eigenvalues are positive. Hence, they form numerical boundary conditions which must be computed from the flow upstream of the actuator disk surface.

The fifth eigenvalue, $\tilde{u} - c$, however becomes negative for subsonic flow and hence represents a physical boundary. The particular characteristic is incoming which means that a physical boundary condition has to be prescribed at this boundary. For an outflow boundary conditions usually the pressure, p_b, is prescribed. In the case of the actuator disk however it may be beneficial to prescribe the mass flow since we have the restriction that continuity of mass is required. Hence the mass flow at location 1 must be equal to $\dot{m}_3 = \rho_3 u_3$ at the other side of the disk. An alternative approach would be to prescribe the pressure, p_1, at the outflow side. This procedure was utilized successfully by Belk et al [69]. To prevent the necessity of specifying p over the entire disk a simple radial equilibrium may be enforced based on:

$$\frac{\partial p}{\partial r} = \left(\frac{\rho v_t^2}{r} \right)_1 \tag{4.17}$$

where v_t is the tangential velocity component at the boundary (index 1).

The state vector $\overline{q}_1$ is now partially determined by the Riemann invariants (quantities that are constant along the characteristic lines) that are valid for the characteristic

directions and partially by the physical boundary conditions. This means that for the outflow side (front side of the disk) the following relations exist:

$$u_1 + \frac{2}{\gamma - 1}c_1 = u_0 + \frac{2}{\gamma - 1}c_0$$

$$v_1 = v_0$$

$$w_1 = w_0$$

$$z_1 = z_0$$

$$\rho_1 u_1 = \rho_3 u_3 \quad \text{or} \quad p_0 = p_b$$

(4.18)

where z_i is the scaled entropy defined by $z_i = \ln(p_i/\rho_i^\gamma)$. Additionally the perfect gas law $c = \sqrt{\gamma p/\rho} = \sqrt{\gamma R T}$ can be used to close the system.

In case the pressure is prescribed both state vectors are known because we have 5 equations and 5 unknowns. The final state variables can be easily found by:

$$\rho_1 = \left(e^{\ln(p_1) - z_0} \right)^{\frac{1}{\gamma}}$$

$$c_1 = \sqrt{\frac{\gamma p_1}{\rho_1}}$$

$$u_1 = u_0 + \frac{2}{\gamma - 1}(c_0 - c_1)$$

(4.19)

In an analogue way the state variables can be obtained once the mass flow is prescribed based on the state at the exit plane of the disk.

Subsonic inflow

At the back side of the the actuator disk an inflow into the the computational domain exists. For subsonic inflow, eq. (4.16) shows that we have one outgoing characteristic and 4 incoming characteristics. Hence, in this case four physical boundary conditions have to be prescribed and one numerical boundary condition follows from the solution.

The combination of flow parameters that are prescribed is arbitrary as long as the system of equations constitute a complete set, i.e. all the state variables can be determined. An attractive set of boundary conditions for the propeller flow case is: the total pressure, p_t, the total temperature, T_t, and the flow direction composed of 2 angles, θ_1 and θ_2. Nevertheless, other combinations may be used as well [70]. The quantities at the outflow side are obtained by the value of the inflow side with the increments (jumps) added. The system can be closed by prescribing the mass flow as was done for the outflow boundary condition.

The inflow boundary relations for the system sketched in 4.3 then become:

$$
\begin{aligned}
p_{t_2} &= p_{t_0} + \Delta p_t \\
T_{t_2} &= T_{t_0} + \Delta T_t \\
\frac{u_2}{q_2} &= d_x \\
\frac{v_2}{q_2} &= d_y \\
\frac{w_2}{q_2} &= d_z \\
\rho_2 u_2 &= \rho_3 u_3 = \dot{m}_3
\end{aligned}
\tag{4.20}
$$

where $d = (d_x, d_y, d_z)^T$ is the normalized velocity vector. Furthermore use is made of the isentropic relations:

$$
\begin{aligned}
\frac{p_t}{p} &= \left(1 + \frac{\gamma - 1}{2}\frac{q^2}{c^2}\right)^{\frac{\gamma}{\gamma - 1}} \\
\frac{T_t}{T} &= \left(1 + \frac{\gamma - 1}{2}\frac{q^2}{c^2}\right)
\end{aligned}
\tag{4.21}
$$

and the equation of state for a perfect gas:

$$
c^2 = \gamma\,(\gamma - 1)\,T = \gamma\frac{p}{\rho}
\tag{4.22}
$$

Once the state vector $\bar{q}_2$ is determined the other quantities can be calculated through:

$$
\begin{aligned}
c^2 &= \gamma\,(\gamma - 1)\,T_{t_2} - \frac{\gamma - 1}{2}q_2^2 \\
p_2 &= \frac{\dot{m}_3 c_2^2}{\gamma d_x q_2} \\
\rho_2 &= \gamma\frac{p_2}{c_2^2} \\
u_2 &= q_2 d_x \\
v_2 &= q_2 d_y \\
w_2 &= q_2 d_z
\end{aligned}
\tag{4.23}
$$

The jumps in the total pressure, the total temperature and the flow angles have to be provided by a separate model either based on an experimental or a numerical propeller model. The flow direction downstream at the disk, given by the normalized

vector, $\overline{d}$, has to be determined from the flow direction upstream of the disk and the incremental flow angles, $\Delta\theta_1$ and $\Delta\theta_2$.

It should be noted that these boundary conditions are appropriate for inviscid flow in the case of steady flow calculations. In reality however the flow domain around the propeller contains typical viscous regions like the nacelle and spinner boundary layer. The problem can be overcome by imposing the (viscous) no-slip boundary condition only at grid points at some small distance away from the disk. This approximation is justified if the boundary layers are extremely thin compared to the disk dimensions (high Re-number flow). Alternatively the boundary layer conditions can be replaced by experimentally observed distributions.

Part II

Experimental and numerical analysis

Chapter 5

Experimental investigation

5.1   Introduction

In this chapter the wind tunnel experiments that were performed to get a further insight in the propeller-wing interactive flow will be discussed.

Although CFD has become quite mature in the last few decades, wind tunnels are still essential tools for aerodynamicists and aircraft designers. Their main tasks can be summarized as: assistance in revealing certain (true) physical phenomena, the generation of experimental data to validate numerical procedures and, last but not least, establishing the performance data in the development of new aircraft concepts. Clearly the role of the wind tunnel has changed in the past few years due to the rapid development of numeric methods of calculation. Still, CFD calculations (Computational Fluid Dynamics) have not rendered the tunnels superfluous [71, 72, 73].

The discussion on the flow characteristics in the area of the propeller slipstream has shown that they are of a complex nature. The phenomena that occur are completely dependent on the disk loading of the propeller which makes the analysis of the aerodynamics involved a difficult task. The variety of calculation techniques dedicated to the problem of propeller-wing interference, as discussed in previous chapters, may very well be capable of clarifying the various effects qualitatively, but the prediction capabilities are still limited in quantitative sense. The problems with respect to the prediction of the flow behavior are mainly due to:

- viscous effects related to boundary development in general and separation specifically, combined with the limited capabilities to incorporate the effect of turbulence

- unsteady effects in the propeller slipstream related to the blade passage frequency

On the other hand, the wind tunnel environment also exhibits typical problems that prevent the acquisition of the true (free flight) characteristics of the propeller-wing configuration. The main topics that need to be addressed in this respect are extensively described in refs [74, 75, 76]. The most important problems are related to:

- The attainable Reynolds and Mach number due to the fact that generally test are performed on a scaled down version of the true configuration

- the corrections due to the presence of tunnel walls

- the turbulence level of the flow (either too high or too low)

In the tests described in this chapter the most important problems are dealt with. Nevertheless an extensive description of all wall corrections that were applied is felt beyond the scope of this thesis. Where appropriate, reference is made to relevant literature for further reading. The experiments discussed herein constitute only a minor part of the experimental data base in the field of propeller wing interference found in open literature. As such, it is only meant to provide insight in specific topics addressed in previous chapters regarding the optimization of propeller-wing configurations. The effects of the propeller position and rotation direction on the model forces as found from the experiments as well as the surface pressure and field data will be discussed. The latter is important to better understand the effect that the slipstream distortion may have on the wing behavior and its relation to the swirl recovery capability of the trailing wing.

Three models will be discussed in subsequent sections:

- a straight wing propeller-nacelle-wing model, denoted as PROWIM(**pro**peller **wing** interference **model**)

- a model consisting of wing with a separated nacelle-propeller unit, denoted as APROPOS (adaptive **prop**eller **positioning** system)

- a scale model of the Fokker F-27 aircraft

5.2   Test set-up and procedures

5.2.1   Wind tunnel

The wind tunnel used during these investigations is the Delft University Low Turbulence Tunnel (LTT) which has an octagonal test section of width $1.80\,m$ and height $1.25\,m$. To compensate for the wall boundary layer displacement effect the test section is slightly divergent which results in a zero static pressure gradient in streamwise direction for the empty test section. The maximum attainable speed is $120\,m/s$,

although in practice the speed is limited to $100\,m/s$. The wind tunnel has low turbulence levels ranging from $Tu = 0.025\%$ at $40\,m/s$ to $Tu = 0.085\%$ at $100\,m/s$. A general description of the facility is given by Veldhuis [77].
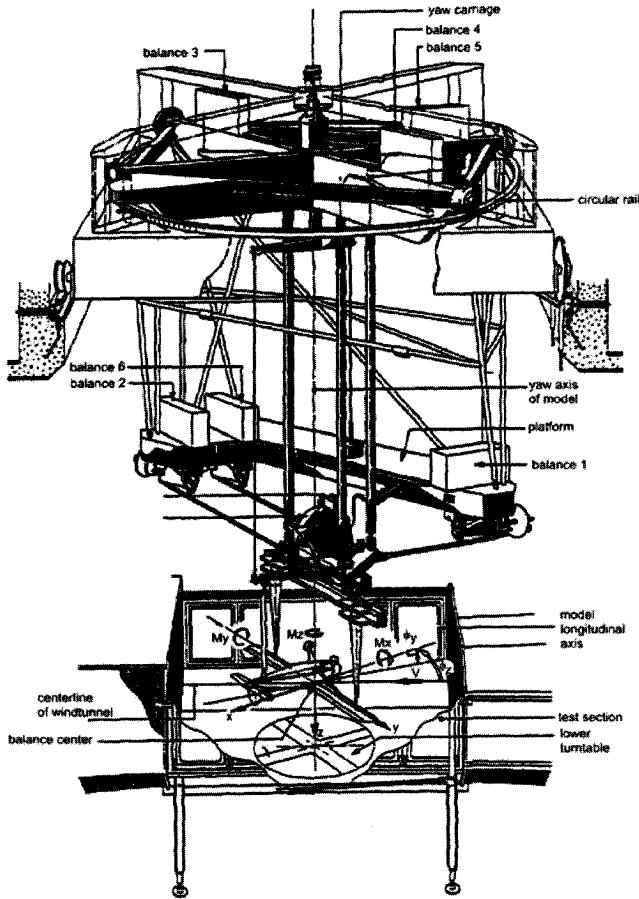

Figure 5.1: *Layout of the six-component external balance system in the LTT.*

5.2.2 Balance system

Force measurements on the models or parts thereof, are performed with an external six-component balance system (Fig. 5.1). The models are connected to the balance either through a three-strut support for complete aircraft models or through a turntable

that acts as a reflection plane. The balance system can be rotated in the horizontal plane enabling a variable yaw angle of complete models or the angle of attack for half models (with their spanwise axis in vertical direction, see Fig. 5.2). A separate rotation mechanism mounted on top of the main carriage allows the angle of attack setting of the 3-dimensional aircraft models by moving the tail strut.
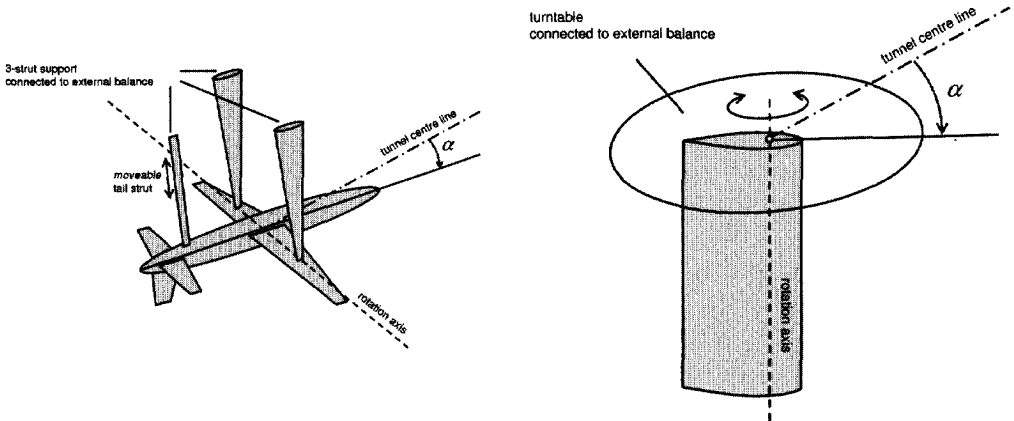
Figure 5.2: *Angle of attack setting of full aircraft model (left) and a wing half model (right) in the LTT.*

All balance data are recorded with a *HP 3852A* Data Acquisition Unit data acquisition system (DACU) that sends the raw data to a UNIX based computer system running a dedicated balance program, denoted textitw3d. The layout of the balance measurement system is sketched in Fig. 5.3.

5.2.3   Motor control unit

A dedicated model motor control unit (MCU) is connected to a PC, that is part of the complete data acquisition system. On this PC, a separate program controls the speed setting of the propeller to an accuracy of approximately 0.02% while monitoring the most important motor parameters like: speed, electrical current, $Volts/Hz$ ratio and motor temperature. In case any of the monitored parameters exceeds predefined limits the system enters an emergency shutdown procedure to prevent loss of the model motor(s).
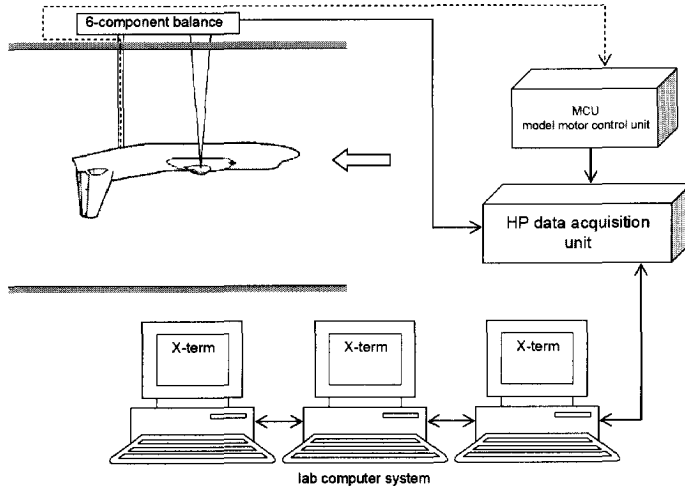
Figure 5.3: *Setup of the LTT data-acquisition system.*

5.2.4 Surface pressure measurements

Part of the surface pressure measurements were performed with a 200-tube multi-manometer that is read out electronically. The data stream is sent directly to the laboratory computer enabling acquisition of 200 pressures in approximately 5 s.

Additional surface pressures were recorded with *scanivalves* (2x48) containing *PDCR-22* pressure transducers (range $\pm 6900\,Pa$). Data points for all local surface pressures were based on a 150 samples average sampled at a frequency of $1000\,Hz$. Switching effects were avoided by allowing a delay time of $16\,ms$ at the start of the measurement sequence. To prevent loss of pressure data accuracy due to transducer drift the *PCDR-22* pressure transducers, that were mounted outside the test section, were calibrated approximately every 10 minutes using an "on-line" calibration unit.

5.2.5 Five hole probe and traversing mechanism

For the application of the quantitative wake analysis technique (section 5.6) field data are needed. Since both the complete velocity vector and the total pressure distribution is required for this, five hole probe measurements were performed.

The five-hole probe that was used for all wake surveys has a diameter of $1.65\,mm$ and a conical head (Fig. 5.4). Cross flow angles were valid within a calibration range of $+45°$ to $-45°$. All measurement data were acquired through the DACU connected to a *HP9000-825* computer.

During the five hole probe measurements, the electronic pressure transducer (ZOC)
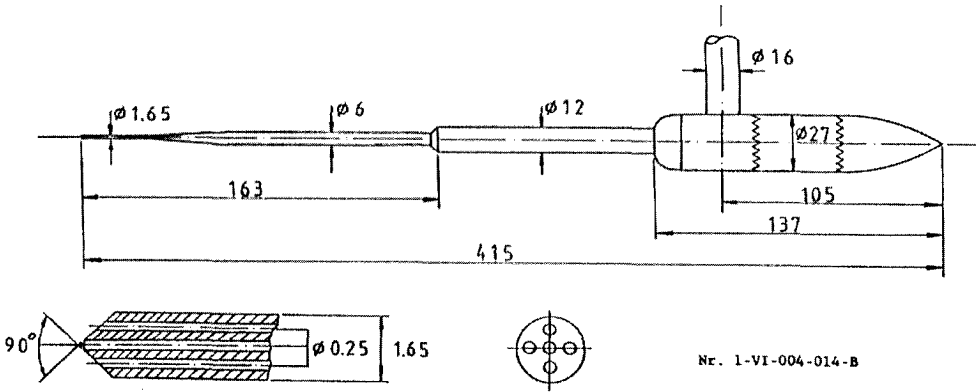
Figure 5.4: *Layout of the five hole probe used during the acquisition of flow field data for the quantitative flow field survey.*
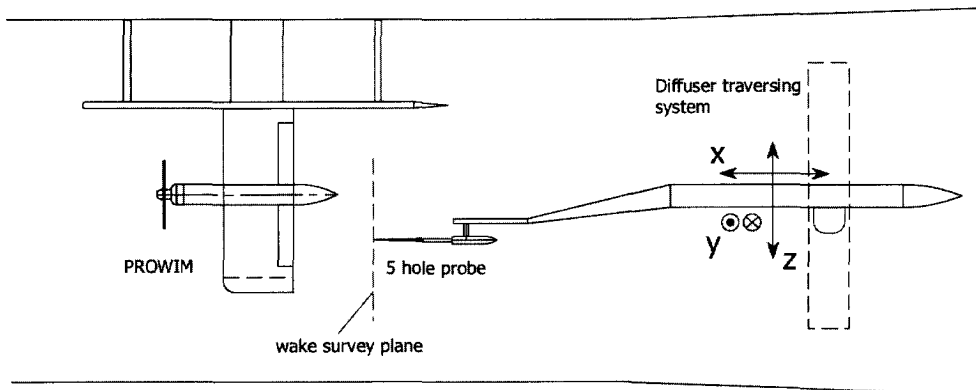

Figure 5.5: *Diffuser traversing system used during the five hole probe surveys.*

was positioned inside the test section and therefore sensitive to possible temperature changes. To compensate for possible errors the transducer was therefore calibrated every 600 data points (approx. 3 minutes).

All test data were reduced on-line yielding the three components of wake velocity, from which circulation and total pressure within the slipstream/wake were calculated.

Traversing of the probe was done through a computer controlled traversing system consisting of a diffuser mounted x, y, z slide and a adjustable sting connected to it (Fig. 5.5).

The accuracy of the traversing system is approximately $0.02\,mm$ in all directions.

To reduce time needed for measuring several model configurations, the pressure measurements were done with the probe in non-nulling mode using a fast pressure transducer reading while the probe was traversing at low speed ($5\,mm/s$). The data-acquisition system was triggered for measurement every $2\,mm$ of y-movement using the signal output of a "40-counter" connected to a shaft optical encoder

The number of samples per pressure hole was fixed at 10 and the sample rate at $10,000\,Hz$. The complete measurement cycle of one survey point took $24\,ms$. This means that the displacement effect ($0.024 \times 5{=}0.12\,mm$) of the traversing probe is negligible compared to the probe diameter [58]. For all flow conditions the measurement grid was build with its borders as closely as possible to the so-called *Poisson area* (see section 5.6.3) to prevent acquisition of unnecessary data. Typically, the total measurement grid behind the model contained about 30,000 to 40,000 data points.

5.2.6   Flow visualization

The boundary layer behavior was investigated qualitatively by using both a fluorescent oil technique (PROWIM model) and the standard tuft technique (F27 model). The oil mixture that was used consisted of *Shell Ondina 32 / 15* containing the fluorescent additive $A - 680$. Still photographs were taken with an Olympus OM-2N camera operated in B-mode with an exposure time of approximately 50 - 60 seconds.

5.3   Models

5.3.1   PROWIM

The first wind tunnel model (Fig. 5.6), denoted PROWIM, consists of a straight wing of aspect ratio $A = 5.33$ with no twist, constant chord and airfoil section (NACA 64_2-A015). Its (half) span is $0.64\,m$. To change the spanwise loading distribution in combination with the effect of the propeller, the model is provided with two flaps of equal span situated inboard and outboard of the nacelle. These flaps will be further denoted as the inboard and the outboard flap respectively. For the propeller on test, the model can be equipped with a 4-bladed metal propeller of $0.236\,m$ diameter that is driven by a $5.5\,kW$ electrical 3-phase induction motor contained inside the nacelle. The propeller speed setting of this motor was controlled using a 200-per-revolution optical encoder mounted on the rotor. Cooling of the motor was done through a closed cooling circuit filled with distilled water that is controlled by the MCU.

The axis-symmetrical nacelle was build as a "minimum body" (body of revolution) mounted with its rotation axis on the MAC-line and at $0.3\,m$ from the wing root. This leads to a dimensionless spanwise propeller position of $y_p/b/2 = 0.469$. During all tests the $\frac{3}{4}R$ blade angle was set to $25°$. The model was attached to the external 6 component balance through a turntable which is flush with the image plate situated at
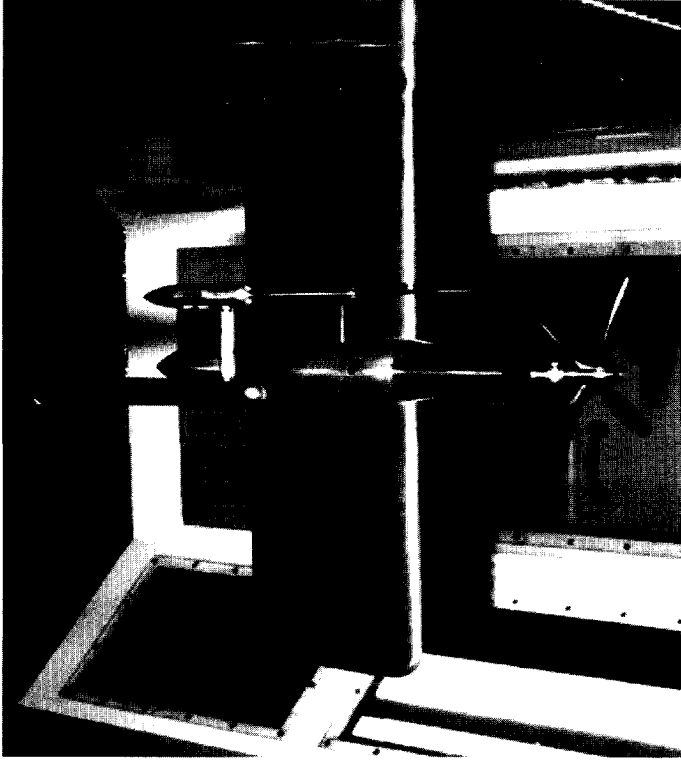
Figure 5.6: *Model PROWIM, installed in the LTT with a five hole probe
mounted directly behind the propeller.*

$0.3\,m$ from the upper wall. To perform surface pressure measurements with *PDCR-22*
transducers, the wing contains a total of 918 pressure orifices located in 18 rows.

In the vicinity of the nacelle, where the slipstream washes the wing, a closer
spacing was used than outside this area. Two pitot tubes were installed at a small
distance behind the propeller to determine the total pressure jump ΔP_t across the
propeller plane which is a measure for the thrust coefficient, T_c.

To define the chordwise pressure every row contained 51 pressure taps. The pres-
sure taps on the flaps indicated in which situations separation effects occurred during
tests with the highest disc loading. This information is needed to decide whether or
not strong viscous effects affect the drag data during flap angle variation tests.

For all thrust settings of the propeller at least 12 rows were washed by the slip-
stream. The dense distribution of rows is necessary to be able to perform a reasonable
induced drag analysis when no spatial velocity field data are known.
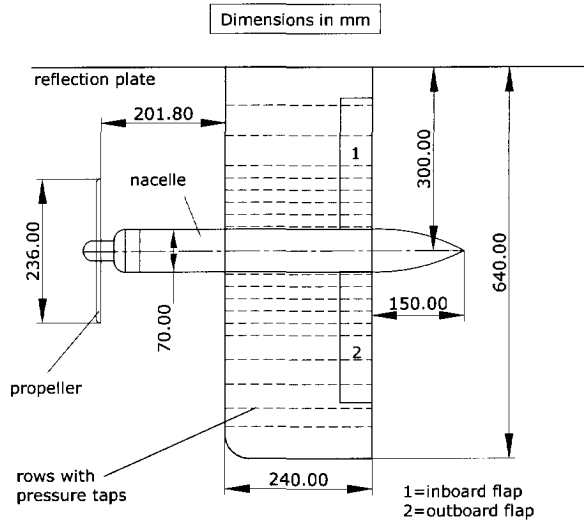
Figure 5.7: *Dimensions of the PROWIM model; Top View.*
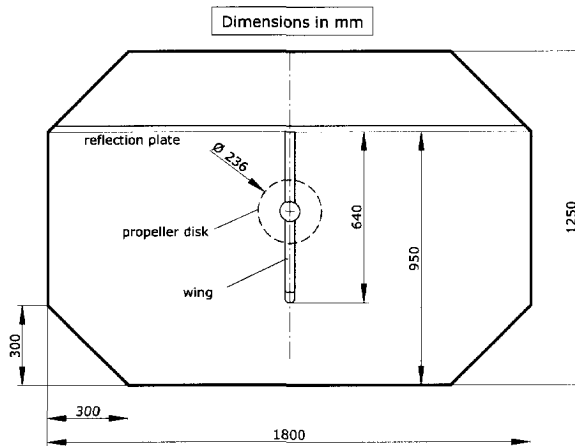
Figure 5.8: *Dimensions of PROWIM installed in the LTT; Front View.*

5.3.2 Flap deflection

During the PROWIM test several flap settings were used for mainly 2 reasons. Firstly, flap deflection can be used to simulate a change in airfoil camber over a part of the wing. In some tests the flaps were therefore deflected differentially (e.g. inboard down, outboard up for an inboard up rotating propeller) to additionally deform the lift distribution in a positive way. The efficiency (effective thrust) should increase in this situation. Since the lift vector is tilted forward at the upgoing blade side and tilted backward at the downgoing blade side the contribution of the lift at the blade upgoing side decreases the induced drag while the contribution of the lift at the blade downgoing side increases it.

The second reason for the use of flap deflection is the influence it has on the performance of the propeller. Knowledge of the magnitude of this effect is necessary for a correct drag bookkeeping and for application of non-interacting propeller codes in existing panel programs.

The maximum flap deflection used during the tests with PROWIM was approx. 6°, which resulted in small, though remarkable, performance increase indicated by a lower overall drag coefficient.

5.3.3 APROPOS

The second windtunnel model referenced as APROPOS is identical with PROWIM except for the fact that it is not provided with flaps and it has no nacelle connected to it (Fig. 5.9). Instead, the nacelle with propeller is supported by a strut which can be traversed with the 3-component traversing system mentioned earlier.

With the propeller-nacelle detached from the wing in the APROPOS layout the separate effect of the propeller slipstream on the wing could be measured and the effect of the propeller position relative to the wing could be investigated.

5.3.4 F27 model

This model is a 1:20 scale model of the prototype of the *Fokker F27* aircraft [78]. The model that is constructed of a combination of brass and wood consists of several parts that can be detached for detail tests (see Fig. 5.10). The span of the high aspect ratio wing ($A = 12$) is $1.45\,m$.

Typical tests that can be performed with this model are related to the static stability under power on and power off conditions. For this purpose the horizontal tail surface can be removed enabling the determination of the characteristics of the fuselage-tail combination. Removing the propellers enables analysis of the propulsion effects. Almost all typical flight conditions can be simulated by deflecting control surfaces like: rudder, elevator, inboard and outboard flaps and ailerons.
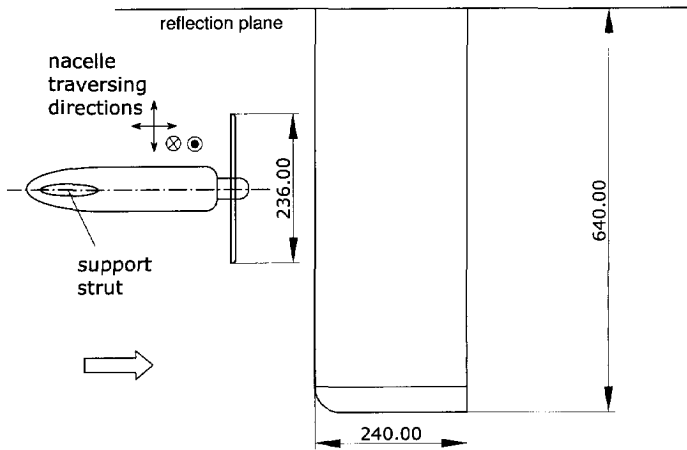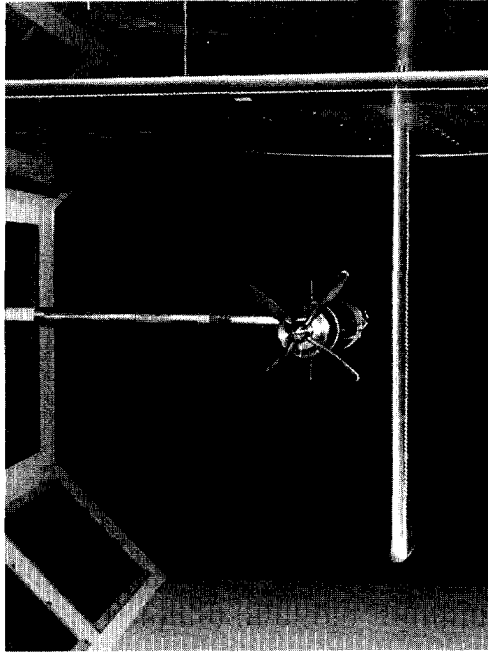
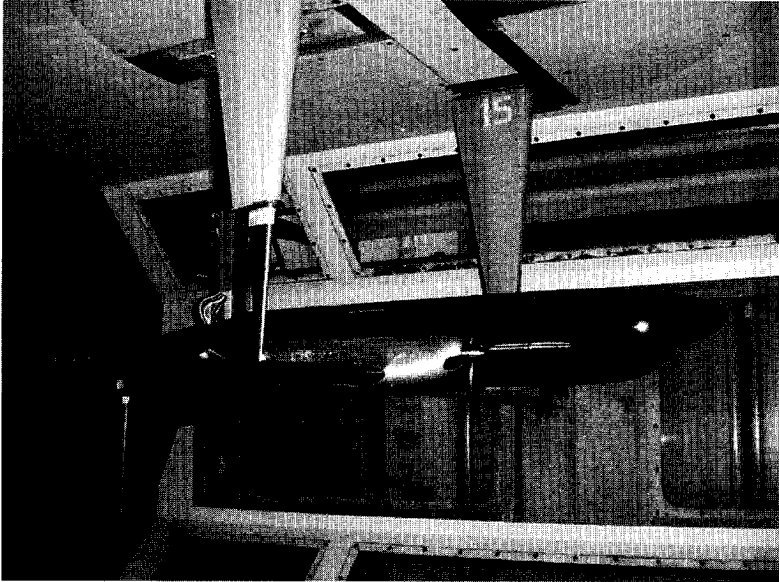Figure 5.9: *Layout and dimensions of the APROPOS model (in mm).*

Figure 5.10: *Fokker F27 model, scale* 1 : 20, *in the LTT.*

Powered flight is simulated by driving two metal propellers, with fixed (preset) blade pitch. For the power-on tests each nacelle contains an electrical 3-phase induction motor with a power of $3.6\,kW$. Since the motors can run in two directions, all relevant cases like inboard up, outboard up and co-rotating propellers can be simulated.

To prevent laminar boundary layer separation at the relatively low chord Reynolds numbers at which the tests are performed, the model is equipped with transition strips at the fuselage and at $30\%c$ of the wing and the empennage surfaces.

5.3.5 Corrections for wind tunnel wall effects

The experimental data were corrected for the following wind tunnel wall effects :

- Model blockage
- wake blockage
- Slipstream blockage
- Lift interference

- Streamline curvature
- Buoyancy
- Support Tare

Details of these corrections and their magnitude for the different models can be found in refs. [75, 74].

5.4 Thrust setting

The required thrust was obtained by setting the propeller speed with the motor control unit (MCU), as described in section 5.2.3.

The speed of both propellers was kept equal by selecting the appropriate control method (M1&M2) in the MCU.

An acceptable thrust simulation is obtained by setting equivalent values for the thrust coefficient T_c and the torque coefficient Q_c for a given angle of attack. This means that in general the blade setting is selected such that the T_c vs. Q_c of the full scale constant speed propeller is resembled as closely as possible.
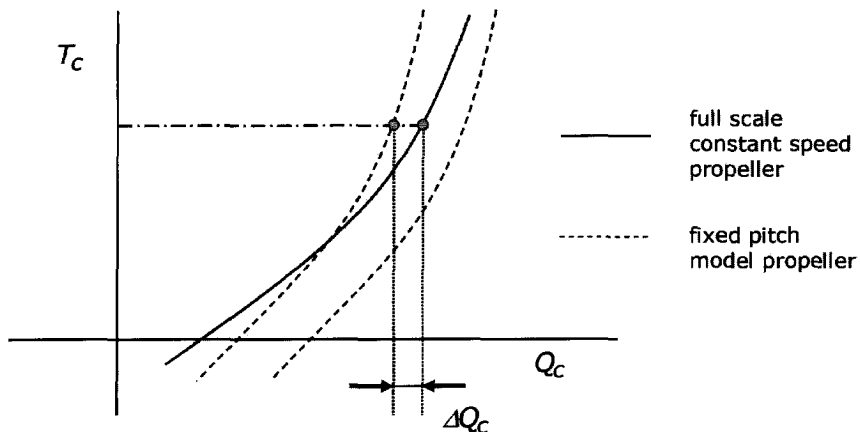
Figure 5.11: *Relation between the thrust coefficient and the torque coefficient for the full scale (variable pitch, constant speed) and the model propeller (fixed pitch, variable speed).*

As indicated in Fig. 5.11 under normal conditions the torque coefficient Q_c, shows a small error, ΔQ_c, which means that the swirl velocity for the given flight condition $(T_c = f(\alpha))$ is slightly different from the swirl component in the case of the full scale aircraft. This effect should be kept in mind when the results are analyzed. Nevertheless its impact is small if merely the trends of the propulsion effects are the goal of the investigations.

The flight condition that can be simulated depends on the value of the power coefficient that can be attained in the wind tunnel environment. Setting the power

coefficient of the full scale (index fs) equal to the model value (index m):

$$C_{p_m} = \frac{P_m}{\rho_m n_m^3 D_m^5} = C_{p_{fs}} = \frac{P_{fs}}{\rho_{fs} n_{fs}^3 D_{fs}^5} \qquad (5.1)$$

results in an expression for the required model power:

$$P_m = P_{fs} \left(\frac{\rho_m}{\rho_{fs}}\right) \left(\frac{n_m}{n_{fs}}\right)^3 \left(\frac{D_m}{D_{fs}}\right)^5 \qquad (5.2)$$

Assuming sea level conditions ρ_m/ρ_{fs} may be set to 1 while the ratio D_m/D_{fs} for the scale model of the Fokker F27 is 20. Thus the required model power depends solely on the speed ratio n_m/n_{fs}. The required speed of the model propeller can be estimated presuming an equal advance ratio of the propeller, $J_m = J_{fs}$. With the data given for the air density and the scale factor, the required model power now becomes:

$$P_m = 0.0025 P_{fs} \frac{V_m}{V_{fs}} \qquad (5.3)$$

Typical numbers to be substituted in eq.(5.3) are: $P_{fs} = 3200\,kW$ (per engine), $V_m = 50\,m/s$ and $V_{fs} = 133\,m/s$ (cruise condition); which results in a required model power of $P_m = 3.0\,kW$, per engine. Consequently cruising flight conditions can be simulated with the available power of $3.6\,kW$ per model motor.

5.5 Experimental results

5.5.1 Force measurements and surface pressure data

PROWIM The characteristics of the PROWIM model were determined in several test campaigns in the Low speed windtunnel LTT. Besides a general investigation of the propeller wing interference effects in a typical cruise condition, off-design configurations with deflected inboard and outboard flaps were investigated.

Most of the measurements were conducted at a dynamic pressure of $1500\,Pa$ ($Re_c = 0.8 \times 10^6$). To increase the thrust coefficient of the propeller with limited power available of the model motor, for some conditions a lower value of $245\,Pa$ ($Re_c = 0.3 \times 10^6$) was chosen. The complete set of test conditions for both the PROWIM and the APROPOS models is given in Table 5.1.

During the tests several parameters were changed, like wing angle of attack, propeller thrust, propeller rotation direction and flap deflection. In all cases with deflected flaps combinations of ($\delta_{f_i} > 0 \wedge \delta_{f_o} < 0$) and ($\delta_{f_i} < 0 \wedge \delta_{f_o} > 0$) were made. The purpose of this procedure was to adapt the lift distribution such that lower overall induced drag would be produced through lift enhancement at the upgoing blade side (UBS) and a lift decrease at the downgoing blade side(DBS). Since a change in

Table 5.1: *Test conditions for the PROWIM and APROPOS model.*

Test	Re_c	J	T_c
PROWIM			
Balance and surface pressures	0.8×10^6	$0.81 \rightarrow 1.20$	$0.0 \rightarrow 0.2$
Flow field survey	0.8×10^6	0.85	0.168
APROPOS			
	0.3×10^6	0.43	0.77
Balance and surface pressures	0.8×10^6	0.90	0.133
	0.8×10^6	0.92	0.120

flap setting in general shifts the zero lift angle of attack, comparing points of equal lift values would produce data points at different α. To prevent modification of the propeller thrust and the slipstream characteristics, the flap angles were selected such that the lift coefficient remained constant for the same angle of attack.

Since the forces acting on the propeller could not be measured separately the effective thrust was determined through a bookkeeping procedure as well as by the measurement of the total pressure jump over the propeller disk.

In case of the bookkeeping procedure the thrust of the propeller is defined as the difference in the tangential force between the propeller on (WNP) and the propeller off (WN) configuration. To determine the wing effect on the propeller thrust, the propeller rotational speed was measured at (approximate) windmill conditions for variable wing angle of attack with and without a constant propeller angle of attack with reference to the undisturbed flow direction (APROPOS case). The constancy of the power "delivered" by the model motor during these test underlines the fact that no measurable change in the thrust occurred. This check was only performed for the propeller positioned at $x_p/c = -0.71$. For other streamwise positions an alternative procedure was followed, as explained further on.

Overall balance data The thrust coefficients for the PROWIM model are quite low; nevertheless the effect of the propeller on the lift coefficient is clearly visible in Fig. 5.12. The change in the lift coefficient due to power effects increases with wing angle of attack as a result of the propeller normal force and the increased dynamic pressure in the slipstream. Besides these two effects the vertical component of the propeller thrust force delivers a contribution to the total lift coefficient.

The relative contributions of these factors can be determined by applying eq.(2.13) for the normal force gradient of the propeller. At $\alpha = 10°$ this leads to the distribution as presented in Table 5.2.

The normal force contribution is relatively low but the vertical component of the

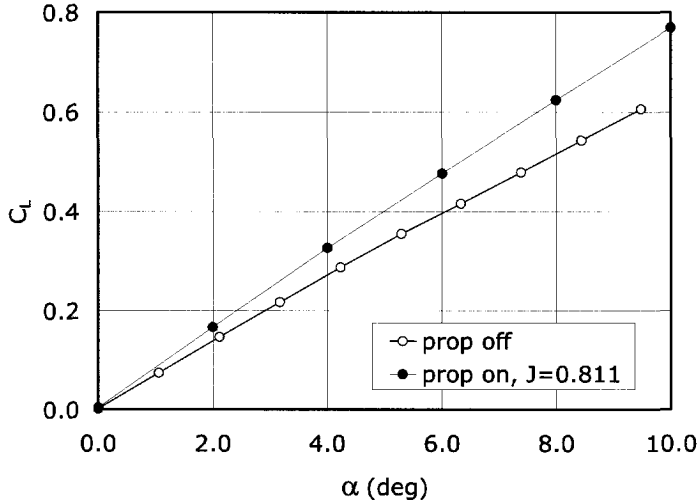Figure 5.12: *Lift coefficient of PROWIM versus α with and without running propeller ; $J = 0.811$; inboard up rotation.*

Table 5.2: *Relative contribution of propeller / slipstream effects on the lift increment due to power of the PROWIM model at $\alpha = 10°$; inboard up rotation.*

Contributor	ΔC_L	Rel. contribution
Propeller normal force	0.012	8.6 %
Vertical thrust component	0.035	25.1 %
Dynamic pressure and loading distr.	0.0924	66.3 %
Total propeller and slipstr. effect	**0.1394**	

thrust force contributes significantly to the total lift. The main effect is, as expected, the influence of the propeller slipstream both through the action of the dynamic pressure increase and the local angle of attack variation that are introduced by the swirl velocity distribution.
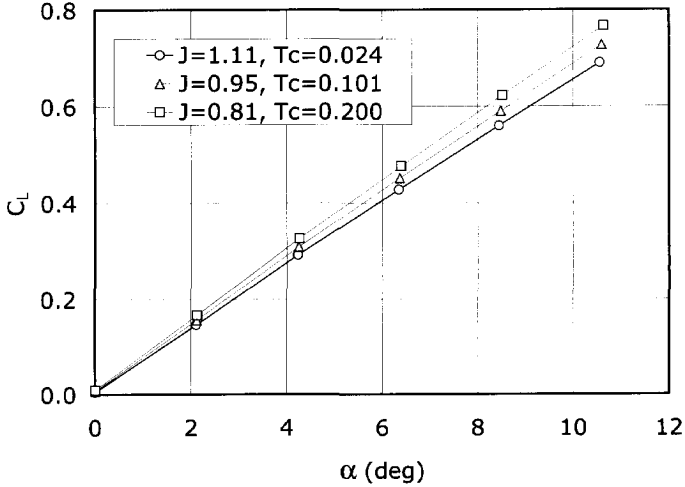
Figure 5.13: *Lift coefficient of PROWIM versus the angle of attack for different power settings of the propeller ; inboard up rotation.*

It is obvious that with increasing power of the propeller (higher thrust) the lift coefficient is enhanced (Fig. 5.13).

The propeller not only alters the lift coefficient, it alters the effective drag coefficient as well. With an elliptic like lift distribution the inboard up rotating propeller should produce lower (induced) drag than the outboard up rotating propeller. As can be seen in Fig. 5.14, indeed a remarkable gain in performance (through effective drag reduction) can be found when comparing propeller inboard up rotation and outboard up rotation. Here the effective drag coefficient, C'_D, is defined as:

$$C'_D = (C_D)_{prop\,on} - (C_D)_{prop\,off} \tag{5.4}$$

This effect is enhanced with the propeller positioned at a spanwise position where the lift distribution is steeper (e.g. the wing tip area) as will be shown later. As shown in Fig. 5.15 the inboard up rotation case produces a higher overall lift of the configuration which contributes to the total performance compared to the outboard up rotating case.
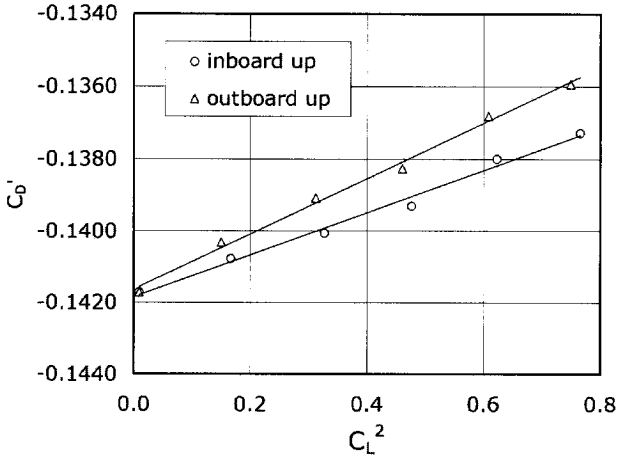
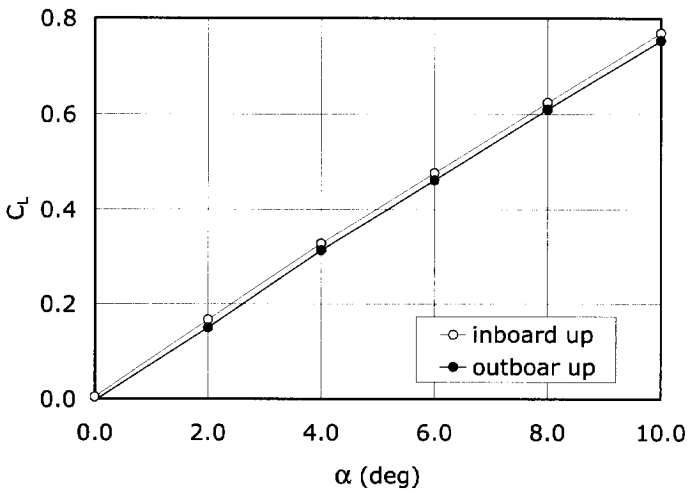Figure 5.14: *Effect of propeller rotation direction on the "drag coefficient", C'_D, of PROWIM ; $J = 0.85$.*

Figure 5.15: *Effect of propeller rotation direction on the lift coefficient of PROWIM; $J = 0.85$.*

The effect of the propeller rotation direction is important since almost all twin-engine propeller powered aircraft have co-rotating propellers which introduces secondary drag forces due to the trimming of the aircraft with asymmetrical aerodynamic loading (rolling and yawing moments, side force). Hence it is evident that application of two inboard up rotating propellers should improve the overall performance from aerodynamical point of view. The optimum loading distribution of the wing with an active tractor propeller is far from elliptical. For an IUR propeller apparently a high lift coefficient is needed inboard and a much lower value at the outboard side of the nacelle.

To check this optimization technique experimentally, some PROWIM tests were performed with flaps deflected differentially thus approximating the required lift distribution. In Fig. 5.16 the effective drag versus the wing lift coefficient is given for two combinations of flap settings. Clearly a reduction of the effective drag (i.e. propulsive force) can be realized by introducing an adaptation of the loading distribution. Of course application of flap deflection is not the appropriate method to optimize the wing lift distribution. In practice a combination of twist and airfoil shape (camber) adaptation is a more attractive way to attain the optimum loading (see chapter 6).
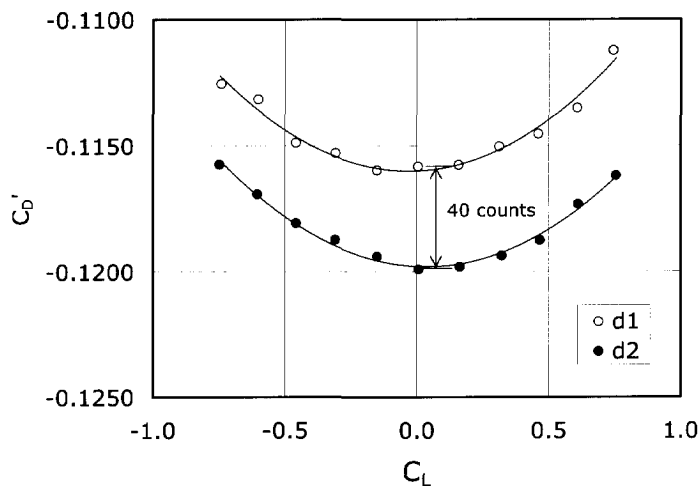

Figure 5.16: *Effect of differential flap deflection on the effective drag coefficient ; d1=flap setting $\delta_1 : \delta_{f_i} = \delta_{f_o} = 0°$, d2=flap setting $\delta_2 : \delta_{f_i} = 4°, \delta_{f_o} = -4.52°$*

Pressure distributions To get detailed information about the extent of the slipstream influence on the wing surface pressure measurements were carried out at different flow conditions. In Fig. 5.17 the pressure distributions are presented for the

propeller off case for three angles of attack $\alpha = 0°, 4°$ and $10°$. The pressure distribution is quite smooth in chordwise and spanwise direction although the presence of the nacelle is clear. Due to the increase in the vertical component of the velocity at both sides of the nacelle for $\alpha > 0°$ a higher flow angle of attack is introduced which results in more negative C_p values close to the nacelle.
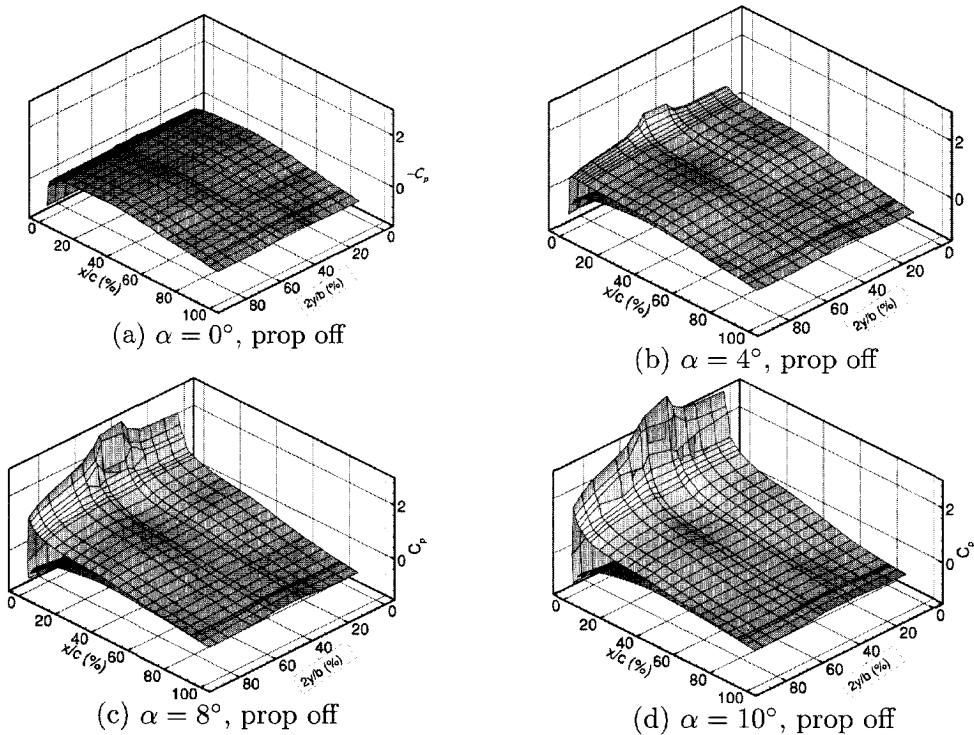

(a) $\alpha = 0°$, prop off

(b) $\alpha = 4°$, prop off

(c) $\alpha = 8°$, prop off

(d) $\alpha = 10°$, prop off

Figure 5.17: *Surface pressure distributions on PROWIM for the propeller off case (x=chordwise direction , y=spanwise direction)*

In Fig. 5.18 the pressure distributions for the case of the running propeller are presented while Fig. 5.19 contains typical 2-dimensional chordwise distributions.

The increase in the local lift at the UBS, due to the increased dynamic pressure and the increased local angle of attack, is clearly visible. Note that the stagnation pressure coefficient is higher than its normal value of 1.0, found for the configuration without running propeller.
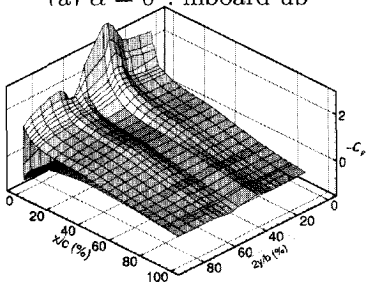
Fig. 5.19 shows that the strongest effects on the pressure distribution are found at the side of the upgoing propeller blade inside the slipstream. At the downgoing blade side the effects of dynamic pressure increase and angle of attack change due to swirl more or less compensate each other, as expected.
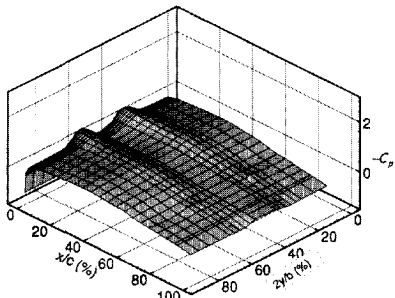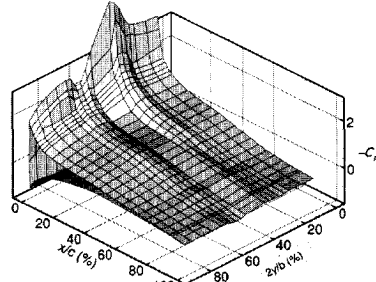
(a) $\alpha = 0°$, inboard up
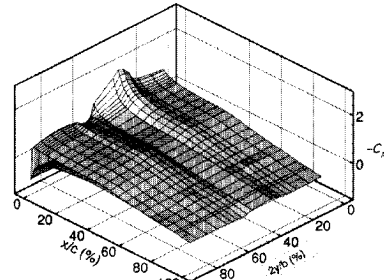
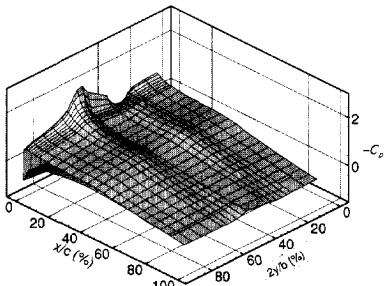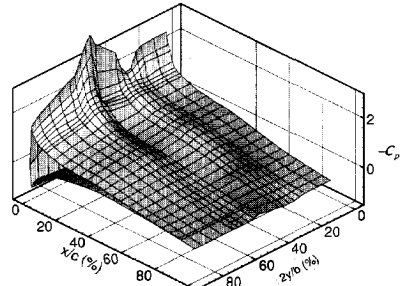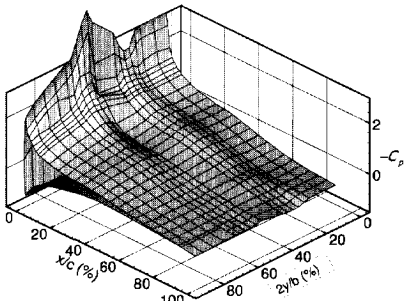(b) $\alpha = 4°$, inboard up

(c) $\alpha = 8°$, inboard up

(d) $\alpha = 10°$, inboard up

(e) $\alpha = 4°$, outboard up

(f) $\alpha = 8°$, outboard up

(g) $\alpha = 10°$, outboard up

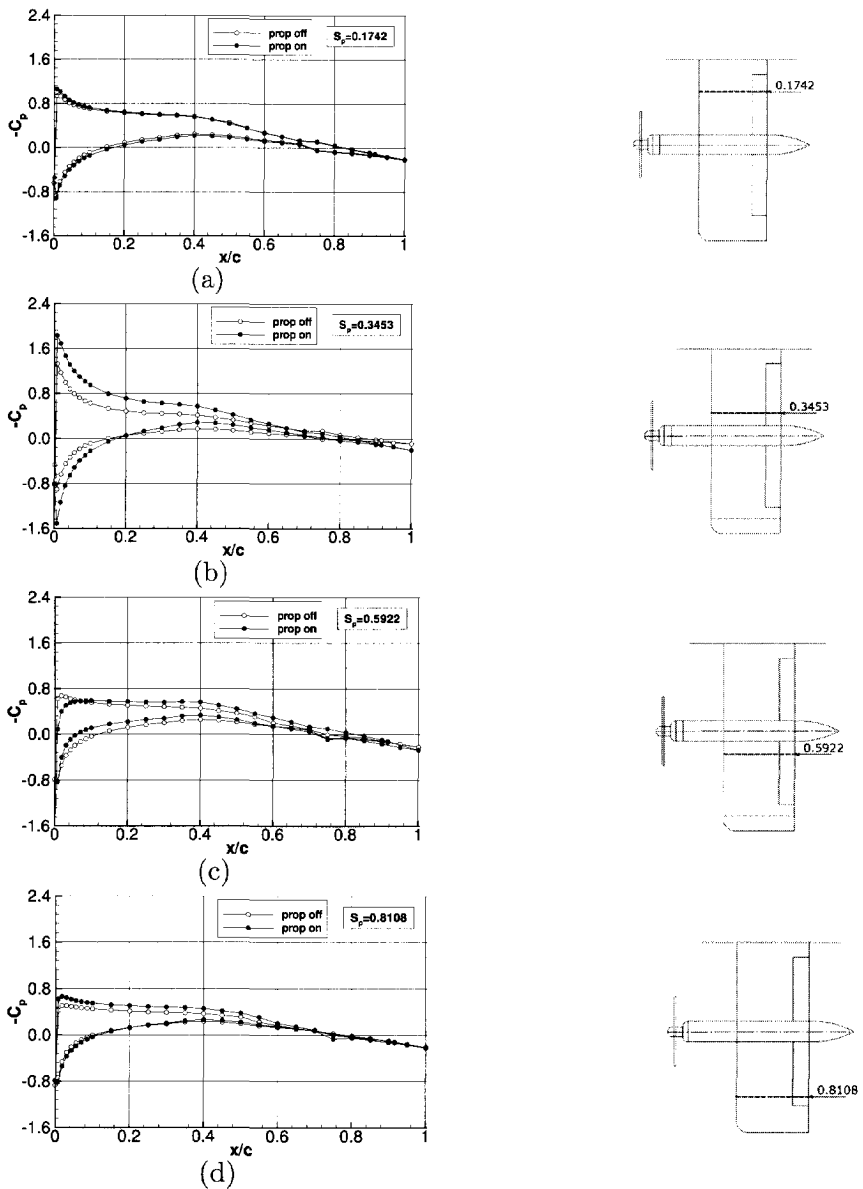Figure 5.18: *Surface pressure distributions on PROWIM for the propeller on case ; $J = 0.85$.*

Figure 5.19: *Effect of propeller slipstream on the surface pressure distribution of PROWIM ; $\alpha = 4.2°; J = 0.85;$ inboard up running propeller.*

The effect of the propeller slipstream on the boundary layer development can be seen in the pressure distribution for $\alpha = 10°$ in Fig. 5.20. The laminar separation bubble, at approximately $x/c = 0.02$, which is present for the measurements with the propeller off, is completely removed when the slipstream is present. The turbulent flow introduced by the propeller apparently has a strong influence on the development the boundary layer [27].
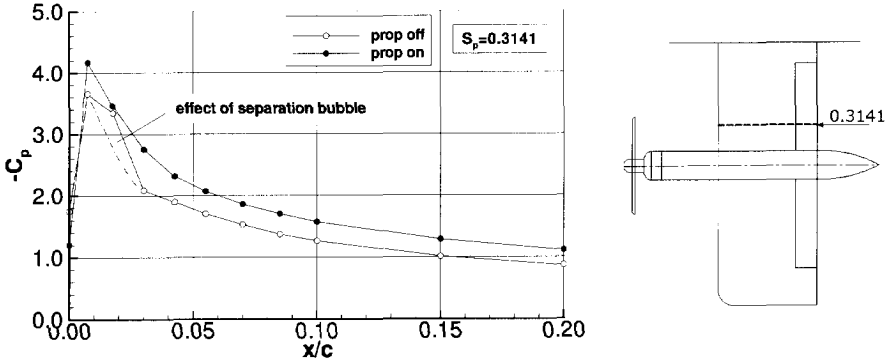

Figure 5.20: *Propeller slipstream effect on the presence of a laminar separation bubble ; J=0.85 ; $\alpha = 10°$.*

Normal and tangential force distribution   The chordwise pressure distributions were integrated to give the local values of the normal and tangential force coefficients. The latter of course excludes the contribution of the friction forces acting on the wing surface which increase on the wing part washed by the propeller slipstream.

Due to both the effects of the total pressure rise within the slipstream and the propeller induced swirl velocity the distributions of the normal and tangential force coefficients are strongly distorted.

Fig. 5.21 shows the spanwise distribution of the tangential force coefficient, C_t, for $\alpha = 0°$ and $10°$. For convenience, the data points in spanwise direction in the following figures are connected in the area of the nacelle ($0.414 < y/b/2 < 0.523$) although no data are available in this region.

The effects of the slipstream on C_t are quite small for $\alpha = 0°$. Nevertheless a strong influence is found for $\alpha = 10°$. For the propeller off case a more negative tangential force is found close to the nacelle due to the increased local angle of attack induced by the nacelle (enhanced leading edge suction). With the propeller active, the inboard side shows an even more negative C_t contribution due the swirl in the slipstream while for the nacelle's outboard side more positive values (less suction) are found. The outboard up rotating propeller shows the opposite effects as expected.
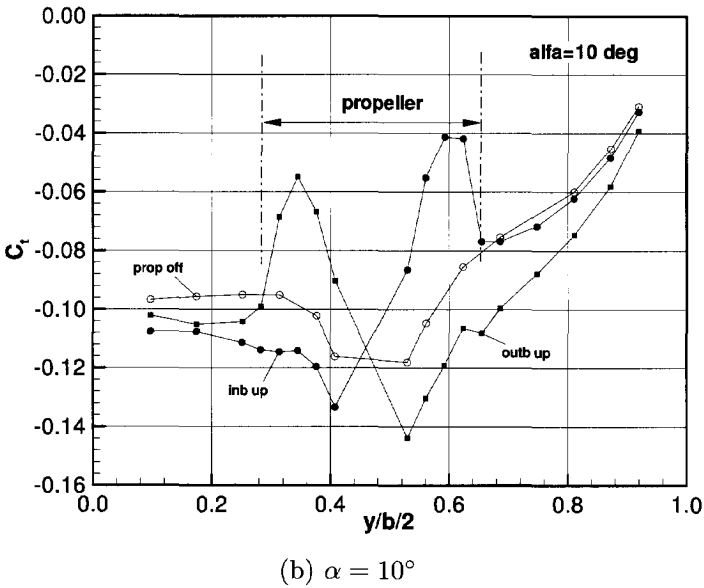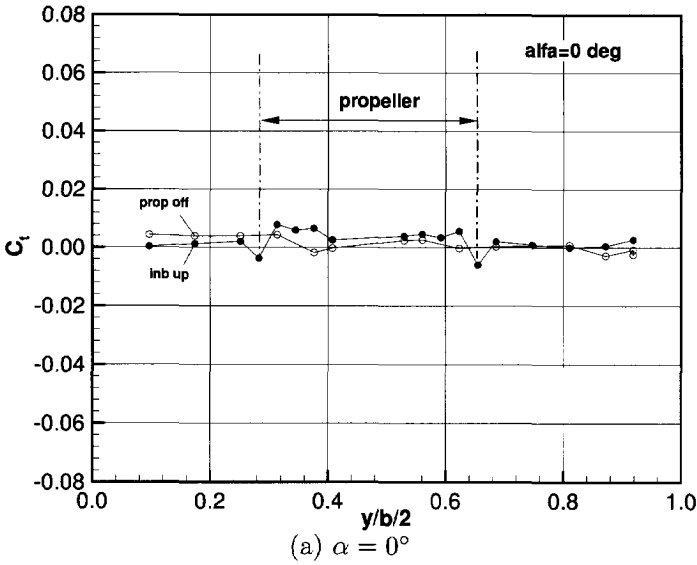
(a) $\alpha = 0°$

(b) $\alpha = 10°$

Figure 5.21: *Effect of the propeller on the distribution of the tangential force coefficient of PROWIM ; J = 0.85.*

Taking into account the increased leading edge suction at the UBS of the nacelle the key to a further reduction of the drag could be found in enhancing the effects on the UBS and diminish them at the DBS.

The overall performance of the propeller-wing configuration is for a considerable part determined by the spanwise loading distribution which is reflected by the normal force coefficient as depicted in Fig. 5.22. Significant distortion of the propeller off distribution is found when the propeller is active. From the curves it becomes clear that the change in the wing loading is not restricted to the wing part washed by the slipstream. Hence numerical codes that are used to predict the typical propeller-wing interference effects should incorporate power effects outside the slipstream envelope.
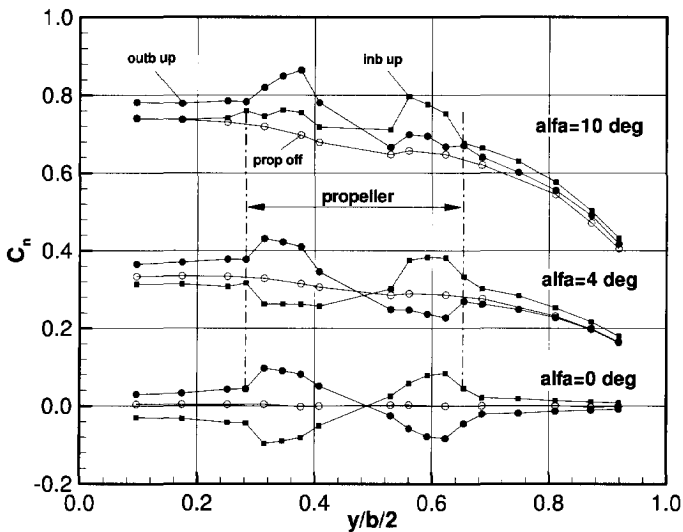

Figure 5.22: *Effect of the propeller on the normal force distribution of PROWIM for $\alpha = 0°$, $4°$ and $10°$; $J = 0.85$*

When comparing the normal force coefficients for $\alpha = 0°$ and $\alpha = 10°$, a different behaviour is found going from wing root to the tip. For $\alpha = 10°$ the decrease of the normal force at the DBS is much smaller, if not absent, due to the opposite effects of the axial velocity and rotational (swirl) velocity contributions. Consequently, the wing's span efficiency factor, e, which is directly related to the lift distribution and which is normally independent of the angle of attack, now changes with this angle.

Flow visualization This study was performed only for PROWIM and the test conditions were not exactly identical to the test conditions during the pressure and balance measurements. Nevertheless, the flow visualization study with the fluorescent

oil technique provides a qualitative analysis of the most important effects of the propeller on the wing.

The most interesting pictures are presented in Fig. 5.23 and Fig. 5.24. It should be noted that the colour changes in spanwise direction (chordwise stripes) are caused by adhesive tape that was put on the model surface to protect the pressure tabs from being contaminated by the fluorescent oil.

Fig. 5.23a, which presents the prop off condition at $\alpha = 0°$, clearly shows a separation bubble which is typical for the airfoil used in the wing (NACA-64$_2$A015). The separation is located at approximately 52% while reattachment is found around 66%. Notice that a fairly large area of the wing root is influenced by the boundary layer of the turntable. Also in the nacelle/wing juncture area a strong effect is found as the laminar boundary layer has become completely turbulent. The transition to a turbulent boundary layer is caused by the horseshoe vortices that develop as a secondary juncture flow.

In Fig. 5.23b the propeller is active at an advance ratio of $J \approx 0.85$. The influence of the slipstream is clearly visible. Although it is difficult to determine whether the flow in the washed area of the wing is laminar or turbulent or transient [27], it looks like a turbulent flow. Due to the action of the propeller the separation bubble is completely removed in the slipstream wetted area of the wing and the flow over the nacelle has changed compared to the prop off situation. It is interesting to notice that there is a small forward shift in the position of the separation bubble present at the wing inboard side. This indicates that the influence of the propeller is not completely confined to the area of the wing washed by the slipstream.

Fig. 5.24 shows the influence that a change in power output of the propeller has on the wing and nacelle. The area of separated flow at the wing trailing edge, that exists for the given angle of attack of $\alpha = 8°$, seems to the become smaller as the propeller power output is increased from $J = 1.059$ (Fig. 5.24a) to $J = 0.849$ (Fig. 5.24b). This is the direct result of the flow guiding effect that the propeller slipstream exhibits in the slipstream wetted area. Additionally a small change in the flow over the nacelle due to the change in power output is found.

5.5.2   APROPOS

Spanwise propeller position   The spanwise gradient of the lift distribution at the position where the slipstream washes the wing plays an important role with respect to the possible performance benefits introduced by the propeller. This was already shown in earlier investigations [10, 11, 79]. Gentry et al [80] who investigated the effects of propellers located at more inboard positions, state that changes in the nacelle position and inclination have very little effect on the performance for the cruise wing configuration. The experiments that were performed with the APROPOS test set-up, however, shows that this statement needs to be reviewed.

First of all the influence of the spanwise propeller position was investigated. In

prop off $\alpha = 0°, \delta_{f_i} = 0°, \delta_{f_o} = 0°$

(a)

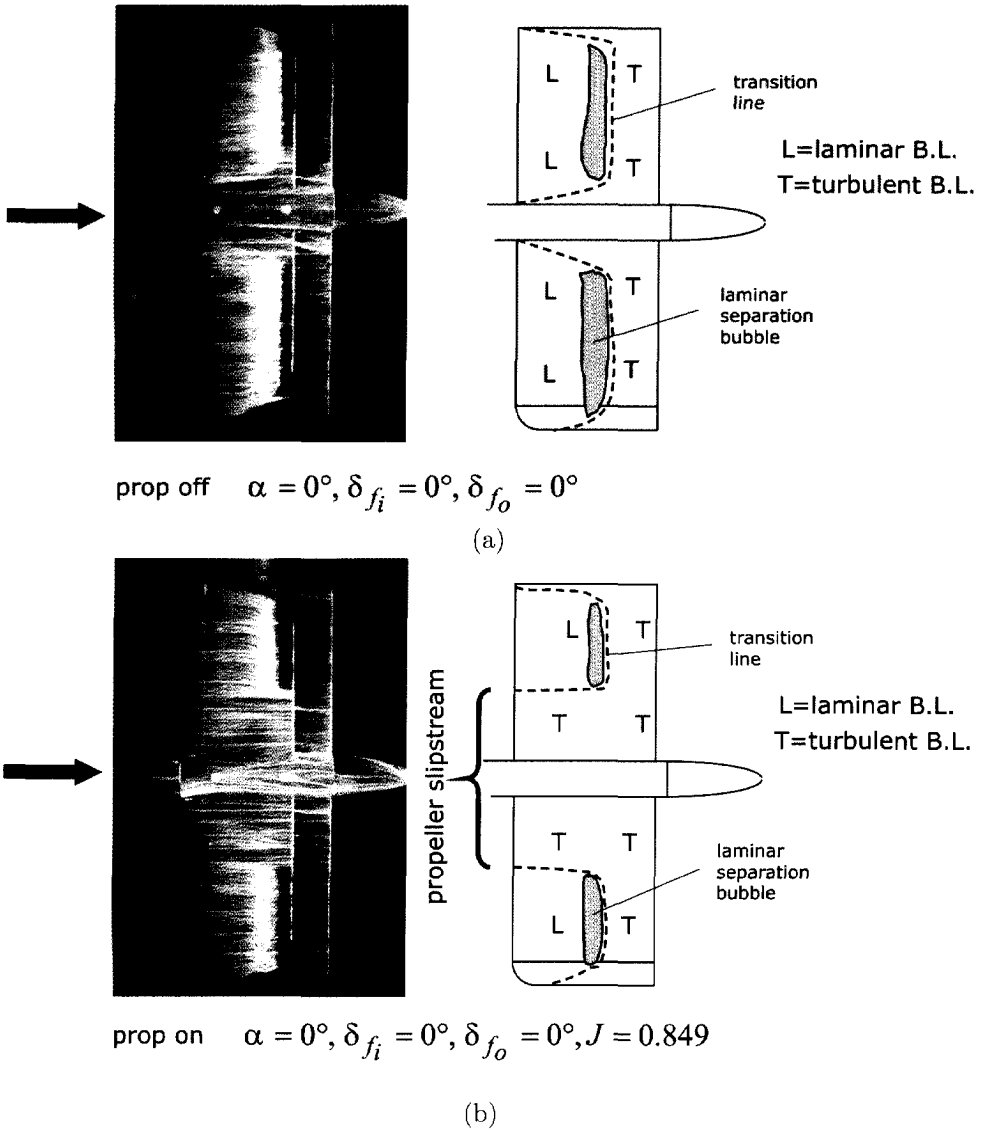prop on $\alpha = 0°, \delta_{f_i} = 0°, \delta_{f_o} = 0°, J = 0.849$

(b)

Figure 5.23: *Flow visualization on PROWIM using a fluorescent oil technique ; comparison of prop off (a) and prop on (b) condition at $\alpha = 0°$.*

prop on $\alpha = 8°, \delta_{f_i} = 0°, \delta_{f_o} = 0°, J = 1.059$

(a)

prop on $\alpha = 8°, \delta_{f_i} = 0°, \delta_{f_o} = 0°, J = 1.059$

(b)

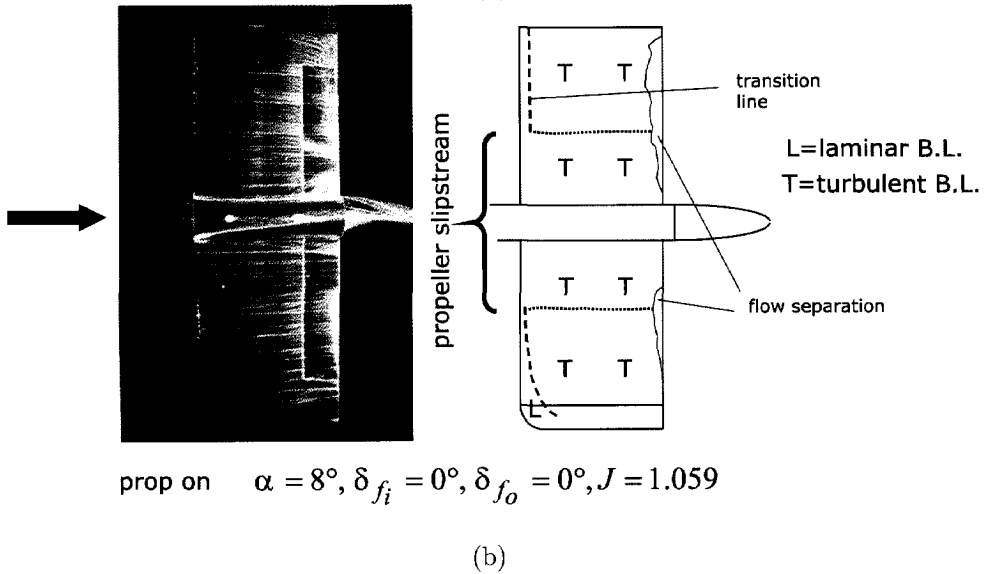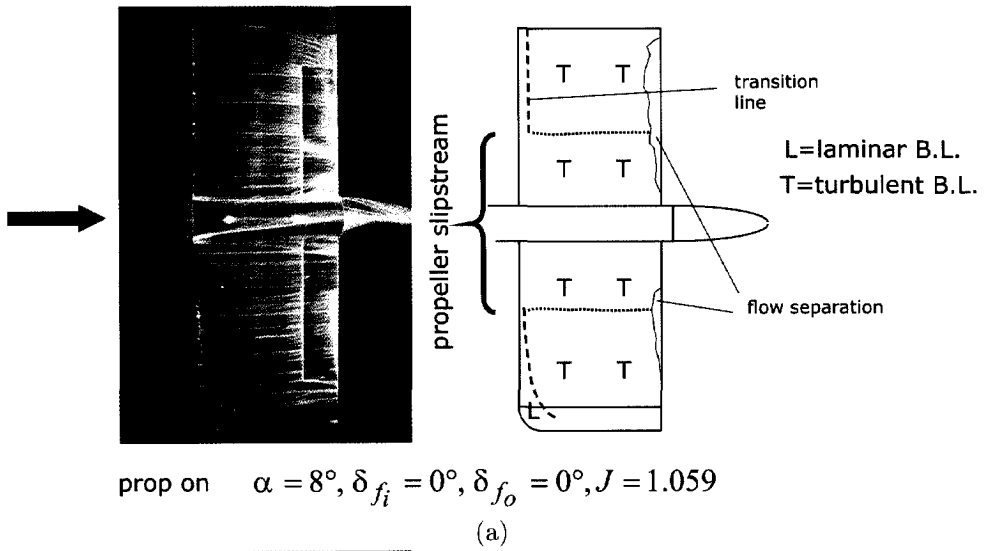Figure 5.24: *Flow visualization on PROWIM; comparison of two thrust conditions at $\alpha = 8°$.*

Fig. 5.25 and Fig. 5.26 the effects of the spanwise position is presented for a rather low thrust condition.

(a) $\alpha = 1.05°$
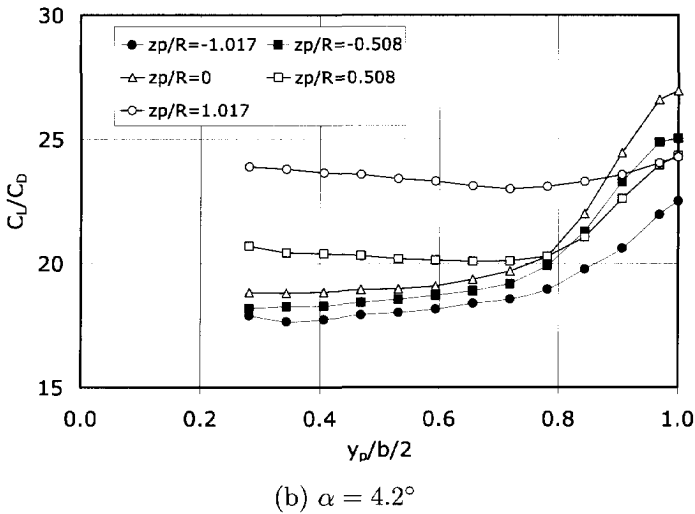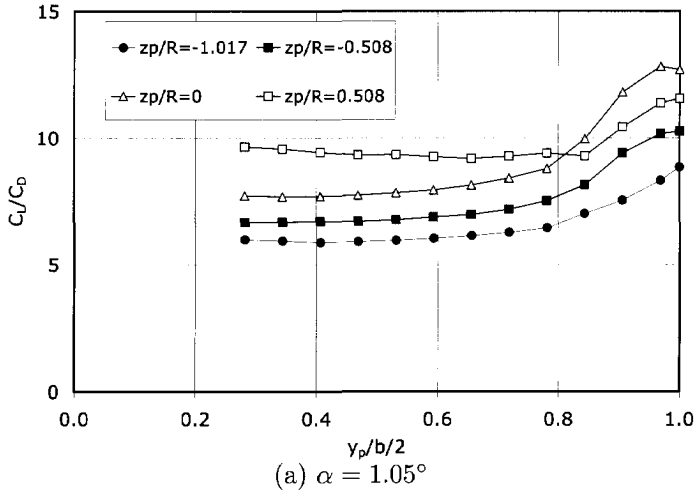

(b) $\alpha = 4.2°$

Figure 5.25: *Effect of the propeller spanwise location, y_p, on the lift/drag ratio of the APROPOS wing for several vertical propeller locations, z_p; $J = 0.92$; $T_c = 0.025$; $\alpha_p = 0°$.*

The different curves in Fig. 5.25 correspond to different vertical positions of the propeller, which will be discussed further on in more detail. As expected, the

performance of the wing improves when the propeller is moved in the direction of the
wing tip indicated by the increasing wing lift/drag ratio.

The reason for this change in the lift/drag ratio can be found in an increase in the
lift coefficient combined with a concurrent reduction of the drag coefficient towards
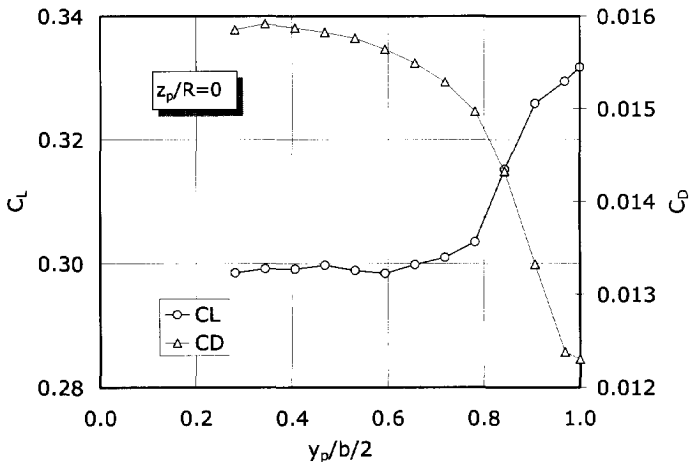the tip, as indicated by the curves in Fig. 5.26 for $\alpha = 4.2°$.

Figure 5.26: *Effect of the propeller spanwise location on the lift and the drag
coefficient of the APROPOS wing; $z_p = 0$; $J = 0.92$; $T_c = 0.025$;
$\alpha = 4.2°$; $\alpha_p = 0°$.*

Apparently the vorticity field (swirl) induced by the inboard up rotating propeller
attenuates the wing tip vortex influence. As a result, the effective aspect ratio of
the wing is increased which leads to lift increase and drag decrease. Test with the
propeller rotating in the same direction as the wing tip vortex (outboard up) revealed
negative effects, as expected. Tests at several angles of attack and vertical propeller
positions (see Fig. 5.25) have shown that the effect at the wing tip is maximum
when the slipstream centerline is exactly in line with the wing tip vortex. Although
the spanwise propeller position strongly affects the performance for positions close to
the wing tip, it should be remarked that small changes in y_p for realistic positions
$(0.25 < y_p/b/2 < 0.30)$ show negligible effects.

Vertical propeller position   Since the current twin-engined turboprop aircraft
all show quite different vertical propeller positions with reference to the wing, the
z_p coordinate (Fig. 5.27) was changed in the APROPOS tests to investigate the
performance effects. The experimental results of these tests are also compared to
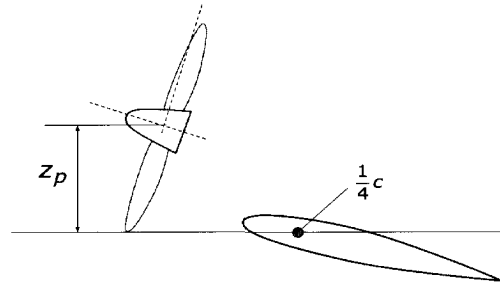theoretical predictions in chapter 6.

Figure 5.27: *Definition of the vertical propeller coordinate, z_p.*

The tests showed that the vertical propeller position has a remarkable effect on the performance of the wing.

For realistic spanwise locations of the propeller a high position is beneficial with respect to the wing lift/drag ratio, mainly due to a lift enhancement induced by the combination of dynamic pressure increase at the wing's upper surface and contraction of the slipstream which leads to increased flow angles of attack.

To study this phenomenon in more detail additional balance measurements were performed for variable z_p positions of the propeller. During these test the propeller was located at $y_p/b/2 = 0.281$ and $x_p/R = -1.44$. Both low thrust and high thrust conditions were analyzed. In Fig. 5.28 the behavior of the wing lift/drag ratio versus the propeller vertical position is presented for three angles of attack: $\alpha = 4°$, $8°$ and $12°$.

The vertical position of the propeller clearly influences the wing performance where the higher values of C_L/C_D are found for the most positive values of z_p in the case of the low thrust coefficient of $T_c = 0.137$. For the higher thrust coefficient, however, the trend of the curves changes somewhat. A relative peak is found for slightly negative z_p values (Fig. 5.28b). The cause of this behavior is easily explained by the lift and drag curves depicted in Fig. 5.29. Whereas only moderate changes in C_L and C_D occur for the lower thrust coefficient a more pronounced effect of the propeller slipstream can be noticed for the higher thrust case.

The peak around $z_p = -0.2$ in Fig. 5.28b for $\alpha = 4°$ is provoked by the combination of a reduction in the drag coefficient and a reasonable lift coefficient in this location. The local drag minimum is likely to be caused by the fact that for z_p value close to zero a smaller part of the immersed part of the wing is washed by the slipstream annulus that contains increased dynamic pressure. This principle is illustrated in Fig. 5.30.

The increase in the lift coefficient, that is found when the propeller is moved from negative to positive z_p values, is attributed to the effect of the contraction of the slipstream. For high z_p/R values this results in a local wing angle of attack increase
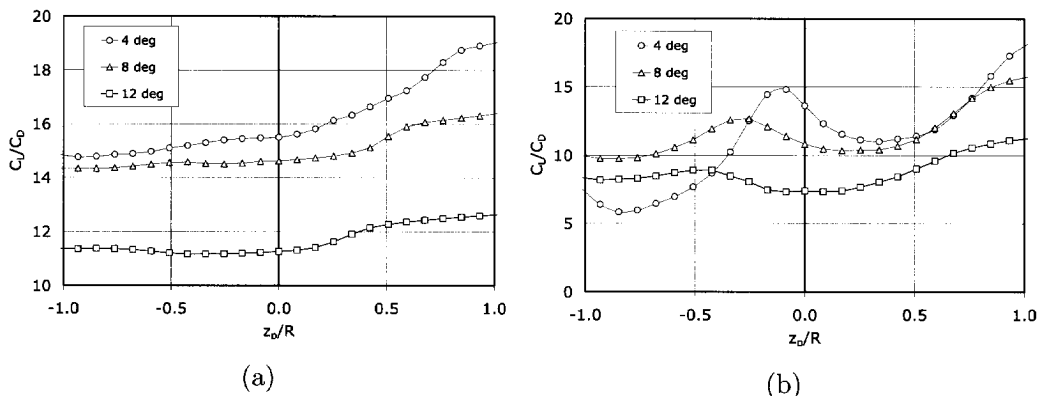
Figure 5.28: *Effect of vertical propeller position on the lift/drag ratio of APRO-POS; (a) low thrust ($J = 0.9$; $T_c = 0.137$) ; (b) high thrust ($J = 0.433$; $T_c = 0.985$).*

and a lift increment; for the lower z_p/R values an opposite effect occurs.

For $\alpha = 4°$ the maximum value of the lift coefficient is found for $z_p/R = 0.51$. This configuration is visualized in Fig. 5.31. Here the average dynamic pressure increase at the wing position reaches its maximum value. For lower values of z_p/R the pressure deficit in the core of the slipstream, which is caused by the nacelle wake, results in lower lift coefficients. The fact that the lift does not increase for $z_p/R = -0.51$ indicates that the swirl velocity in the slipstream also plays a role in the lift enhancement process. In case the slipstream centerline is located underneath the wing chord reference line the inboard up rotating propeller strengthens the cross flow at the lower wing surface in the direction of the wing tip. Thus the overall wing lift is reduced.

Summarizing one can state that the wing may benefit from the presence of the propeller since C_L/C_D rises for the higher propeller positions. The trends that were found seem to confirm the (limited) observations by other researchers that the projection of the propeller plane onto the wing strongly influences the local wing lift.

Streamwise propeller position   Several windtunnel investigations indicate the necessity to take into account the strong aerodynamic interactions that can occur for unconventional positions of the propeller. An important configuration is the one where the propeller is located close to the wing.

Especially for over-the-wing (OTW) propeller configurations favorable interference effects can be obtained. Johnson and White [81], for example, found significant performance improvements at a climb lift coefficient of 0.7 over design which had the
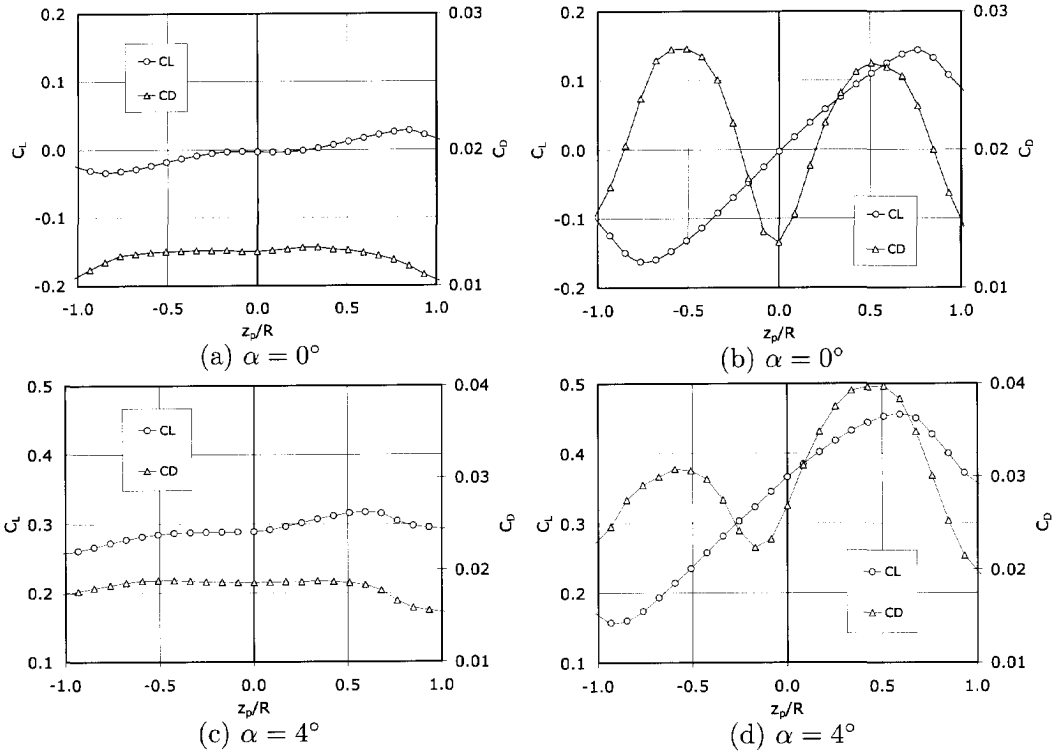
Figure 5.29: *Effect of propeller vertical position on the lift and drag coefficient of the APROPOS wing at $\alpha = 0°$ and $\alpha = 4°$; (a+c) low thrust ($J = 0.9$; $T_c = 0.137$) ; (b+d) high thrust ($J = 0.433$; $T_c = 0.985$)*
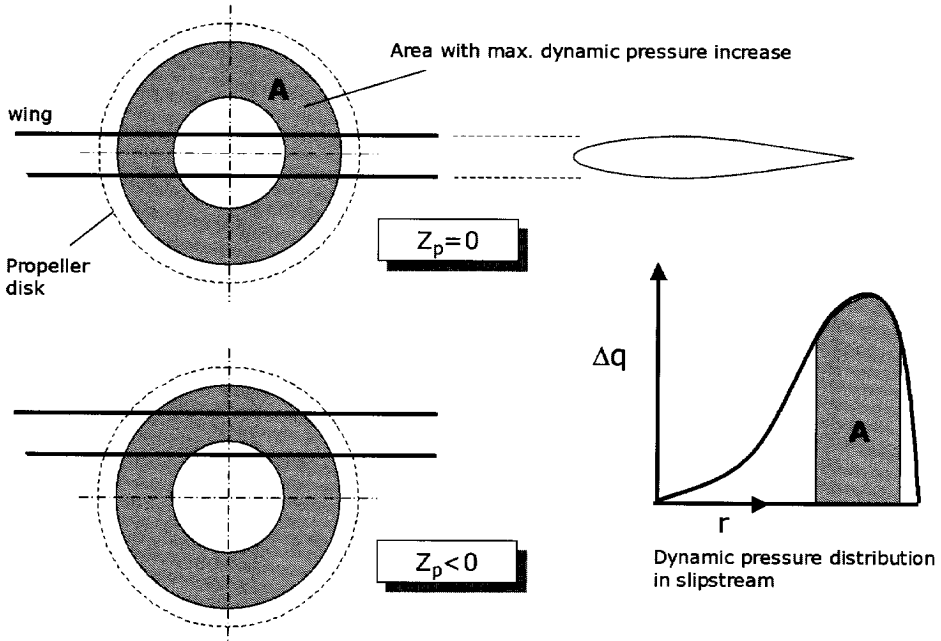
Figure 5.30: *Increase in average dynamic pressure over the wing due to off-centre position of the propeller ($z_p \neq 0$).*
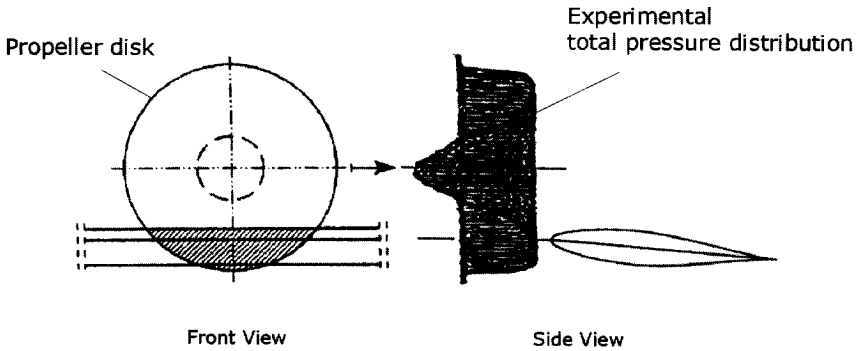
Figure 5.31: *APROPOS propeller/wing configuration for maximum lift increment due to the propeller slipstream; $\alpha = 4°$; Veldhuis [12].*

propeller in front of the wing. The aerodynamic effects were also studied by Cooper et al [82]. They also showed that beneficial interaction effects were attainable for wings with deflected flaps. Remarkable and unexpected is their conclusion that the efficiency of the propeller was maintained. Johnson et al [81] used a full 3D-aircraft model to check the effects of an OTW propeller under climb and cruise conditions. With this arrangement a clear reduction of the wing drag for an increasing thrust coefficient could be achieved. A beneficial side effect of their configuration was that the aft location of the propulsion system produced stabilizing pitching moment contributions originating from the propeller normal forces located behind the aircraft center of gravity.
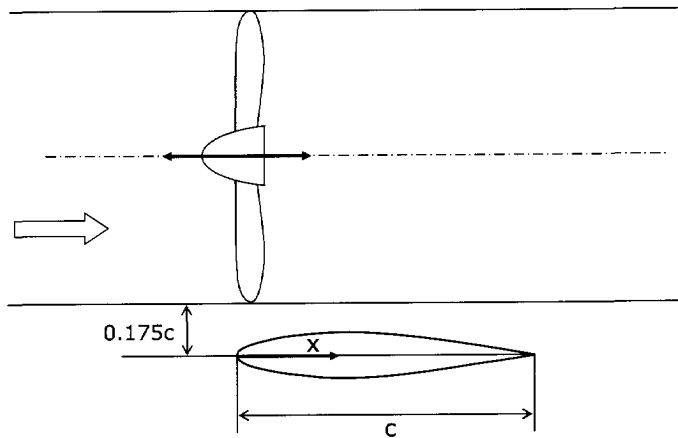
Figure 5.32: *Over-The-Wing (OTW) propeller arrangement tested with the APROPOS test set-up.*

Bearing this in mind the interference effects that occur for closely coupled propeller wing configuration in OTW fashion, the APROPOS set-up was used to vary the streamwise propeller position for a typical high propeller configuration.

During these experiments it was noticed that no significant influence of the propeller streamwise placement was found for positions well ahead in front of the wing leading edge. However, for the propeller placed very close to the wing, i.e. in an OTW fashion, remarkable strong interference effects were found. Although the wing angle of attack may very well have an important influence on the magnitude of the OTW propeller effect, this investigation was only performed at a (corrected) angle of attack of $\alpha = 4.2°$.

Significant gains in lift and reductions in wing drag were experienced when positioning the propeller above the wing (Fig. 5.32). In Fig. 5.33 the wing lift and drag coefficient versus the streamwise propeller position are presented. The propeller

Figure 5.33: *Effect of propeller streamwise position on the wing lift (a) and the drag (b) coefficient of APROPOS for the low and high thrust condition; $\alpha = 4.2°$.*

plane was perpendicular to the undisturbed flow direction, and it was positioned to give a tip clearance of 17.5%c of the chord above the wing $\frac{1}{4}c$ line.

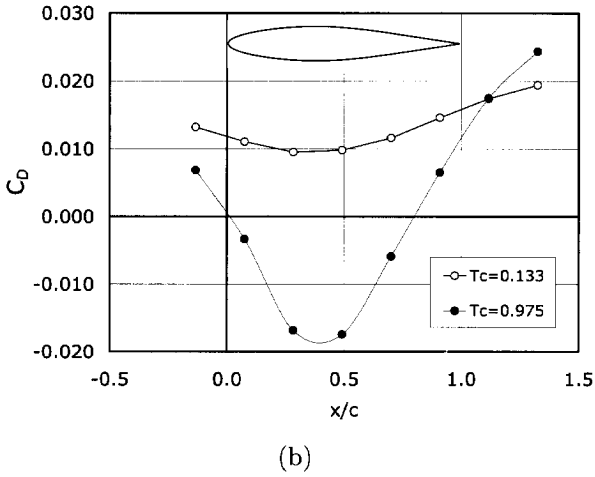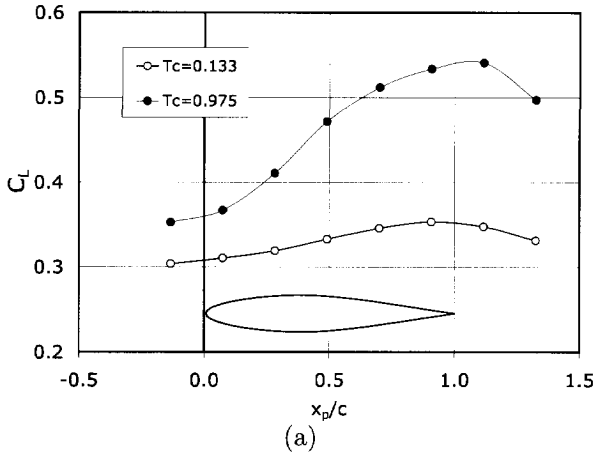Where the influence of the streamwise position is noticeable but small for the low thrust coefficient, the high thrust condition results in very high lift and even negative wing drag, for propeller positions just above the wing. The favorable effects show a maximum with regard to the wing drag, for propeller locations around $x_p/c = 0.40$ and they decrease when moving the propeller further backward. Nevertheless the wing lift still increases in this direction, a result which is supported by Gentry et al [80]. The key aerodynamic feature is the propeller induced flow over the wing causing increased lift and reduced drag. Especially the strong inflow into the propeller disk and the slipstream contraction, which enhance the leading edge suction has a strong influence on this drag reduction. As a result of the low drag value at $x_p/c = 0.40$ the wing lift to drag ratio also demonstrates a maximum at this propeller position, as indicated in Fig. 5.34.
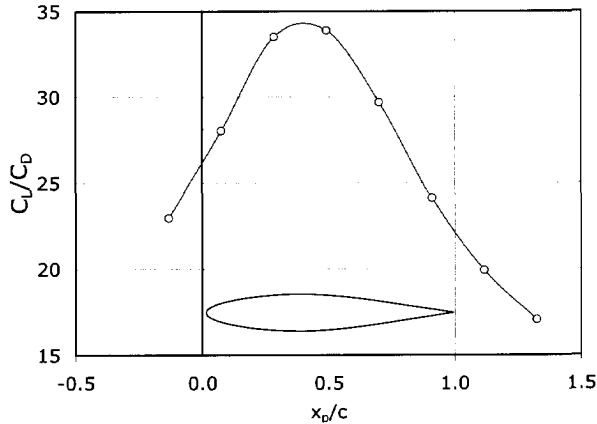
Figure 5.34: *Effect of propeller streamwise position on APROPOS wing lift/drag ratio at low thrust ; $J = 0.905$; $T_c = 0.133$; $\alpha = 4°$.*

In general, for a propeller position close to the wing, reductions in the wing drag might be associated with a drop in propeller efficiency (or propeller thrust for given power setting). For this reason a performance indication obtained from the configuration in which both the propeller and the wing are combined is more representative for the overall benefits. Therefore, to judge the total propeller effect the drag change of the wing can be treated as a propeller thrust augmentation. In this case an effective propulsive efficiency can be chosen:

$$\eta_{eff} = \frac{T_c - \Delta C_D \frac{S}{D^2}}{P_c} \qquad (5.5)$$

Since no internal balance was present to measure the thrust of the propeller separately, the total pressure across the propeller disk was measured. Integration over the disk then yields the effective thrust of the propeller. This was done for two positions of the propeller $x_p/c = 0.50$ (denoted A) and $x_p/c = -0.71$ (denoted B) respectively. For the high thrust condition ($J = 0.43$) values of $T_c = 0.7701$ and $T_c = 0.785$ were found for the positions A and B respectively. As expected the thrust coefficient for A is somewhat lower due to the increased flow velocity over the wing upper surface.
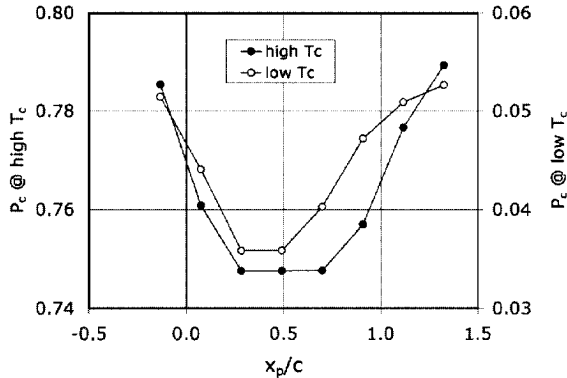
Figure 5.35: *Model motor power coefficient versus streamwise propeller position* ; $\alpha = 4.2°$.

Fortunately the power required for this T_c-value is also reduced (Fig. 5.35). Apparently the effect of the wing proximity on the propeller performance is relatively small. If we look at the value of η_{eff} we find that it changes from 0.346 at position B to 0.408 at position A in the high thrust case. For the low thrust case this value changes from $\eta_{eff} = 0.793$ at position B to $\eta_{eff} = 0.851$ at position A. This is a remarkable performance improvement. Again it should be noted that the OTW positioning of the propeller reveals an increment in lift and a reduction in drag. Johnson et al [81], who performed comparable tests, always found a drag rise which cannot be explained based on the results from the APROPOS tests.

In Fig. 5.36 some examples of the pressure distributions at the spanwise location of the propeller centre line are presented. The C_p curves in these figures should be on top of each other since the angle of attack in this case is $\alpha = 0°$ and the wing profile is symmetrical (NACA64$_2$-A015). Fig. 5.36a, that was generated for the low thrust condition, shows that for the propeller positioned well ahead of the wing leading edge almost a symmetrical pressure distribution is indeed found whereas the propeller positioned above the wing results in a noticeable effect on C_p. As indicated before this is the direct effect of inflow into the propeller disk and the contraction of the

Figure 5.36: *Effect of streamwise propeller position and thrust condition on the surface pressure distribution of the APROPOS model at $\alpha = 0°$; (a) comparison of x-position at $T_c = 0.133$; (b) $x_p/c = 0.54$ and $T_c = 0.77$.*

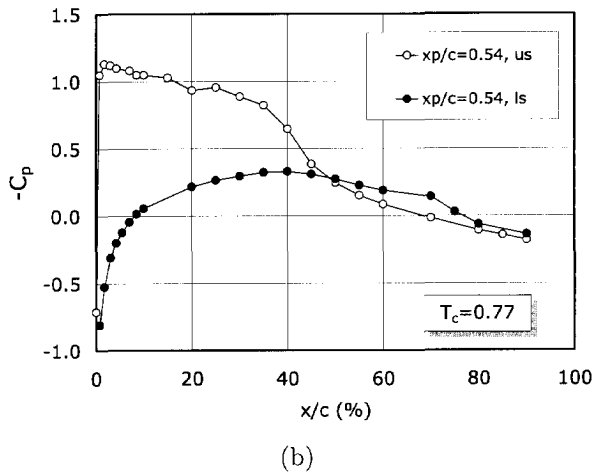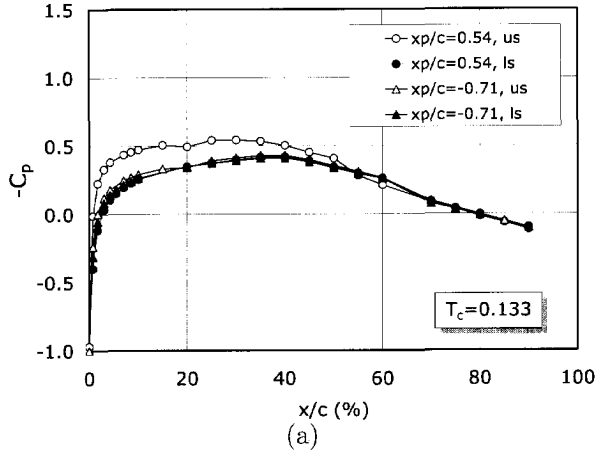slipstream. Comparing Fig. 5.36a and Fig. 5.36b, where the latter shows the OTW configuration but now for higher propeller thrust, immediately confirms the strong influence of the stronger slipstream contraction leading to increased asymmetry in the pressure distribution.

Although some propeller positions seem to result in considerable benefits it should be noted that the connection between the nacelle and the wing generally reduces the lift, changes the lift curve slope and increases the drag. Therefore practical implementation of an OTW propeller arrangement certainly requires further detailed research.

Additional aspects of the OTW configuration will be treated in Chapter 6, based on CFD-calculations on the APROPOS model.


Effect of propeller inclination   As described earlier, a fixed position of the propeller with reference to the wing brings about a strong deformation of the slipstream symmetry when the wing is given a positive angle of attack. In principle this causes detrimental effects with regard to the induced drag of the wing. When looking at the propeller itself it is important to understand that the wing generally introduces upflow in the propeller disk area. Thus the correct setting of the tilt down angle for minimum alternating loads on the blades depends typically on the streamwise position of the propeller. It should be noted that significant flow non-uniformity might also be introduced by the presence of the nacelle when it is positioned at some non-zero angle of attack. The fact that this has a negative effect on the propeller is another reason to explore the possible advantageous effects of a Propeller-Tilt-Down configuration, further denoted as PTD. Propeller thrust line tilt down may be used to improve power-on longitudinal stability through reduction of in-plane normal forces and increase of the vertical position of the thrust axis with reference to the aircraft's c.g.

Normally the angle of incidence given to a propeller is limited to approximately $2°$ which effectively reduces the cyclic loading due to the wing upwash generated skewed flow field. To verify the possible performance effect of PTD configurations experimentally much bigger angles were analyzed.

Although all the tests were performed for different y_p and z_p values combined with several propeller incidence angles, α_p, only the results for $y_p/b/2 = 0.469$ and $z_p/R = 0$ will be presented here.

In Fig. 5.37 the lift and the drag coefficient of the APROPOS model are given versus the propeller angle of attack, α_p.

The tilting-down of the propeller evidently leads to improved performance of the wing through an increase in the lift and a significant decrease in the drag. This results in a notable rise of the lift/drag ratio, as indicated in Fig. 5.38. Note that the underlying cause is principally different from the effect of vertical displacement of the propeller since now the velocity distribution in the slipstream has undergone a major
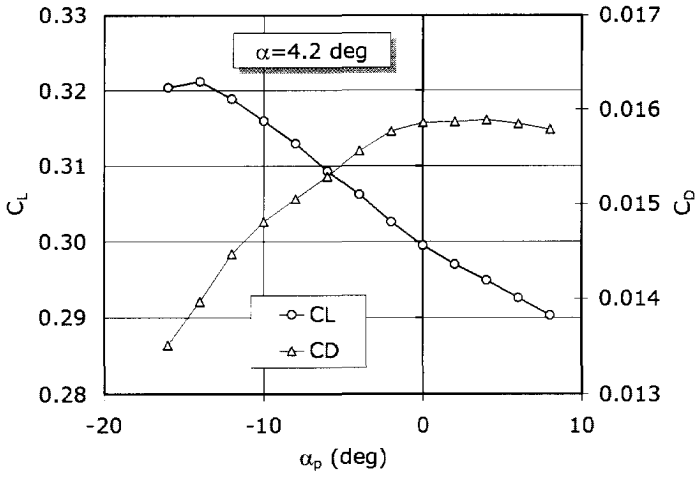
(a)
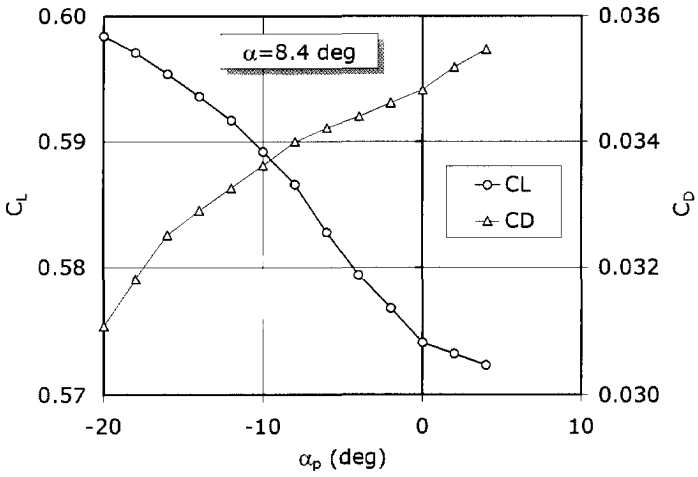
(b)

Figure 5.37: *Effect of propeller angle of attack on the wing lift and drag coefficient of APROPOS ; $J = 0.92$; (a) $\alpha = 4.2°$; (b) $\alpha = 8.4°$.*

change (Veldhuis [12]). These experimental results are qualitatively in agreement with the results produced by the optimization code that is discussed in Chapter 7.
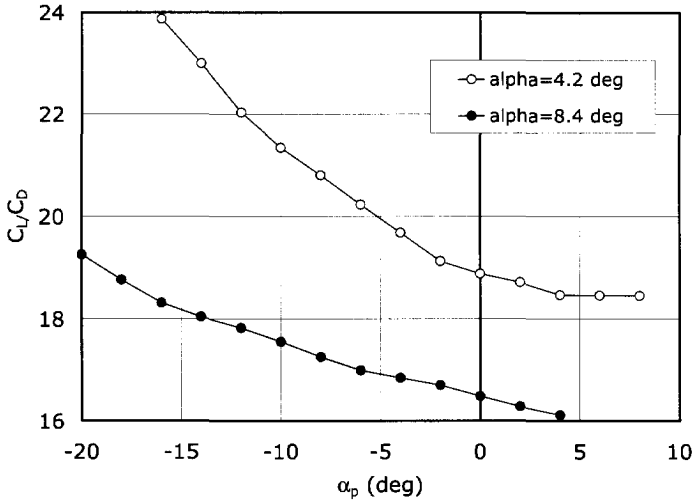
Figure 5.38: *APROPOS wing lift/drag ratio versus the propeller angle of attack relative to the wing chord reference line ; J* = 0.92.

Note that the (small) negative normal force acting in the propeller plane and the (small) reduction in effective thrust hardly reduces the positive effects of the PTD. In contrast to the OTW layout, an innovative configuration with application of propeller tilt down angles up to approximately 15° should not raise major problems from the structural point of view. In chapter 6 the discussion on this layout is extended, based on numerical predictions.

5.5.3   F27 MODEL

The models PROWIM and APROPOS that were used during the earlier experimental test campaign produced valuable results and provided detailed insight in the complex flow that is associated with a slipstream washing a trailing wing. The main disadvantages of these models, however, are reflected in their geometry and layout. Since in both cases a half model was used in the windtunnel the reflection plate to which the wing is mounted acts as a plane of symmetry in all cases. This means that the models do not allow investigation of the (common) case of co-rotating propellers. Further disadvantages are the lack of a fuselage and empennage which are known to generate small effects on the propeller wing interaction phenomena and last but not least the rather low aspect ratio ($A = 5.33$) of both half models.

To extend the experimental research on the propeller effects somewhat further, in the same windtunnel environment, additional tests were carried out on the F27 model that was described in section 5.3.4.

The tests on the F27 model were restricted to the investigation of:

- the overall propeller effect

- the effect of propeller rotation direction

- the effects of the propeller slipstream on the flow behavior close to stall

Reynolds number effects The Reynolds number that is selected during propeller-on tests is important for two reasons:

- A low Reynolds number results in a development of the boundary layer that significantly differs from the full scale behavior. This may lead to premature separation effects when the propeller induced wing angle of attack increases for the high thrust cases

- A Reynolds number that is set to high (for the given model scale) hinders the setting of a high thrust coefficient.

The latter can be seen as follows. The ratio C_T/C_P (thrust for a given power) can be written as:

$$\frac{C_T}{C_P} = \frac{\frac{T}{\rho n^2 D^4}}{\frac{P}{\rho n^3 D^5}} = \frac{T}{P} nD \tag{5.6}$$

with the efficiency of the propeller:

$$\eta = \frac{TV}{P} \tag{5.7}$$

eq. (5.6) becomes:

$$\frac{C_T}{C_P} = \frac{\eta}{J} \tag{5.8}$$

The propeller efficiency is quite constant over a range of Reynolds number which means that the thrust coefficient for a given power coefficient is large for low values of J which can be realized at low wind speed for a certain maximum propeller speed.

To determine a suitable wind speed for the propeller-on tests several runs with varying Reynolds numbers were performed. The lift curve, presented in Fig. 5.39 demonstrates a clear Reynolds dependency especially when the Reynolds number (based on $\bar{c}$) is reduced to a value of $Re = 2.5 \times 10^5$.

During the preliminary propeller-on run it became clear that the highest thrust coefficient could only be realized by performing tests with the lower Reynolds number of $Re_{\bar{c}} = 0.25 \times 10^6$. As a consequence the propeller rotation effects for the high and low thrust cases should be treated separately when conclusions are drawn since the latter were partly obtained at higher Reynolds numbers.
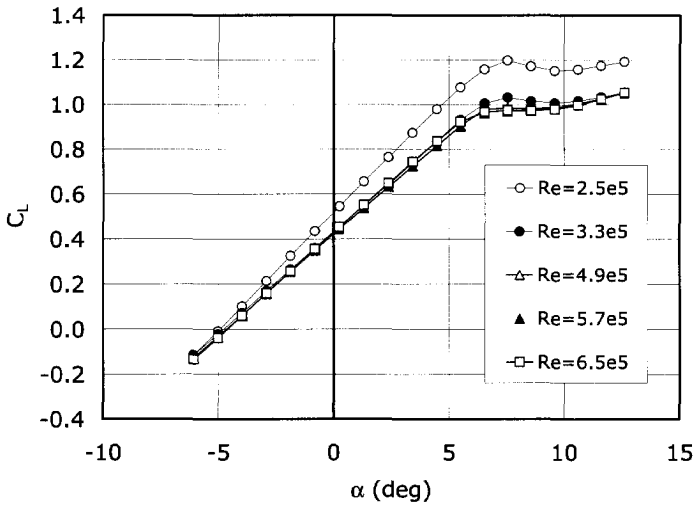
Figure 5.39: *Reynolds number effect on the lift curve of the F27; configuration WFNV.*

Effect of rotation direction The experiments were performed on the model without horizontal tail (configuration WFNV). In this way only the effects of the slipstream on the behavior of the wing were investigated without disturbances introduced by the horizontal tail. It should be noted that the impingement of the slipstream on the horizontal tail also affects the total lift and drag (Obert [45]) but this effect is small and the analysis of the secondary contribution is considered beyond the scope of these investigations.

The three propeller rotation cases that were studied are:

- co-rotating propellers (right when looking upstream), referred to as : "co-right"

- inboard-up rotating propellers, referred to as : "inb-up "

- outboard-up rotating propellers, referred to as : "outb-up "

The main difference between the three propeller rotation cases is the change in propeller induced angle of attack in the area washed by the slipstream due to the swirl velocity distribution. The effect of the propeller rotation direction was tested for two ranges of thrust coefficient referred to as "low thrust" and "high thrust". The installed thrust coefficient was approximated by subtracting the propeller on and propeller-off drag coefficient for $\alpha = 0°$. In Fig. 5.40 the measured thrust coefficient, T_c, versus the advance ratio is presented.
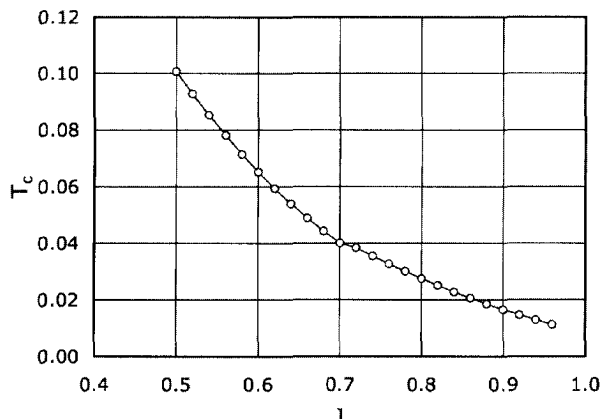
Figure 5.40: *Thrust coefficient of the F27 versus advance ratio;* $\beta_{0.75R} = 25°$

The low thrust case typically represents the cruise condition of the aircraft. Only moderate effects of the rotation direction are expected since the swirl velocity relative to the flight speed is small. The maximum angle of attack change in the wing area washed by the propeller slipstream , that was approximated with the BEM code (see Appendix A) is approximately : $\Delta\alpha = 5°$ at $r/R = 0.75$.

Fig. 5.41 shows the effect of the rotation direction for a rather low thrust coefficient of $T_c = 0.025$ as well as the wind milling propeller and the propeller off condition. The inboard up rotating propeller demonstrates the highest value of the lift curve slope, C_{L_α}, in the linear part and hence produces the highest lift force at a given angle of attack. This is an expected behavior since the slipstream rotates in the direction opposite to that of the tip vortices. The same behavior was found for PROWIM although the effects were much stronger due to the more outboard position of the propeller and the smaller aspect ratio. Even if the propeller distance from the wing tips is large for the F27 model its influence on the effective aspect ratio of the wing apparently is still noticeable. The curve for the co-rotating propellers (not depicted in Fig. 5.41), is fairly close to the inb-up curve since in this case one propeller causes a positive and the other a negative effect on the lift curve slope. The difference of both the prop-on cases with prop-off case again arises from the contribution of the increased dynamic pressure in the slipstream area and the propeller normal force. As expected, the wind milling case (co-right) produces the lowest lift curve slope due to the strong dynamic pressure loss in the slipstream.

A closer look at the prop-on curve beyond $\alpha = 6°$ reveals a lift coefficient for the outb-up case that is slightly higher than the one for inb-up case. Here an important other phenomenon of the slipstream becomes visible, namely the impact on the boundary layer development.
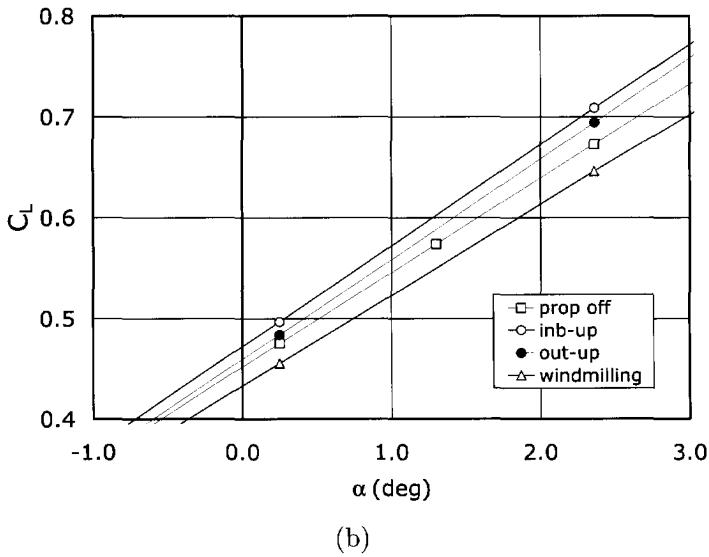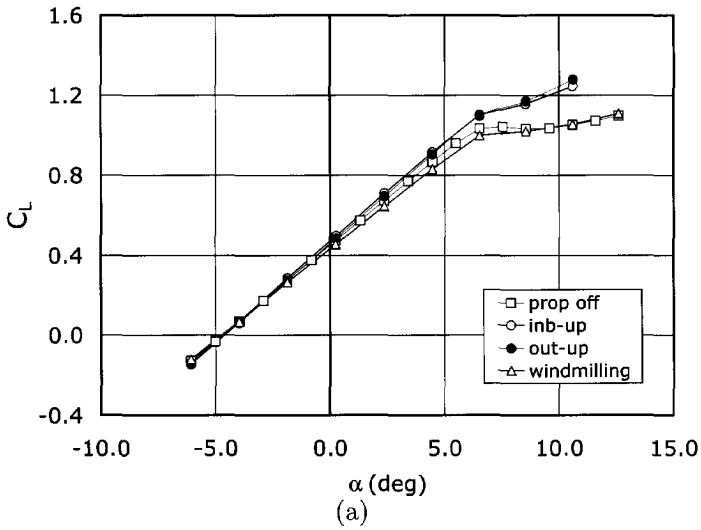
Figure 5.41: *Effect of propeller rotation direction and wind milling on the lift curve ; (a) full curve ; (b) detail around cruise angle of attack ; $Re = 0.41 \times 10^6$; $T_c = 0.025$; $\beta_{0.75R} = 25°$.*
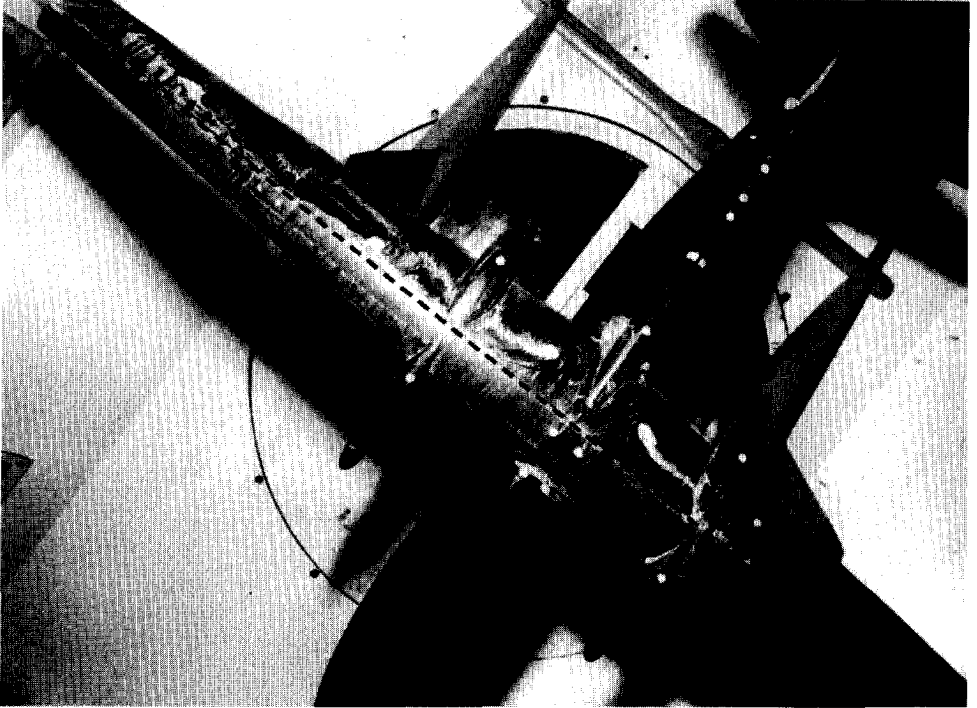
Figure 5.42: *Flow visualization on the upper surface of the F27-model at α = 6.5° angle of attack. The flow separates at approx. 50% of the chord. The thin dotted line indicates the tripping wire at 50% chord [66] ; prop off.*

From earlier experiments on the F27 in gliding flight (Spigt and van Gelder [83]) significant separation was found on the wing upper side beyond $\alpha = 5°$(Fig. 5.42). In the outb-up rotation case the propeller induced swirl velocity reduces the effective wing angle of attack at the inboard side of the nacelle. Therefore the lift coefficient increases a little bit in this case. It should be noted that this effect is stronger on the full scale aircraft since the high angle of attack case corresponds to a much higher thrust setting of the propellers characteristic for the landing phase of the aircraft.

Further evidence of the flow straightening effects of the slipstream is found from still images that were extracted from video recording of the F27 at high angles of attack. In this case a single line of tufts was used an indicator for flow separation. In Fig. 5.43 the situation for $\alpha = 12°$ is presented.

prop off, port wing

prop on, port wing

$\alpha = 12°$

$T_c = 0.025$

Clean

prop on, starboard wing

Figure 5.43: *Comparison of the flow visualization using tufts for the prop off and prop on case of the F27; top view.*

In the prop-off case significant flow separation is found at the nacelle inboard side

(see port wing). With both propellers running co-right, the downgoing propeller side (at the right of the port nacelle) shows a remarkable reduction of the flow separation (tufts aligned with the main stream). The nacelle inboard side of the starboard wing, where the propeller increases the local angle of attack, shows a smaller guiding effect, as expected. The effect of the thrust coefficient for a constant angle of attack is presented in Fig. 5.44. Although the effects are relatively small the outboard up rotating propeller clearly shows the lowest increase in the lift coefficient. In case of the lower advance ratios the inboard up rotating propellers are superior.

Not only the slipstream influence on the lift coefficient but also the way it affects the overall performance of the aircraft is important. A convenient way to examine this is through a plot of the lift-drag polar. The result for the lower thrust coefficient is presented in Fig. 5.45.

Now an important problem arises since the drag coefficient, which incorporates the thrust coefficient becomes unequal to zero. For the low angle of attack a clear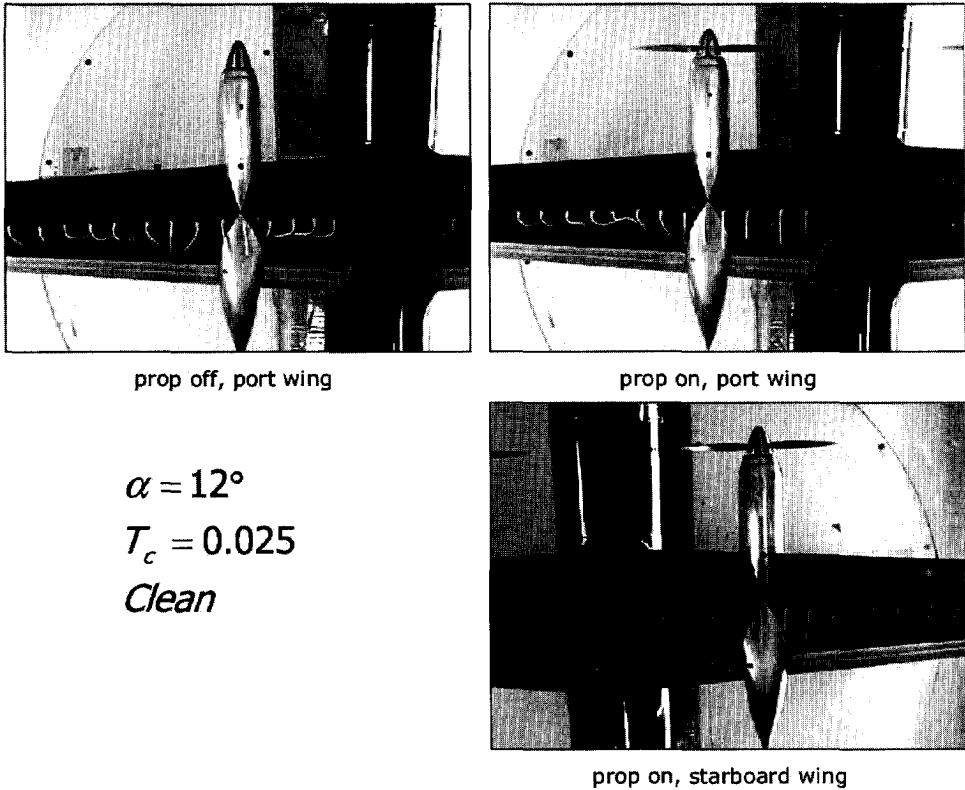 excess in thrust is discernible, hence a violation of the thrust-drag equilibrium is manifest. This observation is supported by Ref. [78] where data for the normal cruise condition of the F27 are presented. This problem is mainly due to the relative low Reynolds at which the tests were performed resulting in an inaccurate drag coefficient compared tot the full scale situation. Additionally, the low Reynolds number at which the propeller performs its work leads to a further discrepancy between the model and the full scale polar. Instead of an exact representation of the cruise flight condition of the full scale aircraft the data shown in Fig. 5.45 may be used to acquire quantitative effects of typical turboprop arrangements.

As the lift increase due to the slipstream guiding effect at high angles of attack can be seen clearly comparing the prop off and prop on curves in Fig. 5.45a. The effect of the propeller rotation direction on the drag coefficient, as shown in the detail plot of Fig. 5.45b, confirms the (small) beneficial effects of the inboard up rotating propeller. At a typical cruise lift coefficient of $C_L = 0.4$, the difference between the outboard up and the inboard up rotating propeller is 4 drag counts in favour of the latter. The difference between the two propeller rotation cases depends on the lift coefficient. One may expect that with increasing lift acting on the wing, the relative effects of the opposite swirl distribution introduce larger changes in the drag. Fig. 5.46 shows that the positive influence of the inboard up rotation increases for the higher C_L values.

Flap deflection As indicated by the optimization results and the experiments on PROWIM a specific change in the spanwise loading may lead to a reduced drag for given lift. In general a smoothly varying twist or camber distribution is required to attain the true optimum loading. Nevertheless it is also possible that a small change in the loading distribution provoked by a small flap deflection, may as well lead to a performance enhancement.
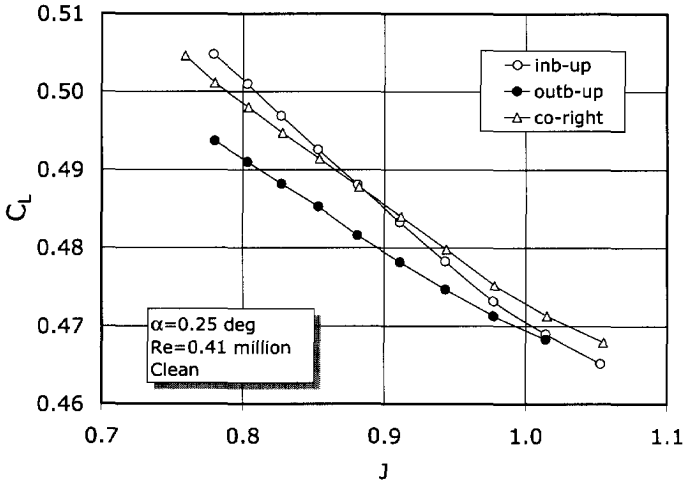
(a)
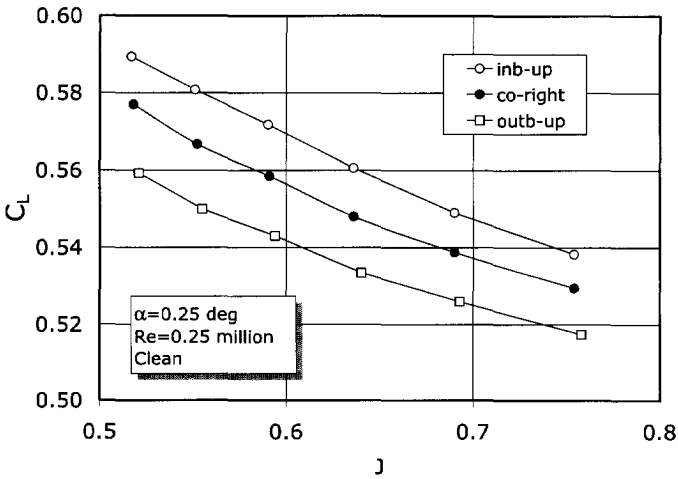
(b)

Figure 5.44: *Effect of the propeller rotation direction and the advance ratio on the lift coefficient ; $\alpha = 0.25°$; (a) $Re = 0.41 \times 10^6$; (b) $Re = 0.25 \times 10^6$.*
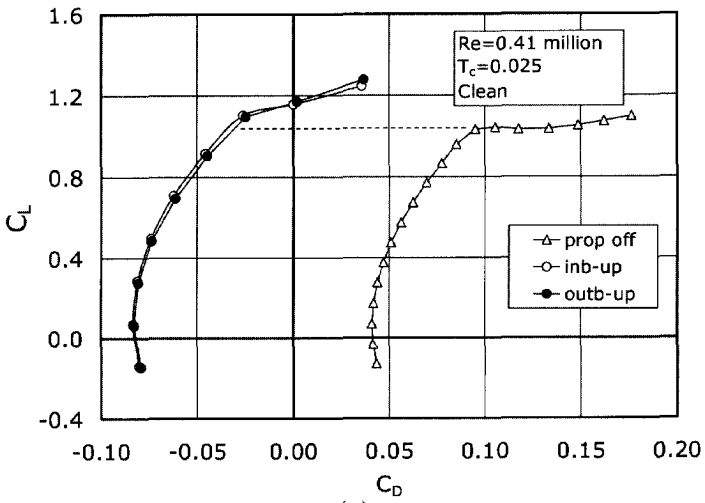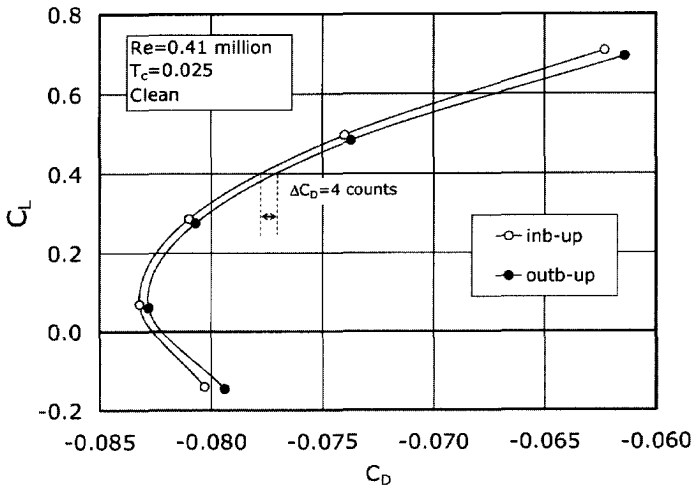
Figure 5.45: *Lift-Drag polar for the F27 at $T_c = 0.025$ in the clean configuration ; (a) complete prop on and prop off curves ; (b) detail for the prop on case.*
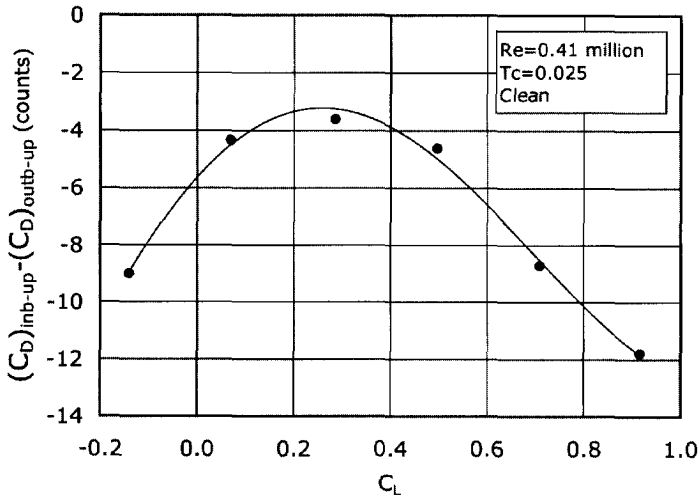
Figure 5.46: *Difference in drag coefficient for the inboard up and the outboard up rotation case ; F27 in clean configuration.*

On the F27 model a loading variation was created by a deflection of $\delta_{f_i} = 28°$ of the inboard flap only[1].

Fig. 5.47 presents a part a the measured lift-drag polar at the same thrust coefficient as the one used for the clean configuration.

The lift coefficient for given model angle of attack is higher due to the extended flaps. However, this is associated with a higher drag coefficient for a given lift. Closer examination reveals a small but noticeable difference with the clean configuration when the inboard up and outboard rotation case are compared. As indicated by the data in Fig. 5.48, where the difference in effective drag coefficient is depicted, the power effects lead to larger differences between the inboard and outboard up rotation case.

This behavior indicates that unquestionably a strong relationship exists between the loading distribution and the swirl distribution in the slipstream. When the loading distribution is changed the optimum propeller swirl has to be adjusted accordingly and vice versa.

---

[1]Normally the deflection of the inboard and the outboard flap are coupled in a ratio of approximately 2:3.
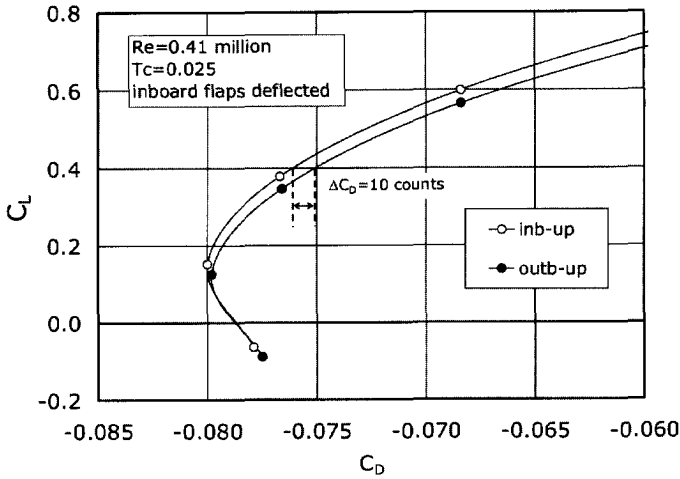
Figure 5.47: *Lift-Drag polar for the F27 at T_c = 0.025 with deflected inboard flap, δ_{f_i} = 28° ; (a) complete prop on and prop off curves ; (b) detail for the prop on case.*
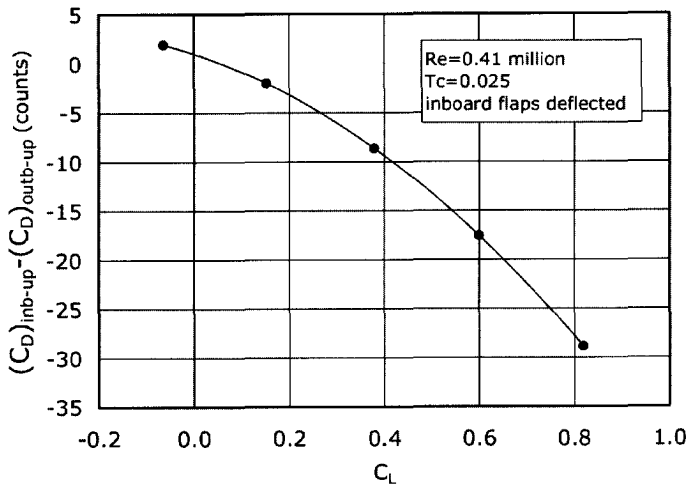
Figure 5.48: *Difference in drag coefficient for the inboard up and the outboard up rotation case for the F27 with extended inboard flaps.*

5.6 Quantitative wake analysis

5.6.1 Introduction

The interaction between a propeller and wing and the associated vortex flow field is very complex. Therefore an optimization of the configuration with theoretical prediction techniques will only be successful if quite detailed data are available on the characteristics of the slipstream/wing interactive flow. For that reason a detailed flow field survey at 1 chord length behind the PROWIM model was performed. Analysis of the flow field on a simple rectangular wing performed by de Leeuw [84] showed that the 1 chord location provides acceptable results when a thin five hole probe is used.

One of the earlier attempts to explain the different phenomena that occur when a propeller slipstream interacts with a trailing wing was made by Aljabri and Hughes [46]. Their analysis, however, is restricted to a quasi 2-dimensional wing (with endplates) thus omitting the (strong) effect of the wing tip vortex. Samuelson [85] describes the flow field around several propeller wing configurations and includes a discussion on the velocity field in qualitative sense. Although an extensive amount of vector plots is produced in [85] no attempt is made to derive configuration characteristic values (like lift, profile drag and induced drag) from the survey data.

The flow field surveys that are described hereafter, exhibit some interesting perspectives:

1. The three dimensional visualization of the flow field reveals important qualitative information on the deformation process of the wake which can be important for the aerodynamic design of the wing and trailing surfaces and for the modeling of vortex formation in CFD-codes.

2. The components of drag can be measured separately. Thus the quantitative results of the wake survey may be of use for the validation of codes where the calculation of profile drag and induced drag are generally performed with different calculation models.

The main objectives of the quantitative flow analysis behind the propeller-wing model were:

- to learn more about the ability of a quantitative wake survey to produce accurate information about the lift and the drag components when a propeller slipstream interacts with a wing

- to explore the geometry of the deformed slipstream and vortex wake downstream of the wing

- to improve the understanding of the complex vortex wake structure as it is important for future optimization of propeller-wing configurations.

The analysis method as described hereafter was programmed in a FORTRAN code referred to as *WAKE* [86]. This code is currently used for quantitative wake analysis of both experimental and numerical field data [87, 88].

5.6.2   Theoretical background of the wake analysis method

In this section a brief review of the theory behind the quantitative wake analysis method is given. A further discussion on this subject is presented by Maskell [70], Betz [69], Rentema [74] and Wu et al. [72]. The power of the method that is used in quantitative wake analysis is the ability to distinguish the profile drag from the vortex related induced drag of the configuration. First of all the assumptions on which the model is based should be outlined. The first assumption that is made is a flow that is steady (time-averaged) and incompressible at the field survey plane (FSP) which is positioned somewhere behind the model. Secondly, the closed wind tunnel has a constant effective cross section which means that the effective boundary of the stream is defined as the displacement surface of the boundary layer on the wind tunnel walls.

To determine the signs of the variables a right-handed axis system is used with the x-axis pointing in the streamwise direction and the z-axis pointing up in vertical direction.

Wake drag integrals   The drag of a body positioned in a control volume as depicted in Fig. 5.49 can be found from the change in momentum in the direction of the undisturbed flow. The upper, lower and the side planes of the control volume are parallel and positioned just outside the wall boundary layer.
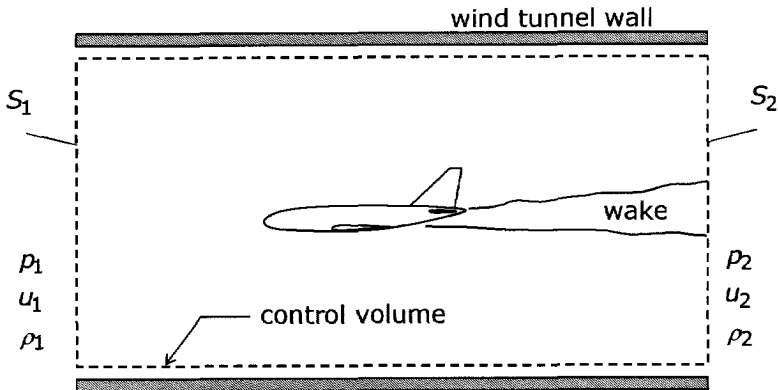
Figure 5.49: *Control volume approach used in the quantitative wake analysis.*

Considering the conditions at plane S_1 and S_2 upstream and downstream of the

body respectively the drag may be written as :

$$D = \iint\limits_{S_1} \left(p_1 + \rho u_1^2\right) dydz - \iint\limits_{S_2} \left(p_2 + \rho u_2^2\right) dydz \tag{5.9}$$

Introducing the total head H :

$$H = p + \tfrac{1}{2}\rho \left(u^2 + v^2 + w^2\right) \tag{5.10}$$

equation (5.9) may be rewritten as :

$$D = \iint\limits_{W} \left(H_\infty - H_2\right) dydz +$$
$$\tfrac{1}{2}\rho \iint\limits_{S} \{\left(u_1^2 - v_1^2 - w_1^2\right) - \left(u_2^2 - v_2^2 - w_2^2\right)\}dydz \tag{5.11}$$

where W denotes the wake area part of S_2. Since the total head is constant everywhere outside the vortical area of the flow the first integral is limited to the wake downstream of the object.

To limit the second integral to the wake also, Betz [69] introduced an artificial velocity-component u^* which differs from u only in the wake area:

$$H_\infty = p + \tfrac{1}{2}\rho(u*^2 + v^2 + w^2) \tag{5.12}$$

The difference between Betz' velocity and the undisturbed flow velocity is called the perturbation velocity $u"$:

$$u" = u* - U_\infty \tag{5.13}$$

Substituting (5.12) and (5.13) into the drag relation (5.11) results in :

$$D = \iint\limits_{W} \{(H_\infty - H_2) + (u_2^* - u_2)(u_2^* + u_2 - 2U_\infty)\}dydz +$$
$$\tfrac{1}{2}\rho \iint\limits_{S} \{\left(u_1"^2 - v_1^2 - w_1^2\right) - \left(u_2"^2 - v_2^2 - w_2^2\right)\}dydz \tag{5.14}$$

This equation holds for any steady incompressible flow of a fluid with constant viscosity. To express the contribution of a perturbation velocity a wake integral is introduced (Maskell [70]) for the wake-blockage velocity u_b :

$$u_b = \frac{1}{2S} \iint\limits_{W} \left(u_2^* - u_2\right) dydz \tag{5.15}$$

The perturbation velocity, $u"$, can be considered as a constraint correction to the Betz' formula, due to the presence of the wind tunnel walls. Maskell [70] derived the relation between $u"$ and u_b by considering a system of a bound vortex and a source-sink combination in the flow:

$$\tfrac{1}{2}\rho \iint\limits_{S} \left(u_1^2 - u_2^2\right) dydz = -2\rho u_b^2 S \tag{5.16}$$

Substituting (5.16) into (5.14) leads to :

$$D = \iint\limits_{W} \{(H_\infty - H_2) + \tfrac{1}{2}\rho\,(u_2^* - u_2)\,(u_2^* + u_2 - 2U_\infty)\}dydz$$
$$-2\rho u_b^2 S + \tfrac{1}{2}\rho \iint\limits_{S} \{(v_2^2 + w_2^2) - (v_1^2 + w_1^2)\}dydz \tag{5.17}$$

The first two terms are considered by Betz as the profile drag while the last term is supposed to be the vortex drag or induced drag.
Comments:

- Although this seems to be a reasonable definition it might be questioned. One could likewise decide to split the contributions into one part that is related to the viscosity, called the profile drag and the remainder being the vortex or induced drag.

- It should be noted that for the case where a propeller is running the energy supply to the flow increases the value of H_2 which means that the profile drag may become negative.

- In the program *WAKE*, the induced drag is defined as being the result of local non-viscous normal forces, such as lift, generated by the wind tunnel model. The remainder is defined as the profile drag.

The problem with formulation of the last integral of eq.(5.17) is that it must be evaluated over the entire cross section of the wind tunnel (i.e. flow data need to be available in the complete S_2 plane). This problem can be solved in the following way.
Introduce the continuity equation :

$$\frac{\partial v}{\partial y} + \frac{\partial w}{\partial z} = -\frac{\partial u}{\partial x} = f \tag{5.18}$$

the axial vorticity component :

$$\xi = \frac{\partial w}{\partial y} - \frac{\partial v}{\partial z} \tag{5.19}$$

and two scalar functions $\phi(y, z)$ and $\psi(y, z)$ such that the following conditions are satisfied:

$$v = \frac{\partial \psi}{\partial z} + \frac{\partial \phi}{\partial y} \tag{5.20}$$

$$w = -\frac{\partial \psi}{\partial y} + \frac{\partial \phi}{\partial z} \tag{5.21}$$

When equations (5.20) and (5.21) are substituted in (5.18) and (5.19) we obtain :

$$\frac{\partial^2 \psi}{\partial y^2} + \frac{\partial^2 \psi}{\partial z^2} = -\xi \tag{5.22}$$

$$\frac{\partial^2 \phi}{\partial y^2} + \frac{\partial^2 \phi}{\partial z^2} = f \tag{5.23}$$

With known values of ξ and f in the wind tunnel cross section the values of the scalars ϕ and ψ can be calculated applying the right boundary conditions (Rentema [58]).

The last integral of (5.17) can now be written as:

$$\iint\limits_S (v^2 + w^2)dydz = \iint\limits_S \left(\frac{\partial}{\partial y}(\psi w) - \frac{\partial}{\partial z}(\psi v)\right)dydz$$
$$- \iint\limits_S \left(\frac{\partial}{\partial y}(\psi w) - \frac{\partial}{\partial z}(\psi v)\right)dydz + \iint\limits_S (\psi \xi - \varphi f)\,dydz \tag{5.24}$$

Applying Stokes' theorem and the 2-dimensional form of the divergence-theorem to the first two integrals on the right hand side of eq. (5.24) the following line integrals are found:

$$\oint\limits_{b_i} \psi v_t ds + \oint\limits_{b_i} \varphi v_n ds \tag{5.25}$$

Here boundary b_i is determined by the intersections between S_1 and S_2 and the wind tunnel side walls. The velocities v_t and v_n denote respectively the tangential and the normal component of the velocity vector at boundary$b$.

Because ψ is chosen zero at the boundary, the first integral of (5.25) vanishes. The second integral also vanishes since there is no mass flow through the wind tunnel wall and consequently $v_n = 0$.

Thus, only the last integral of eq. (5.24) remains to be used in eq. (5.17).

The axial vorticity is zero outside the wake which restricts the vortex drag integral to :

$$D_v = \tfrac{1}{2}\rho \iint\limits_W \psi_2\,\xi_2\,dydz + \tfrac{1}{2}\rho \iint\limits_S (\varphi_1 f_1 - \varphi_2 f_2)\,dydz \tag{5.26}$$

The term $\psi_1 \xi_1$ has disappeared because at the upstream side of the model $\xi_1 = 0$.

The second integral of eq. (5.26) represents the contribution of the crosswise components of the vorticity vector which still has to be evaluated by taking the surface integral over the test section cross planes S_1 and S_2. Yet, if the flow is considered two-dimensional in these planes the velocity gradient f disappears and the integral can be simplified. This is the case when the planes S_1 and S_2 are positioned far upstream and downstream of the model respectively.

Wu et al [89] have shown that under normal conditions the variable quantities $\varphi_1 f_1$ and $\varphi_2 f_2$ are equal, hence their contributions cancel each other.

When the survey plane S_1 is taken far upstream f_1 vanishes thus simplifying the equation for the vortex drag as :

$$D_v = \tfrac{1}{2}\rho \iint\limits_W \psi_2\,\xi_2\,dydz - \tfrac{1}{2}\rho \iint\limits_W \phi_2\,f_2\,dydz \tag{5.27}$$

In general the contribution of the second integral is negligible outside the wake thus integration is performed over the wake only. De Leeuw [84] verifies this vortex drag

formula with experiments on a simple half-wing model. He concludes that for the clean
wing configuration the transverse vorticity contribution is very small $(0.04\% - 0.13\%$
of the vortex drag).

5.6.3 Boundary conditions

Eq. (5.22) and eq. (5.23) have to fulfill the boundary condition $\psi = 0$ at the wind
tunnel walls to ensure they will form streamlines in the 2-dimensional space. To be
able to calculate the values of ψ and φ over the measurement area only the boundary
conditions at the wind tunnel walls will have to be translated to the boundary of this
measurement area.
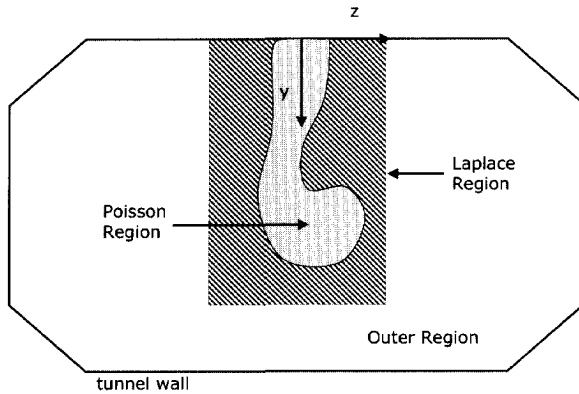
Figure 5.50: *Splitting the test section cross plane.*

Therefore the test section cross plane is split into 3 areas (Fig. 5.50) into:

- an outer region between the measurement area and the wind tunnel walls

- a quasi- 2-dimensional area denoted "Laplace-region"

- an inner region, completely being enclosed by the Laplace-region, denoted "Pois-
  son region"

where the Poisson-region is the only one containing vorticity. For the Laplace-region
we may write :

$$\Delta\psi = 0$$
$$\Delta\varphi = 0$$

(5.28)

and for the Poisson-region :

$$\Delta\psi = -\xi$$
$$\Delta\varphi = f \tag{5.29}$$

In the outer region the scalar variable φ may be chosen constant, for example zero. In case φ represents the 2-dimensional velocity potential the choice $\varphi = 0$ means the flow is irrotational and perpendicular to the measurement plane. In reality however the velocity components v and w are unequal to zero in the outer region. This indicates that φ does not represent a velocity potential. The advantage of this choice for φ is the favorable effect on the calculation of ψ. Using eq. (5.20) and eq. (5.21) we may write:

$$\frac{\partial\psi}{\partial z} = v$$
$$-\frac{\partial\psi}{\partial y} = w \tag{5.30}$$

Thus ψ represents a 2-dimensional stream function.

Because there is no mass flow through the wind tunnel walls the surface normal gradient of φ should be zero. The boundary conditions that has to be applied to solve the Poisson-equations (5.22) and (5.23) can now be summarized as follows :

- $\frac{\partial\psi}{\partial z} = v \wedge \varphi = 0$ at the boundary $z = $ constant

- $\frac{\partial\psi}{\partial y} = -w \wedge \varphi = 0$ at the boundary $y = $ constant

- $\psi = 0 \wedge \frac{\partial\varphi}{\partial y} = 0$ at the boundary where the model is connected to the wind tunnel wall

Equations (5.22) and (5.23) can now be solved using a (standard) Poisson-Solver.

5.6.4   Wake Lift integral

The local lift coefficient can be found following the classical wing theory. When a planar wake is assumed the local distributed vorticity strength of the wake that leaves the wing at the trailing edge is given by:

$$\gamma(y) = \int\limits_{-\infty}^{\infty} \xi dz \tag{5.31}$$

The magnitude of the distributed vorticity strength is related to the bound vorticity strength through:

$$\Gamma = \int\limits_{y_1=y}^{\infty} \gamma(y_1) dy_1 \tag{5.32}$$

Integration of the local lift coeffient, given by $l(y) = \rho V\Gamma(y)$, leads to the total lift force:

$$L = \rho U_\infty \int\limits_{y=-b/2}^{+b/2} \int\limits_{y_1=y}^{+\infty} \int\limits_{z=-\infty}^{+\infty} \xi(y_1, z) dz dy_1 dy \qquad (5.33)$$

Of course the integration can be restricted to the vortical wake since outside this area ξ becomes zero.

Based on an analysis of the momentum equation in vertical direction of the given control volume Maskell [90] derives a slightly different form. An additional term is added given by:

$$\Delta L = \rho \iint\limits_W (u_2^* - u_2) \, w_2 dy dz \qquad (5.34)$$

which is the loss of momentum due to the loss of energy in the wake. Although this term is generally very small [90, 91] it has been added to the lift integral of eq. 5.33, since its (positive) contribution may not be negligible in the propeller slipstream.
Remarks:

1) Due to the fact that the integration in the survey plane is performed sequentially in z- and y-direction, effectively only the vertical component of the side-force acting on the wing is obtained. This implies that the normal force distribution that for example acts on a winglet can not be calculated correctly with the method described above.

2) A second important remark should be made regarding eq.(5.33). Since the wake behind the wing deforms, the assumption of a planar wake is not correct. This means that from the shed vorticity the direction and the location of the inducing (lift) force acting locally on the wing can not be determined exactly. Therefore calculation of the integral in eq.(5.33) through successive integration in z- and y-direction in principal produces a wrong picture in areas where the vortex sheet has rolled up, as occurs at the wingtip. An example of this phenomenon is sketched in Fig. 5.51.

In fact the integration should be performed first in s- and then in t-direction which are locally perpendicular and parallel to the vortex sheet respectively. This is practically unrealizable in a fully developed tip vortex where the sheet is stretched in lateral direction and rolled up into one vortex core. Although this is a clear limitation in the use of eq. (5.33) a reasonable representation of the local lift distribution will be obtained using the classical theory. Only in areas with strong vortex roll up (e.g. the wing tip area) deformations of the lift distribution are expected and at larger distance behind the wing.

5.6.5 Wake analysis of experimental data

Flow field survey data To understand the balance and the surface pressure data discussed earlier better, flow field surveys were performed behind PROWIM. Time
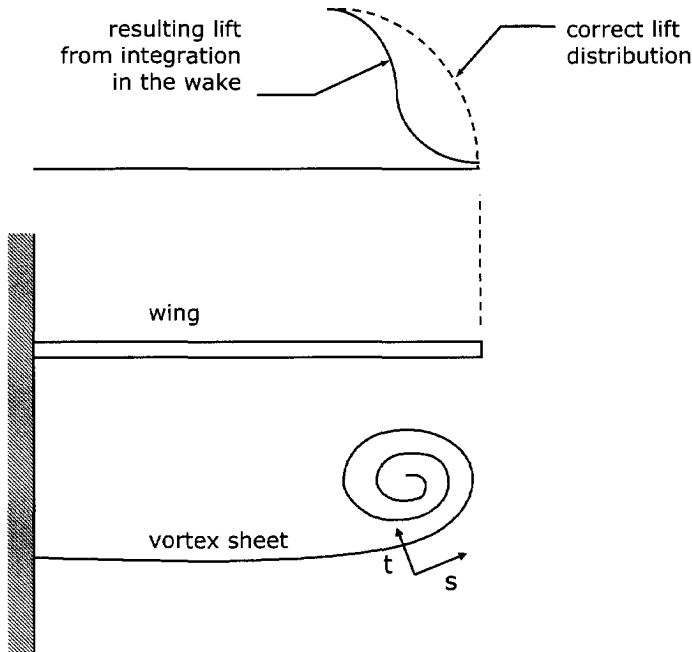
Figure 5.51: *Mis-interpretation of the lift distribution close to the wingtip due to vortex wake roll-up.*

averaged slipstream and wake measurements were performed at 1 chord length behind the wing trailing edge. The propeller was rotating inboard up with an advance ratio of $J = 0.85$.

To be able to analyze slipstream influence on wing profile drag, induced drag and lift distribution, a grid spacing of only $2mm$ ($h/\frac{b}{2} = 0.0003125$) was chosen in both directions. This very fine grid was selected to uncover enough detail of the flow field to draw qualitative conclusions. To check the necessity of taking so many data points some calculations with fewer data points were performed afterwards. By skipping measurement data the effect of grid density on the calculated axial vorticity was found [79].

Quite coarse measurements grids can be used if only qualitative information is requested. Yet, the variables that depend on the value of ξ like the local lift coefficient and the induced drag coefficient show a clear effect of grid density. Based on these analyses a choice of the $2mm$ grid spacing seems to be appropriate to ensure accurate

integration of flow data over the wake area.

Flow structure for the prop off case Fig. 5.52 displays the total pressure coefficient for the propeller off case at $\alpha = 0°, 4°$ and $10°$. The strong deficit which occurs in the wing wake and the wing tip vortex are clearly visible. Besides the total head loss behind the nacelle with the pressure tubes installed, there is a distinct effect of the horseshoe vortex at the wing/wall junction. For $\alpha = 4°$ and $10°$, when the wing generates lift, the total head loss in the tip vortex core becomes very pronounced.

The wake starts to deform significantly for the higher angles of attack which may have consequences for the theory applied above where a planar wake was assumed. Near the root, the wake of the wing shows a disturbance (see arrow in Fig. 5.52b) which becomes larger at higher angles of attack. This is caused by a small streamwise gap between the trailing edges of the inboard flap and the wing. The fact that this small geometrical disturbance generates a measurable effect demonstrates the power of the flow field analysis.

An interesting and accurate way of presenting the flow field is to consider the axial vorticity ξ as given in Fig. 5.53.

All important vorticity, confined in either sheets or distinct vortices, becomes visible. Sometimes the total pressure loss also forms a good indicator for the presence of vortical flow as long as the position of the viscous wake (with lower C_{p_t} values as well) is known and taken into account.

In Fig. 5.53a, for $\alpha = 0°$, two vortex pairs appear, originating from the horseshoe vortices generated by the nacelle/wing connection. At $\alpha = 4°$ the vortices with negative ξ merge and the field rotates in anti-clockwise direction due to the cross flow induced by the wing. Since the wing now produces lift, the wake rolls up resulting in a strong vortex with very high ξ-value at the tip. Moving from the tip to the root the trailing vorticity becomes weaker. This is easily explained by considering the spanwise gradient of the lift which decreases when moving in the direction of the wing root.

Flow structure for the prop on case With the propeller running the structure of the flow field changes radically.

In Fig. 5.54 the cross flow vectors are depicted for $\alpha = 4°$. Although this type of graph is easily generated (even on-line during the measurements) it exhibits no significant additional information on the flow field compared to the axial vorticity plots. In fact the interpretation of the cross flow vectors may result in a completely wrong perception of the real flow field since distinct vortices can not be distinguished accurately [92].

Fig. 5.55 shows the combination of the cross flow vectors and the total pressure contour lines both at the propeller location and the tip region. The wing tip vortex is easily recognizable from the vector field whereas the slipstream geometry is not
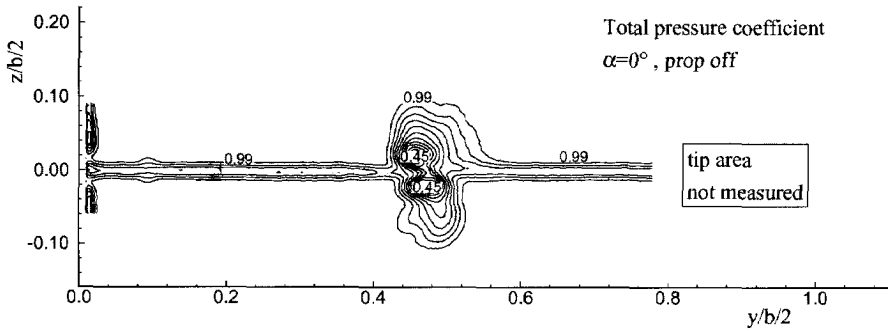
(a) $\alpha = 0°$
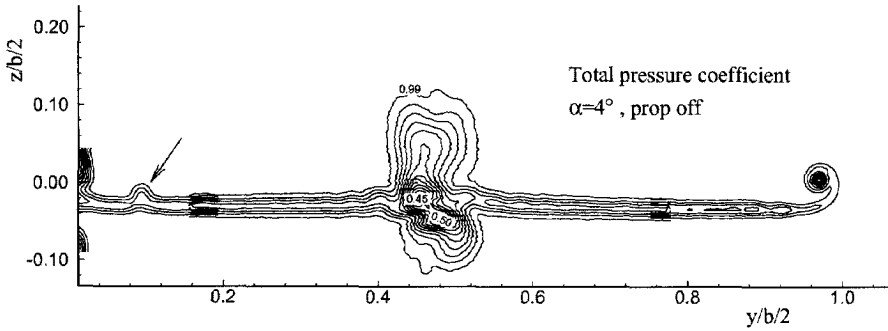
(b) $\alpha = 4°$
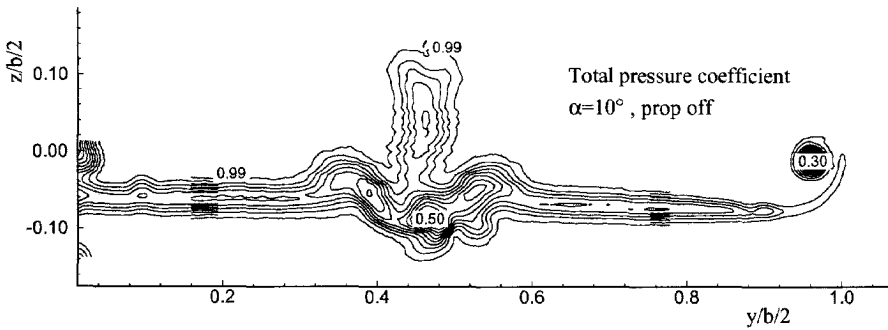
(c) $\alpha = 10°$

Figure 5.52: *Total pressure distribution for the propeller off case of PROWIM. The total pressure loss above and below the nacelle in the center is the result of the installed total pressure probes.*

(a) $\alpha = 0°$

(b) $\alpha = 4°$

(c) $\alpha = 10°$
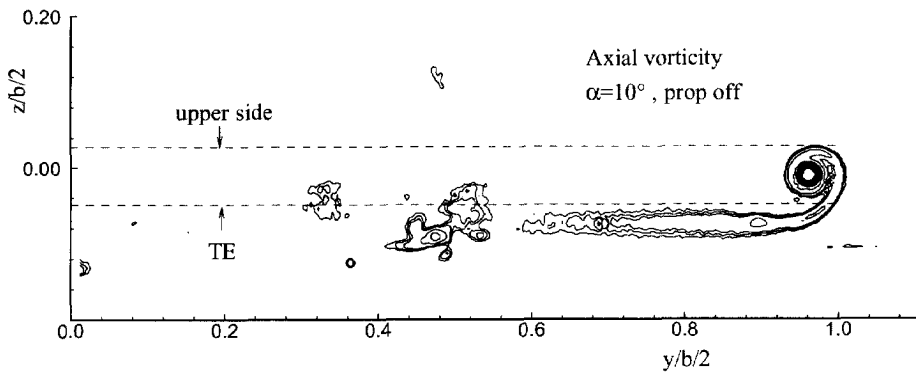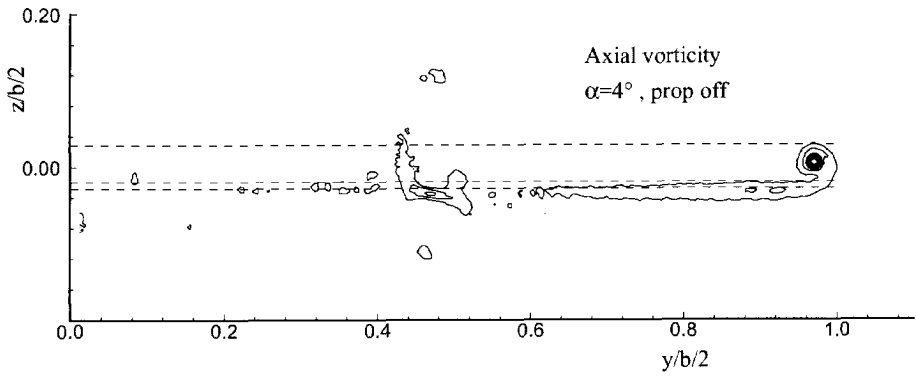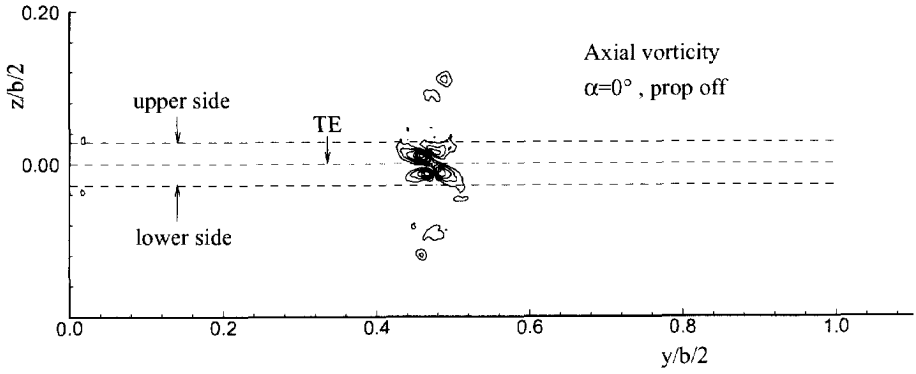
Figure 5.53: *Axial vorticity, ξ, for the propeller off case of PROWIM.*
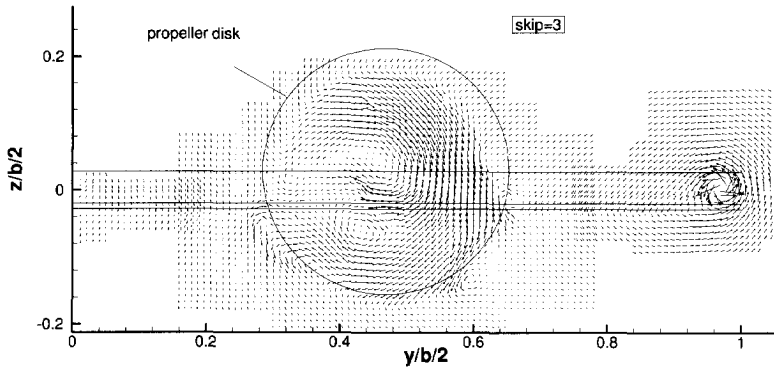
Figure 5.54: *Cross flow vectors for $\alpha = 4°$; prop on.*

clearly defined by the cross flow vectors.

As can be seen in the C_{p_t}-plots of Fig. 5.56 a strong total head rise occurs in the slipstream. The strong spatial gradients in the total pressure distribution that normally occur at the location of the propeller disk are remarkably well preserved towards the slipstream boundary.

Apparently the decay of the vorticity between the propeller position and the survey plane is limited. This can also be seen in the axial vorticity plots of Fig. 5.58, where distinct boundaries are visible. The wake of the nacelle is completely embedded in the slipstream which is substantially distorted by the wing, as expected.

The slipstream contour at $\alpha = 0°$ is sheared in lateral direction but still maintains its original circular shape reasonably well. Increasing the wing angle of attack, however, results in a strongly deformed shape gradually turning into an "inverted T" shape for $\alpha = 10°$. The horseshoe vortex at the wing root is still visible.

In Fig. 5.57 three-dimensional views of the total pressure rise at $\alpha = 0°$, $4°$ and $10°$ are given for the prop on case. The total pressure loss in the wing wake and the tip vortex is clearly visible while the slipstream area shows a total pressure gain due to the power delivered by the propeller. Apparently the flow field in the vicinity of the wing part washed by the slipstream is strongly distorted as the slipstream and the wing wake merge into a rather complex flow pattern.

Though hard to see in these 3D views of the data for $\alpha = 10°$, the total pressure rise is higher at the side of the downgoing propeller blade due to the increased local blade angle of attack. Due to the swirl introduced by the propeller the slipstream rotates resulting in a displaced total pressure field. This is clearly shown in Fig. 5.56c where at $\alpha = 10°$ the peak in the total pressure value has moved in the propeller rotational direction. This, of course has implications for the aerodynamic load on the trailing wing.

(a) Mid section
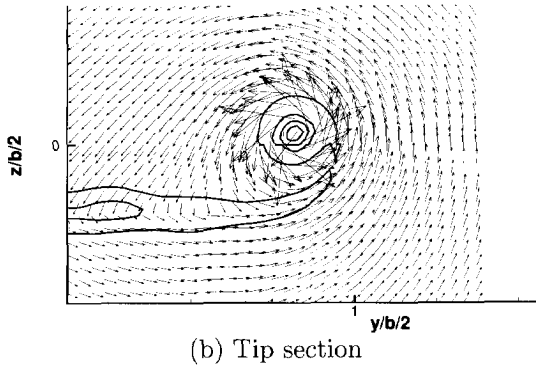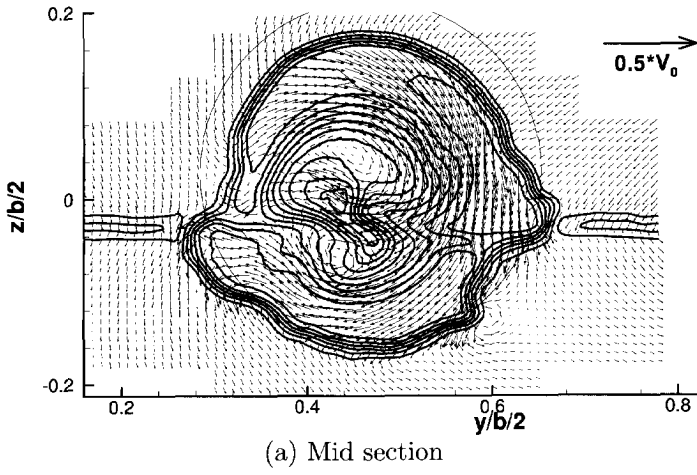
(b) Tip section

Figure 5.55: *Cross flow vectors combined with total pressure contours for* $\alpha = 4°$ *; prop on ; (a) mid section ; (b) the tip section.*

(a) $\alpha = 0°$

(b) $\alpha = 4°$

(c) $\alpha = 10°$
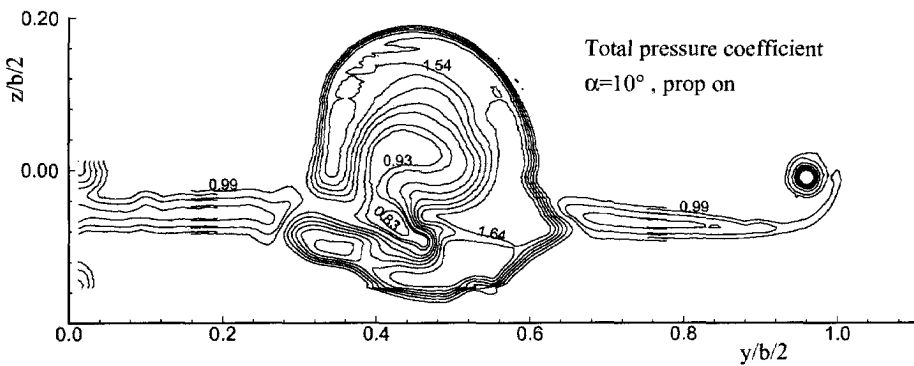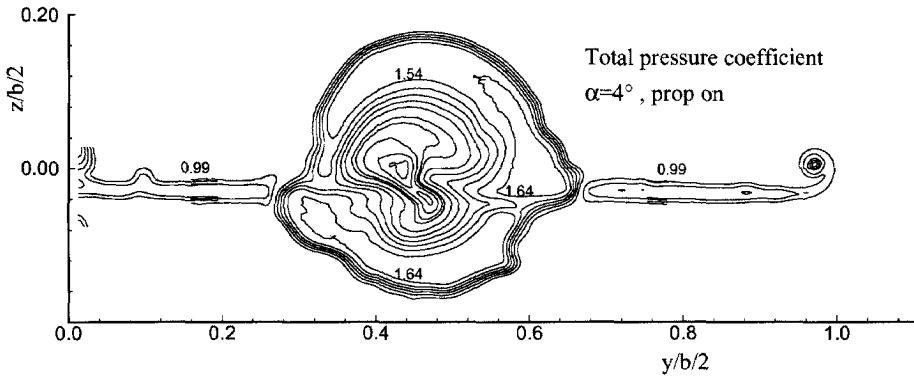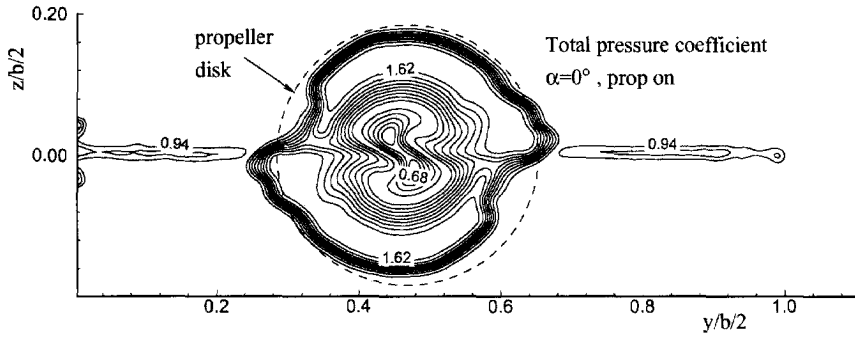
Figure 5.56: *Contour-lines of the total pressure coefficient, C_{p_t}, for the propeller on case.*

(a) $\alpha = 0°$

(b) $\alpha = 4°$

(c) $\alpha = 10°$
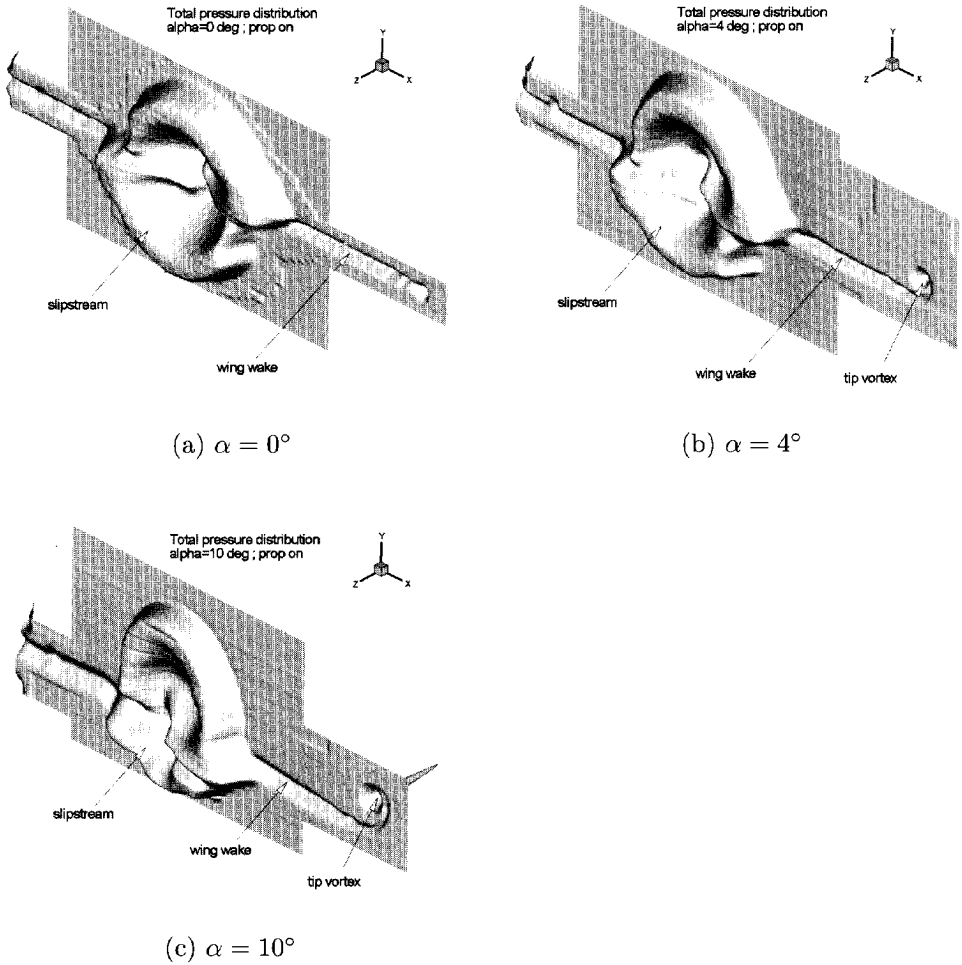
Figure 5.57: *Three-dimensional view of the total pressure distribution behind PROWIM, showing the total pressure loss in the wing wake and the tip vortex and the total pressure gain in the slipstream ; (a) $\alpha = 0°$; (b) $\alpha = 4°$; (c) $\alpha = 10°$.*

To be able to find the propeller effects on the wing loading distribution again plots with the axial vorticity distribution were produced (Fig. 5.58).

Returning to equation (5.27), the second integral generally represents approximately 2% of the total induced drag (de Leeuw [84]), which means that a strong axial vorticity (in the first integral) is indicative for a high induced drag contribution. Although it is difficult to relate a ξ-peak in the survey plane to a corresponding spanwise coordinate on the wing, due to (unknown) wake deformation between the wing and the survey plane, the effects of the propeller blade tip vortices and the wing tip vortex are very pronounced.

When viewed from behind, the tips of the propeller blades produce anti-clockwise vortices. These vortices create a narrow zone with high positive ξ-values at the outer border of the slipstream. The root parts of the propeller blades produce negative vorticity which is spread out inside the nacelle wake area.

As can be seen in Fig. 5.58a for $\alpha = 0°$, the rotational symmetry of the slipstream is clearly influenced by the presence of the wing. The boundary is sheared in lateral direction at the passage of the wing so that the slipstream boundaries at the upper and lower wing surface are at different spanwise stations. A convenient explanation of this phenomenon can be found in the way the slipstream influences the wing lift distribution. Fig. 5.58 shows that strong vorticity is shed from the junction of the wing surface and the edge of the slipstream, which is indicative of the high gradient of spanwise load on the wing. To explain the effect, the vorticity is considered as being contained in 3 discrete vortices as sketched in Fig. 5.59. As a result both slipstream halves shift in opposite spanwise directions near the intersections between the wing and the slipstream outer boundary. The areas with negative ξ-values at these locations confirm this explanation. Also the clockwise rotating center vortex with positive ξ is clearly visible in Fig. 5.58. At $\alpha = 10°$ both slipstream halves have shifted in opposite directions due to the strong influence of the wing tip vortex.

Although the five hole probe measurements were all performed at a rather low thrust coefficient the contraction of the slipstream is still visible, especially at $\alpha = 0°$ in Fig. 5.56a where the propeller disk contour was added as a dotted line.

Summarizing these results it should be stated that the deformation which occurs in the wake is strongly related to the lift distribution of the propeller/wing combination. Therefore, for a accurate prediction of the propeller interactive flow field CFD-codes are required that somehow incorporate the slipstream distortion.

Quantitative wake analysis In this paragraph the results of the field data are compared to the data that were found from the surface pressure and the balance measurements.

Although the wing has some straightening effect on the flow, the basic circular shape of the slipstream is maintained and substantial swirl velocities remain within the slipstream downstream of the wing. This becomes clear when the lift distribution found from integration in the wake is examined.
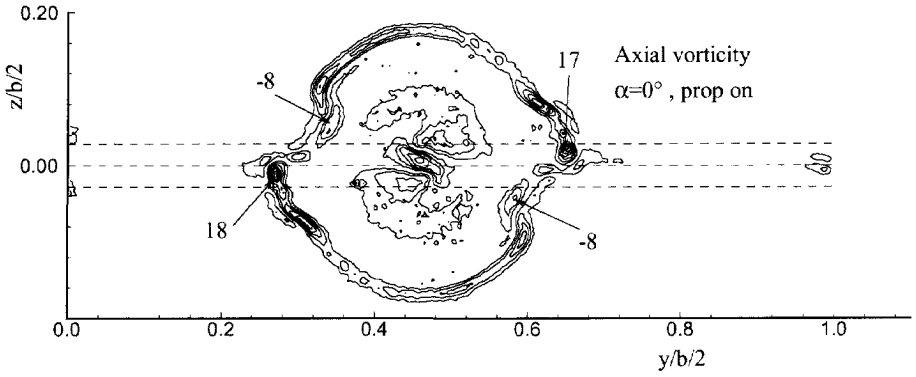
(a) $\alpha = 0°$
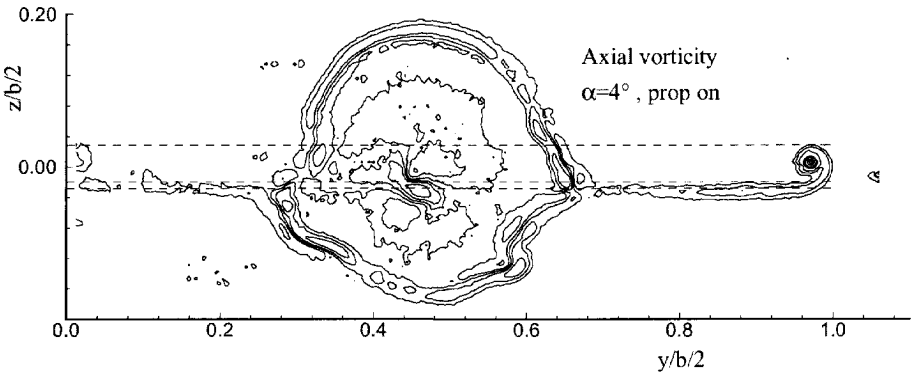
(b) $\alpha = 4°$
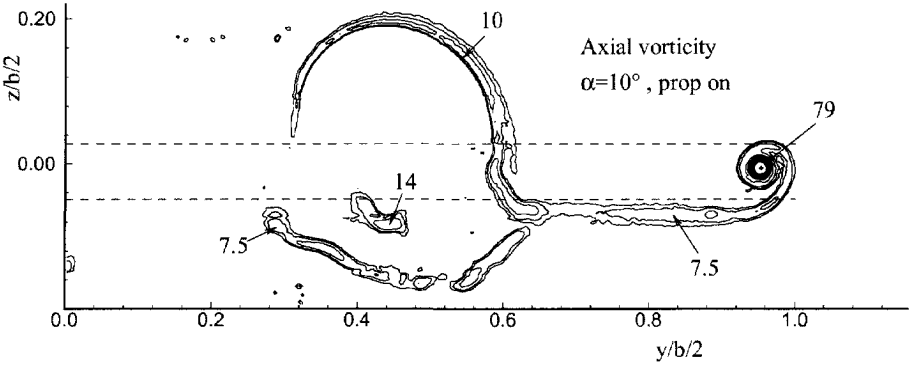
(c) $\alpha = 10°$

Figure 5.58: *Contour-lines of the axial vorticity, ξ, for the propeller on case.*
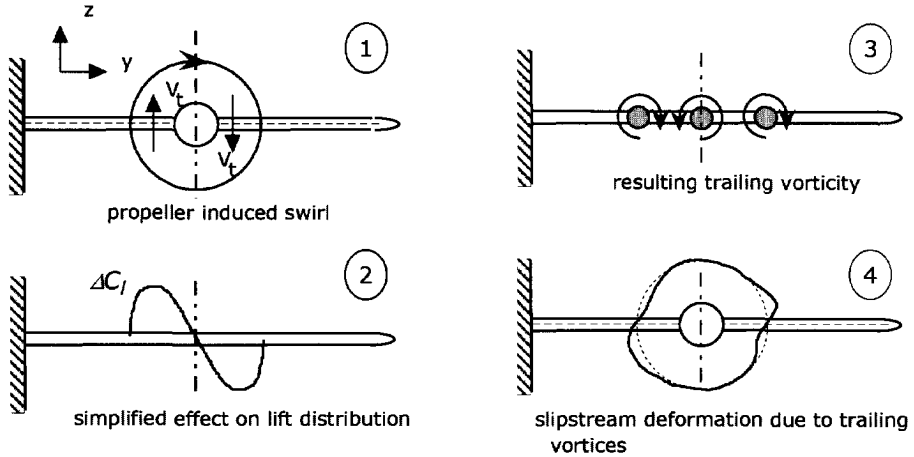
Figure 5.59: *Explanation for the spanwise shearing of the propeller slipstream induced by the trailing vorticity field.*

In Fig. 5.60 the distribution of the local lift, represented by eq. (5.33), is presented for $\alpha = 4°$ and $\alpha = 10°$ together with the results of the integrated surface pressure measurements. A small difference between the lift acquired with both techniques outside the slipstream area is notable in these figures.

The reason for this discrepancy is still unclear but is expected to be a result of an accumulation of several small errors within both measurements. The most striking difference, between the flow field survey curves and the results of the surface pressure measurements, is the opposite effects in the area washed by the slipstream. The latter represent the pressure effects at the wing only, hence no contribution of the lift forces that act on the propeller blades are incorporated in the data. The flow field data, on the other hand, contain the lift contribution of the complete configuration.

Obviously the normal forces acting in the propeller plane exceed the lift variations at the wing which are generated by the slipstream. This means in fact that a considerable swirl is still present in the slipstream after passage of the wing. Here again it is important to note that the wake position, where a certain value of the local lift is found, cannot be directly connected to a known wing spanwise location. This problem is associated with the integration procedure that is performed in vertical direction for all spanwise stations.

The increased loading at the downgoing blade is clearly visible as the peak in the local lift coefficient becomes higher than the values at the inboard side. From these figures it is reasonable to conclude that optimisation of the wing alone with prescribed propeller input data, as suggested by Kroo [10], Miranda [11] and Veldhuis [93] should
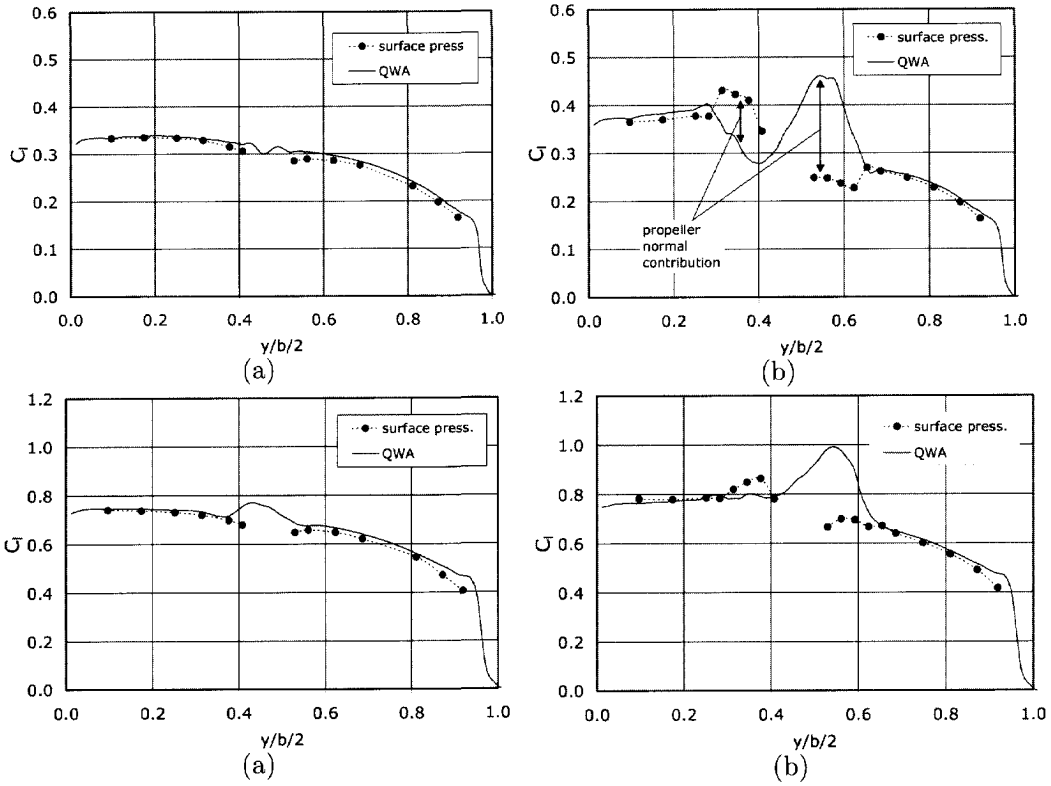
Figure 5.60: *Comparison of the lift distributions found from the integrated sur-face distributions and from the quantitative wake analysis (QWA) ; (a) $\alpha = 4°$, prop off; (b) $\alpha = 4°$, prop on; (c) $\alpha = 10°$, prop off; (d) $\alpha = 10°$, prop on.*

be replaced by an optimisation of the complete propeller/wing combination in which the most important interaction effects are integrated.
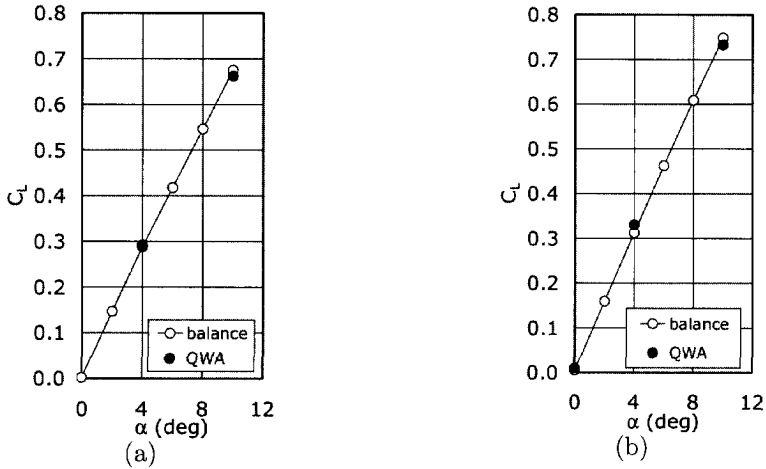
Figure 5.61: *Comparison of the overall lift coefficients found from external balance measurements and the quantitative wake analysis.*

Comparison with balance measurements   The final results of the wake surveys are compared with the balance measurements in Fig. 5.61 and Fig. 5.62. If we look at the effect of the propeller on the separate contributions of induced drag and profile drag we see that mainly the profile drag component is influenced as a result of the strong positive P_t-effect. The results of the calculations for $\alpha = 4°$ and $\alpha = 10°$ are presented in Table 5.3.

It is clear that the drag found in the case of a running propeller includes the thrust component and therefore becomes negative (Fig. 5.62). From Table 5.3 it can be concluded that the favorable effect of the propeller, a negative $(\Delta C_{D_p})_{prop}$, becomes slightly less (about 14 counts) when the angle of attack is increased from $\alpha = 4°$ to $10°$. It is, however, impossible to determine whether this is caused by a change of the wing profile drag or by a change in the slipstream characteristics due to angle of attack. Separate measurements of the propeller thrust, with an internal balance, are necessary to draw conclusions in this respect.

Although the flow field surveys produce a drag coefficient that is slightly smaller than the drag from the external balance measurements, the agreement between the two methods is quite good. The comparison of the overall lift coefficients is even better. The agreement is better for the prop-off case (maximum difference of 2%)
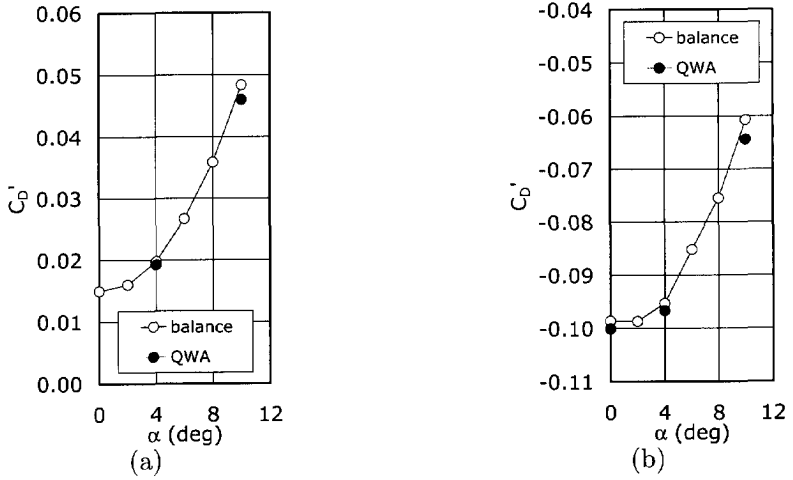
Figure 5.62: *The overall drag coefficients, C'_D, found from external balance measurements and the quantitative wake survey.*

than for the prop-on case (maximum difference of 5%). No convenient explanation for this phenomenon is available at this moment.

Table 5.3: *Propeller influence on the wing lift and drag.*

Component	Case	$\alpha = 4°$	$\alpha = 10°$
C_{D_p}	prop on	-0.10609	-0.09411
	prop off	+0.01600	+0.02661
	$(\Delta C_{D_p})_{prop}$	-0.12209	-0.12072
C_{D_v}	prop on	+0.00717	+0.02774
	prop off	+0.00324	+0.01935
	$(\Delta C_{D_v})_{prop}$	+0.00393	+0.00839
C_D	prop on	-0.09893	-0.06637
	prop off	+0.01924	+0.04596
	$(\Delta C_D)_{prop}$	-0.11817	-0.11233
C_L	prop on	+0.3302	+0.7328
	prop off	+0.2917	+0.6618
	$(\Delta C_L)_{prop}$	+0.0385	+0.0710

Chapter 6

Numerical analysis and verification

6.1 Introduction

To obtain further details of the propeller-wing interactive flow field both experimental and numerical techniques are required. In this chapter the results of the different calculation techniques, discussed in the previous chapters, will be presented. Where appropriate, comparison with available experimental results, either found in open literature or generated with the windtunnel models, described in Chapter 5 will be made.

This chapter is organized as follows. First the VLM-calculations will be discussed in which the effects of propeller position and angle of attack are investigated. Especially their effect on the so-called effective propulsive efficiency is addressed. Secondly panel calculations performed with two different codes are discussed. It will be shown that in this case a swirl recovery is needed to acquire acceptable lift and drag data. The last part of this chapter is dedicated to the discussion of results obtained with the Navier-Stokes solver *FLUENT*. The flow details obtained from these calculations are shown to be in close agreement with experimental data.

6.2 VLM-calculations

During these calculations various typical parameters, which are to be selected in the preliminary design process, were varied in a specified range. The parameters that were investigated include:

- streamwise propeller position

- spanwise propeller position

- propeller angle of attack

- propeller rotation direction

- profile drag contribution

In the next sections the most important results obtained with the VLM-code are presented. The code, denoted VLM4, combines the calculation of the wing characteristics and the complete propeller characteristics by allowing the deformation of the propeller inflow field as sketched in Fig. 6.1.

To verify the significance of the propeller effects, the experimental results obtained with the APROPOS test set-up, will be used for comparison purposes and examples of calculations on the Fokker F50 will be discussed. In the selection of the propeller position with respect to wing Fig. 6.2 will be used as a guide.
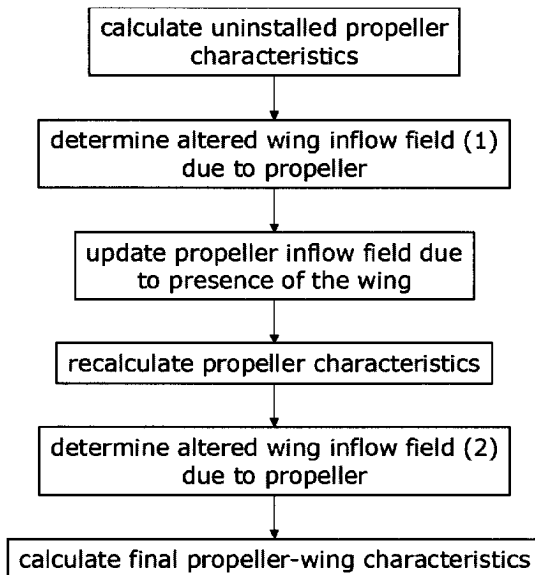
Figure 6.1: *Propeller-wing calculation sequence in the VLM calculations (code VLM4).*
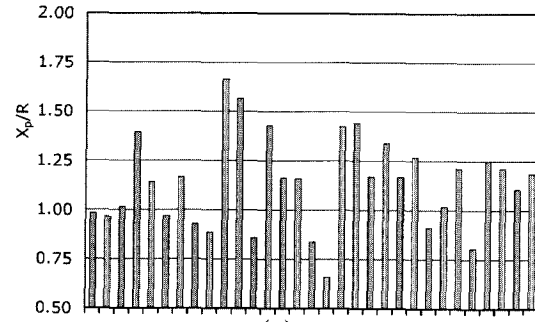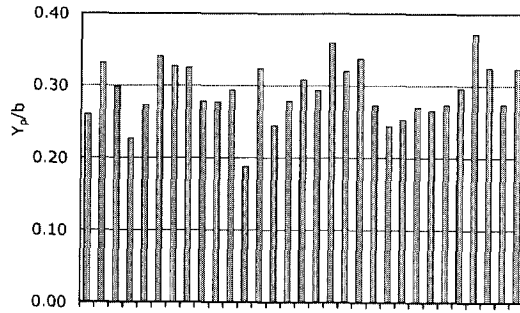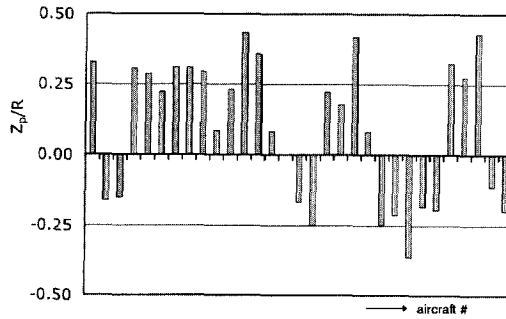
Figure 6.2: *Propeller position (x_p, y_p, z_p) as found for typical twin-engined propeller aircraft (see Appendix B).*

6.2.1   Validation of BEM-analysis

The VLM code incorporates a separate BEM-analysis of the propeller. The prediction capability of this (see Appendix A) was first investigated by comparing typical results with data available from experiments.

The first comparison is made on the basis of a propeller denoted 5868-9 with Clark-Y airfoil sections described in Ref. [94].
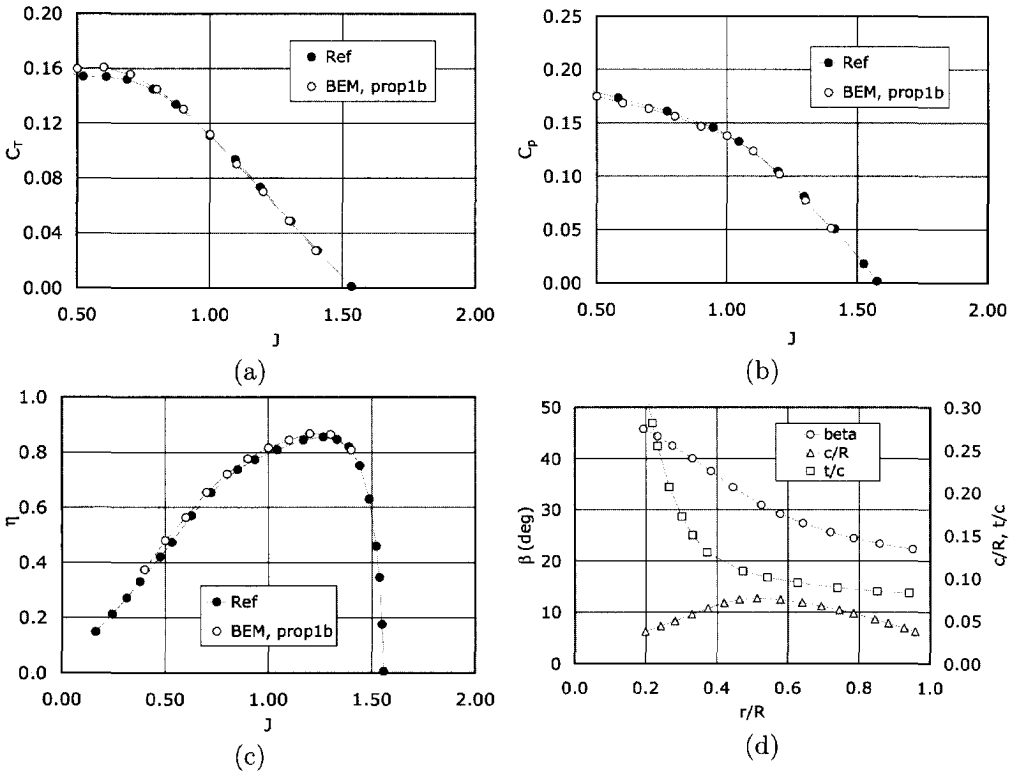
Figure 6.3: *Comparison of Prop1b-BEM analysis results with data from [94] (indicated with 'Ref') ; $\beta_{0.75R} = 30°$.*

Fig. 6.3 contains the calculation results for various rpm's and a blade setting of $\beta_{0.75R} = 30°$. In general a very good agreement between the predicted and the experimental data is found. The success of the BEM-code in this case is probably due to the fact that the propeller is lightly loaded. Hence no severe viscous effects

like flow separation occur on the blades.

The results of a second case that was investigated are presented in Table 6.1. The details of the model propeller that was tested in the Delft University Low Speed windtunnel are presented in ref. [95]. Again the agreement between the BEM-code and the reference data is acceptable. The difference between the experimental and the predicted data is likely due to inaccuracies in the $C_l - \alpha$ and the $C_d - \alpha$ curves that are used as input for the BEM-code.

Table 6.1: *Experimental and calculated propeller characteristics from ref.[95] (denoted with 'Ref') compared to the results found with the Prop1b-BEM code for a small scale model propeller ; $\alpha_p = 0°$.*

Case		0.00	0.20	0.289	0.438	0.591	0.753	0.922
					J			
C_T	Ref, exp.		0.128	0.121	0.102	0.070	0.050	0.009
	Ref, calc.	0.138	0.129	0.123	0.104	0.071	0.050	0.009
	Prop1b-BEM			0.123	0.108	0.084	0.052	0.012
C_p	Ref, exp.		0.070	0.070	0.069	0.064	0.049	0.022
	Ref, calc.	0.069	0.074	0.075	0.073	0.065	0.049	0.024
	Prop1b-BEM			0.074	0.074	0.067	0.051	0.025
η	Ref, exp.		0.370	0.495	0.645	0.740	0.745	0.300
	Ref, calc.	0.0	0.350	0.475	0.630	0.730	0.745	0.300
	Prop1b-BEM			0.479	0.638	0.741	0.760	0.450

Based on the given results, the BEM code (*prop1b*) was implemented as the main propeller-input module in the VLM-code. Furthermore the jump conditions at the propeller disk that were determined with this BEM-code are used in the definition of the actuator disk model used for the Navier-Stokes calculations.

6.2.2 Propeller normal force

To validate the propeller normal force effect on the propeller-wing performance three methods were compared prior to the incorporation in the VLM-code: the method of ESDU [29], (denoted by the E-method), the original approach described by Ribner (R-method) and the direct calculation based on the BEM-analysis (B-method). Table 6.2 contains the result for the calculation of the normal force gradient for a simple test case ($D = 0.3m$, $B = 6$, $c_b = 0.3m$, $J = 1.5$, $T_c = 0.067$) for the three methods mentioned above.

Typical differences that were found between the E- and the R-method are in the $\pm 15\%$ range which is approximately equal to the absolute accuracy of the E-method

Table 6.2: *Comparison of normal force gradients calculated with the E-R and B-method for a simple, lightly loaded propeller.*

Method	$C_{N_{p_\alpha}} = d(N_p/(\rho n^2 D^4))/d\alpha$
ESDU (E)	0.457 rad^{-1}
Ribner (R)	0.518 rad^{-1}
Blade Element Method (B)	0.416 rad^{-1}

as discussed in ref. [29]. The B-method shows a somewhat lower value which is likely to be caused by a to low drag coefficient of the blade airfoil sections. Besides this simple test case further calculations were performed on cases discussed in open literature.

The first case is a Fokker-50 propeller that was tested under different angles of attack in a low speed windtunnel [96]. The normal force coefficient that was found for this propeller is presented in Fig. 6.4. There is a remarkable difference between the experimental values and the predictions following from the E- and the B-method. Since the theoretical methods in general agree well with experiments, the experimental normal force values presented are probably wrong and the data contained in [96] should be regarded with some care. However, the thrust coefficients are very close to the theoretical values as can be seen in Fig. 6.5. A possible explanation for this is the fact that the thrust and the normal force were determined with different strain gauges during the experiments.

The second case is a low speed windtunnel test on a propeller-nacelle-wing configuration [97, 98] (see Fig. 6.6) that was tested in a cooperative effort in the Indonesian Low speed windtunnel, ILST.

Fig. 6.7 shows the contribution of the propeller, C_{L_p}, to the total lift coefficient of the propeller-wing configuration for a thrust coefficient of $T_c^* = 2.5$. The experimental results were obtained using the same rotating balance technique [97] as discussed in Fig. 6.4. In Fig. 6.7, the difference between the curves denoted with 'total' and 'axial' represents the contribution of the propeller normal force. Recalculating these data according to the definition given in [11], an experimental value of the normal force coefficient of $C_{N_{p_\alpha}} = 0.00477$ deg^{-1} is found whereas the theoretical value from the E-method becomes $C_{N_{p_\alpha}} = 0.0011$ deg^{-1}. Again a remarkable difference between the experimentally obtained results and the predicted values. Therefore it might be concluded that there was a problem with this specific test set-up or the way the rotating balance data were processed.

To check whether the data of refs. [96, 97, 98] were indeed questionable, further test cases were defined. The first case was obtained from the data available in
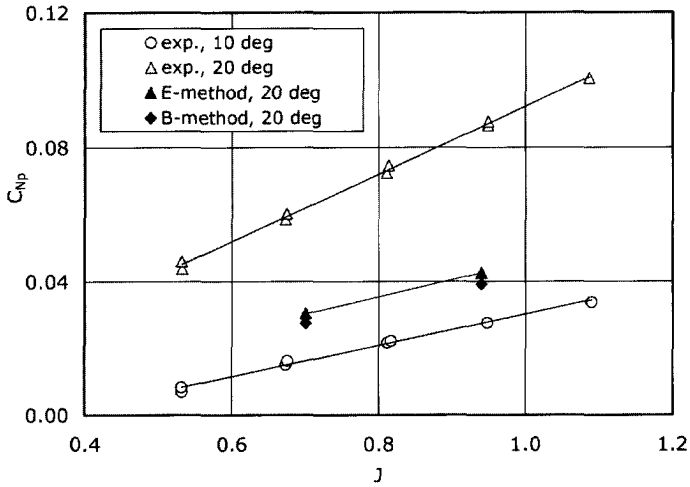
Figure 6.4: *Propeller normal force coefficient versus the advance ratio for a propeller angle of attack of $\alpha_p = 10°$ and $\alpha_p = 20°$ from ref [96] compared to the values predicted with the E- and the B-method.*
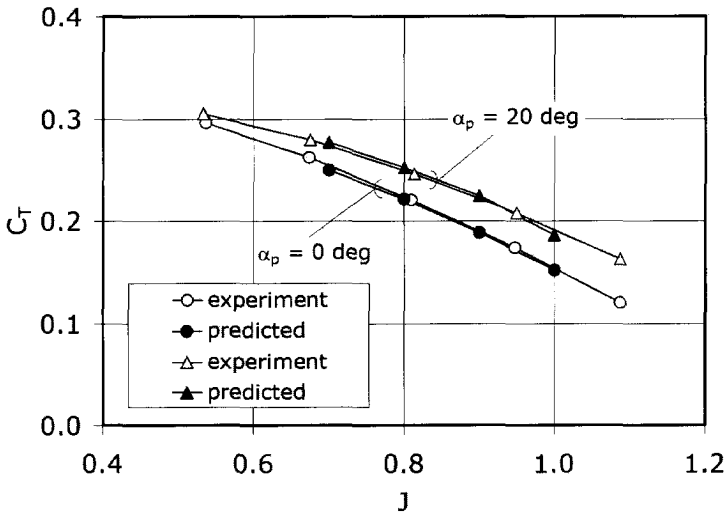
Figure 6.5: *Comparison of experimental thrust coefficients (ref [96]) and values predicted with the B-method.*
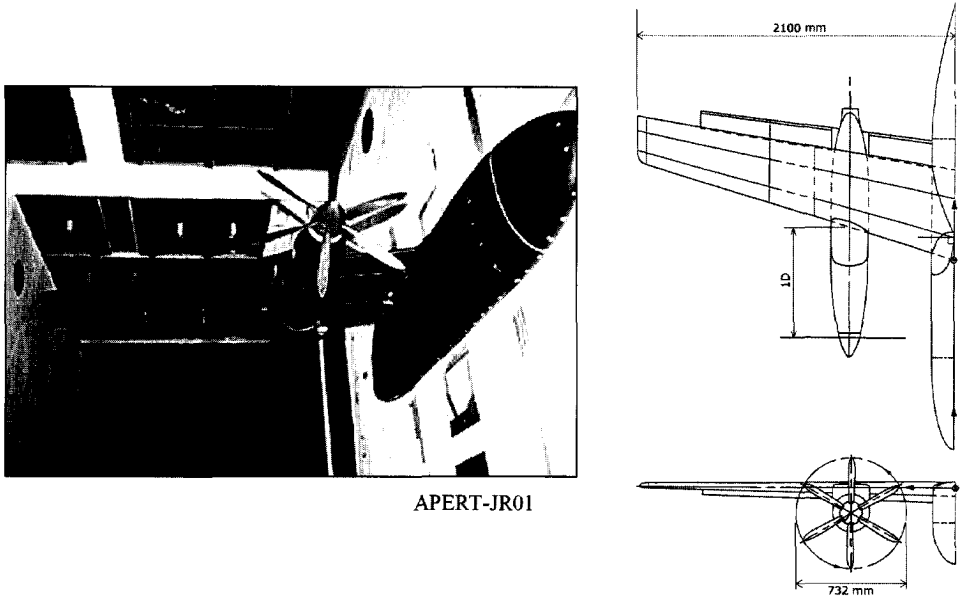
APERT-JR01

Figure 6.6: *APERT-JR01 propeller-nacelle-wing model [97].*
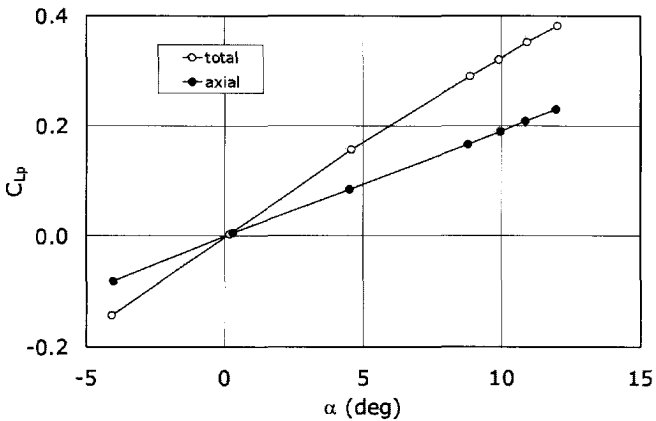
Figure 6.7: *Propeller contribution to the lift force acting on the APERT model;*
$T_c^* = 2.5$. *The difference between the open (total contribution) and closed symbol (contribution of tilted thrust vector) indicates the propeller normal force contribution.*

ref [32]. Mc. Lemore and Cannon tested a four-bladed propeller with a diameter of $D = 1.625\,m$ in a low speed windtunnel in an angle of attack range of $0° \rightarrow 180°$. For comparison with the E-method the following test conditions were selected: $J = 1.6$, $C_T = 0.122$, $\beta_{0.75R} = 40°$. The experimentally found value of $C_{N_{p\alpha}} = 0.331\,rad^{-1}$ agrees very well with the value resulting from the E-method: $C_{N_{p\alpha}} = 0.329\,rad^{-1}$.
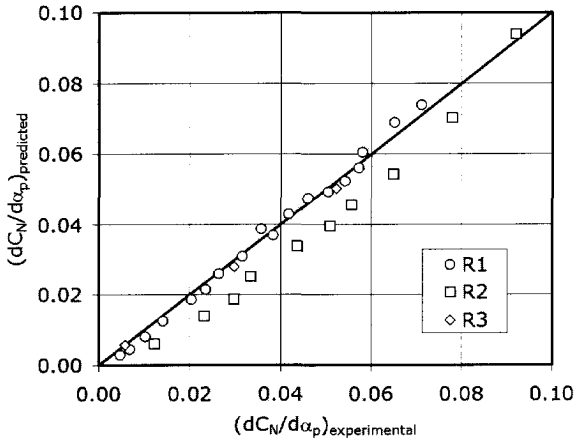
Figure 6.8: *Comparison of predicted (E-method) and experimental normal force gradients, $dC_{N_p}/d\alpha_p$; R1=ref.[30], R2=ref.[13], R3=ref.[31]*

The last comparison of data was taken from separate propeller tests described in refs. [30, 13, 31]. In Fig. 6.8 the values of the normal force gradient as predicted with the E-method are compared with experimental values. In general the E-method leads to acceptable results. Based on the comparison between de E-, R- and B-method the E-method was chosen to be implemented in the VLM-calculation process, especially for its ease of use.

6.3 VLM results

6.3.1 Comparison between VLM-calculations and experimental data

PROWIM To validate the prediction capabilities of the code a comparison was made with existing experimental data.

First of all the lift coefficients of PROWIM, obtained with the balance, the wake survey method and the enhanced VLM-method are compared in Fig. 6.9.

(a) prop off   (b) prop on
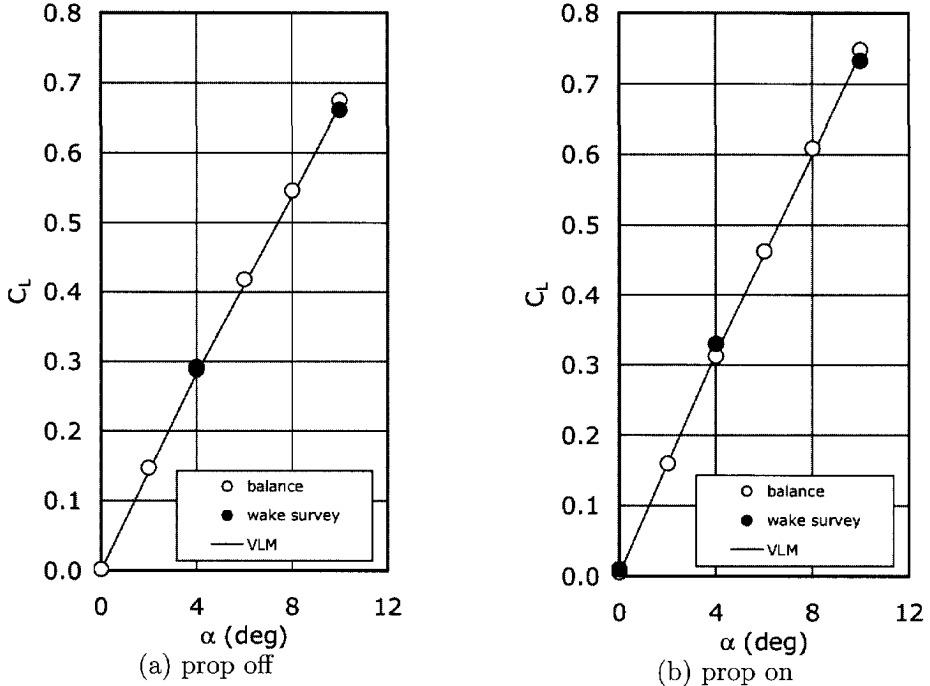
Figure 6.9: *Comparison of experimental and calculated lift coefficient of PROWIM. Propeller on case : $J = 0.85$, $T_c = 0.168$.*

As can be seen an excellent agreement between the three methods is found. Apparently the VLM-method predicts the propeller effects on the overall lift coefficient of the configurations accurately. For values above $\alpha = 10°$ serious flow separation is expected which leads to strong divergence between the experimental results and the theoretical prediction.

In general an accurate value of the drag coefficient is very difficult to capture due to difficulties in the estimation of the profile drag. Nevertheless, the VLM-code gives a reasonable prediction of the total drag coefficient, as can be seen in Fig. 6.10 where the effective "drag" coefficient is presented ($C'_D = C_D - \Delta C_{D_{prop}}$). The differences compared to the experimental values are likely to be caused by inaccuracies in the profile drag data read by the VLM-code. The fact that a reasonable agreement is found supports the conclusion that the typical propeller effect; a drag rise in the propeller washed area due to dynamic pressure increase, is effectively envisaged by

the code.

(a) prop off   (b) prop on
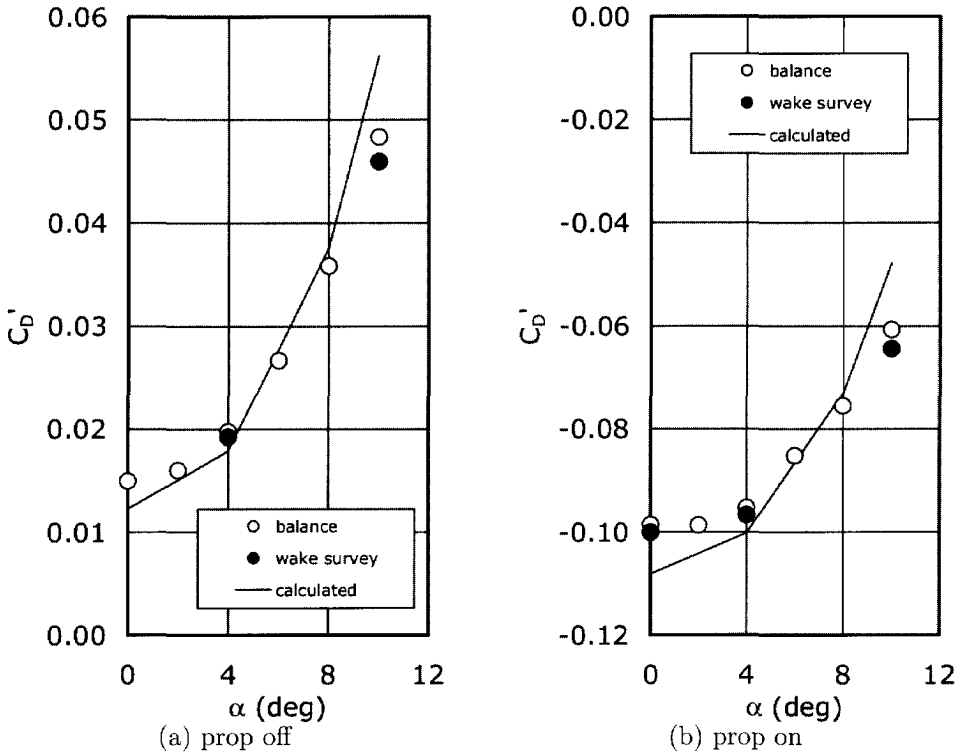
Figure 6.10: *Comparison of experimental and calculated effective drag coefficient* $(C'_D = C_D - \Delta C_{D_{prop}})$ *of PROWIM. Propeller on case ; $J = 0.85$; $T_c = 0.168$.*

The success of the code's predictive capabilities depends on the accuracy of the spanwise loading distribution, both in form and magnitude. For this reason the calculated spanwise lift coefficient of PROWIM is compared at three angles of attack in Fig. 6.11. The agreement is very acceptable for all three angles of attack and a clear deformation of the elliptic shape as a result of the slipstream swirl velocity component is found. Nevertheless, the lift coefficient on the nacelle inboard side is somewhat overestimated by the VLM-code due to the fact that decambering due to boundary layer development is not taken into account. The sharp changes in the experimental lift distribution are softened to some extent by the code, possibly as a result of smoothened slipstream velocities in the BEM analysis.
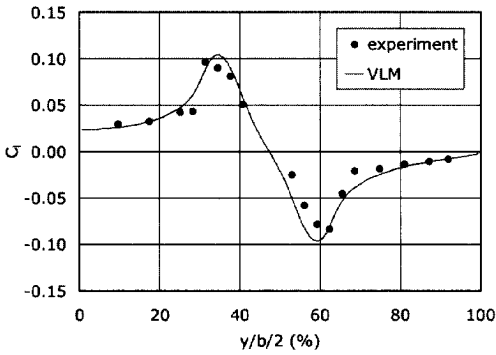
(a) $\alpha = 0°$
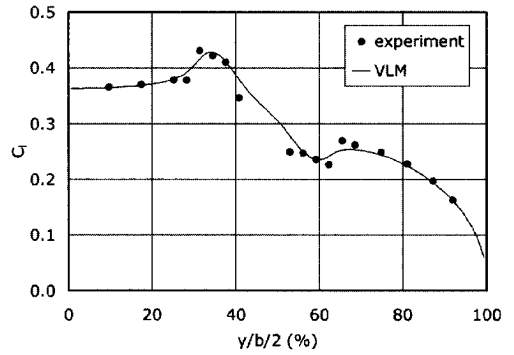
(b) $\alpha = 4°$
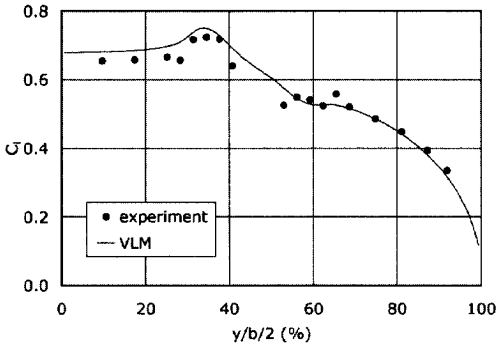
(c) $\alpha = 8°$

Figure 6.11: *Comparison of the experimental and the calculated lift distribution from the PROWIM experiment ; propeller rotating inboard up ; $J = 0.85$; $T_c = 0.168$; (a) $\alpha = 0°$; (b) $\alpha = 4°$; (c) $\alpha = 8°$.*

APROPOS   The experiments with the APROPOS model were used as a second
test case to check the accuracy of the VLM-code. Typical characteristics that were
obtained during the wind tunnel tests were simulated for variable propeller spanwise
and vertical position and the propeller angle of attack.
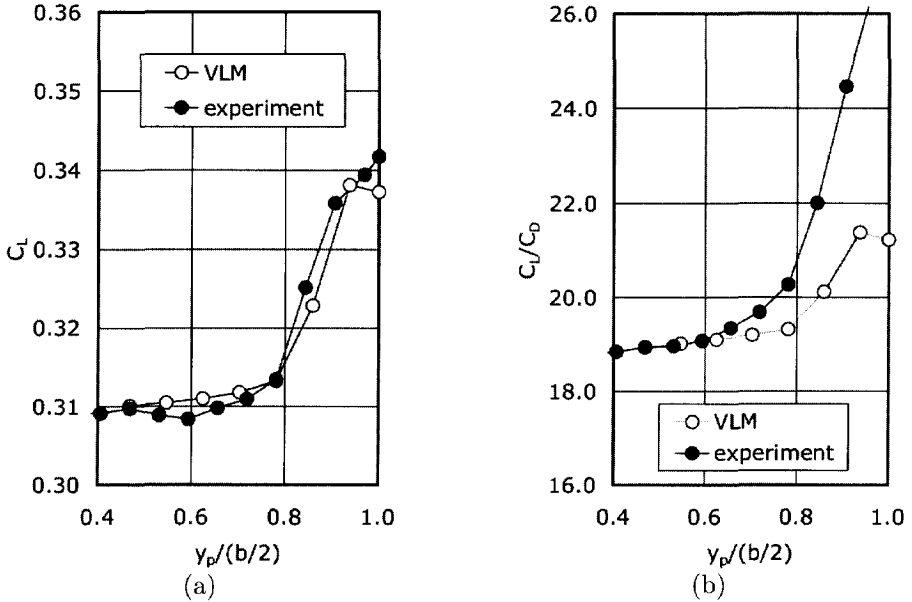
Figure 6.12: *Comparison between experimental and predicted (VLM-method) ef-
fect of the propeller spanwise direction ; APROPOS at $z_p = 0$; (a)
lift coefficient ; (b) lift/drag ratio.*

Fig. 6.12 shows the effect of the spanwise propeller position on the lift coefficient.
The agreement between the theoretical and the experimental curves is acceptable. As
with experiments the theoretical models adequately predict the performance increase
when the propeller is traversed in the direction of the wing tip. Looking at the
lift/drag ratio shows that the VLM-code produces a lower value which has to be
attributed to a problem with the proper calculation of the profile drag coefficient for
the more outboard locations of the propeller.

The effect of the propeller vertical position with respect to the wing seems to
indicate a serious problem in the VLM-method. As indicated in Fig. 6.13, the trend
of variation of the lift coefficient with z_p is predicted to some extent but the lower C_L
at negative z_p that is found in the experiments is not found in the VLM-result. Since
the experimental drag coefficient versus z_p is more closely resembled this indicates
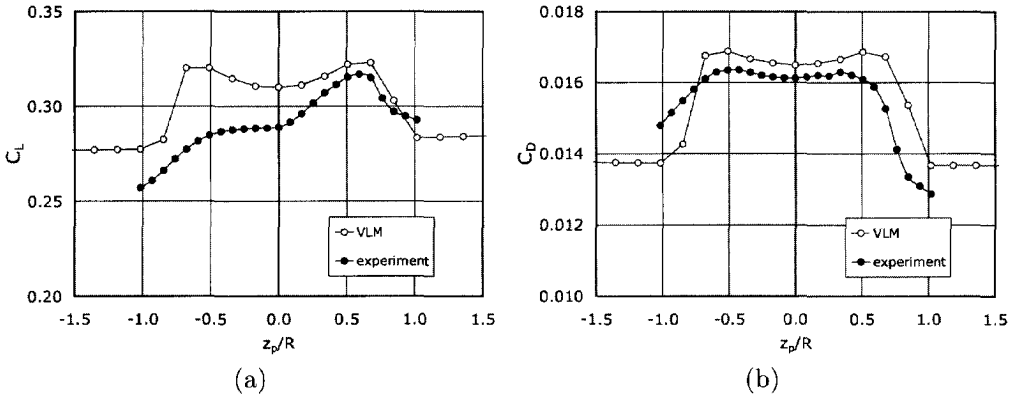
Figure 6.13: *Comparison between experimental and predicted (VLM-method) effect of the propeller vertical direction ; APROPOS ; (a) lift coefficient ; (b) drag coefficient.*

that the problem in Fig. 6.13 is caused by the code's assumption that the slipstream does not deform nor displace in vertical direction. In the case of the experiments the slipstream displaces as a function of the propeller vertical position which manifests itself in noticeable changes in the local wing angle of attack in the area washed by the slipstream. This vertical displacement and deformation is not modelled in the (linear) VLM-code. The drag change with vertical propeller position is mainly due to the changes in the dynamic pressure distribution over the wing. Hence errors in the local angles of attack at the wing airfoil section have smaller influence and the experimental and the computed curves exhibit a more similar trend.

The comparison between the two methods with respect to the effect of the propeller angle of attack is depicted in Fig. 6.14. Both for the lift coefficient and the lift/drag ratio of the wing a very acceptable agreement is found. This success is principally attributable to the part of the propeller-model in the VLM-code that allows the development of asymmetrical distributions in the slipstream axial and swirl velocities.

Fokker 50   Additional verification of the predictive capabilities of the VLM-code was recieved by comparing results obtained from flight tests on the Fokker 50 aircraft [99]. During these test the lift distribution over the wing was obtained by performing pressure measurements in chordwise direction using pressure belts. Two typical flight conditions were considered: a high thrust case (HTC) where $\alpha = 6.1°$, $T'_c = 0.63$, $J = 1.0$ and a low thrust case (LTC) where $\alpha = -0.2°$, $T'_c = 0.11$, $J = 1.63$. The calculation model of the Fokker 50 that was used (denoted Model50) differs slightly from the original aircraft. The main difference with the original F50 model is the
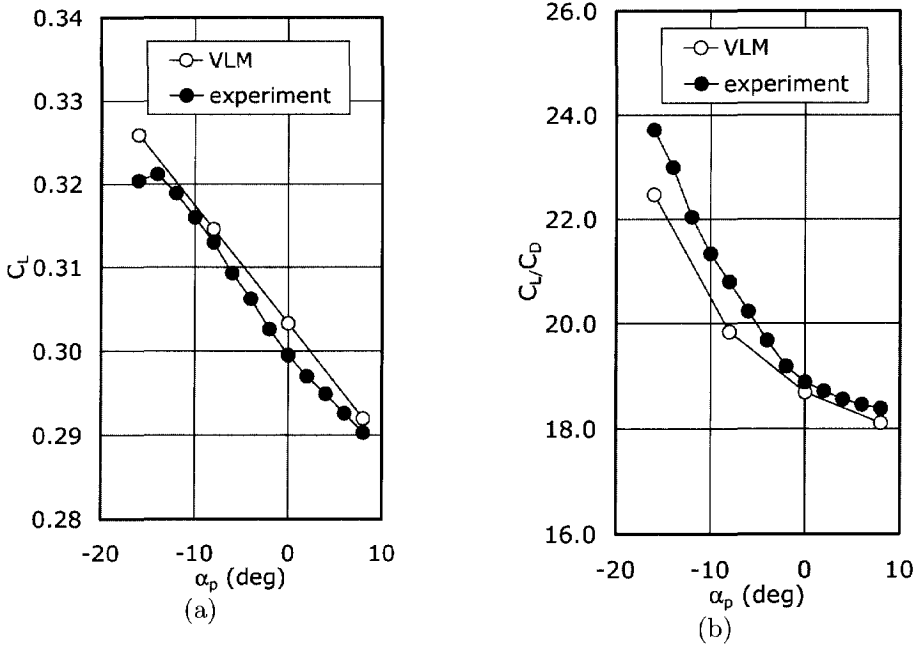
Figure 6.14: *Effect of the propeller angle of attack predicted with the VLM-code and compared to the experimental results of APROPOS ; (a) lift coefficient ; (b) lift/drag ratio*

small increase in the wing span to $b = 30m$. Additional model characteristics are summarized in Table 6.3 and Table 6.4.

Table 6.3: *F50 airfoil characteristics obtained from XFOIL [100].*

Airfoil	NACA 64_2415 (tip)	NACA 64_2421 (root)
$\alpha_0(°)$	-3.194	-3.382
$a_0(rad^{-1})$	6.956	7.227

To arrive at an accurate prediction of the characteristics it is important to model both the fuselage and the nacelle adequately since they tend to lower the local lift coefficient considerably. The effect of the fuselage/nacelle model that was implemented in the VLM-code is presented in Fig. 6.15 for $\alpha = 0°$. Here the clean wing (W) is compared with the wing-nacelle-fuselage (WNF) combination for the case without

Table 6.4: *Wing data used for the F50-like configuration (Model50)*

wing span	b	30.0	m
wing area	S	70	m^2
aspect ratio	A	12	-
dihedral 0.0b/2-0.25b/2	γ	0.0^0	-
dihedral 0.25b/2-b/2		2.5^0	
sweep at 0.25c	$\Lambda_{0.25}$	1.24^0	-
sweep at 0.40c	$\Lambda_{0.4}$	0.0^0	-
chord root	c_r	3.46	m
chord tip	c_t	1.37	m
taper ratio	λ	0.4	-
mean aerodynamic chord	$\bar{c}$	2.6	m
mean geometric chord	c_g	2.4	m
twist root	ε_r	0.0^0	-
twist tip	ε_t	-2.0^0	-
incidence angle (@ root)	i_w	3.27^0	-
airfoil root	-	NACA 64_2421	-
airfoil tip	-	NACA 64_2415	-

the propeller(s) active. Indeed a considerable lift loss occurs at the location of the fuselage and the nacelle.

With the effects of the wing and the nacelle incorporated, the spanwise lift distributions for the low thrust case and the high thrust case were calculated (see Fig. 6.16).

The results of the flight test [99] are compared with the results obtained from the VLM-method and an advanced Euler method, described in ref. [101]. As can be seen in Fig. 6.16b the propeller slipstream generates a significant disturbance of the spanwise lift distribution. Although the associated flow over the real aircraft in flight is very complex, the VLM-method, employing the full interaction model (FIM), combined with the fuselage/nacelle model, predicts the local lift coefficient remarkably well. Considering the complexity of the Euler flow model and the level of flow detail that can typically be obtained with such a model, the VLM-method produces lift distribution data that are of equal quality. In the wing tip area the Euler-curve shows an overestimation of the lift coefficient whereas the VLM-method shows the expected down-sloping curve.

The same situation is found for the high thrust case (Fig. 6.16c and Fig. 6.16d. It should be noted that for both the LTC and the HTC the agreement between the theoretical predictions and the experiment for the port side is better than for the
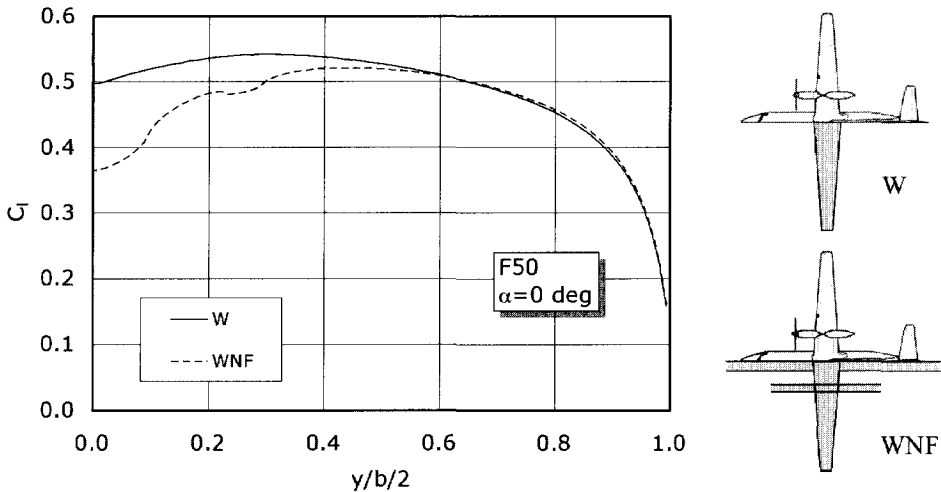
Figure 6.15: *Lift distributions predicted with VLM for the clean wing (W) and the wing-nacelle-fuselage (WNF) configuration ; Fokker 50 model at $\alpha = 0°$; props off.*

starboard side. No satisfactory explanation for this fact has been found to date.

6.3.2 Application of flap deflection

Although most of the calculations performed in this thesis are focused on the cruise condition of the aircraft, the case with flaps deployed was investigated as well. Again Model50 was used to check the various phenomena that occur in the propeller-wing interaction case. The selected flap layout is representative for a F50-like aircraft: $b_f/b = 0.521$, $c_f/c = 0.18$ and δ_f ranges from 0° to 30°. The parameter $C_{l_\delta}/C_{l_\alpha}$, that is needed to model the effect on the wing lift distribution [102], was set to 0.56 based on data obtained from [45]. Due to the higher wing loading with flaps deployed the upwash in front of the wing is enhanced, which in turn leads to considerable flow non-uniformity in the propeller plane. This fact necessitates the usage of the full interaction mode (FIM) of the program.

In general the flow of a wing with extended flaps is very complex due to the strong variation of the wing loading distribution in spanwise direction which leads to strong flap end vortices. Furthermore the initially flat wing wake is distorted adding further complexity to the flow pattern. It is therefore expected that the prediction capability of the program based on the VLM technique is limited.
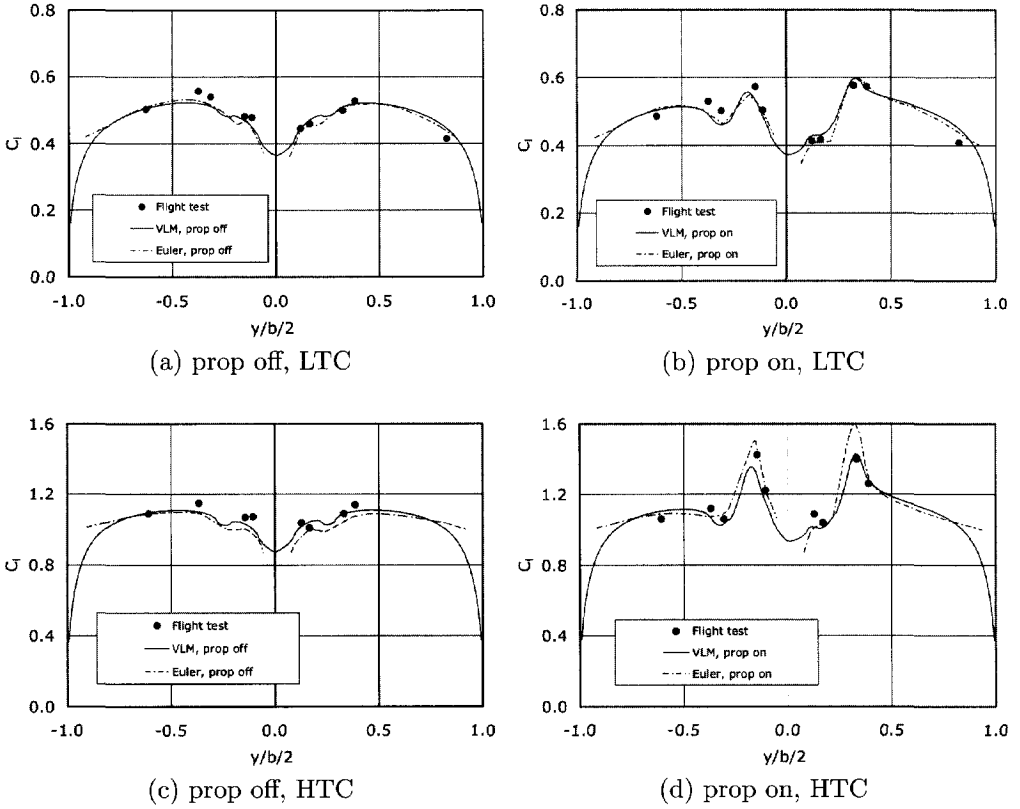
Figure 6.16: *Spanwise lift distributions found with an advanced Euler code [101] and the VLM-method compared with experimental results [99] ; Fokker-50 in the low thrust case ; (a) prop off ; (b) prop on,and the high thrust case ; (c) prop off ; (b) prop on.*
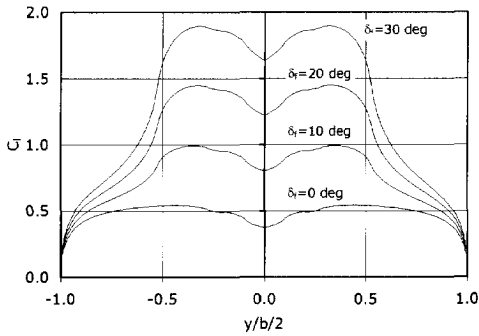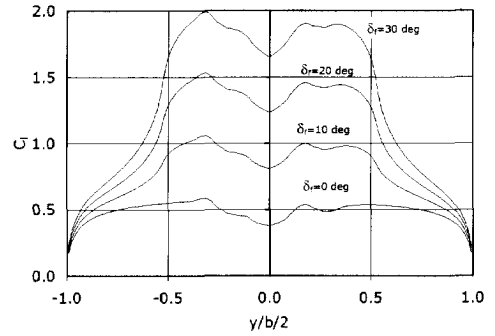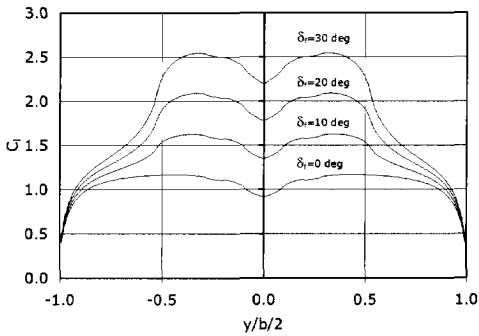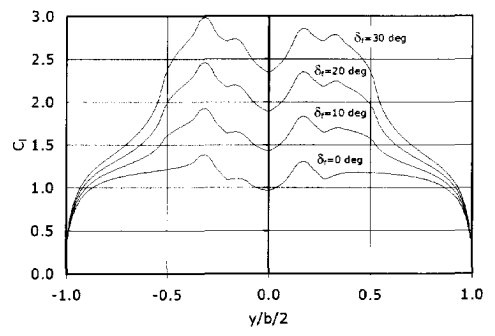
Figure 6.17: *Effect of moderate flap deflection on the lift distribution as pre-dicted with the VLM-code ; Model50 ; (a),(c) prop off ; (b),(d) prop on.*

Fig. 6.17 contains the lift distributions predicted with the VLM-code for both the low speed case ($V_{tas} = 75\,m/s$) and the high speed case ($V_{tas} = 119\,m/s$) that were used earlier for Model50. In the prop on case (right figures) the propellers are again co-rotating right. It can be seen that for moderate flap deflection, up to $\delta_f = 30°$, the form of the lift distributions does not change significantly but only a linear scaling is observed. It is questionable whether this behaviour will occur in practice when the (strong) flap end vortices interact with the propeller slipstream.
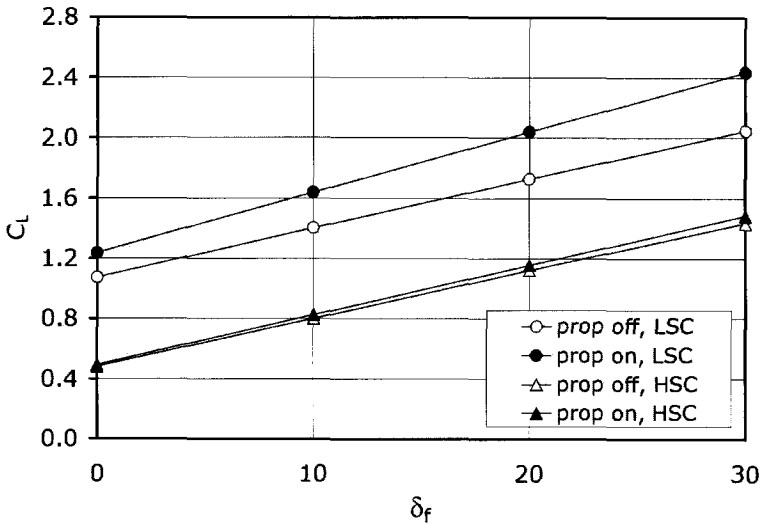
Figure 6.18: *Influence of moderate flap deflection on the lift coefficient of Model50 for the HSC and the LSC.*

The variation of the lift coefficient with the flap angle is presented in Fig. 6.18. As expected, C_L changes linearly with δ_f. But what is more important: the power effect is more pronounced for the LSC where the slipstream velocities have a stronger impact than in the HSC.

Further evidence of the calculation capability of the VLM-code in the case of deployed flaps was found by comparing the results with the data obtained by Obert [45]. In this reference the propeller slipstream effect on the stability and control of multi-engined aircraft is discussed. The data taken from [45] are for the Fokker-50 both in the case of retracted and deployed flaps ($\delta_f = 26.5°$).

In Fig. 6.19 the data are compared for the prop off and the prop on condition. As can be seen quite a close agreement between the data is found. Hence it may be concluded that even for complex flow problems when the propeller action is combined
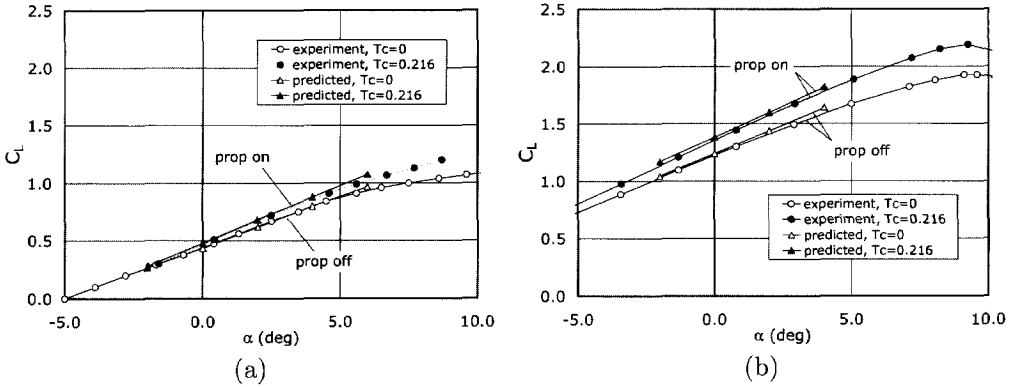
Figure 6.19: *Lift coefficient of the Fokker 50 obtained with the VLM-code com-*
pared to the results found in ref. [45] ; (a) flaps retracted ; (b)
flaps deployed, $\delta_f = 26.5°$.

with deployed flaps reasonable performance data are obtained.

6.3.3   Streamwise propeller position

By changing the propeller streamwise position with respect to the wing the aero-
dynamic coupling between the propeller and the wing changes. The swirl velocity
maintains its value (obtained directly behind the propeller plane) whereas the axial
velocity at the wing increases when distance x_p increases.

In case of high cruising speed the increase in the axial flow velocity directly affects
the critical Mach number, M_{cr}. This critical Mach number, should be high enough
to prevent excessive effects of compressibility induced drag rise ("drag divergence").
To check the impact of the propeller induced axial flow, M_{cr} can be calculated by
considering the critical pressure coefficient:

$$C_{p_{cr}} = \frac{2}{\gamma M_\infty^2} \left(\left(\frac{2 + (\gamma - 1) M_\infty^2}{\gamma + 1} \right)^{\frac{\gamma}{\gamma - 1}} - 1 \right) \tag{6.1}$$

This pressure coefficient is representative for the lift and drag behavior of the airfoil
at the given angle of attack. The development of the axial velocity in streamwise
direction changes the local flow velocity over the airfoil when x_p is changed. When
the value of $C_{p_{cr}}$ is kept constant this gives the change of M_{cr} with x_p. An example
of this relation is presented Fig. 6.20 for two values of the axial inflow factor, a,
and $M_{cr_{propoff}} = 0.7$. Clearly the presence of the propeller lowers the critical Mach
number considerably but the change with the propeller streamwise position is very
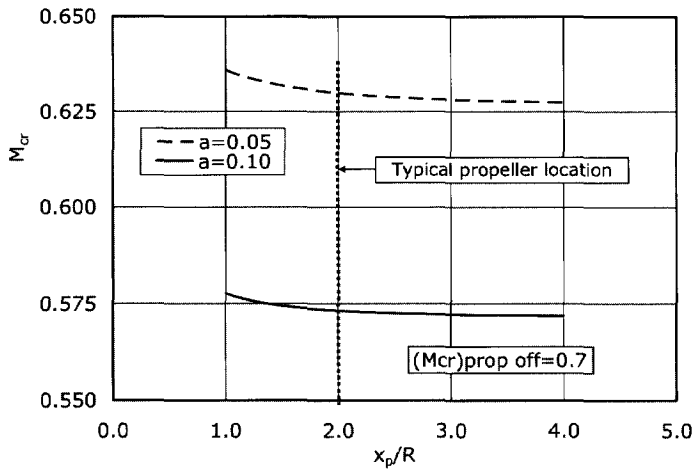
Figure 6.20: *The effect of propeller streamwise position, x_p, on the critical Mach number for two typical axial inflow factors representative for the cruise condition ; $(M_{cr})_{prop\ off} = 0.7$.*

limited. One may conclude that the selection of x_p for any tractor propeller wing configuration is not determined by the influence on the critical Mach number.

Ref.[103] presents results of windtunnel tests on a full 3D-aircraft model. Both the propeller streamwise location and the nacelle thickness were varied. It was found that the installations with the propeller close to the wing ($x_p/\bar{c} < 0.25$ ahead of the wing leading edge) produced a higher propulsive efficiency, η_p, than the configuration with the propeller further ahead, for thin nacelles (D_{nac}/t from 0.5 to 1). For a thicker nacelle ($D_{nac}/t = 1.5$) the 0.25c and the 0.40c propeller locations produced approximately the same efficiency.

To verify these findings the effect of different streamwise positions was analyzed for the Fokker 50 like configuration, Model50. Both a typical high speed case ($J = 1.63$, $T_c = 0.046$) and a low speed case ($J = 1.00$, $T_c = 0.251$) were used for this analysis. It should be noted that in these calculations the full interaction between the propeller and the wing was modeled (FIM).

The effect of the nacelle thickness on the propulsive efficiency was analyzed by comparing 3 different values of $D_{nac}/\bar{c}$ with the case without nacelle. The results of these calculations are summarized in Fig. 6.21.

Evidently an increasing distance between the propeller and the wing leads to a higher propulsive efficiency, η_p, as indicated by Fig. 6.21. The effect of the nacelle thickness was modeled by taking into account the distortion of the lift distribution and the changes in the friction drag acting on the nacelle. The curves of all nacelle cases
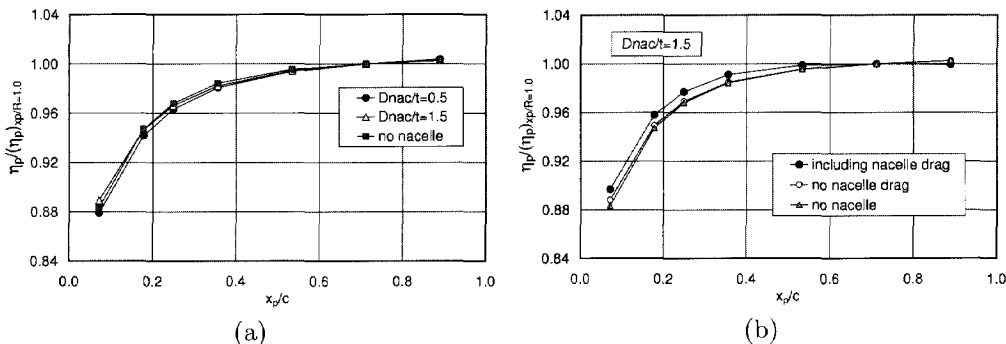
Figure 6.21: *Effect of propeller streamwise position and nacelle thickness on the propulsive efficiency of Model50; high speed case.*

show the same trend and they are very close to each other. This disagrees with the results found in ref. [103]. Since there is no physical reason why the $x_p/c = 0.25c$ case should produce the highest efficiency the results of ref.[103] are probably influenced by secondary flow effects like changes in the nacelle wing juncture flow for the various nacelles that were investigated. Note that all data are corrected to a constant lift coefficient. The effect of this correction procedure can be found in Fig. 6.22.

The source for the higher propulsive efficiency with increasing distance to the wing LE can be found in the higher lift coefficient due to the augmented dynamic pressure at greater distances from the propeller disk. This effect is depicted in Fig. 6.23a where the ratio between the lift coefficient for a given propeller position and the one found at $x_p/R = 2.0$ is given. Although the slipstream velocity distributions are quite different for the low speed case (LSC) and the high speed case (HSC) the ratio $C_L/(C_L)_{x_p/R=2.0}$ changes almost identically with x_p.

Fig. 6.23b shows a different trend for the high speed and the low speed case when $x_p/R < 1.5$. To determine the cause of this behaviour the drag coefficient is split into profile drag and induced drag.

The profile drag behaves similarly for both cases in that increasing propeller distance results in higher C_{D_p} values due to dynamic pressure effects. However, the induced drag behaves differently when the propeller approaches the wing. In the low speed case the thrust force is relatively high and the propeller induced velocity components compared to the undisturbed velocity are higher than in the high speed case. This apparently leads to stronger propeller induced angle of attack effects for the propellers that are in close proximity of the wing. It is obvious that the smaller total drag values for the propeller close to the wing in the low speed case are attributed to the smaller induced drag values. These low values in turn are the result of the lower lift coefficient in this case combined with the stronger distortion of the

(a)   (b)
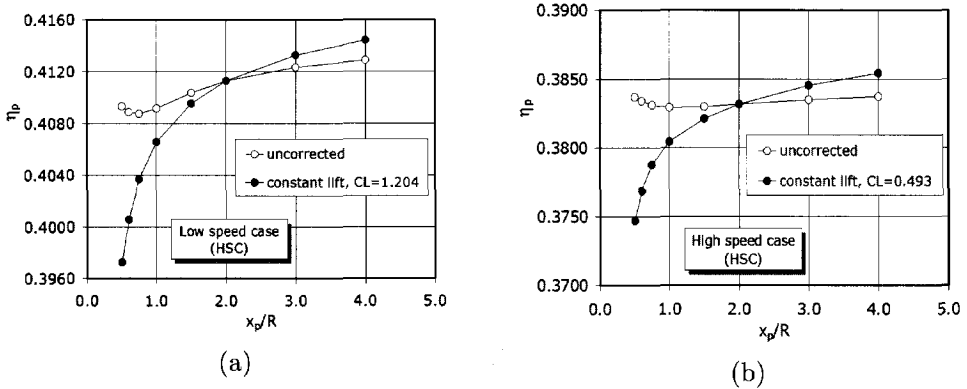
Figure 6.22: *Propulsive efficiency versus the propeller streamwise position of Model50 for a typical low speed and high speed case taking the full interaction of the propeller and the wing into account.*

propeller induced axial and tangential velocity components.

For $x_p/R > 1.0$ both C_{D_i} curves show a negative gradient, which could be anticipated since due to the higher local lift coefficient, in the slipstream washed area of the wing, stronger swirl recovery due to the presence of the wing occurs.

The range over which the propeller was translated was chosen rather wide to be able to identify the streamwise effect as completely as possible. For practical reasons, however, the choice for the propeller streamwise position is constrained by the space needed for the engine in relation to the wing structural layout. Therefore the variation of x_p is to be seen only as an "aerodynamic test case" without taking into account the problems related to the nacelle-wing structure. However, in a practical range of $x_p/R = 1.5 - 2.0$ still a noticeable effect on the propulsive efficiency is found. This is in agreement with the experiments performed on the APROPOS model [104].

One may conclude that from the fuel consumption point of view a propeller position not too close to the wing leading edge is beneficial.

6.3.4   Spanwise propeller position

The effect of the spanwise propeller position was analyzed with Model50 again for the high speed case (HSC) and the low speed case (LSC). To keep the configuration more realistic than considered in the experimental campaign for PROWIM, the spanwise propeller position was changed over a small range of $y/(b/2) = 0.20 - 0.28$ only. The spanwise loading distributions are presented in Fig. 6.24 while the characteristic
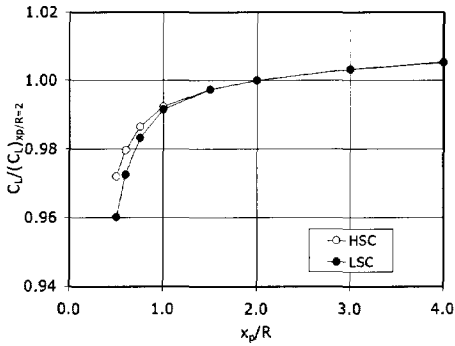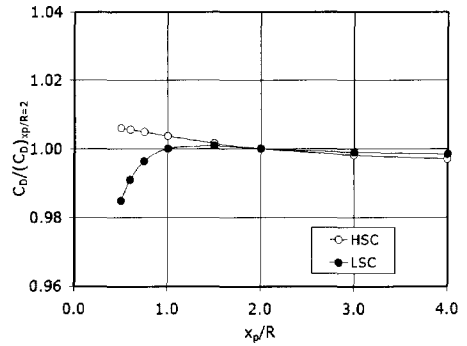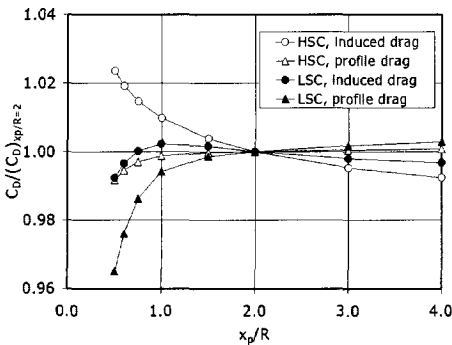
Figure 6.23: *Effect of propeller streamwise position on the wing of model 1 for the low speed case (LSC) and the high speed case (HSC) ; (a) the lift coefficient ; (b), the total drag coefficient ; (c) the drag coefficient components.*

coefficients are given in Table 6.5.
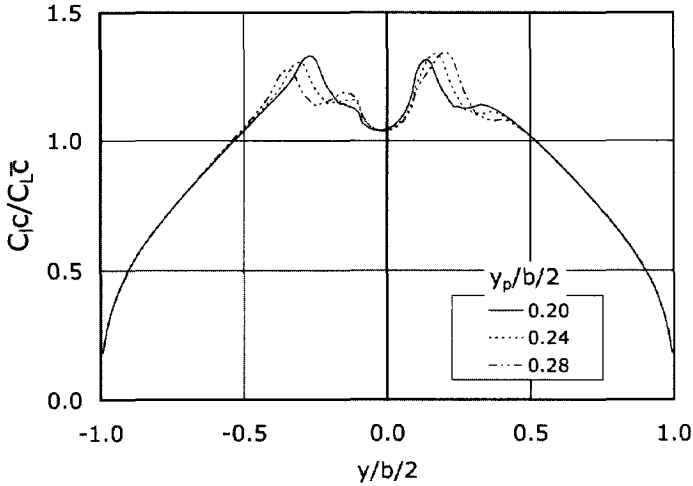
Figure 6.24: *Spanwise loading distribution for three lateral propeller positions ;*
Model50 ; high speed case.

Table 6.5: *Influence of spanwise propeller position on lift coefficient, rolling mo-*
ment coefficient and effective propulsive efficiency ; Model50.

High speed case			
$y_p/(b/2)$	C_L	$C_{m_{roll}}$	$(\eta_p)_{corr}$
0.20	0.5459	-0.001136	0.35209
0.24	0.5464	-0.001105	0.35210
0.28	0.5466	-0.001077	0.35226
Low speed case			
$y_p/(b/2)$	C_L	$C_{m_{roll}}$	$(\eta_p)_{corr}$
0.20	1.2965	-0.002805	0.39967
0.24	1.2955	-0.002765	0.39966
0.28	1.2929	-0.002714	0.39984

The small shift in the propeller position is clearly visible in the spanwise loading
given as $C_l c/C_L \bar{c}$ versus $y/b/2$. Although the most outboard position produces a
somewhat higher propulsive efficiency, as expected, the differences between the three

positions are too small to be of significance for the design process. This result can be attributed to the fact that the lift distribution is rather flat for the given propeller position. Again it should be mentioned that more outboard propeller positions raise additional problems with respect to the aircraft control in case of engine failure.

6.3.5 Vertical propeller position

The influence of the vertical propeller position was analyzed by several researchers [105, 104, 12, 1]. Due to the non-uniform distributions of the slipstream velocity component changes in the vertical position are expected to change the overall performance considerably. An indication of this phenomenon was already found during the experiments on the APROPOS model (see Chapter 5).

The effect of the vertical position of the propeller is mainly due to the change in the vertical velocity component at the location of the control point. Moreover, the propeller loading is affected by the altered inflow field generated by the wing.

To study these effects simulations were conducted for a range of $z_p/R = -0.5 \rightarrow 0.5$. This range is somewhat beyond that found for typical twin powered propeller aircraft as indicated by the data from the provisional aircraft database (Appendix A). Although from an aerodynamical analysis point of view a wide test range of z_p/R might be interesting, it is obvious that values $|z_p/R| > 0.25$ lead to very low/high nacelles. This in turn might then lead to excessive high nacelle-wing interference drag.
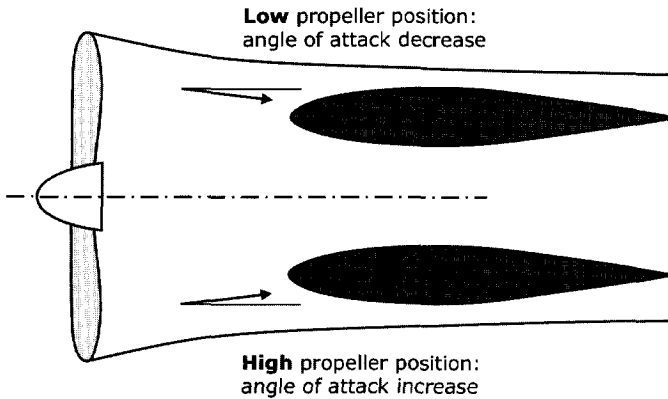
Figure 6.25: *Effect of the slipstream contraction on the local wing angle of attack.*

As can be seen in Fig. 6.25 the high propeller position causes a local angle of attack increment while the low position shows the opposite. This inflow effect, which

is dictated directly by the contraction of the slipstream tube, influences the wing lift. The magnitude of the inflow effect is related to the propeller x_p-position since the slipstream contraction varies in streamwise direction.
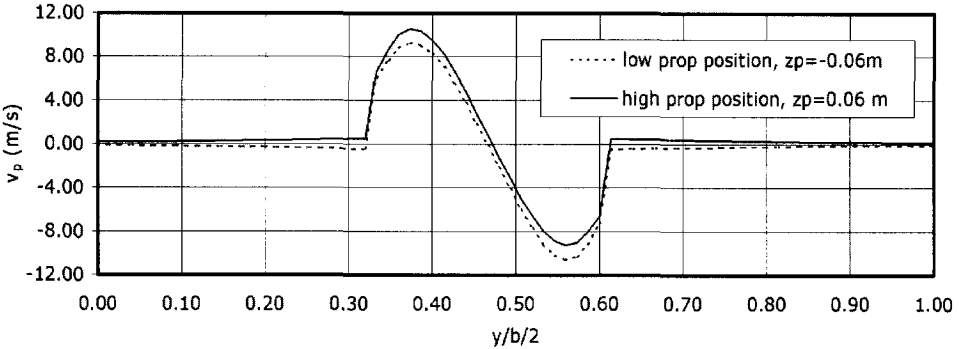
Figure 6.26: *Vertical propeller induced velocity at the PROWIM wing showing the effect of inflow into the slipstream due to the radial velocity contribution.*

In Fig. 6.26 a typical example of the effect is presented for the PROWIM model. Indeed the high propeller position leads to more positive values of the vertical velocity component caused by the slipstream. As a direct result of this inflow effect, the lift coefficient for the high propeller position is higher than for the low position as depicted by the lift coefficient ratio for the two cases in Fig. 6.27. Since the contraction is highest close to the propeller disk, the C_L-ratio grows for x_p/R close to zero.

The effects of the vertical propeller position on the characteristics of Model50 were examined by selecting 5 positions spaced $0.25R$ apart. Separate calculations showed that no significant changes occur for intermediate positions.

Fig. 6.28 gives an impression of the effect of z_p on the lift and the drag coefficient. The results are expressed in the form of a ratio between the values found at the specific location and $z_p/R = 0$. Note that in this case the angle of attack effects due to slipstream contraction are smaller than for the PROWIM model due to the higher value of x_p/R.

The first thing that can be noticed is the minimum in the lift coefficient found at $z_p/R = 0$. Apparently the overall dynamic pressure increase over the wing part immersed in the slipstream increases somewhat when the propeller is put at an off-zero position (see Fig. 5.30). The reason for this is to be found in the distribution of the axial velocity increase in the slipstream. In case of $z_p/R = 0$ part of the wing is hit by the velocity deficit area in the middle of the slipstream whereas for higher or lower positions a more filled axial velocity profile interacts with the wing. On
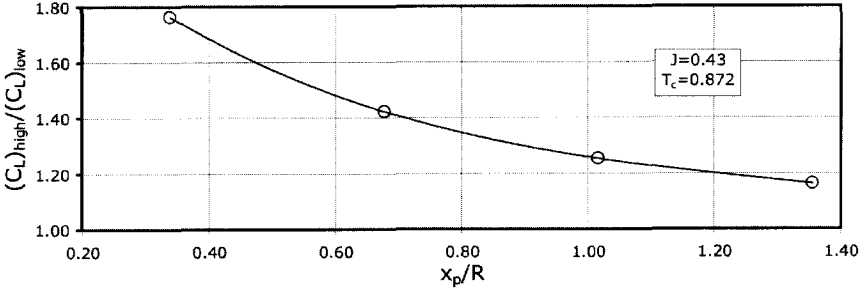
Figure 6.27: *Ratio of PROWIM wing lift coefficient for high ($z_p/R = 0.508$) and low ($z_p/R = -0.508$) propeller position versus the propeller streamwise position relative to the wing.*
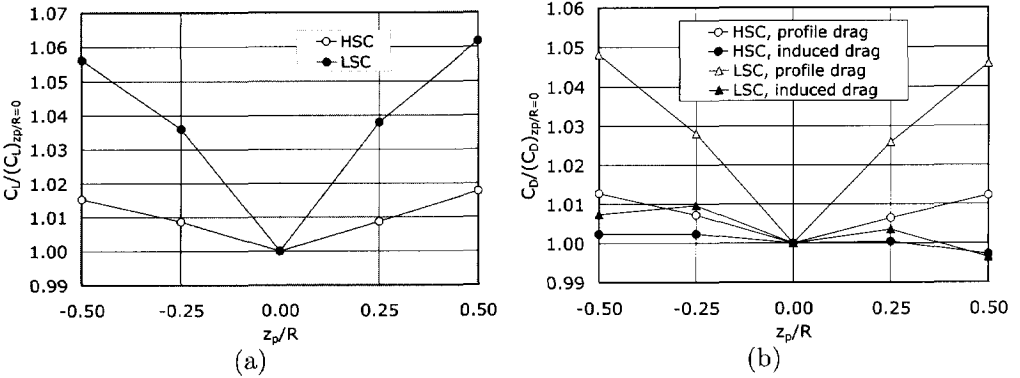
Figure 6.28: *Effect of vertical propeller position on the lift coefficient (a) and the drag coefficient (b) of Model50 calculated for the high speed and the low speed case.*

average this leads to higher dynamic pressure over the wing which increases the lift and the drag. The drag coefficient is mostly affected by a change in the profile drag component showing variations up to 5% while the induced drag doesn't alter more than 1% for the given range of propeller positions.

Comparing the variations of lift with z_p of Fig. 6.28 with the earlier found trends in the experimental data for PROWIM, the lift coefficient seems to be overestimated for the low propeller positions. A possible cause for this discrepancy is the code's inability to take the slipstream deformation into account. From the experimental investigations on PROWIM a considerable deformation was found.

Since the propulsive efficiency is directly correlated with the total lift and drag values, a more acceptable value of η_p can be obtained by applying a correction such that the lift coefficient resembles that of Fig. 5.29d, i.e. lower values for negative z_p.
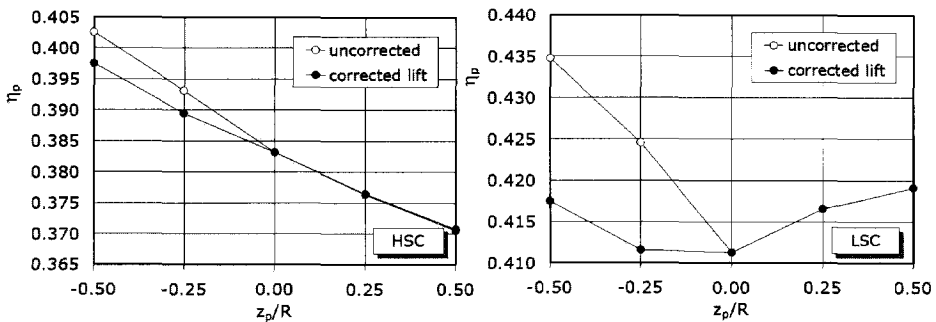
Figure 6.29: *Uncorrected and lift corrected values of the effective propulsive efficiency versus the vertical propeller position ; high and low speed case for Model50.*

The original and the (lift) corrected values of η_p are presented in Fig. 6.29. Note that, in contrast with the lift and drag distributions of Fig.6.28 for both the uncorrected and the lift-corrected case, no symmetry with respect to $z_p/R = 0$ is found. The higher η_p-values for the low propeller position are caused by the increased efficiency (and thrust) of the propeller due to the reduced inflow velocity in the propeller plane.

Especially the high speed case, which is representative for the cruise condition of the aircraft, shows a considerably higher propulsive efficiency for the low propeller positions.

6.3.6 Propeller angle of attack

In the experiments described in Chapter 5 we found remarkably strong effects of propeller angle of attack changes with respect to the wing reference chord line. As with the PROWIM model the effects of changing α_p were investigated for Model50 as well.

Fig. 6.30 shows the breakdown of the total lift coefficient. For decreasing propeller angle of attack the wing lift increases slightly due to the upwash encountered by the wing immersed in the slipstream.
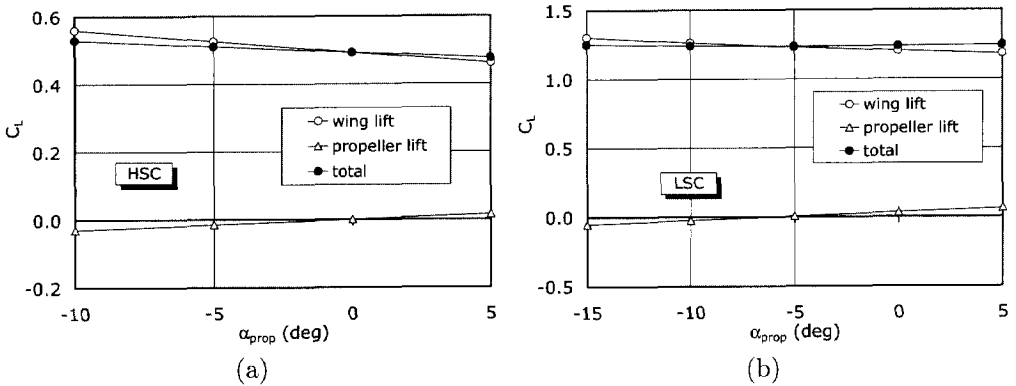
Figure 6.30: *Components of the lift coefficient for Model50 versus the propeller angle of attack; (a) high speed case; (b) low speed case.*

However, the direct lift force that acts on the propeller (denoted 'propeller lift') lowers the total lift as a result of tilting down the thrust vector and the negative propeller normal force that is associated with negative α_p. The trend for both the high speed case and the low speed case is similar, though the changes due to α_p are somewhat stronger for the latter.

To compare the α_p-effects on the lift and the drag, ratios were defined taking the values at $\alpha_p = 0°$ as a reference. Fig. 6.31 shows the results for C_L and C_D, where the latter is again split in profile drag and induced drag.

Small increments in the lift coefficients are found in the low speed case with decreasing α_p while more significant effects are predicted for the high speed case. In the latter case the most prominent contribution is due to the change in the wing lift. By lowering the advance ratio, as is done in the low speed case, the relative contribution of the propeller normal force increases, leading to a smaller change of C_L with decreasing α_p.

The picture for the drag coefficient becomes more complex since the total "drag" force is constituted of three components: profile drag, induced drag and propeller
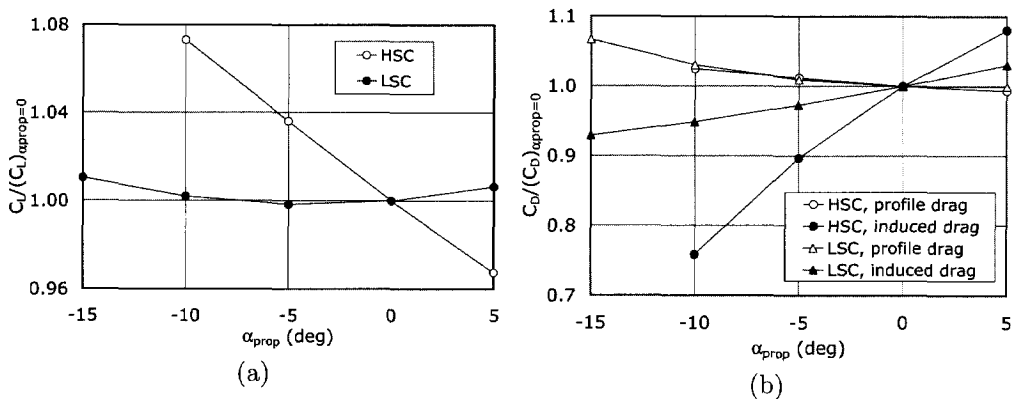
Figure 6.31: *Effect of propeller angle of attack on the lift (a) and drag (b) ratios for Model50. The values at $\alpha_p = 0°$ were taken as a reference.*

"drag" (in fact thrust).

In Fig. 6.31b the drag ratio $C_D/(C_D)_{\alpha_p=0}$ is shown for both flight cases. Once more the effect of lowering the propeller angle of attack is more pronounced for the high speed case. That is: the relative change in the drag coefficient is higher which of course has to be partially contributed to the lower absolute values of the drag coefficient in this case. The change in the profile drag coefficient is negligible, which could be expected from the fact that the average dynamic pressure in the slipstream is hardly affected by changes in the propeller angle of attack. The induced drag , on the other hand, diminishes expressively as a consequence of the increased upflow in front of the wing.

The combined effects on the changed lift and drag contributions leads to favourable propulsive efficiencies for low values ofα_p, as indicated by Fig. 6.32. In the high speed (cruise) case η_p rises approximately 9.5% by changing α_p from 0° to$-10°$. This performance improvement is interesting enough to be considered further in design studies of tractor propeller wing configurations.

6.3.7   Propeller rotation direction

As indicated in Chapter 3, the propeller rotation direction directly influences the overall performance of the aircraft. Experimental proof for this phenomenon was found in Chapter 5. From a theoretical point of view the configuration with inboard-up rotating propellers is expected to produce the highest efficiency due to the favorable interaction between the slipstream swirl velocity and the wing lift distribution. To examine the effect of the rotation direction on a realistic configuration, some calcula-
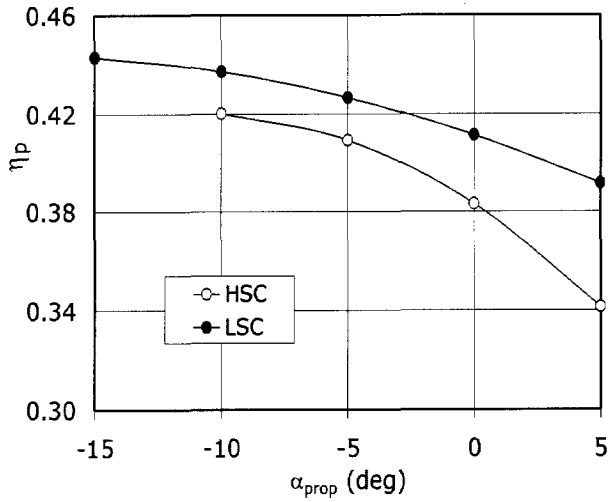
Figure 6.32: *Propulsive efficiency of Model50 versus the propeller angle of attack for the high speed and the low speed case.*

tions on Model50 were performed for the 3 relevant cases: inboard-up (IU), co-right (CR) and outboard-up (OU) rotating propellers. The most important results are summarized in Table 6.6.

Table 6.6: *Influence of propeller rotation direction on the lift coefficient and the propulsive efficiency of Model50.*

High speed case		
Rotation direction	C_L	η_p
inboard Up	0.4986	0.38550
co-right	0.4974	0.38466
outboard up	0.4962	0.38388
Low speed case		
Rotation direction	C_L	η_p
inboard Up	1.2468	0.41577
co-right	1.2439	0.41518
outboard up	1.2408	0.41458

The IU case, indeed produces the highest propulsive efficiency for both flight conditions, but the magnitude of the effects is rather small. The propulsive efficiency for the IU case is only 0.23% higher than for the (conventional) CR-case for the high speed (cruise) condition. For the low speed case this even reduces to 0.14% in favor of the IU-configuration. These values are lower than found during earlier experiments and calculations on the PROWIM model. The reason is the much smaller propeller diameter over wing span ratio, D/b.

6.3.8　Propeller loading

When the thrust of the propeller is changed both the direct contributions of the propeller forces to the overall performance as well as the slipstream shape and velocity components are drastically changed. As an example the capability to predict the effects of changes in propeller thrust loading on the propeller-wing combination is presented in Fig. 6.33 and Fig. 6.34.

(a)　　　　　　　　　　　　　　　　(b)
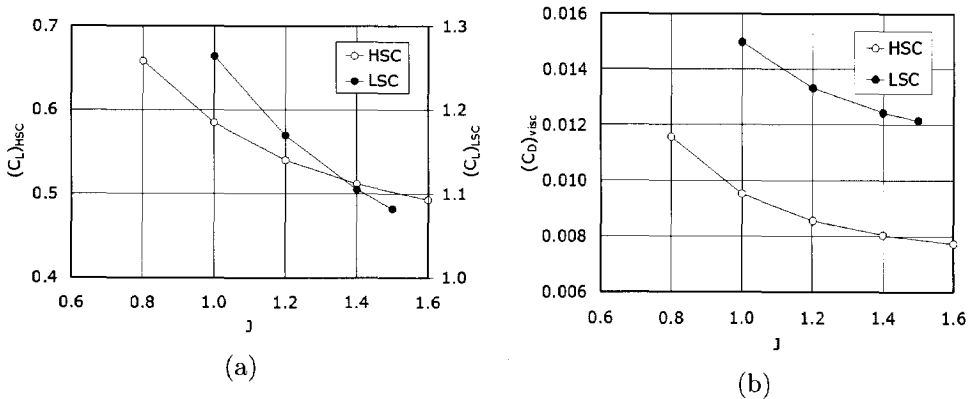
Figure 6.33: *Variation of Model50 wing lift (a) and drag (b) coefficient with changing propeller advance ratio for the two typical flight cases: HSC and LSC.*

The expected increase in the wing lift and drag coefficient with increasing propeller loading (i.e. lower advance ratio, J) is presented in Fig. 6.33. The curve for the LSC is steeper because of the higher basic loading.

Where changes in the dynamic pressure lead to a comprehensible effect on lift and drag, the changes in the slipstream velocity distributions constitute a somewhat different change in the wing characteristics. The swirl velocity in the slipstream initially represents a loss in propulsive efficiency of the propeller. However, due to the presence of the wing a part is recovered due to the wing guiding effect. This
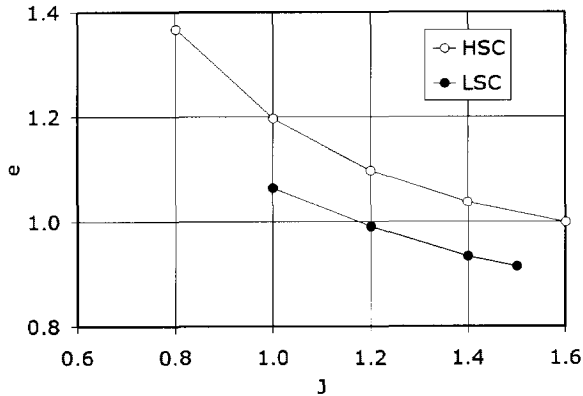
Figure 6.34: *Wing span efficiency factor, versus the propeller advance, J ratio of Model50 for the two cases investigated : HSC and LSC.*

directly leads to a relative reduction of the wing induced drag compared to the prop-off condition, a description of which was discussed earlier.

The recovery of a part of the swirl loss is reflected in the change in wing span efficiency factor (Fig. 6.34) which clearly rises with increasing propeller loading i.e. lower advance ratio. This is consistent with earlier theoretical observations.

6.3.9 The interaction step

The significance of completing the full interaction scheme, e.g. take into account the propeller effects on the wing and vice versa, was assessed by comparing the final results of step 1 (no wing effect on the propeller) and step 2 (full interaction) in the scheme of Fig. 6.1.

To assess whether full interaction is needed a comparison is made between the lift distributions found for both situations. In Fig. 6.35 this is expressed in the form of a difference between the local lift coefficient found for step 1 and step 2: ΔC_l. Again the calculations were performed for both the high speed and the low speed case.

A noticeable difference exists, especially in the vicinity of the propeller where the effect of the slipstream is the most prominent. The fact that larger values of ΔC_l are found for the low speed case is trivial since for this condition a higher lift is produced by the wing which causes a stronger deterioration of the inflow field of the propeller.

Typical differences between the lift coefficient, the drag coefficient and the propulsive efficiency are shown in Table 6.7. From these results it may be concluded that all propeller-wing calculations should be performed in the full interaction mode (FIM).
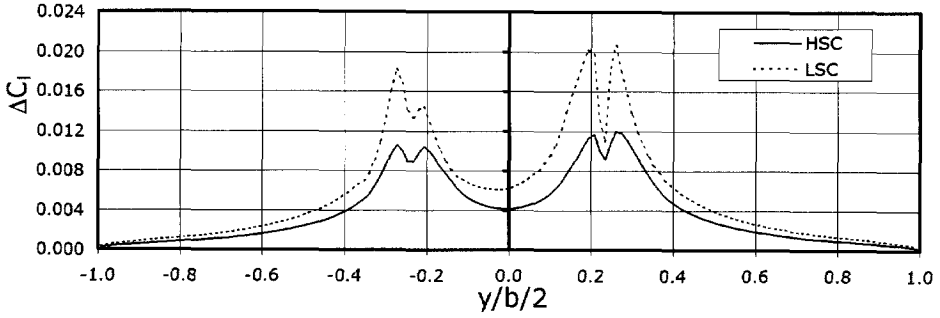
Figure 6.35: *Difference between the local lift coefficient distribution of the 'no interaction case' and the 'full interaction case' as calculated on Model50 for the high (HSC) and the low speed case (LSC).*

Table 6.7: *Comparison of calculation results on Model50 for step 1 (single interaction, SIM) and step 2 (full interaction, FIM)*

High speed case							
Iteration	α	C_L	C_{D_i}	$C_{D_{visc}}$	$C_{L_{tot}}$	$C_{D_{tot}}$	η_p
1 (SIM)	0	0.4971	0.00617	0.00773	0.4971	-0.01994	0.38422
2 (FIM)	0	0.4929	0.00625	0.00772	0.4929	-0.01988	0.38316
Low speed case							
Iteration	α	C_L	C_{D_i}	$C_{D_{visc}}$	$C_{L_{tot}}$	$C_{D_{tot}}$	η_p
1 (SIM)	6	1.2090	0.03605	0.01383	1.2431	-0.13258	0.41433
2 (FIM)	6	1.2042	0.03631	0.01379	1.2382	-0.13160	0.41128

The propulsive efficiency changes 0.3% for the high speed while a 0.7% change is found for the low speed case. The suggestion, offered by some authors, that the wing effect on the propeller (in case of the tractor propeller located well ahead of the wing) can be neglected, should therefore be questioned.

6.3.10 Over the wing propeller arrangement

The last configuration that was investigated with the VLM-method is the over-the-wing (OTW) propeller arrangement. Several researchers investigated over–the-wing (OTW) arrangement of the propulsion system for the capability of increased lift and reduced drag. Over-the-wing jets were investigated by Sawyer et al [106] Putnam [107], Cooper et al [82] while Johnson et al [81], Veldhuis [12] and Luijendijk [108] examined the aerodynamics of an over-the-wing propeller configuration. All investigations were intended to determine whether the jet/propeller inflow was effective in producing favorable interference effect.

For jets placed close to the wing surface increased lift and reduced drag were found [107, 82], as a result of the entrainment of free-stream flow into the jet. Especially for jets placed in close proximity to the wing strong changes in streamline curvature were found leading to distortion of the wing loading distribution (both in spanwise and chordwise direction).

Very interesting results were obtained with the over-the-wing propeller arrangement of Johnson et al [81]. For a lift coefficient of 0.7 a significant performance improvement was found with a maximum for the propeller positioned at 0.2c above the wing. Cooper et al [82] performed both a numerical and an experimental analysis on a low aspect ratio rectangular wing. In the numerical model the propeller effect was modeled by a streamtube enclosing the slipstream. By controlling the inflow and outflow for the streamtube the effect of streamline distortion due to the propeller could be modeled. During the experiments a propeller positioned at 0.1c above the wing was used.

Although the numerical calculations (panel method) underestimated the effect of the OTW arrangement on lift and drag the variation with streamwise position was similar to that of the experiments. A maximum lift increment was found for the propeller located above the trailing edge ($x_p/c = 1.0$) whereas a maximum in wing drag reduction was found for a mid-chord location ($x_p/c = 0.5$).

Based on these positive results and the code's flexibility to change the propeller-wing layout easily, it was decided to gather additional information on an OTW arrangement on a Model50 like configuration.

In the OTW layout the propeller clearance from the wing upper surface is $0.15R$ and streamwise positions in the range $x_p/R = -1.0$ to 2.0 were selected.

In Fig. 6.36 the effect of the streamwise propeller position on the free wing lift and drag is depicted. For this OTW layout the full interaction model of the program is absolutely essential because of the strong effect of the wing induced flow field on

the propeller.
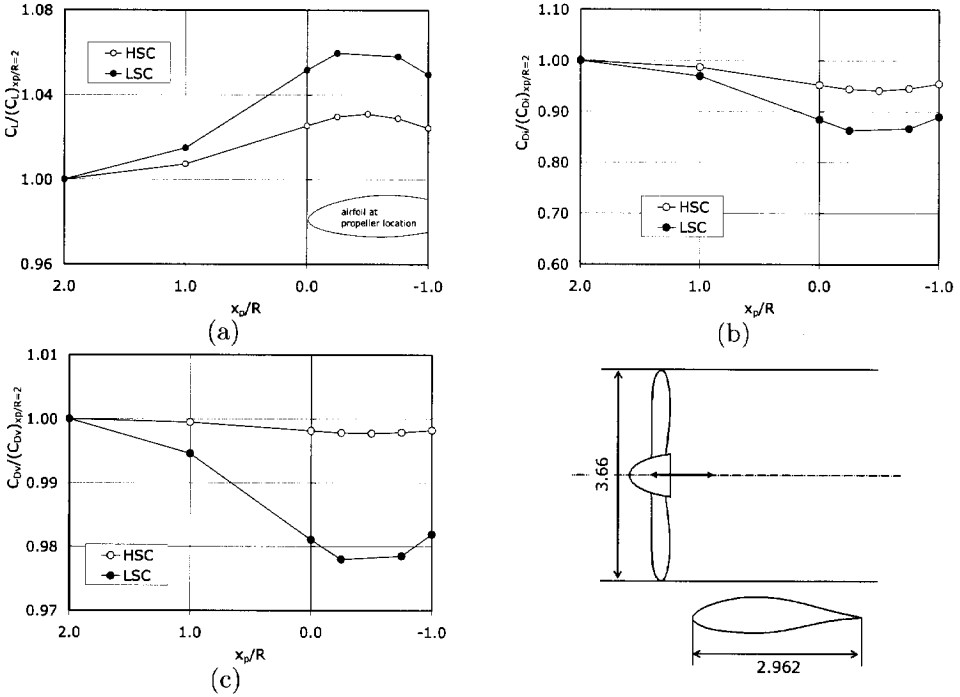
Figure 6.36: *Effect of the propeller streamwise location for the OTW-configuration of Model50 expressed relative to $x_p/R = 2.0$; (a) wing lift coefficient ; (b) wing induced drag coefficient ; (c) wing profile drag coefficient.*

As described earlier, the velocity increase at the wing's suction side reduces the axial velocity increase due to lower blade effective angles of attack in this situation. As a consequence the propeller thrust and the power are reduced considerably, which means that for final conclusions on the performance aspects of the OTW configuration only the total (i.e. propeller + wing) coefficients have to be used. Note that the lift and drag coefficients in Fig. 6.36 are based on the wing only. The changes that occur for changing x_p/R are the result of adaptation of the streamline curvature outside the slipstream according to the model described in Appendices C and F. Apparently the lift coefficient peaks at $x_p/R = 0.5$ while the lowest value of the drag coefficient is also found at this location. Expressed in the local wing chord this value is equivalent to $x_p/c = 0.31$, which is close to the value found by Johnson et al [81]. At this position

the contracted slipstream apparently generates the highest leading edge suction.

Comparing the values of x_p/c for maximum lift enhancement and drag reduction found in open literature combined with the data from the APROPOS experiments and the calculations on Model50 quite some scatter is observed (optimum x_p between 0.5 and 1.0). Although no clear explanation for this fact could be found, the variation in x_p/c is expected to be caused by the way the different airfoils react to the streamline deformation induced by the contracting slipstream.

Before final conclusion about possible beneficial or detrimental effects of an OTW propeller arrangement can be drawn it is important to consider the propulsive efficiency of the complete configuration.

The lift and drag data depicted in Fig. 6.36 were acquired by changing the propeller streamwise location for a constant value of the advance ratio, J. Due to the higher flow speed at the wing upper side, however, the effective advance ratio of the propeller decreases, leading to a reduced thrust and shaft power as well as a change in the propeller efficiency.
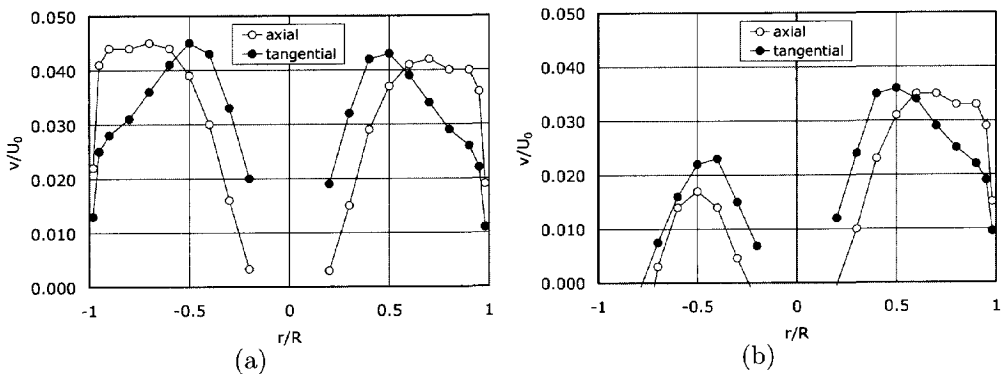
Figure 6.37: *The axial and the tangential velocity directly behind the propeller ; (a) propeller well in front of the wing, $x_p/R = 2.0$; (b) propeller above the wing, $x_p/R = -0.5$*

A typical example of this reduction in propeller loading, as calculated with the BEM-analysis is presented in Fig. 6.37. In this figure the positive values of r/R represent positive values of z ($\psi > 0$) and negative values represent negative z ($\psi < 0$). Hence the data on the left side are produced by the blade closest to the wing. Whereas the slipstream is more or less symmetrical for $x_p = 2.0$ (Fig. 6.37a), it becomes highly asymmetrical in case the propeller is positioned above the wing (Fig. 6.37b). In the latter case even negative axial and swirl velocities are generated by the lower propeller blade. This deformation evidently initiates changes in the propulsive efficiency of both the propeller and the wing.
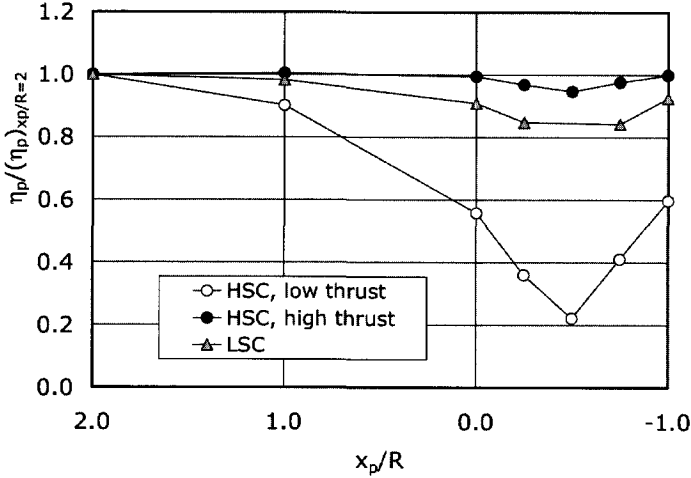
Figure 6.38: *Effect of the propeller streamwise position in the OTW configuration on the propulsive efficiency expressed relative to $x_p/R = 2.0$; constant J and $\beta_{0.75R}$.*

A nice example of the effect of the OTW configuration on the propulsive efficiency is given in Fig. 6.38. In this case the propeller was set at the same HSC and LSC power conditions as sketched earlier and the values of J and $\beta_{0.75R}$ remained constant while moving the propeller downstream. The value of η_p drops considerably when the propeller is positioned over the wing. This is not surprising since the propeller efficiency itself is diminished due to the higher incoming flow speed and the deformation of the inflow field. The strongest effects (relative to $x_p/R = 2.0$) are found for the high speed case because of the relative low axial and swirl velocities generated by the propeller. Any disturbance created by the wing will effectively change the propulsive efficiency stronger than in the case of high thrust that is found in the low speed case. The existence of this effect may be acknowledged by considering the solid symbols in 6.38. In this situation the HSC is combined with a higher thrust setting (the one normally used for the LSC) and the curve immediately jumps to higher η_p-values.

To arrive at a fair comparison of the OTW configurations with variable x_p we need to analyse the performance characteristics at equal thrust and power setting. This means that with the increasing inflow velocity for a propeller approaching the wing, a new combination of J and $\beta_{0.75R}$ needs to be set. By changing the propeller settings calculations could be performed for a total (constant) power of $816\,kW$ per propeller.

In Fig. 6.39 the effect of this procedure is summarized. As can be seen, all
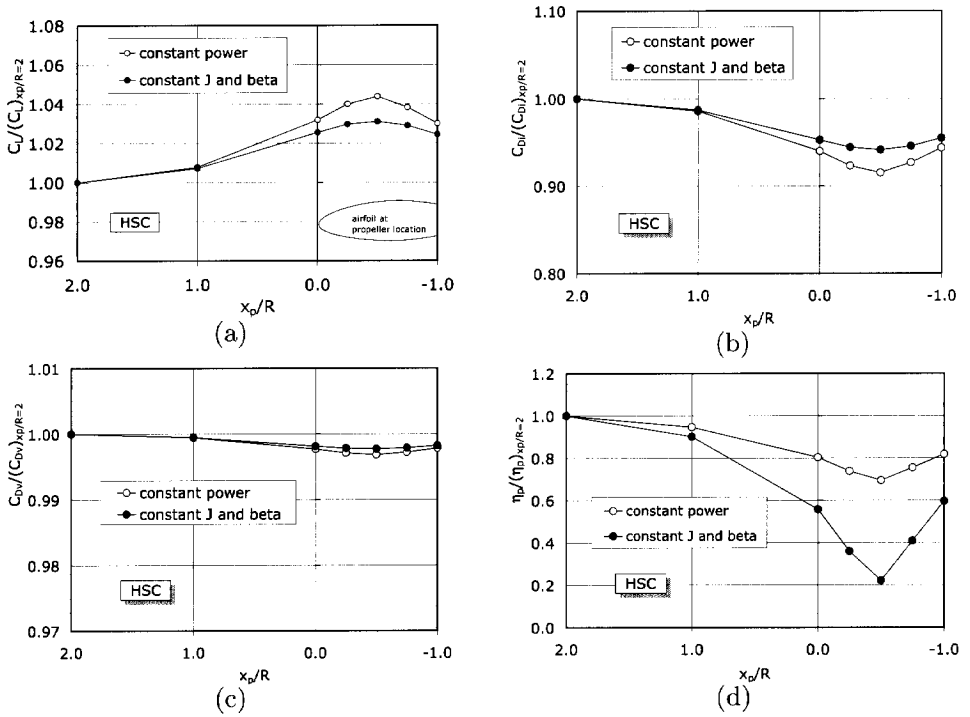
Figure 6.39: *Comparison between constant power and constant J (at given $\beta_{0.75R}$) for the OTW-configuration of Model50 expressed relative to $x_p/R = 2.0$; (a) wing lift coefficient ; (b) wing induced drag coefficient ; (c) wing profile drag coefficient ; (d) propulsive efficiency.*

characteristics are affected by the new propeller setting. Due to the stronger pro-
peller induced velocities the contraction of the slipstream increases which results in
higher lift lower drag and increased propulsive efficiency for the propeller position
above the wing. Especially the effect on η_p is noticeable. This is a direct result of
the increased propeller efficiency which leads to higher thrust for given shaft power.
Although the slipstream velocity components show higher values, the distribution is
still asymmetrical. This problem is the main cause for the reduction in the overall
propulsive efficiency for an OTW-layout for an twin-engined Fokker 50 like aircraft
configuration.

The discrepancy between the results of APROPOS and Model50, with respect to
the optimum propeller position for highest lift and lowest drag, are most likely caused
by the fact that in the VLM-calculation model the slipstream location is not modified
by the wing induced velocity field.

It should be noted that the analysis of the OTW-configuration was performed for
a value of $z_p/R = 1.15$, which is the position closest to the wing. However, due to
weaker wing effects on the propeller the propulsive efficiency increases with higher
values of z_p/R. Some results of this effect are presented in Fig. 6.40.
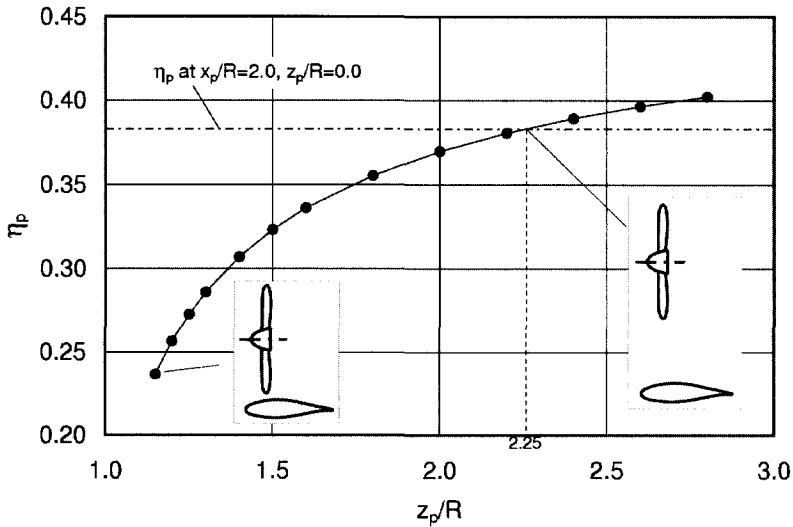
Figure 6.40: *The influence of the vertical propeller position, z_p/R, on the propul-
sive efficiency for the OTW-layout of Model50 ; $x_p/R = -0.5$; high
speed case.*

Apparently at $z_p/R = 2.25$ the value of η_p becomes equal to the one found for
the 'standard' layout of the propeller-wing configuration $(x_p/R = 2.0, z_p/R = 0.0)$

and higher value are reached beyond this z_p value. Nevertheless, problems from the structural and maintenance point of view will prevent the implementation of such a high OTW positioned propeller.

Although variation of the streamwise coordinate, x_p, for an OTW-layout has a strong influence on the noise radiation effects (shielding by the wing) and structural behaviour of the OTW-configuration the conclusions drawn by several researchers on the benefits for the performance in the sense of high propulsive efficiency in the cruise phase of the aircraft could not be founded. There is a certain benefit for the wing lift and drag but compared to the "original" tractor layout of Model50 ($z_p = 0$, $x_p/R = 2.0$) a considerable loss in η_p (34%!) is found for the high speed case. Unless new ways are found to reduce the loss in propeller efficiency the OTW-configuration does not seem attractive to be implemented for a typical twin-engined turboprop aircraft.

6.4 Panel method results

6.4.1 Introduction

The main disadvantage of the VLM method is the limited level of detail that is obtained. Typical characteristics that could be obtained with a potential flow code like the chordwise pressure distribution and the wake rollup to a certain extent determine the important phenomena that occur in the propeller-wing interactive flow.

To acquire additional detail the next step in complexity is the application of panel methods. As this approach is still used in the design process of propeller wing configurations some calculation results as well as the limitations of the method will be discussed hereafter.

The codes that were used during these investigations are PDAERO [55] and FASD [109]. PDAERO uses the slipstream envelope model as described in Chapter 3. For this so-called "full-interaction model" various references are available [56, 55]. In this case the effect of the aircraft structure on the velocity components induced by the propeller and the slipstream is not neglected.

FASD incorporates either the simple "add on" model in which the velocity and total pressure data inside the slipstream tube (see Appendix D) are either based on experimental data or calculated with he slipstream tube model (Appendix D). The data are extrapolated to the panel collocation points. Typical examples of this approach can be found in [110, 111, 112, 113, 114, 57, 54].

Although quite reasonable agreement with experimental results is obtained in most cases typical difficulties appear in the set-up of the calculation. The first problem is the limited number of panels that is generally used to prescribe the propeller disk and the trailing slipstream envelope. As a result of this the generated flow field represents the true situation only to a limited degree. Another problem is found in the way the

slipstream is positioned with respect to the wing. Since experiments show that strong deformations occur in the slipstream shape, any (arbitrary) user defined position of the slipstream (and its strength) may lead to erroneous velocity components at the wing.

Without going into the details of all relevant cases described in open literature a general conclusion may be drawn. Due to the limitations discussed so far an overestimation of the changes in the local wing lift due to the propeller effects is found. This leads both to deviations in the lift distribution and the integrated overall lift value. Subsequently errors in the induced drag arise.

Although the full interaction model (PDAERO) is the most sophisticated surface singularity model that is used for the calculation of the PROWIM model, there are clear limitations that affect the final results. The main contributors to errors will be treated shortly hereafter.

6.4.2   Propeller normal force

The propeller at a non-zero angle of attack generates a normal force in the plane of rotation. With the actuator disk model implemented in the panel code no resultant normal force will be found.

Since the propeller normal force , N_p, is not calculated as part of the final result care must be taken when comparing the predicted result with existing balance data.

For positive angles of attack the experimental results should produce somewhat higher lift values than the panel code. Yet, in practice both the calculated and the experimental value sometimes agree reasonably due to a known compensating error introduced by the lack of viscosity in the flow calculation. During the experiments the wing airfoils are effectively de-cambered by the boundary layer that develops along the wing surface. Hence the inviscid panel code produces higher lift values that partly compensate the error in the lift force due to the propeller normal force effects.

6.4.3   Propeller model and slipstream geometry

Since the actuator disk model is based on inviscid, incompressible theory, certain limitations with respect to the generated velocities occur. In the PDAERO model for example the effect of the propeller is included by prescribing a mean total enthalpy jump across the disk; the value of which is determined by the propeller operating conditions like T_c and J. The mean enthalpy jump, ΔH, across the actuator disk is determined by eq. 3.83 while the velocity jump properties are derived from eq. 3.66.

In a realistic propeller-wing interactive flow field the position of the slipstream and its shape vary strongly in the proximity of the wing. Although an approximate position may be selected by the user it is not practical to repeat such a procedure for all power conditions (T_c values) that are investigated. Hence a constant location and

form of the slipstream is selected for all flow conditions neglecting the shearing effect and the deformation (see Chapter 5) that are found during the experiments.

When the propeller is placed at an angle of attack, either due to the selection of the incidence angle of the thrust axis or due to the wing induced upwash field, the slipstream will continue downstream with an average position somewhere between the free stream direction and the thrust axis line. The free stream will tend to deflect the slipstream back in streamwise direction while the normal force generated by the propeller tends to do the opposite. In PDAERO (and most other panel codes) these effects are not modelled automatically.

A slipstream which runs parallel with the propeller axis, with a constant cross-sectional shape, seems to be the most practical layout of the slipstream boundary for most loading cases.

It should be noted that a serious limitation of the PDAERO panel code is the assumption of a uniform distribution of jump conditions on the propeller disk where in reality almost in every flow condition non-uniform distributions are found at the location of the propeller disk.

6.4.4   PDAERO calculations on PROWIM / APROPOS

The first analysis of the PROWIM and the APROPOS models was performed with the higher order panel method, PDAERO. In line with the assumptions and limitations used in this method the calculations are restricted to the incompressible case with undeformed wake shapes and uniform total enthalpy jumps across the propeller disk. The computational results will be compared to the experimental results that were discussed in Chapter 5.
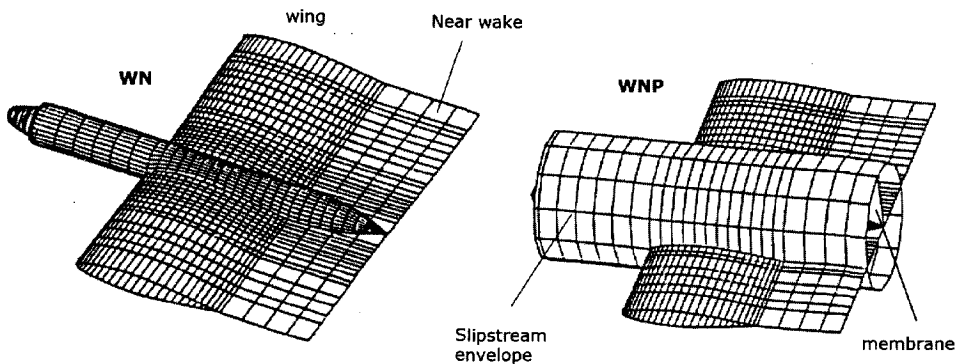
Figure 6.41: *Panel layout for the PROWIM model as used for the PDAERO calculations ; left: prop off ; right prop on.*

A typical layout of the panelling of the PROWIM model is presented in Fig. 6.41. The APROPOS model which has the same propeller and wing geometry but without the nacelle is set up in the same way.
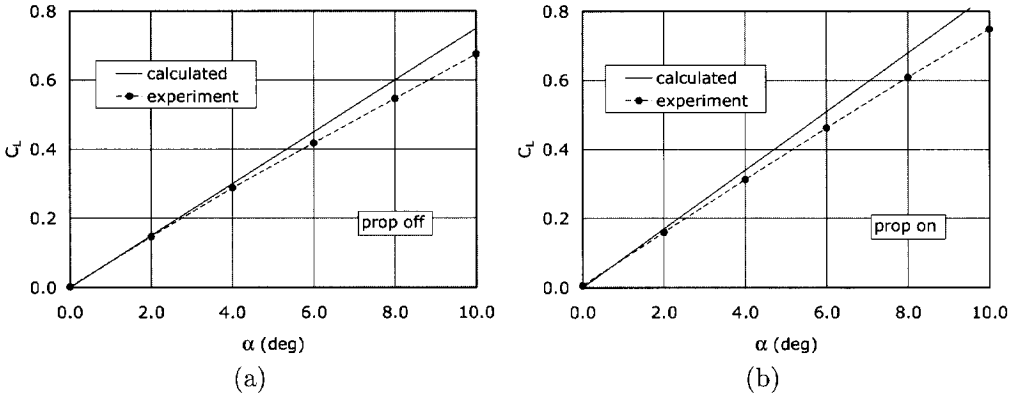
Figure 6.42: *Comparison of experimental and predicted (PDAERO) lift coeffi-
cient for PROWIM ; J = 0.85 ; (a) prop off ; (b) prop on.*

First of all the lift coefficients as calculated with the panel code are compared with experimental results from Chapter 5. In Fig. 6.42 the overall lift coefficient is depicted both for the propeller off and the propeller on configuration. The lift enhancement due to the propeller is clearly visible but a distinct difference in the lift curve slope exists between the experiments and the calculations.

The main cause for this discrepancy is the omission of the viscous effect in the panel code (no decambering effect exists). This reasoning is supported by the comparison of the lift distributions in Fig. 6.43a. In the propeller off case a fair agreement is only found if the model angle of attack is lowered around 0.4° compared to the experimental value. The true problem with the panel code becomes visible when the lift distributions for the powered models are compared (Fig. 6.43b and -c). The code fails to predict the changes in the local lift coefficient in the slipstream washed area due to the limitations imposed by the single slipstream tube with uniform loading. Especially the errors in the swirl velocity component play a major role in this respect. The code's inability to predict the secondary flow phenomena, like flow boundary layer thickening and small areas of flow separation that were found in the experiment, adds to the limited agreement with the experimental results. A noticeable effect occurs for the $\alpha = 4°$ case where the agreement is reasonable for the nacelle outboard side whereas the lift coefficient is strongly overpredicted for the nacelle inboard side.

This is also reflected in the comparison of the surface pressure distributions, pre-sented in Fig. 6.44. Since the local C_l not only depends on the propeller induced
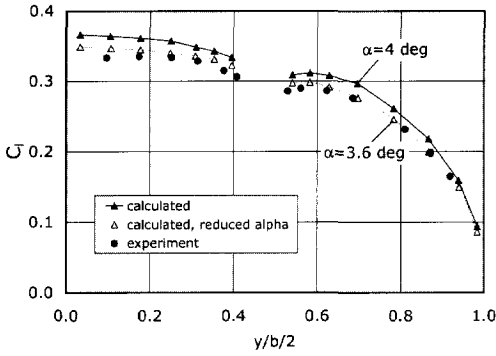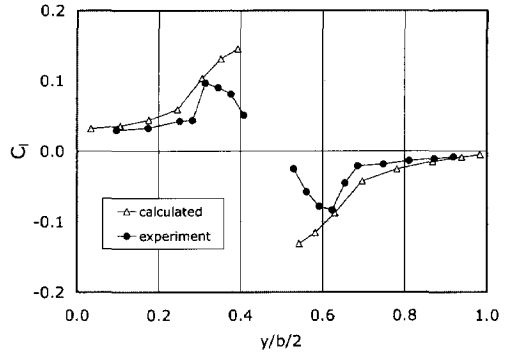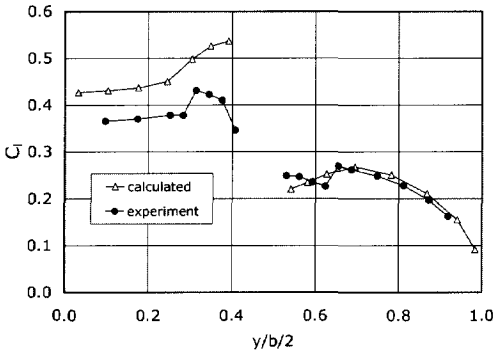
Figure 6.43: *Lift distribution of PROWIM from the PDAERO calculation compared to experimental values ; $J = 0.85$; (a) prop off, $\alpha = 0°$; (b) prop oon, $\alpha = 0°$; (c) prop on $\alpha = 4°$.*
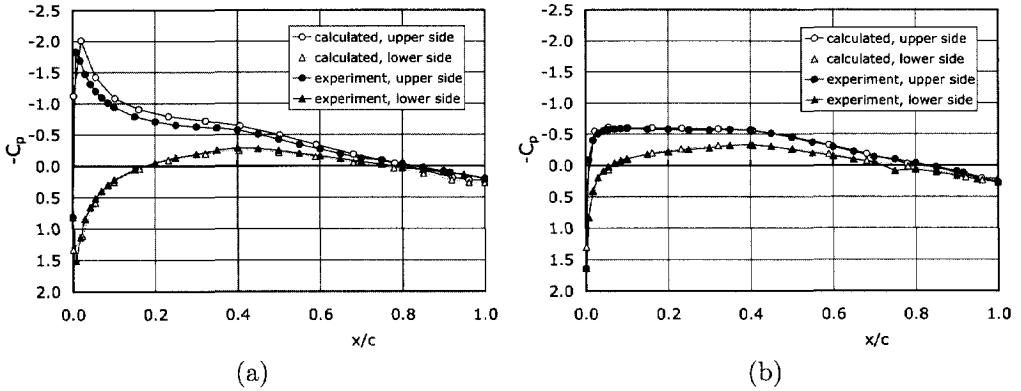
Figure 6.44: *PROWIM surface pressure distribution inside the slipstream washed area ; (a) $y/b/2 = 0.35$; (b) $y/b/2 = 0.60$; $\alpha = 4°$, $J = 0.85$.*

inflow field but is affected by the vorticity distribution of the trailing vortex sheet and its deformed geometry as well, it is expected that implementation of only a partly relaxed wake shape in the code is the cause for this error in the predicted local lift.

The limited effect of the nacelle in the discrepancy between the experimental and the predicted characteristics can be anticipated by calculations of the APROPOS model. In this case the wing is combined with a (free flying) actuator disk model which results in much simpler panel layout.

Fig. 6.45 shows a comparison of the lift coefficient for three different spanwise propeller locations. The trend is more or less the same as found for PROWIM. The induced drag of the model, depicted in Fig. 6.46, shows a fair agreement when the C_{D_i} data are compared at equal lift coefficients. It should be noted that the comparison is performed only at a rather low thrust coefficient of $T'_c = 0.31$. Even in this case the slipstream model of PDAERO fails to produce acceptable distributions of the axial and tangential velocity components, as can be seen in Fig. 6.47. Consequently, the errors in the calculations are expected to increase for the higher power loadings.

Although the trends in the panel calculation results seem to predict the propeller effects on the wing (and not vice versa) reasonably, it is impossible to derive definite conclusions about guidelines to improve the propeller-wing layout based on these data since the form of the induced drag distribution in spanwise direction is wrong. Hence it is difficult to predict performance improvements for propeller-wing layouts with the suggested panel model that incorporates a single slipstream envelope.

$$y_p/(b/2) = 0.28 \qquad y_p/(b/2) = 0.47 \qquad y_p/(b/2) = 0.78$$
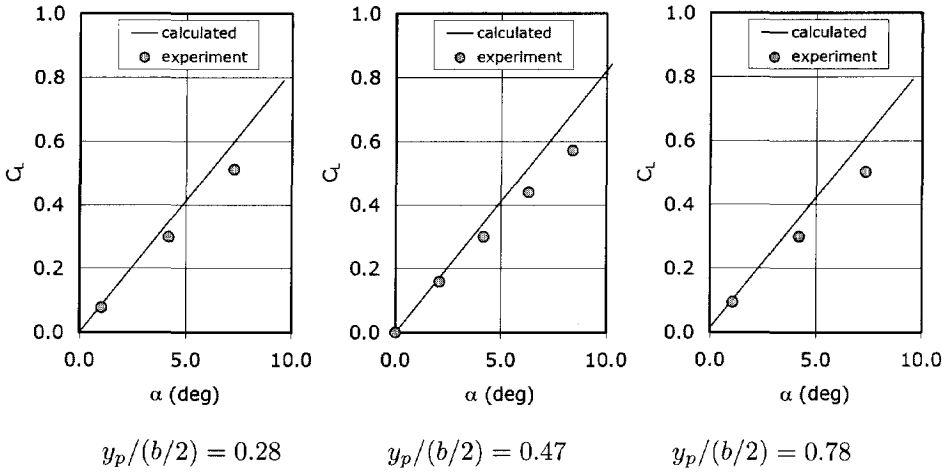
Figure 6.45: *Comparison of calculated (PDEAERO) and experimental lift co-efficients of APROPOS for three spanwise propeller positions ; $T_c' = 0.31, J = 0.92$.*

$$y_p/(b/2) = 0.28 \qquad y_p/(b/2) = 0.47 \qquad y_p/(b/2) = 0.78$$
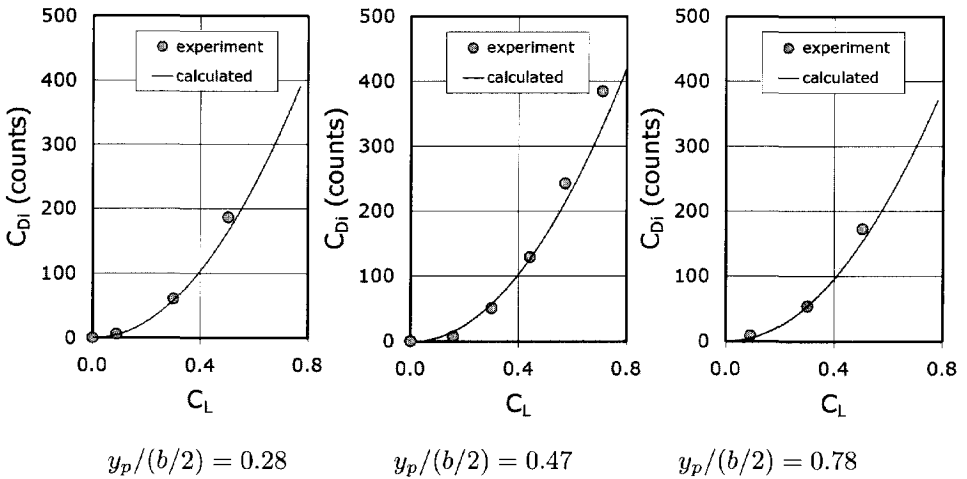
Figure 6.46: *Comparison of calculated (PDAERO) and experimental induced drag coefficients of APROPOS for three spanwise propeller positions ; $T_c' = 0.31, J = 0.92$.*
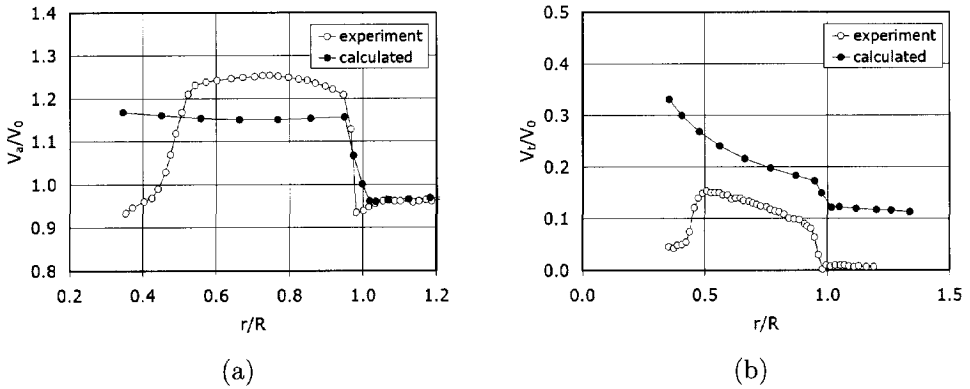
Figure 6.47: *Typical example of axial (a) and tangential (b) velocity profiles at $\psi = 90°$ and $0.57R$ behind the propeller used in the PDAERO analysis of APROPOS ; $\alpha = 4.2°$, $J = 0.85$.*

6.4.5   FASD calculations on APROPOS and Fokker 50

To derive some understanding of the typical differences between the PDAERO model and the simpler FASD 'add-on' model, additional panel calculations were performed on the same APROPOS model and a typical Fokker 50 model [115].

The slipstream velocity data needed for the inclusion into the panel model were first acquired from experimental 5-hole probe data taken behind the propeller (chapter 5).

From the experiments the total velocity vector as a function of the spatial coordinate, was available as well as the energy increase in the slipstream, $\Delta E = 1 + \Delta P_t / q_\infty$. These values were extrapolated to the collocation points of the panels in the slipstream immersed part of the wing [115].

For comparison purposes the analytical procedure of the vortex tube model (Appendix D) was applied as well. In this case the velocity components are directly found at the positions of the collocation points as they form a part of the slipstream routine input.

The panel models of APROPOS and the simplified F50 model are depicted in Fig. 6.48 and Fig. 6.49 respectively.

6.4.6   Apropos results

Since the slipstream position and its geometry is not known a priori, a location with respect to the wing must be selected by the user. In this case two layouts are chosen:
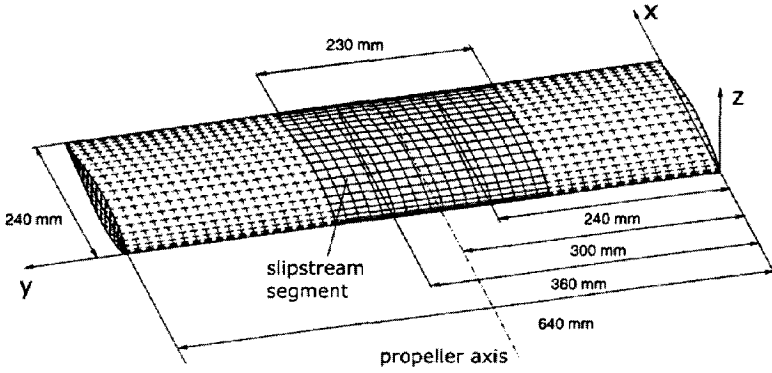
Figure 6.48: *APROPOS panel model used in the FASD panel method analysis.*
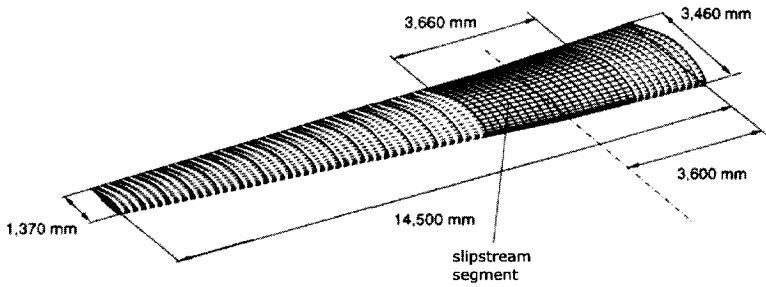
Figure 6.49: *Fokker 50 panel wing model without nacelle used in the FASD panel analysis.*

the slipstream fixed in the free-stream direction (denoted 'flow fixed') and the slip-
stream completely deflected in the direction of the propeller axis (denoted 'wing fixed').
The APROPOS model was calculated with two different slipstream approaches: ex-
perimental data and predicted data (Blade Element Method).
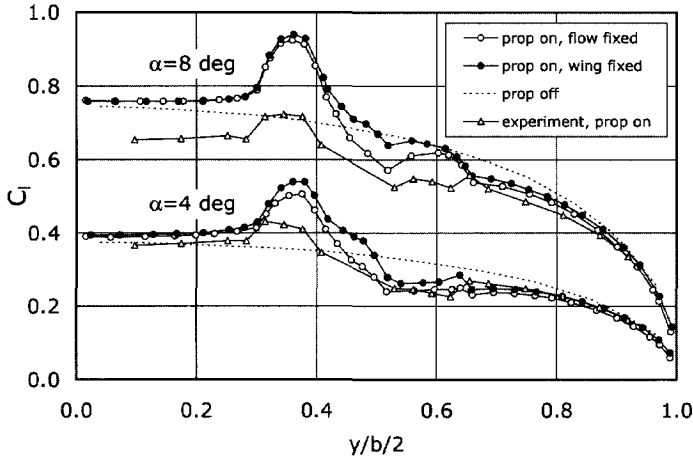
Figure 6.50: *Lift distributions of the APROPOS wing for two slipstream layouts
('flow fixed' and 'wing fixed') ; $T_c = 0.133$; The experimental slip-
stream is generated from 5hole probe data obtained directly behind
the propeller.*

Typical lift distributions that were found with these methods are compared to
the experimental values, in Fig. 6.50. As was found with the single tube model
in PDAERO, the lift of the wing is strongly overpredicted. This is mainly due to
the absence of the decambering effect of the boundary layer. Another remarkable
difference between the experimental and the calculated results is the stronger effect
of the swirl velocity in the predictions. This difference can be attributed to the lack
of swirl recovery, a phenomenon that is always present in the real viscous flow.

With respect to the two layouts of the slipstream apparently both fail to predict the
experimental results. To find out whether errors are introduced by the extrapolation
technique used to determine the velocities at the collocation points the effect of the
slipstream definition was checked. The circulation strength that is needed in the
slipstream "tube-model" was found by matching both the propeller induced axial
and tangential velocities as closely as possible to the experimental values that were
found directly behind the propeller. Fig. 6.51 shows that, although differences occur
between the two models, they match closely enough to rule out significant influence
on the prediction errors found in Fig. 6.50.
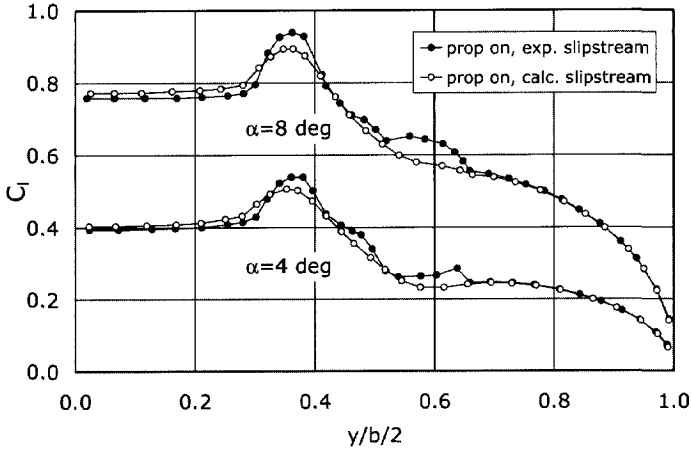
Figure 6.51: *Comparison of APROPOS lift distributions found with the experimental slipstream and the slipstream "tube-model".*

When the results of the FASD add-on code are compared to the PDAERO results it becomes clear that incorporating a known slipstream velocity field (for example from experimental data of an uninstalled propeller) produces a more realistic form of the lift distribution. However, the absolute accuracy of the two approaches is limited.

Being aware of the known limitations, the FASD code was used for additional analysis of the propeller interaction effects. In this case the effect of the vertical and the horizontal position of the propeller with respect to the wing was investigated for the APROPOS and the F50 model, as sketched in Fig. 6.52.

First of all the wing lift and the wing drag of APROPOS for variable z_p/R are presented in Fig. 6.52. C_L rises with increasing z_p until a local maximum is found at about $z_p/R = -0.2$. A second, higher, local maximum is reached at $z_p/R = 0.6$. The values for C_D exhibit two local maxima at about $z_p/R = -0.4$ and $z_p/R = 0.6$, whereas a local minimum is found at $z_p/R = 0.2$.

Although the absolute values for the aerodynamic coefficients predicted by FASD differ from those of the experiments (Chapter 5), important similarities of the general behaviour are found. The lift rises with increasing z_p/R position to a maximum which is found at approximately $z_p/R = 0.6$, for all cases. The tendency to a local minimum is found in the experiments as well due to the average decrease in the dynamic pressure in the slipstream for a propeller positioned directly in front of the wing ("donut-effect").

Even while the panel code only calculates the induced drag component compared to the full inviscid plus viscous drag in the experiment, the behaviour of the drag

(a)   (b)
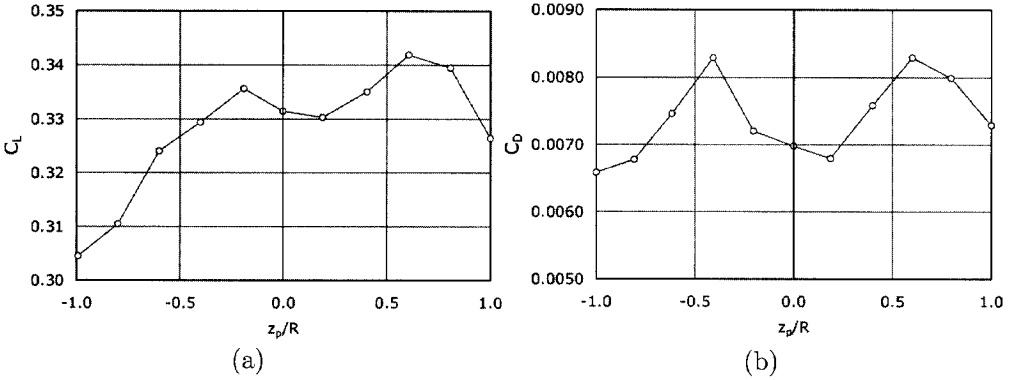
Figure 6.52: *Effect of the propeller vertical position on the lift and drag coefficient of APROPOS(propeller in front of the wing); slipstream calculated from the slipstream "tube-model".*

coefficients is similar. The difference between the local minima and maxima are stronger in the calculated results due to the fact that the swirl recovery is the major driving force for the effects on the wing drag.

(a)   (b)
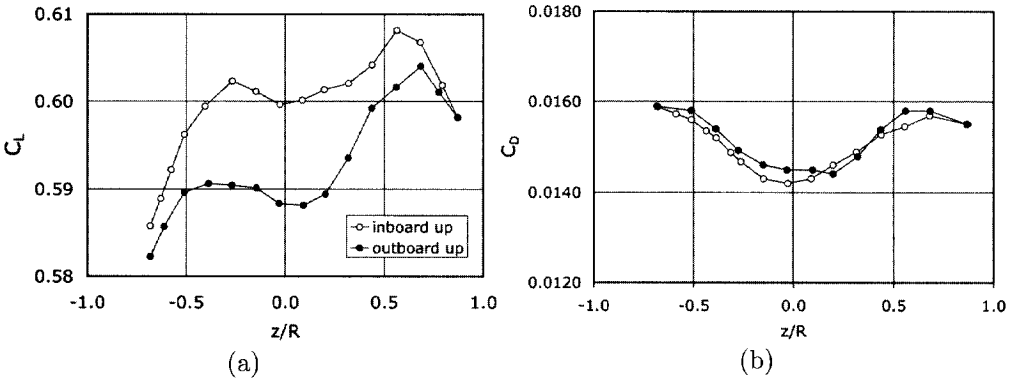
Figure 6.53: *Effect of the vertical propeller position on the lift and drag coefficient for the Fokker 50 case at low thrust (inboard up and outboard up rotating propeller).*

To verify whether the conclusions obtained with the APROPOS model could be translated to a more realistic case the Fokker 50 wing was investigated as well. As shown in Fig. 6.53, the behaviour of the lift and the drag coefficient with vertical

propeller position is comparable to the APROPOS model. Looking at the scales in the figure it should be noted again that the effect of changing z_p/R is relatively small for the low thrust case (typical for cruise). The advantage of inboard up rotation on the lift and the drag, as was already described in previous chapters, are confirmed by the data presented in Fig. 6.53: for inboard up rotation a higher lift coefficient and a lower (induced) drag coefficient are obtained.

6.4.7   Over the wing arrangement

The last check on the capabilities of the FASD panel code with respect to the prediction of propeller wing interference effects was performed by looking again at the OTW arrangement.

For the APROPOS model the propeller was moved in the direction of the trailing edge with the propeller axis at $z/R = \frac{4}{3}$ above the wing. The calculations were performed with slipstream characteristics provided by slipstream model that was designed to incorporate the contraction of the slipstream [115].
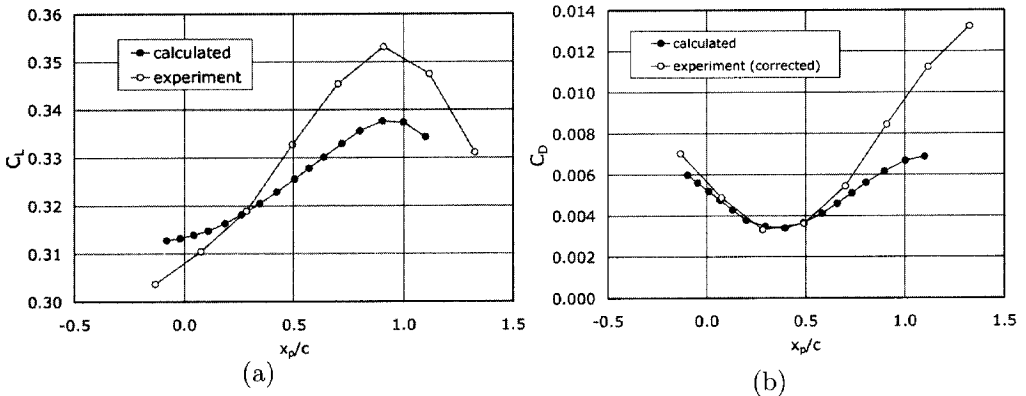
Figure 6.54: *Effect of the propeller streamwise position on the lift and the drag coefficient of the APROPOS wing ; $T_c = 0.133$.*

Fig. 6.54 shows the results of the FASD calculations for a propeller positioned in OTW arrangement above the APROPOS wing. For comparison purposes the experimental values that were discussed in Chapter 5, are presented as well. The value of C_L rises with the increased streamwise position above the wing until a maximum is reached at about $x_p/c = 0.9$. This trend is found in the experiments as well. The main reason for the discrepancy in the local values of C_L is attributed to the fact that in the experiment a quite bulky nacelle was present that induces a distorted flow field (mainly axial velocity increase) that may lead to stronger effects on the lift

coefficient. The calculated drag coefficient is compared to an experimental value that was corrected for the profile drag (obtained from a separate *XFOIL* [116] calculation) since the panel code delivers only the effect on the induced drag. As can be seen, a fair agreement is found with the local minimum at $x/c = 0.4$ in both cases. Apparently the panel code FASD, which uses the "ad-on slipstream", performs reasonably in the OTW case since the level of distortion of the slipstream in the real flow case is limited with the slipstream passing over the wing. Hence the approximation of an axis-symmetrical slipstream envelope as used in the slipstream tube-model ('sliptube') is acceptable in this case.

(a)   (b)
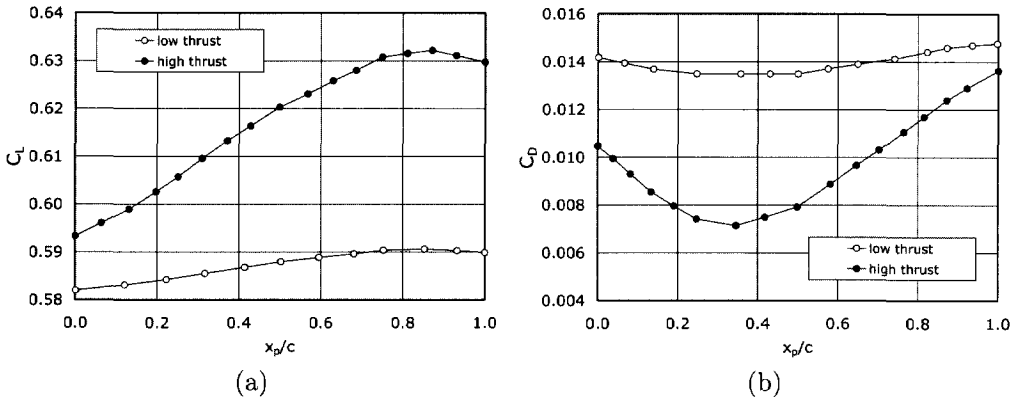
Figure 6.55: *Effect of the propeller streamwise position, x/c, on the lift and drag coefficient of the Fokker 50 model ; low and high thrust case for cruise angle of attack.*

The influence of the streamwise position on the simplified Fokker 50 model (Fig. 6.55) was investigated as well. In this case the cruise condition was calculated for a high and a low thrust case, as discussed in Chapter 5. The results, shown in Fig. 6.55, indicate that the same effects as found for APROPOS layout emerge. This means that from the lift and drag point of view the OTW shows benefits for a propeller wing combination that is typical for modern turbo prop aircraft.

6.5   Navier-Stokes calculations

6.5.1   Introduction

To circumvent the problem of explicitly prescribing the slipstream position and its development in space ENS calculations were performed and compared to the experimental data of Chapter 5. Results of ENS calculations on typical propeller-wing

models, found in open literature, have shown that application of this approach can predict both the overall aerodynamic configuration characteristics as well as the details of the surrounding flow.

The successful use of the multiblock Euler- and Navier Stokes codes for propeller-wing interference effects has previously been demonstrated [117, 101, 118, 119]. An interesting analysis of the steady and the unsteady case of uninstalled propellers as well as a propeller-wing configuration is presented in [120]. The paper describes two distinct approaches to the general aerodynamic analysis of propeller flow fields. A three-dimensional compressible Euler code and a general purpose 3D CFD codes (Navier-Stokes solver) were used to compare predicted propeller and wing pressure distributions with experimental data. The overall conclusion is that both codes produce results that compare well with data obtained from experiments. However, as with many descriptions presented in open literature the discussion in [120] is restricted to the presentation of the basic phenomena that occur. No supplementary comment is given on the specific aspects of the interaction between the propeller and the wing and the different flow characteristics that influence the performance of the configuration.

In subsequent sections the calculations that were performed on PROWIM and an OTW arrangement will be discussed and comparison with experimental data will be presented. Although the application of the Euler equations lead to reasonable agreement with experimental data, the full (Reynolds averaged) Navier-Stokes equations were applied here to acquire the detailed effects of the propeller on the viscous drag.

As the calculation results depend on aspects like grid set-up and grid density, turbulence modelling etc. [63], some information is provided on the various choices that were made before the final results are presented.

6.5.2   The numerical model

The numerical model was derived directly from the experimental PROWIM model, although some adaptations were needed to arrive at an acceptable number of grid cells pertaining the most important flow features.

First of all a simplification of the spinner region was introduced (elliptical nose) in order to make the topology simpler in that area. Secondly the two total head probes directly behind the propeller that were used during some of the windtunnel tests and their support are absent. It is obvious that substituting the front part of the nacelle (including the spinner) with an elliptical nose produces some changes in the flow field; the effects are expected to influence the drag, but they are supposed to play a negligible role on the wing pressure distribution that is mainly determined by the swirl velocity distribution further away from the nacelle.

Although the absence of the two total head probes and the support clearly affects

the flow field data in the wake, the effect on the lift distribution is assumed to be negligible.

An overview of the surface layout of the PROWIM model as used in the ENS-calculations is presented in Fig. 6.56 and Fig. 6.57.
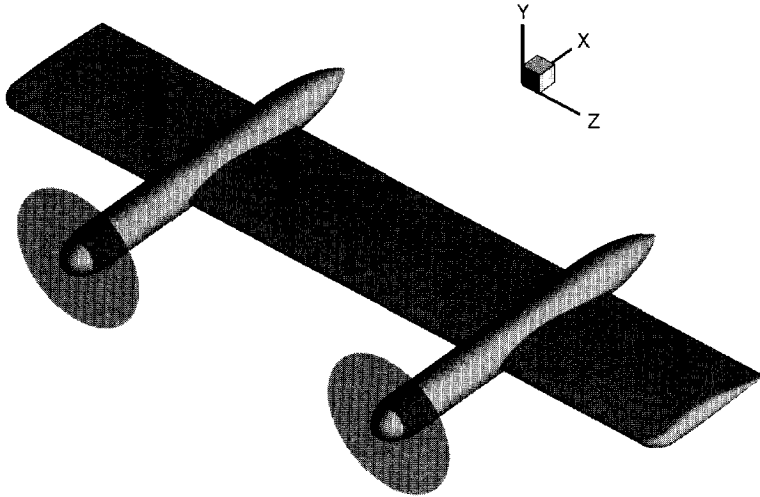
Figure 6.56: *Layout out full 3D wing model based on PROWIM dimensions*

6.5.3   Computational domain and boundary conditions

The computational domain is defined by the surfaces of the model and an external box, as shown in Fig. 6.58.

To define the front and the back plane, the chord length was taken as the reference length. In these terms the front face of the box is placed three chords upstream of the spinner, while the rear face is placed six chords downstream the trailing edge of wing. The streamwise extent of the flow domain is limited compared to suggestions presented in open literature [63, 121], to fit the model in the available computer memory. Separate domain size studies in 2D flow showed that acceptable results can be expected, though. In lateral direction the size is the same as that of the windtunnel test section. A simplification is introduced with respect to the corners: the octagonal shape is reduced to a rectangular one, which is expected to have negligible influence at the location of the wing. The distance between them corresponds to the width of the test section.

The dimensions of the domain thus defined are supposed to be large enough to
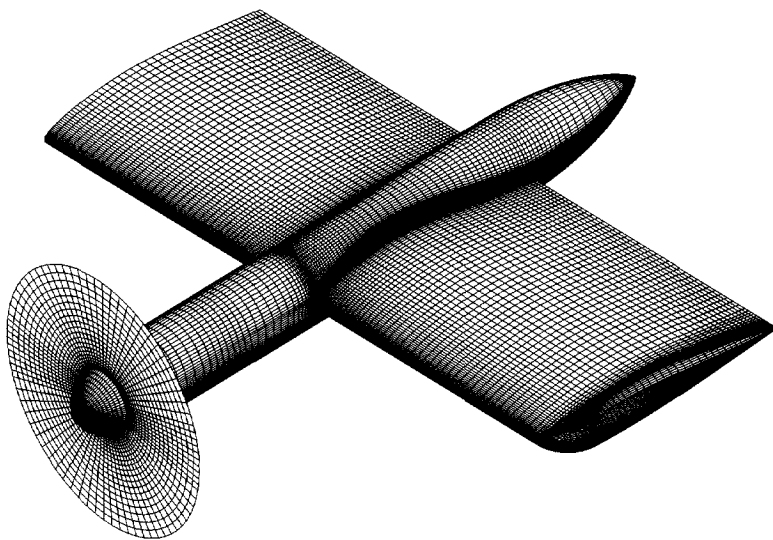
Figure 6.57: *Model surface grid distribution on wing, nacelle and actuator disk (finest level)*

prevent serious errors due to the prescription of the boundary conditions close to the model.

With the data known from the windtunnel experiment the velocity is described at the inlet plane (denoted 'velocity inlet' with $V = 50\,m/s$) while at the outlet plane an undisturbed static pressure is prescribed (denoted 'pressure outlet').

Velocity inlet boundary condition requires, besides the velocity itself, input values for k and ε if one of the $k - \varepsilon$ models is chosen. The turbulent kinetic energy and its dissipation ratio are also required when Reynolds Stress Modeling (RSM) is selected. Again known data of the windtunnel experiments were used for this purpose. The viscosity ratio, μ_t/μ was fixed to 1 in order to simulate an incoming flow that, even if calculated as being fully turbulent, was as close as possible to the conditions of a laminar flow.

Pressure outlet boundary conditions require the specification of a gauge pressure and values for k and ε, as well.

Symmetry boundary conditions assume a zero flux of all quantities across the boundary (being the normal velocity, as well as the normal gradient of other flow variables) equal to zero.

The propeller was modeled using an actuator disk approach (see Chapter 4). The effect of the propeller is obtained by specifying a pressure rise in terms of total pressure
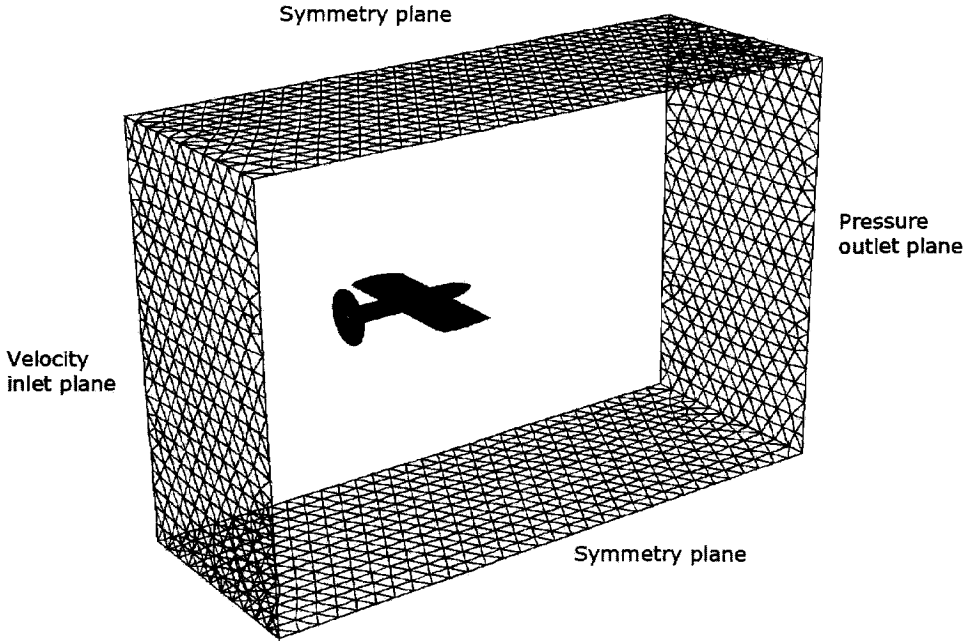
Figure 6.58: *Part of the computational domain (side walls not visualized) for the $\alpha = 0°$ case.*

jump, swirl velocity and radial velocity.

On the surfaces of the model the 'no slip condition' is maintained and near wall treatments for the computation of the boundary layer have been defined separately.

6.5.4   Near wall treatment

It is well known that the turbulent boundary layer can be subdivided into an inner and a outer region. The first is characterized by the so-called law of the wall while the second, denoted wake region, depends on the pressure distribution [122].

The inner region can be divided into three subregions: the viscous sub layer ($0 \leq y^+ \leq \approx 5$), the log-layer ($30 \leq y^+ \leq 350$) and the buffer layer (in between). In our case non equilibrium wall functions have been selected as the standard near-wall treatment for all the calculations involving turbulence models. This approach partly accounts for effects of pressure gradients giving better accuracy in all those cases in which the flow departs from equilibrium conditions. For more detailed information

see [63] and [21].

6.5.5 Operating conditions, settings, configurations

It is useful to remark that values for the pressure are given in terms of gauge pressure. The reference value for the static pressure is always 101325 Pa.

Table 6.8: *Operating conditions and flow setting for the NS-calculations.*

General flow settings					
Static Press [Pa]	ρg [kg/m^3]	μ [kg/(ms)]	T [k]	Re	M
101325	1.225	$1.79 \cdot 10^{-5}$	288.16	$8.2 \cdot 10^5$	0.15

Velocity inlet plane		
Velocity [m/s]	Tu [%]	μ_t/μ
50	0.06	1

Pressure outlet plane		
Gauge press. [Pa]	Tu [%]	μ_t/μ
0	0.06	1

Operating conditions maintained and the input values for the boundary conditions in all the calculations as shown in Table 6.8 have been given so as to recreate the same conditions of the experiments in the windtunnel.

The velocity magnitude of the incoming flow was fixed at 50 m/s, but specified in terms of x-y components. For calculations in which the angle of attack was different from zero this is a simpler procedure than rotating the model in the tunnel. The latter would have required the creation of a new grid for different angles of attack. As a consequence two symmetry surfaces, the upper and the lower one, were turned into velocity inlets.

The gauge static pressure was set to zero at pressure outlet, since the influence of the model on pressure in that location is supposed to be negligible.

The other parameters (turbulence intensity and turbulent viscosity ratio) were set in order to create a laminar-like flow at the velocity inlet. Even if these characteristics are certainly different at the boundary outlet, the same values were kept at the pressure outlet to create no discontinuities in the boundary conditions: it must be kept in mind that for angles of attack different from zero boundary inlets and outlets have edges in common. Moreover, no detrimental effects have been noticed with respect to this choice.

6.5.6   The grid

The need to have a good resolution near the surfaces of the model and in the slip-stream of the propeller, and the necessity to save computer resources limiting the total number of cells, led to the selection of a hybrid grid as the best choice for the current investigation.

Hexahedral cells that were used close to the model surface are generated in a structured multiblock approach which led to a complicated topology (74 blocks for the complete grid). In the outer part of the flow domain tetrahedral cells were used as the required accuracy is limited in this region. Fig. 6.59 shows a part of the topology solutions adopted (Grid-3).
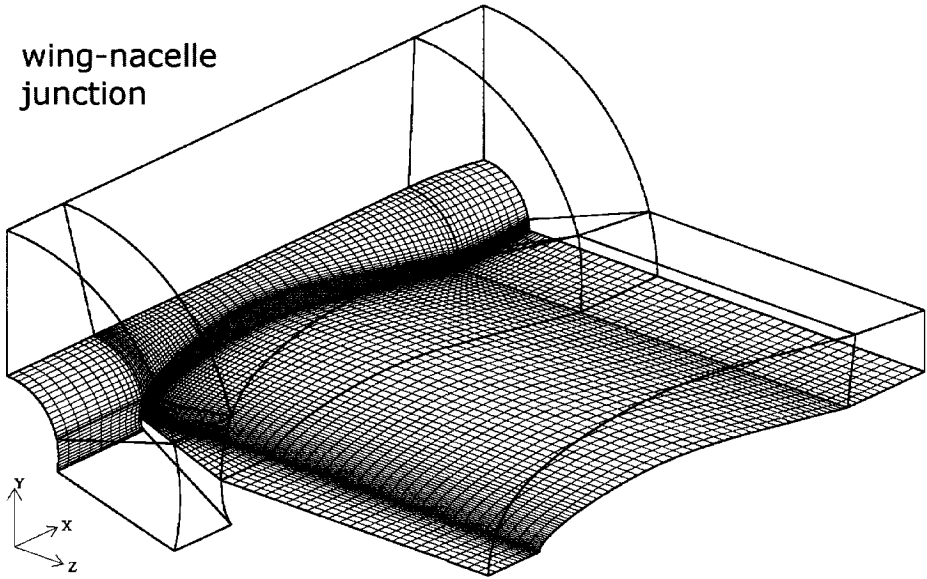
Figure 6.59: *Part of the block topology of PROWIM showing the wing-nacelle junction.*

6.5.7   Configurations tested

Calculations were run on three different grids, for two different angles of attack, 0° and 4°, with the propeller active and removed, using two turbulence models (Realizable k-ε and RSM). Besides this, one inviscid flow case was tested.

The course grid, denoted Grid-1, was created with approximately 140,000 cells. Moreover, a simplification was introduced: the wing-tip was cut off and a symmetry surface was attached at the wing on that side. This grid appeared to be useful, as a first approach, to see if the hybrid grid solution (hexahedral cells close to the model and tetrahedral cells in the remaining part), adopted to discretize the computational domain worked properly. Additionally, useful information was obtained with respect to convergence and residual history in relation to the roughness of the grid and the use of turbulence models.

The final grid, denoted Grid-3, contained approximately 1 million cells. Here the wing tip was added and the numerical domain extended to its final shape. It was used to compare numerical data to experimental data. An intermediate (Grid-2) of apprimately 500,000 cells was used for additional calculations.

Small changes, in terms of local grid refinement, were made on Grid-3 in some simulations where more accuracy was required in particular regions. In one, local refinement on both sides of the propeller was used in order to obtain greater accuracy in estimation of the thrust. In the other, local refinement was used in the wing-tip vortex-core region to see which improvements could be obtained in calculating the sharp total-pressure-loss and high-vorticity peaks in this area.

6.5.8   Selection of the turbulence model

Two turbulence models were used in the current investigation: "Realizable k-ε" (RKE) and a "Reynolds stress model" (RSM). The former uses a Boussinesq approximation to model turbulence and two additional transport equations (for the turbulence kinetic energy and the turbulent dissipation rate) that have to be solved. The latter directly solves the transport equations for the Reynolds stresses together with an equation for the dissipation rate, leading to seven additional equations in 3D [123].

The arguments that led to the choice of these two models are briefly discussed.

Since even the most refined grid (Grid-3), could not have the very high resolution recommended for an accurate computation of the boundary layer, some tests on a simple 2D configuration were performed. The purpose of these tests was to understand which turbulence model was the most robust, in relation with a relatively coarse grid spacing in the boundary layer area.

The configuration chosen for this purpose is the PROWIM airfoil. A 2-dimensional grid with the same hybrid structure as that of the three-dimensional one was created to avoid any undesirable effects related with the topology. Through successive refinements three 2-dimensional models (denoted Grid-1-2D, Grid-2-2D and Grid-3-2D) were obtained with a grid structure similar to that of a vertical cross section of the 3-dimensional grids.

The results thus obtained were then compared with the ones from a 2D panel code combined with integral boundary layer equations, *XFOIL* [100]

Table 6.9: *Results of 2D calculations on the intermediate (Grid-2-2D) and the final grid (Grid-3-2D) with different turbulence models.*

GRID-2-2D						
Turb. model	α[deg]	C_l	C_d	p_{t_s} [Pa]	Flow	p_{t_∞} [Pa]
Inviscid	4	NA	NA	1532	sss	1527
SA	0	0.000	0.011	1524	no sep.	1534
	4	0.423	0.012	1524	s	1534
RNG k-ε	0	0.000	0.009	1523	no sep.	1534
	4	-	-	-	nnn	-
Real. k-ε	0	0.000	0.013	1525	no sep.	1534
	4	0.425	0.015	1524	no sep.	1534
RSM	0	0.000	0.011	1525	no sep.	1534
	4	0.433	0.014	1523	no sep.	1534
GRID-3-2D						
Turb. model	α[deg]	C_l	C_d	P_{t_s} [Pa]	Vel. vectors	p_{t_∞} [Pa]
SA	0	0.000	0.012	1540	no sep.	1534
	4	0.423	0.014	1539	no sep.	1534
RNG k-ε	0	-	-	-	sss	-
	4	-	-	-	sss	-
Real. k-ε	0	0.000	0.013	1540	no sep.	1534
	4	0.427	0.015	1539	no sep.	1534
RSM	0	0.000	0.0076	1540	no sep.	1534
	4	0.450	0.0092	1536	no sep.	1534

SA=Spalart Almaras model, RNG=Renormalization Group, Real.=Realizable, RSM=Reynolds Stress Model

The results obtained are shown in Table 6.9. For comparison, the reference values for C_l and C_d obtained from *XFOIL* are:

$$\alpha = 0° \left\{ \begin{array}{l} C_l = 0.000 \\ C_d = 0.0065 \end{array} \right. \text{ and } \alpha = 4° \left\{ \begin{array}{l} C_l = 0.446 \\ C_d = 0.0071 \end{array} \right.$$

In Table 6.9, the values of C_L, C_D, static pressure in the stagnation point, p_{t_s} and reference total pressure (p_{t_∞}, taken at the velocity inlet) are summarized for different configurations. The symbols in the column "Flow" refer to the behavior of the flow at the trailing edge: "no sep." means that the flow behaves as expected (i.e. no separation in accordance with windtunnel tests and *XFOIL* calculations), "s" means that a very small recirculation zone is found, whereas "ss" and "sss" denotes a bigger and very large recirculation zone respectively. As can be seen both the Realizable $k-\varepsilon$ model and the RSM model lead to acceptable values of the lift coefficient compared to the experimental data.

From calculations with *XFOIL* it is known that the boundary layer remains laminar for a large part of the airfoil, as a consequence drag calculations using turbulence models will always be affected by a great error since transition is not accounted for. As expected, this leads to an overestimation of the drag coefficient.

From the preliminary calculations it was concluded that the realizable $k - \varepsilon$ and the RSM would produce the best results in relation with a relatively coarse grid. Hence, these models were chosen for the simulations on the three dimensional model.

6.5.9   Actuator disk boundary conditions

With the actuator disk approach the propeller action is averaged in spatial sense and is specified in terms of jumps in the total pressure , the tangential velocity and the radial velocity. To specify the jumps experimental data [58] were used and an external *fortran* routine was created to produce the boundary conditions at the disk. In the experiments, values for the total pressure, the tangential velocity and the radial velocity were measured in two cross sections, inboard and outboard side, at a survey station placed at $0.266D$ ($63mm$) behind the propeller.

These data were then approximated using polynomial functions in order to obtain analytical expressions for the variables profiles; the functions thus obtained were then easily interpolated with the *fortran* program to obtain the complete distribution at the location of the propeller.

Typical examples of data derived from experimental measurements and polynomial functions are shown and compared in Fig. 6.60. Both the total pressure rise over the propeller disk and the tangential (swirl) velocity distribution are depicted.

Due to the complexity of the flow in the vicinity of the nacelle the shape functions show a small deviation from the experimental data. This is not important since the major propeller wing interference effects are initiated at a more outboard position (i.e. large values of r/R).

The effect of the angle of attack on the performance of the blades is clearly visible
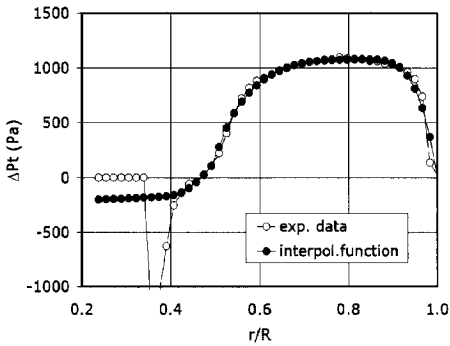
(a) outboard
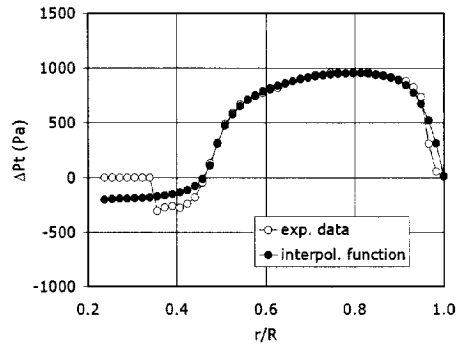
(b) inboard
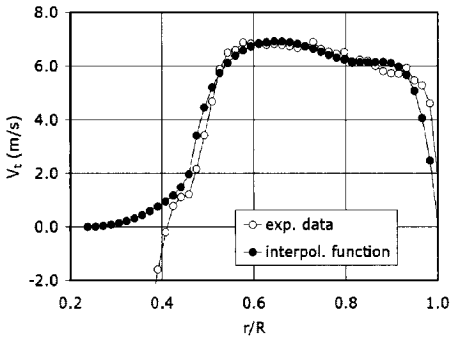
(c) outboard
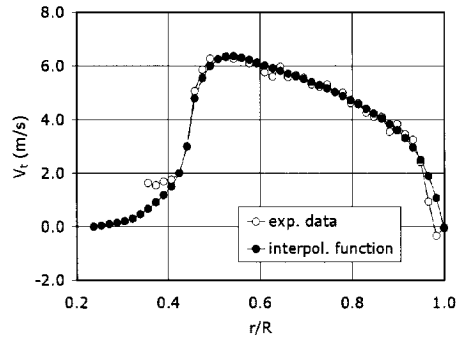
(d) inboard

Figure 6.60: *Example of the total pressure rise (upper figures) and the tangential velocity profile (lower figures) for the experimental slipstream and interpolating function used for the boundary layer profile ; $\alpha = 4°$; left: nacelle outboard side , right: nacelle inboard side.*

as the outboard side benefits from an increased local incidence and so generates a higher pressure jump, whereas on the inboard upgoing blade the pressure rise is lower, hence the effect is the opposite. Since the survey station used in the measurements was physically limited by the presence of the nacelle, the interpolating polynomials had to be extended to the spinner surface.

Once analytical functions were available, values all over the disk surface were determined through linear interpolation.

With respect to the propeller boundary conditions, as taken from the experiments, two important remarks should be made.

1) The swirl velocity distribution near the hub proved to be difficult to model. Without having available experimental data in this region it was decided to extend the swirl velocity distribution curves with a constant value.

2) It is probable that the contribution of the measured axial velocity component to the swirl velocity (in case on non-zero angle of attack) has been overestimated. This consideration originates from the fact that the flow accelerates strongly (in axial direction) in the $63mm$ that separate the propeller from the survey station in which data were acquired.

6.5.10   Results

Hereafter some of the NS-calculation results will be discussed. Particular attention will be paid to Grid-3 because the higher refinement level assures greater accuracy and because it models the complete configuration including the wing tip, it allows comparisons with windtunnel experiments.

Some considerations on accuracy and convergence, in relation to the different grids, are discussed where results from *XFOIL* calculations and 2D NS-calculations are included for comparison.

With respect to the turbulence modelling, the differences found between the RKE model and the RSM are briefly discussed.

Pressure distributions, lift and drag coefficients and wake qualitative investigation for the various configurations tested are presented and compared with experimental data. Results from windtunnel experiments include both balance and surface pressure measurements by Philipsen [124] and calculations based on wake surveys from Rentema [58] and Veldhuis [125].

Besides this the flow field behavior behind the propeller at different survey stations is discussed in detail; its evolution and the influence of the geometry are investigated and the most important aspects in relation to the accuracy of the propeller boundary conditions are highlighted. Finally a few conclusions on the effects of radial velocity and the rotation direction of the propeller are drawn.

Convergence and accuracy   In all cases a smooth behavior of the residuals was found. No convergence problems occurred with the two turbulence models used; even

on Grid-1, in which grid density is very low, the solution converged and was stable. Of course this provides no information on the accuracy of the solution; since in that grid there were no cells in the boundary layer, near wall treatment (wall functions) could easily lead to errors. These errors are reflected first of all in the calculation of the boundary layer. However, it was not the purpose of these calculations to investigate the detailed behavior of the boundary layer. Much more important for the current work, was to determine the accuracy of pressure distributions and of the general behavior of the flow field. This has been achieved using data from windtunnel experiments, 2D *FLUENT* calculations and *XFOIL*.

In Fig. 6.61 a comparison is made between Grid-1 and Grid-3 for the propeller off case. Because the two grids differ for the presence of the wing tip, pressure distribution comparisons were limited to the wing inboard side, since here the tip flow influence is negligible.

Moreover, for the wing cross section at the root, also the results from *XFOIL* and from 2D *FLUENT* calculations were used. In this particular zone a symmetry surface was defined as boundary condition, leading to a behavior of the flow very close to a two-dimensional one.

For the c_p distribution at the root (i.e. at the intersection between the wing and the symmetry surface) the flow can be considered quasi-two dimensional. The program *XFOIL* should be considered an excellent reference for these comparisons since it is specially suited for 2D airfoil calculations including the effects of viscosity and moderate compressibility [100]. Two-dimensional *FLUENT* calculations are included to see how much the solution changes when grid refinement is used and possible 3D-effects of the wing are removed.

For $\alpha = 0°$, the differences between the various grids are small. It is important to notice that a transition bubble is found with *XFOIL*; this phenomenon is not predicted by the NS-code since turbulent models calculate a turbulent flow starting from the leading edge. The laminar separation was also found during the windtunnel experiments through oil visualization at approximately 52% and reattachment at 66% of the chord [124] whereas *XFOIL* computed transition at 65%.

For $\alpha = 4°$, three dimensional effects produced by the nacelle and by the tip influence the flow field in the zone inboard of the nacelle. Hence the agreement between the 2D NS-calculation and the *XFOIL* is expected to be superior to the 3D NS-data.

Comparing the different curves it becomes clear that increasing the angle of attack from $0°$ to $4°$, differences between Grid-1 and Grid-3 occur due to the thickening of the boundary layer which is not captured well enough by Grid-1. The 2D-calculation with the NS-code proves that the finest grid leads to a very close agreement with the *XFOIL* data. Therefore this grid density of Grid-3 is expected to be acceptable for the 3-dimensional calculations of PROWIM.

It is interesting to observe how the transition bubble moves forward on the upper side with increasing angle of attack. As a consequence the prediction accuracy of the
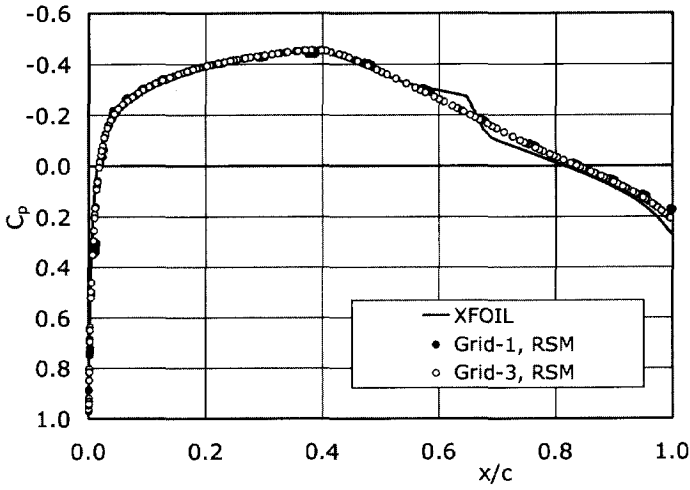
(a) $\alpha = 0°$
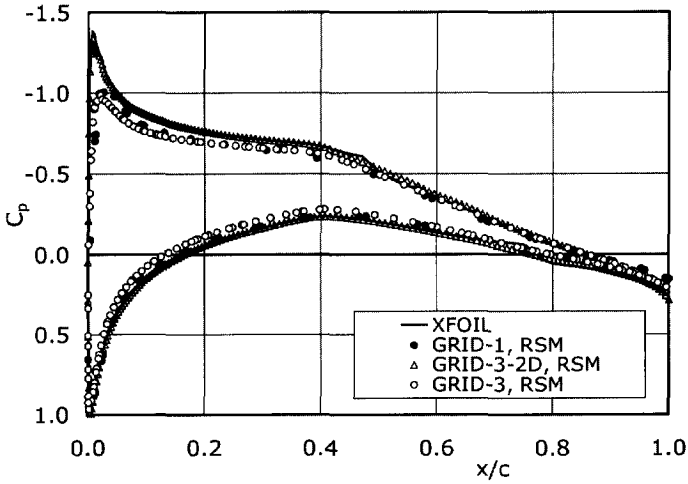
(b) $\alpha = 4°$

Figure 6.61: *Comparison of chordwise pressure distributions for various grid layouts ; propeller off*

drag coefficient of the NS-code compared to the experimental data is expected to be limited.

Comparison between the RKE model and the RSM In this paragraph differences noticed in the behavior of the two turbulence models are briefly discussed.

Regarding the pressure distribution on the surface of the model the differences are very small everywhere except in the stagnation point on the spinner and in the peak values of static pressure that can be found at the intersection between the wing and the nacelle for $\alpha = 4°$, here RSM calculated values are about $50\,Pa$ higher than those from the RKE model. The stagnation point on the spinner deserves more attention because here the two models behave differently. The RKE model produced a significant error in computing the static pressure as can be seen in Table 6.10.

Table 6.10: *Influence of selection of the turbulence model on the static pressure in the stagnation point at the spinner nose of PROWIM.*

Case	α[deg]	Static pressure [Pa]		Total pressure Ref. [Pa]
		RKE	RSM	
Propeller off	0	1970	1524	1530
	4	1776	1522	1530
Propeller on	0	1852	1516	1520
	4	1743	1516	1520

In case of the RKE model, vector plots in the vicinity of the stagnation point showed erroneous velocity vectors with a small outward component where the vectors for the RSM were perfectly aligned with the surface.

It is difficult to say what led to such a difference on the spinner (also because stagnation points all along the wing were caught well by both the models).

Another noticeable difference between RKE model and RSM was found during the investigation of the wake. First of all it should be remembered that a small modification of the trailing edge of the nacelle was introduced when creating the grid: the sharp corner was cut off and a small facet created to avoid grid collapsing problems. This facet is responsible for local increased vorticity and total pressure loss peaks. Almost in all the test cases (except for $\alpha = 0°$ propeller off) the RSM seems to strengthen these effects, but it is hard to say which model performs better since the experimental data refer to a configuration in which the cut was not present.

Fig. 6.62 shows some examples in terms of total pressure loss comparing the two turbulence models. Minor differences are found in the main area of interest, the nacelle and the slipstream washed area. The tip vortex is not included in these figures as differences showed to be very small in that zone.

prop off

prop on
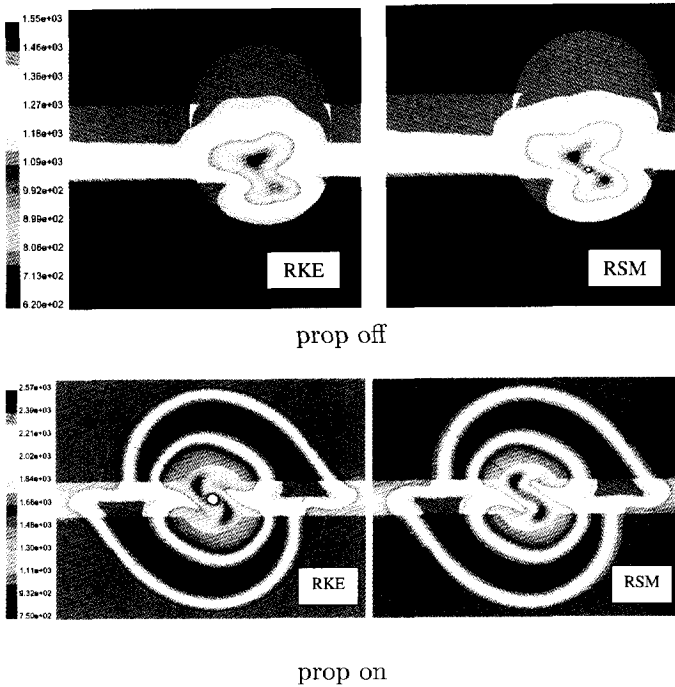
Figure 6.62: *Example of total pressure distribution ([Pa]) at 1 chord length behind the wing found with the RKE model (left) and the RSM (right).*

Finally, values for C_L, C_D are summarized in 6.11: differences in the calculated lift and the drag coefficient are small with a slight tendency of the RSM to produce higher values.

Table 6.11: *Comparison of the lift and the drag coefficients calculated with the RKE model and the RSM.*

		propeller off		propeller on	
		$\alpha = 0°$	$\alpha = 4°$	$\alpha = 0°$	$\alpha = 4°$
C_D	RKE	0.0169	0.0230	-0.0929	-0.0857
	RSM	0.017	0.0231	-0.0926	-0.0842
C_L	RKE	0.000	0.2909	0.0040	0.3167
	RSM	0.000	0.3052	0.0043	0.3192

6.5.11   Final NS-results

Propeller-off   The final results of the NS-calculations on PROWIM refer to the finest grid (Grid-3). In Fig. 6.63 the predicted static pressure distribution on the surface of the model is depicted. The pressure gradients in spanwise direction are moderate except for the wing-nacelle juncture region. At that location a typical pattern is obtained that demonstrates a small loss of lift. Although the pressure distribution changes dramatically (large differences between wing upper and lower side) when the angle of attack is increased from $\alpha = 0°$ to $4°$, still a rather small spanwise gradient is maintained. This is important with respect to the changes that the slipstream exhibits when it strikes the wing.

Although some disturbances are found at the wing tip (because its peculiar shape), it is expected that the wing tip flow pattern has only minor influence on the propeller-wing interactive flow at the more inboard located position.

From an integration of the surface distributions of the pressure and the shear forces the lift and the drag coefficients were obtained.

In Table 6.12 the values for C_L and C_D are collected and compared to the results from the windtunnel experiments reported in Chapter 4 (the error is expressed based on differences with the balance measurement data).

Apparently a fair agreement is obtained regarding the lift coefficient while the estimation of the drag coefficient is affected by a greater error that increases when the angle of attack is set from $0°$ to $4°$. The predicted lift coefficient shows a close agreement with the experiments. Its non-zero value for $\alpha = 0°$ that is due to the asymmetry introduced by the presence of the wing-tip, is computed satisfactory. For
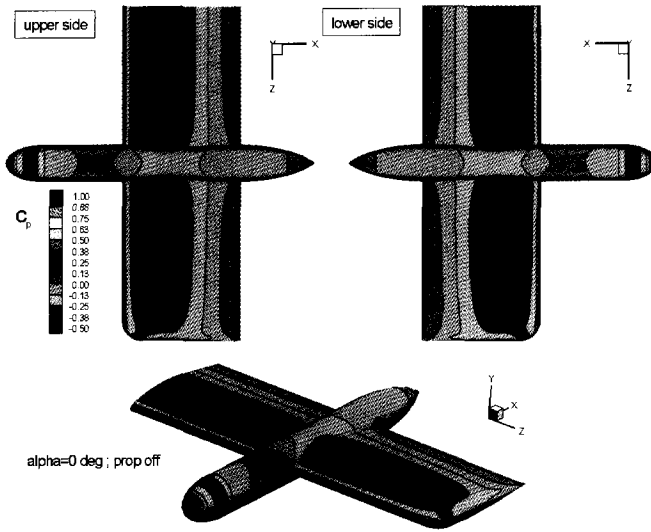
(a) $\alpha = 0°$
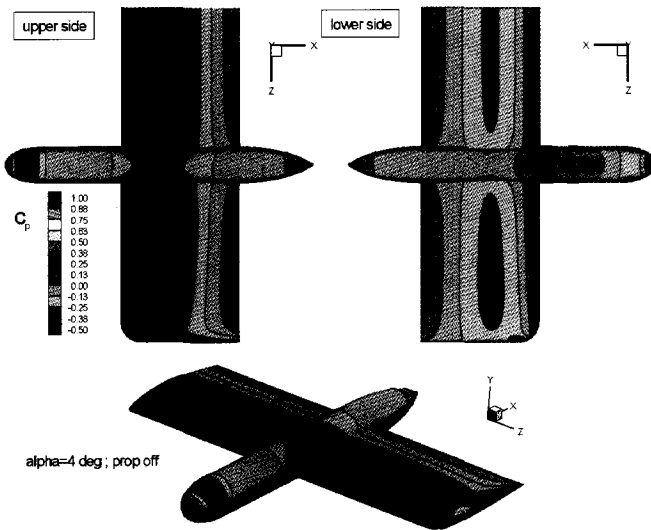
(b) $\alpha = 4°$

Figure 6.63: *Static surface pressure distribution on PROWIM; propeller off.*

Table 6.12: *Comparison of numerical results obtained from Grid-3 with quantitative wake measurements (QWA) and balance measurements. All data are corrected for the propeller thrust force contribution*

		propeller off		propeller on	
		$\alpha = 0°$	$\alpha = 4°$	$\alpha = 0°$	$\alpha = 4°$
C_D	RKE	0.0169	0.023	-0.0929	-0.0857
	RSM	0.017	0.0231	-0.0926	-0.0842
	QWA	-	0.0192	-0.1016	-0.0989
	Balance data	0.015	0.0198	-0.0986	-0.0916
C_L	RKE	0	0.2909	0.004	0.3167
	RSM	0	0.3052	0.0043	0.3192
	QWA	-	0.2917	0.0099	0.3302
	Balance data	0	0.288	0.0055	0.3135

$\alpha = 4°$ the results ($C_{L_{propoff}} = 0.291$, $C_{L_{propon}} = 0.317$) from RKE model are surprisingly close to the experimental one ($C_{L_{propoff}} = 0.288$, $C_{L_{propon}} = 0.314$).

As expected, the drag coefficient is affected by a greater error. This has to be ascribed mainly to the fact that the wing boundary layer is calculated as being turbulent, while flow visualization [124] showed a large area in which the flow is laminar (no artificial transition was applied during the experiments). Yet, it can be noticed that error in the drag coefficient becomes smaller when the propeller is active. This can be explained from the fact that the area on the model surface in which the flow is laminar becomes smaller because the flow in the slipstream of the propeller is fully turbulent. As a result of this the flow field computed using a turbulence model becomes more similar to the real one and the error introduced by the viscous contribution of the C_D decreases.

When comparing the results it should be kept in mind that the symmetry surface, that models the reflection plate at the wing root, changes the physics of the flow in that zone. As a result of this, higher C_L values and lower C_D values would be expected from the numerical model. Because of the lack of experimental pressure data close to the reflection plate it is difficult to quantify these effects, but a closer look at the wing root region in Fig. 5.60 shows that the effect on the total lift coefficient is probably quite small.

Note that all the values reported in Table 6.12 for the propeller-on configuration are corrected for the contribution of the thrust force. In order to obtain these thrust values as accurately as possible; a first level of local refinement on both surfaces of

the fan was performed. Results thus obtained were then compared (Table 6.13) with the one from the BEM-analysis (prop1b).

Table 6.13: *Thrust of the PROWIM propeller calculated with the NS-code and the Blade Element Method (prop1b) ; $V = 50\,m/s$; $RPS = 249\,Hz$; $J = 0.85$.*

Case	Thrust [N]	
	$\alpha = 0°$	$\alpha = 4°$
RKE	24.81	24.82
RKE (propeller local refinement)	26.07	25.97
RSM	24.80	24.79
BEM (*prop1b*)	26.56	-

The results of both calculation techniques show a very close agreement. There are no appreciable differences in thrust estimation between the two turbulence models and the local refinement provides a considerable improvement. Hence, thrust results from the configuration "RKE (propeller local refinement)" were used to calculate C_D values (and C_L when $\alpha = 4°$) in all the "propeller-on" cases reported in Table 6.12.

Table 6.14: *Viscous and pressure contribution to the drag coefficient for the various calculations performed on PROWIM.*

Case	Turbulence model	α [°]	$C_{D_{visc}}$	$C_{D_{press}}$
Propeller off	RKE	0	0.01114	0.00575
	RSM	0	0.01122	0.00580
	RKE	4	0.01085	0.01219
	RSM	4	0.01025	0.01281
Propeller on	RKE	0	0.01187	0.00611
	RSM	0	0.01207	0.00617
	RKE	4	0.01163	0.01289
	RSM	4	0.01133	0.01467

In Table 6.14 the viscous and the pressure contribution to the drag coefficient are reported separately, which shows the importance of the viscous contribution to the total drag. With the propeller slipstream known to influence the viscous part considerably the relevance of performing viscous Navier-Stokes-calculations rather than Euler-calculations becomes inevitable for a final design calculation.

To get an idea of the prediction capability of the code some flow field related properties were visualized. Since the propeller slipstream has significant impact on the vortical flow field in the model area washed by the slipstream, the development of capturing of vorticity components is important.

Fig. 6.64 shows a contour plot of the axial vorticity for the model without running propeller. The junction between the nacelle and the wing produces secondary flow phenomena as a result of the nacelle boundary running into the high pressure area at the wing leading edge. This interaction leads to a double vortex system that is nicely captured by the code, indicating that the grid density is high enough to prevent premature diffusion of important flow parameters like total pressure and vorticity.

plane at $x/c = 0.10$ plane at $x/c = 2.0$
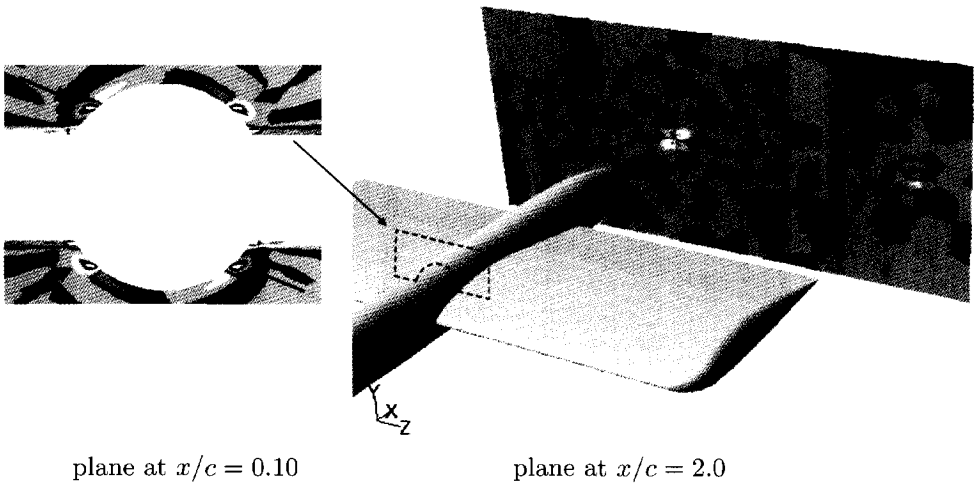
Figure 6.64: *Contours of axial vorticity showing the double vortex pairs that is generated by the wing-nacelle juncture ; prop off ; $\alpha = 0°$.*

Another indicator of an good behavior of the numerical model is shown by the flow field path lines combined with the total pressure loss in the wake, an example of which is presented in Fig. 6.65.

Two regions of interest are shown: the nacelle region and the wing-tip. The nacelle wake and the tip-vortex are both caught by the numerical analysis.

The wake behavior was investigated through the visualization of the total pressure and the axial vorticity, which enabled direct comparison with the wake survey measurements discussed in Chapter 5.

The contour plots of the total pressure are given in terms of total pressure loss coefficient defined as:

$$\Delta C_{p_t} = \frac{p_t - p_{t_0}}{\frac{1}{2}\rho U_0^2} + 1 \tag{6.2}$$
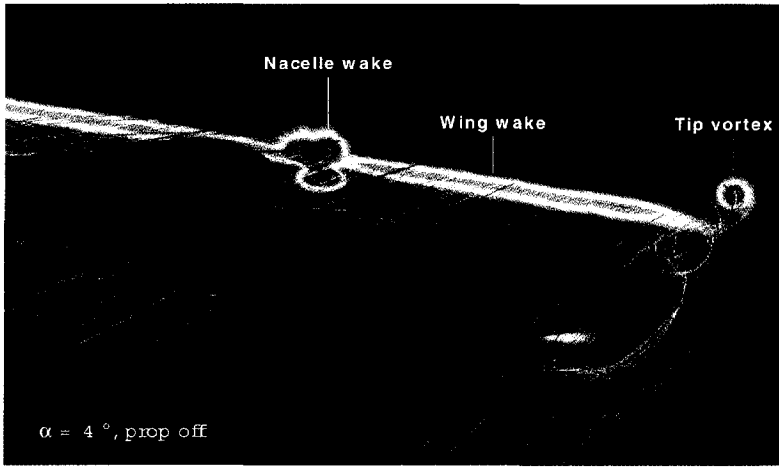
Figure 6.65: *Combined flow path lines and contours of total pressure loss behind showing the wake and the tip vortex structure ; $\alpha = 4°$; prop off.*

where p_{t_0} and U_0 are the reference values for the total pressure and the velocity respectively, defined at the inlet boundary inlet .

The vorticity is plotted in normalized form analogue to the convention used for the experimental data:

$$\tilde{\xi} = \frac{b/2}{U_0}\xi \tag{6.3}$$

where $b/2$ is the model semi span $(0.64m)$.

Fig. 6.66 and Fig. 6.67 show the wake of PROWIM for two different angles of attack (propeller off) combined with data from the windtunnel investigation.

Qualitatively the flow field calculated with the NS-code shows a good agreement with the experimental data. At an angle of attack of $0°$ the two high total pressure loss spots, coming from the upper and lower surface of the nacelle, and the horse shoe vortices, originated by the wing-nacelle connection, are well resolved (Fig. 6.66a).

As the angle of attack increases, differences between NS-calculations and the experimental data become more prominent. It should be remembered in this respect that small modifications of the trailing edge of the nacelle were introduced when creating the calculation domain and the total pressure probes behind the propeller were not incorporated in the calculations. Typical differences are found in the contour plots of the axial vorticity, as presented in Fig. 6.67. For $\alpha = 0°$ a good agreement is found with respect to the vorticity distribution behind the nacelle but for $\alpha = 4°$ the horse shoe vortices become harder to distinguish (Fig. 6.67b) since their relative strength is low compared to the vorticity sheet produced by the wing.
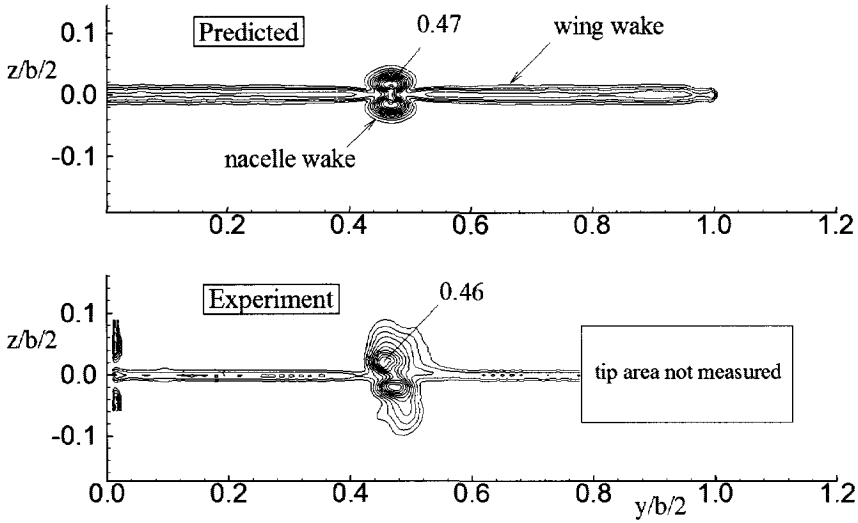
(a) $\alpha = 0°$
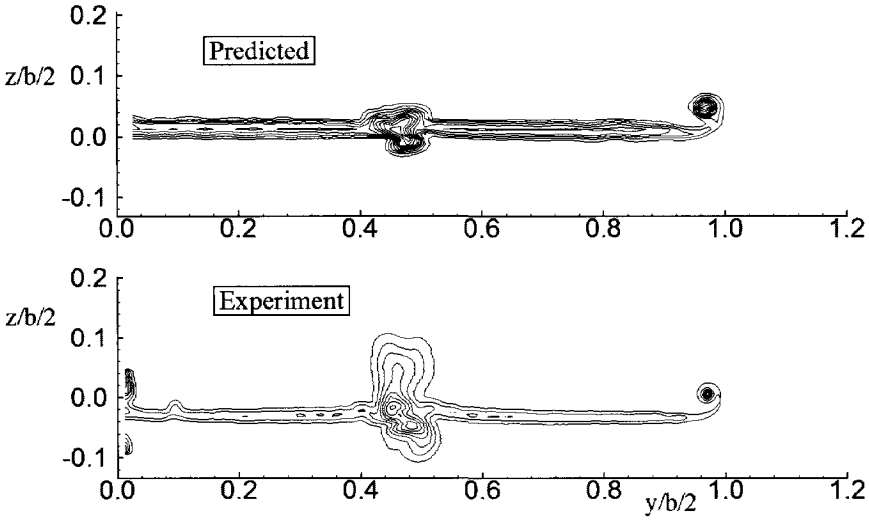
(b) $\alpha = 4°$

Figure 6.66: *Contour lines of constant total pressure coefficient, prop off ; (a)*
$\alpha = 0°$, (b) $\alpha = 4°$.
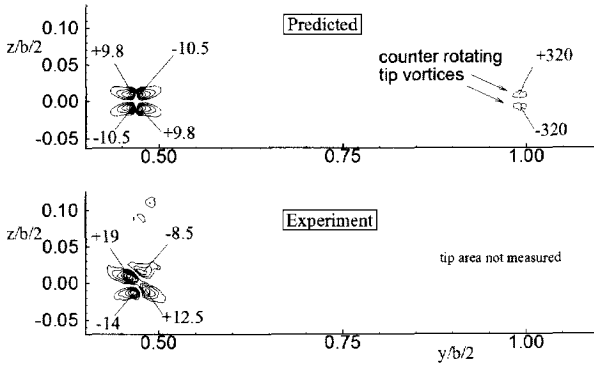
(a) $\alpha = 0°$
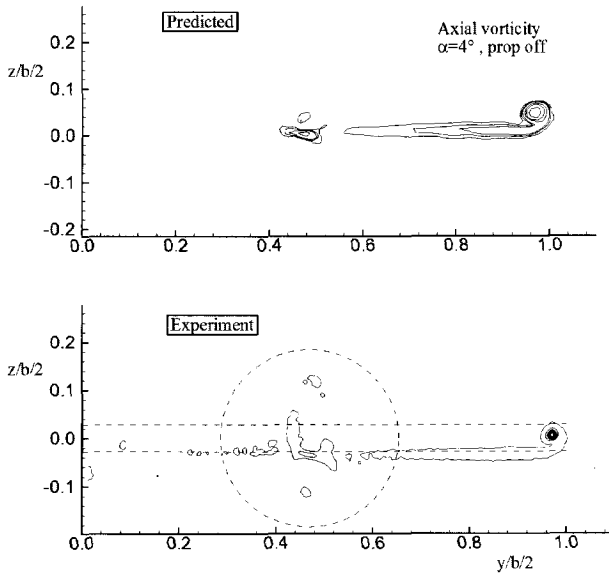
(b) $\alpha = 4°$

Figure 6.67: *Contour lines of constant axial vorticity, (a) $\alpha = 0°$ and (b) $\alpha = 4°$; prop off.*

Although the tip vortex is represented quite well, at least in qualitative sense, the peak value of the axial vorticity differs from the one found in the experiments. However, it should be remarked that the tip vortex has a very sharp peak in the core compared to the distribution of the various parameters in the remaining part of the flow domain. A local refinement level in the wing tip zone was performed but this did not lead to significant changes in the surface pressure distribution and the lift and drag forces acting on the model.

Propeller-on case   The results for the propeller on configuration show the expected strong effect of the swirl velocity component in the slipstream. As expected, a dramatic change in the total pressure distribution is found as well, leading to a very complex flow pattern.

First of the static pressure distribution over the model is depicted in Fig. 6.68 for $\alpha = 0°$ and $4°$.

The combined effect of the changes in the local angle of attack due to swirl and the total pressure rise in the slipstream washed area is clearly visible. The changes are especially visible in Fig. 6.68a for $\alpha = 0°$ (as for both angles of attack the same contour levels were chosen).

The local pressure distribution in the slipstream washed area is mainly determined by the development of the dynamic pressure in the slipstream, and the swirl distribution. As expected from the actuator disk theory, the mean value of the dynamic pressure rises in x-direction and a deformation takes place as sketched in Fig. 6.69 for $\alpha = 0°$.

In Fig. 6.70 a comparison between the experimental pressure distribution and predicted one is presented for the $\alpha = 4°$ case, for two spanwise positions inside the slipstream. Despite the boundary layer modelling restrictions in the NS-code, the agreement is good.

As can be seen in Fig. 6.71 the total pressure rise in the slipstream and its deformation are nicely predicted by the NS-code.

Some problems, however, arise at the upper side of the calculated slipstream envelope as can be noticed in Fig. 6.71b. At this location the total pressure distribution shows increased numerical diffusion due to the slipstream entering a part of the calculation domain where bigger cells are used. A clear indication of this problem can also be found in Fig. 6.72 where a surface of constant value of the total pressure is depicted. Clearly the total pressure is diminished at the slipstream upper side and at some distance behind the model (again due to the coarser grid in that region). Nevertheless, this effect is not expected to influence the propeller wing interactive flow field significantly.

The decay of the vorticity between the propeller position and the wake survey plane (at 1 chord length behind the wing trailing edge) is limited, as can be seen in the axial vorticity plots of Fig. 6.73 where distinct boundaries are visible at 1 chord

(a) $\alpha = 0°$

(b) $\alpha = 4°$
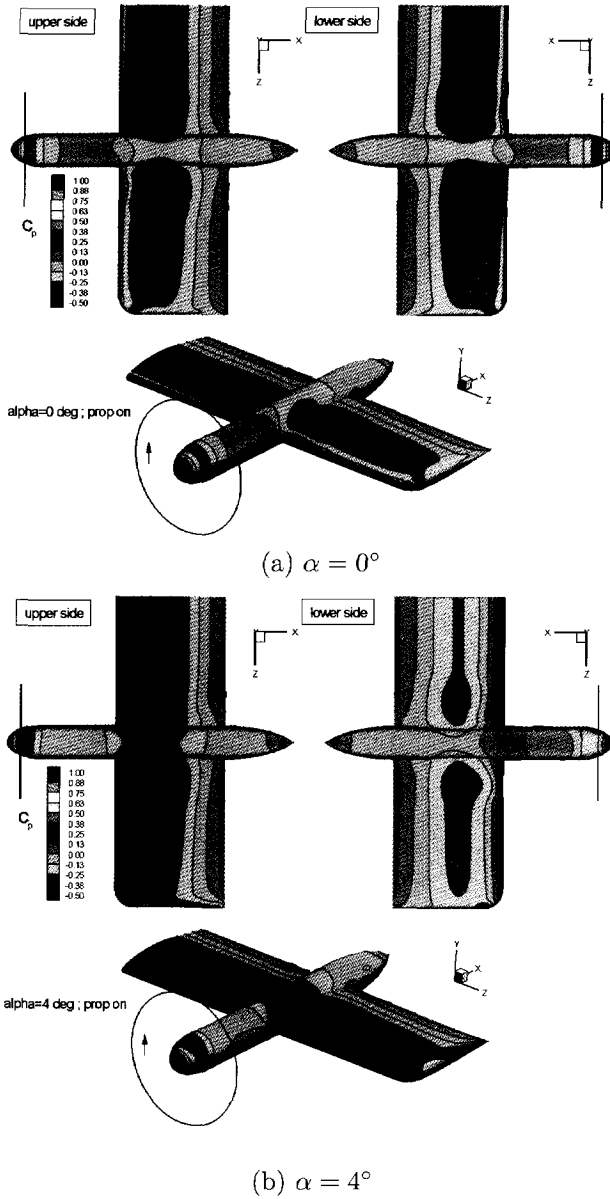
Figure 6.68: *Static surface pressure distribution at $\alpha = 0°$ (upper figures) and $\alpha = 4°$ (lower figures) ; propeller on.*
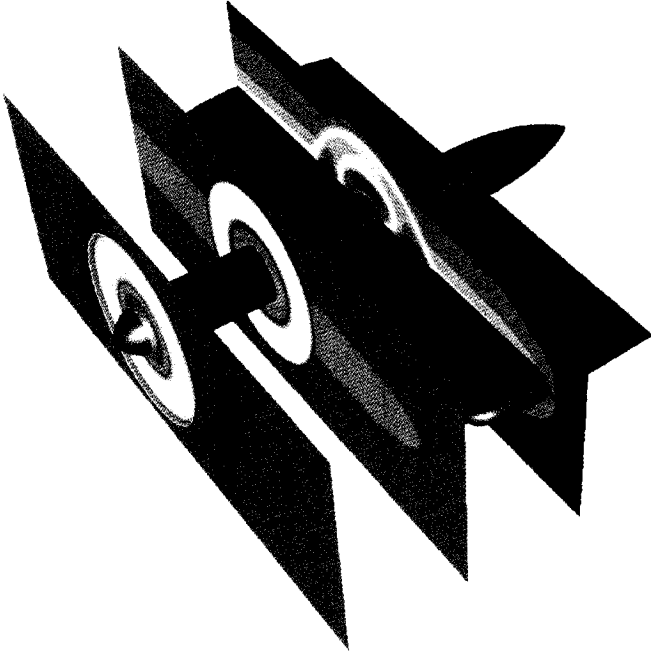
Figure 6.69: *Development of the dynamic pressure in the slipstream showing the streamwise increase and deformation due to the presence of the wing ; $\alpha = 0°$.*
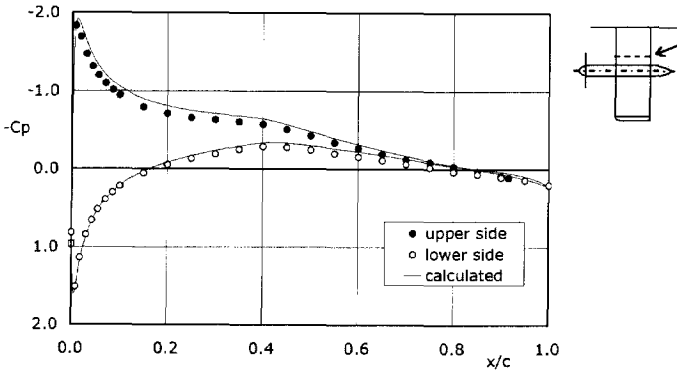
(a)
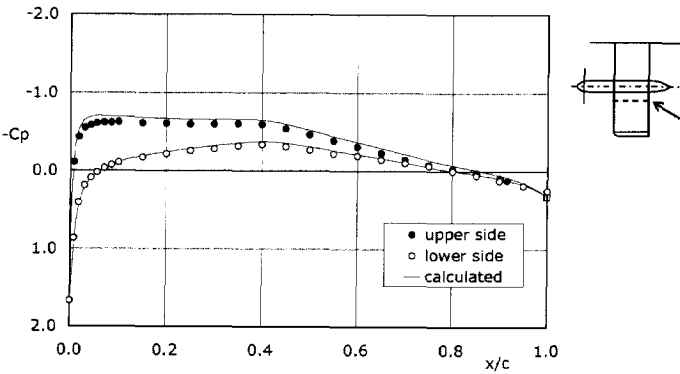
(b)

Figure 6.70: *Experimental and calculated pressure distribution at $\alpha = 4°$; prop on ; (a) $y/b/2 = 0.345$; (b) $y/b/2 = 0.623$.*

(a) $\alpha = 0°$

(b) $\alpha = 4°$
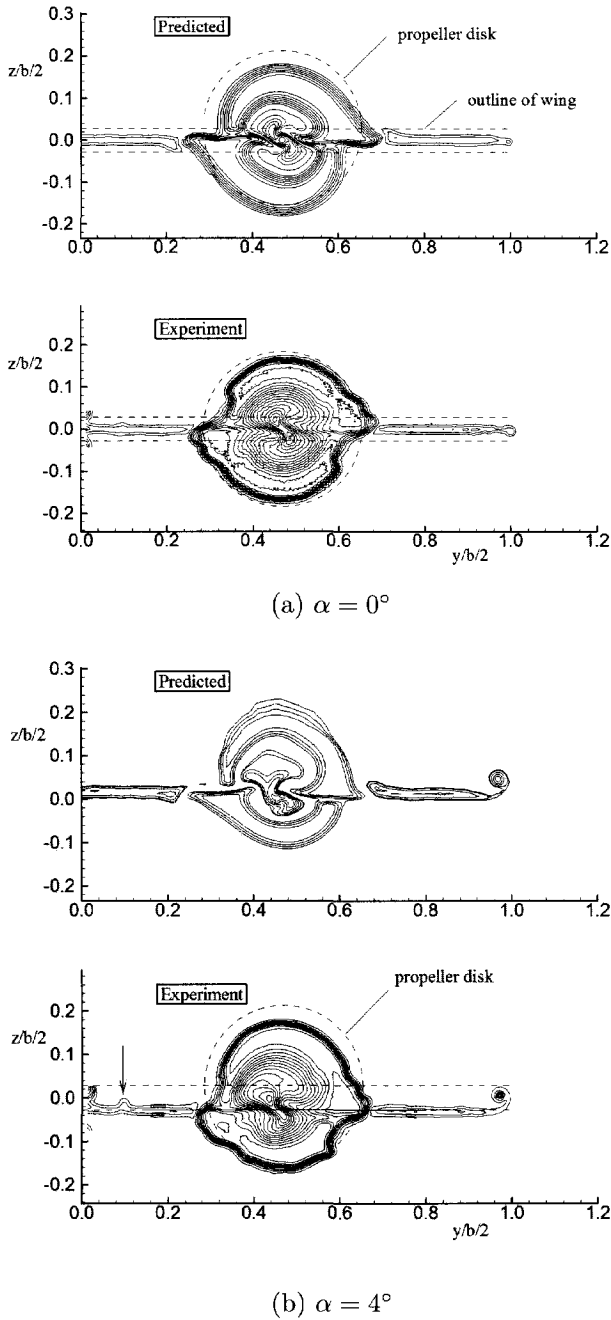
Figure 6.71: *Predicted and experimental contour lines of constant total pressure coefficient at 1 chord behind the wing; prop on ; (a) $\alpha = 0°$; (b) $\alpha = 4°$.*
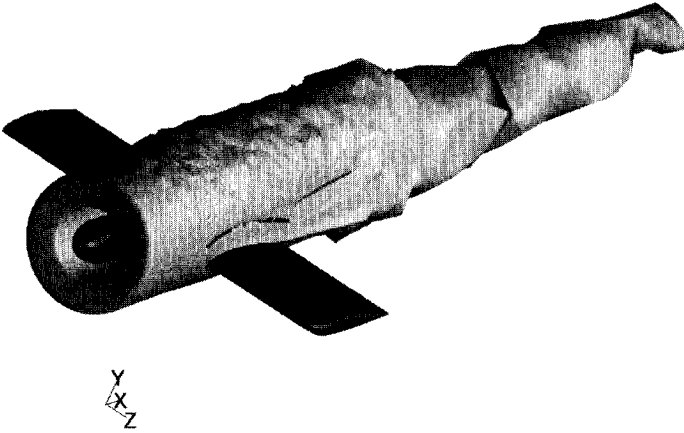
Figure 6.72: *PROWIM with surface of constant total pressure value (p_t = 1800 Pa), showing the effect of grid coarsening above and behind the model ; prop on ; $\alpha = 4°$.*

behind the model. Again the qualitative agreement between the experimental flow field and the predicted results is good.

Quantitative Wake Analysis   To gather more information from the calculated flow field data a quantitative wake analysis was performed on the calculated data in the same way as was done for the experimental 5-hole probe data described in Chapter 5.

A typical number of grid points in the wake survey plane (WSP) during the experiment was 30,000–40,000 whereas the WSP in the Navier-Stokes calculations contained 5000 data points.

In Fig. 6.74 examples of the calculated and experimental local lift distribution, are presented for $\alpha = 4°$. A small difference is visible between the lift acquired with both techniques. Although in general the agreement between the calculated and the measured lift distribution is quite satisfactory, typical differences are found in the wing tip region. The calculated curves show a smaller spanwise lift gradient due to the limited number of cells and the increased dissipation of the tip vortex. Small differences in the lift distribution in the vicinity of the propeller slipstream between the calculated and the experimental results are due to the simplified actuator disk representation of the propeller, which does not exactly constitute the exact velocity and pressure distributions of the real flow. In this respect the quantitative flow analysis also provides information about the quality of the actuator disk approach.
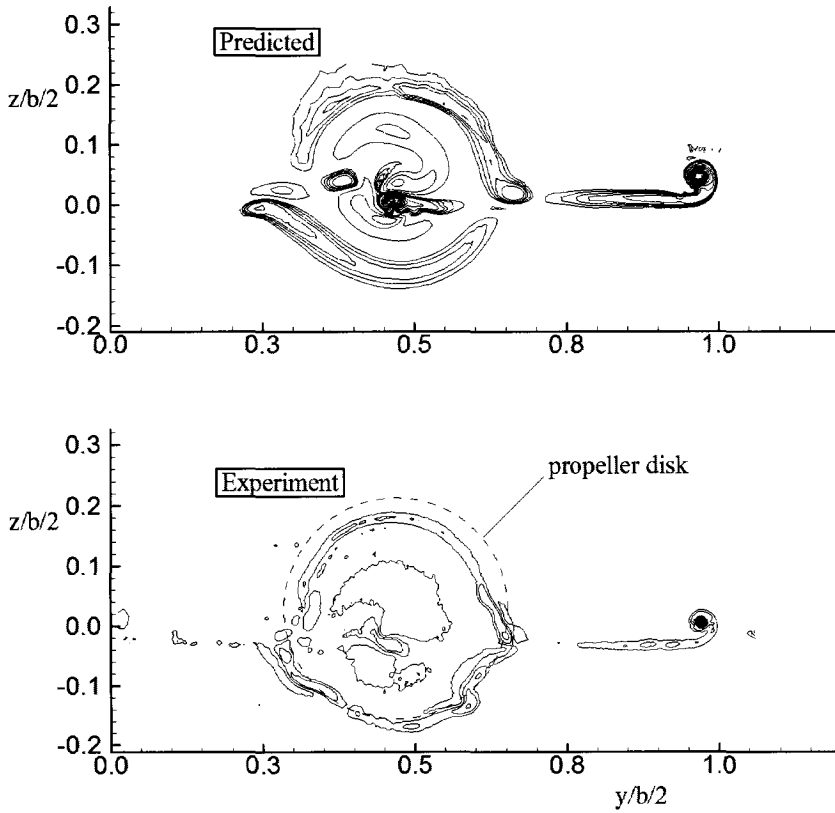
Figure 6.73: *Comparison of predicted and experimental contour lines of constant axial vorticity at 1 chord behind the model ; prop on ; $\alpha = 4°$.*
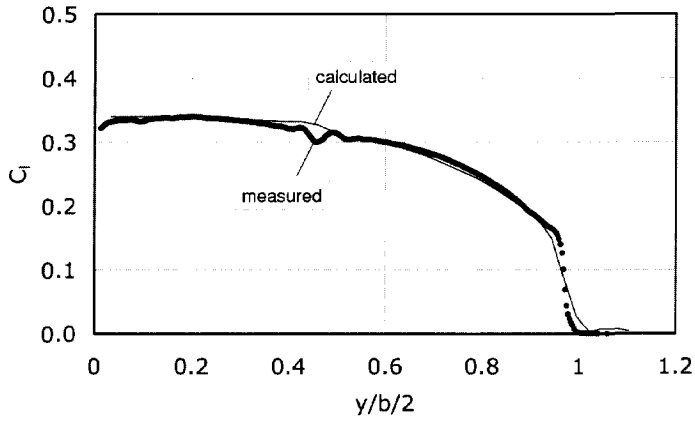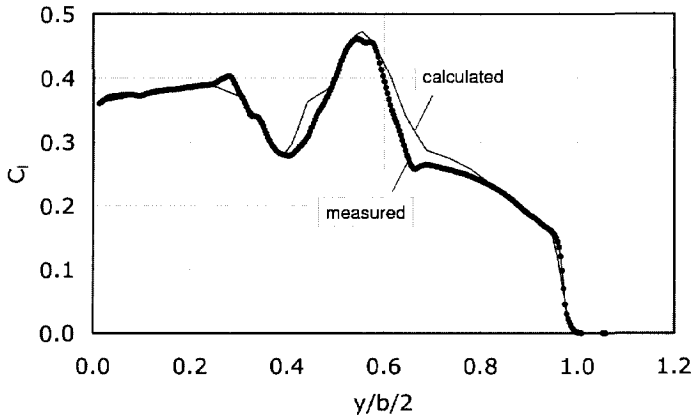
Figure 6.74: *Measured and calculated lift distributions from wake analysis for* $\alpha = 4°$; *(a) prop off ; (b) prop on.*

Comparison with balance measurements   The final results of the numerical
and the experimental wake surveys are compared with the balance measurements in
Table 6.15.

Table 6.15: *Comparison of calculated and measured lift and drag coefficients for
the PROWIM model.*

Method	α	prop	C_L	C_D'
CALC.	0	off	0.000	0.0109
wake	4	off	0.288	0.0171
analysis	0	on	0.003	-0.0985
	4	on	0.310	-0.0910
CALC.	0	off	0.000	0.0170
surface	4	off	0.291	0.0231
forces$^{(*)}$	0	on	0.004	-0.0926
	4	on	0.319	-0.0857
EXP.	0	off	0.000	0.015
balance	4	off	0.288	0.0198
data	0	on	0.006	-0.0986
	4	on	0.314	-0.0916

In these data the drag coefficient, C_D', found in the case of a running propeller,
includes the thrust component and therefore becomes negative. From Table 6.15 it
can be concluded that the wake survey of the CFD data produce a lift coefficient
that is very close to the balance data. For $\alpha = 4°$, both in the case of prop off
and prop on, the lift coefficient is (almost) exactly reproduced. Although the flow
field surveys produce a drag coefficient that is slightly smaller than the drag from
the external balance measurements, the agreement between the three techniques is
such that the QWA technique in CFD calculations results can be successfully utilized.
This conclusion is supported by the findings reported in ref [126].

Propeller rotation effect   With respect to the propeller rotation direction of the
propeller, one should remember that in the numerical models discussed so far and
during the windtunnel investigations, the propeller rotated "inboard up". Within the
current numerical model it was possible to reverse the rotating direction very easily
by changing the propeller boundary conditions. To determine whether inboard up
rotation was as beneficial as found in Chapter 5 a numerical test case was run for
$\alpha = 4°$ using the RKE model.

The new configuration indeed led to a small performance decrease of the complete
model, i.e. a slightly lower lift coefficient and a small increase of the drag coefficient,

while the thrust was unchanged: $C_L = 0.2997$; $C_D = -0.0839$; $T = 24.80\,N$. An explanation for this effect of the rotation direction was already presented in Chapter 5.

Over the wing propeller A last comparison between earlier data and the results of the NS-code was made on the over-the-wing configuration (see Chapter 5).

The purpose of these calculations was to confirm whether the trends found during the windtunnel tests and the preliminary calculations performed in Chapter 5 would be supported by the NS-approach.
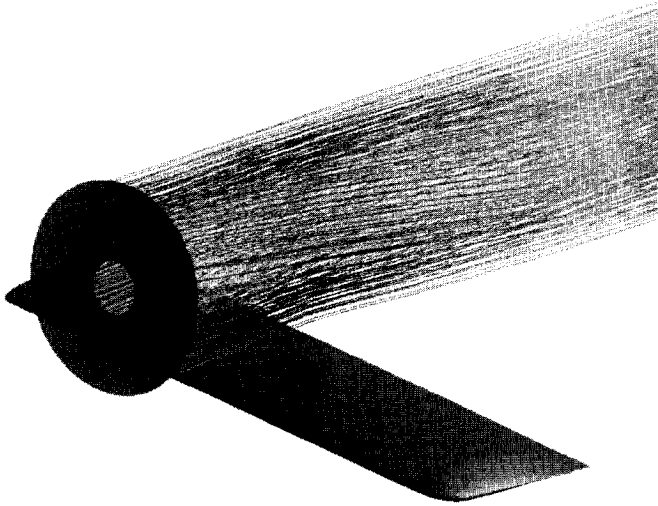
Figure 6.75: *Layout of the OTW model with flow path lines emanating from the actuator disk surface.*

The numerical model was simplified compared to the APROPOS model in the sense that the nacelle was not modeled. Fig. 6.75 shows the wing model with the propeller at a forward position with flow path lines originating from the actuator disk surface. To check the effect of the propeller position above the wing, in total 9 positions at streamwise locations between $x_p/c = -0.840$ and $x_p/c = 1.25$ were investigated.

The absence of the nacelle in the computational model led to a simple model with the main advantage that the same grid could be used for all propeller positions. Hence, a significant reduction of the time needed in the pre-processing (modelling)

phase was obtained. Moreover, due to the use of 1 grid more reliable comparison is expected between the different configurations.

To simulate the propeller flow, the actuator disk model was adopted again for two reasons. First of all the interference effects in the OTW configuration are purely based on angle of attack changes imposed by the propeller on the wing and vice versa. Hence, the details of the flow inside the slipstream (particularly the swirl distribution) are unimportant. Secondly it has been shown during earlier research [20, 119] that there is a close resemblance between the flow field generated by an actuator disk and a full blade modelling and small difference are only to be expected in the vicinity of the propeller. The major disadvantage of the actuator disk model is the fact that the jump conditions have to be known a priori. This problem was again easily overcome with the availability of thrust and flow field data found in the experiments performed.

From the data obtained in the flow field close to the nose of the model it could be concluded that the propeller effect on the wing manifests itself purely through an angle of attack change. The inflow into the slipstream produces a local effect on the chordwise lift distribution as shown in Fig. 6.76 and Fig. 6.77. In these figures only the upper side pressure distribution is depicted as the effect of the propeller on the lower side turned out to be rather small.
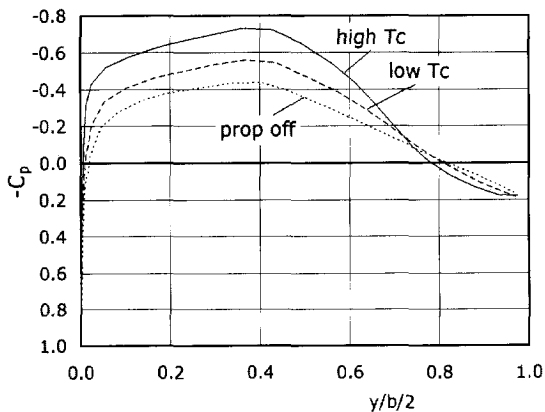
Figure 6.76: *Effect of OTW propeller on the chordwise pressure distribution directly below the slipstream ; $x_p/c = 0.75$; $y_p/b/2 = 0.47$; low $(T_c = 0.174)$ and high $(T_c = 0.52)$ thrust coefficient.*

As can be seen in Fig. 6.76 an increase in the thrust coefficient directly leads to a stronger contraction of the slipstream which in turn produces lower pressures at the wing upper side for given value of x_p/c.
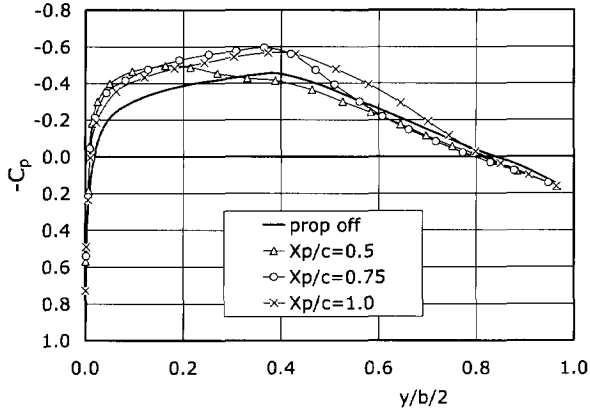
Figure 6.77: *The effect of the streamwise propeller location on the wing pressure distribution ;* $y_p/b/2 = 0.47$ *;* $T_c = 0.174$.

Changing the streamwise position of the propeller (Fig. 6.77), however, changes the chordwise pressure distribution considerably into a form that is different from the one found at the same lift coefficient produced by an angle of attack change.
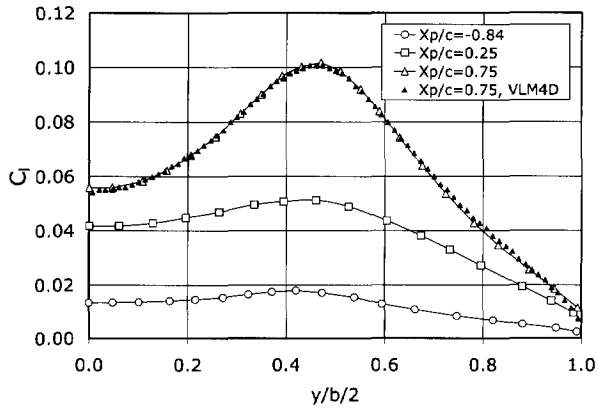
Figure 6.78: *Spanwise lift distribution for three streamwise propeller locations ;* $\alpha = 0°$ *;* $T_c = 0.18$ *; inboard up rotation ; solid symbols show the results of the VLM-analysis.*

Integration of the pressure distribution produces spanwise lift distributions as sketched in Fig. 6.78. Here the effect of the local flow angle of attack increase is observable by the local rise in C_l which peaks close to the spanwise location of the propeller ($y_p/b/2 = 0.47$). Due to the fact that the swirl velocity (and possible errors in its input values) does not play an important role for the overall performance of the OTW-configuration the trend found in Fig. 6.78 perfectly agrees with the result of the much simpler VLM calculation approach as discussed in Chapter 5.

In Fig. 6.79 the calculation results are compared to experimental data. An excellent agreement is found indicating that the deformation that takes place in the NS-approach allows a realistic propeller induced angle of attack. The static slipstream envelope used in the VLM and the panel method approach clearly show problems in this respect.

(a)

Low thrust case

(c)

(d)

High thrust case
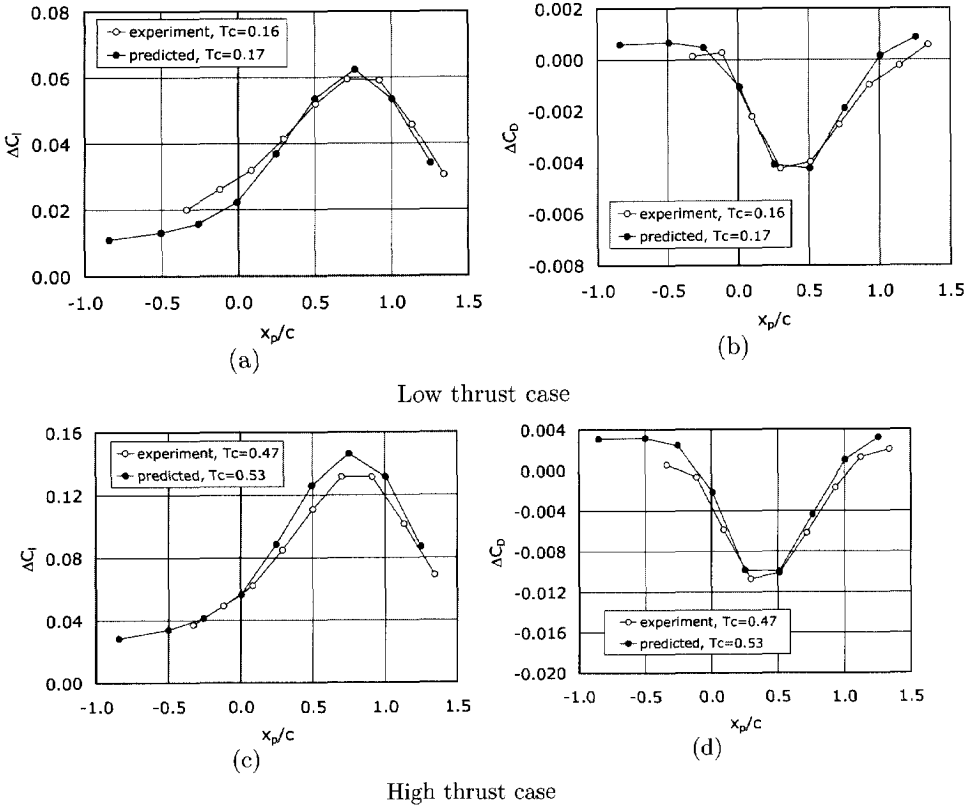
Figure 6.79: *Effect of the propeller streamwise position in the OTW arrangement on the lift coefficient (left) and the drag coefficient (right).*
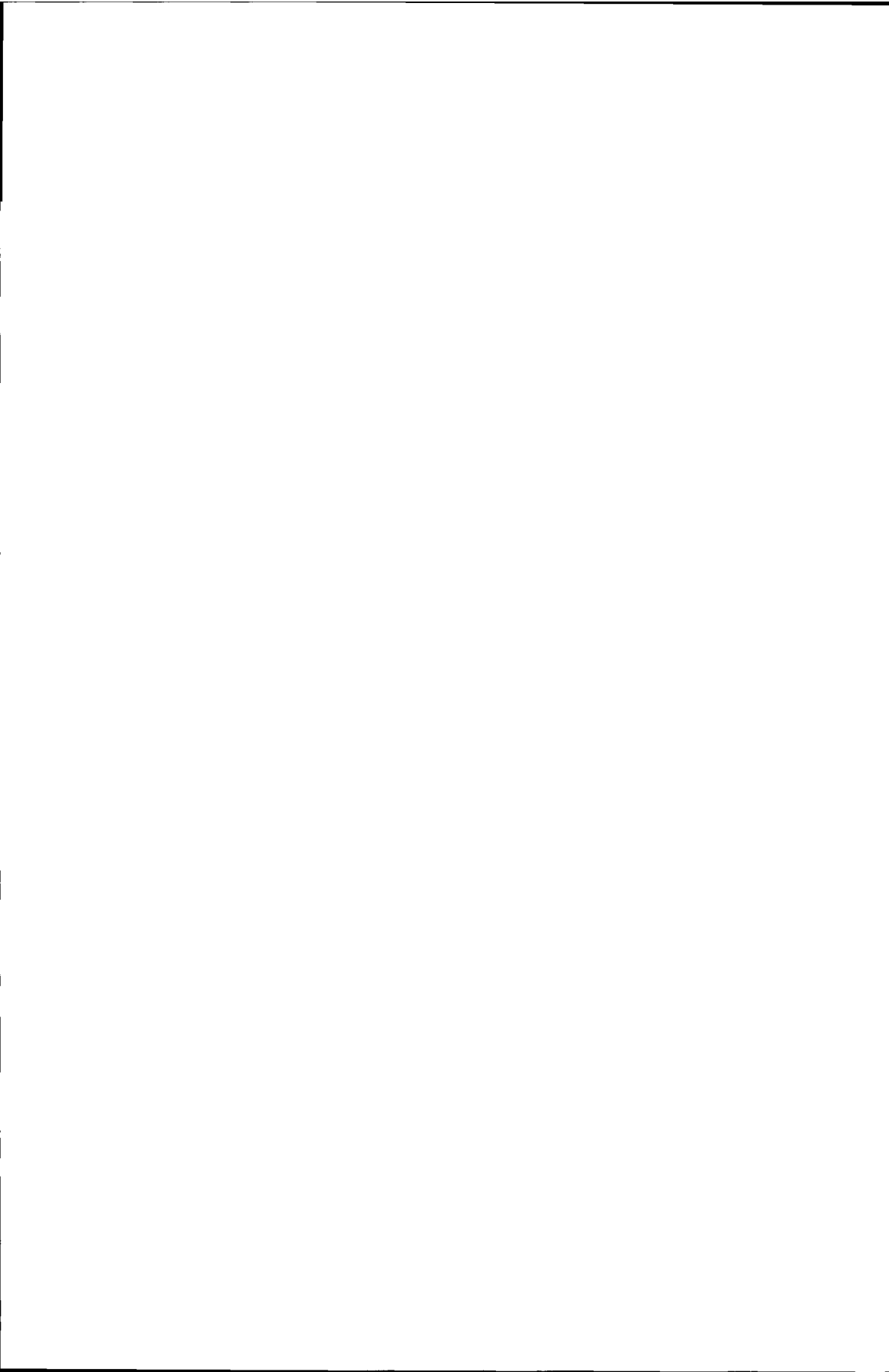
Part III

Optimization

Chapter 7

Optimization of tractor propeller-wing configurations

7.1 Introduction

Modern CFD code based on the Navier-Stokes equations contribute, without doubt, to a better understanding of the problem of propulsion integration they generally lack an important feature: a design optimization option. Optimization programs are important in the preliminary design phase when the main design parameters like the location of the propulsion system have to be chosen. Since these methods should be fast enough to quickly assess the consequences of changes in the global shape of the configuration they are often based on elementary momentum considerations and relatively simple numerical schemes.

To obtain a propeller wing configuration that is optimized for high performance in a specified flight regime both elements should be designed simultaneously taking into account the most important interference effects. To arrive at the final design two approaches may be followed:

- Separate design of the propeller and the wing based on either experimental or numerical data where the wing characteristics are analyzed for given propeller condition. This procedure is further denoted as the Analysis Approach

- Integrated design of the propeller and the wing where the optimized wing loading is calculated based on a given input of the propeller. With the obtained optimum wing loading the wing geometrical parameters can be calculated. This procedure is denoted as the Optimization Approach.

In the Analysis Approach the optimum propeller wing combination is in fact a heuristic process where an initial wing designed without incorporating propulsion ef-

fects is subjected to a given propeller slipstream flow. Analysis of the experimental
or numerical results then leads to new choices for the complete configuration. After
several, laborious, iteration steps, an acceptable configuration may be found for the
specified flight condition. Subsequent tests or calculations on the off-design condi-
tions finally determine whether the design is acceptable or not from aerodynamic or
structural point of view.

The Optimization Approach uses geometric shape functions and is coupled to
two-dimensional or three dimensional flow solvers. Inverse optimization programs use
aerodynamic shape functions and are coupled to flow solvers based on the lifting line
theory and a Trefftz plane analysis. Although this process is probably much faster
than the A-approach again additional tests or calculations are needed to determine
the characteristics under off-design conditions. With the contribution of the propeller
in the optimization process, a different lift distribution than the optimal 'clean wing'
distribution will be found.

In the next sections the Optimization Approach, which was implemented in two
optimization programs, *optimizer* and *pwopt2,* will be treated in more detail and some
calculation results will be discussed in short.

7.2   Fourier approach

7.2.1   Lift and drag

The first approach for an optimization of the wing in a tractor propeller wing arrange-
ment is based on a rather straightforward procedure.

To be able to find the induced drag of a wing from the lift distribution it is
important to reconsider the effects of the axial and swirl velocity distribution in the
slipstream. The local effective angle of attack of a wing airfoil section is given by:

$$\alpha_{eff} = \alpha - \alpha_i \tag{7.1}$$

Here α is the geometric angle of attack and α_i the angle induced by the wing vortex
system and the propeller slipstream.

The induced angle of attack consists of two parts:

$$\alpha_i = \alpha_{i_w} + \alpha_{i_p} \tag{7.2}$$

where index w is for the wing vortex system and p for the propeller vortex system.

According to the Prandtl Lifting Line Theory, the local induced angle of attack
at spanwise position y_0, induced by the wing vortex system, can be found from the
spanwise distribution of vorticity:

$$\alpha_{i_w}(y_0) = \frac{-1}{4\pi U_\infty} \int\limits_{-b/2}^{+b/2} \frac{(\frac{d\Gamma(y)}{dy})dy}{y_0 - y} \tag{7.3}$$

For a small α_i the lift and induced drag of the wing become:

$$L = \rho U_\infty \int\limits_{-b/2}^{+b/2} \Gamma(y)dy \qquad (7.4)$$

$$D_i = \rho U_\infty \int\limits_{-b/2}^{+b/2} \alpha_i(y)\Gamma(y)dy \qquad (7.5)$$

An optimum spanwise loading (proportional to $\Gamma(y)$) gives a minimum induced drag at a given design lift coefficient. To prepare the equations for the optimization process the spanwise circulation distribution is represented as a Fourier sine series consisting of N terms:

$$\Gamma = 2U_\infty b \sum_{n=1}^{N} A_n \sin(n\theta) \qquad (7.6)$$

where the physical spanwise co-ordinate y has been replaced by θ, through: $y = -\frac{b}{2}\cos\theta$ and A_n are the Fourier coefficients. In case the spanwise lift distribution is symmetrical only n odd terms remain (see Fig. 7.1).

The lift per unit span can now be written as:

$$l(\theta) = \rho U_\infty \Gamma(\theta) = 2\rho U_\infty^2 b \sum_{n=1}^{\infty} A_n \sin(n\theta) \qquad (7.7)$$

where A_n are the Fourier coefficients.

Introducing the propeller induced axial velocity increase factor $a(\theta) = V_{ax}(\theta)/U_\infty$ the local lift per unit span changes to:

$$l(\theta) = \rho U_\infty \Gamma(\theta)(1 + a(\theta)) = 2\rho U_\infty^2 b \sum_{n=1}^{\infty} A_n \sin(n\theta)(1 + a(\theta)) \qquad (7.8)$$

Integration over the span gives the slipstream influenced wing lift:

$$L = 2\rho U_\infty^2 b \sum A_n \frac{b}{2} \int\limits_{0}^{\pi} \sin(n\theta)(1 + a(\theta))\sin(\theta)d\theta \qquad (7.9)$$

For the induced drag an analogue analysis can be followed. Rewriting eq. (7.9) in dimensionless form leads to

$$C_L = 2 \cdot AR \cdot \sum_n A_n \int\limits_{0}^{\pi} \sin(n\theta)\sin(\theta)(1 + a(\theta))d\theta \qquad (7.10)$$
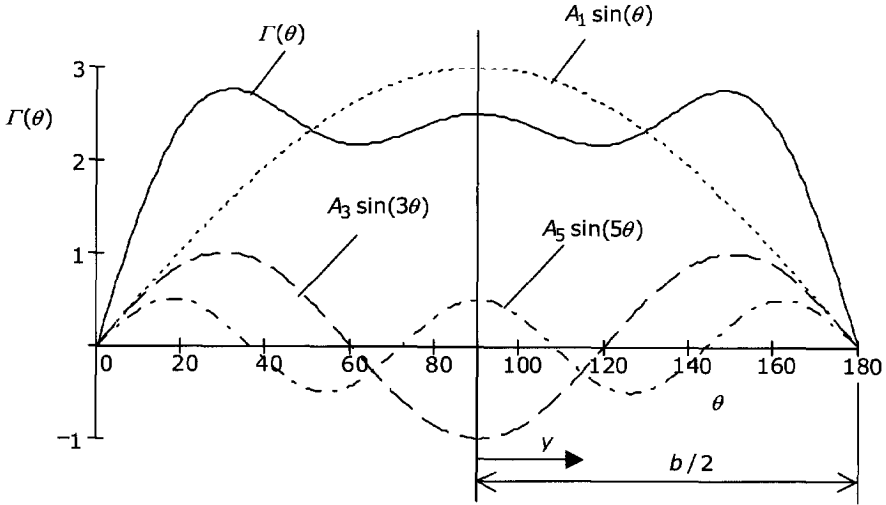
Figure 7.1: *Symmetrical spanwise circulation distribution represented by Fourier sine series*

where AR is the aspect ratio of the wing[1].

For the propeller-off case $(a = 0)$ the lift coefficient can be written as:

$$C_L = \pi \cdot AR \cdot A_1 \tag{7.11}$$

This is the well known lifting line result where the lift coefficient depends only on the first Fourier coefficient, A_1.

Without further proof we state that in an analogous way the following expression for the induced drag coefficient in inviscid flow exists when a propeller slipstream is present:

$$C_{D_i} = 2 \cdot AR \cdot \sum_n \sum_k n A_n A_k \int_0^\pi \sin(n\theta) \sin(k\theta)(1 + a(\theta))d\theta + \\ 2 \cdot AR \cdot \sum_n A_n \int_0^\pi \alpha_{i_p}(\theta) \sin(n\theta) \sin(\theta)(1 + a(\theta))d\theta \tag{7.12}$$

where $\alpha_{i_p}(\theta)$ is the propeller induced angle of attack at the local spanwise wing position.

---

[1]written as AR to prevent confusion with the Fourier coefficients

Once the lift and induced drag coefficients are calculated, the wing efficiency can simply be found by:

$$e = \frac{C_L^2}{\pi A C_{D_i}} \tag{7.13}$$

For a given wing lift distribution the Fourier coefficients A_n can be calculated and the total wing lift, the induced drag and the efficiency factor can be evaluated using eq. (7.10),(7.12) and (7.13).

It has to be noticed that the expressions stated above are based on the following simplifications:

- The wing trailing vortex sheet is assumed to be flat and lying in the plane $z = 0$.

- The propeller induced velocities have to be known in advance. The influence of the wing induced velocity field on the propeller flow is not represented directly. A correction is applied afterwards.

- There are still no viscous effects, which means that the contribution of section profile drag is assumed to be zero

7.2.2   Optimization of the lift distribution

As can be seen from eq. (7.12), the induced drag expression consists of two terms. The contribution of the second term can either be negative or positive depending on both the signs of the swirl distribution and the Fourier coefficients. This indicates that a non-elliptic optimum lift distribution might be found for minimum induced drag when the propeller is running.

The optimum is now found by specifying that the partial derivative of the induced drag with respect to all the Fourier coefficients of order higher than one should be zero. This can easily be seen by assuming that $\partial C_{D_i}/\partial A_n \neq 0$ for a certain value of n. This means that the additional lift distributions related to the given value of A_n can be changed such that C_{D_i} becomes lower, for a constant value of the wing lift coefficient. The minimum is reached when $\partial C_{D_i}/\partial A_n = 0$. Thus:

$$\frac{\partial C_{D_i}}{\partial A_n} = 0 \quad n = 2, 3, ..., \infty \tag{7.14}$$

Define:

$$I_{nk} = \int_0^\pi \sin(n\theta)\sin(k\theta)(1 + a(\theta))d\theta \tag{7.15}$$

$$J_n = \int_0^\pi \alpha_{i_p}(\theta)\sin(n\theta)\sin(\theta)(1 + a(\theta))d\theta \tag{7.16}$$

Note that $I_{nk} = 0$ when $n \neq k$. Using eq. (7.14) the Fourier coefficients for the optimum lift distribution in inviscid flow, become:

$$A_n = \frac{-J_n}{2nI_{nn}} \qquad n = 2, 3, ..., \infty \qquad (7.17)$$

7.2.3   Program OPTIMIZER

The method described above was implemented in a computer program called *optimizer*. With this code it is possible to find the optimum lift distribution for minimum induced drag for any tractor propeller/wing arrangement of arbitrary shape.

The user can either select input of experimental data for the slipstream or generate artificial data using a simple slipstream model ([93]). The main input consists of :

- wing geometry (aspect ratio and chord distribution)

- the propwash data (axial and tangential velocity increase, a and a' respectively)

- propeller diameter and position

- the required lift coefficient

In case the propeller is put at an angle of attack to the flow the distribution of the factors a and a' should be given according to the increased values at the upgoing blade side and vice versa. If only data are available for the setting $\alpha_p = 0°$ at the position of the propeller plane instead of the wing location, the program will calculate the propwash data according to the following scheme.

The axial velocity increase at a certain distance x_p behind the propeller is given by $a_x(x_p) = u_p(x_p)/V_\infty$. According to a velocity potential formulation as described by Smelt & Davies [37], which is based on an analogy with magnetic shell theory, the axial velocity increase, as a function of x, can be estimated by :

$$a(x_p) = a_0 \left(1 + \frac{1}{\sqrt{(\frac{R}{x_p})^2 + 1}} \right) \qquad (7.18)$$

where a_0, is the axial velocity factor at the position of the propeller plane ($x_p = 0$). The flow velocity in the direction of the thrust line is given by $V_\infty \cos(\alpha_p)$ whereas the velocity perpendicular to this line is $V_\infty \sin(\alpha_p)$. The slipstream centerline will therefore deviate from the thrust line, by an angle $\alpha_{c.l.}$ given by:

$$\tan(\alpha_{c.l.}) = \frac{V_\infty \sin(\alpha_p)}{V_\infty(1 + a(x_p)) \cos(\alpha_p)} = \frac{\tan(\alpha_p)}{(1 + a(x_p))} \qquad (7.19)$$

To account for the "upwash effect" given by $\alpha_{c.l.}$ the local swirl velocity at the wing position is corrected through:

$$a_{t_{corr}} = \tan(\alpha_w + \alpha_p - \alpha_{c.l.} + \arctan(a_t(y))) \qquad (7.20)$$

where $a_t(y) = v_t(y)/V_\infty$, is the uncorrected swirl velocity factor.

To account for the "upwash effect" given by $\alpha_{c.l.}$ the angle α_{i_p} used in eq. (7.12) is corrected through :

$$(\alpha_{i_p})_{cor} = \alpha_{i_p} - \alpha_{c.l.} \qquad (7.21)$$

7.2.4 Contribution of the propeller at angle of attack

As indicated in Chapter 2 the induced angle of attack is substantial for closely mounted propeller-wing configurations. The propeller at angle of attack will, in addition to moments, produce a thrust and a normal force. In *optimizer*, the propeller angle of attack effect on the performance of the optimized propeller/wing configuration is calculated through usage of the E-method described in Appendix A.

After the normal force gradient of the propeller is calculated, conversion from the propeller to the wing reference parameters gives:

$$\frac{dC_{N_p}}{d\alpha_p} \cdot \frac{\pi}{4} \frac{D^2}{S_w} = \frac{dC_{N_p}}{d\alpha_p} \cdot g \qquad (7.22)$$

Besides the secondary, slipstream generated, propeller effect, the primary contribution of the propeller to wing lift and drag is given by :

$$\begin{aligned}
\Delta C_L &= (C_{N_p}\cos(\alpha_p') + T_c\sin(\alpha_p')) \cdot g \\
\Delta C_D &= (C_{N_p}\sin(\alpha_p') - T_c\cos(\alpha_p')) \cdot g
\end{aligned} \qquad (7.23)$$

where, the propeller geometrical angle α_p' is defined by:

$$\alpha_p' = \alpha_p + \alpha_w \qquad (7.24)$$

The change in wing lift and drag generated by the propeller, with reference to the situation $\alpha_p = 0$, is therefore given by :

$$\begin{aligned}
\Delta C_L' &= T_c'\sin(\alpha_p') - T_{c_0}'\sin(\alpha_{p_0}') + \Delta C_{N_w}\cos(\alpha_p') - \Delta C_{N_{w_0}}\cos(\alpha_{p_0}') \\
\Delta C_D' &= -T_c'\cos(\alpha_p') + T_{c_0}'\sin(\alpha_{p_0}') + \Delta C_{N_w}\sin(\alpha_p') - \Delta C_{N_{w_0}}\sin(\alpha_{p_0}')
\end{aligned} \qquad (7.25)$$

where :

$$T_c' = \frac{2D^2}{S_w}T_c \quad ; \quad T_c = \frac{T}{\rho V^2 D^2} \quad ; \quad \Delta C_{N_w} = \frac{dC_{N_w}}{d\alpha_p}\alpha_{eff}$$

and index 0 refers to the situation $\alpha_p = 0$. To correct the wing efficiency, given in eq. (7.13), the lift and the drag change are incorporated in the calculation resulting in an effective efficiency defined as:

$$e_{eff} = \frac{(C_L + \Delta C_L)^2}{\pi A(C_{D_i} + \Delta C_D')} \qquad (7.26)$$

Thrust and normal force coefficients are determined by the effective propeller angle of attack:

$$\alpha_{eff} = \alpha_p + \alpha_w + \alpha_{upflow} \qquad (7.27)$$

7.2.5   Realization of the optimum lift distribution

After the discussion about the acquisition of the optimum lift distribution for a given propeller/wing combination the next logical step is to define how the required distribution can be obtained. To get some understanding of the magnitude of the changes to an initial wing design, a simple analysis is suggested here.

Eq. (7.9) in dimensionless form can be written as:

$$C_l(\theta)\,\frac{c(\theta)}{b} = g(\theta) = 4\sum_{n=1}^{\infty} A_n \sin(n\theta)(1 + a(\theta)) \qquad (7.28)$$

The requirement for the wing now becomes:

$$C_{l_\alpha}(\theta)(\alpha_g(\theta) - \alpha_i(\theta) - \alpha_0(\theta))\frac{c(\theta)}{b} = g(\theta) \qquad (7.29)$$

Since α_i is fixed by the given vorticity distribution along the span, the user may select an appropriate value for the following parameters to fulfill the requirement of eq. (7.29):

- the two-dimensional lift curve slope, C_{l_α}

- the geometrical airfoil angle of attack which is determined by the twist distribution, α_g

- the zero lift angle of attack of the airfoil, α_0

- the chord/span ratio of the airfoil, c/b

It is clear that the wing design of an optimum wing with installed propeller is complicated due to the difference between the optimum lift distribution and the "normal" elliptic-like distribution, especially at transonic speeds. In general the profile shape should be modified to prevent unwanted viscous and compressibility effects in the part of the wing that is immersed in the slipstream.

Since leading and trailing edge of the wing are normally kept straight and the airfoil type will not change strongly in spanwise direction, in general the most attractive way to generate the optimum wing lift distribution may be an adaptation of the twist distribution or the camber distribution of the airfoils.

Due to deformation of the airfoil shape as a result of wing twist, a combination of twist adaptation and variation of section shape will be employed in practice, though.

The induced angle of attack at the location of the wing is given by:

$$\alpha_i(\theta) = \arctan\left(\frac{v_{n,wing}(\theta) + w_p(\theta)}{U_\infty + u_p(\theta)}\right) \qquad (7.30)$$

Table 7.1: *Calculated effect of camber on the lift coefficient of NACA x415 air-foils series ; inviscid case at $\alpha = 5°$.*

Airfoil	Camber (%)	C_l
NACA1415	1	0.748
NACA2415	2	0.878
NACA3415	3	1.008
NACA4415	4	1.138
NACA5415	5	1.267
NACA6415	6	1.395

in which v_n is the total downwash at the wing due to the trailing vortex system ($v_n > 0$, defined positive in negative z-direction).

To get an idea about the magnitude of the required changes of the wing geometry, the optimum wing twist distribution with constant airfoil section, the local twist angle found from:

$$\varepsilon(\theta) = \frac{g(\theta)}{C_{l_\alpha}} + \alpha_i + \alpha_0 + \alpha_r \qquad (7.31)$$

may be calculated.

When the twist distribution is kept constant and both the leading edge and the trailing edge remain straight (as seen from above) the required lift distribution can be realized by adaptation in the camber distribution.

The change in the lift coefficient due to camber effects becomes:

$$\Delta C_l = \frac{\partial C_l}{\partial \tau} \Delta \tau \qquad (7.32)$$

where τ is the camber of the airfoil section.

To obtain quantitative information about the typical change in the airfoil camber that are to be expected for an optimized wing geometry in the presence of a rotating propeller, a simple analysis may be based on the NACA 4 series airfoils, NACA$xyzz$. Here x is the maximum deflection of the camber line as a percent of the airfoil chord, c. The second digit, y, designates the position of the maximum camber line deflection, $x_{\tau_{max}}$, in terms of tenths of c while the last two digits, zz, designate the airfoil thickness, t, as a percent of c. The effect of changing the camber of the airfoil is a linear change in the zero lift angle of attack or, alternatively, a change in the lift coefficient at $\alpha = 0°$, as can be seen in Table 7.1 and Fig. 7.2.

From the calculated airfoil data both the change in the lift coefficient with the camber and with the angle of attack can be determined. It appears that both values are approximately the same, i.e. $C_{l_\tau} = 0.1152 \ (\%\tau)^{-1} \approx C_{l_\alpha} = 0.1138 \ (\text{deg}^{-1})$.
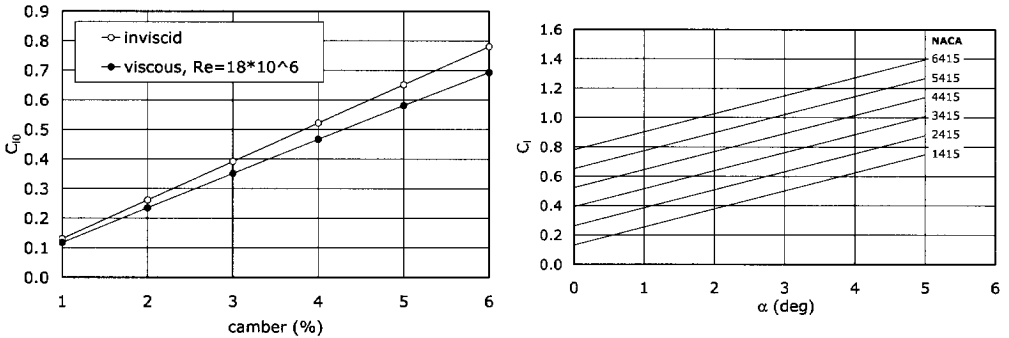
Figure 7.2: *Effect of camber on the lift coefficient of a NACA x415 airfoil series ;*
left: Inviscid C_l-α curves ; right: comparison of inviscid and viscous
calculations at $Re = 18 \cdot 10^6$. Transition was fixed at 5 % at upper
and lower side.

Both airfoil camber adaptation and twist adaptation can be used to change the
local lift coefficient needed to arrive at the optimized loading distribution from either
of the two methods derived above.

7.2.6   Generation of propeller slipstream data

To find the correct interference effect that the slipstream imposes on the wing, the
axial and the tangential flow velocities, which together form the velocity vector
(u_p, v_p, w_p), must be incorporated as stated in the equations for the lift and the
drag coefficient. In the current program it is possible to import experimental slip-
stream data or calculate the propeller induced velocities with a simplified slipstream
model. In the latter case (u_p, v_p, w_p) is calculated with the slipstream tube model (see
Appendix D). In this model, the vorticity in the slipstream originally concentrated on
a finite number of helical vortex sheets, is replaced by two superimposed continuous
distributions of vorticity: axial and tangential vorticity. Using a Biot-Savart calcula-
tion algorithm the propeller induced velocity vector is then found in the Trefftz plane.
In case the propeller is put at a positive angle of attack to the flow the induced veloc-
ity distribution should be given according to the increased values at the down-going
blade side and vice versa. If only data are available for the setting $\alpha_p = 0°$ at the
position of the propeller plane instead of the wing location, the program will calculate
the propwash data according to the scheme given in section 7.2.3.

7.3 Trefftz plane analysis

The effect of the profile drag in the optimization process cannot be implemented easily in the Fourier approach. For this reason an alternative method was developed which allows minimization of the total (induced plus viscous) drag for a given lift coefficient.

7.3.1 Lift and induced drag

In this analysis the so-called Trefftz plane method is applied to the propeller wing configuration. The method, based on Munk's stagger theorem [127], was originally applied to wing tail configurations but may be extended to propeller-wing configurations as well, as indicated by Kroo [10]. Initially the influence of the wing on the propeller is neglected, which implies that the propeller is far upstream or downstream of the wing. Hence the total downwash at infinity, used in the optimization process, is a superposition of the downwash due to all lifting surfaces and the downwash generated by the propeller at infinity. An inverse numerical optimization is applied here, based on a flow solver which utilizes a lifting line theory to model the lifting surfaces combined with a Trefftz plane analysis. The bound circulation is modeled using a quadratic distribution function similar to the method of Kuhlman [128]. Examples of comparable optimization codes were already described by Miranda & Brennan [11], Kroo [10] and Veldhuis [93]. These approaches differ from the current analysis in the way the lift distribution is modeled. The authors mentioned above, for example, proposed a technique where the lift distribution is given as a Fourier sine series combined with axial and tangential velocities induced by the propellers (see section 7.2.3).

Using the Trefftz analysis technique, the drag can be calculated by considering the momentum balance of a control surface S which surrounds the configuration Fig. 7.3. In subsequent paragraphs the most important calculation and derivation results will be summarized. Further details about the technique in general can be found in refs. [129, 130, 131, 14]. In the following analysis the effects of compressibility will be neglected since most propeller aircraft operate in the (low) subsonic speed regime.

For a steady, incompressible, inviscid flow the conservation equations of mass, momentum and energy, applied to control volume V surrounded by control surface S become :

$$\iint_S \rho(V \cdot n)dS = 0$$

$$\iint_S \rho V(V \cdot n)dS = -\iint_S (pn)dS + F \tag{7.33}$$

The second equation states that the time rate of change of linear momentum is equal to the sum of the forces acting on the control volume. Here F is the force acting on the fluid inside the control volume (generally zero), ρ is the density, V
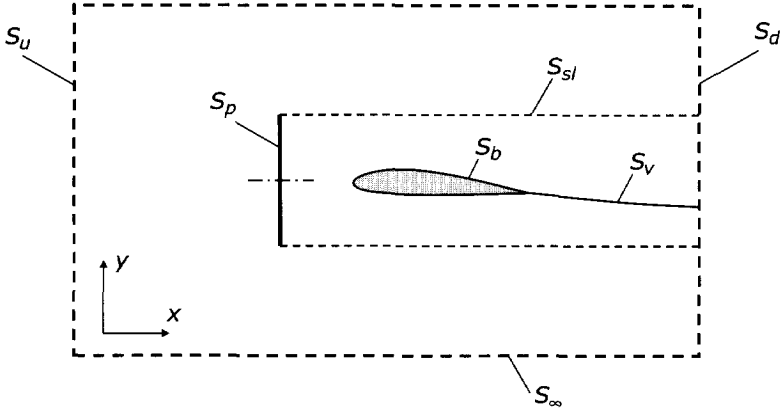
Figure 7.3: *Layout of the control volume and the control surface as used in the Trefftz plane analysis.*

is the velocity vector and n is the outward pointing normal vector to the control surface. Since for the moment the viscous forces acting on a body with surface S_b are neglected, the only resulting force in x-direction will be the induced drag, D_i. The control surface S consists of several sub surfaces, as indicated in Fig. 7.3: $S = S_u + S_d + S_\infty + S_b + S_v + S_p + S_{sl}$. We can now apply some known boundary conditions:

- on S_b : $V \cdot n = 0$

- on S_∞ : $V \cdot n = 0$ and $n_x = 0$

- on S_v : $V \cdot n = 0$ and p is continuous (vortex sheet fully developed)

- on S_{sl} : $V \cdot n = 0$ and p is continuous (stream surface)

Hence the surface integrals (7.33) can be reduced to:

$$0 = \iint\limits_{S_u + S_d} \rho(V \cdot n) dS$$

$$D_i = - \iint\limits_{S_u + S_d + S_p} (pn_x + \rho u(V \cdot n)) dS \tag{7.34}$$

The propeller thrust is defined by:

$$T_{tot} = - \iint\limits_{S_p} (pn_x + \rho u \, (V \cdot n)) \, dS \qquad (7.35)$$

Thus the second integral of (7.34) may be rewritten as:

$$D_i = - \iint\limits_{S_u + S_d} (p \, n_x + \rho u(V \cdot n)) \, dS + T \qquad (7.36)$$

When there is an active propeller with surface S_p there will be an energy increase which may be regarded as negative dissipation. Introducing the velocity potential Φ the induced drag can be written as:

$$D_i = - \iint\limits_{S_u + S_d} \left(pn_x + \rho \frac{d\Phi}{dx} (\nabla \Phi \cdot n) \right) dS + T \qquad (7.37)$$

Let us introduce the perturbation potential, φ, defined as $\Phi = U_\infty x + \varphi_x$, then eq. (7.37) can be further simplified leading to the so-called Trefftz plane analysis. In the Trefftz plane (S_T) it is assumed that the flow is fully developed which means that no velocity gradient and pressure gradient exist in streamwise direction. With $S_D = S_T$, the final result becomes:

$$D_i = \frac{\rho}{2} \iint\limits_{S_T} \left(-\varphi_x^2 + \varphi_y^2 + \varphi_z^2 \right) dS + T \qquad (7.38)$$

which can be further simplified accepting the fact that $\varphi_x^2 = 0$ in the Trefftz-plane. It should be noted that in this analysis , based on inviscid theory, the velocity change that normally occurs in the vortex cores is neglected:

$$D_i = \frac{\rho}{2} \iint\limits_{S_T} \left(\varphi_y^2 + \varphi_z^2 \right) dS + T \qquad (7.39)$$

Now exclude force from eq. (7.39) since the interest is focused to the optimization of the induced drag for a given propeller condition (fixed thrust force and torque). This simplification is allowed as long as the thrust force and the propeller torque do not change significantly when adapting the geometry of the wing behind the propeller. In general, this is the case for all practical designs where the distance between propeller and wing is not small.

The perturbation potential φ is built up of a disturbance due to the wing/body (index b) and a disturbance due to the propeller (index p).

Neglecting $\partial\varphi/\partial x$ (the flow is fully developed), the induced drag (without the thrust contribution) becomes:

$$D_i' = \frac{\rho_\infty}{2} \iint\limits_{S_T} (\varphi_{b_y}^2 + \varphi_{b_z}^2)\, dS + \rho_\infty \iint\limits_{S_T} (\varphi_{b_y}\varphi_{p_y} + \varphi_{b_z}\varphi_{p_z})\, dS +$$
$$\frac{\rho_\infty}{2} \iint\limits_{S_T} (\varphi_{p_y}^2 + \varphi_{p_z}^2)\, dS \qquad (7.40)$$

Using Green's identity the integral over S_T is transformed into an integral over the curve(s) C_T formed by the intersection of the wake and the Trefftz plane.

The first integral of eq. (7.40) is rewritten in the form:

$$\iint\limits_{S_T} \left((\frac{\partial\varphi}{\partial y})^2 + (\frac{\partial\varphi}{\partial z})^2 \right) dS = \int\limits_{C_T} \frac{\partial\varphi}{\partial \mathrm{n}}\varphi\, dC - \iint\limits_{S_T} \varphi \left(\frac{\partial^2\varphi}{\partial y^2} + \frac{\partial^2\varphi}{\partial z^2} \right) dS \quad (7.41)$$

while the second integral becomes :

$$\iint\limits_{S_T} (\nabla\varphi_p \cdot \nabla\varphi_b)dS = \int\limits_{C_T} \varphi\,(\nabla\varphi_p \cdot n)\; dC - \iint\limits_{S_T} \varphi \left(\frac{\partial v_p}{\partial y} + \frac{\partial w_p}{\partial z} \right) dS \quad (7.42)$$

where $\nabla\varphi_p = V_p = (u_p, v_p, w_p)^T$ is the velocity vector induced by the propeller.

At the Trefftz plane the second terms in the right hand side of eq. (7.41) and (7.42) vanish. The jump in the velocity across the wake is equivalent to the local circulation. Hence with $\Delta\varphi = \Gamma$ and $\partial\varphi/\partial n = v_n$, the induced drag in the Trefftz plane becomes:

$$D_i' = \frac{\rho_\infty}{2} \int\limits_{C_T} \Gamma_b(v_{n_b} + 2(v_{n_p}))\, dC + \frac{\rho_\infty}{2} \iint\limits_{S_p} (v_p^2 + w_p^2)dS \qquad (7.43)$$

Three terms can be distinguished:

$$A_i = \frac{\rho_\infty}{2} \int\limits_{C_T} \Gamma_b v_{n_b}\; dC \qquad (7.44)$$

which is the induced drag without the presence of a slipstream

$$A_p = \rho_\infty \int\limits_{C_T} \Gamma_b\, v_{n_p}\, dC \qquad (7.45)$$

which is the propeller-wing interaction effect. And finally:

$$A_s = \frac{\rho_\infty}{2} \iint\limits_{S_p} (v_p^2 + w_p^2)\; dS \qquad (7.46)$$

which is the "swirl loss" of the propeller.

Now eq. (7.43) can be written as a "drag" coefficient:

$$C'_{D_i} = \frac{1}{V_\infty^2 S_{ref}} \int_{C_T} \Gamma_b(v_{n_b} + 2(v_{n_p})) \, dC \; + \; \sum_{k=1}^{N_p} C_k^* \tag{7.47}$$

with :

$$C_k^* = \frac{1}{V_\infty^2 S_{ref}} \iint_{S_p} \left(v_p^2 + w_p^2 \right) \, dS \tag{7.48}$$

and N_p is the number of propeller (2 or 4).

Without further proof it is stated that in an analogue way the following relation can be derived for the lift coefficient:

$$C_L = \frac{2}{V_\infty^2 S_{ref}} \int_{C_T} \Gamma_b \left((V_\infty + u_p) \cos \zeta \right) dC \tag{7.49}$$

where u_p is the axial velocity increase due to the propeller and ζ is the wing dihedral angle. Since we will only deal with the Γ-distribution of the "body" the subscript b will be omitted in the following analysis.

7.3.2 Viscous drag

An optimization in which only the induced drag is minimized, may result in a lift distribution that differs considerably from the one in which the total drag is minimized. The wing profile drag contribution can be found from:

$$C_{D_v} = \frac{1}{V_\infty^2 S_{ref}} \int_{C_T} C_{d_v} \left(V_\infty + u_p \right)^2 c \, dS \tag{7.50}$$

The profile drag coefficient can be determined either through the input of two-dimensional airfoil characteristics or alternatively by using empirical relationships. The relation between local lift and drag coefficient (for a given airfoil) is estimated using a simple quadratic relation:

$$C_{d_v} = f(C_l) = C_{d_0} + f_1 C_l + f_2 C_l^2 \tag{7.51}$$

with the local lift coefficient being :

$$C_l = \frac{1}{c} \left(\frac{2 \left(V_\infty + u_p \right) \cos \zeta}{V_\infty^2} \Gamma \right) = \frac{\Gamma'}{c} \tag{7.52}$$

the viscous drag becomes :

$$C_{D_v} = \frac{1}{V_\infty^2 S_{ref}} \int\limits_{C_T} (V_\infty + u_p)^2 (a_0 + a_1\Gamma + a_2\Gamma^2)dC \tag{7.53}$$

Expressions (7.47), (7.49) and (7.53) may now be employed to find an optimum load distribution ($\Gamma = \Gamma(y)$) in which for a given lift coefficient and propeller setting, the drag coefficient is minimized.

7.3.3   Optimization formulation

With the equations for the vortex drag, the viscous drag and the lift established, the problem of finding the optimum loading distribution remains.

The problem is to find either a minimum induced drag or a minimum total drag, given certain constraints. Typical constraints that may be imposed for a complete aircraft are:

- lift constraint (loading for a target lift coefficient)

- pitching moment constraint (aircraft is trimmed)

- root bending moment constraint (to minimize structural loading and stresses)

Since, in this thesis, the emphasis is on the propeller-wing configuration, the optimization of the spanwise loading distribution will be limited to minimization of the drag for a given, predefined design (or "target") lift coefficient, $C_{L_{des}}$. Hence the problem can be stated in the following way: determine the load distribution function, $\Gamma(s)$ that minimizes the functional $C_{D_i} + C_{D_{visc}}$ that is subject to the lift constraint $C_L = C_{L_{des}}$.

The equations for the induced drag and the viscous drag that are needed in the optimization process are given by eq. (7.47), (7.49) and (7.53).

To perform the optimization an object function is needed that incorporates the constraint given. For this purpose the method of Lagrange multipliers is introduced.

If the function that is to be minimized (extreme value at this point) is defined as the drag coefficient and for the constraint function, J, the lift $C_L - C_{L_{des}}$ is taken, the optimization problem reduces to:

$$\begin{aligned} I &= F + \lambda J \\ &= C_{D_i} + C_{D_{visc}} + \lambda \left(C_L - C_{L_{des}} \right) \end{aligned} \tag{7.54}$$

where the Lagrange multiplier, λ, is to be determined.

As indicated in Appendix G, a necessary condition for a function to have an extremum is that its differential vanishes. Consequently, the necessary condition for

the functional I to have an extremum is that its variation vanishes as well. Given that δy is an arbitrary variation in y, the condition $\delta y = 0$ implies that:

$$f_y - \frac{df_{y'}}{dx} = 0 \tag{7.55}$$

Apparently the parameters of eq. (7.55) can be replaced as follows: $f \mapsto \int C_D$, $y \mapsto \Gamma(s)$, $y' \mapsto \Gamma'(s)$, $x \mapsto s$, where $\int C_D$ represents the total drag integral(s) of both the induced and the viscous drag as given by eq. (7.47) and (7.53). Eq. (7.55) then states:

$$\frac{\partial \int C_D}{\partial \Gamma} = \frac{d}{ds}\left(\frac{\partial \int C_D}{\partial \Gamma'}\right) \tag{7.56}$$

In general (especially when propellers are active) the loading distribution is so complex that it cannot be described by analytical functions. This makes the evaluation of (7.56) in a direct form impossible. Consequently it is obvious that some discretization is needed to solve the optimization problem.

For the point at which the discretization is applied, prior to the solution of the problem, we have two options.

When first the circulation distribution is discretized expressions for the drag and the lift will be found in terms of the unknown discretization variables. Following this approach a set of algebraic equations is obtained the solution of which requires the calculation of double integrals. Because of the rather high calculation effort and the reduced accuracy of this approach the second option, described hereafter, will be employed.

First of all, to form the first variation δI of I with respect to the first variation of the circulation distribution, we write:

$$\Gamma(s) = \Gamma^*(s) + \delta \Gamma(s) \tag{7.57}$$

and

$$\lambda = \lambda^* + \delta \lambda \tag{7.58}$$

where the optimal solution for the circulation distribution is given by $\Gamma^*(s)$ while λ^* is the optimal value for the Lagrange multiplier, λ.

Next, the variations of the object function I, as given by (7.54) is calculated by substitution of the expression for $\Gamma(s)$ and λ from (7.57) and (7.58).

The normal velocity can be written as:

$$v_n(s) = V_\infty^2 S_{ref} \int g(s,t)\Gamma(t)dt \tag{7.59}$$

where $g(s,t)$ is the influence function that expresses the effect of the gradient in the circulation distribution at the spanwise station t on the normal velocity at station s.

Then, $I + \delta I$ becomes:

$$
I + \delta I = \frac{1}{V_\infty^2 S_{ref}} \int_{C_t} (\Gamma^*(s) + \delta\Gamma(s)) g(s,t) (\Gamma^*(t) + \delta\Gamma(t)) ds dt +
$$

$$
\frac{2}{V_\infty^2 S_{ref}} \int_{C_t} (\Gamma^*(s) + \delta\Gamma(s))(V_p \cdot n(s)) ds + \sum_{k=1}^{N_p} C_k^* +
$$

$$
\frac{1}{V_\infty^2 S_{ref}} \int_{C_t} (V_\infty + u_p(s))^2 \left(\begin{array}{c} a_0(s) + a_1(s)\,(\Gamma^*(s) + \delta\Gamma(s)) + \\ a_2(s)\,(\Gamma^*(s) + \delta\Gamma(s))^2 \end{array} \right) ds +
$$

$$
(\lambda^* + \delta\lambda) \left(\frac{2}{V_\infty^2 S_{ref}} \int_{C_t} (\Gamma^*(s) + \delta\Gamma(s))\,(V_\infty + u_p(s))^2 \cos\nu\, ds - C_{L_{des}} \right)
$$

$$
(7.60)
$$

As stated earlier, the necessary condition for attaining an extremum of the object function (minimum drag) is that its variation δI vanishes for arbitrary values of $\delta\Gamma(s)$ and $\delta\lambda$. The variation δI can be found by subtracting I from eq. (7.60). Neglecting second order terms like $\delta\Gamma^2$ and $\delta\Gamma\delta\lambda$ this leads to an integral for δI whose integrand must be zero. Hence:

$$
\frac{2}{V_\infty^2 S_{ref}} \int_{C_t} g(s,t)\Gamma^*(s) ds + \frac{(V_\infty + u_p(s))^2}{V_\infty^2 S_{ref}} (a_1(s) + 2a_2(s)\Gamma^*(s)) +
$$

$$
\frac{2\lambda^*}{V_\infty^2 S_{ref}}\Gamma^*(s)\,(V_\infty + u_p(s)) \cos\nu = 0
$$

$$
(7.61)
$$

This equation, containing the unknown Lagrange multiplier and the unknown optimum circulation distribution $\Gamma^*(s)$, must hold for all values of the spanwise coordinate, s.

Combined with the constraint $C_L = C_{L_{des}}$:

$$
\frac{1}{V_\infty^2 S_{ref}} \int_{C_t} \Gamma^*(s)\,(V_\infty + u_p(s)) \cos\nu ds = C_{L_{des}}
$$

$$
(7.62)
$$

eq. (7.61) leads to a system of equations that can be constructed for all spanwise stations defined. Note that in the inviscid case and for the propeller off condition we have $u_p = v_p = w_p = C_{d_v} = 0$ eq. (7.61) reduces to:

$$
v_n + \lambda \cos\nu = 0
$$

$$
(7.63)
$$

which is the classical result of Munk [127] stating that the normal velocity is constant along the span and proportional to the cosine of the dihedral angle of the wing.

7.3.4   Numerical approach

A direct integration in eq. (7.61) is possible only for simple bound circulation distributions. With the propellers active a strong deformation of the elliptic-like distribution is, however, expected which makes discretization based on an approximate shape of the circulation distribution necessary. An example of such model can be found in refs [128, 129, 130, 131].

To perform the discretization of the governing equations the contour C_t in the Trefftz plane is divided into linear elements referred to as panels.

Assuming the strength of the vortex sheet to change linearly in spanwise direction the bound circulation becomes a quadratic function of s because $\gamma(s) = \partial\Gamma/\partial s = c_0 + c_1 s$. Looking at eq. (7.61) we need to work out the integral over the function $g(s, t)$ which represents the downwash at location s.

With the given quadratic distribution of the circulation an approach comparable to the one described by Munk [127] is employed. The situation for the panel i is sketched in Fig. 7.4.

For $\gamma(s)$ at location s_l and s_r we may write respectively:

$$\gamma(s_l) = c_{0,i} = \frac{\Gamma_{i-1} - \Gamma_i}{h}$$
$$\gamma(s_r) = c_{0,i} + c_{1,i}s' = \frac{\Gamma_i - \Gamma_{i+1}}{h} \tag{7.64}$$

where $h = \Delta s_l = \Delta s_m = \Delta s_r$ is the panel width. In eq. (7.64) the coefficient $c_{0,i}$ and $c_{1,i}$ can easily be obtained. To find the bound circulation at the local coordinate s' a simple integration suffices:

$$\Gamma(s') = \int_{s'} \gamma(s')ds' + \Gamma(s_l) \tag{7.65}$$

Once the piecewise varying coefficients, $c_{m,k}(m = 1, 2 \; ; \; k = 1, 2, ..., n)$ are available the normal velocity due to a single panel element, j at location s can be obtained by applying the relation derived by Munk that is based on the panel layout sketched in Fig. 7.4:

$$v_{n_j}(s) = \int_{p_j} \frac{c_{0,j} + c_{1,j}s'}{4\pi |r|} \cos(\beta - \alpha_i)\, ds' \tag{7.66}$$

where β, α and $|r|$ are functions of s.

Expanding eq. (7.66), based on the geometry given in Fig. 7.5 gives the normal velocity due to a panel $i(p_i)$ on control point j:

$$v_{n_{j,i}}(s) = \Gamma_{i-1} \int_{p_i} B_{i,j}l_{1,i}(s)ds + \Gamma_i \int_{p_i} B_{i,j}l_{2,i}(s)ds + \Gamma_{i+1} \int_{p_i} B_{i,j}l_{3,i}(s)ds \tag{7.67}$$
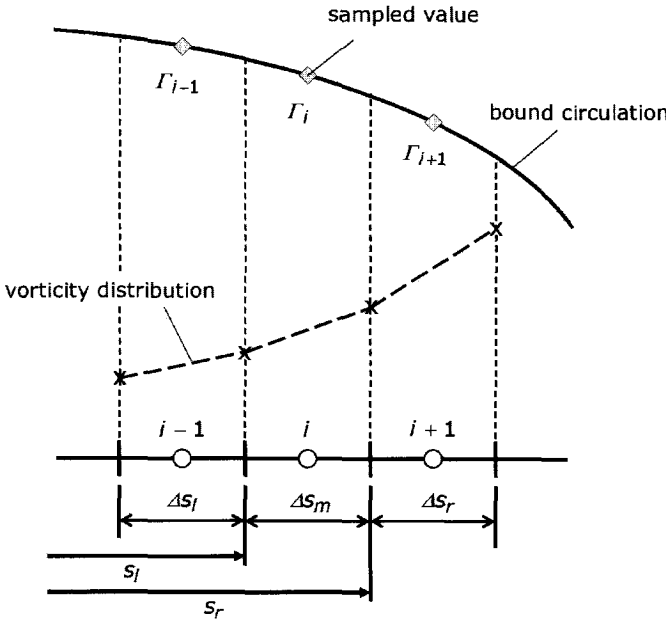
Figure 7.4: *Distribution of bound circulation and vorticity around panel i.*

where:

$$l_{1,i} = 2\left(\frac{s}{\Delta s_m(\Delta s_l + \Delta s_m)} + \frac{1}{\Delta s_l + \Delta s_m}\right)$$

$$l_{2,i} = 2\left(\frac{1}{\Delta s_l + \Delta s_m} + \frac{1}{\Delta s_m + \Delta s_r}\right)\frac{s}{\Delta s_m} - 2\left(\frac{1}{\Delta s_l + \Delta s_m}\right) \qquad (7.68)$$

$$l_{3,i} = -2\left(\frac{s}{\Delta s_m(\Delta s_r + \Delta s_m)}\right)$$

and $B_{i,j}$ is a geometrical parameter that depends solely on the panel distribution layout:

$$B_{i,j} = \frac{\cos\alpha_i\left\{\begin{array}{c} y_{p_2} - y_{p_1} + \\ s'\cos(\alpha_j) \end{array}\right\} + \sin\alpha_i\left\{\begin{array}{c} z_{p_2} - z_{p_1} + \\ s'\sin(\alpha_j) \end{array}\right\}}{s'^2 + 2s'\left\{\begin{array}{c} \cos\alpha_j\,(y_{p_2} - y_{p_1}) + \\ \sin\alpha_j\,(z_{p_2} - z_{p_1}) \end{array}\right\} + (y_{p_2} - y_{p_1})^2 + (z_{p_2} - z_{p_1})^2} \qquad (7.69)$$

The terms in the integrals of (7.104) are all in the form:
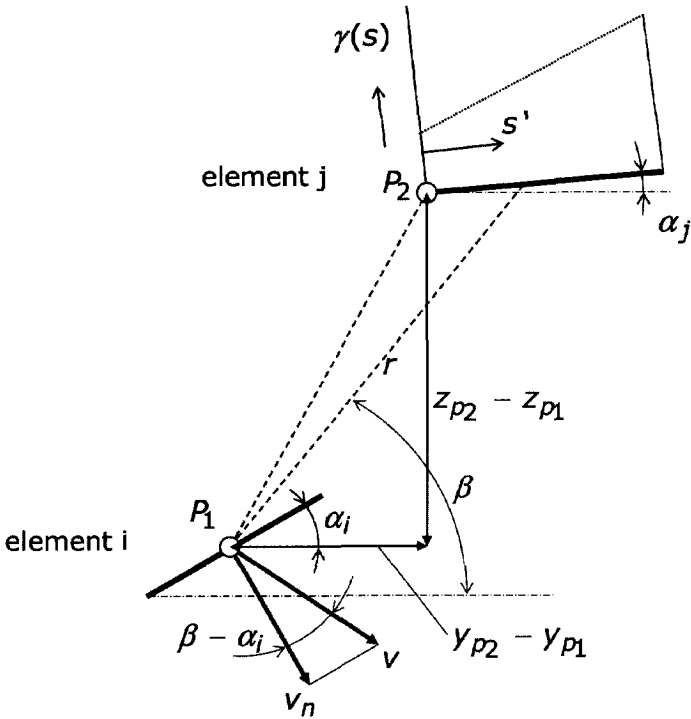
Figure 7.5: *Panel layout for the calculation of the downwash velocity on panel i.*

$$\Gamma_k \int \frac{a_k(s)}{b_k(s)} ds \quad k = i-1, i, i+1 \tag{7.70}$$

where:

$$
\begin{aligned}
a_k(s) &= c_{1,k} + c_{2,k}s + c_{3,k}s^2 \\
b_k(s) &= d_{1,k} + d_{2,k}s + d_{3,k}s^2
\end{aligned}
\tag{7.71}
$$

The expression (7.67) for the normal velocity can now be written as a summation of panel integrals. With the implementation of the discretization outlined above the following expression for the total normal velocity induced at panel j:

$$v_{n_j} = \sum_{p=1}^{n} \sum_{k=i-1}^{i+1} \Gamma_k \int \frac{a_k(s)}{b_k(s)} ds \tag{7.72}$$

Here p is the panel counter.

Substitution of this expression in the extremizing condition of eq. (7.61) yields:

$$\frac{2}{V_\infty^2 S_{ref}} \sum_{p=1}^{n} \sum_{k=i-1}^{i+1} \Gamma_k^* \int_p \frac{a_k(s)}{b_k(s)} ds + \frac{(V_\infty + u_p(s))^2}{V_\infty^2 S_{ref}} \left(a_1(s) + 2a_2(s)\Gamma^*(s)\right) +$$

$$\frac{2\lambda^*}{V_\infty^2 S_{ref}} \Gamma^*(s) \left(V_\infty + u_p(s)\right) \cos\nu = 0 \tag{7.73}$$

Moreover, the constraint for the lift coefficient can be replaced by a summation as well:

$$C_{L_{des}} = \frac{2}{V_\infty^2 S_{ref}} \sum_{p=1}^{n} \Gamma_p^* \left(V_\infty + u_p\right)^2 \cos\nu \Delta s_p \tag{7.74}$$

where Δs_p is the panel width of panel p. Eq. (7.73) and (7.74) constitute a system of linear equations expressed in the unknown parameters Γ^* and λ^* which can be solved using standard techniques.

With the optimum loading known the relevant aerodynamic coefficients of the propeller-wing configuration can be calculated with relations (7.47),(7.49) and (7.53) discussed.

7.3.5   Calculation results

Initial calculations   In the next sections some calculation results of both methods presented above will be discussed. For convenience the method based on the Fourier analysis (program *optimizer*) is referred to as the F-method whereas the optimization approach based on the Trefftz plane analysis combined with the Lagrange multiplier technique is denoted as the T-method in subsequent sections.

To validate the optimization program(s) first the PROWIM model was analysed. The propeller induced velocities are adapted from the measured flow-field behind the tractor propeller of the APROPOS configuration.

During the initial calculations, an axis-symmetrical slipstream was used which is equal to the case of a zero (effective) propeller angle of attack. Furthermore, induced flow angle at the propeller plane due to the wing upflow is neglected.

The configuration was optimized for the constrained lift value $C_{L_{des}}$ = 0.4.

An easy check on the accuracy of the optimization programs can be obtained by considering the propeller-off case. Without the slipstream distorting the incoming flow to the wing, the optimum loading distributions that are predicted should be elliptical and the span efficiency factor, defined as:

$$e = \frac{C_L^2}{\pi A C_{D_i}} \tag{7.75}$$
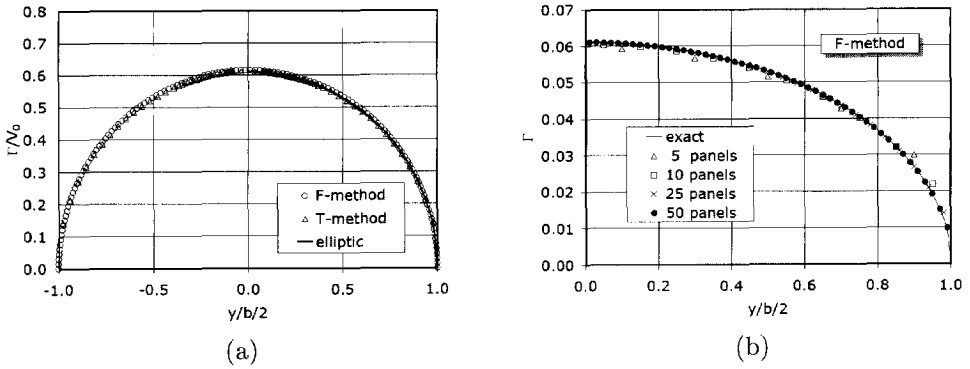
Figure 7.6: *Optimized loading distribution for a straight wing without propeller active as predicted with both the F- and the T-method ; (a) comparison of methods ; (b) effect of number of panels (F-method).*
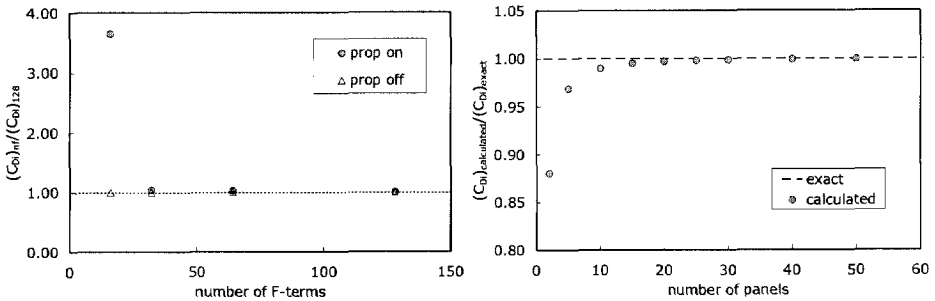
Figure 7.7: *Effect of the number of Fourier terms in the F-method and the number of panels in the T-method ; Left: F-method , prop on ($a_t = 0.1$ over the complete propeller radius) and prop-off ; Right: T-method, prop-off.*

should become 1.

In Fig. 7.6 the results for a propeller-off case are shown. As seen in Fig. 7.6a indeed the elliptical loading is found.

Fig. 7.6b and Fig. 7.7 show clearly that the accuracy of both methods depends on the number of control points (i.e. number of Fourier terms) in the F-method or the number of panels in spanwise direction in the T-method. For the propeller off case the F-method reaches the theoretical value of $e = 1$ already for 1 Fourier term because of

(a)   (b)
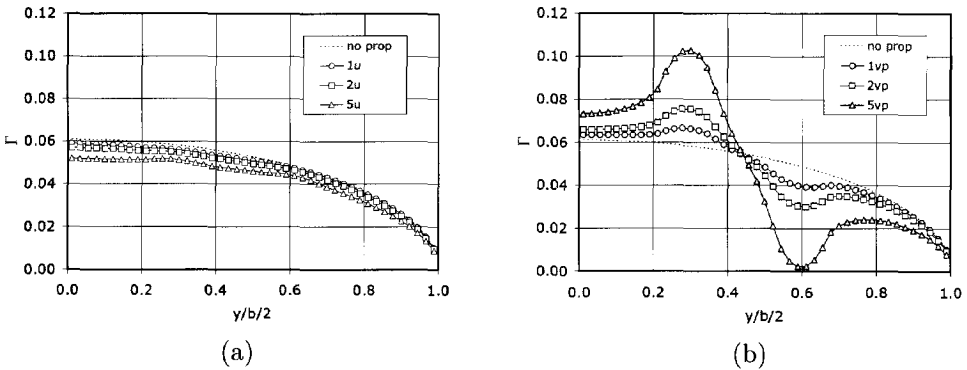
Figure 7.8: *Effect of the axial (a) and the tangential velocity component (b) on the lift distribution of the optimized APROPOS configuration : both components are multiplied by factors 1,2 and 5.*

its procedure that is capable of exactly reproducing the elliptical loading (see section 7.2). For the case with a propeller running, however, the number of Fourier-terms (F-terms) must be increased considerably. It appears that the change of the induced drag versus the nrumber of F-terms levels of at 128 terms. The accuracy the T-method can be found in Fig. 7.7 (prop off case). The solution converges to the theoretical optimum of $e = 1$ with increasing number of panels. With a model containing 25 panels the induced drag is already computed with an accuracy of 0.2%.

Effect of slipstream velocity components When the propeller slipstream is included in the optimization process, the optimal distributions will change and the elliptical distribution of the clean wing configuration is distorted. To get an idea about the effect of the individual velocity components on the optimal circulation distribution both the axial and the swirl component were changed by multiplying the original components depicted in Fig. 7.8 with an arbitrary factor (1,2 and 5).

When only the axial velocity is taken up in the optimization process, the circulation distribution starts to deviate from the expected elliptical one (7.8a). An increase of the axial velocity will result in an increase of the lift on the geometry. However, due to the lift constraint , the mean value of the circulation is decreasing when the axial velocity is increased.

For the swirl velocity a quite different result is obtained, as illustrated in Fig. 7.8b. In the wing upwash region, the local circulation is increased and for the wing downwash region, the local circulation is decreased. This effect, due to a change in local angle of attack, is strengthened when the swirl velocity is increased, as expected.
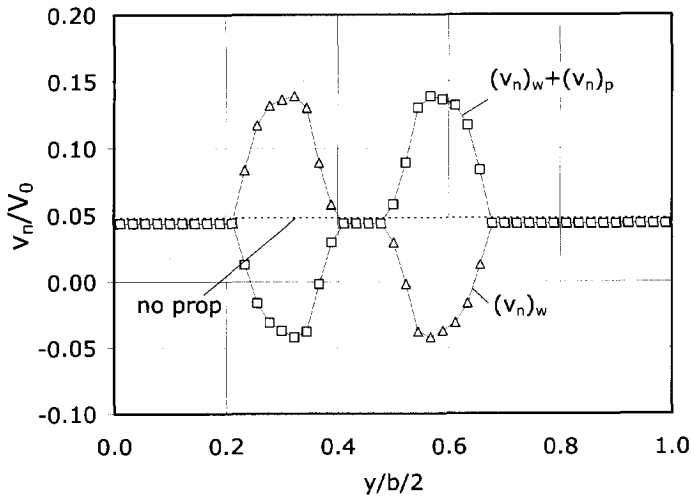
Figure 7.9: *The downwash velocity, v_n/V_∞, in the Trefftz plane behind the APROPOS model at $C_{L_{des}} = 0.4$ for an inboard up rotating propeller ; effect of the wing (w) and the propeller swirl velocity (p).*

Downwash and induced drag The optimizated propeller-wing configuration is obtained when the downwash distribution reaches an optimum. In this respect it is interesting to consider the downwash velocities that are calculated by the optimization program.

In Fig. 7.9 the downwash at the Trefftz plane as calculated with the T-method is depicted for the inboard-up rotating propeller of APROPOS at $C_{L_{des}} = 0.4$.

A lift increase at the up-going blade side results in an increase of the downwash behind the wing. When the downwash due to the swirl is now superimposed, the resulting downwash is opposite to the one directly induced by the propellers at position of the wing.

The local induced drag as calculated with the T-method is presented in Fig. 7.10 for the inboard-up rotating propeller.

As can be seen, the induced drag at the upwash region results in a negative local induced drag contribution due to a more forward rotated lift vector. In the downwash region, the local induced drag is increased. The positive and negative drag contributions at both sides of the thrust axis are of unequal magnitude due to the gradient in wing lift distribution. In case of the running propeller a considerable wing drag reduction can be established when the forward rotated force is larger than the
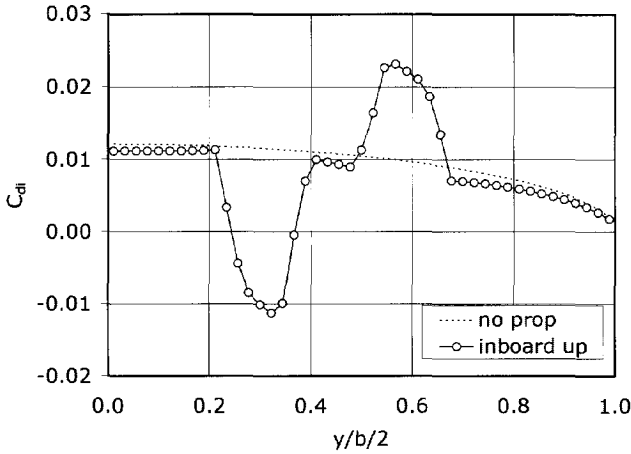
Figure 7.10: *Comparison of the spanwise distribution of the induced drag coef-*
ficient for the wing-only and for an inboard up rotating propeller
calculated with the T-method; APROPOS at $C_{L_{des}} = 0.4$.

Table 7.2: *The effect of the rotation direction on the induced drag of APROPOS*
at $C_{L_{des}} = 0.4$

Case	C_{D_i}
Propeller off	0.00954
Inboard up rotation	0.00781
Outboard up rotation	0.00900
Co-rotating right	0.00840

backward rotated force.

The resulting induced drag values are presented in Table 7.2. As can be seen, the inboard-up rotating propellers lead to a most favourable configuration with respect to the minimum induced drag. The outboard-up rotating case results in the least favourable configuration. For the co-rotating case, both the positive and negative contributions of the starboard and port wing result in an intermediate induced drag.

Viscous drag contribution   To get further insight in the effects of the viscous drag component in the optimization process some additional calculations on the APROPOS
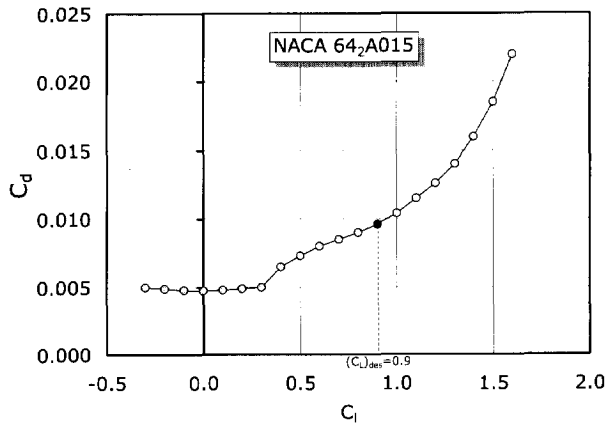
Figure 7.11: *Drag curve of the NACA 64_2-A015 airfoil taken from ref. [132], used in the optimization process to express the effects of the viscous drag component.*

model were performed.

First of all the drag-curve of the airfoil NACA 64_2A015, that is used in the model was estimated based on data given in ref. [132] (see Fig. 7.11).

As can be seen at low lift coefficients, between -0.3 and 0.3, the curve is rather flat ("low drag bucket"). Consequently, an optimization with a constrained lift value in that particular range will hardly result in a changed optimal lift distribution. To demonstrate the influence of the profile drag into the optimization results the constrained value of the design lift coefficient for the current calculation, is set equal to $C_{L_{des}} = 0.9$.

The calculation results obtained with the T-method in the cases with and without the profile drag contribution is depicted in Fig. 7.12 for the inboard up rotating propeller.

When both drag contributors are used in the optimization process, the optimal lift distribution is somewhat changed compared to the inviscid case. Due to the high values of the local angle of attack, some (though limited) viscous drag effects occur. Apparently the inclusion of the profile drag results in a reduction of the high local lift values and a shift of the loading to a more outboard position.

Fig. 7.13 shows the influence of the profile drag in the optimization process on both the induced and profile drag distribution for an inboard up rotating propeller. The changes, ΔC_{d_i} ("dCdi") and ΔC_{d_v} ("dCdv"), are the result of the optimization including the viscous effects minus the result based on the induced drag only. The
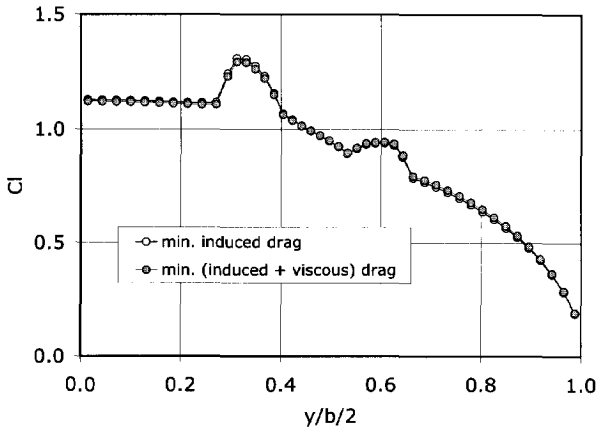
Figure 7.12: *Effect of the inclusion of the viscous drag component in the opti-mization process ; APROPOS at $C_{L_{des}} = 0.9$.*

Table 7.3: *Effect of the viscous drag component on the wing drag coefficient for various optimization cases of APROPOS at $C_{L_{des}} = 0.9$.*

Case	Minimization	C_{D_i}	C_{D_p}	$C_{D_{tot}}$
Inboard up	C_{D_i}	0.04371	0.01067	0.05438
Inboard up	$C_{D_i} + C_{D_p}$	0.04373	0.01063	0.05436
Outboard up	C_{D_i}	0.04629	0.01054	0.05683
Outboard up	$C_{D_i} + C_{D_p}$	0.04631	0.01051	0.05682

local profile drag distribution is calculated afterwards. Fig. 7.13 shows clearly that the local profile drag is reduced on the upwash region due to a decrease of the local lift values resulting in a reduction of the local induced drag. On the outboard region of the wing, where a lower lift is found than on the inboard region, both the local induced drag and the local profile drag increase.

The values of the drag coefficients of the wing are given in Table 7.3 for both the inboard-up as well as the outboard-up rotating propeller. It should be noted that the differences are very small for this test case. Nevertheless, it is clear that for the inboard up rotating propeller the induced drag is larger when the sum of the induced drag and the profile drag is minimized than when the induced drag alone is optimized.
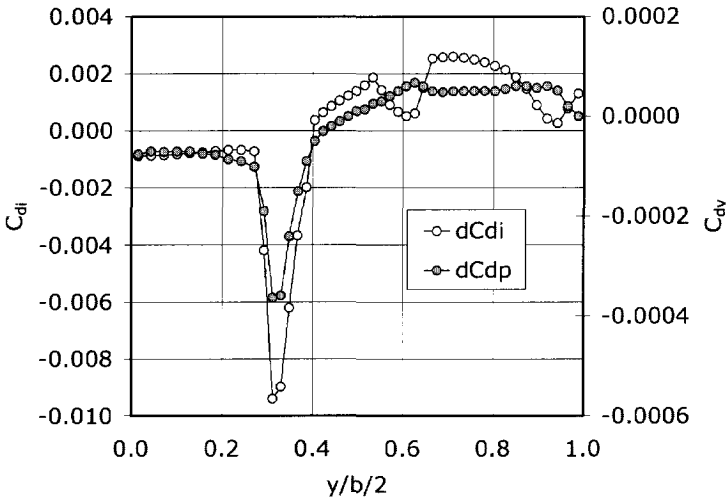
Figure 7.13: *Spanwise distribution of changes in induced and the profile drag coefficient due to inclusion of the viscous drag contribution in the optimization process ;APROPOS at $C_{L_{des}} = 0.9$.*

However, the profile drag becomes smaller towards a more optimized value. The total drag, as a result of the optimization of the sum of the induced and viscous drag, is less than it would have been if only the induced drag was minimized and the viscous drag was added afterward.

Optimization of F50-like configuration   The previous optimization results on a simple propeller-wing model showed the possibilities to obtain a higher performance when the wing is changed according to the typical impact that the propeller has on the wing. The APROPOS layout, though, does not represent a very practical configuration compared to modern turbo-props.

Hence, to estimate the possible effects of the wing optimization a more realistic propeller wing configuration is investigated. For this purpose a typical Fokker 50 like configuration (further denoted as F50 model) was selected (Fig. 7.14).

Two typical cases were investigated : the so-called "high speed case" and the "low speed case" (Table 7.4).

The slipstream data for these cases, which were taken from Janssen [133], are symmetrical with respect to the propeller axis i.e. the propeller is positioned perpendicular to the local flow. Hence it is assumed that the upflow in front of the wing is compensated for.

Table 7.4: *Flight conditions for a typical low speed and high speed case of the Fokker 50 aircraft [133] as employed in the optimization process.*

Parameter	high speed	low speed
density, $\rho[\text{kg/m}^3]$	0.934	0.872
temperature, $T[\text{K}]$	264	261
true airspeed, $TAS[\text{m/s}]$	119.5	75
revolutions per second, $n[\text{Hz}]$	20	20
blade angle, $\beta_{0.75R}[\,^\circ\,]$	37.61	33.78
advance ratio, J	1.633	1.025
design lift coefficient, $C_{L_{des}}$	0.6	1.2
thrust coefficient, T_c	0.10	0.60

The effect of the rotation direction on the optimal lift distribution was investigated by examining three different cases:

- inboard up rotating propellers (Case A)

- outboard up rotating propellers (Case B)

- co-rotating propellers (Case C)

Looking at the current fleet of turbo-prop aircraft, we see that the configuration with two co-rotating propellers is the actual situation (like the *F50*) for most aircraft. The (unconventional) inboard up and outboard up (*BA Jetstream 41*) rotation case may be beneficial to reduce trimming drag and directly enhance the performance of the aircraft.

Propeller rotation direction   In Fig. 7.16 the optimum bound circulation distribution and the lift coefficient distribution respectively as calculated with the T-method, are presented for the F50 case.

In this case the optimization problem was limited to finding minimum induced drag for a given lift coefficient ($C_{L_{des}} = 0.6$ for the high speed case and $C_{L_{des}} = 1.2$ for the low speed case). As was found for the APROPOS model the circulation distribution differs significantly from the elliptical one that is found for a clean wing configuration due to the action of the propeller. Both the local circulation strength and the local lift coefficient show a jump going from the inboard to the outboard side of the wing, since the magnitude of the lift vector tilted forward is bigger than the one tilted backward. As a consequence the propeller produces both positive and negative contributions to the drag induced at the spanwise locations. The negative
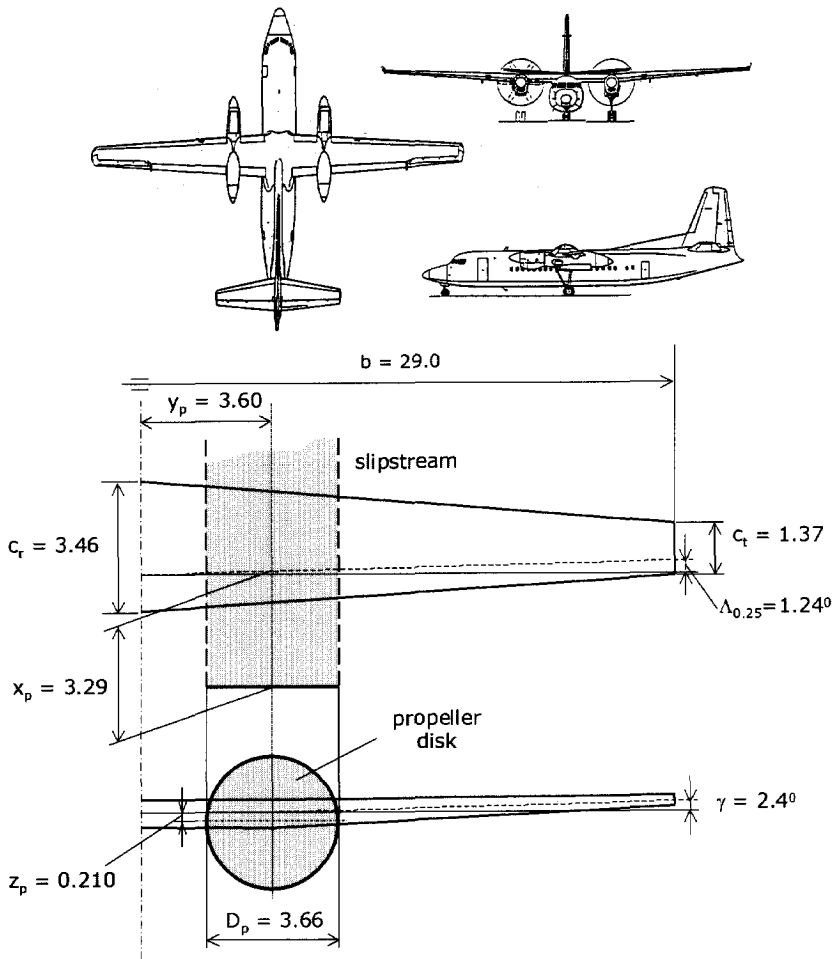
Figure 7.14: *Fokker 50 configuration investigated in the optimization process.*

contribution at the up going blade (UBS) side exceeds the positive contribution at the downgoing blade side (DBS) resulting in the reduction of the overall induced drag (Fig. 7.18).

The effects described are directly related to the selected form of the spanwise lift distribution which shows a negative gradient going from the wing root to the wing tip. Thus the best rotation direction seems to be prescribed by the form of the spanwise lift distribution. In case of a backward swept wing, where the root lift is generally
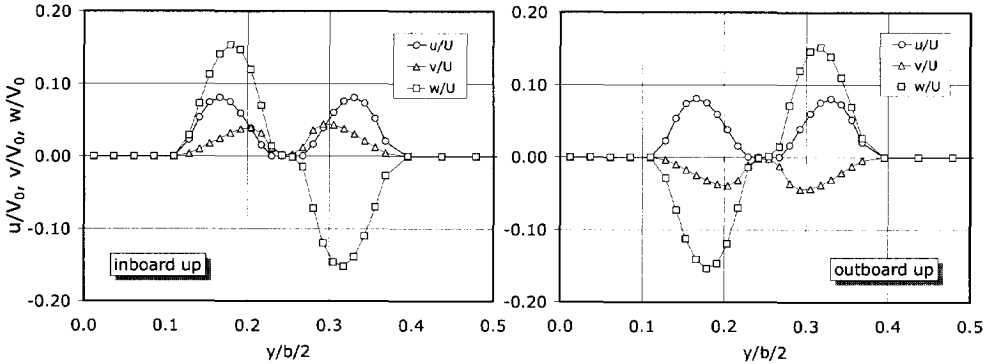
Figure 7.15: *Slipstream velocity distributions applied for the F50 high speed case ; Left: inboard up rotation ; Right: outboard up rotation.*
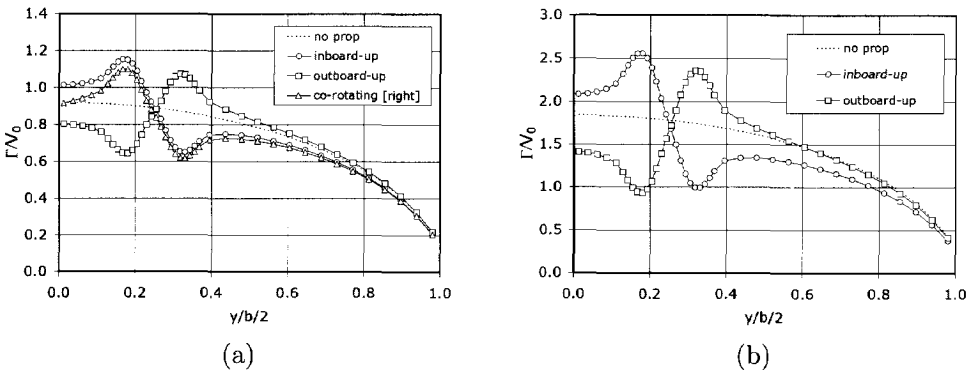
Figure 7.16: *Optimal spanwise bound circulation distribution for different rotation directions ; F50 model at $C_{L_{des}} = 0.6$; (a) high speed case ; (b) low speed case.*

smaller than the lift at the tip, outboard up rotation could be beneficial.

For the inboard up rotating propeller the local profile drag contribution is sketched in 7.19. The "scrubbing drag", which is the net profile drag increase due to the higher dynamic pressure in the slipstream is clearly visible. The higher value at the inboard side is the result of the higher lift coefficient in this area compared to the outboard side.
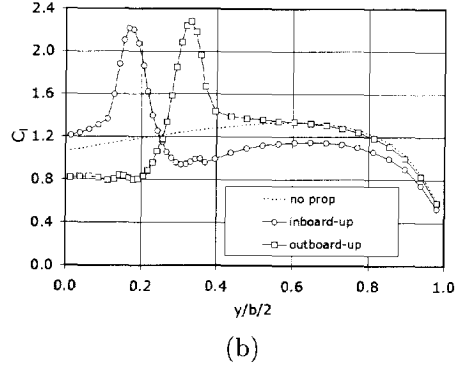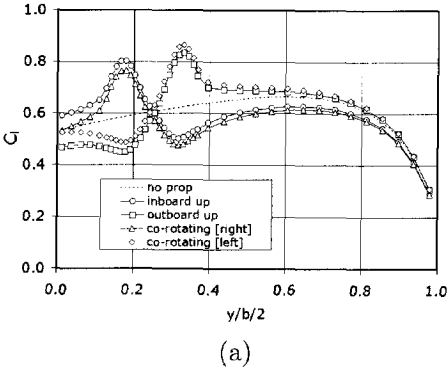
Figure 7.17: *Optimized local lift distribution for the F50 model ; (a) high speed case ; (b) low speed case*
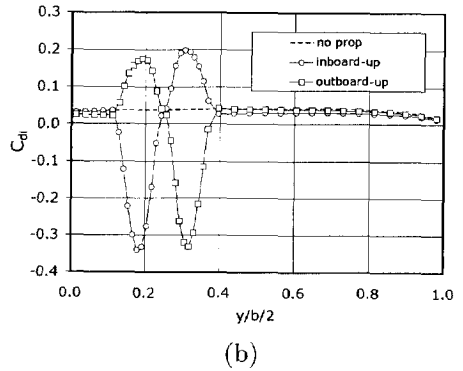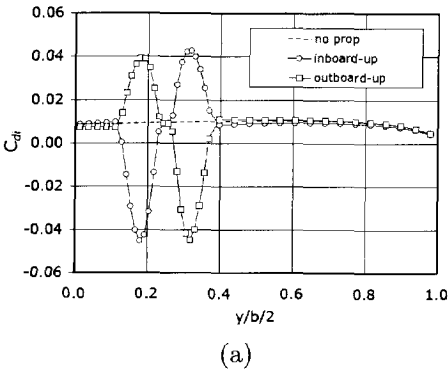
Figure 7.18: *Induced drag distribution for optimized loading on F50 model ; (a) high speed case ; (b) low speed case.*
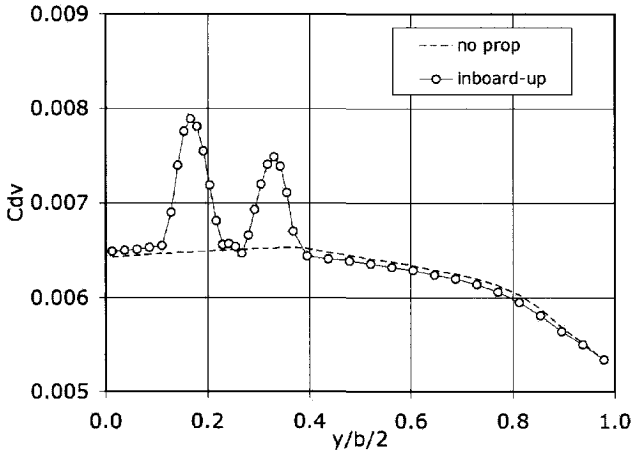
Figure 7.19: *Distribution of the profile drag coefficient for the optimized loading of the Fokker 50 in the high speed case ; inboard up rotation.*

Optimum twist and chord distribution   As described in eq. (7.29) the sectional shape can now be adapted to realize the optimum lift distribution. In Fig. 7.20 the optimum twist distribution is presented when the local chord and airfoil shape are left unaltered. The resulting maximum twist angle is about 4° for the high speed case and 10° for the low speed case. These strong differences in the twist distributions indicate that the optimized wing geometry can only be attained for a specific flight condition (generally the cruise condition). Since the mission fuel required is mainly determined by the cruise phase of the airplane, the optimum should be sought for the cruise lift coefficient. It is clear that the twist distribution, as given in Fig. 7.20, should be "smoothed" resulting in a wing efficiency value lower than the given optimum.

In 7.3.5 the optimum local chord distribution for the high speed case is sketched in case the twist is left unchanged. Clearly this results in very unrealistic chord values. Hence, a twist and a camber adaptation seem to be the only acceptable design variables.

It should be remarked that for the low speed case the relative magnitude of the slipstream velocities has increased compared to the high speed case. This makes the results somewhat less accurate since in the Trefftz plane analysis the perturbation velocities were assumed to be small. Due to the higher slipstream velocities the wing induced drag in the low speed case with inboard up rotation is about 60 counts lower than for outboard up rotation. For the high speed case this influence is limited to approximately 10 counts in favor of the inboard up rotation case (Table 7.5).
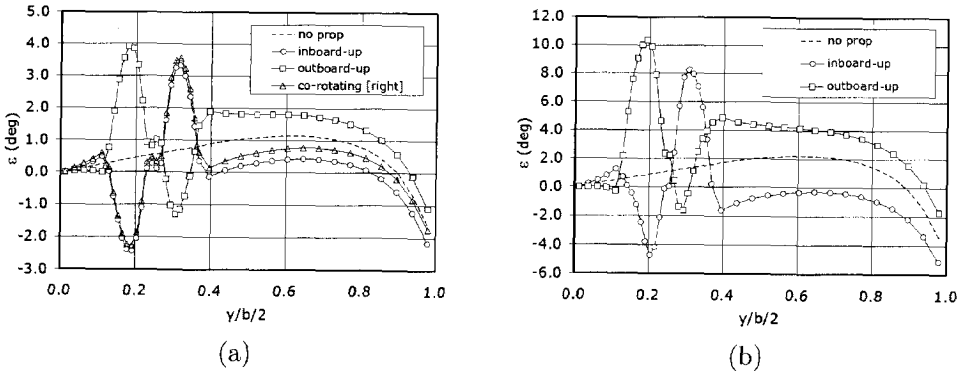
Figure 7.20: *Optimum twist distribution for the high speed case of the Fokker 50 aircraft ; (a) high speed case ; (b) low speed case.*
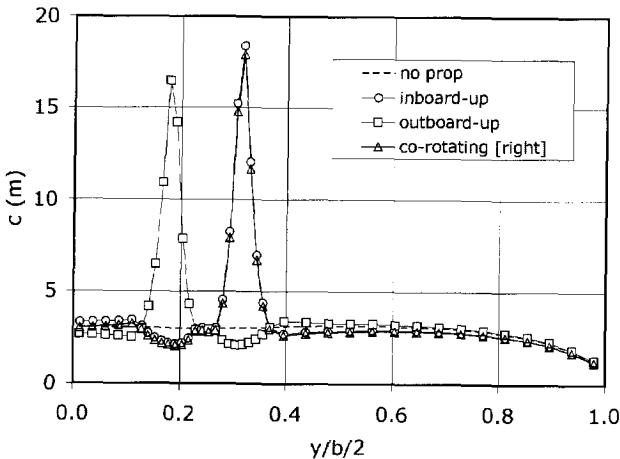
Figure 7.21: *Optimum chord distribution for the high speed case of the Fokker 50 aircraft at $C_{L_{des}} = 0.6$.*

Propeller at angle of attack As indicated by the experiments on the PROWIM model, the wing performance may be significantly influenced by the propeller angle of attack with respect to the wing reference chord line. The so-called PTD-configuration (propeller-tilt-down) used by Veldhuis [12, 93] suggests a reduction of overall wing induced drag.

Table 7.5: *Effect of the propeller rotation direction on the lift and drag coefficient for the F50 high speed case (original and optimized configuration) at $C_{L_{des}} = 0.6$.*

Rotation	Configuration	α	C_L	C_D
inboard-up	original	-0.925	0.6	0.012744
outboard-up	original	-0.850	0.6	0.013358
inboard-up	optimized	-1.400	0.6	0.012216
outboard-up	optimized	-1.400	0.6	0.012946
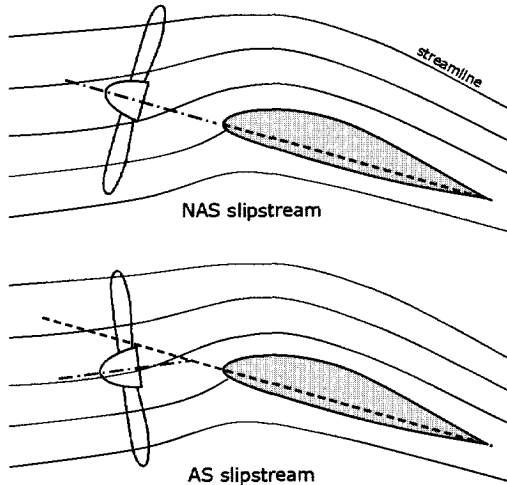
Figure 7.22: *The generation of an non-axi-symmetrical (NAS) and axi-symmetrical (AS) slipstream as a result of the propeller angle of attack with reference to the local streamlines.*

To quantify the effects of the propeller angle of attack in the optimization process a test with both an axi-symmetrical (AS) slipstream and a non-axi-symmetrical (NAS) (see Fig. 7.22) slipstream was performed with the F-method . In this case the effect of the viscous drag component was not taken into account and the optimization of the loading distribution was performed for a design lift coefficient of $C_{L_{des}} = 0.4$. The tangential slipstream velocities that were used for a typical F50-case are depicted in Fig. 7.23

Note that the NAS slipstream represents the case where the propeller axis is fixed
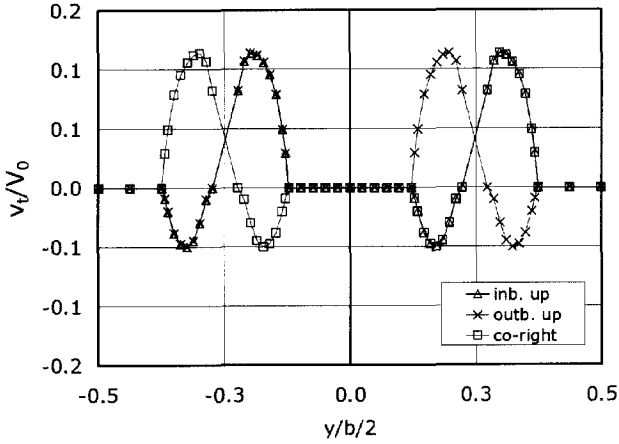
Figure 7.23: *Example of non-axi-symmetrical slipstream (NAS) tangential velocity distributions used in the optimization of an F50 model.*

to the wing at an angle of $\alpha_p = 0°$ with reference to the wing reference chord line. Hence the effective propeller angle of the wing becomes positive due to both the positive wing angle of attack (required to obtain the design lift coefficient) and the upflow in front of the wing due to the positive wing loading. Contrary to this situation the AS slipstream implies that the propeller axis is always pointing in the direction of the local flow (Fig. 7.22).

The wing efficiency as calculated by the F-method is given in Fig. 7.24 for both slipstream distributions and the three cases, A, B and C mentioned earlier. For the AS slipstream only a slight difference between the 3 cases is found, case B being the most promising. Apparently the efficiency of the wing increases as the propeller is brought down to create a more symmetrical slipstream compared to the one obtained with a positive effective propeller angle of attack, $\alpha_{p_{eff}} > 0$.

The swirl velocities used in the calculations for the AS slipstream are equal on both sides of the propeller axis. As a consequence due to the relatively high downwash generated by the downgoing blade the performance benefit resulting from tilting the lift vectors almost vanishes. Accordingly, a swirl velocity distribution with lower values at the DBS and higher values at the UBS should increase the wing efficiency factor.

In the case of the AS slipstream, the effect of the propeller induced flow field results in wing efficiency factor that exceeds the value 1 found for elliptic loading distributions for wing-only configurations. The reason for this performance increase relative to the
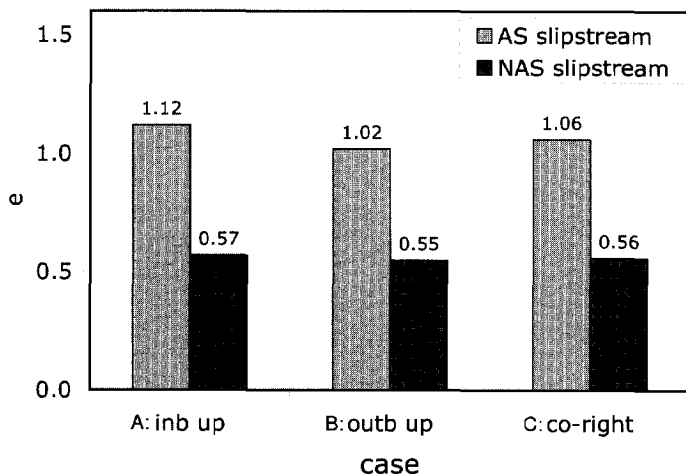
Figure 7.24: *Wing efficiency of cases A,B and C for the axi-symmetrical (AS) and the non-axi-symmetrical (NAS) slipstream* ($\alpha_{p_{eff}} > 0°$) *for the F50 model at* $C_{L_{des}} = 0.4$.

"clean" elliptic wing loading is the propeller induced flow field. It should be remarked that the theoretical maximum of $e = 1$ can be derived for a wing in an undisturbed flow field with a flat trailing wake. When the condition of the oncoming flow changes, through action of the propeller, there is no reason why the optimum value of $e = 1$ should not be exceeded. Kroo [10] subscribes this phenomenon in his theory.

To increase the performance of the propeller-wing configuration further, a logical consequence from this analysis would be to generate a swirl velocity distribution with even more favorable characteristics.

When α_p becomes more negative, the local blade angle of attack of the downgoing blade increases while that of the upgoing blade becomes smaller. This results in an asymmetrical slipstream. Since the lift vector at the side of higher local lift coefficient is tilted forward and the lift vector at the other side is tilted backward a net drag reduction remains. Accordingly, a swirl velocity distribution with lower values at the DBS and higher values at the UBS should increase the wing efficiency factor. Besides this, the whole slipstream will be placed at an angle which attenuates the forward tilting process (resulting in increased leading edge suction) at both sides of the nacelle.

The obvious way to accomplish this is utilization of a bigger negative propeller angle of attack (propeller tilt down). In this way two beneficial effects are combined. First the swirl distribution itself will become more favorable, secondly the whole slipstream will be placed at an angle which attenuates the forward tilting process at both sides of the nacelle.
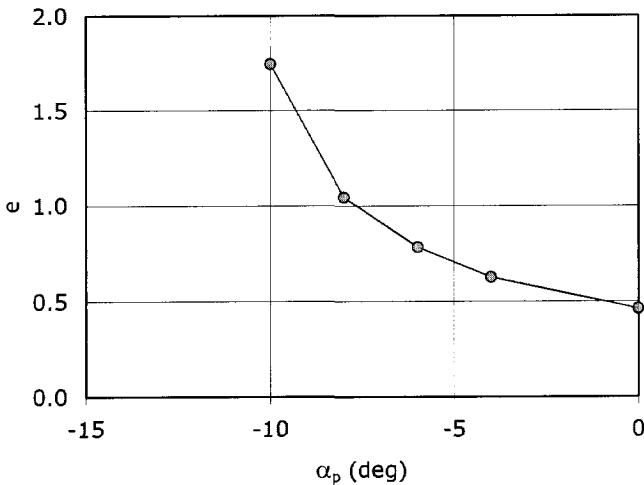
Figure 7.25: *Effect of the propeller angle of attack on the wing efficiency for a NAS slipstream.*

The following cases are all based on slipstream velocities generated with the BEM propeller model, adapted for angle of attack effects, as discussed in Chapter 2. The propeller loading characteristics employed in the next examples are more or less typical for a Fokker 50 like geometry, although only rough estimates of the slipstream velocities are found. This is due to the fact that no further detailed information of the Fokker 50 propeller was available (like slipstream velocities for the propeller under angle of attack and the so-called "Blade Tape", containing C_L and C_D as functions of α, Re and M). The slipstream data from the BEM-model are only meant to incorporate a more or less realistic propeller angle of attack effect in the calculations. Therefore no further comparison with experimental data is presented at this point.

For a negative propeller angle of attack both the axial and swirl velocity distribution become highly non-axi-symmetric. As discussed earlier this effect, in which the upwash on the inboard side is increased compared to the downwash generated on the outboard side, could be exploited to improve wing performance. As can be seen in Fig. 7.25, a significant performance improvement is found for increasingly negative α_p. This is the result of the strong upwash effect tilting the local lift vector forward.

Since the induced drag produced by the wing is generally written as $C_L^2/\pi Ae$, this effect can be regarded as an increase of the effective wing aspect ratio. In our case the effective aspect ratio changes from 6 for $\alpha_p = 0°$ to approx. 21 for $\alpha_p = -10°$. It should be remarked that, in contrast with what one would expect, the reduction
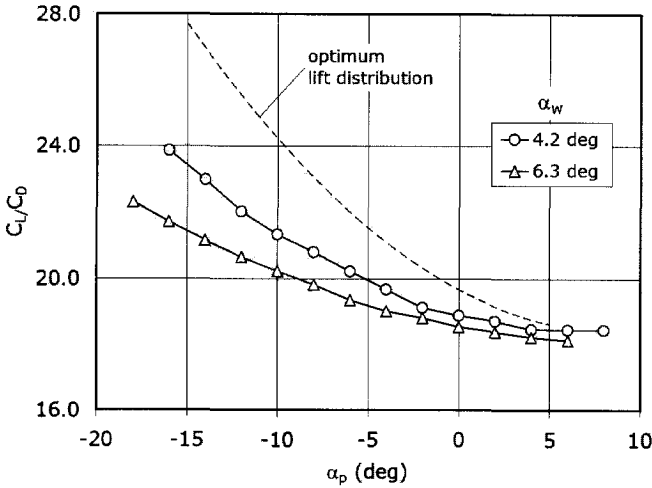
Figure 7.26: *Effect of the propeller angle of attack, α_p, on the wing efficiency for various wing angles of attack, α_w on the lift/drag ratio found from the APROPOS experiment ; $J = 0.92$.*

of wing lift and effective thrust, through direct forces acting on the propeller (see eq. (7.25)), are smaller than the benefits in the sense of reduction of the overall induced drag.

An inevitable disadvantage of a configuration with high negative values of α_p (denoted as the Propeller-Tilt-Down or *PTD*-configuration) is of course the appearance of cyclic blade loading. The resulting variation in blade stresses with azimuthal position and the possible increase in noise level are problems to be addressed before a PTD-configuration can be practically implemented.

The given effects for the optimized propeller-wing configuration, are qualitatively in agreement with experimental results of the APROPOS model.

Fig. 7.26 illustrates the effect of the propeller angle of attack on the lift/drag ratio. In this case the propeller spanwise position was $y_p/b/2 = 0.469$ and its height position $z_p = 0$. In the same figure the theoretical curve is given for $\alpha_p = -4°$ found with the F-method. The trend is remarkably comparable to the experimental result. The differences are mainly caused by the fact that the experimental lift distribution is not optimized. Therefore the induced drag reduction and thus the performance could in practice even be higher. Apparently the performance benefit is not disturbed by viscous losse, which might occur when local flow angles at the wing become to high.

The effect of the propeller angle of attack was investigated again with the T-
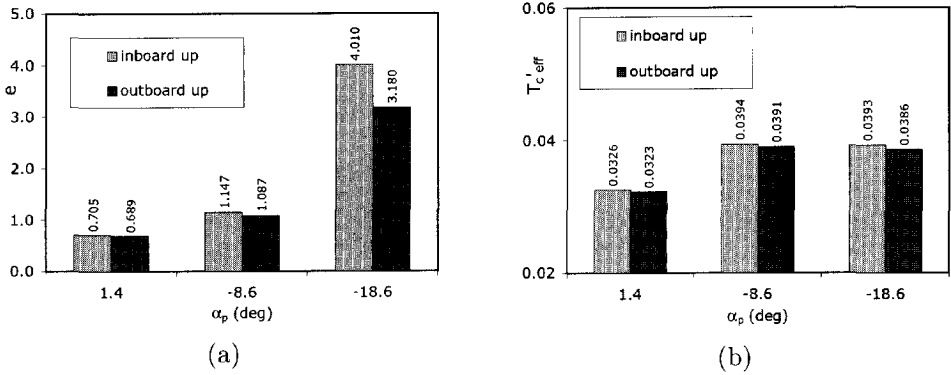
Figure 7.27: *Effect of propeller angle of attack on the wing span efficiency factor (a) and the effective thrust coefficient (b), $T'_{c_{eff}}$, of the F50 model in the high speed case.*

method for the given F50-like configuration. The normal force gradient of the six-bladed propeller was taken from windtunnel tests on a generic propeller-wing model (APERT-JR01), data of which were published by Kusomo et al. [98]. To express the performance of the propeller-wing configuration incorporating the direct forces acting on the propeller we use :

$$T'_{c_{eff}} = -(C_{D_i} + \Delta C_{D_p} + \Delta C_{D_i}) \tag{7.76}$$

with :

$$\Delta C_{D_i} = (C_{D_i})_{no\,prop} - (C_{D_i})_{prop}$$

$$= \frac{2C_L^2 \cdot \Delta C_{L_p} + \Delta C_{L_p}^2}{\pi A\,e} \tag{7.77}$$

where index p denotes the effect due to the propeller. Again the profile drag is ignored in the optimization process.

Fig. 7.27 shows the effect of propeller angle of attack on the wing span efficiency factor, e for the F50 model. The odd values of the propeller angle of attack at the x-axis are due to the restricted values of α_p that were available from the BEM-program that was used to determine the velocity components in the slipstream.

The highest "effective thrust" is found at relatively large negative angles of attack. Apparently the benefits of the wing drag reduction due to the presence of the propeller increase with negative propeller-angle of attack, α_p.
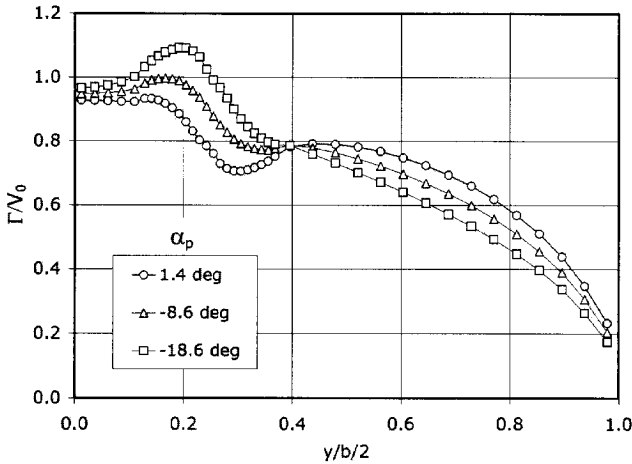
Figure 7.28: *Effect of propeller angle of attack, α_p, on the optimum circulation distribution of the F50 model; propellers rotating inboard up.*

Again the configurations with inboard up rotating propellers demonstrate a superior performance compared to the outboard up rotating cases. In Fig. 7.28 the optimum circulation distribution is presented for several propeller angles of attack . Apparently the propeller angle of attack strongly influences the form of the optimum distribution.

Spanwise propeller position   With the presented methods it becomes easy to analyze the effect of the spanwise position of the propeller. In Fig. 7.29 the wing induced drag coefficient of the APROPOS model, as calculated with the T-method, is plotted as a function of the spanwise propeller position denoted as y_p.

The wing efficiency increases for the inboard up rotation case and decreases for the outboard up rotation when the propeller is moved towards the tip. Apparently a wing with tip mounted propeller is the most advantageous. This has already been proven by several authors [12, 14, 10, 11]. Evidence was also found from the experimental data of the APROPOS tests, discussed in chapter 5.

Streamwise propeller position   Besides the spanwise propeller position the effect of different streamwise positions was also analyzed for the optimized configurations. Again the APROPOS model was used in combination with the F-method. The results, given in Fig. 7.30, show that the effect of a change in x_p/R seems to have a much smaller influence on the wing efficiency than changing the propeller angle of attack,
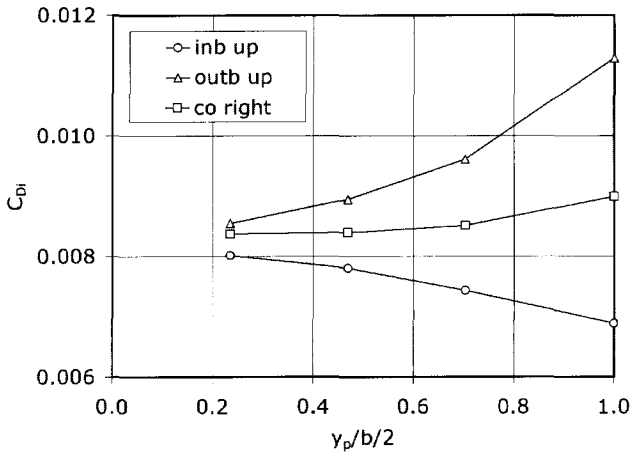
Figure 7.29: *Effect of the propeller spanwise position, y_p, on the induced drag coefficient of APROPOS at $C_{L_{des}} = 0.4$.*

α_p.

The reason for this is the fact that with increasing x_p/R the axial flow velocity within the slipstream tube increases whereas the effective angle between slipstream center line and wing reference line decreases. Apparently the two effects compensate each other such that e is changed only slightly. Again the APROPOS tests indicate that the influence of streamwise position is negligible [104, 12]. Further evidence of the restricted influence of the propeller streamwise position was found in the VLM-calculations discussed in chapter 5.

7.3.6 Comparison of optimization and analysis

The cases presented in the previous paragraphs were all based on a typical cruise lift coefficient, since this is the most important condition with regard to minimization of the required mission fuel. It should be clear, however, that the optimum lift distribution, obtained through an adaptation of wing twist and camber distribution, may result in a lower wing performance for off-design points. Solution of this problem requires a computer code based on an analysis-approach. In subsequent sections the optimization process was analyzed using the panel method FASD.

To verify whether the panel code confirms the optimization results, calculations were performed on both the original and the optimized configuration using the panel code FASD. With the details of these calculations described more extensively in ref.
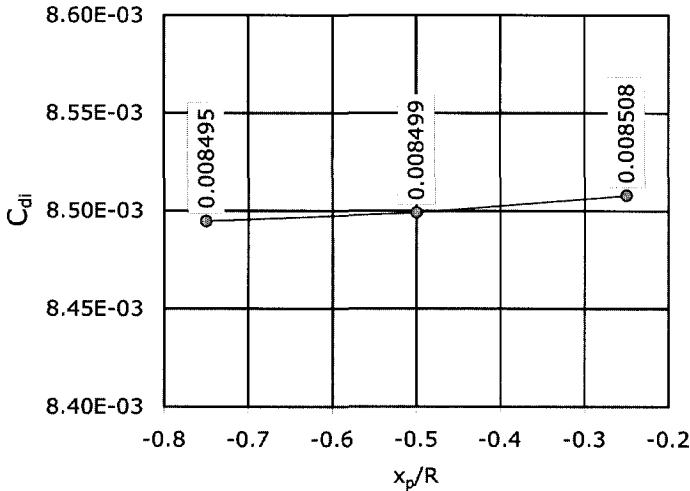
Figure 7.30: *Effect of the streamwise propeller position on the induced drag of APROPOS at $C_{L_{des}} = 0.4$; AS slipstream.*

[14] the main conclusions will be summarized here.

Fig. 7.31 shows an overview of the simplified F50 panelled geometries that were investigated with the FASD program. The original wing planform was compared with a modified wing nacelle modelled and with the optimized wing found from the results described in section 7.2.2. As can be seen in the lower part of Fig. 7.31 the optimization was realized by adapting the twist distribution in the wing area washed by the slipstream.

To incorporate the power effects the slipstream velocity components and the pressure rise in all prop on cases were determined with the *sliptube* model (see Appendix D). In this case both the typical low speed case (LSC) and the high speed case (HSC) were investigated.

All calculations have been performed on a symmetrical configuration i.e. only the contra-rotating case is investigated. The number of strips in spanwise direction used in the analysis is equal to the number of panels used in the optimisation of the configuration. Except for the outboard segment on which a cosine distribution is applied, the panel distribution is uniform.

High Speed Case First calculations were carried out at the Mach number for the 'high speed' case equal to $M = 0.35$. For every flow case the angle of attack is chosen

(a) original wing layout

(b) original nacelle-wing layout

(d) Front view
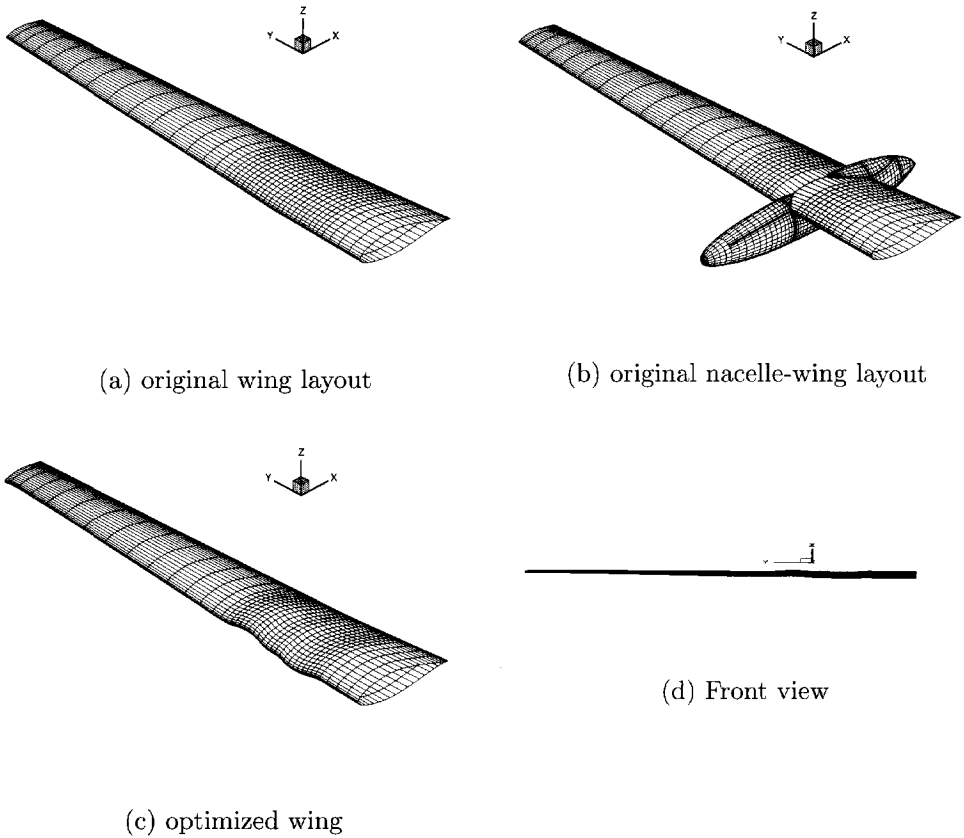
(c) optimized wing

Figure 7.31: *Simplified Fokker 50 wing and wing-nacelle layouts investigated with respect to the effect of optimization.*

such that the resulting lift coefficient is equal to $C_L = 0.6$.

Calculations with the nacelle-wing model indicated that the effect of the (modified) nacelle on the wing pressure distribution was small. As can be seen in Fig. 7.32, the presence of the nacelle does not introduce extensive deterioration of the C_p distribution for a typical low angle of attack case. With this in mind and the fact that the add-on procedure in the panel method is quite laborious, the effect of the optimization on the calculated characteristics was investigated for the model without the nacelle present.

Fig. 7.33 shows the surface pressure distribution for the original wing model and
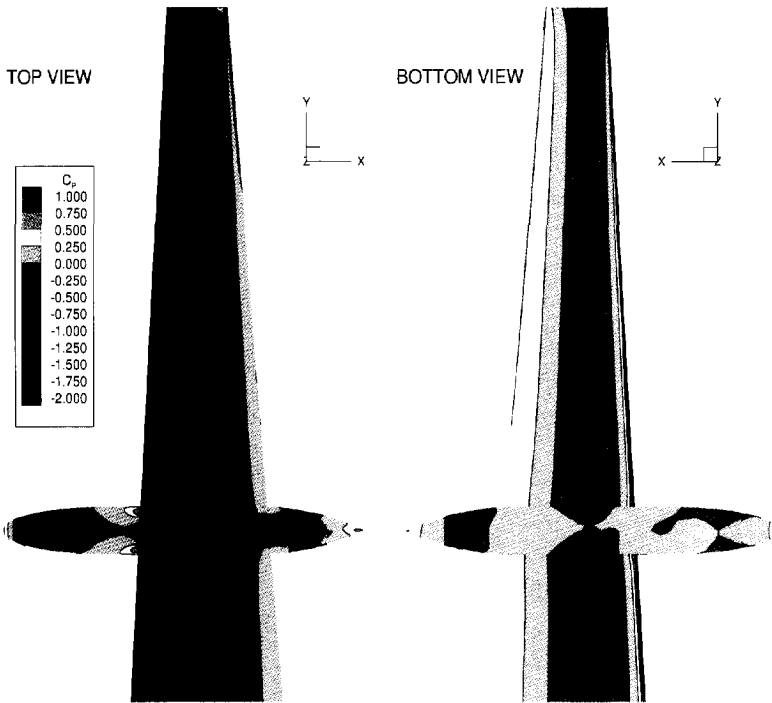
Figure 7.32: *Surface pressure distribution at the upper side (left picture) and lower side (right picture) for the simplified wing nacelle model ; prop off.*

for the optimized wing model where the twist distribution was adapted. As can be seen from these results, the change in angle of attack due to the swirl in the slipstream results in an increase of the pressure on the upper side at the inboard slipstream segment and an increase of the pressure on the lower side at the outboard slipstream segment. When the optimized wing is considered we see that the spatial gradients of the pressure are weakened in chordwise and spanwise direction compared to the original wing.

The lift and drag coefficients, as found from surface pressure integration for the complete configuration, are presented in Table 7.6 and 7.7 for the original and the optimized geometry respectively.

The results exhibit the expected effect since due to the presence of the slipstream, the lift is increased while the drag is decreased. The lift increase for the inboard-up rotating propeller at a configuration angle of attack of $\alpha = -0.925°$ is about 0.02.

(b)
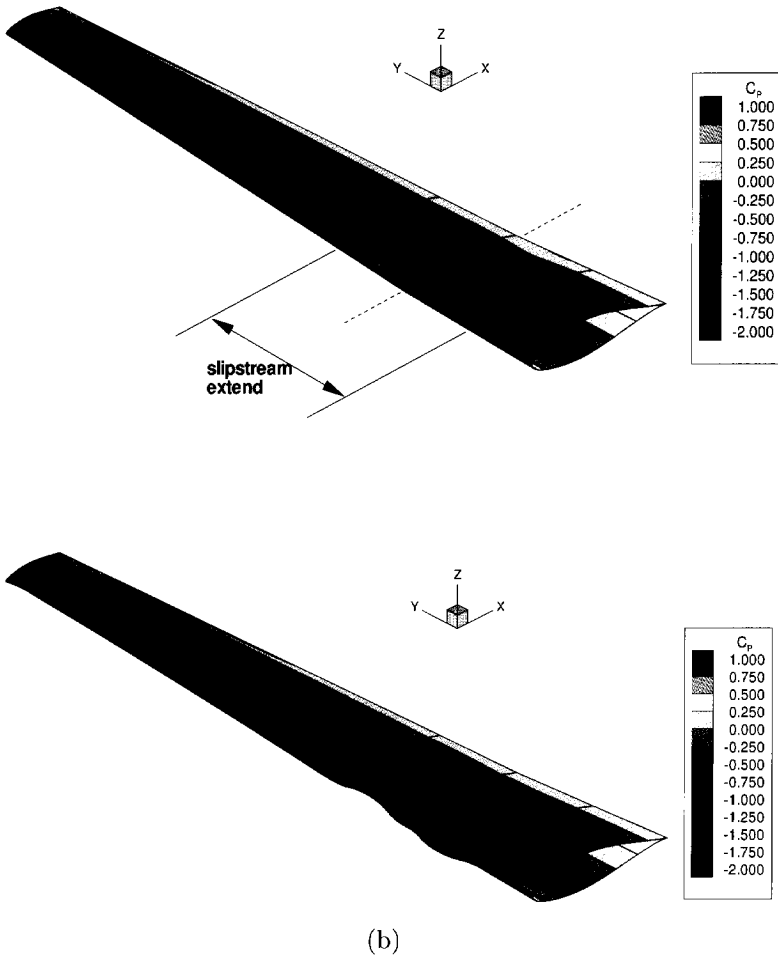
Figure 7.33: *Typical surface pressure distribution for the Fokker 50 original wing model (a) and the optimized wing (b) ; $M = 0.35$; $\alpha = -1°$; prop on ; high speed case.*

For the outboard-up rotating propeller at $\alpha = -0.85°$, the increase in lift is about 0.012. It should be noted that this increase in the lift is only due to the propeller slipstream affecting the flow field at the wing because the contribution of the vertical component of the normal and thrust force on the propeller at the propeller plane is not accounted for.

Table 7.6: *Lift and drag coefficient for the initial wing-nacelle configuration in the high speed case.*

Configuration	$\alpha(°)$	C_L	C_D
prop off	-0.75	0.599	0.01444
prop on, inboard up rotation	-0.925	0.599	0.01274
prop on, outboard up rotation	-0.850	0.600	0.01336

Table 7.7: *Lift and drag coefficient for the optimized wing configuration in the high speed case.*

Configuration	$\alpha(°)$	C_L	C_D
prop off	-1.10	0.599	0.01417
prop on, inboard up rotation	-1.40	0.599	0.01222
prop on, outboard up rotation	-1.40	0.600	0.01295

The drag coefficient decreases due to the presence of the slipstream. For the inboard-up rotating propeller $\alpha = -0.925°$ the drag is decreased about 10 counts and for the outboard-up rotating propeller $\alpha = -0.850°$ about 7 counts. At the lift coefficient of $C_L \approx 0.6$, the difference in drag between the inboard-up and the outboard-up rotating propeller is about 6 counts for the original wing and 7.5 counts for the optimized wing.

Low Speed Case   From the real propeller-wing interference point of view it is not very interesting to consider the low speed case with an inviscid code since strong viscous effects may occur. The case could be typical for the first segment climb of the aircraft, a phase that has a short duration compared to the cruise phase. Hence its impact on the operation of the aircraft with respect to specific fuel consumption is limited. The fact that for this case the lift is higher and the relative effects of the propulsion system are stronger due to the higher slipstream velocity components, however, makes it an interesting case for comparison purposes.

Therefore additional flow calculations were performed with FASD for the low speed case at a Mach number of $M = 0.22$ and a lift coefficient of $C_L = 1.2$.

The lift distribution on the wing of the initial geometry as well as the optimized geometry is given in Fig. 7.34. The wing part washed by the slipstream clearly shows the increase and decrease of the local induced drag generated at the downgoing and the upgoing blade side respectively. When the optimized wing is calculated small
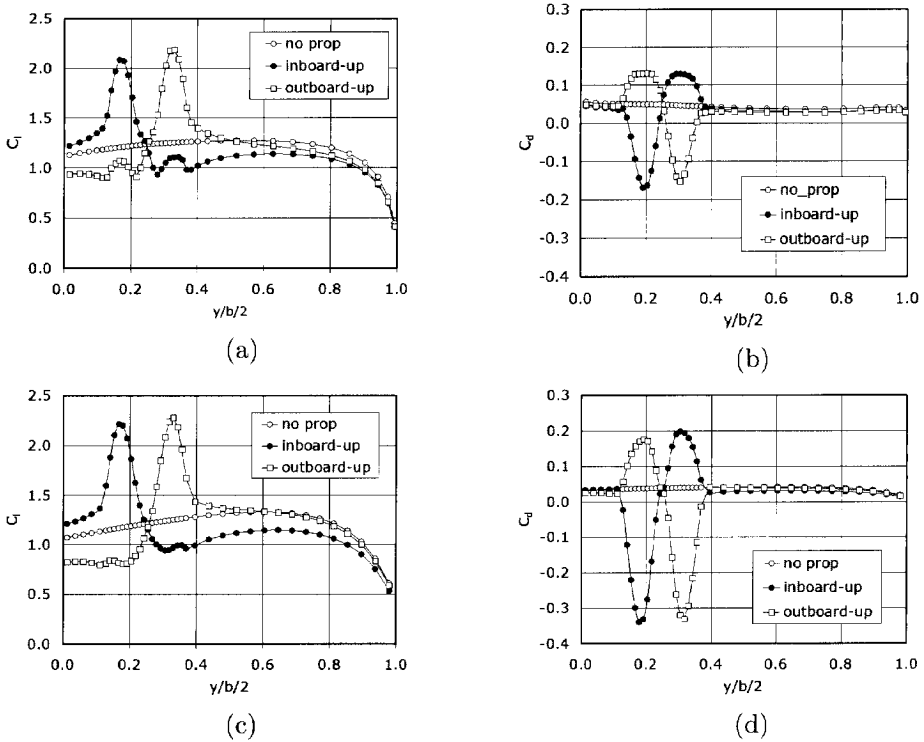
Figure 7.34: *Lift (left) and drag (right) distribution of the initial wing (upper pictures) and the optimized wing (lower pictures) in the low speed case ; $M = 0.22$; $C_L = 1.2$.*

changes in the lift distribution occur (lower part of Fig. 7.34). Especially the peaks in the drag distribution have become sharper compared to the initial wing.

Finally the characteristics of the wing under influence of the slipstream have been calculated for the low speed case as well, the results of which are summarized in Table 7.8.

For the inboard-up rotating propeller at a configuration angle of attack of $\alpha = 4.2°$, the lift increase is about 0.11 and the drag decrease is about 77 counts.

For the inboard-up rotating propeller at $\alpha = 4.4°$, the lift increase is about 0.09 and the drag decrease is about 50 counts. The difference in drag between the inboard-up and outboard-up rotating propeller at the lift coefficient $C_L = 1.2$ is about 40 counts.

The optimized wing was calculated in the low speed case only for the inboard up rotating propeller. At an angle of attack of $\alpha = 3.3°$ and $C_L = 1.2005$ a drag

Table 7.8: *Lift and drag coefficient for the original wing configuration in the low
speed case.*

Configuration	$\alpha(°)$	C_L	C_D
prop off	5.3	1.2005	0.04365
prop on, inboard up rotation	4.2	1.2008	0.02812
prop on, outboard up rotation	4.4	1.1996	0.03217

coefficient of $C_D = 0.02790$ was found, which is only 2 drag counts smaller than that
of the original wing.

Considering the panel calculation results on the optimized F50 wing especially in
the 'high speed' case, a remarkable drag reduction of a propeller configuration can
indeed be established with an optimization of the geometry.

When the results are studied in more detail, the tendency of the results of the
optimized geometry corresponds to the predicted results, but there is a little difference
in the resulting circulation and lift distribution. For example for the inboard-up
rotating propeller, the local lift on the inner wing is smaller and on the outer wing
larger than the optimization results predicted. The consequence is that the resulting
drag distribution differs from the optimal distribution, resulting in an increased drag
with respect to the minimum induced drag. This is probably due to an error in the
optimum twist distribution and the effect of wing thickness.

For the 'low speed' case, the results of the analysis of the optimized geometry are
less satisfactory as would be expected, since no performance increase was found. The
reason for this may be the afore-mentioned differences in propeller induced slipstream
velocities used during the analysis and optimization of the configuration. Another
possibility is that the optimization, performed by a Trefftz plane analysis, is less
suitable for the highly loaded propeller of the 'low speed' case in which the increase
in velocity due to the propeller can not be assumed small anymore.

Final remarks on the optimization process   The following conclusions may be
drawn with respect to the optimization of a wing in a tractor propeller layout.

Aerodynamic optimisation of wings in multi-engined tractor propeller arrange-
ments is discussed and analyzed with two approaches: a simple lifting line Fourier-
analysis and a calculation based on a Trefftz-plane analysis where the conservation
laws of mass, momentum and energy are fulfilled in a control volume surrounding the
configuration.

The computer programs that were developed for the optimization of propeller-wing
configurations in the preliminary design phase enable investigations of the effects of

propeller position, slipstream velocity distribution and adaptations to conventional wing designs.

The example calculations show that the lift distribution for minimum induced drag differs significantly from the elliptic loading.

Furthermore, the propeller angle of attack seems to have a dominant influence on the wing performance. Mounting the propeller at a negative (tilt down) angle with reference to the wing suggests a reduction of overall wing induced drag. This effect is mainly due to the asymmetry in the slipstream velocity distribution that is introduced. However, in an analysis including viscous effects in high subsonic flow there will be a maximum in the attainable effective efficiency since the drag rise with Mach number and separation effects may nullify the local leading edge suction.

For a practical use of a PTD-configuration, it should be noted that small changes in thrust line orientation can produce significant changes in flow field uniformity and thus propeller performance and blade stress levels. This might also affect the overall noise production. In this field, further research is needed taking into account all beneficial and detrimental effects to define the optimum propeller/wing configuration.

It is shown that the inboard-up rotating propeller exhibits a superior performance compared to the conventional co-rotating or the outboard-up rotating case. Further investigation of this configuration will be needed to arrive at a practical implementation of this propeller-nacelle-wing layout.

Some numerical studies show that optimisation of a modern medium speed turboprop aircraft leads to performance increase by adapting the wing shape.

Chapter 8

Conclusions

In this chapter, conclusions on the work accomplished in this thesis are drawn and some recommendations regarding future research for possible improvements are given.

In the previous chapters, various aspects of propeller wing aerodynamic interference were discussed, based on both a numerical and an experimental approach. Calculations were performed at different levels of complexity to be able to find trends in the effect of propeller location on the one hand and reveal possibilities in the optimization of the propeller wing combination on the other. In the following sections the main conclusions regarding the aerodynamic interference between the propeller and the wing will be discussed briefly.

8.1 Experimental approach

The experimental investigations were performed with a limited number of windtunnel models that were all used in the low speed range ($M < 0.3$). Typical twin-engined turboprop aircraft operate in a higher Mach range during their cruise flight but the characteristic trends found during the windtunnel tests are still expected to be predictive for the cruise condition of the full-scale aircraft.

Although every propeller-wing configuration exhibits its own specific features, characteristic conclusions on the interference effects could be drawn from the models used.

Especially the flexible set-up of the APROPOS model proved to be valuable for the determination of the propeller position effects. The simple geometry selected for both PROWIM and APROPOS reduced the numerical modelling complexity. It also prevented unwanted side effects in the form of secondary flow structures that could conceal the primary propeller-wing interactive flow phenomena.

All models were successfully measured with the windtunnel external 6 component balance, delivering directly all relevant forces and moment necessary to draw

conclusions on the overall performance of the configuration in the form of drag at a given lift coefficient. However, limited information was available for the experimental thrust-drag bookkeeping as the thrust of the propeller could not be measured separately. The alternative approach by which the thrust is calculated through the measurement of the total pressure jump across the propeller disk proved to be an acceptable alternative.

The pressure measurements on the model surface were invaluable for the comparison with the numerical calculations performed later on.

Finally the quantitative wake analysis (QWA), performed with the 5-hole probe behind the model, provided detailed insight in the deformation process of the propeller slipstream. This is necessary to estimate possible modelling errors when simplified undistorted slipstream envelopes are used in numerical approaches (for example for the inclusion in a panel code).

The knowledge gained during the windtunnel tests formed the basis for a further analytical and numerical approach of the problem. The primary disadvantages of the windtunnel environment like wall effects and scaling of the Reynolds number were reduced by adapting the boundary conditions in the numerical models accordingly.

8.2   Numerical approach

During the numerical investigations of the propeller-wing interference problem, several models of increasing complexity were developed and adopted. The main reason for the application of this range of models was the ease of use and reduced calculation time per flow case for the simpler models on the one hand, and the ability of delivering relevant flow details by the complex models on the other. All models require some simplification of the propeller influence on the wing, either by accepting time average effects of the propulsive system or by simplification of the propeller itself through the application of an actuator disk representation.

Besides the analysis codes based on: the vortex lattice technique, the surface singularity approach (panel methods) and the solution of the Navier-Stokes equations an optimization code, dnoted *pwopt2*, was developed and applied to determine optimum wing designs in the presence of a slipstream.

The VLM code, which is the most flexible from a problem setup point of view, was coupled with an advanced Blade Element Model allowing a single interaction mode (SIM) and a full interaction mode (FIM). The latter incorporates the effect of the trailing wing on the propeller, a coupling that researchers ignore in most cases.

The optimization code employs the method of multipliers, which combines the Lagrangian method and the penalty function method. The method can handle general wing propeller layouts and it shows to be efficient in calculating optimized wing designs for typical twin engined configurations.

The NS-code that was used delivered the highest level of flow detail about the

propeller-wing configurations. It was combined with an actuator disk approach that allowed input of time-averaged jumps in the propeller domain.

To validate the capabilities of all codes, comparison was made between data obtained during the windtunnel test campaign and data found in open literature.

8.3 Results

The experiments reveal a very complex flow with high levels of vorticity and considerable shearing forces in the wing area that is washed by the propeller slipstream. The unsteady nature of the flow shows a frequency that coincides with the blade passing frequency. However, the time-averaged forces acting on the propeller and the wing dictate the performance of the configuration.

The time-averaged non-uniform velocity and pressure distribution in the slipstream were measured successfully with a 5-hole probe and the data were used as input for subsequent numerical simulations.

The surface pressure measurements clearly showed the effect of the swirl velocity and the increased total pressure due to the propeller. Its local influence is directly coupled to the propeller rotational direction. The force measurements and the surface pressure measurements demonstrated a performance benefit when the propeller rotational direction is inboard up. Small adaptations of the spanwise lift distribution, by applying differential flap deflection on both sides of the nacelle, revealed a small performance increase (higher C_L/C_D at given thrust and power). This finding indicates the possibilities to design optimum wing shapes of which exact shaping and profiling depends on the structure of the incoming slipstream.

With the focus on optimizing the complete propeller-wing configuration the thrust-drag bookkeeping becomes an important issue. Earlier research [35] has already shown that the separate determination of thrust in a closely coupled propeller-wing design is difficult, not to say impossible. The main reason for this conclusion is to be attributed to the difficulties found in the definition of propeller produced thrust and drag and partly in the difficulties in measuring the thrust force and torque separately. The latter problem can be overcome by applying a so-called rotating shaft balance, an instrument that was not available for the experiments performed in this work. Moreover, with respect to the coupling between thrust and drag it seems that in many investigations the accuracy as well as the changes in the propeller thrust forces due to interference received limited attention. This approach is mostly reflected in ignoring the wing effect on the propeller (SIM). The full interaction mode (FIM), that is used in the VLM calculations, showed that even for a normal layout, with the tractor propeller well in front of the nacelle, small effects on the thrust coefficient are found in the range of several drag counts.

A parametric analysis was performed to demonstrate the effects of changing propeller x, y and z direction and the inclination angle with respect to the wing. From

the measurements as well as the numerical simulations the following conclusions may
be drawn.

- Propeller inboard up rotation is beneficial, as higher lift/drag ratios are obtained
  at constant power settings

- The effect of the propeller spanwise position is negligible for locations well within
  the range that is normally used for modern turboprop aircraft. Nevertheless,
  an inboard up rotating propeller positioned close to or at the wing tip delivers
  a considerable performance increase.

- When the vertical position of the propeller is changed, high positioned propellers
  obtain the highest lift coefficients. The drag coefficient, on the other hand, rises
  for both high and low propeller positions and shows a relative decrease for $z_p \approx 0$
  due to the "donut" effect. It is important to notice that the calculations prove
  a low propeller position to be beneficial regarding the propulsive efficiency. The
  reason for this effect is attributed to the reduced propeller inflow distortion due
  to the wing.

- The streamwise variation of the propeller position shows small variations in the
  propulsive efficiency of the configuration. For positions more upstream of the
  wing the propulsive efficiency increases slightly due to the rise in the axial flow
  velocity inside the slipstream and the diminished wing effect on the propeller.

- Negative propeller inclination angle with respect to the wing are generally ben-
  eficial for values less than 15°. The main reason for this positive effect is the
  change in the slipstream velocity distribution where increased asymmetry is
  introduced and the fact that the complete slipstream envelope is rotated to
  produce an average increase in the local wing flow angle of attack.

- The over-the-wing propeller (OTW) location showed very specific characteristics
  in the lift, the drag and the propulsive efficiency. First of all a considerable
  increase in the lift coefficient was observed for aft located propeller positions
  with a maximum C_L close to $x_p/c = 1.0$. The location for minimum drag
  coefficient was found at a more upstream position at $x_p/c \approx 0.3$. Even if the
  OTW arrangement of the propeller shows positive effects on the obtainable lift
  and drag coefficient, calculations showed that the propulsive efficiency of the
  configuration reduces when the propeller is positioned above the wing. Again,
  the strong deformation of the propeller inflow field with a resulting reduction in
  propeller efficiency, is the main cause for this. When the distance between the
  propeller and the wing is increased, however, the propulsive efficiency increases
  and it exceeds the value that is obtained with the same propeller positioned in
  tractor fashion in front of the wing.

The optimisation code proved to be capable of defining optimized wing shapes that are influenced by a typical propeller slipstream. For the optimized wings, generally, the same effects are found as described for the standard layout, i.e. inboard up rotation and increased propeller tilt down angle both lead to a performance increase. Calculations with and without the effect of the viscous drag component, showed a limited effect of the viscous effects on the final optimized wing shape for a given lift coefficient and power setting of the propeller.

The calculations performed with the different codes described here conform to the trends found in the windtunnel experiments. The VLM-approach delivered quite accurate results compared to the panel methods and NS-code. This close agreement was found only after applying a swirl recovery factor (SRF). The absence of the SRF in the panel methods based on the slipstream envelope model, always leads to an overestimation of the slipstream swirl velocity component and hence the local lift effect. In the inclusion method where the slipstream generated velocities and pressure are prescribed on a the slipstream washed panels, SRF can be incorporated without difficulty. Hence this panel method approach is preferred over the slipstream envelope model.

Once accurate results are needed for the propeller-wing interference problem and details of the flow are needed to determine the secondary flow effects that influence the lift and drag performance of the model, the NS-code becomes indispensable.

The calculations with the NS-code produced results that are very similar to the data obtained from the experimental flow field survey.

The NS-approach facilitated the identification of typical flow phenomena, like the deformation of the slipstream when passing the wing. The spanwise distributions of lift and drag are sensitive to the form the velocity distribution in the slipstream as well as the way the slipstream deforms when passing the wing. Hence, a calculation model based on the NS-equation yields a more realistic estimation of the propeller wing interactive flow since the slipstream is allowed to develop and deform freely and no artificial swirl recovery (the application of the SRF) is needed.

The quantitative wake analysis (QWA), as applied to the propeller-wing model, delivered detailed information on the slipstream deformation. This was helpful in the validation of the theoretical prediction codes. The integrated lift and drag data agreed well with the experimental data obtained from the pressure and the balance measurements. Moreover, applying the QWA to field data generated with the NS-code showed that acceptable lift and drag data can be obtained in this case as well.

The measurements and computations on the problem of propeller-wing interference revealed the existence of a highly complex flow with strong vortical flow phenomena combined with significant boundary layer effects. From the fact that performance benefits were found for several adaptations of a "standard" propeller-wing layout and the wing shape, the main conclusion that integrated design of propeller and wing may lead to more fuel efficient aircraft, is justified.

8.4   Concluding remark

Although several topics play a role in the final design stage of a typical multi-engined propeller aircraft, the design space in this thesis was limited to the aerodynamics related areas. The fact that in some cases benefits were found for a certain propeller-wing layout does not necessarily imply that these benefits can be obtained in real practice. Many design considerations that have not been discussed herein are undeniably important for the conclusions on performance benefits. Issues like structural and flutter behaviour, maintenance, asymmetrical power cases (engine out conditions) etc. will have to be addressed before the practical feasibility of alternative tractor propeller–wing configuration can be determined.

≺ – ≻

Appendix A

Engineering methods for the estimation of propeller data

A.1 Introduction

To be able to work with the flow phenomena that occur in propeller flow it is beneficial to shortly restate the typical propeller flow characteristics and discuss methods by which both the propeller force as well as the slipstream parameters can be obtained.

A logical step towards the analysis of the propeller is to consider a propeller that operates in an undisturbed uniform flow generating a slipstream that is free of any disturbance caused by the proximity of a nacelle or any other airframe part. The flow field that is generated is very similar to that of a wing. The local lift on the blade section at any radial position is associated with the local circulation around the blade. This circulation varies from the blade root to the blade tip resulting in the shedding of a vortex sheet from the blade trailing edge, as sketched in Fig. A.1.

The vortex sheets of all blades pass downstream in a helical path together forming the slipstream. The vortex sheets springing from all propeller blades are free to move under their own self-induced influence and the influence of the other sheets. The resulting slipstream shows a contraction as it moves downstream due to the increasing axial velocity inside the slipstream tube. The bound vorticity on the propeller blades and the trailing vorticity generate a propeller induced velocity vector, V_p. This local induced velocity can be added vectorially to the free stream velocity and the local rotational velocity of the blades to form the total local velocity vector in a fixed (Eulerian) frame of reference. Once the slipstream is generated in the form of helical wakes its geometry will change gradually as it progresses downstream. This "deformation" of the slipstream tube is the result of both the contraction and the rolling up of the vorticity sheets into a discrete tip and root vortex. The distance

321

(a)

(b)
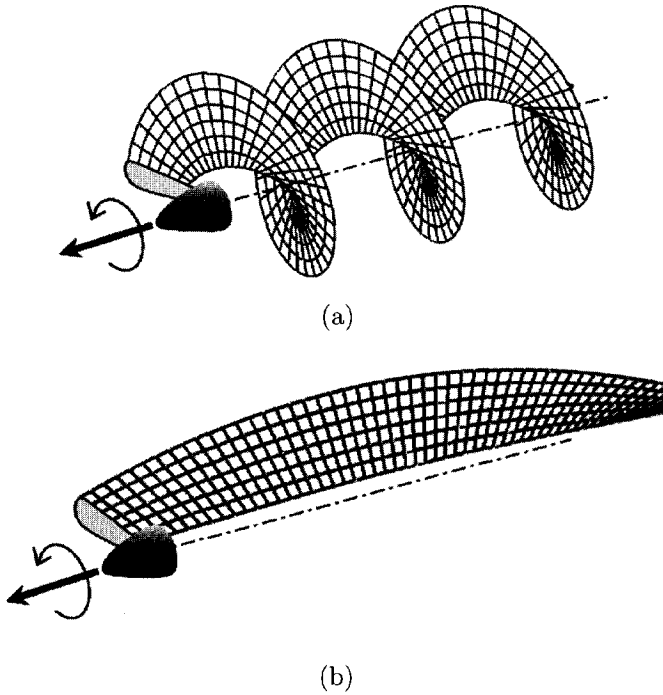
Figure A.1: *Sketch of a vortical wake generated by a propeller blade; (a) high loading (low advance ratio), (b) light loading (high advance ratio); deformation and roll up neglected.*

over which this process takes place is dependent on the propeller loading since this strongly determines the advance ratio of the blade wakes (see Fig. A.1).

For the propeller-wing interference problem a clear description on the effect that the inflow field has on the propulsive efficiency (i.e. the thrust for given flight speed and shaft horse power) is essential. An attractive starting point to describe possible losses and gains for the propeller is found in the description of the so-called free air thrust. This is the thrust of the propeller blades without any other aircraft part present. The efficiency of this propeller can simply be written as:

$$\eta_{fa} = \frac{T_{fa} V_\infty}{P} \tag{A.1}$$

With ΔP_p defined as the power loss arising from profile losses on the propeller blades and ΔP_i the induced losses, the free air efficiency can be written as:

$$\eta_{fa} = 1 - \frac{\Delta P_p}{P} - \frac{\Delta P_i}{P}$$
$$= 1 - \Delta\eta_p - \Delta\eta_i$$

(A.2)

The induced losses are typically the effect of the axial and swirl velocity components generated by the helical vortex sheets that emanate from the blades. In case of interference with other aircraft parts these velocities will of course be strongly affected.

The loss in efficiency due to blade airfoil drag, $\Delta\eta_p$, is related to the drag of the blade airfoil sections and are insofar rather independent on the selection of the 3-dimensional propeller blade geometry[1] and the propeller position relative to other aircraft parts. To reduce the profile losses the airfoil sections will be designed to produce a high lift to drag ratio, C_l/C_d, over a wide range of propeller inflow conditions, i.e. a range of advance ratios that the propeller experiences going from take-off to cruise condition. The final selection of the airfoils is therefore based on a compromise aiming at high efficiency at a specified flight condition (generally the cruise phase) whilst maintaining acceptable penalties for other flight phases. Accordingly the profile loss associated effects are part of the propeller design process which is only loosely related to the propeller wing interference problem.

On the other hand, the induced loss of the propeller is an important issue when treating the propeller wing interaction effects. Because the inflow conditions of the propeller are mainly dictated by the propeller-airframe configuration the loading distribution on the propeller blades and, consequently, the trailing vortex system will change with reference to the uninstalled propeller condition. Even though the free air efficiency is an interesting property as far as propeller design is concerned the most important condition for the treatment of the performance of the complete aircraft will be the installed propeller case. In the next sections first of all the main features of the uninstalled propeller and various methods to calculate the performance will be discussed.

A.2 Propeller coefficients

For propellers different dimensionless coefficients are in use:

$$T_c = \frac{T}{\rho V_\infty^2 D^2}$$

(A.3)

$$T'_c = \frac{T}{q_\infty S_p}$$

(A.4)

---

[1]the spanwise distribution of blade angle and chord

$$T_c* = \frac{T}{q_\infty S_{wing}} \tag{A.5}$$

$$C_T = \frac{T}{\rho n^2 D^4} \tag{A.6}$$

In the discussion of the propeller characteristic the choice for one of these definitions is not always obvious although it is clear that eq.(A.5) enables direct comparison with the aircraft's coefficients since S_{wing} and q_∞ are both selected as the reference variables. In some presentations of the propeller performance the torque coefficient is used to represent the power delivered by the propeller. Standard definitions include:

$$C_Q = \frac{Q}{\rho n^2 D^5} \tag{A.7}$$

and:

$$Q_c = \frac{Q}{\rho V_\infty^2 D^3} \tag{A.8}$$

where Q is the propeller shaft torque.

The power coefficient is defined as:

$$C_p = \frac{P}{\rho n^3 D^5} \tag{A.9}$$

With $P = 2\pi n Q$ an alternative form that is often used is:

$$P_c = 2\pi \frac{Q_c}{J} \tag{A.10}$$

where J is the propeller advance ratio defined as $J = V_\infty/nD$. This advance ratio is a direct indication for the propeller blade section angle of attack and hence the loading as can be seen from the velocity diagram sketched in Fig. A.2.

The propeller efficiency is defined as the ratio between the effective propulsive power and the shaft power, $\eta = TV_\infty/P$, which leads to two alternative expression for the propeller efficiency:

$$\eta = \frac{C_T}{C_p} J \tag{A.11}$$

and:

$$\eta = \frac{C_T}{2\pi C_Q} J \tag{A.12}$$

In the remainder of this text a description of engineering methods is presented that are available for the calculation of the propeller and slipstream characteristics under axial flow conditions (zero inflow angle). Because of their importance for the aircraft's propulsive efficiency, this discussion is limited to the thrust and the torque coefficients only.

$$\alpha = \beta - \tan^{-1}\left(\frac{J}{\pi}\right)$$
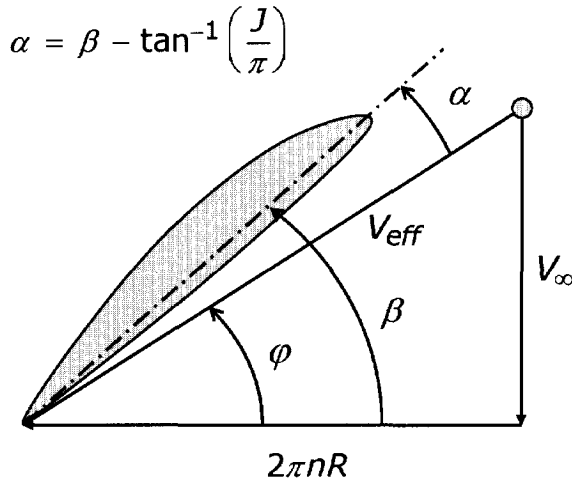
Figure A.2: *Velocity diagram at the propeller tip with the propeller induced velocity components neglected; β is the blade angle; α is the angle of attack.*

A.3 Actuator disk theory

The thrust delivered by a propeller can be achieved by imparting axial momentum to the passing fluid to force a backward motion. The energy associated to the fluid is an inevitable loss. The original theory, as first formulated by Rankine and Froude, excludes the viscous effects, the rotation of the slipstream, and the uneven load distribution, with the scope of evaluating the ideal efficiency of such a propulsive system (also called actuator disc).

The rotor is degenerated into a disc perpendicular to the direction of the thrust, and is capable of sustaining a pressure difference between its two sides, and of generating/imparting linear momentum to the fluid that passes through it. The determination of the thrust requires the evaluation of the mass flow through a stream tube bounded by the disc. In a later refinement the load distribution on the disc was taken into account with the momentum equation, and led to the conclusion that the load (i.e. the pressure difference), in fact, must be constant over the actuator disc to produce optimal thrust (e.g. with minimum energy losses). With this in mind the actuator disk theory is discussed briefly.

The momentum theory of propellers, as proposed decades ago by Rankine and Froude, provides a basic understanding of various aspects related to the performance of propellers. As sketched in Fig. A.3 the propeller is approximated by a infinitely thin
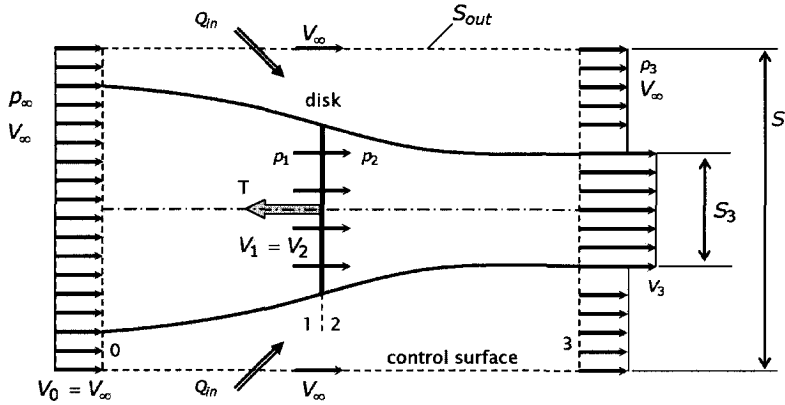
Figure A.3: *Actuator disk model with control volume for the application of the momentum equation.*

actuator disk across which the static pressure rises in a discontinuous way. Important simplifications that are applied in this model can be summarized as follows:

- both the pressure and the velocity are distributed uniformly over the disk

- the rotation (swirl) imparted to the flow as it passes the disk plane is completely neglected

- the flow passing through the propeller disk can be separated from the rest of the flow by a streamtube

- the flow is assumed to be incompressible

In order to apply the momentum theory, four planes, 0 to 3, all perpendicular to the thrust axis, are defined. Planes 0 and 3 are assumed to be lying far upstream and far downstream of the disk respectively. Planes 1 and 2 are positioned just in front of and behind the propeller (Fig. A.3). This means that the local static pressure in the these planes is constant and equal to the undisturbed pressure, p_∞.

A volume exists across the inflow plane, with surface area S, the outflow plane with the same area and the cylindrical surface S_{out}. The flux passing out of the surface across plane 3 minus the flux entering across plane 0 will be:

$$\Delta Q = S_3 V_3 + (S - S_3)V_\infty - S V_\infty \tag{A.13}$$

or:

$$\Delta Q = S_3(V_3 - V_\infty) \tag{A.14}$$

If $V_3 \neq V_\infty$, a flux enters the control volume from the side. When the cylindrical control volume is chosen large enough the external pressure forces cancel out. In this case the momentum equation results in:

$$T = \rho S_3 V_3^2 + \rho (S - S_3) V_\infty^2 - \rho S V_\infty^2 - \rho \Delta Q V_\infty \qquad (A.15)$$

With equation (A.14) this leads to:

$$T = \rho S_3 V_3 (V_3 - V_\infty) \qquad (A.16)$$

where $\rho S_3 V_3$ is equal to the mass flux passing through the propeller plane. Alternatively the thrust of the propeller can be derived from the pressure force acting on the actuator disc plane:

$$T = S_p (p_2 - p_1) \qquad (A.17)$$

where $S_p = S_1 = S_2$ is the propeller disk area.

To relate p_1 and p_2 Bernoulli's equation can be applied both for the domain upstream and downstream of the propeller:

$$p_\infty + \tfrac{1}{2}\rho V_\infty^2 = p_1 + \tfrac{1}{2}\rho V_1^2 \qquad (A.18)$$

$$p_2 + \tfrac{1}{2}\rho V_2^2 = p_\infty + \tfrac{1}{2}\rho V_3^2 \qquad (A.19)$$

Subtracting equation (A.18) from equation (A.19) and noting that the velocity is continuous across the propeller disk ($V_1 = V_2 = V_p$) leads to:

$$p_2 - p_1 = \tfrac{1}{2}\rho (V_3^2 - V_\infty^2) \qquad (A.20)$$

From the continuity equation it follows that: $S_3 V_3 = S_p V_p$. Combining this with equations (A.16), (A.17) and (A.20) results in:

$$V_p = \frac{V_3 + V_\infty}{2} \qquad (A.21)$$

So, we conclude that the velocity at the location of the propeller is equal to the average of the velocity far upstream and far downstream of the propeller. With the propeller induced axial velocity increase at the propeller plane, v_a:

$$V_p = V_\infty + v_a \qquad (A.22)$$

the thrust can be written as:

$$T = 2\rho S_p (V_\infty + v_a) v_a \qquad (A.23)$$

To determine the efficiency of the propeller a relation for the power has to be established. From the increase in kinetic energy of the flow the power can be written as:

$$P = \tfrac{1}{2}\rho S_p (V_\infty + v_a) \left\{ (V_\infty + 2v_a)^2 - V_\infty^2 \right\} \qquad (A.24)$$

or:

$$P = 2\rho S_p v_a (V_\infty + v_a)^2 \tag{A.25}$$

Substitution of equation (A.23) leads to the following important result:

$$P = T(V_\infty + v_a) \tag{A.26}$$

The efficiency of the propeller, η , is the ratio between the useful power, TV_∞ and the power, P, that is absorbed. Hence:

$$\eta = \frac{TV_\infty}{P} = \frac{TV_\infty}{T(V_\infty + v_a)} \tag{A.27}$$

or:

$$\eta = \frac{1}{1 + (\frac{v_a}{V_\infty})} \tag{A.28}$$

Solving equation (A.23) for v_a leads to:

$$v_a = \tfrac{1}{2}\left(-V_\infty + \sqrt{V_\infty^2 + \tfrac{2T}{\rho S_p}}\right) \tag{A.29}$$

With the definition for the thrust coefficient, $T_c = T/(\frac{1}{2}\rho V_\infty^2 S_p)$, the combination of equation (A.28) and (A.29) the efficiency of the propeller can be written as:

$$\eta = \frac{2}{1 + \sqrt{1 + T_c}} \tag{A.30}$$

This means that the propeller efficiency approaches unity when the disk loading (and therefore the thrust coefficient) approaches zero.

Expression (A.30) represents the theoretical maximum value of the efficiency. This value is however not attainable in practice since the momentum equation neglects viscous losses due to the boundary layer on the propeller blades. Moreover, additional induced losses arise due to the loss of lift near the propeller tips. The helically shaped vortex system that is produced as a result reduces the efficiency even further similar to the performance degradation of a wing due to the tip vortices.

Although the actuator disk model, based on the momentum equation, fails to accurately predict the power of a propeller it is very useful for estimating the propeller induced axial velocity in the slipstream, as indicated above.

A.4   Vortex Theory

The actuator disk theory helped in the understanding of propellers but failed to relate the blade loading with the propeller geometry and operating conditions. Prandtl [134] introduced the lifting line theory in which he described the lift of finite wings

in three dimensional flow introducing the idea of a trailing vortex sheet. The basis effect of the vortex sheet is to induce velocities at the location of the wing (or bound vortex) which can be calculated with the Biot-Savart Law. For the special case of an elliptically loaded wing the induced angle of attack will be constant.

In reality, the vortex sheet is not stable and tends to roll up behind the wing into two distinct "tip vortices". If however if the vortex sheet that leaves the wing is assumed to stay flat its position will vary in a state of uniform motion perpendicular to itself. The downwash angle far downstream will then be twice the value as found at the location of the wing. This picture led the way to the vortex theory of propellers assuming that an equivalent vortex system will be produced by the rotating propeller blades (6.3.6).

The vortex theory, developed by Betz [135], assumes a rigid "wake" and can be used to design a minimum induced loss propeller in analogy with the elliptical wing which produces minimum induced drag. The *optimum distribution of the circulation* along the propeller blade produces a propeller with maximum efficiency excluding any viscous losses due the profile drag of the propeller blade sections.

From the known optimum circulation distribution the optimum value of the local loading, expressed in $C_l \cdot c$, is found for one specific operation condition of the propeller. Now combinations of blade angle distributions and chord distributions can be produced delivering an optimum (minimum induced loss) propeller.

If the focus is on the analysis of a given propeller, rather than the design of a new propeller, the vortex theory of propeller is of little use. Especially when the slipstream characteristics of a given propeller are the subject of research a more extended procedure as outline in section A.5 is to be used as a starting point. One concept however that can be described based on the original vortex theory of propellers is the so-called "Tip loss factor", denoted with F. To understand its importance for the description of the inflow field of a propeller the derivation of an expression for F will be summarized here, based on the so-called displacement velocity.

Consider an elementary helical vortex filament being part of in a helical vortex sheet which forms part of the slipstream of a propeller as shown in Fig. A.4. The vortex filament is constrained to move everywhere perpendicular to itself with a velocity w_s, which is the same as the local slipstream velocity. When the local helix angle is φ_s, the axial velocity becomes $w_s \cos(\varphi_s)$ and the circumferential velocity $w_s \sin(\varphi_s)/r_s$, where r_s is the local helix radius. For an observer that is unaware of the angular velocity it seems that the vortex filament has a displacement velocity:

$$v_n = w_s \cos(\varphi_s) \tag{A.31}$$

Betz [135] shows that for a propeller of minimum induced loss the displacement velocity is constant in blade spanwise direction (i.e. radially constant). The axial component and the swirl component of the vortex sheet are then given by:
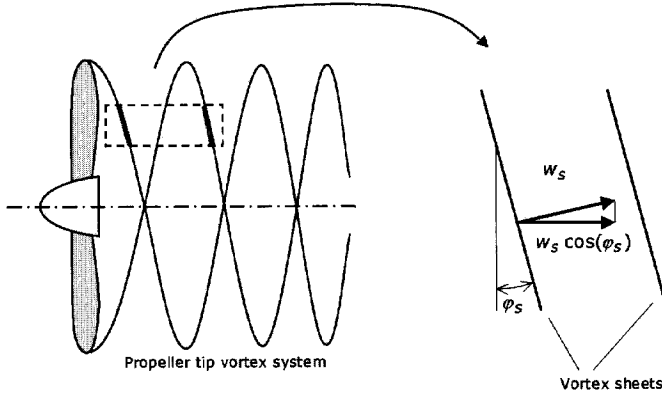
Figure A.4: *True and apparent transport velocity of the vortex sheets behind the propeller blades.*

$$
\begin{aligned}
w_{ax} &= w_s \cos(\varphi_s) = v_n \cos^2(\varphi_s) \\
w_{sw} &= w_s \sin(\varphi_s) = v_n \cos(\varphi_s) \sin(\varphi_s)
\end{aligned}
\tag{A.32}
$$

When the advance ratio is small or the number of blades is high enough the distance between the vortex sheets, produced by two succeeding blades, will be small. Based on this model Prandtl showed that the fluid velocity between the sheets is a fraction F of the vortex sheet velocity.

Prandtl realized that that at small values of r_s the velocity between the vortex sheets will be approximately the same as the local displacement velocity of the sheets. Further he indicated that then local flow velocity at the outer edge of the vortex sheet will be different from the displacement velocity. This flow type now exhibits much similarity with the 2-dimensional flow along the edges of parallel plates in a uniform flow as sketched in Fig. A.5.

For this particular flow field the ratio between the local average flow velocity between the plates, $\overline{v_n}$ and the speed of the plates with reference to the undisturbed flow at great distance from the plate, v_n, becomes:

$$
\frac{\overline{v_n}}{v_n} = \frac{2}{\pi} \arccos(e^{\frac{-\pi d}{s}})
\tag{A.33}
$$

To put this in a form that is directly related to the propeller vortex sheet geometry, distance d is replaced by $R - r$ and s by the distance between the two succeeding tip vortices (index t):
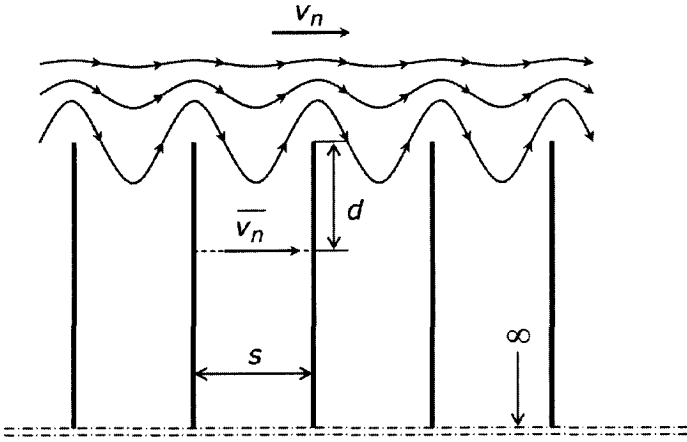
Figure A.5: *Two-dimensional potential flow along a row of semi-infinite parallel plates as used by Prandtl in the derivation of the tip loss factor, F.*

$$s = \frac{2\pi R}{B} \sin(\varphi_{t_3}) \qquad (A.34)$$

where index 3 again indicated plane 3 far downstream of the disk. Thus for a circle with radius r:

$$\frac{\overline{v_{a_3}}}{v_{a_3}} = \frac{\overline{v_{t_3}}}{v_{t_3}} = F \qquad (A.35)$$

where:

$$F = \frac{2}{\pi} \arccos(e^{-f}) \qquad (A.36)$$

and:

$$f = \frac{\pi \, (R - r)}{\frac{2\pi R}{B} \sin(\varphi_t)} = \frac{B \, (1 - \xi)}{2 \sin(\varphi_t)} \qquad (A.37)$$

where $\xi = r/R$. It should be noted that for the limiting case were the propeller is lightly loaded the induced velocities become very small.
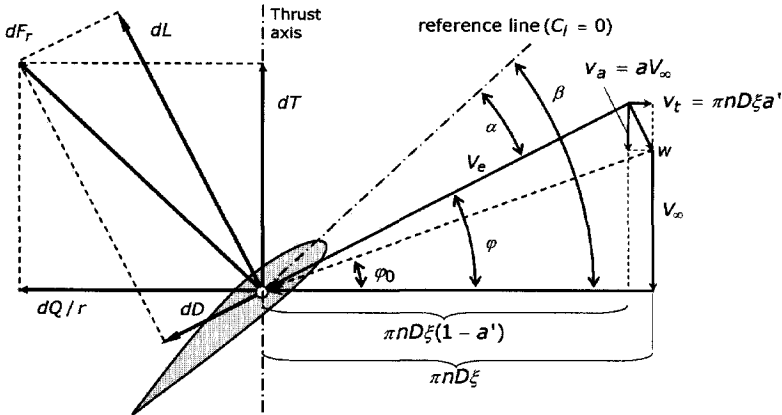
Figure A.6: *Velocity and force diagram acting on a propeller blade element.*

A.5 Blade element theory

As indicated before, in order to estimate the performance of the propeller and assess the slipstream that is generated it is necessary to examine the aerodynamics of the blade in detail. A relatively simple method of predicting the performance of a propeller is the use of blade element theory. The propeller is divided into a number of independent sections along the blade spanwise direction.

Fig. A.6 contains the velocity and force diagram for a blade section positioned at radius , r. Before the forces acting on the propeller can be determined from the known airfoil characteristics of the blade sections, it is necessary to calculate the effective velocity, V_e, or equivalent : the induced velocity components, v_a and v_t.

To calculate the induced velocities one could start using the Biot-Savart law in the process of calculating the velocity induced by every single vortex filament in the slipstream. This leads to a rather laborious calculation technique that not necessarily produces more accurate results than the method based on conservation of momentum as sketched hereafter. In case the number of propeller blades is limited the induced velocity components will exhibit a fluctuating character at the location of the propeller disk. This again makes the Biot-Savart techniques complex since unsteady equations have to be solved. However, a very acceptable result is obtained by considering the case that the number of blades $B = \infty$ [59].

Following a simplified conservation of momentum approach only requires the availability of the Prandtl tip loss factor.

Considering a circular streamtube, between r and $r + dr$ the conservation law of momentum in axial direction becomes:

$$2\pi r dr \rho \left(V_\infty + \overline{v_a}\right) \overline{v_{a_3}} = dT'_0 \tag{A.38}$$

where index 0 refers to the condition were the profile drag of the blade element is zero $(C_d = 0)$. The right hand side, dT'_0, is the force acting on the fluid inside the tube element which is equal to B times the force acting on the blade element. In tangential direction we may write:

$$2\pi r dr \rho \left(V_\infty + \overline{v_a}\right) \overline{v_{t_3}} = \frac{dQ'_0}{r} \tag{A.39}$$

The attribute $C_d = 0$ is essential since the left hand sides of the equations (A.38) and (A.39) are based on an idealized vortex system in which the effect of the profile drag is not represented for the moment. With the lift force dL acting on the blade element the thrust and torque can also be expressed as:

$$dT'_0 = B \, dL \, \cos(\varphi) = B \, C_l \tfrac{1}{2}\rho \, V_e^2 \, c \, dr \, \cos(\varphi) \tag{A.40}$$

$$\frac{dQ'_0}{r} = B \, dL \, \sin(\varphi) = B \, C_l \tfrac{1}{2}\rho \, V_e^2 \, c \, dr \, \sin(\varphi) \tag{A.41}$$

where dL denotes the lift force acting on an element of a single propeller blade. The velocity V_e can be written as :

$$V_e = \frac{V_\infty + v_a}{\sin(\varphi)} = \frac{V_\infty \left(1 + a\right)}{\sin(\varphi)} \tag{A.42}$$

or:

$$V_e = \frac{\Omega r - v_t}{\cos(\varphi)} = \frac{\Omega r(1 - a')}{\cos(\varphi)} \tag{A.43}$$

The axial and tangential velocity ratio at the location of the propeller and at cross section 3 may be approximated by:

$$\frac{\overline{v_a}}{v_a} = \frac{\overline{v_t}}{v_t} = \frac{\overline{v_{a_3}}}{v_{a_3}} = \frac{\overline{v_{t_3}}}{v_{t_3}} = F \tag{A.44}$$

In theory $\overline{v_a}/v_a$ will be different from $\overline{v_{a_3}}/\overline{v_a}$ due to the influence of the bound circulation on the blades and the "development" of the trailing vortex system that is influenced by self-induction. However, the angle φ_{w_3} will differ only slightly from φ_{w_2}. This is especially the case for lightly loaded propellers. Accepting the value of F as calculated by the method described in section A.4, the blade element model now proceeds as follows.

Substitution of eq. (A.44) and (A.40) into eq. (A.38) leads to:

$$4\pi r \rho \left(V + F v_a\right) F v_a = B C_l \tfrac{1}{2}\rho V_e^2 c dr \cos(\varphi) \tag{A.45}$$

or:

$$4\pi r\rho\left(V + Fv_a\right)Fv_a = BC_l\frac{1}{2}\rho\frac{(V+v_a)^2}{\sin^2(\varphi)}cdr\cos(\varphi) \tag{A.46}$$

Thus:

$$\frac{V + Fv_a}{V + v_a}\frac{Fv_a}{V + v_a} = \frac{Bc}{2\pi r}\frac{C_l\cos(\varphi)}{4\sin^2(\varphi)} \tag{A.47}$$

In an analogue way for the tangential direction we find:

$$\frac{V + Fv_a}{V + v_a}\frac{Fv_t}{\Omega r - v_t} = \frac{Bc}{2\pi r}\frac{C_l}{4\cos(\varphi)} \tag{A.48}$$

For the known values of V, Ω, r, B, β and c equations (A.47) and (A.48) constitute a relation between the induced velocities v_a, v_t and the angle φ (or α). The value of the lift coefficient C_l for all blade sections is known at every angle of attack from a look-up table. Remember that α is simply found from $\alpha = \beta - \varphi$. The Prandtl Tip-loss-factor, F, is known for a given value of φ but an initial guess is needed for φ_{t_3} which is unknown at the start of the calculation process.

For a lightly and optimal loaded propeller $V + w_3$ may be approximated as being independent of r. Hence:

$$\tan(\varphi_{t_3}) = \frac{r}{R}\tan(\varphi_{w_3}) \tag{A.49}$$

Using the assumptions based on the use of the Prandtl tip-loss-factor it is beneficial and acceptable to start the calculation process with $\sin(\varphi_{tw_3}) = \frac{r}{R}\sin(\varphi_{w_3})$. Thus factor f in eq. (A.37) becomes:

$$f = \frac{B\left(1 - \frac{r}{R}\right)}{2\frac{r}{R}\sin\left(\varphi_{w_3}\right)} \tag{A.50}$$

Initially the relation between φ_{w_3} and φ must be predicted appropriately. For lightly loaded propellers a start value of $\varphi_{w_3} = \varphi$ is acceptable. For a non-zero flight speed, V_∞, eq. (A.47) and (A.48) may be put in the form :

$$\frac{1 + Fa}{1 + a}\frac{Fa}{1 + a} = \sigma\frac{C_l\cos(\varphi)}{4\sin^2(\varphi)} \tag{A.51}$$

$$\frac{1 + Fa}{1 + a}\frac{Fa'}{1 - a'} = \sigma\frac{C_l}{4\cos(\varphi)} \tag{A.52}$$

where $\sigma = Bc/2\pi r$ denotes the solidity of the propeller blade section. With equation (A.51) the axial induction factor can be determined for all values of φ. Subsequently the value of the tangential induction factor, a', can be calculated with eq. (A.52).

In cases where the axial velocity increase, v_a, is small compared to the undisturbed flow velocity (i.e. cruise condition), the term $(1 + Fa)/(1 + a)$ may be approximated by 1. Thus equations (A.51) and (A.52) become:

$$\frac{a}{1 + a} = \sigma\frac{C_l\cos(\varphi)}{4F\sin^2(\varphi)} \tag{A.53}$$

$$\frac{a'}{1-a'} = \sigma \frac{C_l}{4F\cos(\varphi)} \tag{A.54}$$

These expressions relate the induction factors a and a' with the flow angle φ. To calculate these three variables a third equation is needed which fixes the operating condition of the propeller. For this purpose the advance ratio, J, is used :

$$J = \frac{V}{nD} = \frac{V}{\frac{\Omega}{2\pi}2r\frac{R}{r}} = \pi\xi\frac{V}{\Omega r} \tag{A.55}$$

where $\xi = \frac{r}{R}$. Hence:

$$J = \pi\xi\frac{V(1+a)(1-a')}{\Omega r(1-a')(1+a)} = \pi\xi\tan(\varphi)\frac{1-a'}{1+a} \tag{A.56}$$

Equations (A.53), (A.54) and (A.56) now have to be solved for a, a' and φ by performing an iterative process.

In reality the propeller blade section, beside the lift force, produces a profile drag force which means that eq. (A.40) and (A.41) have to be rewritten as :

$$dT' = B\left(C_l\cos(\varphi) - C_d\sin(\varphi)\right)\tfrac{1}{2}\rho V_e^2\,c\,dr \tag{A.57}$$

$$\frac{dQ'}{r} = B\left(C_l\sin(\varphi) + C_d\cos(\varphi)\right)\tfrac{1}{2}\rho V_e^2\,c\,dr \tag{A.58}$$

With $V_e = V(1+a)/\sin(\varphi)$ and $dP = \Omega dQ$ and the definitions for the thrust and power coefficient:

$$C_T = \frac{T}{\rho n^2 D^4} \tag{A.59}$$

$$C_p = \frac{P}{\rho n^3 D^5} \tag{A.60}$$

equations (A.57) and (A.58) can be rewritten :

$$\frac{dC_T}{d\xi} = J^2 B\frac{c}{R}\frac{(1+a)^2}{8\sin^2(\varphi)}\left(C_l\cos(\varphi) - C_d\sin(\varphi)\right) \tag{A.61}$$

$$\frac{dC_P}{d\xi} = J^2\frac{r}{R}B\frac{c}{R}\frac{\pi}{8}\frac{(1+a)^2}{\sin^2(\varphi)}\left(C_l\sin(\varphi) + C_d\cos(\varphi)\right) \tag{A.62}$$

and the propeller efficiency can be calculated from :

$$\eta = \frac{TV}{P} = \frac{C_T}{C_p}J \tag{A.63}$$

With these equations the system that determines the propeller characteristics is now complete. As input parameters we need the blade geometry (chord and blade angle

distribution) and the characteristics of the blade airfoil sections. The latter may be taken either from experiments or calculations on 2D-airfoils. Two factors that need further attention before appropriate lift and drag coefficients can be used in the BEM-analysis, as discussed above, are the effect of compressibility and the tip relief effect (TRE).

A.6   Effect of compressibility

In contrast to the Mach numbers that are attained on the wing, the local propeller blade section Mach number may be quite high. At a flight speed of $V = 100 \, \text{m/s}$ with a 3.65 m diameter propeller running at an RPM of 2200 in standard atmosphere at height of $h = 3000 \, \text{m}$ the tip Mach number already reaches a value of $M = 0.815$. This means that the lift and drag characteristics taken from experiments or calculations under incompressible conditions should be corrected for compressibility effects. For Mach numbers below 0.7 the Prandtl-Glauert correction may be applied, leading to acceptable results:

$$C_{x_{cor}} = \frac{C_x}{\sqrt{1 - M_\infty^2}} \tag{A.64}$$

where the coefficient C_x is either the lift or the drag coefficient of the blade airfoil section. For $M > 0.7$ the airfoil characteristics have to be corrected through dedicated prediction codes or should directly be taken from appropriate high speed windtunnel tests.

A.7   Tip relief effect

Experiments on rotating propeller blades have shown that the pressure distribution and the local lift curve slope, C_{l_α}, may differ significantly from the 2D-airfoil data of the particular blade section [136]. This phenomenon can be attributed to the existence of centrifugal and Coriolis forces that act on the boundary layer flow over the propeller blades. The total effect is comparable to a favorable pressure gradient. Fig. A.7 shows the situation on the propeller blade. The Coriolis acceleration is given by:

$$a_{cor} = -2\omega \times V_{rel} \tag{A.65}$$

where V_{rel} is the velocity vector relative to the rotating propeller frame of reference. The centrifugal acceleration is given by:

$$a_{cen} = \omega \times (\omega r) \tag{A.66}$$

We see that material in the boundary layer that moves with the propeller is swept outward due to the centrifugal acceleration while the Coriolis force depends on the
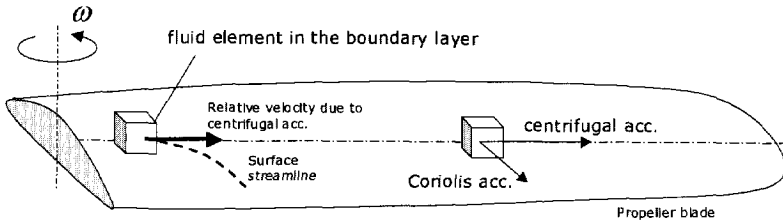
Figure A.7: *Effect of the Coriolis force on the propeller blade boundary layer.*

direction of the relative velocity vector, V_{rel}. In case V_{rel} is directed outward due to the action of a_{cen}, the Coriolis force will be in the direction of the blade trailing edge, as indicated in Fig. A.7

Comparison of results of boundary layer calculations of rotating blades with those of 2-dimensional stationary ones showed that the secondary flow induced over the rotating blades has strong effects by suppressing the boundary layer growth which results in delayed transition and separation of the boundary layer [136].

An indication of these effects can be found from the measurements of Himmel-skamp [137]. Himmelskamp performed measurements on a rotating propeller and determined the local blade section lift coefficients from surface pressure measurements. Some of his results are reproduced in Fig. A.8 where the C_l-α curves at various radial stations are compared with 2D windtunnel data. A significant increase in lift coefficient can be found going from the tip to the hub, combined with separation delayed to a higher angle of attack.

These effects on the lift curve slope can be explained by the influence of the Coriolis force acting on the boundary layer material. Additionally the centrifugal force transports boundary layer material away from the hub. The resulting boundary layer at the inner portion of the blade thus becomes thinner, leading to favorable C_l-α behavior.

To incorporate these effects in the calculation process of the propeller forces the lift coefficients should somehow be corrected. This procedure however is not straightforward since the correction needed depends very much on the state of the local boundary layer. Several attempts have been made to derive a convenient correction formula. A quite acceptable method was developed by ECN and NLR as described by Bosschers [138] in the form of an empirical formula. This method is based on the work of Snel [139] on incompressible boundary layers. The method proposed is particularly suited for high lift conditions were separated flow is affected by the Coriolis force pressure force and shear stresses. An acceptable correlation between the predicted and the measured data was found for some typical wind turbine applications. The empirical relation for the rotational effects on the flow in the stall region is based on the dif-
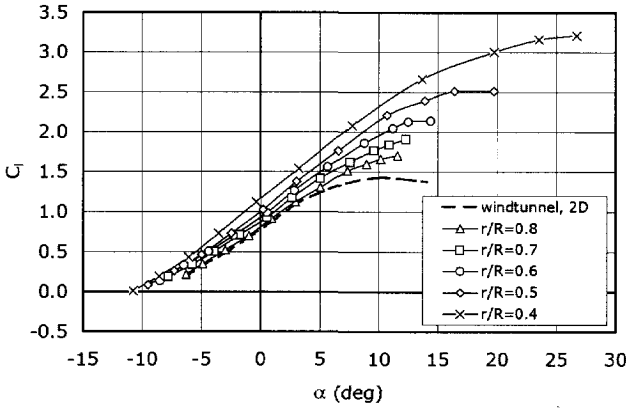
Figure A.8: *Typical example of the effect of blade rotation on the sectional lift coefficient of the propeller blade [137]. Airfoil: Göttingen 625.*

ference between the 2D inviscid and the viscous lift curve slope, C_{l_α}, as expressed by :

$$C_{l_{3D,rot}} = C_{l_{2D,vis}} + \left(C_{l_{2D,inv}} - C_{l_{2D,vis}}\right) \cdot f_c\left(c/R\right) \qquad (A.67)$$

where $C_{l_{3D,rot}}$ is the local blade lift coefficient on the rotating propeller, $C_{l_{2D,vis}}$ and $C_{l_{2D,inv}}$ are the 2D lift coefficients for the viscous and the inviscid flow respectively. The function $f_c(c/R)$ is a function of the chord distribution. Although it is evident that f_c will be affected by parameters like the airfoil shape, local Reynolds number, etc. the following approximation produces interesting results :

$$f_c(c/R) = \tanh\left(3(c/R)^2\right) \qquad (A.68)$$

The procedure as described above should however be treated carefully since the boundary layer transition process may influence the lift enhancement process [140]. The resulting decrease in lift and increase in skin friction drag complicates the effect of blade rotation which in general is thought to increase lift and decrease drag for the inboard blade sections.

A.8   Nacelle effects

In most cases the nacelle has a relative large dimension compared to the blade root chord and the propeller tip radius. The presence of the nacelle therefore alters the
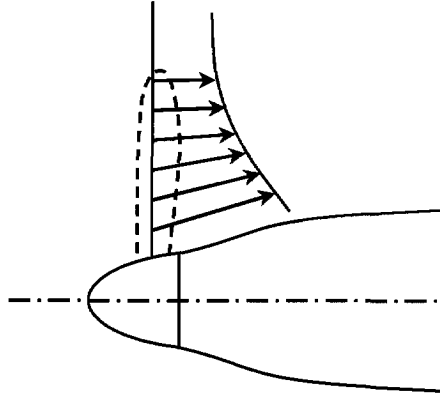
Figure A.9: *Axial velocity increase due to the blockage effect of the nacelle.*

flow field by changing the axial flow velocity, u, and the radial flow velocity, v_r, as sketched in Fig. A.9.

To get a first estimate of the performance of the installed propeller the axial force acting on the nacelle can be estimated by calculating the change in static pressure upstream and downstream of the thrusting propeller. For this purpose the approximate relation as presented by Koning [141] can be used. Downstream of the propeller, the static pressure change becomes:

$$\frac{\Delta P}{\frac{1}{2}\rho V_\infty^2} = +\frac{T_c}{2}\left(1 - \frac{x/R}{\sqrt{(x/R)^2 + 1}}\right) \quad (A.69)$$

while upstream:

$$\frac{\Delta P}{\frac{1}{2}\rho V_\infty^2} = -\frac{T_c}{2}\left(1 + \frac{x/R}{\sqrt{(x/R)^2 + 1}}\right) \quad (A.70)$$

Here x is the distance downstream of the propeller. The axial pressure gradient that exists causes a buoyancy force on the nacelle that can be calculated with the known area distribution $S_n(x)$:

$$\Delta C_{D_{buoy}} = \frac{1}{S_{ref}} \int_0^{L_n} \left(\frac{\Delta P}{\frac{1}{2}\rho V_\infty^2}\right)\left(\frac{dS_n}{dx_n}\right) dx_n \quad (A.71)$$

where S_{ref} is the reference area used in the calculation of drag coefficients, L_n is

the nacelle length. The net thrust of the propeller-nacelle configuration then becomes:

$$C_{T_n} = C_T \left(1 - \frac{S_{ref}}{\pi R^2} \Delta C_{D_{buoy}} \right) \tag{A.72}$$

A.9 Propeller at angle of attack

The effective velocity vector at the blade section in the propeller axis reference system is the sum of the undisturbed flow vector and the induced flow vectors induced by all aircraft parts (index ap) and by the propeller itself (index p) :

$$(V_{eff})_p = (V_\infty)_p + (V_{ap})_p + (V_p)_p \tag{A.73}$$

This velocity vector is defined in the orthogonal propeller axis system, denoted by $(\ )_p$. To find the velocity vector in the cylindrical propeller axis system, denoted by $(\ )_{pc}$, the velocity vectors have to be transformed from the global axis system, X, Y, Z. Thus:

$$(V)_{pc} = M \cdot N \cdot V_{gl} \tag{A.74}$$

where M and N are the transformation matrices respectively from global to orthogonal propeller axis system and from orthogonal to cylindrical propeller axis system. Index gl denotes the global axis system.

The general form of the matrix M is:

$$M = \begin{pmatrix} i \cdot i_p & j \cdot i_p & k \cdot i_p \\ i \cdot j_p & i \cdot j_p & i \cdot j_p \\ i \cdot k_p & i \cdot k_p & i \cdot k_p \end{pmatrix} \tag{A.75}$$

where i, j, k and i_p, j_p, k_p are the unit vectors in the global and the orthogonal axis system respectively and the vector product merely represent the cosine of the angles between the different axes. The matrix N simply becomes:

$$N = \begin{pmatrix} 1 & 0 & 0 \\ 0 & \sin(\theta) & \cos(\theta) \\ 0 & \cos(\theta) & -\sin(\theta) \end{pmatrix} \tag{A.76}$$

In flight there will generally be some angle of attack to the free stream and therefore a component of the forward speed will act in the plane of the propeller that will combine with the rotational component to produce a periodic variation of the angle of attack as the propeller rotates. To get some understanding of the resulting effects on the propeller performance assume the propeller flow is only affected by a plain α_p-effect.

In this case M becomes:

$$M = \begin{pmatrix} \cos(\alpha_p) & 0 & -\sin(\alpha_p) \\ 0 & 1 & 0 \\ \sin(\alpha_p) & 0 & \cos(\alpha_p) \end{pmatrix} \qquad (A.77)$$

and the effective velocity vector, V_{eff}, can be written as :

$$V_{eff} = \begin{pmatrix} V_\infty(1+a)\cos(\alpha_p) \\ V_\infty \sin(\alpha_p)\cos(\theta) \\ V_\infty \sin(\alpha_p)\sin(\theta) + \pi n D\xi\,(1-a') \end{pmatrix} \qquad (A.78)$$

This means that the expressions for the local thrust and power of the blade element change to:

$$\frac{dC_T}{d\xi} = J^2 B \frac{c}{R} \frac{(1+a)^2}{8\sin^2(\varphi')} \left(C_l \cos(\varphi') - C_d \sin(\varphi') \right) \cos^2(\alpha_p) \qquad (A.79)$$

$$\frac{dC_P}{d\xi} = J^2 \frac{r}{R} B \frac{c}{R} \frac{\pi}{8} \frac{(1+a)^2}{\sin^2(\varphi')} \left(C_l \sin(\varphi') + C_d \cos(\varphi') \right) \cos^2(\alpha_p) \qquad (A.80)$$

with:

$$\tan(\varphi') = \frac{V_\infty\,(1+a)\cos(\alpha_p)}{V_\infty \sin(\alpha_p)\sin(\varphi') + \pi n D\xi\,(1-a')} \qquad (A.81)$$

The coefficients now show a periodic variation which will cause an asymmetric loading over the propeller disk and moments about the axes normal to the propeller axis. With the relation between the power and the torque, $P = \Omega Q$, the torque coefficient of the blade sections can be found. Resolving this into the force components in direction normal and lateral to the propeller axis the normal force and lateral force contribution can be calculated through:

$$dN_p = \frac{dQ}{r}\sin(\theta) \quad ; \quad dY_p = \frac{dQ}{r}\cos(\theta) \qquad (A.82)$$

The pitching moment contribution and yawing moment contribution can be found from :

$$dM_p = r\,dT\cos(\theta) \quad ; \quad dM_y = r\,dT\sin(\theta) \qquad (A.83)$$

To find the magnitude of the forces and moments an integration over the propeller disk is needed. The normal force for example can be found from:

$$N_p = \frac{1}{2\pi} \int_{\xi=0}^{1} \int_{\theta=0}^{2\pi} \frac{dQ}{\xi}\sin(\theta)d\xi \qquad (A.84)$$

Appendix B

Aircraft database

To establish an acceptable range of characteristics for the target airplane discussed in this report, a brief database was generated containing data relevant for discussing the problem of propeller-wing interference. The target aircraft, denoted with TA, is compared with existing designs in Tables B.1 to B.5. The geometrical parameters that are used in the database are given in Fig.B.1.
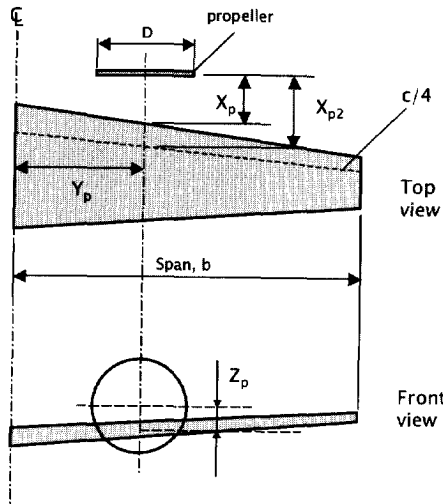
Figure B.1: *Geometrical parameters used in the aircraft database.*

Table B.1: *Typical parameters for some twin-engined propeller powered aircraft (I).*

ID#	Name	P (kW)	V_{cr} (Km/hr)	h_{cr} (m)	M_{cr}	D_p (m)	Disk load (kw/m^2)
1	Antonov AN-32	3760	530	6000	0.47	4.70	216.72
2	ATR-42/300	1342	490	5180	0.43	3.96	108.96
3	ATR-72	1849	526	4575	0.45	3.96	150.13
4	BAe 748-2b	1700	452	4575	0.39	3.66	161.58
5	BAe ATP	1978	496	4575	0.43	4.19	143.45
6	BAe jetstream 31	701	488	4570	0.42	2.69	123.35
7	BAe jetstream 41	1230	547	6100	0.48	2.90	186.22
8	Beech 1900	820	442	7620	0.40	2.78	135.09
9	Beech 1900 D	954	515	7620	0.46	2.78	157.17
10	Beech 99	410	409	3050	0.35	2.33	96.20
11	Beech Super King Air 350	783	576	7315	0.52	2.76	130.87
12	Beechcraft 2000 Starship	895	626	10670	0.59	2.54	176.63
13	CN-235	1305	460	4570	0.40	3.35	148.06
14	Convair CV-580	2797	550	6100	0.49	4.11	210.82
15	DHC -6 Twin otter	486	210	3050	0.18	2.59	92.25
16	DHC -8(dash 8)-100	1491	491	4575	0.42	3.96	121.06
17	Dornier 228-200	579	428	3050	0.36	2.73	98.86
18	Dornier 328-100	1625	620	6100	0.55	3.60	159.65
19	Embraer 110	507	454	3000	0.38	2.36	115.90
20	Embraer 120ER	1342	555	7620	0.50	3.20	166.86
21	Embraer CBA-123	969	648	9150	0.60	2.59	183.92
22	Fairchild Metro 3	746	515	4575	0.45	2.69	131.18
23	Fokker F27	1529	474	6100	0.42	3.87	129.98
24	Fokker 50	1864	526	7620	0.45	3.66	177.17
25	LET 410	533	370	3000	0.31	2.59	101.17
26	LET 610	1358	490	7200	0.44	3.50	141.15
27	Nurtanio N-250	2386	611	7620	0.55	3.81	209.28
28	Piaggio Avanti P-180	597	740	8230	0.67	2.16	162.92
29	Piper Cheyenne 4	1227	620	10670	0.58	2.69	215.81
30	Saab 340b	1305	522	4575	0.45	3.35	148.06
31	Shorts 330	893	352	3050	0.30	2.82	142.98
32	Shorts 360	1062	394	3050	0.33	2.82	170.03
33	TA	1860	520	7000	0.45	3.66	-

Table B.2: *Typical parameters for some twin-engined propeller powered aircraft (II).*

ID#	Name	MTOW	OEW	Range (Km)	Pass.	Year
1	Antonov AN-32	27000	17308	2520	50	1955
2	ATR-42/300	16700	10200	4482	46	1959
3	ATR-72	21500	12500	3889	66	1960
4	BAe 748-2b	21092	12206	2372	58	1966
5	BAe ATP	22930	13595	3444	64	1968
6	BAe jetstream 31	6950	4360	2053	19	1969
7	BAe jetstream 41	10886	6416	1433	29	1969
8	Beech 1900	7530	3947	1578	19	1970
9	Beech 1900 D	7688	4815	2778	19	1990
10	Beech 99	4717	2621	1770	15	1974
11	Beech Super King Air 350	6804	4111	2319	12	1990
12	Beechcraft 2000 Starship	6350	4044	3691	11	1991
13	CN-235	15100	9800	3908	44	1976
14	Convair CV-580	24766	19958	2980	52	1968
15	DHC -6 Twin otter	5670	3180	1198	20	1981
16	DHC -8(dash 8)-100	15650	10251	1546	37	1981
17	Dornier 228-200	5700	3547	600	19	1982
18	Dornier 328-100	13990	8920	1666	33	1982
19	Embraer 110	5300	3200	2050	16	1983
20	Embraer 120ER	11990	7560	3017	30	1983
21	Embraer CBA-123	8500	5640	3521	19	1986
22	Fairchild Metro 3	6577	4164	1065	19	1986
23	Fokker F27	19731	11639	1805	48	1957
24	Fokker 50	19950	12520	2033	50	1985
25	LET 410	5700	3570	1300	19	1988
26	LET 610	14000	9000	2406	40	1988
27	Nurtanio N-250	24800	15700	1270	64	1995
28	Piaggio Avanti P-180	4767	3130	3335	9	1991
29	Piper Cheyenne 4	5466	3431	3375	9	1994
30	Saab 340b	13155	8140	1491	35	1989
31	Shorts 330	10387	6680	876	30	1989
32	Shorts 360	11999	7666	1667	36	1989
33	TA	-	-	-	-	-

Table B.3: *Typical propeller related geometrical parameters for some twin-engined propeller powered aircraft.*

ID#	Name	Y_p (m)	Z_p (m)	X_p (m)	X_{p2} (m)	S_p (m^2)
1	Antonov AN-32	3.80	0.77	2.31	3.42	17.35
2	ATR-42/300	4.07	-0.32	1.91	2.55	12.32
3	ATR-72	4.04	-0.30	2.01	2.64	12.32
4	BAe 748-2b	3.54	0.56	2.55	3.32	10.52
5	BAe ATP	4.18	0.60	2.39	3.18	13.79
6	BAe jetstream 31	2.70	0.30	1.30	1.81	5.68
7	BAe jetstream 41	2.99	0.45	1.69	2.20	6.61
8	Beech 1900	2.70	0.43	1.29	1.89	6.07
9	Beech 1900 D	2.46	0.41	1.23	1.79	6.07
10	Beech 99	1.94	0.10	1.94	2.53	4.26
11	Beech Super King Air 350	2.59	0.32	2.16	2.75	5.98
12	Beechcraft 2000 Starship	1.56	0.55	1.09	2.19	5.07
13	CN-235	4.18	0.60	2.39	3.18	8.81
14	Convair CV-580	3.93	0.17	2.39	3.33	13.27
15	DHC -6 Twin otter	2.76	0.00	1.50	1.94	5.27
16	DHC -8(dash 8)-100	3.99	-0.33	1.66	2.33	12.32
17	Dornier 228-200	2.49	-0.34	0.90	1.47	5.85
18	Dornier 328-100	3.77	0.40	2.56	3.09	10.18
19	Embraer 110	2.45	0.21	1.70	2.34	4.37
20	Embraer 120ER	3.34	0.67	1.87	2.41	8.04
21	Embraer CBA-123	2.13	1.54	4.49	5.02	5.27
22	Fairchild Metro 3	2.37	0.11	1.80	2.26	5.68
23	Fokker F27	3.54	-0.48	2.26	2.98	11.76
24	Fokker 50	3.67	-0.39	2.32	3.09	10.52
25	LET 410	2.36	-0.47	1.18	1.71	5.27
26	LET 610	3.40	-0.32	1.78	2.43	9.62
27	Nurtanio N-250	3.83	-0.37	2.31	3.00	11.40
28	Piaggio Avanti P-180	2.08	0.35	0.87	1.25	3.66
29	Piper Cheyenne 4	2.70	0.37	1.68	2.19	5.68
30	Saab 340b	3.48	0.72	2.03	2.61	8.81
31	Shorts 330	3.12	-0.16	1.56	2.03	6.25
32	Shorts 360	3.20	-0.28	1.67	2.16	6.25
33	TA	3.60	-0.4	2.30	3.10	10.52

Table B.4: *Wing related geometrical parameters for some twin-engined propeller powered aircraft.*

ID#	Name	b	c_r	c_t	$\Lambda_{\frac{1}{4}c}$
1	Antonov AN-32	29.20	3.60	1.26	6.83
2	ATR-42/300	24.57	2.57	1.41	3.10
3	ATR-72	27.05	2.57	1.59	3.10
4	BAe 748-2b	31.23	3.49	1.19	2.90
5	BAe ATP	30.63	3.83	1.53	2.90
6	BAe jetstream 31	15.85	2.19	0.80	0.57
7	BAe jetstream 41	18.29	2.70	0.89	0.57
8	Beech 1900	16.61	2.18	0.91	0.00
9	Beech 1900 D	17.67	2.18	0.91	0.00
10	Beech 99	14.00	2.15	1.07	0.00
11	Beech Super King Air 350	17.65	2.18	0.90	0.00
12	Beechcraft 2000 Starship	16.60	5.53	1.11	24.40
13	CN-235	25.81	3.00	1.20	3.91
14	Convair CV-580	32.12	3.76	1.37	3.00
15	DHC -6 Twin otter	19.81	1.98	1.98	0.00
16	DHC -8(dash 8)-100	25.91	2.56	1.00	0.00
17	Dornier 228-200	16.97	2.38	1.70	8.00
18	Dornier 328-100	20.98	2.48	0.29	0.00
19	Embraer 110	15.32	2.32	1.35	0.00
20	Embraer 120ER	19.78	2.81	1.40	0.00
21	Embraer CBA-123	17.72	2.50	0.99	4.13
22	Fairchild Metro 3	17.37	2.59	0.79	0.90
23	Fokker F27	29.00	3.46	1.40	0.00
24	Fokker 50	29.00	3.46	1.40	0.00
25	LET 410	17.48	2.53	1.27	0.00
26	LET 610	25.60	2.92	1.46	1.00
27	Nurtanio N-250	28.00	2.80	1.45	0.00
28	Piaggio Avanti P-180	14.03	1.82	0.62	0.00
29	Piper Cheyenne 4	14.53	3.12	0.97	0.00
30	Saab 340b	21.44	2.75	0.87	3.60
31	Shorts 330	22.76	1.85	1.85	0.00
32	Shorts 360	19.79	1.78	1.78	0.00
33	TA	29.0	3.46	1.40	0.00

Table B.5: *Propeller models used on typical turbo-prop aircraft*

Model	Aircraft	B	D (ft)	W (lbs)	RPM	SHP	BAF
568F-1	ATR-42-400	6	12.9	393	1200	1896	76
568F-1	ATR-42-500	6	12.9	393	1200	2399	76
568F-1	ATR-72-210	6	12.9	393	1200	2748	76
247F-1E	ATR-72-210	4	13	373	1200	2748	108
14SF-5	ATR-42-300	4	13	320	1200	1896	93
14SF-7	DHC-8-100	4	13	320	1200	2144	93
14SF-11E	ATR-72-200	4	13	320	1200	2401	93
14SF-15	DHC-8-200	4	13	320	1200	2300	93
14SF-15	DHC-8-300	4	13	320	1200	2492	93
14SF-17	CL-215/415	4	13	320	1200	2379	93
14SF-23	DHC-8-100	4	13	320	1200	2144	93
14SF-23	DHC-8-200	4	13	320	1200	2300	93
14SF-23	DHC-8-300	4	13	320	1200	2492	93
14RF-9	EMB-120	4	10.5	232	1300	1782	90
14RF-19	Saab-340B	4	11	232	1384	1869	90
14RF-21	CN-235	4	11	232	1384	1749	90
14RF-23	L-610G	4	11	232	1384	1749	90
TA-prop	TA	6	12	-	1200	1860	92
54H60	C-130, P-3C	4	13.5	960	1020	4600	-
54460	E-2C, C-2A	4	13.5	845	1106	5100	-
63E60	DHC-5, G.222	3	14.5	710	1260	3400	-

RPM = Revolution per minute ; BAF = Blade activity factor ; SHP = Shaft horse power. Source : Hamilton Standard

Appendix C

Slipstream contraction

Due to the velocity increase induced by the propeller the slipstream will contract. This is an important aspect as this results in a region of influence that is smaller than the volume occupied by the cylinder with constant radius R. Besides this the slipstream contraction causes an inflow angle that affects the local angle of attack of the wing.

An attractive way to study the slipstream contraction is to realize that its form is determined by the forces that the propeller exerts on the air. In view of the fact that in general the problem in its most general form is very complex it is beneficial to simplify the propeller again as a this disk. Realizing that the function of the propeller is to generate a force in x-direction it is expected that the axial components of the general force system will dominate the slipstream geometry. Accepting the simplification that these axial forces are constant over the propeller disk we arrive at the definition of the so-called "ideal propeller".

To be able to find the velocities that in their turn determine the slipstream boundary and contraction the flow is simplified even further by neglecting the effects of viscosity and compressibility.

A simple procedure that can be followed to find a first estimate for the contraction, is described here.

The boundary of the slipstream can be modeled as a body of revolution with a radius, R_s, that changes with the axial coordinate, x. By considering the law of continuity the amount of fluid that has passed the propeller disc is equal to the amount found in all cross section of the slipstream. With the acceptance of a uniform velocity distribution this leads to:

$$\pi R_s^2 V_\infty (1 + v_x) = \pi R^2 V_\infty (1 + a) \tag{C.1}$$

Here a is the axial inflow factor representing the axial velocity increment at the

location of the disc. Its value follows from the axial momentum theory of propellers, in which the tangential velocity component, v_t, is neglected :

$$a = \tfrac{1}{2}\left(-1 + \sqrt{1 + \tfrac{8}{\pi}T_c}\right) \qquad (C.2)$$

For a given value of the axial inflow factor the contraction ratio, R_s/R, depends on the streamwise development of the axial velocity perturbation, $v_x(x)$. This function can be determined by considering the Navier-Stokes equations for inviscid, incompressible flow with only an external force in x-direction active. For small perturbations due to the propeller:

$$\rho V \frac{\partial v_x}{\partial x} = -\frac{\partial p}{\partial x} + F_x$$
$$\rho V \frac{\partial v_y}{\partial x} = -\frac{\partial p}{\partial y} \qquad (C.3)$$
$$\rho V \frac{\partial v_z}{\partial x} = -\frac{\partial p}{\partial z}$$

$$\frac{\partial v_x}{\partial x} + \frac{\partial v_y}{\partial y} + \frac{\partial v_z}{\partial z} = 0 \qquad (C.4)$$

The external force only acts on the disc while the pressure, apart form the propeller disc surface, is continuous everywhere. By eliminating the velocity components, v_x, v_y and v_z , from eq. C.3 combined with eq. C.4 the Laplace equation for the pressure is found:

$$\frac{\partial^2 p}{\partial x^2} + \frac{\partial^2 p}{\partial y^2} + \frac{\partial^2 p}{\partial z^2} = 0 \qquad (C.5)$$

The potential function for p can now be obtained by a distribution of doublets of strength $(p_2 - p_1)$ per unit disc area. Point 1 is taken in front of the propeller disc and point 2 directly behind it. The pressure in a point Q located at a distance l_Q from any point on the disc then becomes:

$$p_Q = \frac{p_2 - p_1}{4\pi} \int_S \frac{\partial}{\partial n}\left(\frac{1}{l_Q}\right) dS \qquad \text{for } l_Q > 0 \qquad (C.6)$$

Rewriting eq. C.6 in cylindrical coordinates leads to:

$$p_Q = \frac{p_2 - p_1}{4\pi} \int_0^R \int_0^{2\pi} r_1 \frac{\partial}{\partial x_1}\left(\frac{1}{l_Q}\right) dr_1 d\theta_1 \qquad (C.7)$$

or:

$$p_Q = \frac{p_2 - p_1}{4\pi} \int\limits_0^R \int\limits_0^{2\pi} \frac{x r_1}{[r_1^2 + r^2 - 2rr_1 \cos(\theta_1 - \theta) + x^2]^{3/2}} dr_1 d\theta_1 \tag{C.8}$$

The flow inside and outside the slipstream has a velocity potential and it shows a discontinuity in v_x at the disc. Let the value of p at $r = 0$ be representative for the flow in the slipstream (uniform velocity distribution). In this case the expression for the pressure becomes:

$$\begin{aligned} p &= \frac{p_2 - p_1}{4\pi} \int\limits_0^R \int\limits_0^{2\pi} \frac{x r_1}{[r_1^2 + x^2]^{3/2}} dr_1 d\theta_1 \\ &= \frac{p_2 - p_1}{2} \left(\frac{x}{\sqrt{x^2}} - \frac{x}{\sqrt{R^2 + x^2}} \right) \end{aligned} \tag{C.9}$$

For $x > 0$ this leads to:

$$p = \frac{p_2 - p_1}{2} \left(1 - \frac{x}{\sqrt{R^2 + x^2}} \right) \tag{C.10}$$

Integrating the first expression of (B.3) and combining this with eq. C.10 results in:

$$v_x = \frac{p_2 - p_1}{2\rho V_\infty} \left(1 + \frac{x}{\sqrt{R^2 + x^2}} \right) \tag{C.11}$$

which represents the streamwise development of the axial induced flow velocity in the slipstream. Combining eq. C.1 and eq. C.10 now determines the slipstream radius as a function of the streamwise x-coordinate:

$$\pi R_s^2 V_\infty \left(1 + \frac{p_2 - p_1}{2\rho V} \left(1 + \frac{x}{\sqrt{R^2 + x^2}} \right) \right) = \pi R^2 V_\infty (1 + a) \tag{C.12}$$

At $x = 0$ the axial component becomes aV, hence the term $(p_2 - p_1)/2\rho V$ can be replaced by aV. Working out eq. C.12 results in the contraction ratio, R_s/R:

$$\frac{R_s}{R} = \sqrt{\frac{1 + a}{1 + a\left(1 + \frac{x}{\sqrt{R^2 + x^2}} \right)}} \tag{C.13}$$

Accepting the assumptions made with respect to the actuator disc with uniform axial force distribution over the disc, expression C.13 produces very acceptable values of the contraction ratio. It should be noted however that the introduction of a nacelle has strong effects on the contraction due to the mirror vortex system inside the nacelle geometry. Mindless usage of eq. C.13 then leads to erroneous results.

Appendix D

Slipstream Tube Model

D.1 Vorticity tubes

The calculation of the velocity field induced by the helicoidal vortex sheet model of the slipstream is quit complex. However, the overall induced effects can be modelled by a much simpler model, representing the main features of a given propeller. Such a model is the vorticity tube model. In this model, the helicoidal vortex sheets are replaced by two continuous distributions of vorticity: the axial vorticity and the tangential vorticity, as shown in Fig. D.1

The axial vorticity γ_x is parallel to the axis of rotation and distributed on concentrically placed cylinders (tubes). The tangential vorticity γ_t is distributed on the same cylindrical surfaces but perpendicular to the axial vorticity. For the axial and tangential vorticity distributions yields [1]:

$$\gamma_x = \frac{B}{2\pi r_0} \frac{d\Gamma}{dr} \tag{D.1}$$

$$\gamma_t = \frac{nB}{U_\infty} \frac{d\Gamma}{dr} \tag{D.2}$$

where: B is the number of blades, n is the number of revolutions per second, r is the blade station radial distance, r_0 is the vortex tube radius, U_∞ is the free stream velocity and $d\Gamma/dr$ is the blade spanwise gradient in the circulation with respect.

For an arbitrary blade circulation distribution, the gradient in the circulation distribution is illustrated in Fig. D.2. To be able to calculate the velocity induced by the vorticity tube model the Γ-distribution needs to be given. The source for this may either be a separate BEM-based propeller code (*prop1b*) code or an experimental data set.
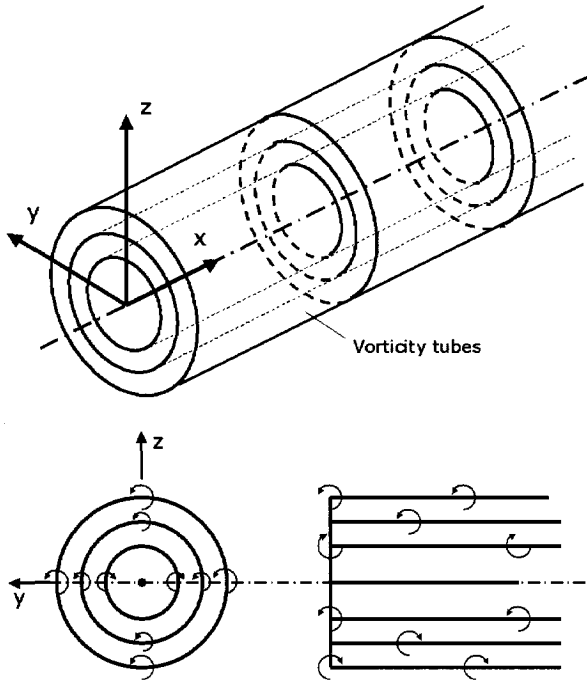
Figure D.1: *The slipstream tube model*

With the given circulation distribution, the calculation of the velocity field induced by the vorticity tube model of the propeller is rather straightforward.

Let the x-axis in a Cartesian coordinate system coincide with the propeller axis, then the velocity vector and its components in x, y and z direction is presented by:

$$V_p = (U_p, V_p, W_p)^T \tag{D.3}$$

The velocity induced at an arbitrary point P by an infinitesimal vortex segment dl and strength Γ is then given by:

$$dV_p = \frac{\Gamma}{4\pi} \frac{r \times dl}{r^3} \tag{D.4}$$

where r is the radius vector from point P to the element.

D.2   Tangential vorticity

Consider a ring vortex of strength Γ_t as sketched in Fig. D.3.
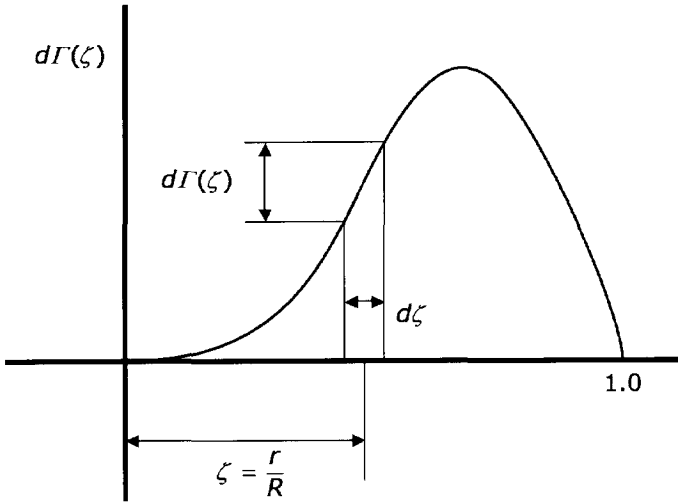
Figure D.2: *Arbitrary radial circulation distribution and notation.*
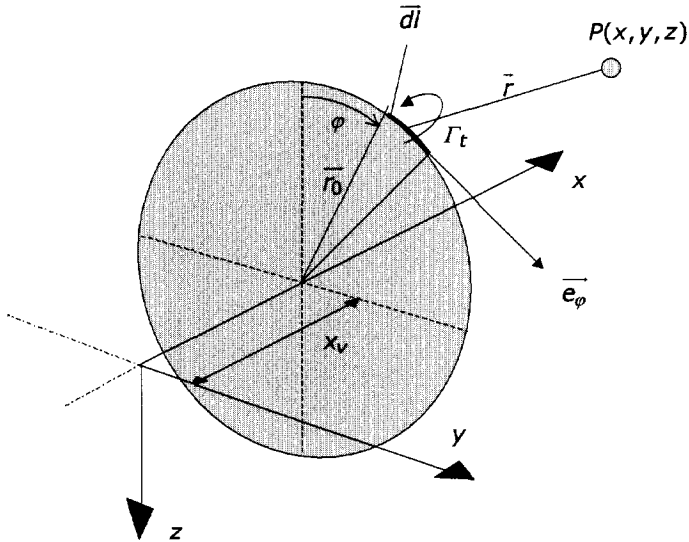
Figure D.3: *Induced velocities in point P due to the tangential vorticity.*

For the infinitesimal small ring element of length dl we can write:

$$dl = |r_0|\, d\varphi e_\varphi \tag{D.5}$$

with:

$$e_\varphi = \begin{pmatrix} 0 \\ \cos\varphi \\ \sin\varphi \end{pmatrix} \tag{D.6}$$

Hence the position vector r becomes:

$$r = \begin{pmatrix} x_v - x_p \\ r_0 \sin\varphi - y_p \\ -r_0 \cos\varphi - z_p \end{pmatrix} \tag{D.7}$$

in which x_v is the position in x-direction of the ring vortex. Combining (D.5), (D.6) and (D.7) gives:

$$
\begin{aligned}
r \times dl &= (r \times e_\varphi) r_0 d\varphi \\
&= \begin{pmatrix} x_v - x_p \\ r_0 \sin\varphi - y_p \\ -r_0 \cos\varphi - z_p \end{pmatrix} \times \begin{pmatrix} 0 \\ \cos\varphi \\ \sin\varphi \end{pmatrix} r_0 d\varphi \\
&= \begin{pmatrix} -y_p \sin\varphi + r_0 \sin^2\varphi + z_p \cos\varphi + r_0 \cos^2\varphi \\ (x_v - x_p) \sin\varphi \\ (x_v - x_p) \cos\varphi \end{pmatrix} r_0 d\varphi \\
&= \begin{pmatrix} -y_p \sin\varphi + z_p \cos\varphi + r_0 \\ (x_v - x_p) \sin\varphi \\ (x_v - x_p) \cos\varphi \end{pmatrix} r_0 d\varphi
\end{aligned} \tag{D.8}
$$

Hence the components of the induced velocities contributions in point P, due to the tangential vorticity are:

$$
\begin{aligned}
du_p &= C(-y_p \sin\varphi + z_p \cos\varphi + r_0) \\
dv_p &= C(x_v - x_p) \sin\varphi \\
dw_p &= C(x_v - x_p) \cos\varphi
\end{aligned} \tag{D.9}
$$

where:

$$C = \frac{\Gamma_t}{4\pi} \frac{r_0 d\varphi}{r^3} \tag{D.10}$$

$$r = \sqrt{(x_p - x_v)^2 + (r_0 \sin\varphi - y_p)^2 + (-r_0 \cos\varphi - z_p)^2} \tag{D.11}$$

To find the resulting induced velocities in point P, the velocities must be integrated over the complete contour of the ring vortex. Hence:

$$V_p = \int\limits_{\varphi=0}^{2\pi} dV_p \tag{D.12}$$

resulting in:

$$u_p = \frac{r_0}{4\pi} \int\limits_{\varphi=0}^{2\pi} \frac{\Gamma_t(-y_p \sin\varphi + z_p \cos\varphi + r_0)d\varphi}{[(x_v - x_p)^2 + (r_0 \sin\varphi - y_p)^2 + (-r_0 \cos\varphi - z_p)^2]^{3/2}} \tag{D.13}$$

$$v_p = \frac{r_0}{4\pi} \int\limits_{\varphi=0}^{2\pi} \frac{\Gamma_t(x_v - x_p) \sin\varphi d\varphi}{[(x_v - x_p)^2 + (r_0 \sin\varphi - y_p)^2 + (-r_0 \cos\varphi - z_p)^2]^{3/2}} \tag{D.14}$$

$$w_p = \frac{r_0}{4\pi} \int\limits_{\varphi=0}^{2\pi} \frac{\Gamma_t(x_v - x_p) \cos\varphi d\varphi}{[(x_v - x_p)^2 + (r_0 \sin\varphi - y_p)^2 + (-r_0 \cos\varphi - z_p)^2]^{3/2}} \tag{D.15}$$

Now, the bound vorticity Γ_t at x_v can be replaced by a distributed vorticity $\gamma_t dx$ between $x = x_v$ and $x = \infty$. For the induced velocities this yields:

$$u_p = a \int\limits_{x=x_v}^{\infty} \int\limits_{\varphi=0}^{2\pi} \frac{(b \sin\varphi - c \cos\varphi)d\varphi dx}{[(x - x_p)^2 + b^2 + c^2]^{3/2}} \tag{D.16}$$

$$v_p = a \int\limits_{x=x_v}^{\infty} \int\limits_{\varphi=0}^{2\pi} \frac{(x - x_p) \sin\varphi d\varphi dx}{[(x - x_p)^2 + b^2 + c^2]^{3/2}} \tag{D.17}$$

$$w_p = a \int\limits_{x=x_v}^{\infty} \int\limits_{\varphi=0}^{2\pi} \frac{(x - x_p) \cos\varphi d\varphi dx}{[(x - x_p)^2 + b^2 + c^2]^{3/2}} \tag{D.18}$$

where:

$$a = \frac{\gamma_t r_0}{4\pi}$$
$$b = r_0 \sin\varphi - y_p \tag{D.19}$$
$$c = -r_0 \cos\varphi - z_p$$

This can be integrated in x-direction, resulting in:

$$u_p = \left[\frac{a}{2} \int\limits_{\varphi=0}^{2\pi} \frac{(b\sin\varphi - c\cos\varphi)(x-x_p)d\varphi}{(b^2+c^2)((x-x_p)^2+b^2+c^2)^{1/2}} \right]_{x_v}^{\infty} \tag{D.20}$$

$$v_p = \left[a \int\limits_{\varphi=0}^{2\pi} \frac{-\sin\varphi d\varphi}{((x-x_p)^2+b^2+c^2)^{1/2}} \right]_{x_v}^{\infty} \tag{D.21}$$

$$w_p = \left[a \int\limits_{\varphi=0}^{2\pi} \frac{-\cos\varphi d\varphi}{((x-x_p)^2+b^2+c^2)^{1/2}} \right]_{x_v}^{\infty} \tag{D.22}$$

which leads to the final expressions for the induced velocities:

$$u_p = a \int\limits_{\varphi=0}^{2\pi} \frac{b\sin\varphi - c\cos\varphi}{b^2+c^2} \left(1 - \frac{x_v - x_p}{\sqrt{(x_v-x_p)^2+b^2+c^2)}} \right) d\varphi$$

$$v_p = a \int\limits_{\varphi=0}^{2\pi} \frac{\sin\varphi d\varphi}{\sqrt{(x_v-x_p)^2+b^2+c^2}} \tag{D.23}$$

$$w_p = a \int\limits_{\varphi=0}^{2\pi} \frac{\cos\varphi d\varphi}{\sqrt{(x_v-x_p)^2+b^2+c^2}}$$

with the coefficients a, b and c according to D.19. The velocity components can be found by performing a numerical summation. For this reason $d\varphi$ is replaced by $2\pi/n$ and φ by $i\Delta\varphi$, where n is the number of summation steps. Consequently the final form of eq. D.23 becomes:

$$u_p = \frac{a}{2} \sum_{i=1}^{n} \frac{b_i \sin(i\Delta\varphi) - c_i \cos(i\Delta\varphi)}{b_i^2+c_i^2} \left(1 - \frac{x_v - x_p}{\sqrt{(x_v-x_p)^2+b_i^2+c_i^2)}} \right) \Delta\varphi$$

$$v_p = a \sum_{i=1}^{n} \frac{\sin(i\Delta\varphi)d\varphi}{\sqrt{(x_v-x_p)^2+b_i^2+c_i^2)}} \tag{D.24}$$

$$w_p = a \sum_{i=1}^{n} \frac{\cos(i\Delta\varphi)d\varphi}{\sqrt{(x_v-x_p)^2+b_i^2+c_i^2)}}$$

with:

$$b_i = r_0 \sin(i\Delta\varphi) - y_p$$
$$c_i = -r_0 \cos(i\Delta\varphi) - z_p \tag{D.25}$$
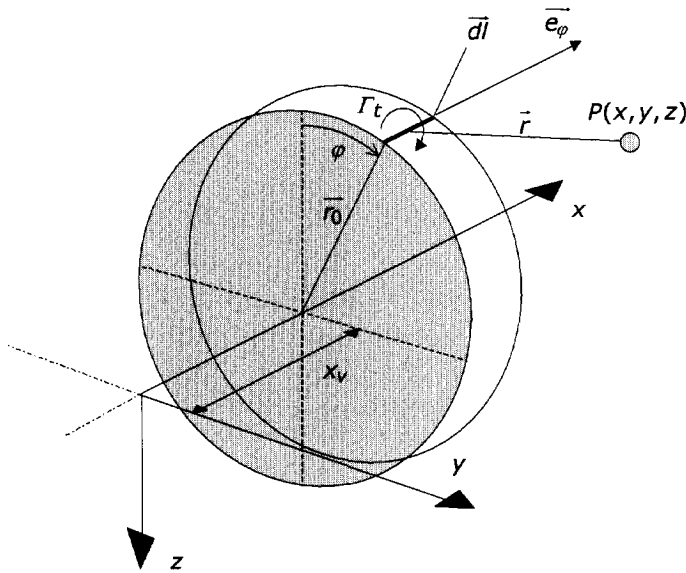
Figure D.4: *Induced velocities in point P due to the axial vorticity.*

D.3   Axial vorticity

In an analogue way the axial vorticity is taken into account: (see Fig. D.4):

$$dl = (dx)e_x = \begin{pmatrix} 1 \\ 0 \\ 0 \end{pmatrix} dx \qquad (D.26)$$

So, combination of D.7 and D.26 gives:

$$
\begin{aligned}
r \times dl &= (r \times e_x)dx \\
&= \begin{pmatrix} x_v - x_p \\ r_0 \sin\varphi - y_p \\ -r_0 \cos\varphi - z_p \end{pmatrix} \times \begin{pmatrix} 1 \\ 0 \\ 0 \end{pmatrix} dx \\
&= \begin{pmatrix} 0 \\ -r_0 \cos\varphi - z_p \\ -r_0 \sin\varphi + y_p \end{pmatrix} dx
\end{aligned}
\qquad (D.27)
$$

Then, the components of the induced velocity contributions in point P, due to the

vortex element aligned in tangential direction are:

$$du_p = 0$$
$$dv_p = C(-r_0 \cos \varphi - z_p)$$
$$dw_p = C(-r_0 \sin \varphi + y_p)$$

(D.28)

where:

$$C = \frac{\Gamma_x}{4\pi} \frac{dx}{r^3}$$

(D.29)

and r is given by eq. D.11. To find the resulting induced velocities in point P, the velocities must be integrated from $x = x_v$ to $x = \infty$. Hence:

$$V_p = \int\limits_{x=x_v}^{\infty} dV_p$$

(D.30)

resulting in:

$$u_p = 0$$

(D.31)

$$v_p = \frac{1}{4\pi} \int\limits_{\varphi=0}^{2\pi} \frac{\Gamma_x(-r_0 \cos \varphi - z_p)dx}{\left[(x - x_p)^2 + (r_0 \sin \varphi - y_p)^2 + (-r_0 \cos \varphi - z_p)^2\right]^{3/2}}$$

(D.32)

$$w_p = \frac{1}{4\pi} \int\limits_{\varphi=0}^{2\pi} \frac{\Gamma_x(-r_0 \sin \varphi + y_p)dx}{\left[(x - x_p)^2 + (r_0 \sin \varphi - y_p)^2 + (-r_0 \cos \varphi - z_p)^2\right]^{3/2}}$$

(D.33)

As was done for the tangential vorticity component, the bound vorticity Γ_x at x_v is now replaced by a distributed vorticity $\gamma_x r_0 d\varphi$ between $\varphi = 0$ and $\varphi = 2\pi$. The expressions for the induced velocities yield:

$$u_p = 0$$

(D.34)

$$v_p = a \int\limits_{x=x_v}^{\infty} \int\limits_{\varphi=0}^{2\pi} \frac{cd\varphi dx}{\left[(x - x_p)^2 + b^2 + c^2\right]^{3/2}}$$

(D.35)

$$w_p = a \int\limits_{x=x_v}^{\infty} \int\limits_{\varphi=0}^{\infty} \frac{-bd\varphi dx}{\left[(x - x_p)^2 + b^2 + c^2\right]^{3/2}}$$

(D.36)

where:

$$a = \frac{\gamma_x r_0}{4\pi}$$
$$b = r_0 \sin \varphi - y_p$$
$$c = -r_0 \cos \varphi - z_p$$

(D.37)

This can be integrated in x-direction, resulting in:

$$u_p = 0 \tag{D.38}$$

$$v_p = \left[\frac{a}{2} \int_{\varphi=0}^{2\pi} \frac{c(x - x_p)d\varphi}{(b^2 + c^2)((x - x_p)^2 + b^2 + c^2)^{1/2}} \right]_{x_v}^{\infty} \tag{D.39}$$

$$w_p = \left[\frac{a}{2} \int_{\varphi=0}^{2\pi} \frac{-b(x - x_p)d\varphi}{(b^2 + c^2)((x - x_p)^2 + b^2 + c^2)^{1/2}} \right]_{x_v}^{\infty} \tag{D.40}$$

The resulting equations for the induced velocities become:

$$u_p = 0$$

$$v_p = \frac{a}{2} \int_{\varphi=0}^{2\pi} \frac{c}{b^2 + c^2} \left(1 - \frac{x_v - x_p}{\sqrt{(x_v - x_p)^2 + b^2 + c^2)}} \right) d\varphi$$

$$w_p = a \int_{\varphi=0}^{2\pi} \frac{-b}{b^2 + c^2} \left(1 - \frac{x_v - x_p}{\sqrt{(x_v - x_p)^2 + b^2 + c^2)}} \right) d\varphi \tag{D.41}$$

with the coefficients a, b and c given by D.37. By performing a numerical integration as described in paragraph D.2 the velocity components can be found.

D.4 Vorticity at the propeller disk

Besides the slipstream envelope the propeller disk also carries (bound) vorticity. When the elementary segment with length dl, as sketched in Fig. D.5 is considered we see:

$$dl = dr e_r = \begin{pmatrix} 0 \\ \sin \varphi \\ -\cos \varphi \end{pmatrix} dr \tag{D.42}$$

So, D.7 and D.41 give:

$$
\begin{aligned}
r \times dl &= (r \times e_r)dr \\
&= \begin{pmatrix} x_v - x_p \\ r_0 \sin \varphi - y_p \\ -r_0 \cos \varphi - z_p \end{pmatrix} \times \begin{pmatrix} o \\ \sin \varphi \\ -\cos \varphi \end{pmatrix} dr \\
&= \begin{pmatrix} -r_0 \sin \varphi \cos \varphi + y_p \cos \varphi + r_0 \cos \varphi \sin \varphi + z_p \sin \varphi \\ (x_v - x_p) \cos \varphi \\ (x_v - x_p) \sin \varphi \end{pmatrix} dr
\end{aligned}
\tag{D.43}
$$
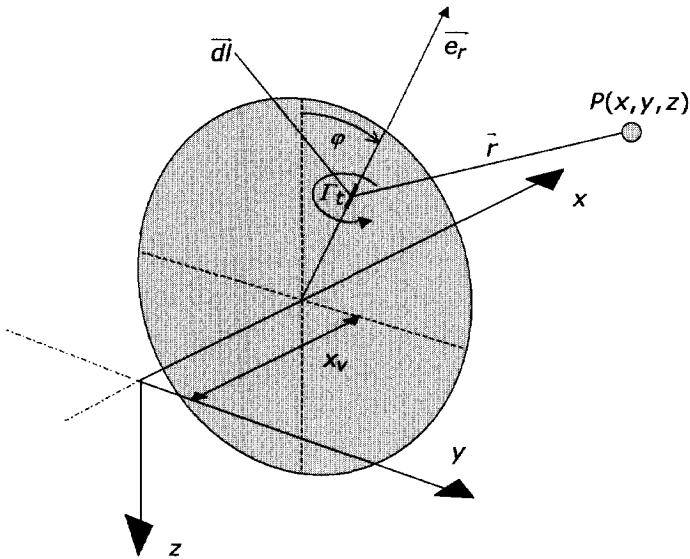
Figure D.5: *Induced velocities in point P due to the vorticity in the propeller plane.*

The components of the induced velocity contributions in point P, due to the tangential velocity are now:

$$
\begin{aligned}
du_p &= C(y_p \cos \varphi + z_p \sin \varphi) \\
dv_p &= C(x_v - x_p) \cos \varphi \\
dw_p &= C(x_v - x_p) \sin \varphi
\end{aligned}
\tag{D.44}
$$

where:

$$
C = \frac{\Gamma_p}{4\pi} \frac{dr}{r^3}
\tag{D.45}
$$

and r according to D.11. To find the resulting induced velocities in point P, the velocities must be integrated over the complete radius of the propeller plane. Hence:

$$
V_p = \int_{r=0}^{R} dV_p
\tag{D.46}
$$

resulting in:

$$
u_p = \frac{1}{4\pi} \int_{r=0}^{R} \frac{\Gamma_p(y_p \cos \varphi + z_p \sin \varphi)dr}{\left[(x_v - x_p)^2 + (r_0 \sin \varphi - y_p)^2 + (-r_0 \cos \varphi - z_p)^2\right]^{3/2}}
\tag{D.47}
$$

$$v_p = \frac{1}{4\pi} \int\limits_{r=0}^{R} \frac{\Gamma_p (x_v - x_p) \cos \varphi \, dr}{\left[(x_v - x_p)^2 + (r_0 \sin \varphi - y_p)^2 + (-r_0 \cos \varphi - z_p)^2 \right]^{3/2}} \qquad (D.48)$$

$$w_p = \frac{1}{4\pi} \int\limits_{r=0}^{R} \frac{\Gamma_p (x_v - x_p) \sin \varphi \, dr}{\left[(x_v - x_p)^2 + (r_0 \sin \varphi - y_p)^2 + (-r_0 \cos \varphi - z_p)^2 \right]^{3/2}} \qquad (D.49)$$

Now, the bound vorticity Γ_p at the propeller plane can be replaced by a distributed vorticity $(\gamma_p/2\pi) d\varphi$ between $\varphi = 0$ and $\varphi = 2\pi$, where γ_p is the sum of the circulation round each blade element at radius r. For the induced velocities this yields:

$$u_p = a \int\limits_{r=0}^{R} \int\limits_{\varphi=0}^{2\pi} \frac{f \, d\varphi \, dr}{\left[(x_v - x_p)^2 + b^2 + c^2 \right]^{3/2}} \qquad (D.50)$$

$$v_p = a \int\limits_{r=0}^{R} \int\limits_{\varphi=0}^{2\pi} \frac{(x_v - x_p) \cos \varphi \, d\varphi \, dr}{\left[(x_v - x_p)^2 + b^2 + c^2 \right]^{3/2}} \qquad (D.51)$$

$$w_p = a \int\limits_{r=0}^{R} \int\limits_{\varphi=0}^{2\pi} \frac{(x_v - x_p) \sin \varphi \, d\varphi \, dr}{\left[(x_v - x_p)^2 + b^2 + c^2 \right]^{3/2}} \qquad (D.52)$$

where:

$$\begin{aligned} a &= \frac{\gamma_p}{8\pi^2} \\ b &= (r_0 \sin \varphi - y_p) \\ c &= (-r_0 \cos \varphi - z_p) \\ f &= y_p \cos \varphi + z_p \sin \varphi \end{aligned} \qquad (D.53)$$

Summarizing the equations for the propeller and slipstream induced velocities yields:

$$\begin{aligned} u_p &= f(\gamma_t, \gamma_p) \\ v_p &= f(\gamma_t, \gamma_x, \gamma_p) \\ w_p &= f(\gamma_t, \gamma_x, \gamma_p) \end{aligned} \qquad (D.54)$$

Again the velocity components can be found by performing a numerical integration as described in paragraph D.2.

The calculation procedure according to eq. D.54 was coded in the program *sliptube*. This program can be combined with any application that requires the value of the slipstream velocity components in a 3-dimensional domain.

References

[1] Miranda, L.R. and Brennan, J.E. : "Aerodynamic Effects on Wingtip-Mounted Propellers and Turbines", AIAA 86-1802, 1986.
[2] Metcalfe, M.P. : "On the Modelling of a Fully-Relaxed Propeller Slipstream", AIAA 85-1262, 1985.

Appendix E

Quantitative Wake Analysis Program, WAKE

E.1 General aspects

Based on the theory presented in preceding paragraphs the code *WAKE* was developed. This program processes flow field data to calculate:

1. total viscous drag

2. total induced drag

3. total lift force

4. the spanwise distribution of the local lift, profile and induced drag coefficient

The procedure can be applied either to wind tunnel data or to data obtained from CFD calculations. In Fig. E.1 the setup of the QWA program WAKE is depicted.

Depending on the position at which the flow field data were taken (for example using a 5-hole-probe) also a reasonable indication of the lift- and drag distribution is calculated. *WAKE* accepts data files containing total pressure distributions and velocity-components in rectangular fields (Fig. E.1).

Throughout the program use is made of dimensionless quantities given by:

$$\tilde{x} = \frac{x}{R}, \quad \tilde{y} = \frac{y}{R}, \quad \tilde{z} = \frac{z}{R}$$

$$\tilde{u} = \frac{u}{U_\infty}, \quad \tilde{v} = \frac{v}{U_\infty}, \quad \tilde{w} = \frac{w}{U_\infty}$$

(E.1)

This leads to the dimensionless axial vorticity, source terms, and circulation:

$$\tilde{\xi} = \frac{\partial \tilde{w}}{\partial \tilde{y}} - \frac{\partial \tilde{v}}{\partial \tilde{z}} = \frac{R}{U_\infty}\xi$$

$$\tilde{\sigma} = \frac{\partial \tilde{v}}{\partial \tilde{y}} + \frac{\partial \tilde{w}}{\partial \tilde{z}} = \frac{R}{U_\infty}\sigma$$

$$\tilde{\psi} = \frac{1}{U_\infty R}\psi$$
(E.2)

$$\tilde{\varphi} = \frac{1}{U_\infty R}\varphi$$

$$\tilde{\gamma} = \int_{\tilde{z}=-\infty}^{\infty} \tilde{\xi}(\tilde{y},\tilde{z})\, d\tilde{z}$$

$$\tilde{\gamma}(\tilde{y}) = \frac{1}{U_\infty}\gamma(y)$$
(E.3)

$$\tilde{\Gamma}(\tilde{y}) = \int_{\tilde{s}=\tilde{y}}^{\infty} \tilde{\gamma}(\tilde{s})\, d\tilde{s}$$

$$\tilde{\Gamma}(\tilde{y}) = \frac{1}{RU_\infty}\Gamma(y)$$

The total lift and the lift distribution are then given by respectively:

$$C_L = (1+\tilde{u}_b)\int_{\tilde{y}=-1}^{1} C_l(\tilde{y})\, d\tilde{y} + \frac{2R^2}{S_{ref}}\iint_w (\tilde{u}^* - \tilde{u})\,\tilde{w} d\tilde{y} d\tilde{z}$$
(E.4)

and:

$$C_l(\tilde{y}) = \frac{2R}{c(\tilde{y})}\int_{\tilde{s}=\tilde{y}}^{\infty}\int_{\tilde{z}=-\infty}^{\infty} \tilde{\xi}\, d\tilde{z} d\tilde{s}$$
(E.5)

The term, u_b due to wake blockage [142] in dimensionless form becomes:

$$\tilde{u}_b = \frac{R^2}{2C}\iint_w (\tilde{u}^* - \tilde{u})\, d\tilde{y} d\tilde{z}$$
(E.6)

To determine the so-called 'Betz velocity', $\tilde{u}^*$ the definition of the following definition of the total pressure is used:

$$p_t = p + \tfrac{1}{2}\left(u^{*2} + v^2 + w^2\right) \tag{E.7}$$

Hence:

$$\tilde{u}^* = \sqrt{\frac{p_{t_\infty} - p}{\tfrac{1}{2}\rho U_\infty^2} + \frac{u^2}{U_\infty^2}} \tag{E.8}$$

The profile drag is split into two separate contributions:

$$C_{D_p} = C_{D_{p_1}} + C_{D_{p_2}} \tag{E.9}$$

The first term, $C_{D_{p_1}}$, is the main contributor to the profile drag while the second term constitutes a small correction that takes the wake blockage into account. Writing the two terms leads to:

$$C_{D_{p_1}} = \frac{R^2}{S_{ref}} \iint\limits_{w} \{1 - C_{p_t} + (\tilde{u}^* - \tilde{u})(\tilde{u}^* - \tilde{u} - 2)\}d\tilde{y}d\tilde{z} \tag{E.10}$$

$$C_{D_{p_2}} = \frac{4\tilde{u}_b^2 C}{S_{ref}} \tag{E.11}$$

where the total pressure coefficient is given by: $C_{p_t} = \frac{p_t - p_{t_\infty}}{q_\infty} + 1$

The induced drag is also split into two parts:

$$C_{D_i} = C_{D_{i_1}} + C_{D_{i_2}} \tag{E.12}$$

As discussed earlier, the second term generally is very small compared to the first. In dimensionless form the contributions are calculated with:

$$C_{D_{i_1}} = \frac{R^2}{S_{ref}} \iint\limits_{w} \tilde{\psi}\tilde{\xi}d\tilde{y}d\tilde{z} \tag{E.13}$$

$$C_{D_{i_2}} = -\frac{R^2}{S_{ref}} \iint\limits_{w} \tilde{\varphi}\tilde{f}d\tilde{y}d\tilde{z} \tag{E.14}$$

Besides the total (integrated values) of the drag coefficient the spanwise distributions of the integrands in the equations for the drag components are calculated as well. In case of the profile drag the local value of the profile drag coefficient, C_{d_p}, is obtained. Contrary to this, a similar explanation can not be maintained for the induced drag coefficient. Now the integrals (E.13) and (E.14) just produce the contribution to the induced drag and an ambiguous relation to the local induced drag coefficient, C_{d_i}, does not exist.

Solution of the Poisson equations

The solution of the Poisson-equations discussed in Chapter 5 is performed using two different fast Poisson-Solvers that can be selected by the user. The first solver, *hwscrt*, that solves the equations on rectangular domains with an equidistant grid, is taken from the well-known *FishPack* library [143].

The second solver, denoted *SPS*, solves the same equations on non-rectangular domain with the ability to use non-equidistant grids. Details on this solver and the range of applicability were described by Veldhuis [86].

Data reduction

To work out the lift and drag formulae practically all variables are first non-dimensionalized. The profile drag can simply be resolved from integration in the survey plane. Determination of the vortex drag though, requires calculation of the axial vorticity ξ and the axial velocity gradient $\partial U/\partial x$. Since the survey plane is build up with a very fine mesh size ($h/\frac{b}{2} = 0.0003125$) no cubic splines fit through the data points is needed as suggested by Brune [144]. Instead a simple and straightforward five point difference scheme is used to acquire the velocity derivatives.

Depending on the geometry of the wake survey grid either the solver *hwscrt* or *SPS* is used to solve the Poisson equations. The latter procedure takes approximately 20-30 times as much CPU time as the *FishPack* routine.
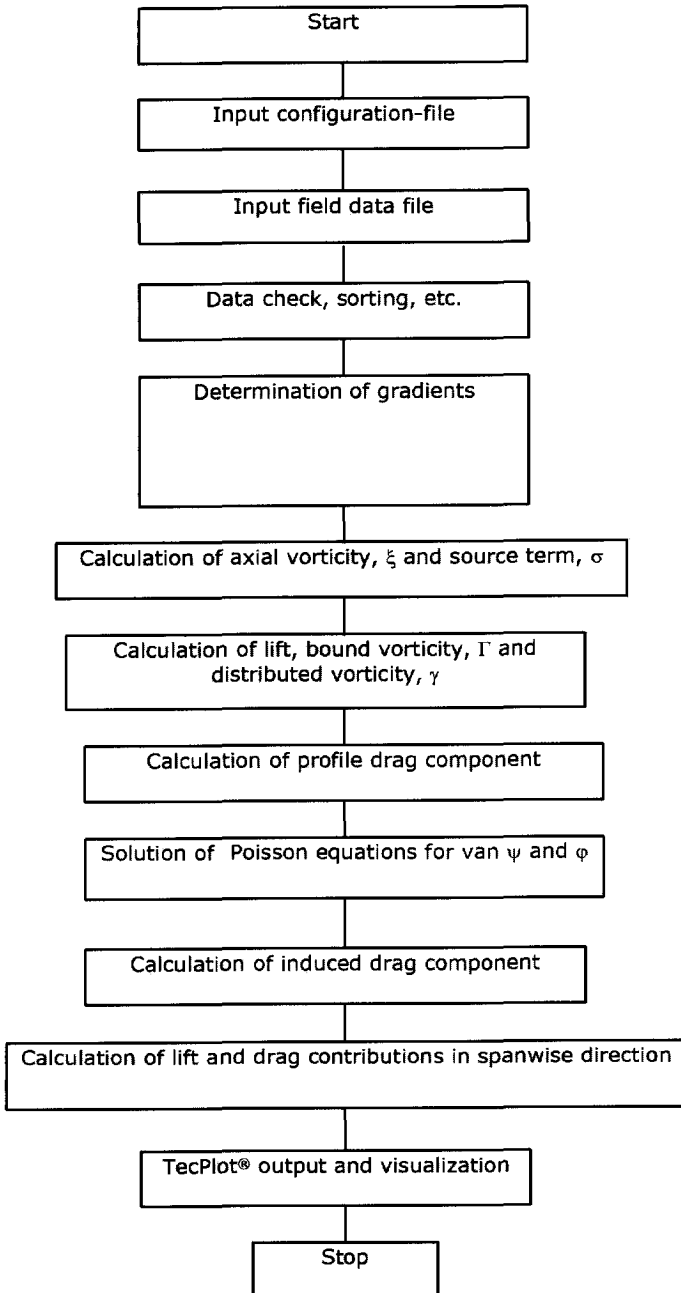
Figure E.1: *Global setup of program WAKE.*
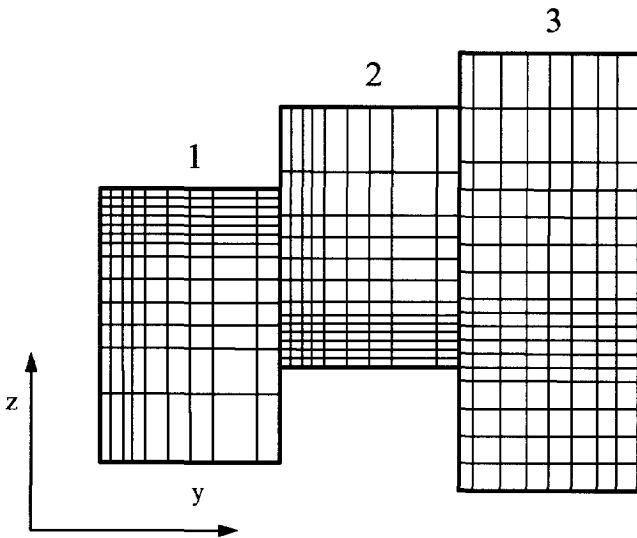
Figure E.2: *Example of typical wake survey data field structure accepted by WAKE, consisting of 3 subfields.*

Appendix F

Modelling of propeller induced velocities

F.1 Introduction

The development of computational methods for the aerodynamic analysis of the propeller-wing interference problem requires some form for the propeller slipstream model that can be readily incorporated in available programs. In the discussion of the VLM-method and the NS solution of the interference problem the need to quantify the main slipstream characteristic parameters like the axial velocity increase $v_a(x, y, z)$, the tangential (or swirl) velocity increase $v_t(x, y, z)$ and the dynamic pressure $q_\infty(x, y, z)$ became apparent.

Since in the current analysis of the propeller-wing characteristics the focus in on the interference problem, there is no need to obtain the details of the flow around the propeller as long as the slipstream induced velocity components at the location of the wing are appropriately predicted.

In most cases, where the streamwise distance between the propeller and the wing is moderate to large a SIM-approach (Single Interaction Mode) is acceptable. Hence a simple description of the slipstream is sufficient and the details of the propeller are unimportant. However, the FIM-approach (Full Interaction Mode) requires the modeling of the propeller as well to be able to determine the effect of the wing on the propeller.

For the purpose of performing both SIM and FIM calculations 4 propeller/slipstream models were developed, a description of which is presented in the following sections.

F.2 Arbitrary model

The first simple model, denoted 'arbitrary model' is used to a perform a quick analysis of the interaction problem by assuming the axial velocity and the tangential (swirl) velocity can be approximated by a sin-function of the form:

$$
\begin{aligned}
\frac{v_a}{V_\infty} &= af \cdot f_1 \sin\left(\zeta^{p_1}\pi\right) \\
\frac{v_t}{V_\infty} &= sf \cdot g_1 \sin\left(\zeta^{p2}\pi\right)
\end{aligned}
\tag{F.1}
$$

where af and sf are multiplication factors selected by the user such that values for the axial and swirl velocities are obtained that are representative for the specific propeller loading condition. The factors p_1 and p_2 are shape factors, again chosen to obtain an acceptable form of the velocity distributions. Their value may be selected based on given representations of experimental data. As discussed earlier a non-zero propeller angle of attack results in a an asymmetry in the loading where the downgoing blade at positive α_p shows a increased loading and the upgoing side a diminished loading. To incorporate this effect of the propeller angle of attack the factors f_1 and g_1 are introduced. The magnitude of these multiplication factors is based on BEM-calculation with non-zero α_p following the procedure discussed in Appendix A. Apparently f_1 and g_1 depend linearly on the effective propeller angle of attack, $\alpha_{p_{eff}}$:

$$
\begin{aligned}
f_1 &= asf_{ax} \cdot \alpha_{p_{eff}} \\
g_1 &= asf_{sw} \cdot \alpha_{p_{eff}}
\end{aligned}
\tag{F.2}
$$

where asf_{ax} and asf_{sw} are the axial and the swirl asymmetry factors obtained from the BEM-analysis, respectively. An example of the slipstream velocity components calculated with the arbitrary model is depicted in Fig. F.1.

It should be noted that in case of known experimental or numerical data used to prescribe the slipstream velocity components the selection of all the parameters that determine v_a and v_t should be based on the representative location of these velocity data (either the propeller or the wing position). Furthermore, the arbitrary slipstream model translates the swirl components into an induced vertical velocity component, v_p. Hence this model is only valid for the cases where the propeller thrust axis is located on the wing reference chord (i.e. $z_p = 0$). A more complete model that contains the effect of the radial component in the slipstream (and thus the effect of contraction), allowing high and low propeller positions ($|z_p| > 0$) is discussed in section F.3.
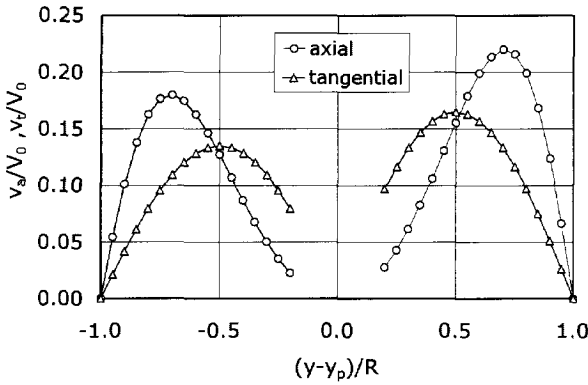
Figure F.1: *Example of the axial and tangential (swirl) velocity distribution according to the arbitrary slipstream model ; $f_1 = g_1 = 1.1$ (right), $f_1 = g_1 = 0.9$ (left), $af = 0.2$, $sf = 0.15$, $p_1 = 2$, $p_2 = 1$.*

F.3 Analytical slipstream model

In the analytical slipstream model, further denoted as ASM, either an user defined slipstream distribution is given or experimental data are synthesized directly.

In case of the synthesized version of the ASM the axial and the tangential velocity components are calculated from:

$$\frac{v_a}{U_\infty} = p_1 \sin\left(\left(\frac{r}{R_s}\right)^{p_2} \pi\right)$$

$$\frac{v_t}{U_\infty} = q_1 \sin\left(\left(\frac{r}{R_s}(1 - q_3) + q_3\right)^{q_2} \pi\right)$$

(F.3)

where the radial coordinate is given by: $r = \sqrt{(y - y_p)^2 + (z - z_p)^2}$.

The shape factors p_1, p_2, q_1, q_2, q_3 are chosen such as to approximate a realistic slipstream that may be given by experimental data. The parameter R_s is the function that describes the contraction of the slipstream (Appendix B). When experimental data are available, the ASM employs spline functions that allow an adequate representation of the true velocity distributions.

Fig. F.2 contains a calculation example of the ASM combined with the experimental data that were used to find the shape factors.
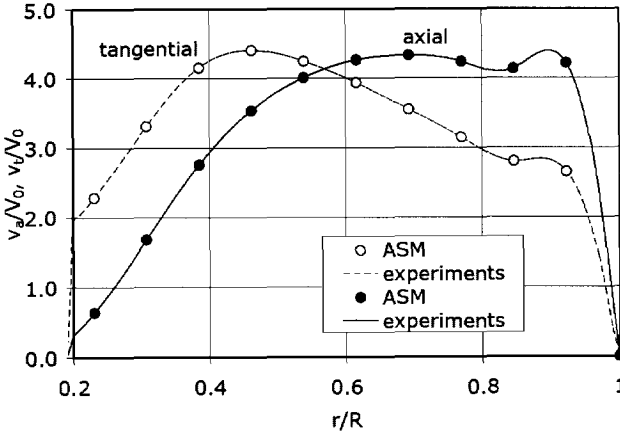
Figure F.2: *Example of axial and tangential velocity distribution acquired with the ASM.*

F.4   Blade element model

When the blade element model (BEM) model is used to calculate the velocity components at the location of the propeller disk, the true geometry of the propeller as well as the exact operating conditions are used.

Fig. F.3 shows a nice example of axial and tangential velocity components for a zero degree propeller of attack ($\alpha_p = 0°$),which leads to a symmetrical slipstream.

Velocity data are obtained at specific coordinates (r, ψ). The wing control points in a Vortex Lattice Method approach, however, can be located in any position with reference to the propeller. This necessitates the application of a cubic spline function through the given (r, ψ). Once these functions are generated the velocity components in the BEM-version are found from:

$$\frac{v_a}{U_\infty} = \Pi_{ax}\left(\frac{r}{R_s}, \psi\right)$$
$$\frac{v_t}{U_\infty} = \Pi_{sw}\left(\frac{r}{R_s}, \psi\right)$$

(F.4)

where ψ is the azimuth angle and the functions Π_{ax} and Π_{sw} represent the cubic spline functions for the axial and the swirl velocity respectively.
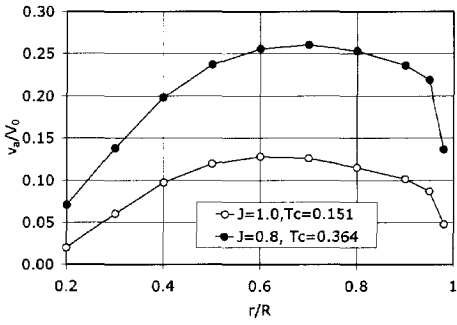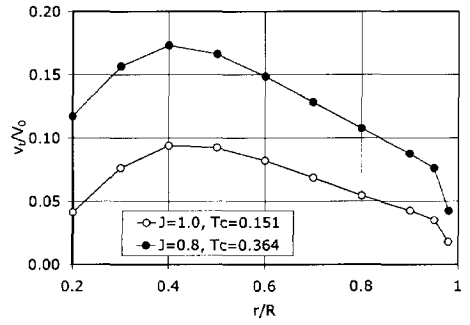
Figure F.3: *Example of axial (a) and tangential (b) velocity distributions ob-
tained with BEM.*

Appendix G

Lagrange multipliers analysis

Assume an extremum (minimum drag) is sought of $f(x_1, x_2, ..., x_n)$ that is subject to the constraint $g(x_1, x_2, ..., x_n)$ (the design lift coefficient). When f and g are functions with continuous first partial derivatives on the open set containing the curve $g(x_1, x_2, ..., x_n)$ an extremum exists when:

$$df = \frac{\partial f}{\partial x_1} dx_1 + \frac{\partial f}{\partial x_2} dx_2 + ... + \frac{\partial f}{\partial x_n} dx_n = 0 \qquad (G.1)$$

but also:

$$dg = \frac{\partial g}{\partial x_1} dx_1 + \frac{\partial g}{\partial x_2} dx_2 + ... + \frac{\partial g}{\partial x_n} dx_n = 0 \qquad (G.2)$$

Now multiply eq. (G.2) by the, as yet undetermined, parameter λ (denoted as the Lagrange multiplier) and combine this with eq. (G.1) into:

$$\left(\frac{\partial f}{\partial x_1} + \lambda \frac{\partial g}{\partial x_1} \right) dx_1 + \left(\frac{\partial f}{\partial x_2} + \lambda \frac{\partial g}{\partial x_2} \right) dx_2 + ... + \left(\frac{\partial f}{\partial x_n} + \lambda \frac{\partial g}{\partial x_n} \right) dx_n = 0 \quad (G.3)$$

It should be noted here that the differentials in eq. (G.3) are all independent. Hence we can set any combination equal to zero and the remainder must still give zero. This requires that:

$$\frac{\partial f}{\partial x_k} + \lambda \frac{\partial g}{\partial x_k} = 0 \quad \forall \ k = 1, 2, ..., n \qquad (G.4)$$

From eq. (G.4) we see that in fact the value of the Lagrange multiplier at the solution of the problem is equal to the rate of change in the maximum value of the objective function, f (of which the extremum is sought) as the constraint is relaxed. If the function that is to be minimized (extreme value at this point) is defined as the drag coefficient and for the constraint function, J, the lift $C_L - C_{L_{des}}$ is taken, the

optimization problem, as given by eq. (G.4) reduces to:

$$\begin{aligned} I &= F + \lambda J \\ &= C_{D_i} + C_{D_{visc}} + \lambda \left(C_L - C_{L_{des}} \right) \end{aligned} \tag{G.5}$$

where the Lagrange multiplier, λ, is to be determined.

The next step to solve this optimization problem is based on the application of the Calculus of Variation.

The utilization of this technique for the current optimization problem is best illustrated by considering the conditions at which an integral shows extremes under constraints in general.

The constraint function may take the form of a definite integral of which the value is fixed, leading to a so-called isoperimetric problem.

Now consider a simple isoperimetric problem that consists of finding a function $y(x)$ that extremizes an integral in the form:

$$I = \int_{x_1}^{x_2} f\left(x, y, y' \right) dx \tag{G.6}$$

relative to twice-differentiable functions on the interval $[x_1, x_2]$, which satisfies the integral constraint

$$J = \int_{x_1}^{x_2} g\left(x, y, y' \right) dx \tag{G.7}$$

and where J is a fixed constant. Additionally end conditions are prescribed: $y(x_1) = y_1$ and $y(x_2) = y_2$ while f and g will be assumed twice-differentiable with respect to their arguments. The selection of this problem is relevant from the standpoint of the drag minimization problem sketched earlier since at a later stage the integral I can be replaced by the drag integral(s) while the fixed value J integral relates to the fixed lift coefficient constraint $C_L - C_{L_{des}} = 0$.

Treating the problem in a general way for the moment, however, leads more clearly to the specific conditions needed for obtaining an optimization, in general.

To find the twice-differentiable function $y(x)$ consider the set $\{y\}$ of all twice-differentiable functions Y on the interval $[x_1, x_2]$, which take on the values y_1 and y_2 at respectively x_1 and x_2. The required set can now be created by introducing a two-parameter family of comparison functions:

$$Y(x) = y(x) + \varepsilon_1 \eta_1(x) + \varepsilon_2 \eta_2(x) \tag{G.8}$$

where $\eta_1(x)$ and $\eta_2(x)$ are arbitrary twice-differentiable functions on $[x_1, x_2]$ such that:

$$\eta_1(x_1) = \eta_1(x_2) = \eta_2(x_1) = \eta_2(x_2) = 0 \tag{G.9}$$

These restrictions ensure that all comparison functions $Y(x)$ satisfy the same end conditions as the extremizing function $y(x)$. Moreover, for every $\eta_1(x)$ and $\eta_2(x)$ the function $Y(x)$ becomes $y(x)$ if $\varepsilon_1 = \varepsilon_2 = 0$.

Returning to the integral functions I and J substitution of an arbitrary comparison function Y leads to:

$$I(\varepsilon_1, \varepsilon_2) = \int\limits_{x_1}^{x_2} f(x, y, y')dx \qquad (G.10)$$

and:

$$J(\varepsilon_1, \varepsilon_2) = \int\limits_{x_1}^{x_2} g(x, y, y')dx \qquad (G.11)$$

Note that the functional relation exists: $J(\varepsilon_1, \varepsilon_2) = J$ for $J = $ constant, which means that ε_1 and ε_2 are not independent. Now, since by definition $y(x)$ extremizes I subject to the constraint (G.7), $I(\varepsilon_1, \varepsilon_2)$ has an extremum relative to the values of ε_1 and ε_2 when $\varepsilon_1 = \varepsilon_2 = 0$. Hence, the isoperimetric problem has become that of finding the condition(s) that $y(x)$ must take when it is known that, for $\varepsilon_1 = \varepsilon_2 = 0$, the function $I(\varepsilon_1, \varepsilon_2)$ of the two variables ε_1 and ε_2 has an extremum subject to the constraint given by $J(\varepsilon_1, \varepsilon_2) = J$ for $J = $ constant.

To implement the method we make use of the Lagrange multiplier that was introduced earlier. The object function now becomes:

$$I^*(\varepsilon_1, \varepsilon_2) = I(\varepsilon_1, \varepsilon_2) + \lambda(\varepsilon_1, \varepsilon_2)$$
$$= \int\limits_{x_1}^{x_2} f^*(x, y, y')dx \qquad (G.12)$$

where the function f^* is defined by $f^* = f + \lambda g$. We know that:

$$\frac{\partial I^*}{\partial \varepsilon_1} = \frac{\partial I^*}{\partial \varepsilon_2} = 0 \text{ for } \varepsilon_1 = \varepsilon_2 = 0 \qquad (G.13)$$

Computing these derivatives leads to:

$$\frac{\partial I^*}{\partial \varepsilon_i} = \int\limits_{x_1}^{x_2} \left(\frac{\partial f^*}{\partial y} \frac{\partial Y}{\partial \varepsilon_i} + \frac{\partial f^*}{\partial y'} \frac{\partial Y'}{\partial \varepsilon_i} \right) dx$$
$$= \int\limits_{x_1}^{x_2} \left(\frac{\partial f^*}{\partial y} \eta_i + \frac{\partial f^*}{\partial y'} \eta_i' \right) dx \qquad i = 1, 2 \qquad (G.14)$$

Because of the fact that y and y' become the extremizing function $y(x)$ and its derivative $y'(x)$ when $\varepsilon_1 = \varepsilon_2 = 0$, eq. (G.13) and eq. (G.14) lead to:

$$\left. \frac{\partial I^*}{\partial \varepsilon_i} \right|_{(0,0)} = \int_{x_1}^{x_2} \left(\frac{\partial f^*}{\partial y} \eta_i + \frac{\partial f^*}{\partial y'} \eta_i' \right) dx = 0 \quad i = 1, 2 \tag{G.15}$$

When the second term in the integrand of eq. (G.15) is integrated by parts and eq. (G.9) is recalled, we get:

$$\int_{x_1}^{x_2} \left(\frac{\partial f^*}{\partial y} - \frac{d}{dx} \left(\frac{\partial f^*}{\partial y'} \right) \right) \eta_i \, dx = 0 \quad i = 1, 2 \tag{G.16}$$

And since η_1 and η_2 are arbitrary, for $i = 1$ or 2 we obtain:

$$\frac{\partial f^*}{\partial y} - \frac{d}{dx} \left(\frac{\partial f^*}{\partial y'} \right) = 0 \tag{G.17}$$

This is the *Euler-Lagrange* equation which the function $y(x)$ must satisfy if it is to extremize integral I that is subject to an integral constraint as given by eq. (G.11). The complete solution of eq. (G.17) will contain two constants of integration as well as the Lagrange multiplier.

At this stage the variation of a real function F (functional) is introduced. The domain of F is a set of real functions $\{y\}$. To determine the change of the functional F corresponding to an assigned change in the value of $y(x)$ for a fixed value of x the variation $\varepsilon \eta(x)$, denoted with δy, is applied to $y(x)$. That is, $y(x)$ is changed to: $y(x) \mapsto y(x) + \varepsilon \eta(x)$ or $y \mapsto y + \delta y$. Furthermore: $y'(x) \mapsto y'(x) + \varepsilon \eta'(x)$ and $\delta y'(x) = \varepsilon \eta'(x)$.

With the given variation in $y(x)$ the corresponding change to the functional F that depends on $y(x)$ becomes:

$$\Delta F = F(x, y + \varepsilon \eta, y' + \varepsilon \eta') - F(x, y, y') \tag{G.18}$$

Expanding this equation in a MacLaurin expansion in powers of ε and neglecting powers of ε higher than 1 finally leads to:

$$\Delta F = \frac{\partial F}{\partial y} \eta \varepsilon + \frac{\partial F}{\partial y'} \eta' \varepsilon \tag{G.19}$$

or

$$\delta F = \frac{\partial F}{\partial y} \delta y + \frac{\partial F}{\partial y'} \delta y' \tag{G.20}$$

where δF is the variation of F that results from the variation δy on $y(x)$. For a functional expressed as an integral:

$$I = \int_a^b f(x, y, y')dx \qquad (G.21)$$

of the kind discussed earlier, the variation becomes: $\Delta I = I(y + \varepsilon \eta) - I(y)$. Hence:

$$\Delta I = \int_a^b f(x, y + \varepsilon \eta, y' + \varepsilon \eta')dx - \int_a^b f(x, y, y')dx$$

$$= \int_a^b \Delta f(x, y, y')dx \qquad (G.22)$$

The variation of I is now defined as the expression resulting when Δf in the last integral is replaced by the first-order approximation, δf:

$$\delta I = \int_a^b \delta f(x, y, y')dx \qquad (G.23)$$

Following the analysis as given above for the object function I^* results in an expression for the variation of I:

$$\delta I = \int_a^b f_y - \frac{d}{dx}(f_{y'}) \delta y dx \qquad (G.24)$$

A necessary condition for a function to have an extremum is that its differential vanishes. Consequently it can be stated that the necessary condition for the functional I to have an extremum is that its variation vanishes as well. Given that δy is an arbitrary variation in y, the condition $\delta y = 0$ implies that:

$$f_y - \frac{df_{y'}}{dx} = 0 \qquad (G.25)$$
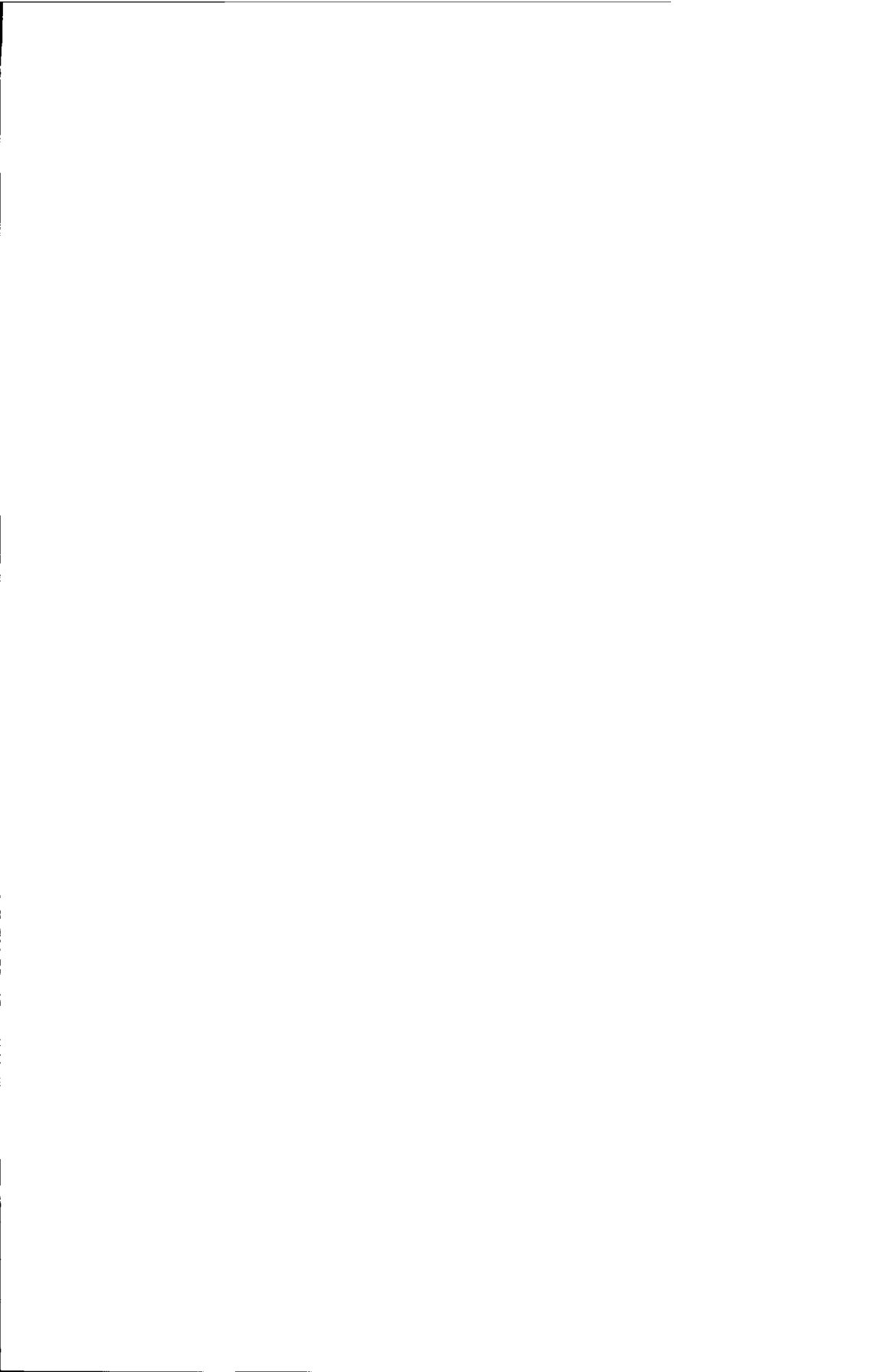
Bibliography

[1] Prandtl, L.: Mutual influence of wings and propeller, NACA Technical Report No. 74, Extract of the First Report of the Goettingen aerodynamic facility, Chap. IV, section 6, 1921.

[2] Poisson-Quinton, Ph.: Technical evaluation report on the Fluid Dynamics Panel symposium on aerodynamics and acoustics of propellers, AGARD AR 213, 1985.

[3] Mikkelsen, D.C.: Summary of Recent NASA propeller research, AGARD CP 366, August 1984, p. 12-1 to 12-22.

[4] Orourke, D. M.: Propfan test assessment propfan propulsion system static test report, NASA-CR-179613, 1986.

[5] Shelby J. and Moore, J.: Performance Estimation for a Highly Loaded Eight-Blade Propeller Combined With an Advanced Technology Turboshaft Engine, NASA TM-80075, April 1979.

[6] Butterworth-Hayes, P.: Aerospace America January 1999.

[7] Trigeiro, W.W.: The Impacts of Regional Jets on Congestion in the NAS,1999, MP 98W0000256V3.

[8] Marotte, B.: Report on Business, 2004.

[9] Babikian, R.: The historical fuel efficiency characteristics of regional aircraft from technological, operational and cost perspectives, PhD Thesis, MIT, June 2001.

[10] Kroo, I.: Propeller/wing integration for minimum induced loss, Journal of Aircraft, Vol. 23 , No. 7 , July 1986. p. 561-565.

[11] Miranda, L.R. and Brennan, J.E.: Aerodynamic effects of wing tip mounted propellers and turbines, AIAA 86-1802 , 1986, p. 221-228.

[12] Veldhuis, L.L.M.: Experimental Analysis of Tractor Propeller Effects on a Low Aspect Ratio Semi-Span Wing, Second Pacific International Conference on Aerospace Science and Technology and the Sixth Australian Aeronautical Conference, Vol. 2, p. 491-498, Melbourne, 20-23 March 1995.

[13] Kuhn, R.E. and Draper, J.W.: Investigation of the aerodynamic characteristics of a model wing-propeller combination and of the wing and propeller separately at angles of attack up to 90, NACA Rep. 1263, 1956.

[14] Veldhuis, L.L.M. and Heyma, P.M.: Aerodynamic optimisation of wings in multi-engined tractor propeller arrangements, ICAS-2000-2.6.4, 2000.

[15] Favier, D.; Maresca, C.; Barbi, C. and Fratello, G.: Experimental and Numerical Study of the Propeller/Fixed Wing Interaction,. AIAA-88-2571, 1988.

[16] Luursema, G.: Comparison of an actuator disk and blade modeling approach in Navier-Stokes calculations on the SR-3 propfan, MSc. Thesis, Fac. of Aerospace Engineering, Delft University of Technology, 1999.

[17] Whitfield, D.L.; Swafford, T.W.; Janus, J.M.; Mulac, R.A. and Belk, D.M.: Three-dimensional unsteady euler solutions for propfans and counter-rotating propfans in transonic flow, AIAA-87-1197, 1987.

[18] Muhammad, H. and Vaart, J.C. van der: Static longitudinal stability and control characteristics of the Fokker F.27 Friendship calculated by simple handbook methods, LR-394, Fac. of Aerospace Engineering, Delft University of Technology, 1983.

[19] Schipholt, G.J. ; Voogt, N. and Hengst, J. van: Investigation of methods for modelling propeller-induced flow fields, AIAA-93-0874 , jan. 1993 , Reno , NV.

[20] Veldhuis, L.L.M. and Luursema, G.: Comparison of an actuator disk and a blade modeling approach in Navier-Stokes calculations on the SR-3 propfan, AIAA-2000-4528, 2000.

[21] Nebiolo. S.: CFD analysis of a basic propeller-nacelle-wing configuration based on the solution of the Navier-Stokes eqautions, MSc. Thesis, Fac. of Aerospace Engineering, Delft University of Technology, 1999.

[22] Theodorsen, Th.: The theory of propellers – Part III, The slipstream contraction with numerical values for two-blade and four-blade propellers, NACA Report 777, 1944.

[23] Broek, J.J.: The use of the total-head rise across the propeller of the De Havilland Canada DHC-2 Beaver as a similitary parameter to simulate power-on flight in the wind tunnel, Raport VTH-190, Dept.of Aerospace Engineering, Delft University of Technology, 1976.

[24] Bencze, D.P.; Smith, R.C.; Welge, H.R. and Crowder,J.P.: Propeller Slipstream Wing Interactions at Mach No. 0.8, SAE 780997, 1978.

[25] Ribner, H.S.: Propellers in yaw, NACA WR-L-219, 1943.

[26] Young, J. de: Propellers at high incidence, Journal of Aircraft, Vol. 2, No. 3, May-June 1965.

[27] Miley, S.J.: Wing laminar boundary layer in the presence of a propeller slipstream, Journal of Aircraft Vol. 25, No. 7, July 1988.

[28] Holmes, B.J.; Howard, R.H. and Miley, S.J.: An investigation of the effects of the propeller slipstream on a laminar wing boundary layer, SAE paper 850859, 1985.

[29] ESDU: In-plane forces and moments on installed inclined propellers at low forward speeds, ESDU Data Sheets, ESDU-89047, 1991.

[30] Lesley, E.P.; Worley, G.F. and Moy, S.: Air propellers in yaw. NACA Rep. 597, 1937.

[31] Wickens, R.H.: Aerodynamic force and moment characteristics of a four-bladed propeller yawed through 120 degrees, NRC LR-454, 1966.

[32] Mc Lemore, H.C. and Cannon, M.D.: Aerodynamic investigation of a four-blade propeller operating through an angle of attack range from $0°$ to $180°$, NACA-TN-3228, 1954.

[33] Anon.: Aerodynamics and acoustics of propellers, AGARD CP-366, october 1984.

[34] Fraser-Mitchell, A.H.: MIDAP guide to drag estimation of aircraft and weapons, Sub. Ch. 5, Propeller installations, British Aerospace, 1980.

[35] Muhammad, H.: Identification of turbo-prop thrust from flight test data, PhD Thesis, Delft University of Technology, 1995.

[36] Rowse, J.H. et al: Propeller / Propfan In-Flight Thrust Determination, SAE-AIR 4065, SAE International, 1993.

[37] Smelt, R. and Davies, H.: Estimation of increase in lift due to a slipstream, ARC R&M 1788, 1937.

[38] ESDU: Lift and longitudinal forces on propeller/nacelle/wing/flap systems, ESDU 88031, April 1997.

[39] Jameson, A.: The Analysis of Propeller Wing Flow Interaction, Analytic Methods in Aircraft Aerodynamics, NASA SP-228, October 1969, pp. 721-749.

[40] Fowler, H.D.: Determination of the influence of propeller thrust on C_L and C_D of an airplane using a triple-slotted flap at various deflections, SAE Paper 690724, 1969.

[41] Marr, R.L.: A Method for analyzing power-on Static Longitudinal Stability, SAE Paper 700238, 1970.

[42] Millikan, C.B.: The Influence of Running Propellers on Airplane Characteristics, J. Aeron. Sciences Vol. 7, No 3, 1940.

[43] USAF: USAF Stability and Control DATCOM, Air Force Flight Dynamics lab., Wright-PattersonAir Force Base, oct. 1960.

[44] Kuhn, R.E.: Semi-Empirical Procedure for Estimating Lift and Drag Characteristics of Propeller-Wing-Flaps Configurations for Vertical- and Short-Take-Off-and-Landing Airplanes, NASA M 1-16-59A, 1958.

[45] Obert, E.: A method for the determination of the effect of propeller slipstream on the static longitudinal stability and control of multi-engined aircraft, Report LR-761, Delft University of Technology, Dec. 1994.

[46] Aljabri, A.S and Hughes, A.C. Wind tunnel investigation of the interaction of propeller slipstream with nacelle/wing/flap/combinations, AGARD, FDP, Aerodynamics and Acoustics of propellers, AGARD DCP 366, paper nr. 21, Toronto, October 1984.

[47] Moran, J.: An Introduction to Theoretical and Computational Aerodynamics, Wiley, ISBN 0-471-87491-4, 1984.

[48] Bertin, J.J.: Aerodynamics for engineers, Prentice Hall, 4th edition, 2002, ISBN 0-13-064633.

[49] Katz, J. and Plotkin, A.: Low speed aerodynamics – From wing theory to panel methods, ISBN 0-07-050446-6, Mc. Graw-Hill, 1991.

[50] Witkowski, D.; Lee, A. and Sullivan, J.: Aerodynamic interaction between propellers and wings, J. of Aircraft, Vol. 26, No. 9, pp.829-836, 1989.

[51] Ardito Marreta, R.M.; Davi, G.; Milazzao, A. and Lombardi, G.: Wing pitching and loading with propeller interference, Journal of Aircraft, Vol. 36, No. 2, pp. 468-471., 1999.

[52] I. Kroo: Annual Review of Fluid Mechanics, Annual Review of Fluid Mechanics, Vol. 33: p. 587-617, 2001.

[53] Hoeijmakers, H.W.M: Panel Methods for Aerodynamic Analysis and Design, AGARD Report R-783, 1991.

[54] Smith, B.A.W.: The flow over a wing/nacelle combination in the presence of a propeller slipstream, First Canadian symposium on Aerodynamics, Ottawa, Ontario, 1989.

[55] Es, G. van: Evaluation of the PDAERO Panel Method with Correct Wing Thickness to Model the Flow of Propeller-Wing-Nacelle Combinations, Fokker Report A-273, 1994.

[56] Beek, C.M. van ; Piers, W.J. and Oskam, B.: Aerodynamic analysis of slipstream/wing/nacelle interference for preliminary design of aircraft configurations, AGARD CP-498, 1991.

[57] Løtstedt, P.: A Propeller Slipstream Model in Subsonic Linearized Potential Flow, ICAS 90-5.4.4, 1990.

[58] Rentema, D.W.E.: Drag and lift calculations based on wake surveys of a propeller-wing combination at several angles of attack, Thesis Report, Fac. of Aerospace Engineering, Delft University of Technology, 1994.

[59] Durand, W.F.: Aerodynamic Theory, Volume IV, Divisions J-M, Springer Verlag, 1935, p. 169-430.

[60] Horlock, J.H.: Actuator disk theory: discontinuities in thermo fluid dynamics , Mc. Graw Hill, ISBN: 0070303606, 1978.

[61] Beek, C.M. van ; Piers, W.J. and Oskam, B.: Aerodynamic analysis of slipstream/wing/nacelle interference for preliminary design of aircraft configurations, AGARD-CP-498, 1992.

[62] Longman, I.M.: On the numerical evaluation of Cauchy principle values of integrals, MTAC 12, 1958.

[63] Tannehill, J.C.; Anderson, D.A. and Pletcher, R.H.: Computational fluid mechanics and heat transfer, Published by Taylor and Francis, ISBN 1-56032-046-X, 1997.

[64] Houtman, E.M.: Numerical simulation of three-dimensional compressible flow, Report HSL TM-96381, Fac.of Aerospace Engineering, Delft University of Technology, 1996.

[65] Whitfield, D.L. and Jameson, A.: Three-dimensional Euler equation simulation of propeller-wing interaction in transonic flow, AIAA-83-0236, 1983.

[66] Jameson, A.; Schmidt, W. and Turkel, E.: Numerical solutions of the Euler equations by finite volume methods using Runge-Kutta time stepping schemes, AIAA-81-1259, 1981.

[67] Osher, F. and Solomon, F.: Upwind differences for hyperbolic systems of con-
     servation laws, 1982.

[68] Spekreijse, S.P.: Multigrid solution of the steady Euler equations, PhD. Thesis,
     CWI, Amsterdam, 1987.

[69] Belk, D. ; Janus, J. and Whitfield, D.: Three-dimensional unsteady Euler equa-
     tions solutions on dynamic grids, AIAA-85-1704, AIAA 18th Fluid dynamics
     and plasmadynamics and lasers conference, July, 1985, Cincinnati, Ohio.

[70] Nishida, B.A.; LANGHI, R.G. and BENCZE, D.: A multiblock/multigrid Euler
     analysis of a propfan transport with wing-mounted nacelles, including slipstream
     effects , AIAA-91-0706, 1991.

[71] Kumar, A. and Hefner, J.N.: Future challenges and opportunities in aerody-
     namics, ICAS 2000-0.2.1, 2000.

[72] Baals, D.D. and Corliss, W.R.: Wind Tunnels of NASA. NASA SP-440, 1981.

[73] Bengelink, R.L.: The Integration of CFD and Experiment: An Industry View-
     point, AIAA 88-2043, 1988.

[74] Barlow, J.B. ; Rae, W.H. and Pope, A.L.: Low-Speed Wind Tunnel Testing,
     3rd edition, John Wiley and Sons , 1999, ISBN 047 1557749.

[75] Garner, H.C., Rogers, E.W.E., Acum, W.E.A. and Maskell, E.C.: Subsonic
     Wind Tunnel Wall Corrections, AGARDograph 109, October 1966.

[76] Ewald, B.F.R. (Ed.): Wind tunnel wall corrections, AGARD AG 336, 1998,
     ISBN 92-836-1076-8.

[77] Veldhuis, L.L.M.: Configuration and Propulsion aerodynamics research on the
     Low Speed Aerodynamics laboratory (in Dutch), Review of project 90-LR-5-S,
     1993, Internal Report LSW 93-1, Fac. of Aerospace Engineering, Delft Univer-
     sity of Technology.

[78] Binkhorst, H.: Windtunnelonderzoek naar de toepassing van een gedeeld richt-
     ingsroer als luchtrem voor de Fokker F27 'Friendship', Memorandum LR M-177,
     Technische Hogeschool Delft, Afdeling Vliegtuigbouwkunde, 1971.

[79] Veldhuis, L.L.M.: Quantitative Wake Surveys Behind a Tractor Propeller/Wing
     Configuration, AIAA 95-3908, 1st AIAA Aircraft Engineering, Technology and
     Operations congress, sept. 1995, Los Angeles, CA.

[80] Gentry,G.L. Jr.; Takallu, M.A. and Applin, Z.T.: Aerodynamic Characteristics
     of a Propeller-Powered High-Lift Semispan Wing, NASA Technical Memoran-
     dum 4541, 1994.

[81] Johnson, J.L. and White, E.R.: Exploratory low speed wind-tunnel investigation of advanced commuter configurations, including an over-the-wing propeller, AIAA-83-2531, 1983.

[82] Cooper, R.K.; McCann, W.J. and Chapleo, A.Q.: Over the wing propeller aerodynamics, ICAS-92-3.2.2, 1992.

[83] Spigt, C.L. en Gelder, A. de: Windtunnelmetingen aan een model van de Fokker F27 'Friendship' uitgevoerd in de lagesnelheidstunnel van de Onderafdeling der Vliegtuigbouwkunde, Memorandum M42, 1959, Technische Hogeschool Delft, Vliegtuigbouwkunde.

[84] Leeuw, A. de: Induced drag; theory, measurements and calculations, Thesis Report, Fac.of Aerospace Engineering, Delft University of Technology, 1993.

[85] Samuelsson, I.: Experimental investigation of low speed model propeller slipstream aerodynamic characteristics including flow field surveys and nacelle/wing static pressure measurements, ICAS 90-3.1.3, 1990.

[86] Veldhuis, L.L.M.: WAKE - Program for the determination of lift and drag from wake surveys, Internal Report LSW 96-3, Fac. of Aerospace Engineering, Delft University, 1996 (in Dutch).

[87] Ganzefles, F.L.A.; Bruin, A. de and Puffert-Meissner, W.: A Quantative Analysis of Viscous and Lift-induced Drag Components from Detailed Wake Measurements behind a Half-Span Model, NLR-TP-2002-320, 2002.

[88] Bruin, A. de and Ganzefles, F.L.A.: Drag and lift analysis from wake surveys at large distances behind a small aircraft model, NLR-TR-2003-071, 2003.

[89] Wu, J.C., Hackett, J.E., Lilley, D.E.: A generalized wake-integral approach for drag determination in three-dimensional flows, AIAA 79-0279, Jan. 1979.

[90] Maskell, E.C.: Progress towards a method for the measurement of components of the drag of a wing of finite span, RAE TR-72232, January 1973.

[91] Rentema, D.W.E.: PROP1: Een eenvoudig computerprogramma voor propellerberekeningen, gebaseerd op de vortex-theorie met Prandtl's tip-verlies factor; met aanpassingen voor berekeningen met invalshoek, TZ-rapport, Delft University of Technology, 1993.

[92] Kraemer, E.; Hertel, J., and Wagner, S.: Euler procedure calculation of the steady rotor with emphasis on wake evolution, AIAA 90-3002-CP, 1990.

[93] Veldhuis, L.L.M.: Optimisation of tractor propeller wing configurations, Journal of Aerospace Engineering, Vol. G., paper G01394, 1994.

[94] Mc Cormick, B.W.: Aerodynamics, Aeronautics and Flight Mechanics, John Wiley and Sons, New York, 1995. ISBN 0-471-57506-2.

[95] Ruysink, H.M.: Een Prestatie-Onderzoek aan Propellers voor Modelvliegtuigen en Mini R.P.V.'s, MSc. Thesis, Delft University of Technology, 1981.

[96] Custers, L.G.M.: Experiences with rotating shaft balances for measurement of total propeller force and moment, NLR TP 94036 L, 1994.

[97] Custers, L.G.M.: Propeller-wing interference effects at low speed conditions, NLR TP-96312, 1996.

[98] Prijo Kusumo, J. ; Gayus, L.G.M. ; Custers, L.G.M. ; de Haij, L.H. and Veld-huis, L.L.M.: Experimental investigation on propeller slipstream effects on a swept wing at low speeds, ICAS-96-4.10.2, Sorrento Italy, Sept. 1996.

[99] Borne, P.C.M. van den and Hengst, J. van: Investigation of propeller slipstream effects on the Fokker 50 through in-flight pressure measurements, AIAA-1990-3084, Applied Aerodynamics Conference, 8th, Portland, OR, Aug. 20-22, 1990.

[100] Drela, M.: XFOIL: An Analysis and Design System for Low Reynolds Number Airfoils, contribution to: Conference on Low Reynolds Number Airfoil Aerody-namics, University of Notre Dame, June 1989.

[101] Kuijvenhoven, J.L.: Validation of propeller slipstream calculations using a multi-block Euler code, AIAA-1990-3035, 1990.

[102] Torenbeek, E.: Synthesis of subsonic airplane design, DUP, ISBN 90-247-2724-3, 1982.

[103] Silverstein, A. and Wilson, H.A.: Drag and propulsive characteristics of air-cooled engine-nacelle installations for large airplanes, NACA Report 746, 1942.

[104] G.W van Es: Experimental investigation of the effect of propeller angle of at-tack and position on the aerodynamic characteristics of a tractor-propeller wing combination, TZ-report, Fac. of Aerospace Engineering , Delft University of Technology, 1993.

[105] Hayes, W.C. and Kuhn, R.E.: Effects of propeller position and overlap on the slipstream deflection characteristics of a wing-propeller configuration equipped with a sliding and Fowler flap, NACA TN 4404, 1958.

[106] Sawyer, R.A. and Mecalfe, M.P.: Jet/Wing interference for an overwing engine configuration, AGARD CP-285, 1980.

[107] Putnam. L.: Exploratory investigation at Mach numbers from 0.4 to 0.95 of the effect of jets blown above a wing, NASA TN D-7367, 1973.

[108] Luijendijk, A.P.M.: Propeller-wing interference study for over the wing positioned propeller configurations, MSc. Thesis, Faculty of Aerospace Engineering, Delft University of Technology, 2002.

[109] Luijendijk, R.P.: Prediction of far field ventral support interference in a subsonic windtunnel by means of a second-order panel method, MSc. Thesis, Fac. of Aerospace Engineering, Delft University of Technology, 1995.

[110] Aljabri, A.S.: The prediction of propeller/wing interaction effects, ICAS 82-4.4.5, 1982.

[111] Aljabri, A.S.; Lyman, V. and Parker, R.J.: Evaluation of Propeller/Nacelle Interactions in the PTA Program, AIAA 86-1552, 1986.

[112] Chandrasekaran, B. and Bartlet, G.: Method for calculating effects of a propfan on aircraft aerodynamics at subsonic speeds, AIAA-83-1216, 1983.

[113] Fox, S.T. and Smetana, F.O.: Integration of Propeller Slipstreams into the Aerodynamic Analyses of Bodies, SAE Paper 810566, 1981.

[114] Hess, J.L.: The Problem of Three-Dimensional Lifting Flow and Its Solution by Means of Surface Singularity Distribution, Comp. Meth. in Appl. Mechanics and Engineering, Vol. 4, No. 3, 1974.

[115] Kohlsmied, F.: Analysis of propeller-wing interference by means of a second order panel method, MSc. Thesis, Faculty of Aerospace Engineering, Delft University of Technology, 1996.

[116] Drela, M. and Youngren, H.: XFOIL 6.94 User Guide, Dec. 2001.

[117] Strash, D.J. and Lednicer, D.A.: Analysis or propeller-induced aerodynamic effects, AIAA-98-2414, 1998.

[118] Colin, P. ; Moreux, V. and Barillier, A.: Numerical study of high speed propeller engine integration on transport aircraft, ICAS-96-4.10.1, September 1996.

[119] Moens, F. and Gardarein, P.: Numerical simulation of propeller-wing interactions for transport aircraft, AIAA-2001-2404, 2001.

[120] Quinlan, N.J. and Eaton, J.A.: Computational analysis of steady and unsteady propeller aerodynamics, Contribution to the DLR Workshop Braunschweig Aspects of Engine Airframe Integration for Transport Aircraft, 1996, Braunschweig, Germany.

[121] Thompson, J.F; Bharat Soni and Nigel P. Weatherrill, N.P.: Handbook of Grid Generation, ISBN: 0849326877, CRC Press, 1998.

[122] White, F.M.: Viscous fluid flow, Mc Graw Hill Inc., ISBN 0-07-100995-7, 1991.

[123] Joel H. Ferziger,J.H. and Milovan Peric,M.: Computational Methods for Fluid Dynamics, ISBN: 3540653732, Springer Verlag, 1999.

[124] Philipsen, I.: Analysis of Propeller/Wing Interference on a Straight Half Wing and Tractor Propeller, MSc. thesis, Delft Univeristy of Technology, 1993.

[125] Veldhuis, L.L.M.: Experimental analysis of the vortex wake structure behind a propeller-wing configuration, AGARD-CP-584, Conf. Proceedings 584, 1996, AGARD Symposium , Trondheim Norway.

[126] Boelens, O.J.; Laban, M.; Beek, C.M. van and Leeden, R. van: Accurate drag computation for a wing/body configuration using multi-block, structured-grid CFD technology, NLR-TP-2001-231 , 2001.

[127] Munk, M.M.: The minimum induced drag of aerofoils, NACA Report 121, 1923.

[128] Kuhlman, J.M.: Higher order Farfield Drag Minimisation for a subcritical Wing Design Code, Journal of Aircraft, Vol. 17, No.9, 1980.

[129] Dam, R.F. van den: Samid, an interactive system for aircraft drag minimization ; Mathematical models and methods, NLR TR 880714, 1998.

[130] Middel, J.: Development of a computer aided toolbox for aerodynamic design of aircraft at subcritical conditions with application to three-surface and canard aircraft, PhD Dissertation, 1992, Delft University of Technology, Delft University Press.

[131] Heyma, P.M.: Analysis and Optimization of a Tractor Propeller-wing configuration, TWAIO-thesis, Fac. of Aerospace Engineering, Delft University of Technology, June 1996.

[132] Abott, H. and Doenhoff, A.E. von: Theory of wing sections, Dover Publications, inc. , New York, 1959, ISBN: 0486605868.

[133] Janssen, M.: An evaluation of methods for the calculation of the flow around propeller at angle of attack, M.Sc Thesis, 1991, Fac. of Aerospace Engineering, Delft University of Technology.

[134] Prandtl, L. and Tiedjens, O.: Applied Hydro- and Aeromechanics, Dover Publ., New York, 1934.

[135] Prandtl, L. and Betz, A.: Schraubenpropeller mit geringstem Energieverlust, Goettinger Nachrichten, 1919.

[136] Bak, C. ; Fuglsang, P. ; Sørensen, N.N. ; Aagaard, M. ; Shen, W.Z. and Sørensen, J.N.: Airfoil characteristics for wind turbines, Risø-R-1065(EN), 1999.

[137] Himmelskamp, H.: Profiluntersuchungen an einem umlaufendenn propeller, Diss. Goettingen, 1945, Max-Planck Institut fuer Stroemungsforschung, Goettingen, Rep. No.7.

[138] Bosschers, J.: Validation of the helicopter code HERO, NLR TP 93418 L, 1993.

[139] Snel, H.: Scaling laws for the boundary layer flow on rotating wind turbine blades, Proceedings of the 4th IEA Symposium on the Aerodynamics of Wind turbines, Rome, 1990.

[140] Bosschers, J. ; Montgomerie, B. ; Brand, A.J. and Rooy, R.P.J.O.M. van: Influence of blade rotation on the sectional aerodynamics of rotational blades, NLR TP 96523 L, Sept. 1996.

[141] Koning, C.: Influence of the propeller on other parts of the airplane structure, In: Durand, W.F. (Ed.) Aerodynamic Theory, Division M, Vol IV.

[142] Betz, A.: Ein verfahren zur direkten Ermittlung des Profielwiderstandes, Zeitschrift fuer Flugtechnik und Motorschiffahrt, Vol. 16, p.42, 1925.

[143] Swartztrauber, P. and Sweet, R.: Efficient FORTRAN programs for the solution of elliptic equations, NCAR TN/IA-109, July 1975.

[144] Brune, G.W. and Bogataj, P.W.: Induced drag of a simple wing from wake measurements, AIAA-90-1934, 1990.

Samenvatting

De prestatie, de stabiliteit en de besturingseigenschappen van propelleraangedreven vliegtuigen hangt sterk samen met de bijdrage die het voortstuwingssysteem levert. Voor het ontwerp van propellervliegtuigen is het daarom van belang nauwkeurig in kaart te brengen hoe de stroming zich manifesteert in het deel van de vleugel dat wordt getroffen door de slipstroom van de propellers. Om de bijdrage van propellers en vleugels apart te kunnen bepalen is het noodzakelijk het gehele interactieproces nauwkeurig te beschouwen; d.w.z.het effect van de propeller op de vleugel en vice versa. Het doel van deze studie is het verkrijgen van beter inzicht in de propeller-vleugel interactie die optreedt bij twee-motorige propellervliegtuigen om daarmee de configuratie van dergelijke vliegtuigen te kunnen optimaliseren.

Bij deze experimentele en numerieke studie werd gebruik gemaakt van 4 verschillende propeller-vleugel configuraties. Tijdens de experimenten werden 2 eenvoudige modellen gebruikt bestaande uit een rechte vleugel voorzien van een dunne, losneembare, motorgondel. Een derde model betrof een schaalmodel van een turboprop vliegtuig (Fokker F27) waarbij het horizontale staartvlak was verwijderd. Bij de numerieke studie werd een vereenvoudigd model van de Fokker 50 beschouwd.

Voor het verkrijgen van inzicht in de optredende fenomenen en het vastleggen van referentiedata voor de numerieke berekeningen werd een experimentele database geproduceerd van krachten, oppervlaktedrukken, stromingsvisualisatie data en stromingsgegevens verkregen uit een veldanalyse achter een van de modellen.

Uit de metingen blijkt dat de axiale en de tangentiële snelheidscomponent in de propellerslipstroom leiden tot een sterke verandering in de draagkrachtsverdeling waardoor de totale lift en weerstand worden beïnvloedt. Bij plaatsing van de propeller voor de vleugel wordt een aanzienlijk lagere vleugelweerstand gevonden door de toegenomen zuiging op de vleugelneus; een verschijnsel dat bekend staat als 'swirl recovery'. De mate waarin de propellerverliezen in de vorm van tangentiële snelheden ('swirl') worden gecompenseerd door de vleugel werd onderzocht door het uitvoeren van 5-gats buis metingen in het zog van een van de modellen. Uit deze kwantitatieve veldanalyse bleek een sterke vervorming van de slipstroom die bij de numerieke analyses niet kan worden verwaarloosd.

Om de afzonderlijke bijdragen van propeller en vleugel te kunnen vaststellen werd de motorgondel bij het tweede windtunnelmodel los genomen en op verschillende posities en invalshoeken t.o.v. de vleugel gepositioneerd. Uit de metingen bleek dat het effect van de verplaatsing van de propeller in stromingsrichting (voor de vleugel) slechts geringe effecten teweeg bracht. Het effect van een variatie van de spanwijdtepositie, de hoogtepositie en de effectieve invalshoek laten echter een beduidende invloed op draagkracht, weerstand en voortstuwingsrendement zien. Met name de toepassing van een meer negatieve propellerinvalshoek lijkt een gunstig effect te hebben op de

prestatie van het propeller-vleugel model door een sterke afname van de weerstand en een toename van de lift. Tevens werd een prestatieverbetering gevonden bij een draairichting van de propellers waarbij het binnenste blad omhoog beweegt.

Aanvullend inzicht in de interactie-effecten werd verkregen via metingen aan een model waarbij de propeller op verschillende posities boven de vleugel werd geplaatst (OTW-configuratie). In tegenstelling tot hetgeen wordt gevonden in de literatuur wordt voor posities vlak boven de propeller weliswaar een grotere draagkracht en lagere weerstand gevonden maar het voortstuwingsrendement neemt af. Dit blijkt te worden veroorzaakt door de sterke reductie van het propellerrendement als gevolg van veranderingen in het aanstroomveld veroorzaakt door de vleugel.

De numerieke simulaties aan de verschillende modellen werden uitgevoerd met 3 verschillende methoden met oplopende complexiteit: een "Vortex-Lattice" methode (VLM), twee panelenmethoden en een Navier-Stokes (RANS) code. De berekeningen laten zien dat m.b.v. de VLM-code een redelijke afschatting van de aërodynamische groothede als lift en weerstand wordt verkregen als in het propellermodel, dat gebaseerd is op een Blad-Element-Model, een 'swirl recovery' factor (SRF) van ca. 0.5 in rekening wordt gebracht. De panelencodes, waarbij het effect van de propeller werd gesimuleerd met een slipstroommodel gebaseerd op een "Tube-model" leidde in alle gevallen tot een overschatting van de slipstroomeffecten op de vleugel. De meeste gedetailleerde data werden verkregen met behulp van de Navier-Stokes code. Omdat hierbij de vervorming van de slipstroom in rekening wordt gebracht, werd een goede overeenkomst met de experimentele data verkregen. De vereenvoudiging van de propeller in deze code in de vorm van een trekkende schijf model, met opgelegde randvoorwaarden volgend uit de experimenten, lijkt daarmee te zijn toegestaan.

Op basis van de uit de experimenten en numerieke simulaties verkregen data werd, tot slot, onderzocht of bestaande propeller-vleugel configuraties kunnen worden geoptimaliseerd. Hiertoe werd een optimalisatie-code ontwikkeld waarbij d.m.v. een aanpassing van de draagkrachtsverdelingen de weerstand, bij gegeven lift, werd geminimaliseerd. Uit deze berekeningen bleek dat voor zowel in de kruisvlucht als in het tweede klimsegment een prestatieverbetering kan worden bereikt door toepassing van de welving of de wrongverdeling in het vleugeldeel dat door propellerslipstroom wordt bestreken.

Dankwoord

Dit proefschrift is mede tot stand gekomen dankzij de hulp van onderstaande personen.

Allereerst de technische staf van de leerstoel Aërodynamica die hulp hebben geboden bij het opzetten van de diverse windtunnelexperimenten.

Diverse studenten die onder mijn begeleiding hun afstudeerwerk hebben verricht aan het probleem van propeller-vleugel interactie.

Ton Veldhuis die als alfa-wetenschapper in de engelse taal- en letterkunde hulp heeft geboden bij het finale correctieproces, zich beseffend dat de alfa- en beta-wetenschappen twee volkomen verschillende werelden zijn.

Collega's die hebben gezorgd voor een prettige en ongestoorde sfeer waarin ik de afgelopen jaren heb kunnen werken.

Tot slot, mijn meest dierbaren, mijn vrouw Ansje en kinderen Lotte en Bart die altijd voor mij klaar stonden, mij op de juiste momenten ontzagen en mij ontelbare keren voorzagen van koffie en thee op mijn werkkamer.

Curriculum Vitae

De auteur van dit proefschrift werd geboren op 16 December 1960 te Denekamp. In 1979 behaalde hij het VWO diploma aan het "Thij-college" te Oldenzaal waarna werd gestart met de studie Luchtvaart- en Ruimtevaarttechniek aan de Technische Universiteit Delft. Tijdens deze studie was hij enkele jaren in dienst als student-assistent met als taak het opzetten van nieuwe practica in de lage snelheids windtunnels van het laboratorium. In 1987 werd de universitaire studie succesvol afgerond met de titel Vliegtuigbouwkundig ingenieur. Het afstudeerwerk werd verricht op het Lage snelheids windtunnellaboratorium op het gebied van Laser Doppler snelheidsmetingen in het zog van een superkritiek profiel. Vanaf 1987 is de auteur aangesteld bij de leerstoel Aërodynamica als universitair docent met als specialisatie experimenteel en numeriek onderzoek op het terrein van de toegepaste vliegtuig-aërodynamica en 'flow control'. Naast het lidmaatschap van diverse onderwijscommissies van de Faculteit Luchtvaart- en Ruimtevaarttechniek is de auteur bestuurslid van de Nederlandse Vereniging voor Luchtvaarttechniek (NVVL).

The author was born on December 16, 1960, in Denekamp, the Netherlands. In 1979 he finished high school at the "Thij-college" in Oldenzaal. In the same year he started the MSc study in Aerospace Engineering at Delft University of Technology , where he graduated in 1987 at the Low Speed Windtunnel Laboratory on Laser-Doppler measurements in the wake of a supercritical airfoil. During his MSc. study the author was employed several years at the Low Speed Windtunnel Laboratory as student-assistent to develop new windtunnel labs for undergraduate students. From 1987 on, he is employed as assistant professor and lecturer in the Aerodynamics Group of the Faculty of Aerospace Engineering to perform experimental and numerical research in the fields of applied aircraft aerodynamics and flow control. Besides the participation in several educational committees at the Faculty of Aerospace Engineering the author is board member of the Dutch Society of Aeronautical Engineers (NVVL).